INTERNATIONAL SOCIETY FOR MICROBIAL ELECTROCHEMISTRY AND TECHNOLOGY: OUTPUTS FROM THE 2018 REGIONAL MEETINGS

EDITED BY: Sarah Glaven, Uwe Schröder, Eileen Hao Yu, Srikanth Mutnuri, Jeffrey A. Gralnick and Chi Ho Chan

PUBLISHED IN: Frontiers in Energy Research

frontiers Research Topics

ISSN 1664-8714
ISBN 978-2-88963-842-0
DOI 10.3389/978-2-88963-842-0

About Frontiers

Frontiers is more than just an open-access publisher of scholarly articles: it is a pioneering approach to the world of academia, radically improving the way scholarly research is managed. The grand vision of Frontiers is a world where all people have an equal opportunity to seek, share and generate knowledge. Frontiers provides immediate and permanent online open access to all its publications, but this alone is not enough to realize our grand goals.

Frontiers Journal Series

The Frontiers Journal Series is a multi-tier and interdisciplinary set of open-access, online journals, promising a paradigm shift from the current review, selection and dissemination processes in academic publishing. All Frontiers journals are driven by researchers for researchers; therefore, they constitute a service to the scholarly community. At the same time, the Frontiers Journal Series operates on a revolutionary invention, the tiered publishing system, initially addressing specific communities of scholars, and gradually climbing up to broader public understanding, thus serving the interests of the lay society, too.

Dedication to Quality

Each Frontiers article is a landmark of the highest quality, thanks to genuinely collaborative interactions between authors and review editors, who include some of the world's best academicians. Research must be certified by peers before entering a stream of knowledge that may eventually reach the public - and shape society; therefore, Frontiers only applies the most rigorous and unbiased reviews.
Frontiers revolutionizes research publishing by freely delivering the most outstanding research, evaluated with no bias from both the academic and social point of view. By applying the most advanced information technologies, Frontiers is catapulting scholarly publishing into a new generation.

What are Frontiers Research Topics?

Frontiers Research Topics are very popular trademarks of the Frontiers Journals Series: they are collections of at least ten articles, all centered on a particular subject. With their unique mix of varied contributions from Original Research to Review Articles, Frontiers Research Topics unify the most influential researchers, the latest key findings and historical advances in a hot research area! Find out more on how to host your own Frontiers Research Topic or contribute to one as an author by contacting the Frontiers Editorial Office: researchtopics@frontiersin.org

INTERNATIONAL SOCIETY FOR MICROBIAL ELECTROCHEMISTRY AND TECHNOLOGY: OUTPUTS FROM THE 2018 REGIONAL MEETINGS

Topic Editors:
Sarah Glaven, United States Naval Research Laboratory, United States
Uwe Schröder, Technische Universitat Braunschweig, Germany
Eileen Hao Yu, Newcastle University, United Kingdom
Srikanth Mutnuri, Birla Institute of Technology and Science, India
Jeffrey A. Gralnick, University of Minnesota Twin Cities, United States
Chi Ho Chan, University of Minnesota Twin Cities, United States

Citation: Glaven, S., Schröder, U., Yu, E. H., Mutnuri, S., Gralnick, J. A., Chan, C. H., eds. (2020). International Society for Microbial Electrochemistry and Technology: Outputs From the 2018 Regional Meetings. Lausanne: Frontiers Media SA. doi: 10.3389/978-2-88963-842-0

Table of Contents

frontiers in Energy Research

EDITORIAL
published: 29 May 2020
doi: 10.3389/fenrg.2020.00091

Editorial: International Society for Microbial Electrochemistry and Technology: Outputs From the 2018 Regional Meetings

Sarah M. Glaven[1], Eileen Yu[2], Jeffrey A. Gralnick[3], Chi Ho Chan[3], Srikanth Mutnuri[4] and Uwe Schröder[5]*

[1] Naval Research Laboratory, Washington, DC, United States, [2] School of Chemical Engineering and Advanced Materials, Newcastle University, Newcastle upon Tyne, United Kingdom, [3] BioTechnology Institute, University of Minnesota, St. Paul, MN, United States, [4] Applied Environmental Biotechnology Laboratory, Department of Biological Sciences, BITS Pilani K. K. Birla Goa, Sancoale, India, [5] Institute of Environmental and Sustainable Chemistry, Technische Universität Braunschweig, Braunschweig, Germany

Keywords: microbial electrochemical technologies (MET), electromicrobiology, International Society for Microbial Electrochemistry and Technologies, microbial electrochemistry, electroactive bacteria

Editorial on the Research Topic

International Society for Microbial Electrochemistry and Technology: Outputs From the 2018 Regional Meetings

The International Society for Microbial Electrochemistry and Technology (ISMET) is the premier scientific society for all research involving microorganisms and electron exchange. Founded in 2011, ISMET is a highly interdisciplinary community of researchers ranging in expertise from fundamental microbiology and molecular genetics to electrochemistry and engineering. ISMET scientists study the complex interactions between living microbial cells and conductive surfaces. They leverage their understanding of the unique ability of some microorganisms to perform extracellular electron transfer (EET) to develop novel, sustainable processes and applications in biotechnology. New applications are sprouting up in areas such as microbial bioelectronics and new investigations have shown that electroactive bacteria can even be found in the human gut microbiome (Light et al., 2018). These new investigations and technologies reflect the fact that ISMET is more relevant than ever.

The term "microbial electrochemical technology" is built into the ISMET name, but what does it mean? According to Schroder et al. (2015), microbial electrochemical technologies (METs) are "applications or processes that utilize the electrochemical interaction of microbes and electrodes." The observation of bacteria interacting electrochemically with an electrode was first made over 100 years ago (Potter, 1911). Within the last 20 years what was a phenomenological observation has been put to technological use. METs have been developed for alternative energy production, wastewater treatment, and even biofuels production through the process of microbial electrosynthesis. An attractive aspect of METs is the fact that they enable carbon cycling; simple organic molecules in the sediment can be captured as biomass and electricity on anodes, and CO_2 can be captured using the reducing power of an electrode at the cathode back into products or electricity from renewable sources.

The underlying molecular pathways and processes that result in EET in electroactive bacteria has been heavily studied in attempts to improve the efficiency and productivity of METs. Genetic engineering has been used to determine the molecular underpinnings responsible for carrying charge between cells and extracellular electron acceptors of the two model EET organisms,

OPEN ACCESS

Edited by:
Pierangela Cristiani, Ricerca Sul Sistema Energetico, Italy

Reviewed by:
Mirella Di Lorenzo, University of Bath, United Kingdom

****Correspondence:***
Sarah M. Glaven
sarah.glaven@nrl.navy.mil

Specialty section:
This article was submitted to Bioenergy and Biofuels, a section of the journal Frontiers in Energy Research

Received: *31 March 2020*
Accepted: *28 April 2020*
Published: *29 May 2020*

Citation:
Glaven SM, Yu E, Gralnick JA, Chan CH, Mutnuri S and Schröder U (2020) Editorial: International Society for Microbial Electrochemistry and Technology: Outputs From the 2018 Regional Meetings. Front. Energy Res. 8:91. doi: 10.3389/fenrg.2020.00091

Geobacter sulfurreducens and *Shewanella oneidensis*. Researchers that study EET in the absence of an electrode or technological application, such as direct interspecies electron transfer, sometimes refer to their field as electromicrobiology, but much crossover exists and electromicrobiology is inherent to research conducted by the ISMET community. From a purely ecological perspective, the study of METs can inform our understanding of which bacteria connect with and communicate to metals and minerals in the environment, or to each other as part of the biogeochemical cycle.

The regional meeting special collection represents the spectrum of ISMET research occurring globally in both academic and government laboratories. The ISMET currently represents three broad geographical regions: ISMET North America (NA), ISMET Europe (EU), and ISMET Asia-Pacific (AP). A large, international meeting is held every other year to bring as much of the community together as possible. In between, regional ISMET meetings are held that highlight the work of talented postdocs and graduate students and feature innovative new concepts in METs. In 2018, the three regional meetings were held in Newcastle, United Kingdom (EU-ISMET September 12–14), St. Paul, Minnesota, USA (October 10–12, NA-ISMET), and Goa, India (November 13–16, AP-ISMET). Each meeting had its own focus; from applied uses of bioelectrochemical systems in Newcastle, to fundamental microbiology and electrochemistry in Minnesota, to wastewater treatment in Goa. Research articles span from characterization of new electroactive bacteria (Onderko et al.) to the effect of electrode topography on biofilm formation (Moß et al.), to the growing area of electrofermentation (Joshi J. et al.; Rosa et al.) and effective methods for wastewater treatment (Sugioka et al.). Summaries of all 2018 ISMET regional meetings and information on upcoming meetings can be found at www.is-met.org.

The EU-ISMET meeting was hosted at Newcastle University in Newcastle upon Tyne, UK, a city that boasts the invention of the first microbial fuel cell (MFC) by Potter (1911). EU-ISMET researchers continue to lead the way in the application of METs for microbial electrosynthesis, bioremediation and water treatment. The regional meeting special collection captures just some of this exciting work. An emphasis on detection and remediation of water contaminants is highlighted in the work of Olias et al. and Mani et al., respectively, for using electrodes for atrazine detection and azo-dye remediation. Following on this theme, new technologies using floating MFCs to monitor wastewater while simultaneously harvesting energy are described by Cristiani et al. METs are typically based on cost-effective graphitic materials, the properties and characteristics of which are described by Roubaud et al. and Pötschke et al. One limiting factor in microbial fuel cells is the reaction rate at the cathode. EU-ISMET researchers are working to solve this problem using novel ideas. For example, Izadi et al. showed how acidophilic iron-oxidizing bacteria could be used as biocathode catalysts. Ramírez-Moreno et al. compared different approaches for cathodes used in desalination reactors, a growing application area for METs. We also saw exciting articles on engineered living electronic materials and their (You et al.).

The NA-ISMET meeting in St. Paul, Minnesota, USA, was hosted by a lively group of ISMET researchers from the University of Minnesota and focused primarily on fundamental molecular biology and biochemistry of EET. The articles published as part of this special collection reflect a focus on basic research and invite the reader to learn about topics ranging from the discovery and characterization of new EET organisms (Jangir et al., Ortiz-Medina and Call, and Onderko et al.), to the evolutionary relationship among cellular redox carriers (Campbell et al.). EET is a redox balancing act and papers captured here explore the importance of considering how different routes for electron exchange affect METs (Joshi K. et al.; Duhl and TerAvest). Cellular structures, known in *S. oneidensis* as outer membrane extensions, may aid in long range electron transfer (Chong et al.) and were shown here to be activated by cell surface attachment.

In Goa, the AP-ISMET community is focused on bioelectrochemical (and electrochemical) approaches for decentralized sanitation. The meeting took place at the Birla Institute of Science and Technology (BITS), Pilani, Goa, India. The BITS Pilani campus boasts both a small and large scale demonstration site for treatment of wastewater using constructed wetlands coupled to electrochemical chlorination. In this special collection, Talekar and Mutnuri describe membrane selection to maximize such systems. The vibrant research community of the AP-ISMET pushes the boundaries on how MET can be implemented to overcome issues such as ethanol fermentation, as described by Joshi J. et al.

An ongoing discussion within the ISMET community for both veteran scientists and those new to this area is the issue of nomenclature. As the ISMET community grows and becomes inclusive of additional disciplines (e.g., bioelectronics and synthetic biology), it is important to recognize terminology preferred by the established community in order to communicate our science and strengthen the existing lexicon. At each regional meeting this year the issue of ISMET nomenclature was highlighted as a top priority and culminated in a terminology survey. The survey considered terminology in four areas including The Field, The Process, The Technology, and The Microorganisms. The results of the survey are now shared on the ISMET website: https://is-met.org/ismet-terminology-survey/. ISMET researchers overwhelming preferred the term "microbial electrochemistry" to describe their field, and "extracellular electron transfer" to describe the process of electrons moving in and out of the cell. When microbes mediate the process of EET between the cell and a mineral or electrode, ISMET researchers preferred the term "microbial electrocatalysis." Researchers were asked which term they prefer to describe the systems that they use to study and innovate with electroactive bacteria. Over half of all respondents to the poll prefer to use the term "bioelectrochemical system." ISMET recognizes that the use of specific terms to define an individual's research is important and that terms are only useful if they are adopted by a field. Therefore, the results of this survey are not meant to be prescriptive but can serve as a reference point for those new to the ISMET community.

The ISMET community is strong and interest in microbial electrochemistry and electromicrobiology continue to attract

talented scientists to explore the technological possibilities and basic science of this field. In the coming years, ISMET regional sections will expand to include Africa and South America. As we grow in new directions we consider what new tools must be brought to bear on our field in order to advance technology beyond what we have previously envisioned. This will include bringing in the tools of synthetic biology to specifically design and engineer electroactive organisms, standardization of lab-scale electrochemical reactors, and the ability to predict EET capabilities from newly sequenced genome and metagenome assemblies. In addition, we have only just scratch the surface on understanding natural mechanisms of EET and this work must continue in order to improve MET. We look forward to what comes next for this dynamic research area that truly is the definition of interdisciplinary.

AUTHOR CONTRIBUTIONS

All authors listed have made a substantial, direct and intellectual contribution to the work, and approved it for publication.

REFERENCES

Light, S. H., Su, L., Rivera-Lugo, R., Cornejo, J. A., Louie, A., Iavarone, A. T., et al. (2018). A flavin-based extracellular electron transfer mechanism in diverse Gram-positive bacteria. *Nature* 562, 140–144. doi: 10.1038/s41586-018-0498-z

Potter, M. C. (1911). "Electrical effects accompanying the decomposition of organic compounds," in *Proceedings of the Royal Society of London. Series B, Containing Papers of a Biological Character 84*, 260–276.

Schroder, U., Harnisch, F., and Angenent, L. T. (2015). Microbial electrochemistry and technology: terminology and classification. *Energy Environ. Sci.* 8, 513–519. doi: 10.1039/C4EE03359K

Conflict of Interest: The authors declare that the research was conducted in the absence of any commercial or financial relationships that could be construed as a potential conflict of interest.

frontiers in Energy Research

ORIGINAL RESEARCH
published: 05 March 2019
doi: 10.3389/fenrg.2019.00018

Scratching the Surface—How Decisive Are Microscopic Surface Structures on Growth and Performance of Electrochemically Active Bacteria?

Christopher Moß[1], *Sunil A. Patil*[1,2] *and Uwe Schröder*[1]*

[1] *Institute of Environmental and Sustainable Chemistry, Technische Universität Braunschweig, Braunschweig, Germany,*
[2] *Department of Earth and Environmental Sciences, Indian Institute of Science Education and Research, SAS Nagar, India*

This study elucidates the role of micrometer-scale electrode surface structures on the growth and the electrochemical performance of mixed culture electrochemically active biofilms (EAB). For this purpose, copper electrodes were machined to generate micro-scale surface structures (roughness and waviness) ranging from a few μm to over 100 μm, which were characterized using confocal laser scanning microscopy (CLSM). The structured electrodes were used to cultivate acetate based, mixed culture, anodic EAB in order to establish relationships between the surface properties and (i) the growth behavior and (ii) the stationary electrocatalytic properties of the resulting EAB. On short time scale, the initial growth phase is shown to be significantly influenced behavior by the surface topology. The long term electrocatalytic biofilm performance, however, does not show any dependence on the surface structures and does thus not profit from the increased specific surface area and micro-scale surface area due to the increasing 3-dimensionality. The results of this study are of great importance for a more systematic development of tailored electrodes for microbial electrochemical technologies.

Keywords: microbial electrochemistry, microbial fuel cells, microbial electrochemical technologies, surface topography, copper, confocal microscopy, micro-structures, *Geobacter*

OPEN ACCESS

Edited by:
Subba Rao Chaganti,
University of Windsor, Canada

Reviewed by:
Mohanakrishna Gunda,
Qatar University, Qatar
Matteo Grattieri,
The University of Utah, United States

***Correspondence:**
Uwe Schröder
uwe.schroeder@tu-bs.de

Specialty section:
This article was submitted to Bioenergy and Biofuels, a section of the journal Frontiers in Energy Research

Received: *16 December 2018*
Accepted: *11 February 2019*
Published: *05 March 2019*

Citation:
Moß C, Patil SA and Schröder U (2019) Scratching the Surface—How Decisive Are Microscopic Surface Structures on Growth and Performance of Electrochemically Active Bacteria? Front. Energy Res. 7:18. doi: 10.3389/fenrg.2019.00018

INTRODUCTION

Biofilm electrodes are the core functional element of the great majority of bioelectrochemical systems (BES), such as microbial fuel cells (MFC). A high biofilm electrode performance is thereby decisive for a future success of the respective microbial electrochemical technology. In order to increase this performance, the research community has been using biological and materials science approaches. Biological strategies aim at the improvement of the electrochemically active bacteria and their communities and involve the application of, e.g., sophisticated cultivation procedures (e.g., Riedl et al., 2017), and genetic tools (Li et al., 2018). Major tasks of materials science on the other hand are the improvement of the underlying electrode material toward improved bacterial attachment (Saito et al., 2011; Guo et al., 2013) and interfacial electron transfer (Guo et al., 2014) and, most importantly, the creation of electrodes that are able to host a large number of microbial cells. The latter aspect aims to create electrodes with a large surface area and thus to improve the ratio of electrode surface area to reactor volume for a high bioelectrochemical turnover.

Over the past decade, multiple examples for surface structuring—from the nm to mm scale—or the application of porous electrodes with various pore dimensions (Chen et al., 2012; Ketep et al., 2014; Massazza et al., 2015; Baudler et al., 2017)—have been published. For a more thorough overview on the respective electrode materials, the reader may be directed to one of the recent review articles (Guo et al., 2015; Xie et al., 2015).

Looking into the above literature reveals that research on large-surface area electrodes for microbial electrochemical technologies has, to date, been performed mainly on an empirical basis and non-systematically. A comparison of literature from different labs or between different studies is often difficult due to the use of varying electrode materials and hence differing microorganisms and differing surface chemistries. The latter aspect has recently been highlighted in a publication by Champigneux et al. (2018). Further, many studies use only short experimental time scales that do not allow assessing the long-term bioelectrochemical performance of proposed electrode materials and structures and thus their suitability for technical application.

This study aims to systematically investigate the influence of micro-structures on growth behavior and bioelectrocatalytic performance of electrochemically active biofilms (EABs). Copper was used as the anode material for its excellent bioelectrochemical properties (Baudler et al., 2015) and the ease of mechanical surface processing. The metal was structured by mechanical turning and sanding, followed by thorough optical characterization. Mixed culture EABs were cultivated on these electrodes using acetate as the substrate, in order to assess the impact of the surface structures on the electrochemical biofilm behavior.

EXPERIMENTAL SECTION

Electrode Surface Modification and Characterization

The working electrodes were made of Copper rods (99.999%, ChemPur Feinchemikalien und Forschungsbedarf GmbH, Germany) with a diameter of 1 cm. The rods were cut into disks with a height of 0.6 cm. The surface of each cylinder was insulated with epoxy resin (R&G Faserverbundwerkstoffe GmbH, Germany) leaving the circular top base area open to pose as the Cu disc working electrodes.

Surface structures on the Cu disc surfaces were created by a modified turning process leading to wavelike structures of up to 130 μm in height (**Table S2**). Polished and roughened electrodes were prepared by using sandpapers of grain sizes between 2.12 and 82 μm (**Table S3**). Morphological characterization of the electrode surface was done using a Leica TCS SPE DM5500 confocal microscope. Before the microscopic analysis, every electrode sample was cleaned with isopropanol and immersed into 0.1M H_2SO_4 solution to remove any dirt or reactive impurities which could have been introduced during the manufacturing process. For micro-structured electrodes, a 10x air objective (Leica HC PL Fluotar 10x/0.3NA) was used to measure the sample electrode at 5 different spots not only at random locations but also at locations from the middle to the edge of the respective electrodes. This procedure was used to validate the turning process and to make sure the structures were uniform across the electrode surface. For polished and roughened electrodes, a 50x air objective (Leica HC PL Fluotar 50x/0.8NA) was used to measure at 10 randomly chosen locations on the electrode surfaces. Processing of the microscopic data was done using the software Leica Map 7.0.

Bioelectrochemical Setup and Experimental Conditions

The bioelectrochemical experimental setup consisted of a customized 1 L capacity round bottom glass reactor containing 600 mL of modified standard cultivation medium composed of phosphate buffer, 7.5 mL mineral and vitamin solutions (Balch et al., 1979) and 10 mM acetate. To achieve a high degree of comparability and to minimize statistic deviations up to six biofilm electrodes were cultivated simultaneously in every setup, each cell containing at least one electrode of every category (**Figure 2**, **Table S2**). The electrodes were placed concentrically in distance of roughly 4 cm around the reference electrode (Ag/AgCl, sat. KCl, Sensortechnik Meinsberg, Germany) to minimize potential shifts between the electrodes. A graphite rod of 4 cm length and 1 cm diameter was used as the counter electrode and was placed beside the reference electrode (**Figure S1**). At startup and after medium replacement for each batch cycle, the medium was deaerated by sparging nitrogen for at least 15 min. Additionally, fresh medium was deaerated for at least 15 min before it was added to the reactor for medium replenishments. The reactor was sealed using butyl rubber stoppers to maintain anaerobic conditions in the reactor. As a microbial inoculum source, a secondary culture containing mostly *Geobacter anodireducens* enriched from the primary wastewater of the wastewater treatment plant Steinhof, Braunschweig (Germany) was used (Baudler et al., 2014). To allow for a reproducible inoculation procedure, 6 mL bacterial suspension with an OD of 1 (measured using a UV-VIS spectrophotometer—Dr. Lange, Spektralphotometer CADAS 100) was added to the medium at the start of each experiment. The multi-electrode (6 working electrodes) setup was established using a VMP-3 potentiostat (Bio-Logic Science Instruments SAS, France) and an N-Stat Box (Bio-Logic Science Instruments SAS, France). To monitor the bioelectrocatalytic current generation, the Cu working electrodes were poised at −0.2V vs. Ag/AgCl reference electrode by using chronoamperometry (CA). The bioelectrochemical experiments were conducted for five batch cycles (roughly 70 days in total), over which the incubation temperature was constantly held at 35°C. The abiotic control tests confirmed the electrochemical stability of Cu electrodes under the tested electrochemical and biochemical conditions. This is well in accordance with the previous reports (Baudler et al., 2015). The experimental data in this study are based on at least two independent replicates for every individual electrode, measured in independent reactors. All error bars in this study represent the corrected sample standard deviation of the respective bioelectrochemical measurements.

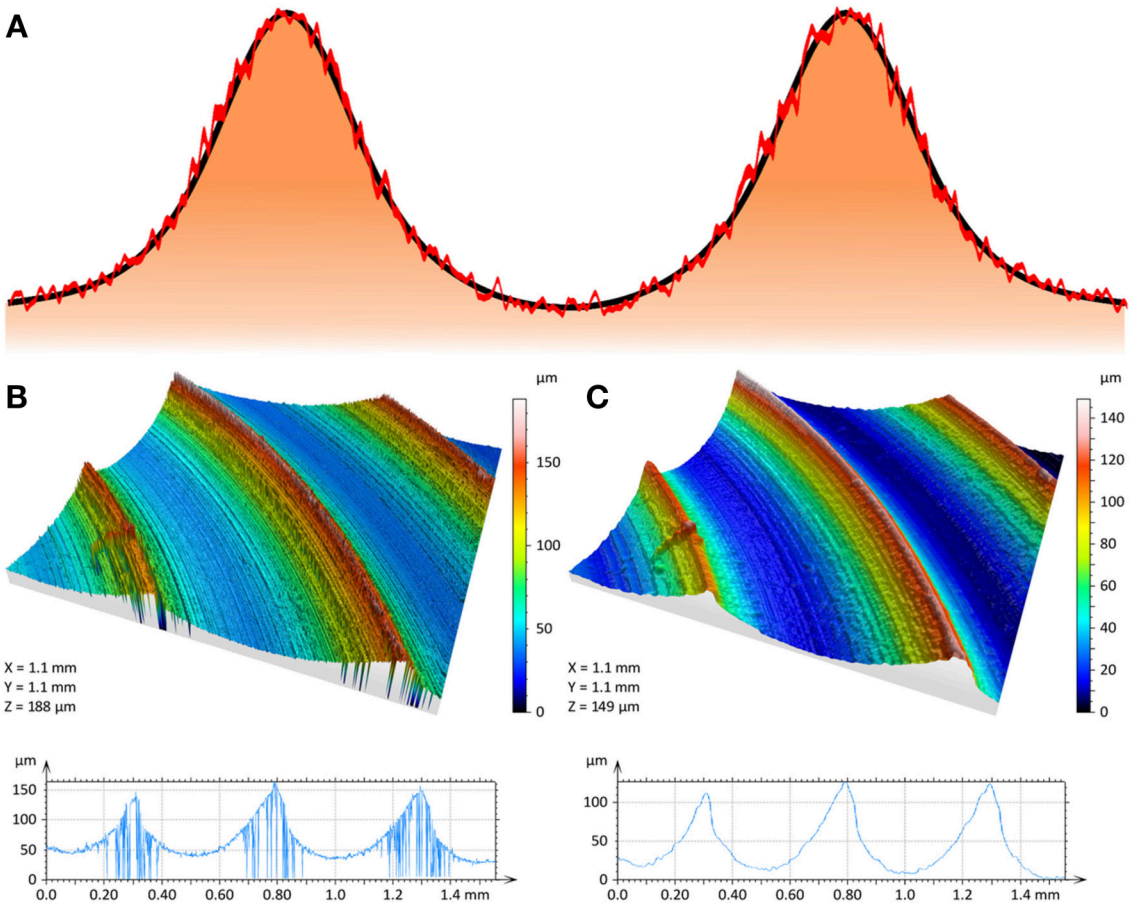

FIGURE 1 | (A) Schematic view of the Copper surface profile generated through the turning process. The black and red borders represent, respectively, the waviness and roughness features of the surface. 3D-Images (top) and 2D-Profiles of the electrode surfaces (bottom); **(B)** unfiltered surface with measurement errors and **(C)** surface after application of a morphological filter.

Biofilm Electrode Characterization Using Confocal Laser Scanning Microscopy (CLSM)

After completion of the bioelectrochemical experiments, the biofilm electrodes were submerged in phosphate buffer solution for confocal microscopy. Measurements were done with a 25x water immersion objective (Leica HCX IRAPO L 25x/0.95NA) as reflection images. It should be noted that the penetration depth of the laser into the biofilms was around 60 µm, which means that information could only be obtained on this part of the biofilm. CLSM images were processed using the software Leica Map 7.0.

RESULTS AND DISCUSSION

Characterization of Electrode Surfaces by CLSM

To correlate bioelectrochemical data with electrode surface properties, detailed knowledge of the surface shape is required. Generally, there are two different approaches to achieve this: manufacturing well defined surfaces or using thoroughly characterized surfaces. In this study, copper electrodes were micro-structured by a turning method. This method creates wavelike patterns of different sizes (**Figure 1**, **Figure S3**) on the electrode surface with a ratio of the height of the peaks compared to their distance of around 0.15 (**Figures 1B,C**). The turning process also introduces roughness to the electrode surface (**Figure 1A**). Since it was not possible to precisely define the dimensions and shape of the electrode surface structures in the manufacturing process, the prepared electrodes had to undergo a thorough surface characterization. Yet, trying to quantify the "real" surface area of an electrode equals to the so called coastline paradox—the closer we look at a given surface area, the more resolved surface structures become and the more they contribute to the determined surface area value (Kirkby and Mandelbrot, 1982; Hanaor et al., 2014). Thus, the real surface area is not a fixed value but it strongly depends on the used characterization technique[1]. We used

[1]For a thorough discussion on the real and projected surface area of electrodes and their determination the reader may be referred to a fundamental publication by Trasatti and Petrii (1992).

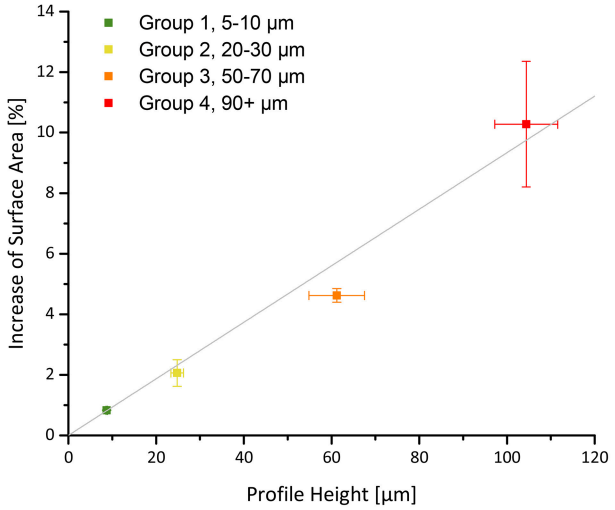

FIGURE 2 | Increase of waviness surface area of micro-structured electrodes compared to a polished electrode (point of origin).

confocal laser scanning microscopy, CLSM, as an optical surface characterization method to obtain representative topographical data. It has a lateral resolution of about 1 µm—the size dimension of a typical electrochemically active bacterium. Since any surface area enlargement by structures below cell size level cannot be accessed by a bacterium as a surface for growth, this study focuses on structures on bacterial scale and above. The surface structure can be separated into two components: Whilst structures around the bacterial level [represented by the roughness profile of the surface (**Figure 1A**)] technically increase the surface area, they do not provide additional area for bacterial/biofilm growth. The micro-structures introduced by the turning process are significantly larger than the electroactive bacteria which makes the additional area provided by these structures available for EAB growth [represented by the waviness profile (**Figure 1A**)].

Due to the occurrence of high-slope areas on the surface profile, artifacts appeared in the resulting CLSM images (**Figure 1B**). To determine the structure size correctly and to quantify the waviness and roughness of the surface, it is important to separate artifacts, roughness and waviness. A morphological filter (Leach, 2010) was therefore used to remove the artifacts (**Figure 1B**) while retaining the electrode geometry (**Figure 1C**). Accordingly, the waviness profile was defined to include the wavelike patterns introduced in the turning process while smaller surface structures were defined as roughness (**Table S1**). Removing smaller topological features, which are not part of the waviness profile using a high pass filter (Leach, 2010) leads to a clear separation of roughness and waviness according to the definition above.

There are several approaches to derive average structure heights from microscopic data. The most basic way is to extract several 2D-profiles and calculate the average structure height. However, this can be a cumbersome approach, which hardly accounts for the variance of surfaces with lower regularities. Using a method which accounts for the whole set of surface data can be helpful to increase representability and reproducibility of the obtained values. In this study, we used a watershed algorithm (Scott, 2009; Leach, 2010) to estimate the height of the respective surface structures. This algorithm generates one data point per dale representing the difference between the lowest point of the dale and the lowest point of the surrounding peaks. Average heights and standard deviations obtained by this method are presented in **Table S2**. Based on the distribution of their average structure heights, the micro- structured electrodes were classified into four groups and were studied accordingly. Groups 1, 2, 3, and 4 represent structure heights of 5–10, 20–30, 50–70, and above 90 µm, respectively. Group "0" is used to represent the polished electrodes with 0 µm structure height. A quantification of the waviness surface area shows an increase of up to 12% as compared to flat electrodes (**Figure 2**).

To estimate potential effects of the superimposing roughness, another set of electrodes was prepared and their roughness was measured by CLSM. Commonly the roughness of a surface is quantified using roughness parameters such as the dimensionless mathematical roughness factor, the arithmetical mean deviation (R_a) and the core roughness depth (R_k).

The dimensionless roughness factor is represented by the quotient of 3D real surface area and 2D geometrical surface area, however it carries no information on the axial dimensions of the sample. The R_a represents the standard height deviation from the center of the roughness profile. The R_k is calculated from the Abbott-Firestone-curve (Whitehouse, 2002; Leach, 2010) of the sample where the value of R_k accounts for the axial region representing the majority of the surface area. While both of these parameters carry information on the axial component of the surface, R_k offers a more accurate picture in terms of the height of the roughness profile compared to R_a (**Figure S2**). The results of the roughness measurement are displayed in **Table S1** in terms of the areal parameters S_a and S_k; the used sandpapers are listed in **Table S3**. It can be seen that the roughness values extend from 0 for a polished surface to a value slightly above the roughness of the micro-structured surfaces.

Bioelectrochemical Behavior of Micro-Structured Copper Electrodes

The bioelectrochemical performance of the optically characterized Cu electrodes was assessed by cultivating EABs at the respective electrodes at a constant potential of −0.2 V (vs. Ag/AgCl) for 5 batch cycles spanning over ∼70 days (see **Figure S4**) and analyzing the resulting bioelectrocatalytic current flow. For statistical evaluation, the electrodes were grouped according to their average structure heights (**Table S2**).

Effect of Micro-Structuring on Initial Attachment of Microbial Cells and Biofilm Growth

The growth and metabolic activity of anodic electrochemically active bacterial can be monitored directly following the oxidative current generation of the biofilm electrode. In this study, we analyzed the onset time (or lag time) of the current generation as a parameter to compare the initial biofilm formation on the differently micro-structured electrodes. For an accurate

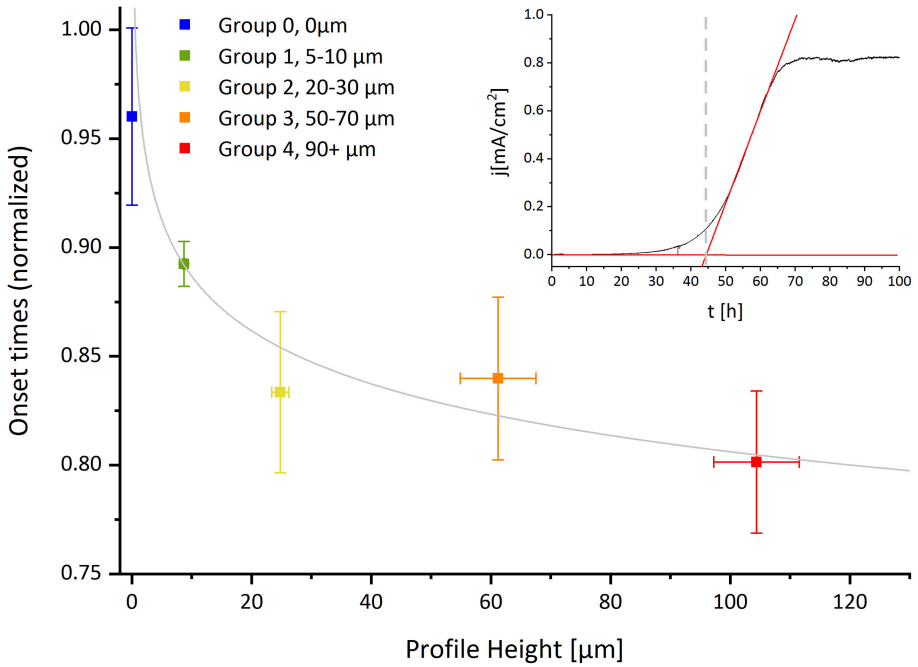

FIGURE 3 | Main figure: Onset times for the bioelectrocatalytic current generation normalized to the slowest value, as a function of the electrode's average structure heights. Inset Figure: Illustration of the graphical method to determine the onset (lag) time of the biofilm formation from the chronoamperometric curve.

comparison, both a definition for the onset (lag) times and a method to obtain reproducible and robust values are needed. In view of this, we define the onset or lag time of current output in a BES system as the time point where an exponential increase in current density can be observed. As a method to measure the onset times, we suggest the use of a graphical method (**Figure 3**, inset figure), wherein the onset time is obtained through a linear fit on the exponentially increasing current during the startup of the BES experiments. The onset time is then defined as the intersection of the resulting line with the origin of the Y-axis. The results obtained through this procedure for different electrodes are shown in **Figure 3** with all data being normalized to the electrode with the longest onset time. The onset times ranged from 43 h for a micro-structured electrode with an average structure height of 106 µm to 56 h for a polished electrode with 0 µm height. Some of the data show a significant experimental variance of up to 10%. It is most likely that these variations in the lag time are to be attributed mainly to a non-uniform, turbulent flow regime of the buffer medium in the stirred batch reactors. Further impacts on the onset of the biofilm formation could be the cultivation temperature (Patil et al., 2010) and the number of active cells in the inoculum. Apart from the variance of the individual data, a clear effect of the micro-structuring on the current onset times can be seen (**Figure 3**). Thus, with growing structure heights, the onset times decrease significantly, with the largest effect of 20% lag time reduction for structure heights of around 100 µm. Hereby the strongest decrease can be observed for group 2 (structure height 20–30 µm). Further increasing the structure size seems less impactful, as the reduction between groups 2, 3, and 4 is—due to the comparatively high sample standard deviation—statistically not significant.

We attribute the observed enhancement in the start-up of the biofilm growth mainly to the axial component introduced by the micro-structures which influences the medium flow on the electrode surface. This can result in a reduction of sheer forces which favors the initial irreversible attachment of the microbial cells as well as the resulting biofilm growth (Alnnasouri et al., 2011). While small structures are close to the size of single cells of e.g., *Geobacter* species (Caccavo et al., 1994) and may therefore favor the attachment of single cells, they may be too small to support the formation of large cell clusters (Lebedev et al., 2014) and thick biofilms to an extent that translates into a significant decrease of current onset times. These effects can be mainly expected for larger structure heights.

Effect of Micro-Structuring on Bioelectrocatalytic Current Densities

Micro-structuring increases the specific surface area, i.e., the electrode's (real) surface area compared to its projected (geometric)[1] surface area, significantly and also increases the area available for bacterial colonization. In our study, this is represented by the waviness profile (see **Figure 2**). To study the impact of the degree of surface structuring on the electrochemical biofilm performance, we extracted the maximum current densities of the respective biofilm electrodes measured in a series of semi-batch experiments (see **Figure S4**) over the course of five batch cycles (corresponding to a duration of ∼70 days). It can be seen that the current densities of

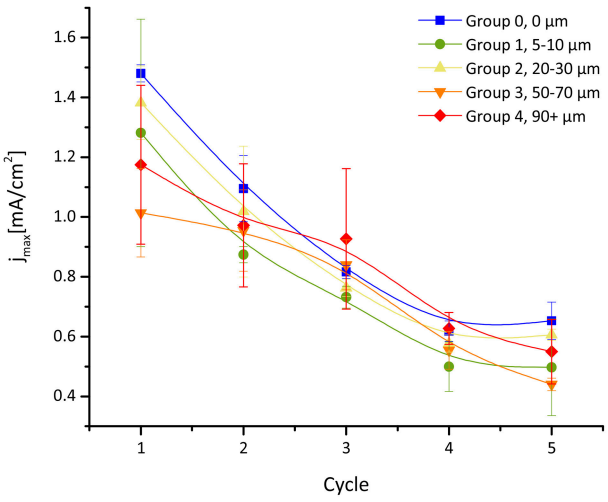

FIGURE 4 | Maximum bioelectrocatalytic current densities over the course of 5 batch cycles (70 days) for different micro-structured Cu electrodes [derived from CA data (**Figure S4**)].

all electrodes range between 1 and 1.5 mA/cm^2 for the first batch cycle. The maximum currents however starts declining over time during the subsequent batch cycles finally reaching a constant level of 0.5–0.7 mA/cm^2 in cycles 4 and 5. Such behavior has been observed before (Babauta and Beyenal, 2014) and has been attributed to the maturation of the biofilm and associated limitations resulting from mass transfer (Renslow et al., 2013), electron transport (Liu and Bond, 2012) or proton accumulation (Torres et al., 2008).

To exclude any influence of copper as the electrode material, graphite electrodes were tested under the same conditions and showed a comparable behavior (**Figure S5**). A clear or significant relation between average structure height and maximum current density was not observed—neither in the early stages of the experiment nor for the mature biofilms which are achieved after 3 cycles or roughly 40 days of operation (**Figure 4**). It is difficult to evaluate the behavior in the early stages due to the high variance, which indicates that biofilm growth is still an important factor at this point.

The results of these experiments lead to the conclusion that micro-structuring did not significantly influence the EAB performance, in particular on a longer time scale. It can be followed that there is no direct relationship between the electrodes' specific surface area or micro-scale surface area and the biofilm electrode performance. This leads to the conclusion that limitations introduced by axial biofilm growth and or structural changes occurring during maturation are leveling off the effect of the increase surface area. This is consistent with EIS measurements of the mature biofilms showing a long time constant process governing most of the resistance of the system which indicate intrinsic limitations of the biofilm transport processes (**Figure S6**). Thus, micro-scale surface area is most likely not a critical parameter for EAB performance.

CLSM Based Analysis of EAB Grown on Micro-Structured Electrodes

To obtain information on biofilm structure, CLSM measurements on the EAB grown on electrodes with different average structure heights (**Table S2**) were performed after the batch experiments. Digital camera and CLSM images are shown in **Figure 5** and a schematic representation based on the CLSM images of EAB is shown in **Figure 6**. For all electrodes it was evident that the micro-structures were completely overgrown by the biofilm (**Figures 5a,c**). On the electrodes with larger micro-structures, the biofilm did adapt to the underlying structure while overgrowing it, thereby showing a wavelike shape (**Figure 5c**). **Figure 5b** shows a 3D-image of a biofilm grown on a polished electrode. The height distribution illustrates a fairly high surface roughness which is not related to the underlying structure. It seems that only larger surface structures can translate into a change in the EAB growth pattern while smaller asperities do not influence the biofilm growth on a large enough scale to be perceived (**Figure 5**). **Figure 5d** shows a 3D-image of a part of the micro-structured electrode (**Figure 5c**). Despite the high surface roughness of the biofilm, the wavelike shape of the underlying surface structure can be observed.

The difference in height between the hills and the dales roughly equals the height of the underlying structure (**Figure 5d**). Since the biofilm performance limitations are likely due to the axial growth of the biofilm, the same limitations as for a flat surface apply to any point on the micro- structured surfaces, which leads to an electrode behavior adopting that of flat 2D-electrodes. Following this argumentation, a 3D-electrode behavior can only be achieved by structures that are significantly larger than the height of the biofilm. Thus, rather than the specific surface area of an electrode, the amount of available projected surface area seems to be the performance defining factor for typical biofilm electrodes. This is consistent with the high currents achieved in studies on macro-structure electrode designs (Chen et al., 2012).

Effect of Surface Roughness on Initial Attachment of Microbial Cells and EAB Growth

The focus of the above sections was on the waviness profile, neglecting the impact of surface roughness. To characterize the influence of the roughness profile on our measurements and thus to avoid mixing up the effects of roughness and waviness on the current onset times, additional short-term experiments with roughened electrodes were conducted (**Figure S7**). The electrodes were abraded with sandpapers to create different roughness profiles (**Figure S2**). On those electrodes, biofilms were grown under the same conditions as for the micro-structured electrodes. For the roughened electrodes (**Figure 7**, red symbols), no clear decrease of the current onset times can be seen as compared to the polished electrodes. Also, no clear relation between their core roughness depth and onset times can be derived. Thus, it appears that if there is an effect of the surface roughness on the onset times it is overruled by the experimental variance. It follows that whereas structures above

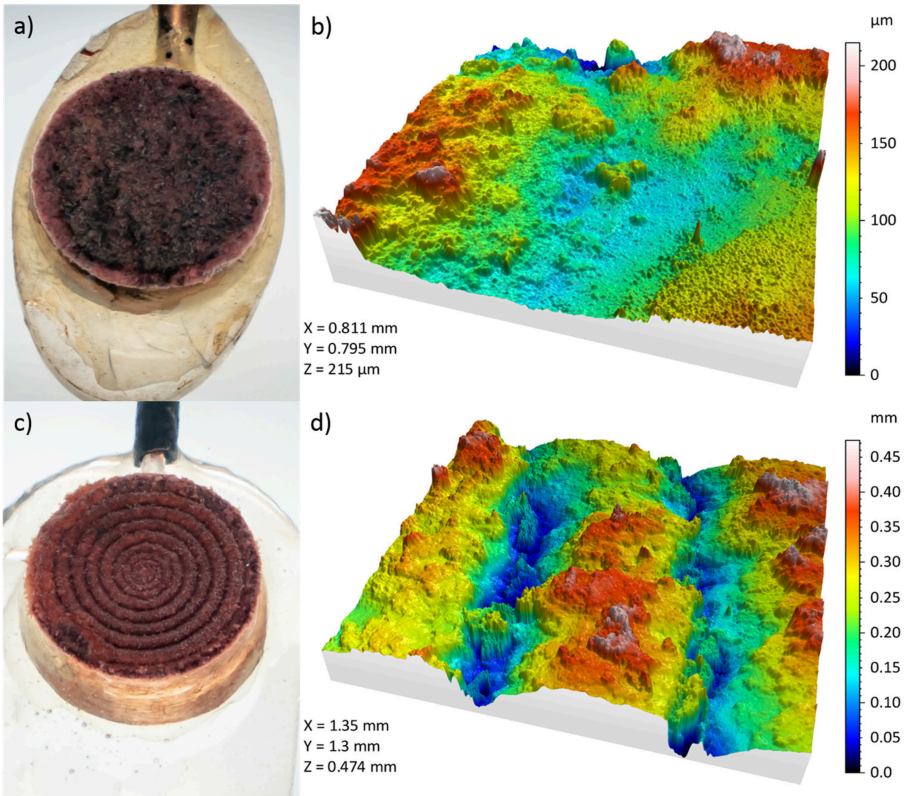

FIGURE 5 | Digital **(a)** and CLSM **(b)** images of the EAB grown on a polished electrode. Digital **(c)** and CLSM **(d)** images of the EAB grown on a micro-structured electrode (average structure height 110 µm).

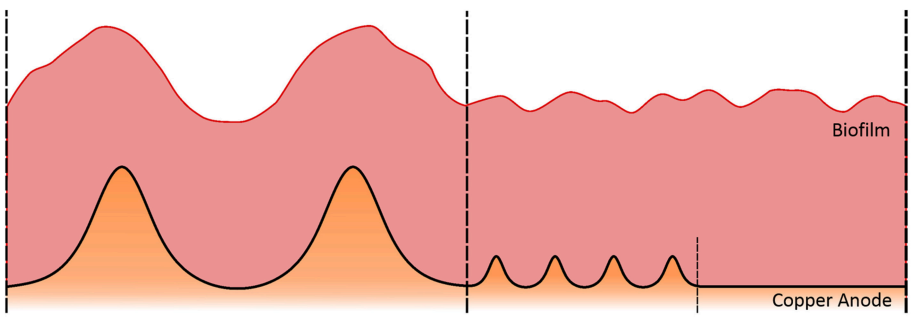

FIGURE 6 | Schematic picture showing electrode structures of different sizes overgrown by a microbial biofilm.

20 µm have a measurable effect on the biofilm development, µm-sized surface roughness does not (Pierra et al., 2018). The above findings appear to contradict recent findings of the Bergel group (Champigneux et al., 2018), who found a significant reduction of the lag time upon increasing surface roughness. The introduced roughness level in that paper, however, was in the low nm range, which seems to underline that a completely smooth electrode surface impedes bacterial colonization and already a nm-based roughness can improve colonization, e.g., by increasing the adhesive forces between bacteria and a sample (Boyd et al., 2002).

CONCLUSIONS

In this study, we systematically assessed the role of micro-structures and surface roughness on the initial growth and the long-term behavior of acetate grown, mixed culture electroactive biofilms. We used copper as electrode material based on its excellent bioelectrochemical properties (Baudler et al., 2015) and the ease of mechanical surface processing. Based on our experimental results we can derive the following four major conclusions:

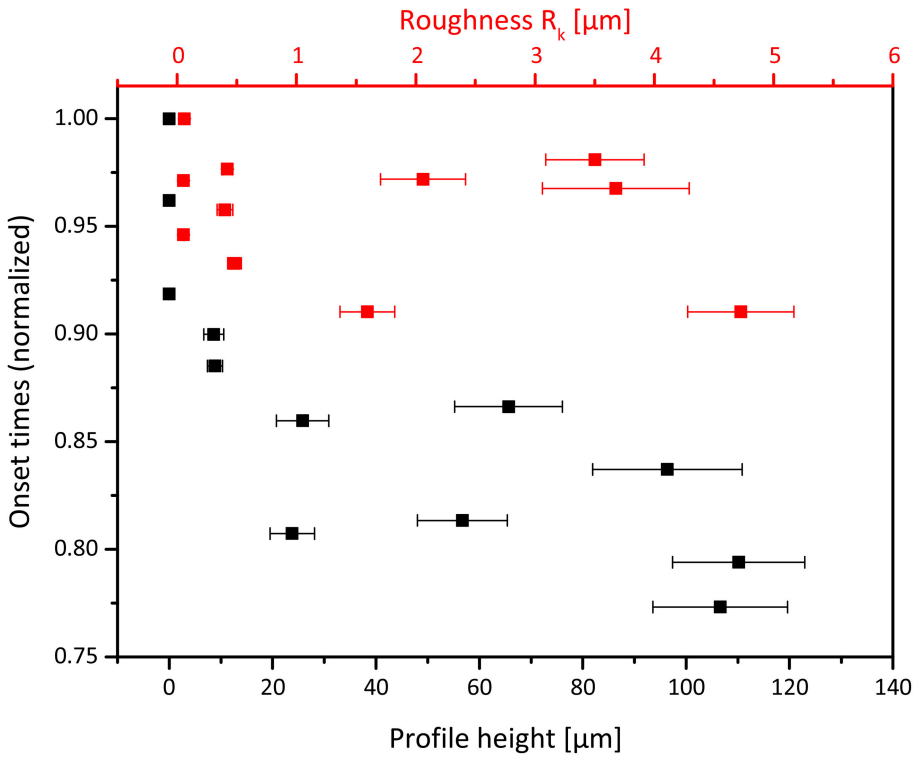

FIGURE 7 | Effect of electrode surface roughness (red) and micro-structures (black) on current onset times.

(I) The (long term) electrochemical performance (i.e., the achievable current density) of typical anodic mixed culture based biofilm electrodes is not significantly influenced or cannot be enhanced by surface structures in the dimension of up to 100 µm.

This finding has to be judged in the light of the thickness of a respective EAB. The electrochemical performance of biofilms that reach a thickness in the dimension of or are larger than the underlying electrode structure, does not profit from the increased specific surface area and micro-scale surface area due to the increasing 3D of these structures. By overgrowing the electrode structures, possible 3D effects are leveled off leading to a performance comparable to a 2D electrode surface. Especially for small structures, the biofilm shape (and thus performance) does not show significant difference to a flat electrode surface. As the size of the microstructure gets closer to the expected biofilm thickness, it becomes evident that the biofilm is adapting to the electrode structure and its increasing 3D.

(II) The projected surface area describes the surface area sufficiently accurate.

Based on the above finding, surface structures that are significantly smaller than the dimension (thickness) of the biofilm can be neglected in the calculation of the surface area. Thus, the projected surface area is a sufficiently accurate means to quantify the electrode surface area.

(III) Surface structures that are much larger than a bacterial cell reduce the onset time (lag time) of the biofilm formation; pure surface roughness does not.

Our experiments show that introducing surface structures (like a waviness) of up to 100 µm height strongly decreases EAB cultivation time. The strongest lag time reduction takes place between 0 and 20 µm structure height. The surface roughness on the other hand has no influence on the biofilm growth. We interpret this finding that at an electrode surface overflowed by a culture medium, surface structures that are considerably larger than the size of a bacterial cell influence the medium flow and reduce the lateral sheer force of the overflowing solution which leads to a preferred settling of cells inside of these structures. Apparently, a pure surface roughening, producing structures in the size dimension of a bacterium, does not lead to an improved bacterial settling at the electrode surface.

(IV) The duration of bioelectrochemical experiments needs be long enough to reach stationary biofilm conditions.

Many studies on EABs are performed at comparatively short time scales, in which the studied biofilms have not reached maturation. Often, the studied biofilms are still in their growth phase and have not reached their final constitution (Abbaszadeh Amirdehi et al., 2018). For the evaluation of the suitability of an electrode material for application in a bioelectrochemical system, however, the study of the

long-term behavior is of utmost importance, since many effects, visible at short time scale, are likely to level off at longer time scales and are thus not of importance for electrode development.

The above statements need to be considered in relation to the studied biofilm systems (and their thickness). Thus, µm-thin anodic (Read et al., 2010; Carmona-Martínez et al., 2013) or cathodic (Kazemi et al., 2015) biofilms may profit much more from a micro-structuring than the here described *Geobacter* dominated mixed culture biofilm.

AUTHOR CONTRIBUTIONS

All authors listed have made a substantial, direct and intellectual contribution to the work, and approved it for publication.

ACKNOWLEDGMENTS

CM gratefully acknowledges financial support provided by the NTH-Research Unit ElektroBak—Innovative materials and concepts for microbial electrochemical systems. SP acknowledges the Alexander von Humboldt Foundation for financial support through a Humboldt Research Fellowship for experienced researchers program. We also thank the Deutsche Forschungsgemeinschaft (DFG) for support (DFG grant SCHR 753/10-2).

SUPPLEMENTARY MATERIAL

The Supplementary Material for this article can be found online at: https://www.frontiersin.org/articles/10.3389/fenrg.2019.00018/full#supplementary-material

REFERENCES

Abbaszadeh Amirdehi, M., Saem, S., Zarabadi, M. P., Moran-Mirabal, J. M., and Greener, J. (2018). Microstructured anodes by surface wrinkling for studies of direct electron transfer biofilms in microbial fuel cells. *Adv. Mater. Interfaces* 5:1800290. doi: 10.1002/admi.201800290

Alnnasouri, M., Lemaitre, C., Gentric, C., Dagot, C., and Pons, M. N. (2011). Influence of surface topography on biofilm development: experiment and modeling. *Biochem. Eng. J.* 57, 38–45. doi: 10.1016/j.bej.2011.08.005

Babauta, J. T., and Beyenal, H. (2014). Local current variation by depth in geobacter sulfurreducens biofilms. *J. Electrochem. Soc.* 161, H3070–H3075. doi: 10.1149/2.0131413jes

Balch, W. E., Fox, G. E., Magrum, L. J., Woese, C. R., and Wolfe, R. S. (1979). Methanogens: reevaluation of a unique biological group. *Microbiol. Rev.* 43, 260–296.

Baudler, A., Langner, M., Rohr, C., Greiner, A., and Schröder, U. (2017). Metal-polymer hybrid architectures as novel anode platform for microbial electrochemical technologies. *ChemSusChem* 10, 253–257. doi: 10.1002/cssc.201600814

Baudler, A., Riedl, S., and Schröder, U. (2014). Long-term performance of primary and secondary electroactive biofilms using layered corrugated carbon electrodes. *Front. Energy Res.* 2:30. doi: 10.3389/fenrg.2014.00030

Baudler, A., Schmidt, I., Langner, M., Greiner, A., and Schröder, U. (2015). Does it have to be carbon? Metal anodes in microbial fuel cells and related bioelectrochemical systems. *Energy Environ. Sci.* 8, 2048–2055. doi: 10.1039/C5EE00866B

Boyd, R. D., Verran, J., Jones, M. V., and Bhakoo, M. (2002). Use of the atomic force microscope to determine the effect of substratum surface topography on bacterial adhesion. *Langmuir* 18, 2343–2346. doi: 10.1021/la011142p

Caccavo, F., Lonergan, D. J., Lovley, D. R., Davis, M., Stolz, J. F., and Mcinerneyl, M. J. (1994). Oxidizing dissimilatory metal-reducing microorganism. *Microbiology* 60, 3752–3759.

Carmona-Martínez, A. A., Harnisch, F., Kuhlicke, U., Neu, T. R., and Schröder, U. (2013). Electron transfer and biofilm formation of Shewanella putrefaciens as function of anode potential. *Bioelectrochemistry* 93, 23–29. doi: 10.1016/j.bioelechem.2012.05.002

Champigneux, P., Renault-Sentenac, C., Bourrier, D., Rossi, C., Delia, M.-L., and Bergel, A. (2018). Effect of surface nano/micro-structuring on the early formation of microbial anodes with Geobacter sulfurreducens: experimental and theoretical approaches. *Bioelectrochemistry* 121, 191–200. doi: 10.1016/j.bioelechem.2018.02.005

Chen, S., He, G., Liu, Q., Harnisch, F., Zhou, Y., Chen, Y., et al. (2012). Layered corrugated electrode macrostructures boost microbial bioelectrocatalysis. *Energy Environ. Sci.* 5:9769–9772. doi: 10.1039/c2ee23344d

Guo, K., Donose, B. C., Soeriyadi, A. H., Prévoteau, A., Patil, S. A., Freguia, S., et al. (2014). Flame oxidation of stainless steel felt enhances anodic biofilm formation and current output in bioelectrochemical systems. *Environ. Sci. Technol.* 48, 7151–7156. doi: 10.1021/es500720g

Guo, K., Freguia, S., Dennis, P. G., Chen, X., Donose, B. C., Keller, J., et al. (2013). Effects of surface charge and hydrophobicity on anodic biofilm formation, community composition, and current generation in bioelectrochemical systems. *Environ. Sci. Technol.* 47, 7563–7570. doi: 10.1021/es400901u

Guo, K., Prévoteau, A., Patil, S. A., and Rabaey, K. (2015). Engineering electrodes for microbial electrocatalysis. *Curr. Opin. Biotechnol.* 33, 149–156. doi: 10.1016/j.copbio.2015.02.014

Hanaor, D. A., Ghadiri, M., Chrzanowski, W., and Gan, Y. (2014). Scalable surface area characterization by electrokinetic analysis of complex anion adsorption. *Langmuir* 30, 15143–15152. doi: 10.1021/la503581e

Kazemi, M., Biria, D., and Rismani-Yazdi, H. (2015). Modelling bio-electrosynthesis in a reverse microbial fuel cell to produce acetate from CO_2 and H_2O. *Phys. Chem. Chem. Phys.* 17, 12561–12574. doi: 10.1039/C5CP00904A

Ketep, S. F., Bergel, A., Calmet, A., and Erable, B. (2014). Stainless steel foam increases the current produced by microbial bioanodes in bioelectrochemical systems. *Energy Environ. Sci.* 7, 1633–1637. doi: 10.1039/C3EE44114H

Kirkby, M. J., and Mandelbrot, B. B. (1982). *The Fractal Geometry of Nature*. San Francisco, CA: W. H. Freeman.

Leach, R. K. (eds.). (2010). "Surface topography characterization," in *Fundamental Principles of Engineering Nanometrology* (Amsterdam: Elsevier), 211–262.

Lebedev, N., Strycharz-Glaven, S. M., and Tender, L. M. (2014). High resolution AFM and single-cell resonance raman spectroscopy of *Geobacter sulfurreducens* biofilms early in growth. *Front. Energy Res.* 2:34. doi: 10.3389/fenrg.2014.00034

Li, M., Zhou, M., Tian, X., Tan, C., McDaniel, C. T., Hassett, D. J., et al. (2018). Microbial fuel cell (MFC) power performance improvement through enhanced microbial electrogenicity. *Biotechnol. Adv.* 36, 1316–1327. doi: 10.1016/j.biotechadv.2018.04.010

Liu, Y., and Bond, D. R. (2012). Long-distance electron transfer by *G. sulfurreducens* biofilms results in accumulation of reduced c-type cytochromes. *ChemSusChem* 5, 1047–1053. doi: 10.1002/cssc.201100734

Massazza, D., Parra, R., Busalmen, J. P., and Romeo, H. E. (2015). New ceramic electrodes allow reaching the target current density in bioelectrochemical systems. *Energy Environ. Sci.* 8, 2707–2712. doi: 10.1039/C5EE01498K

Patil, S. A., Harnisch, F., Kapadnis, B., and Schröder, U. (2010). Electroactive mixed culture biofilms in microbial bioelectrochemical systems: the role of temperature for biofilm formation and performance. *Biosens. Bioelectron.* 26, 803–808. doi: 10.1016/j.bios.2010.06.019

Pierra, M., Golozar, M., Zhang, X., Prévoteau, A., De Volder, M., Reynaerts, D., et al. (2018). Growth and current production of mixed culture anodic biofilms remain unaffected by sub-microscale surface roughness. *Bioelectrochemistry* 122, 213–220. doi: 10.1016/j.bioelechem.2018.04.002

Read, S. T., Dutta, P., Bond, P. L., Keller, J., and Rabaey, K. (2010). Initial development and structure of biofilms on microbial fuel cell anodes. *BMC Microbiol.* 10:98. doi: 10.1186/1471-2180-10-98

Renslow, R. S., Babauta, J. T., Majors, P. D., and Beyenal, H. (2013). Diffusion in biofilms respiring on electrodes. *Energy Environ. Sci.* 6, 595–607. doi: 10.1039/C2EE23394K

Riedl, S., Brown, R. K., Klöckner, S., Huber, K. J., Bunk, B., Overmann, J., et al. (2017). Successive conditioning in complex artificial wastewater increases the performance of electrochemically active biofilms treating real wastewater. *ChemElectroChem* 4, 3081–3090. doi: 10.1002/celc.201700929

Saito, T., Mehanna, M., Wang, X., Cusick, R. D., Feng, Y., Hickner, M. A., et al. (2011). Effect of nitrogen addition on the performance of microbial fuel cell anodes. *Bioresour. Technol.* 102, 395–398. doi: 10.1016/j.biortech.2010.05.063

Scott, P. J. (2009). Feature parameters. *Wear* 266, 548–551. doi: 10.1016/j.wear.2008.04.056

Torres, C. I., Marcus, A., and Rittmann, B. E. (2008). Proton transport inside the biofilm limits electrical current generation by anode-respiring bacteria. *Biotechnol. Bioeng.* 100, 872–881. doi: 10.1002/bit.21821

Trasatti, S., and Petrii, O. A. (1992). Real surface area measurements in electrochemistry. *J. Electroanal. Chem.* 327, 353–376. doi: 10.1016/0022-0728(92)80162-W

Whitehouse, D. (eds.). (2002). "Profile and areal (3D) parameter characterzation," in *Surfaces and Their Measurement* (London: HPS), 48–95.

Xie, X., Criddle, C., and Cui, Y. (2015). Design and fabrication of bioelectrodes for microbial bioelectrochemical systems. *Energy Environ. Sci.* 8, 3418–3441. doi: 10.1039/C5EE01862E

Conflict of Interest Statement: The authors declare that the research was conducted in the absence of any commercial or financial relationships that could be construed as a potential conflict of interest.

frontiers in Energy Research

ORIGINAL RESEARCH
published: 26 June 2019
doi: 10.3389/fenrg.2019.00060

Electrochemical Characterization of *Marinobacter atlanticus* Strain CP1 Suggests a Role for Trace Minerals in Electrogenic Activity

*Elizabeth L. Onderko[1], Daniel A. Phillips[2], Brian J. Eddie[3], Matthew D. Yates[3], Zheng Wang[3], Leonard M. Tender[3] and Sarah M. Glaven[3]**

[1] National Research Council, Washington, DC, United States, [2] American Society for Engineering Education, Washington, DC, United States, [3] Center for Bio/Molecular Science and Engineering, Naval Research Laboratory, Washington, DC, United States

OPEN ACCESS

Edited by:
Subba Rao Chaganti, University of Windsor, Canada

Reviewed by:
Feng Zhao, Institute of Urban Environment (CAS), China
Falk Harnisch, Helmholtz Centre for Environmental Research (UFZ), Germany

***Correspondence:**
Sarah M. Glaven
sarah.glaven@nrl.navy.mil

Specialty section:
This article was submitted to Bioenergy and Biofuels, a section of the journal Frontiers in Energy Research

Received: *15 March 2019*
Accepted: *03 June 2019*
Published: *26 June 2019*

Citation:
Onderko EL, Phillips DA, Eddie BJ, Yates MD, Wang Z, Tender LM and Glaven SM (2019) Electrochemical Characterization of Marinobacter atlanticus Strain CP1 Suggests a Role for Trace Minerals in Electrogenic Activity. Front. Energy Res. 7:60. doi: 10.3389/fenrg.2019.00060

The marine heterotroph, *Marinobacter atlanticus* strain CP1, was recently isolated from the electroautotrophic Biocathode MCL community, named for the three most abundant members: *Marinobacter*, an uncharacterized member of the *Chromatiaceae*, and *Labrenzia*. Biocathode MCL catalyzes the production of cathodic current coupled to carbon fixation through the activity of the uncharacterized *Chromatiaceae*, renamed as "*Candidatus* Tenderia electrophaga," but the contribution of *M. atlanticus* is currently unknown. Here, we report on the electrochemical characterization of pure culture *M. atlanticus* biofilms grown under aerobic conditions and supplemented with succinate as a carbon source at applied potentials ranging from 160 to 510 mV vs. SHE, and on three different electrode materials (graphite, carbon cloth, and indium tin oxide). *M. atlanticus* was found to produce either cathodic or anodic current that was an order of magnitude lower than that of the Biocathode MCL community depending on the oxygen concentration, applied potential, and electrode material. Cyclic voltammetry, differential pulse voltammetry (DPV), and square wave voltammetry (SWV) were performed to characterize putative redox mediators at the electrode surface; however no definitive redox peaks were observed. No effect on current was observed when genes encoding a putative rubredoxin (ACP86_RS07295), as well as a putative NADH:flavorubredoxin oxidoreductase (ACP86_RS07290), were deleted to evaluate their role in EET. The addition of either riboflavin or excess trace mineral solution increased anodic current by ca. an order of magnitude under the conditions in which Biocathode MCL is typically grown. These results indicate that *M. atlanticus* has a non-negligible ability to utilize electrodes as an electron acceptor, which can be enhanced by the presence of excess trace minerals already available in the growth medium. The ability of *M. atlanticus* to utilize trace minerals as electron shuttles with extracellular electron acceptors may have broader implications for its natural role in biogeochemical cycling.

Keywords: *marinobacter*, bioelectrochemical system (BES), biofilm, microbial electrochemistry, mineral cycling

INTRODUCTION

Marinobacter spp. are considered "biogeochemical opportunitrophs" due to their metabolic flexibility (Singer et al., 2011), diverse substrate utilization, and wide geographic range including hydrocarbon-contaminated water (Gauthier et al., 1992), saline soil (Martin et al., 2003), and hot springs (Shieh et al., 2003). Based on their prevalence in subsurface environments (Edwards et al., 2003), demonstrated ability to oxidize iron (Edwards et al., 2003; Bonis and Gralnick, 2015), and identification in biocathode microbial communities (Erable et al., 2010; Debuy et al., 2015; Rowe et al., 2015; Wang et al., 2015b; Stepanov et al., 2016), *Marinobacter* spp. are thought to perform extracellular electron transfer (EET), however, no mechanism has been identified.

Marinobacter atlanticus strain CP1 was recently isolated from the Biocathode MCL community, named for the three most abundant members: *Marinobacter*, an uncharacterized member of the *Chromatiaceae*, and *Labrenzia* (Wang et al., 2015b; Bird et al., 2018). The Biocathode MCL community was originally enriched from seawater at 310 mV vs. SHE and is proposed to catalyze electron transfer from an electrode to oxygen and carbon dioxide for growth due to the activity of the uncharacterized *Chromatiaceae* [renamed "*Candidatus* Tenderia electrophaga" (Eddie et al., 2016)]. "*Ca.* Tenderia electrophaga" is an electroautotroph that cannot currently be cultivated in isolation and expresses proteins required for CO_2 fixation through the Calvin-Benson-Bassham cycle. *Marinobacter* and *Labrenzia* are heterotrophs (unable to fix CO_2) and presumably receive fixed carbon through the activity of "*Ca.* Tenderia electrophaga." Metagenomic and 16S rRNA gene sequencing have shown that the relative abundance of *M. atlanticus* was negatively correlated with cathodic current (Malanoski et al., 2018), and relative activity of *M. atlanticus* tracked with relative abundance in a complementary study (Eddie et al., 2016). In addition, preliminary testing of *M. atlanticus* grown under the same conditions as Biocathode MCL and supplemented with an organic carbon source indicated some capacity to generate anodic current (Wang et al., 2015b), possibly indicating a competing electron transfer (ET) process to that of "*Ca.* Tenderia electrophaga."

In the present study, we build on these previous observations to confirm whether *M. atlanticus* is an electroactive organism in order to further understand its electrochemical contribution, if any, to Biocathode MCL. *M. atlanticus* bioelectrochemical systems (BES) were established using oxygenated artificial seawater medium under identical conditions to those used for Biocathode MCL, but were supplemented with succinate (26 mM) as a carbon source and electron donor. Current production was evaluated at four different applied potentials (160, 260, 310, and 510 mV vs. SHE) and on three different electrode materials commonly used in BES [carbon cloth, graphite blocks, and indium tin oxide (ITO)]. We hypothesized that *M. atlanticus* biofilms would produce anodic current from succinate oxidation at potentials sufficiently positive to act as an electron acceptor once oxygen became limiting. At more negative potentials, we hypothesized that *M. atlanticus* may behave as a biocathode in the presence of O_2 based on the observation that this strain can oxidize iron. When configured as a biocathode, *M. atlanticus* still requires supplemental carbon to grow since it cannot fix CO_2, therefore succinate was also provided here.

The genome of *M. atlanticus* does not contain large multi-heme *c*-type cytochromes, such as those known to facilitate EET in well-known electroactive (EA) organisms like *Geobacter sulfurreducens* (Otero et al., 2018) and *Shewanella oneidensis* MR1 (Coursolle et al., 2010). Features ascribed to an $Fe–S_4$-containing protein were previously observed in the Biocathode MCL biofilm (Yates et al., 2016) and within the Biocathode MCL community *M. atlanticus* expresses the gene for rubredoxin (Eddie et al., 2017), a class of small $Fe–S_4$ proteins commonly involved in electron transfer events (Zanello, 2013; Liu et al., 2014). While rubredoxin has not yet been identified as a component of an EET conduit, synthetic biofilms employing rubredoxin as the charge mediator are capable of electron transfer between an electrode and a multi-copper enzyme and achieved even higher current densities than corresponding systems using cytochrome *c* (Altamura et al., 2017); therefore, its function as an ET mediator in *M. atlanticus* was explored.

For both the wild type (WT) and mutant strains, either anodic or cathodic current was generated, depending on the electrode potential and material used. No difference in current production was observed between the two strains. The presence of protein or small molecule redox mediators was investigated using cyclic voltammetry (CV), square wave voltammetry (SWV), and differential pulse voltammetry (DPV). While no definitive features corresponding to endogenous redox-active species were observed, the addition of exogenous redox-active species, riboflavin or excess trace mineral solution, resulted in approximately an order of magnitude increase in current production. This result suggests that soluble trace redox mediators available in the medium can facilitate EET in *M. atlanticus* BES. The use of soluble redox mediators may represent a more general role for *M. atlanticus* in biogeochemical cycles in the environment.

MATERIALS AND METHODS

Construction of In-frame Deletion Mutants

M. atlanticus CP1 was previously isolated by plating cells from the Biocathode MCL electrode biofilm and restreaking for pure colonies (Wang et al., 2015b). Following isolation, the strain was stored as a glycerol stock at −80 °C. To cultivate this strain, an aliquot of the glycerol stock was struck on a fresh BB agar plate [18.7 g of Difco Marine Broth (MB) 2216 (Becton Dickinson, Franklin Lakes, NJ, USA), 5.0 g of tryptone, 2.5 g of yeast extract, 5.0 g of sodium chloride and 15.0 g of agar per one liter], and a single colony selected to inoculate overnight cultures. In-frame deletions of the *M. atlanticus* gene for a putative rubredoxin (locus: ACP86_RS07295) and a putative NADH:flavorubredoxin oxidoreductase (locus: ACP86_RS07290) were generated by overlap PCR (Warrens et al., 1997) according to an approach previously described for *M. atlanticus* (Bird et al., 2018). Briefly, 500 bp DNA fragments upstream and downstream

of the target gene open reading frame were amplified from *M. atlanticus* genomic DNA using the primer pairs a/b and c/d (**Table S1**), respectively. The two PCR products were annealed at their overlapping region and amplified using primers a and d. The resulting 1 kb PCR fragment was digested with *Bam*HI and *Sac*I and cloned into the plasmid pSMV3 (Saltikov and Newman, 2003), which contains the kanamycin resistance gene for selection following conjugation, and the *sac*B gene for counterselection. The resulting gene deletion plasmids, pZW1207 for the rubredoxin gene and pZW2018 for the oxidoreductase gene, were transformed into *Escherichia coli* DH5α λ*pir* strain (UQ950) for maintenance. Following growth and plasmid isolation, pZW1207 and pZW2018 were transformed into *E. coli* strain WM3064 by electroporation. Conjugation was carried out as previously described (Bird et al., 2018). Briefly, the *M. atlanticus* recipient strain was grown in Marine Broth (MB) 2216 (Becton Dickinson, Franklin Lakes, NJ, USA) overnight at 30 °C with shaking while the WM3064 donor strain was grown in lysogeny broth (LB) (10.0 g of tryptone, 5.0 g of yeast extract, and 10.0 g of sodium chloride per liter) supplemented with 50 μg/mL kanamycin and 600 μM diaminopimelic acid at 37 °C for 5 h with shaking. 400 μL of each strain was mixed, pelleted, and resuspended in 400 μL LB prior to selection on MB agar plates supplemented with 50 μg/mL kanamycin. The in-frame deletion mutants for the rubredoxin gene and NADH:flavorubredoxin oxidoreductase gene (hereafter denoted as Δ*rub* and Δ*roo*, respectively, for convenience) were further counter-selected on MB agar plates supplemented with 6% sucrose and verified by PCR with primers a/d and internal primers e/f (**Table S1**).

Description of Bioelectrochemical System and Inoculation

All biofilm electrochemical experiments were performed in 250 mL (total volume) water-jacketed bioelectrochemical systems (BES) (Pine Instruments, Durham, NC) set up under aerobic conditions except where specifically noted below. Reactors contained a Ag/AgCl reference electrode (3 M KCl, Bioanalytical Systems, Inc.) and carbon cloth counter electrode (4 × 6 cm). All potentials reported here are vs. the standard hydrogen electrode (SHE; +210 mV vs. Ag/AgCl [3 M KCl]). Working electrodes were either 3 × 6 cm carbon cloth (Zoltek PX30 woven carbon fabric, PW06 weave, Zoltek Corporation), 2 × 2.5 cm ITO (Corning 1737, Delta Technologies, Limited), or 3.5 × 1 × 0.3 cm graphite block (grade AXF-5Q, POCO Graphite, Inc.). Prior to use, ITO electrodes were cleaned in concentrated sulfuric acid (Trammell et al., 2011), rinsed with ultrapure deionized water (Millipore-Sigma, Burlington, MA), sandwiched between two titanium washers using a titanium nut and bolt to connect the ITO to a titanium wire, and autoclaved dry. Graphite electrodes were prepared as previously described (Yates et al., 2016). Briefly, electrodes were gently sanded, sonicated, and soaked in 1 N HCl overnight. Graphite electrodes were then rinsed with ultrapure deionized water and allowed to soak in fresh ultrapure water until use. Carbon cloth electrodes were soaked overnight in 1 N HCl, then rinsed repeatedly until all HCl was removed. Working and counter electrodes were connected to a potentiostat via titanium wire and titanium nuts, bolts, and washers. Current densities were reported using the geometric surface areas of 36, 9.7, and 5 cm^2 for carbon cloth, graphite, and ITO electrodes, respectively. Reactors contained ca. 200 mL artificial seawater (ASW) medium (Emerson and Floyd, 2005) (per 1 L: 27.50 g NaCl, 3.80 g $MgCl_2 \bullet 6H_2O$, 6.78 g $MgSO_4 \bullet 7H_2O$, 0.72 g KCl, 0.62 g $NaHCO_3$, 2.79 g $CaCl_2 \bullet 2H_2O$, 1.00 g NH_4Cl, 0.05 g K_2HPO_4) supplemented with 7 g/L sodium succinate dibasic hexahydrate as a carbon source, and 1 mL/L Wolfe's Mineral Solution (per 1 L: 1.5 g nitrilotriacetic acid, 3.0 g $MgSO_4 \bullet 7H_2O$, 0.5 g $MnSO_4 \bullet H_2O$, 1.0 g NaCl, 0.1 g $FeSO_4 \bullet 7H_2O$, 0.1 g $CoCl_2 \bullet 6H_2O$, 0.1 g $CaCl_2$, 0.1 g $ZnSO_4 \bullet 7H_2O$, 0.01 g $CuSO_4 \bullet 5H_2O$, 0.01 g $AlK(SO_4)_2 \bullet 12H_2O$, 0.01g H_3BO_3, 0.01 $Na_2MoO_4 \bullet 2H_2O$). The medium was brought to a final pH of 6.5–6.8 with CO_2. BES temperature was maintained at 30 °C using a Haake AC200 (Thermo Scientific) recirculating water bath with continuous stirring (200–250 rpm).

A single colony of *M. atlanticus* WT, Δ*rub M. atlanticus*, or Δ*roo M. atlanticus* was used to inoculate a 3 mL culture of low calcium artificial seawater (lcASW) medium (Bird et al., 2018) (same as ASW except with a reduced concentration of calcium chloride, 0.05 g/L $CaCl_2 \bullet 2H_2O$, to promote planktonic growth) supplemented with 7 g/L sodium succinate dibasic hexahydrate (carbon source and electron donor) and 1 mL/L Wolfe's Mineral Solution. The resulting culture was allowed to grow aerobically for ca. 40 h which resulted in an optical density at a wavelength of 600 nm (OD600) of ca. 0.9 for all strains. Approximately 1 mL was used to inoculate each BES, where the inoculum was normalized such that all BES received the same number of cells.

Electrochemical Measurements

Working electrodes (carbon cloth, graphite block, or ITO) were poised at 160, 260, 310, or 510 mV vs. standard hydrogen electrode (SHE) and chronoamperometry was recorded on a multichannel potentiostat (Solartron 1470E) under software control (Multistat; Scribner). Prior to inoculation, abiotic current was measured in all BES until it became steady; that is, it no longer increased in either the anodic or cathodic direction (3–24 h). Chronoamperometry is presented as the average of triplicate reactors overlaying the spread of high and low current.

For chronoamperometry of WT *M. atlanticus* reported in **Figure 1**, triplicate BES were measured at each potential. Following chronoamperometry, biofilm samples were preserved in RNA*later* (ThermoFisher Scientific, USA) for future analysis. Laser scanning confocal microscopy (LSCM) of WT *M. atlanticus* biofilms reported in **Figure 3** were obtained from a separate, independent set of BES grown on carbon cloth electrodes at all potentials. For comparison between WT and Δ*rub* as shown in **Figure 5**, a separate independent set of triplicate BES were grown on carbon cloth electrodes at each potential and biofilm samples were again preserved in RNAlater (ThermoFisher Scientific, USA) for future analysis. Separate, independent BES were grown for SWV and DPV as described in the **Supplementary Materials**. For comparison of electrode materials, triplicate BES containing WT *M. atlanticus* were grown at 310 mV vs. SHE. At the

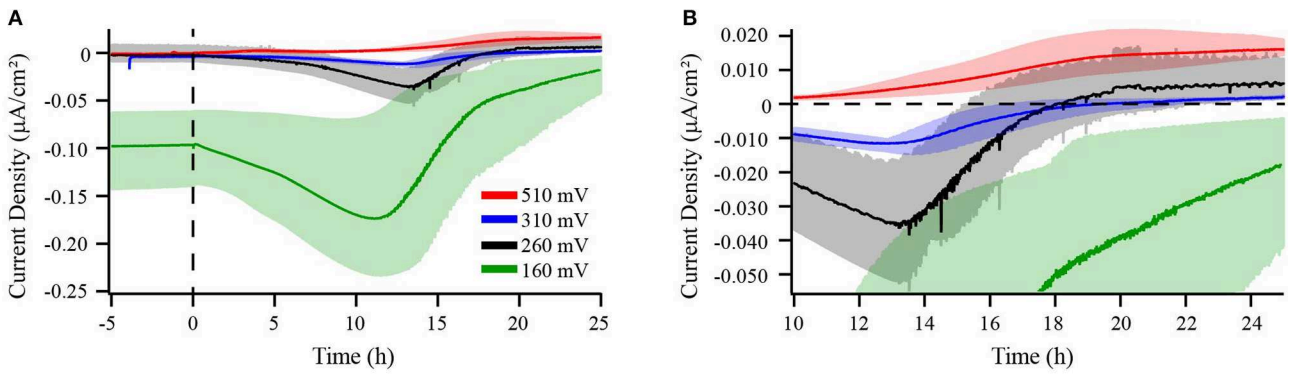

FIGURE 1 | Chronoamperometry of *M. atlanticus* biofilms grown at 510 (red), 310 (blue), 260 (black), and 160 (green) mV vs. SHE. Current produced by both abiotic and biotic BES is shown in panel **(A)**. Panel **(B)** shows a zoomed-in view of current production where 0 $\mu A/cm^2$ is indicated by a dashed line. Bioelectrochemical systems (BES) equipped with carbon cloth working and counter electrodes were inoculated with wild type (WT) *M. atlanticus* and current was monitored over time. Solid lines represent an average of triplicate measurements and shaded areas represent the maximum and minimum values obtained.

conclusion of the experiment, biofilm samples were taken for LSCM or for cyclic voltammetry (CV) (**Figure S3**).

Dissolved Oxygen Measurements

A NeoFox (Ocean Optics, Largo, FL, USA) small footprint phase fluorometer was coupled with the Foxy R-series oxygen sensor probe (Ocean Optics, Largo, FL, USA) and an O-series non-linear probe assembly for temperature correction (Ocean Optics, Largo, FL, USA). Oxygen sensors were factory calibrated and O_2 concentration was recorded per the manufacturer's instructions. The oxygen sensor probe was sterilized using a 10% bleach solution and inserted through a septum into the BES. Oxygen measurements were recorded in two of the triplicate reactors grown on carbon cloth electrodes at 310 mV as described above.

Laser Scanning Confocal Microscopy

Electrodes for microscopy were collected at the conclusion of chronoamperometry measurements as noted above and submerged in Live/Dead staining solution [1 μL/mL 5 mM SYTO9 and 1.5 μL/mL 20 mM propidium iodide in ASW medium] for 30 min in the dark at room temperature, rinsed once with ASW medium, and then placed into a Nunc Lab-tek #1.0 borosilicate chambered cover glass (Thermo Fisher Scientific, Rochester, NY, USA). Fluorescence images of unfixed, stained cells from each electrode sample were acquired with a Nikon A1RSi confocal microscope using a CFI Plan Apochromat Lamba 20X, 0.75 numerical aperture objective over 184.32 μm to 245.76 μm square fields of view (0.18–0.24 μm/px) with 0.95–1.1 μm Z-step intervals. Pinhole widths varied from 20.43 to 26.82 μm depending upon the thickness of the Z-stack images for resolution of voxels deeper within the optical sections. SYTO9 and PI fluorescence spectra were excited with the LU-N4 laser unit at 489.4 nm (SYTO9) and 561.5 nm (propidium iodide). Emission data were collected using 525/50 (SYTO9) and 595/50 (PI) filters and detected with the DU4 GaAsP PMT detector. The images were recorded and processed into maximum intensity projections using identical settings with the NIS Elements software (Nikon Instruments, Melville, NY, USA). Three random fields of view were imaged from one electrode for each potential or electrode material and representative images are shown.

Addition of Electron Transfer Mediators

A third set of independent *M. atlanticus* electrode biofilms were grown as described above on carbon cloth electrodes at 310 mV vs. SHE. Riboflavin (3.5 μM, $n = 3$) or sterile-filtered excess trace minerals [1 mL of Wolfe's Mineral Solution (5X), $n = 2$] were added to either abiotic BES after 2.5–5 h, or to *M. atlanticus* electrode biofilms after ca. 40 h and chronoamperometry was recorded.

RESULTS

Electrochemical Characterization of Wild Type *Marinobacter atlanticus* Grown on Carbon Cloth Electrodes

The electrochemical behavior of *M. atlanticus* was first characterized across a range of applied potentials (160, 260, 310, or 510 mV) for 25 h on carbon cloth electrodes in oxygenated artificial seawater medium where succinate (26 mM) was provided as both the electron donor and carbon source (*M. atlanticus* does not fix CO_2) and O_2 served as the electron acceptor in sealed BES. The 25 h experimental time frame was selected in order to (1) capture images of the biofilm that would reveal the morphology shortly after reaching peak current, and (2) save biofilms for future transcriptomics studies before cells entered into stationary phase where current no longer increased.

Carbon cloth electrodes were initially selected because they are commonly employed in BES and typically used by our lab to cultivate Biocathode MCL at 310 mV. The most positive potential of 510 mV was selected based on the typical applied potential for anode experiments by our group using *G. sulfurreducens* (Strycharz-Glaven and Tender, 2012). The potentials of 260 and 160 mV were selected to allow for characterization at

more negative potentials while avoiding the onset of abiotic oxygen reduction observed in our system at ca. 150 mV. Prior to inoculation, abiotic current resulting from electrode interactions with the medium was measured until the current became steady (3–24 h) and is reported as negative time in **Figures 1**, **4**, **5**. Dashed lines represent the time point at which BES were inoculated. When biofilms were grown at 160, 260, or 310 mV, cathodic (negative) current immediately began to increase (**Figure 1** and **Figure S1**). After 12–14 h, cathodic current reached a maximum and began to decrease. This transition occurred when the O_2 concentration in the bulk medium of a BES with the electrode poised at 310 mV decreased to ca. 12% (**Figure 2**). Cathodic current is not observed in the absence of cells suggesting that it may be the result of biofilm-mediated electron transfer from the electrode to O_2 which cannot be sustained as the surface environment of the electrode becomes anoxic due to increasing biomass from both electrode-attached and planktonic cell growth as described below. Biofilms in BES with electrodes at 260 and 310 mV generated anodic current after 16–18 h, once the bulk O_2 concentration in the 310 mV reactor had decreased to ca. 4%. After approximately 20 h, anodic current production slowed, but remained steady, suggesting ET continues between the biofilm and electrode. Biofilms grown on electrodes at 160 mV never produced anodic current, indicating that this potential is too negative to act as an electron acceptor for the biofilm. *M. atlanticus* biofilms grown at 510 mV exclusively produced anodic current which increased steadily within the first 12 h after inoculation, followed by a more rapid increase after 12 h, corresponding to when O_2 becomes limiting in the reactor (**Figures 1**, **2** and **Figure S1**). Similarly to biofilm electrodes poised at 260 and 310 mV, the anodic current began to level off around 20 h after which it increased more slowly. The coulombic efficiency estimated for complete oxidation of succinate (26 mM) in the highest anodic current-producing BES was 0.00064% (calculations available in **Supplementary Materials**). Loss of succinate in the BES due to anodic current would be in the nM range (total mol e- transferred/12 mol e- per mol succinate/volume of the BES), which would not be distinguishable from succinate oxidation coupled to oxygen reduction and therefore was not measured. *M. atlanticus* was not found to grow when a carbon cloth electrode poised at 310 or 510 mV was provided as the only available electron acceptor when the BES was made anoxic by sparging with CO_2 and N_2 prior to inoculation (data not shown). This finding, together with the observation that anodic current no longer increases once O_2 is limiting, supports that idea that biofilm cells may access the electrode as O_2 becomes limiting for maintenance, but not growth.

Planktonic cell growth was observed in all BES due to the presence of succinate as the electron donor and carbon source and O_2 as the electron acceptor. As has been previously demonstrated (Bird et al., 2018), planktonic growth was limited due to the concentration of calcium chloride in the artificial seawater medium. Final current was not correlated with the final planktonic OD_{600} of *M. atlanticus* (**Table S2**) indicating that planktonic cells do not make a significant contribution to current, and the

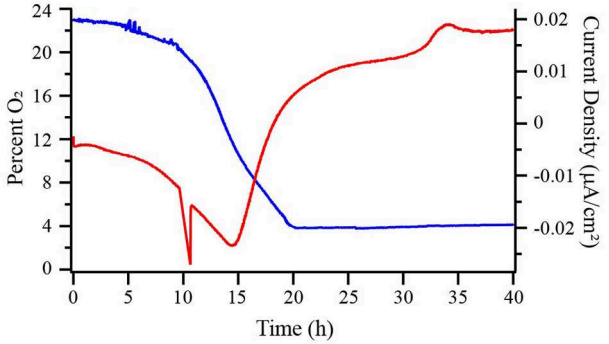

FIGURE 2 | Percent dissolved oxygen (DO) in the bulk medium (blue) and chronoamperometry (red) of a wild type (WT) *M. atlanticus* bioelectrochemical system (BES) with a carbon cloth working electrode poised at 310 mV vs. SHE. Representative trace of duplicated experiments is shown.

effect of O_2 limitation was not explored further. At all potentials, LSCM of *M. atlanticus* biofilms showed cells attached as a biofilm to the carbon cloth fibers (**Figure 3**). Biofilms grown at applied potentials of 260, 310, or 510 mV overwhelmingly stained green (Live/Dead) indicating that the cell membranes remain mostly intact. Qualitatively, biofilms grown at more negative electrode potentials contained a higher ratio of propidium iodide-stained cells (red), indicating compromised cell membranes which is often associated with cell death.

To test whether observed current required *M. atlanticus* whole cells or cellular by-products only, sterile-filtered spent culture medium from Culture-grown cells was used to inoculate BES and current production monitored (**Figure S2**). No current production was observed above baseline abiotic current. Replacing the medium in *M. atlanticus* BES after maximum current was achieved had no effect on current (data not shown), indicating no contribution to current by planktonic cells.

Electrochemical Characterization of *M. atlanticus* on Different Electrode Materials Grown at 310 mV

In order to assess the electrochemical behavior of *M. atlanticus* across a range of materials commonly used in BES, chronoamperometry and cyclic voltammetry (CV) were performed on biofilms grown on carbon cloth, graphite block, and ITO electrodes at 310 mV. This electrode potential was selected because it is the potential at which Biocathode MCL was originally enriched and is typically used for Biocathode MCL electrochemical characterization. For both carbon cloth and graphite electrodes, anodic current increased over time (**Figure 4A**) in contrast to cathodic current observed for Biocathode MCL. The initial increase in cathodic current observed at 310 mV on carbon cloth electrodes (**Figure 4A**) was not observed on graphite block or ITO electrodes. Biofilms grown on ITO electrodes produced an order of magnitude less current than those on carbon

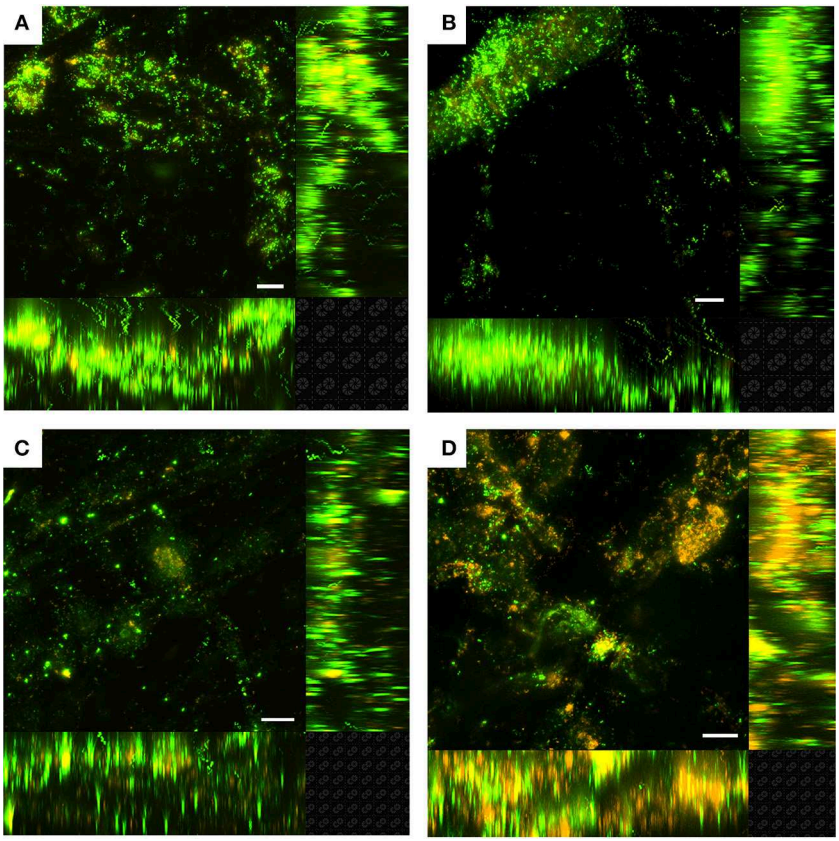

FIGURE 3 | Laser scanning confocal microscopy (LSCM) of Live/Dead-stained *M. atlanticus* biofilms grown on carbon cloth electrodes poised at **(A)** 510 mV, **(B)** 310 mV, **(C)** 260 mV, and **(D)** 160 mV vs. SHE after ca. 25 h. Fluorescence associated with SYTO9 is shown in green (live) and fluorescence associated with propidium iodide is shown in red (dead). Representative images are shown from triplicate reactors. The white scale bar represents 20 μm.

cloth or graphite which never increased above the abiotic cathodic background and fewer cells were observed associated with the electrode surface (**Figures 4B–D**). Anodic current produced at 310 and 510 mV on graphite and carbon cloth electrodes was similar; however, it is difficult to assess whether biomass coverage on the electrode surface was comparable based on microscopy due to the 3-dimensional nature of the carbon cloth fibers. The majority of biofilm-associated cells stained green (Live/Dead) for all electrode materials, consistent with results presented above for biofilms grown at 310 mV and indicating living cells with intact cell membranes.

In order to characterize putative redox mediators associated with *M. atlanticus,* CV was performed on abiotic and *M. atlanticus*-colonized carbon cloth, graphite block, and ITO electrodes (**Figure S3**). The appearance of redox peaks in the presence of cells was inconsistent between electrode materials and could not be distinguished from the abiotic controls. SWV (**Figure S4**) and DPV (**Figure S5**) were also applied in an attempt to further resolve redox peaks from the faradaic current by excluding the capacitive charging currents arising from the electrode; however, no consistent peak could be resolved.

Electrochemical Characterization of Wild Type and Rubredoxin Deletion Strains of *M. atlanticus*

To explore the possibility that small Fe–S_4 proteins play a role in either EET or the survival of *M. atlanticus* as an electrode biofilm, biofilms of the Δ*rub M. atlanticus* and Δ*roo M. atlanticus* strains were electrochemically characterized vs. the WT strain on carbon cloth electrodes. No difference in the overall current trend was observed over 25 h between the Δ*rub* strain and the WT strain at any potential (**Figure 5**), or the Δ*roo* strain and the WT strain at 310 mV (**Figures S1**, **S6**). At the end of the 25–30 h growth period, OD_{600} was measured, found to be similar between reactor conditions, and was not correlated with current production (**Table S2**).

Addition of Exogenous Mediators Enhances Anodic Current in *M. atlanticus* Biofilms

The low current density and absence of redox features in voltammetry may indicate low abundance and/or low rate constants of redox mediators involved in the heterogeneous ET reaction, such as trace metals and minerals or small molecules

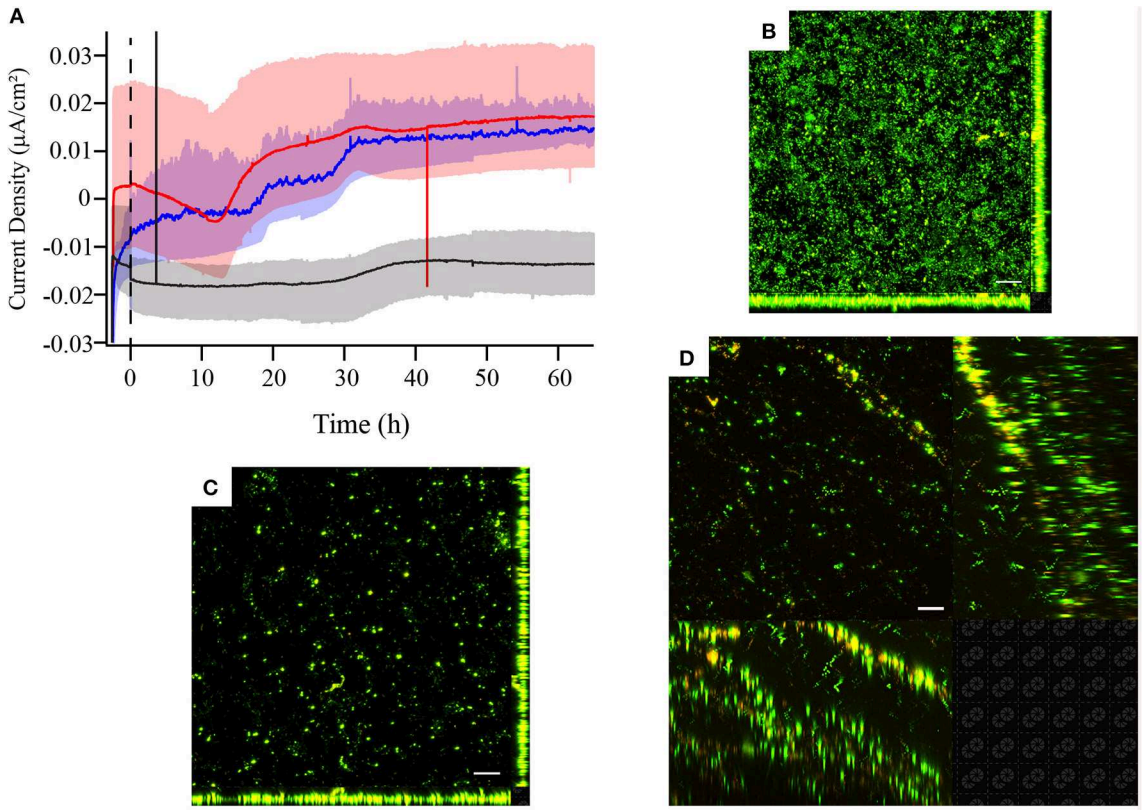

FIGURE 4 | (A) Chronoamperometry and laser scanning confocal microscopy (LSCM) of Live/Dead-stained *M. atlanticus* biofilms grown on **(B)** graphite, **(C)** ITO, or **(D)** carbon cloth working electrodes poised at 310 mV vs. SHE. Microscopy was performed ca. 66 h after inoculation. Fluorescence associated with SYTO9 is shown in green (live) and fluorescence associated with propidium iodide is shown in red (dead). Representative images are shown from triplicate reactors. The white scale bar represents 20 μm.

found in the reactor medium. To test this possibility, a 5X higher concentration of trace mineral mixture was added to BES after WT *M. atlanticus* biofilms grown at 310 mV on carbon cloth electrodes reached maximum current (**Figure 6**). Current immediately began to increase and, after ca. 25 h, was an order of magnitude greater than the current produced prior to the addition of excess trace minerals. No change in the abiotic current was observed after adding excess minerals, either under aerobic conditions, or when the BES was made anoxic to mimic the conditions at the electrode surface once a biofilm is present. In all cases, the excess minerals were exposed to oxygen prior to addition to BES (**Figure S7**). When 5X trace mineral solution was added prior to inoculation, anodic current due to biofilm growth also increased to a maximum that was approximately an order of magnitude higher than is typically observed; however, current did not plateau until 60 h after inoculation (**Figure S8D**). Current was monitored for 40 h after the addition of excess minerals, at which point the experiment was discontinued and the working electrode of a representative BES that had 5X sterile-filtered trace minerals added was removed to test for cell viability by CLSM. Imaging by CLSM indicated that addition of trace minerals had some effect on cell membrane integrity as indicated by the increase in cells that stained red (Live/Dead) as compared to those observed for *M. atlanticus* grown at an applied potential of 310 mV under typical conditions (**Figure S9**). Qualitatively, the surface coverage of the electrode biofilms appears similar to those where no excess minerals were added, which might indicate the cells are limited in their use of the electrode as an electron acceptor by an electron shuttle. When CV was performed after the addition of minerals, a redox peak with a midpoint potential of ca. 180–200 mV was observed associated with *M. atlanticus* biofilms as well in abiotic BES under anaerobic conditions (**Figure S10**). Due to oxygen reduction features, it is unknown if this peak is also present in abiotic BES under aerobic conditions. The observation of this peak may be due to a change in the redox chemistry of charge carriers under anaerobic conditions, such as when a biofilm is present, as well as an increase in their concentration.

Some iron-reducing bacteria, such as *S. oneidensis* MR-1 (Kotloski and Gralnick, 2013), access extracellular electron acceptors, including electrodes, via secreted small molecule redox shuttles including flavins. Flavins can interact with ET proteins in the periplasm or inner membrane of the cell, if such proteins are present, and facilitate EET. It has previously been shown that *E. coli*, which does not naturally participate in EET, is only able to use riboflavin as a shuttle when genetically engineered to express

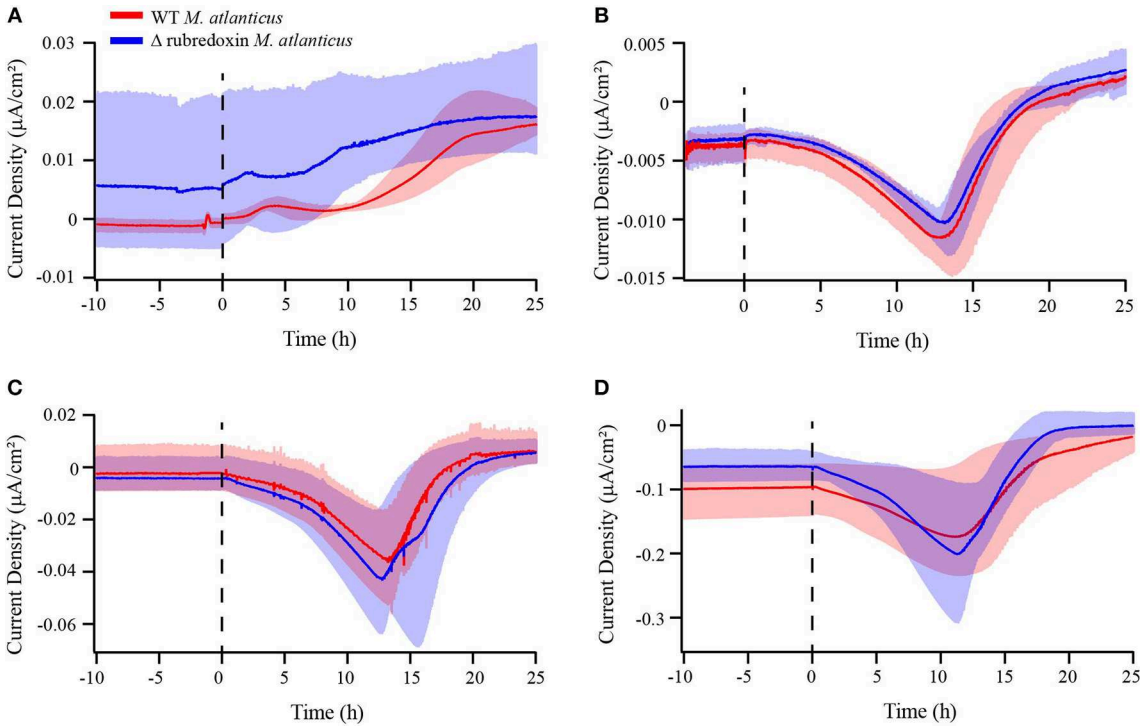

FIGURE 5 | Chronoamperometry of wild type *M. atlanticus* (red) and rubredoxin deletion (Δ*rub*) (blue) biofilms on carbon cloth working electrodes poised at **(A)** 510, **(B)** 310, **(C)** 260, and **(D)** 160 mV vs. SHE. The dashed line indicates the time of inoculation. Solid lines represent an average of triplicate measurements and shaded areas represent the maximum and minimum values obtained.

the *S. oneidensis* Mtr pathway (Jensen et al., 2016). In order to determine whether *M. atlanticus* can naturally use soluble redox shuttles for EET, riboflavin (3.5 μM) was added to BES at a concentration similar to that previously shown to stimulate EET in engineered *E. coli*. Addition of riboflavin resulted in roughly an order of magnitude increase in current (**Figure 6**). In comparison, when the same amount of riboflavin was added to BES containing WT *E. coli* modified electrodes (OD_{600} >0.600), no increase in current was observed (**Figure S11**), demonstrating that *M. atlanticus* has some innate capacity to perform EET with redox shuttles.

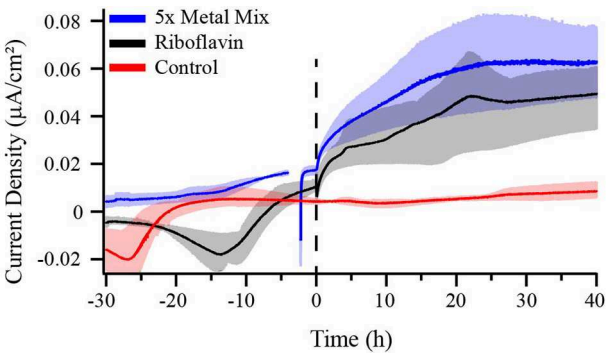

FIGURE 6 | Chronoamperometry of *M. atlanticus* biofilms grown on carbon cloth electrodes poised at 310 mV vs. SHE with either no additions to the growth medium (red), 1 mL of sterile-filtered Wolfe's Mineral Solution added after ca. 48 h post inoculation (blue), or 3.5 μM riboflavin (final concentration) added after ca. 30 h post inoculation (black). Solid lines represent an average of triplicate (control and riboflavin addition) or duplicate (mineral mix addition) bioelectrochemical systems (BES) and the shaded areas represent the maximum and minimum values obtained.

DISCUSSION

The aim of this study was to electrochemically characterize *M. atlanticus*, recently isolated from the Biocathode MCL community. The relative abundance of *M. atlanticus* within Biocathode MCL has been shown to be negatively correlated with current, and previous work suggests that this strain has some capacity for EET on its own (Wang et al., 2015b; Bird et al., 2018); however no mechanism has been proposed. Results presented here show that *M. atlanticus* biofilms grown over a range of electrode potentials and materials resulted in the production of very low, but non-negligible, anodic and cathodic current which depended both on the electrode potential and concentration of O_2. Cathodic current generated in the presence of O_2 by *M. atlanticus* biofilms grown on carbon cloth at 310 mV was at least an order of magnitude lower than comparable Biocathode MCL biofilms grown at the same potential (Malanoski et al., 2018), and anodic current was 4 orders of magnitude lower than typical *G. sulfurreducens* bioanodes (Strycharz-Glaven and

Tender, 2012), which would be expected if EET is not tied directly to the energy-generating processes of the cell. The production of cathodic current, even in the presence of the electron donor succinate, suggests that *M. atlanticus* could scavenge additional electrons from the electrode. Voltammetric analyses did not reveal any clear biofilm-associated redox peaks, differing markedly from the Nernstian current-voltage response observed during CV of Biocathode MCL (Yates et al., 2016). One explanation, inferred from the very low current, is that the redox signal associated with a redox mediator, either cell-associated or a component of the growth medium, is simply too low to detect.

Biofilms grown on carbon cloth electrodes at 260, 310, or 510 mV vs. SHE produced anodic current after a period of 12–18 h, consistent with a decrease in the concentration of O_2 measured for BES at 310 mV. These results suggest that at more positive electrode potentials, *M. atlanticus* is able to use the electrode as an electron acceptor to relieve the buildup of reducing equivalents generated from succinate oxidation once O_2 has been depleted. The absence of anodic current at 160 mV on carbon cloth electrodes, coupled with the noticeable increase in the number of propidium iodide-stained cells, supports the hypothesis that this potential is too negative for the electrode to act as a suitable electron acceptor. *M. atlanticus* biofilms achieve the highest anodic current density at 510 mV, whereas anodic current generated at 260 and 310 mV is about the same. Despite the ability of biofilms to transfer some electrons to an electrode, *M. atlanticus* was unable to grow under anaerobic conditions when the electrode was provided as the sole electron acceptor at 310 or 510 mV. This result is consistent with our previous observation that *M. atlanticus* is able to reduce small amounts of iron under anaerobic conditions in ASW medium, even though this metabolism does not appear to support growth (Bird et al., 2018). No difference in maximum anodic current was observed between the WT strain and Δ*rub* and Δ*roo* strains of *M. atlanticus,* indicating that neither of these proteins are involved in EET to an electrode. While there is a second rubredoxin present in the *M. atlanticus* genome, due to the degree of sequence similarity with AlkG of *Pseudomonas putida* it is likely to be part of the alkane degradation pathway (Kok et al., 1989; Wang et al., 2015a).

Electrochemical characterization of *M. atlanticus* biofilms on carbon cloth, graphite block, and ITO electrode surfaces showed that the electrode material has an effect on the maximum current production as well as whether biofilms initially behave as biocathodes at 310 mV. Graphite block electrodes resulted in the greatest anodic current density, followed by carbon cloth, then ITO. Some of this difference may be attributed to inaccuracies in calculated current density by using the geometric surface area, where ITO is a much smoother surface than carbon cloth or graphite. In addition, micro-features associated with the electrode topography may result in different chemical gradients (O_2 or pH) at the electrode surface that affect current. The extent of *M. atlanticus* colonization, as measured by LSCM of Live/Dead-stained biofilms grown on these electrode surfaces, showed a robust biofilm on the graphite electrode, a fairly even biofilm coating on the carbon cloth fibers, and a sparse biofilm on the ITO electrodes. The biofilm coverage on these electrode surfaces agrees well with the overall current density produced in each case. These results suggest that current production is linked to the presence of metabolically active cells.

It is unclear why cathodic current generated by *M. atlanticus* biofilms at 310 mV only occurs on carbon cloth. The weave of the carbon cloth itself may contribute to this phenomenon if dissolved O_2 is retained among the fibers, providing an electron acceptor that can be slowly released to the growing biofilm. Carbon cloth is a widely used electrode surface in microbial electrochemistry; however, the manufacturing process of carbon cloth only results in 99% carbon atoms (Zoltek Corporation) and surface modifications may be added to improve various properties. It is unknown whether such surface modifications may have an effect here.

The most significant observation was that the addition of excess trace minerals (5X) or riboflavin (3.5 μM) resulted in an order of magnitude increase in anodic current production at 310 mV on carbon cloth electrodes, the same conditions under which Biocathode MCL is typically grown. Conversely, the addition of riboflavin to *E. coli* biofilms resulted in no change in current production. It has previously been reported that the addition of nanomolar concentrations of Cu^{2+} or Cd^{2+} to *S. oneidensis* MR-1 grown in microbial fuel cells resulted in a 1.3-fold increase in power density due to the combined effects of increased biofilm formation and increased riboflavin production (Xu et al., 2016). *M. atlanticus* possesses the required genes for riboflavin biosynthesis (Wang et al., 2015a), but not for the riboflavin exporter found in *S. oneidensis*; therefore, it seems unlikely that a similar mechanism is responsible in this case.

The presence of cells was required for the observed increase in anodic current with the addition of either riboflavin or excess trace minerals, suggesting that sustained turnover of these redox shuttles is catalyzed by the cells at 310 mV. The addition of excess minerals in the presence of the biofilm or when the medium was made anaerobic in abiotic reactors resulted in a discernable redox peak with a midpoint potential (E_m) around 180–200 mV. This peak is likely a component of the trace mineral solution and may be available to the biofilm as a redox mediator. If this is the case, the E_m offers insight into biofilm current production at the various potentials tested here. At potentials above 200 mV, the unknown redox-active species may be partially oxidized by the electrode, and thus could serve as an electron-accepting shuttle between the cell and electrode. Below 200 mV, a higher proportion of the redox mediator would be maintained in the reduced state by the electrode and unable to accept electrons from cells. This is consistent with anodic current at potentials of 260 mV and above, and cathodic current only at 160 mV. Drawing from these results, we can imagine a scenario under which trace minerals serve as electron transfer mediators within the Biocathode MCL community between the electrode and heterotrophic constituents, contributing to the overall electron flux of the biofilm. Depending on the direction of electron flux at 310 mV generated by *M. atlanticus*, anodic or cathodic, this contribution may compete with, or enhance, cathodic ET by "*Ca.* Tenderia electrophaga." If other heterotrophic constituents of Biocathode MCL also participate in mineral cycling, this

effect could be amplified. The low availability of organic carbon in Biocathode MCL reactors (no organic carbon added), as well as microaerobic conditions at the electrode surface, limits heterotrophic growth. If mineral cycling can provide additional electron donors or acceptors it may explain the persistence of heterotrophic community members in Biocathode MCL even after many years of subculture. This finding may also have important implications for how *Marinobacter* spp. interact with minerals in the environment and should be further explored. For example, *Marinobacter* spp. may be able to take up oxidized or reduced trace minerals allowing for sustained cell maintenance during periods of electron donor or acceptor limitation.

In the BES configuration used in this study, it is not possible to determine if cells within the biofilm, but at a distance from the electrode surface, contribute to current as they do for conductive *G. sulfurreducens* biofilms. Because this system is not intentionally made anaerobic, cells at the periphery of the biofilm may utilize O_2 as an electron acceptor, creating an anoxic environment near the electrode surface. LSCM imaging did not indicate the cells at the outer portion of the biofilm were compromised once O_2 is depleted, suggesting that some other electron acceptor is available. Whether this is some oxidized component of the medium or other cells within the biofilm remains unclear and measurements of biofilm conductivity are warranted.

CONCLUSION

Marinobacter spp. are ubiquitous marine opportunitrophs identified in metal-rich environments and within electrode-associated biofilms. Here we demonstrated that *M. atlanticus* is able to generate very low levels of anodic and cathodic current, an indicator of its ability to perform EET outside of the Biocathode MCL community. Constituents of electrochemically active microbial communities that produce low levels of current on their own should not be discounted and may have important roles for the function of the community as a whole (Doyle and Marsili, 2018). Anodic current can be enhanced at 310 mV through addition of riboflavin and excess minerals. These findings have important implications for how *Marinobacter* spp. may interact with minerals in the environment and suggests that trace minerals could be scavenged for use as electron donors or acceptors under otherwise limiting conditions.

With respect to the role for *M. atlanticus* within Biocathode MCL, results presented here indicate the possibility that competing ET processes to "*Ca.* Tenderia electrophaga" occur at a poised electrode potential of 310 mV vs. SHE depending on the concentration of O_2 present. Anodic current produced by *M. atlanticus* at 310 mV is low relative to Biocathode MCL, but it is possible that a cumulative effect may occur if other heterotrophic members of the community are also able to produce anodic current.

DATA AVAILABILITY

All datasets generated for this study are included in the manuscript and/or the **Supplementary Files**.

AUTHOR CONTRIBUTIONS

EO and SG devised experiments and wrote the manuscript. EO performed electrochemical measurements on *M. atlanticus*. DP and BE performed microscopy and imaging. MY and LT helped perform SWV and DPV measurements and analysis of electrochemical data. ZW generated the *M. atlanticus* deletion strains used in this study. This research was performed while the author EO held an NRC Research Associateship award at The Naval Research Laboratory.

FUNDING

This work was funded through the NRL Base 6.1 program and the Office of the Assistant Secretary of Defense for Research and Engineering Applied Research for the Advancement of S&T Priorities program.

SUPPLEMENTARY MATERIAL

The Supplementary Material for this article can be found online at: https://www.frontiersin.org/articles/10.3389/fenrg.2019.00060/full#supplementary-material

REFERENCES

Altamura, L., Horvath, C., Rengaraj, S., Rongier, A., Elouarzaki, K., Gondran, C., et al. (2017). A synthetic redox biofilm made from metalloprotein-prion domain chimera nanowires. *Nat.Chem.* 9, 157–163. doi: 10.1038/nchem.2616

Bird, L. J., Wang, Z., Malanoski, A. P., Onderko, E. L., Johnson, B. J., Moore, M. H., et al. (2018). Development of a genetic system for *Marinobacter atlanticus* CP1 (sp. nov.), a Wax Ester producing strain isolated from an autotrophic biocathode. *Front. Microbiol.* 9:03176. doi: 10.3389/fmicb.2018.03176

Bonis, B. M., and Gralnick, J. A. (2015). Marinobacter subterrani, a genetically tractable neutrophilic Fe(II)-oxidizing strain isolated from the Soudan Iron Mine. *Front. Microbiol.* 6:719. doi: 10.3389/fmicb.2015.00719

Coursolle, D., Baron, D. B., Bond, D. R., and Gralnick, J. A. (2010). The Mtr respiratory pathway is essential for reducing flavins and electrodes in *Shewanella oneidensis*. *J. Bacteriol.* 192, 467–474. doi: 10.1128/JB.00925-09

Debuy, S., Pecastaings, S., Bergel, A., and Erable, B. (2015). Oxygen-reducing biocathodes designed with pure cultures of microbial strains isolated from seawater biofilms. *Int. Biodeterior. Biodegr.* 103, 16–22. doi: 10.1016/j.ibiod.2015.03.028

Doyle, L. E., and Marsili, E. (2018). Weak electricigens: a new avenue for bioelectrochemical research. *Bioresour. Technol.* 258, 354–364. doi: 10.1016/j.biortech.2018.02.073

Eddie, B. J., Wang, Z., Hervey, W. J., Leary, D. H., Malanoski, A. P., Tender, L. M., et al. (2017). Metatranscriptomics supports the mechanism for biocathode electroautotrophy by "Candidatus Tenderia electrophaga". *Msystems* 2. doi: 10.1128/mSystems.00002-17

Eddie, B. J., Wang, Z., Malanoski, A. P., Hall, R. J., Oh, S. D., Heiner, C., et al. (2016). 'Candidatus *Tenderia electrophaga*', an uncultivated electroautotroph from a biocathode enrichment. *Int. J. Syst. Evol. Microbiol.* 66, 2178–2185. doi: 10.1099/ijsem.0.001006

Edwards, K. J., Rogers, D. R., Wirsen, C. O., and Mccollom, T. M. (2003). Isolation and characterization of novel psychrophilic, neutrophilic, Fe-oxidizing, chemolithoautotrophic alpha- and, gamma-Proteobacteria from the deep sea. *Appl. Environ. Microbiol.* 69, 2906–2913. doi: 10.1128/AEM.69.5.2906-2913.2003

Emerson, D., and Floyd, M. M. (2005). Enrichment and isolation of iron-oxidizing bacteria at neutral pH. *Environ. Microbiol.* 397, 112–123. doi: 10.1016/S0076-6879(05)97006-7

Erable, B., Vandecandelaere, I., Faimali, M., Delia, M. L., Etcheverry, L., Vandamme, P., et al. (2010). Marine aerobic biofilm as biocathode catalyst. *Bioelectrochemistry* 78, 51–56. doi: 10.1016/j.bioelechem.2009.06.006

Gauthier, M. J., Lafay, B., Christen, R., Fernandez, L., Acquaviva, M., Bonin, P., et al. (1992). Marinobacter-hydrocarbonoclasticus gen. nov., sp. nov., a New, Extremely Halotolerant, Hydrocarbon-Degrading Marine Bacterium. *Int. J. Syst. Bacteriol.* 42, 568–576. doi: 10.1099/00207713-42-4-568

Jensen, H. M., Teravest, M. A., Kokish, M. G., and Ajo-Franklin, C. M. (2016). CymA and exogenous flavins improve extracellular electron transfer and couple it to cell growth in Mtr-expressing *Escherichia coli*. *Acs Synthetic Biol.* 5, 679–688. doi: 10.1021/acssynbio.5b00279

Kok, M., Oldenhuis, R., Vanderlinden, M. P. G., Meulenberg, C. H. C., Kingma, J., and Witholt, B. (1989). The *Pseudomonas oleovorans* alkBAC operon encodes two structurally related rubredoxins and an aldehyde dehydrogenase. *J. Biol. Chem.* 264, 5442–5451.

Kotloski, N. J., and Gralnick, J. A. (2013). Flavin electron shuttles dominate extracellular electron transfer by *Shewanella oneidensis*. *Mbio* 4. doi: 10.1128/mBio.00553-12

Liu, J., Chakraborty, S., Hosseinzadeh, P., Yu, Y., Tian, S. L., Petrik, I., et al. (2014). Metalloproteins containing cytochrome, iron-sulfur, or copper redox centers. *Chem. Rev.* 114, 4366–4469. doi: 10.1021/cr400479b

Malanoski, A. P., Lin, B. C., Eddie, B. J., Wang, Z., Hervey, W. J., and Glaven, S. M. (2018). Relative abundance of "Candidatus Tenderia electrophaga' is linked to cathodic current in an aerobic biocathode community. *Microb. Biotech.* 11, 98–111. doi: 10.1111/1751-7915.12757

Martin, S., Marquez, M. C., Sanchez-Porro, C., Mellado, E., Arahal, D. R., and Ventosa, A. (2003). Marinobacter lipolyticus sp nov., a novel moderate halophile with lipolytic activity. *Int. J. Syst. Evol. Microbiol.* 53, 1383–1387. doi: 10.1099/ijs.0.02528-0

Otero, F. J., Chan, C. H., and Bond, D. R. (2018). Identification of different putative outer membrane electron conduits necessary for Fe(III) Citrate, Fe(III) Oxide, Mn(IV) Oxide, or electrode reduction by geobacter sulfurreducens. *J. Bacteriol.* 200:e00347–18. doi: 10.1128/JB.00347-18

Rowe, A. R., Chellamuthu, P., Lam, B., Okamoto, A., and Nealson, K. H. (2015). Marine sediments microbes capable of electrode oxidation as a surrogate for lithotrophic insoluble substrate metabolism. *Front. Microbiol.* 5:784. doi: 10.3389/fmicb.2014.00784

Saltikov, C. W., and Newman, D. K. (2003). Genetic identification of a respiratory arsenate reductase. *Proc. Natl. Acad. Sci. U. S. A.* 100, 10983–10988. doi: 10.1073/pnas.1834303100

Shieh, W. Y., Jean, W. D., Lin, Y. T., and Tseng, M. (2003). Marinobacter lutaoensis sp nov., a thermotolerant marine bacterium isolated from a coastal hot spring in Lutao, Taiwan. *Can. J. Microbiol.* 49, 244–252. doi: 10.1139/w03-032

Singer, E., Webb, E. A., Nelson, W. C., Heidelberg, J. F., Ivanova, N., Pati, A., et al. (2011). Genomic potential of Marinobacter aquaeolei, a biogeochemical "Opportunitroph". *Appl. Environ. Microbiol.* 77, 2763–2771. doi: 10.1128/AEM.01866-10

Stepanov, V. G., Xiao, Y., Lopez, A. J., Roberts, D. J., and Fox, G. E. (2016). Draft genome sequence of Marinobacter sp. strain P4B1, an electrogenic perchlorate-reducing strain isolated from a long-term mixed enrichment culture of marine bacteria. *Genome Announcements* 4:e01617–01615. doi: 10.1128/genomeA.01617-15

Strycharz-Glaven, S. M., and Tender, L. M. (2012). Study of the mechanism of catalytic activity of G. Sulfurreducens biofilm anodes during biofilm growth. *Chemsuschem* 5, 1106–1118. doi: 10.1002/cssc.201100737

Trammell, S. A., Dressick, W. J., Melde, B. J., and Moore, M. (2011). Photocurrents from the direct irradiation of a donor-acceptor complex contained in a thin film on indium tin oxide. *J. Phys. Chem. C* 115, 13446–13461. doi: 10.1021/jp2023988

Wang, Z., Eddie, B. J., Malanoski, A. P., Hervey, W. J., Lin, B., and Strycharz-Glaven, S. M. (2015a). Complete genome sequence of *Marinobacter* sp. CP1, isolated from a self-regenerating biocathode biofilm. *Genome Announc.* 3:e01103–01115. doi: 10.1128/genomeA.01103-15

Wang, Z., Leary, D. H., Malanoski, A. P., Li, R. W., Hervey, W. J., Eddie, B. J., et al. (2015b). A previously uncharacterized, nonphotosynthetic member of the chromatiaceae is the primary CO2-fixing constituent in a self-regenerating biocathode. *Appl. Environ. Microbiol.* 81, 699–712. doi: 10.1128/AEM.02947-14

Warrens, A. N., Jones, M. D., and Lechler, R. I. (1997). Splicing by overlap extension by PCR using asymmetric amplification: an improved technique for the generation of hybrid proteins of immunological interest. *Gene* 186, 29–35. doi: 10.1016/S0378-1119(96)00674-9

Xu, Y. S., Zheng, T., Yong, X. Y., Zhai, D. D., Si, R. W., Li, B., et al. (2016). Trace heavy metal ions promoted extracellular electron transfer and power generation by Shewanella in microbial fuel cells. *Bioresour. Technol.* 211, 542–547. doi: 10.1016/j.biortech.2016.03.144

Yates, M. D., Eddie, B. J., Kotloski, N. J., Lebedev, N., Malanoski, A. P., Lin, B. C., et al. (2016). Toward understanding long-distance extracellular electron transport in an electroautotrophic microbial community. *Energy Environ. Sci.* 9, 3544–3558. doi: 10.1039/C6EE02106A

Zanello, P. (2013). The competition between chemistry and biology in assembling iron-sulfur derivatives. Molecular structures and electrochemistry. Part I. {Fe(S^{γ}_{Cys4})} proteins. *Coordination Chem. Rev.* 257, 1777–1805. doi: 10.1016/j.ccr.2013.02.006

Zoltek Corporation. *Technical Datasheet ZOLTEK^{TM} PX30 Fabric (PW03, PW06, SW08) [Online]. ZOLTEK Corporation*. Available online at: http://zoltek.com/datasheets/ (accessed March 15, 2019).

Conflict of Interest Statement: The authors declare that the research was conducted in the absence of any commercial or financial relationships that could be construed as a potential conflict of interest.

frontiers in Energy Research

ORIGINAL RESEARCH
published: 31 July 2019
doi: 10.3389/fenrg.2019.00070

Enhancement of Ethanol Production in Electrochemical Cell by *Saccharomyces cerevisiae* (CDBT2) and *Wickerhamomyces anomalus* (CDBT7)

Jarina Joshi[1]*, *Pradip Dhungana*[1], *Bikram Prajapati*[1], *Rocky Maharjan*[1], *Pranita Poudyal*[1], *Mukesh Yadav*[1], *Milan Mainali*[1], *Amar Prasad Yadav*[2], *Tribikram Bhattarai*[1] and *Lakshmaiah Sreerama*[3]

[1] Central Department of Biotechnology, Tribhuvan University, Kirtipur, Nepal, [2] Central Department of Chemistry, Tribhuvan University, Kirtipur, Nepal, [3] Department of Chemistry and Earth Sciences, Qatar University, Doha, Qatar

OPEN ACCESS

Edited by:
Sarah Glaven,
United States Naval Research Laboratory, United States

Reviewed by:
Darren Greetham,
University of Huddersfield, United Kingdom
Richa Arora,
Lovely Professional University, India

***Correspondence:**
Jarina Joshi
jarinarjoshi@gmail.com;
jarina@biotechtu.edu.np

Specialty section:
This article was submitted to Bioenergy and Biofuels, a section of the journal Frontiers in Energy Research

Received: 28 May 2019
Accepted: 11 July 2019
Published: 31 July 2019

Citation:
Joshi J, Dhungana P, Prajapati B, Maharjan R, Poudyal P, Yadav M, Mainali M, Yadav AP, Bhattarai T and Sreerama L (2019) Enhancement of Ethanol Production in Electrochemical Cell by Saccharomyces cerevisiae (CDBT2) and Wickerhamomyces anomalus (CDBT7). Front. Energy Res. 7:70. doi: 10.3389/fenrg.2019.00070

Bioethanol (a renewable resource), blended with gasoline, is used as liquid transportation fuel worldwide and produced from either starch or lignocellulose. Local production and use of bioethanol supports local economies, decreases country's carbon footprint and promotes self-sufficiency. The latter is especially important for bio-resource-rich land-locked countries like Nepal that are seeking alternative transportation fuels and technologies to produce them. In that regard, in the present study, we have used two highly efficient ethanol producing yeast strains, *viz*., *Saccharomyces cerevisiae* (CDBT2) and *Wickerhamomyces anomalous* (CDBT7), in an electrochemical cell to enhance ethanol production. Ethanol production by CDBT2 (anodic chamber) and CDBT7 (cathodic chamber) control cultures, using 5% glucose as substrate, were 12.6 ± 0.42 and 10.1 ± 0.17 mg·mL^{-1} respectively. These cultures in the electrochemical cell, when externally supplied with 4V, the ethanol production was enhanced by 19.8 ± 0.50% and 23.7 ± 0.51%, respectively, as compared to the control cultures. On the other hand, co-culturing of those two yeast strains in both electrode compartments resulted only 3.96 ± 0.83% enhancement in ethanol production. Immobilization of CDBT7 in the graphite cathode resulted in lower enhancement of ethanol production (5.30 ± 0.82%), less than free cell culture of CDBT7. CDBT2 and CDBT7 when cultured in platinum nano particle coated platinum anode and neutral red-coated graphite cathode, respectively, ethanol production was substantially enhanced (52.8 ± 0.44%). The above experiments when repeated using lignocellulosic biomass hydrolysate (reducing sugar content was 3.3%) as substrate, resulted in even better enhancement in ethanol production (61.5 ± 0.12%) as compared to glucose. The results concluded that CDBT2 and CDBT7 yeast strains produced ethanol efficiently from both glucose and lignocellulosic biomass

hydrolysate. Ethanol production was enhanced in the presence of low levels of externally applied voltage. Ethanol production was further enhanced with the better electron transport provision i.e., when neutral red was deposited on cathode and fine platinum nanoparticles were coated on the platinum anode.

Keywords: electrochemical cell, lignocellulosic biomass, *Saccharomyces cerevisiae*, *Wickerhamomyces anomalous*, *Saccharum spontaneum*, bioethanol

INTRODUCTION

Dependence on petroleum-based transportation fuels is a major challenge for developing countries which don't have fossil fuel reserves. The challenge is severe in the landlocked countries such as Nepal (Joshi et al., 2011). In fact, landlocked countries spend a major share of their GDP to import fossil fuels via other countries. Given the above, serious attempts are being made to develop alternative energy sources that are expected to alleviate the above challenge. Bioethanol is one of those renewable and eco-friendly fuels (Khatiwada and Silveira, 2011). Besides being used as a fuel, bioethanol can also be used for other purposes such as making bioplastics (Rose and Palkovits, 2011) and development of ethanol fuel cells for electricity generation (Saisirirat and Joommanee, 2017).

Second generation biofuels such as bioethanol (obtained from lignocellulose) can be produced in rural as well as urban areas using easily available lignocellulosic biomass. Lignocellulose is the most abundant biomass worldwide with annual production of about 1,000 giga-metric tons. The biomass is a mixture of cellulose, hemicellulose, lignin and other contents such as pectin. Cellulose and hemicelluloses upon degradation produces fermentable sugars, e.g., glucose and xylose. These sugars can be further converted into important products, including ethanol, by fermentation. The extent of ethanol that can be produced by lignocellulosic biomass depends on composition of sugars, which varies in plants and the habitat in which they grow (Hermosilla et al., 2017; Joshi et al., 2018). To date the cost of ethanol production from lignocellulosic biomass depends on technique used. The better the technique, the lower is the cost of production (Haque and Epplin, 2012).

Yeasts such as *S. cerevisiae* are widely used for ethanol fermentation. Yeasts with high salt and ethanol tolerance are most valuable in this process. Further to produce ethanol efficiently from lignocellulosic hydrolysates, yeasts should be able to utilize both glucose as well as pentoses such as xylose and arabinose. This is because lignocellulosic biomass is rich in both glucose and xylose (a pentose) (Joshi et al., 2018). This is the main drawback of using *S. cerevisiae* alone as it cannot ferment both glucose and xylose. Accordingly, identifying yeast strains that can ferment both glucose and xylose is critical, if not, at the least use two different strains of yeast that are capable of utilizing these sugars independently. In this study, we have identified and used highly efficient, salt and ethanol tolerant, yeast strains, *viz., S. cerevisiae* (CDBT2) (Joshi et al., 2014) and xylose utilizing *W. anomalous* (CDBT7) for ethanol production using lignocellulosic biomass.

For enhancing ethanol production, electro-fermentation technology that merges traditional fermentation with electrochemistry can be adopted. Electro-fermentation is a novel process in which the microbial fermentative metabolism may be controlled electrochemically. The benefits of this process are that for the process (i) is selective, (ii) increases sugar (carbon) utilization efficiency, (iii) minimizes the use of additives for redox balance or pH control, (iv) enhance cell growth and (v) in some cases enhance product recovery (Schievano et al., 2016). The electrodes used in the electrochemical cell can act as electron sinks, as source of electrons or polarize ions present in microbes that allow an unbalanced growth. Such electrochemical modifications also exert significant effects on not only metabolism and cellular regulation, but also on interspecies interactions as well as the selection of microbial populations (Moscoviz et al., 2016). The novel yeast strains of *S. cerevisiae* (CDBT2) and *W. anomalous* (CDBT7), identified in our laboratory, are used in this study to determine better utilization of glucose and xylose from lignocellulosic biomass and enhancement in ethanol production in an electrochemical cell. The lignocellulosic biomass used in the study was obtained from *Saccharum spontaneum* pretreated with hot water at 100°C for 2 h followed by 0.5 M hydrochloric acid hydrolysis (Joshi et al., 2018).

MATERIALS AND METHODS

Materials

Woven graphite felt (10 mm thickness) was purchased from Nippon Co., Nippon, Japan. Platinum wire (0.2 mm diameter), high grade neutral red, ethanol, and thionyl chloride were purchased from Sigma Chemical Co., St. Louis, MO, USA. Electrochemical cell (ECC) vessels made up of Pyrex glass were purchased from Adams and Chittenden Scientific Glass Co., California, USA. Nafion 117 membrane was purchased from DuPont Co., Wilmington, DE, USA. Hydrogen hexachloroplatinate (IV) hexahydrate (Kanto Chemicals Company, Japan) was kindly provided by Prof. Dr. Amar Prasad Yadav, Central Department of Chemistry, Tribhuvan University, Nepal. D-Glucose, dinitro salicylic acid (DNSA), sodium potassium tartrate, yeast extract, peptone, ammonium sulfate and sodium alginate were purchased from Hi-Media Company, Bangalore, India. All other chemical were of analytical grade and were available locally.

Biomass samples of *S. spontaneum* was harvested from the premises of Tribhuvan University Campus, Kirtipur, Kathmandu, Nepal during the month of August. The sampling

location was 27.6818°N and 85.2865°S. The aerial portion of the collected sample was air dried for 24 h and cut into about 2 cm pieces. It was further dried in oven at 60°C for 24 h. The dry samples were ground using a blender. The blended biomass was sieved using 250–500 μm sieves and packed into plastic pouches for further use in fermentation studies.

Methods

Ethanol Production in Electrochemical Cell

Development of CDBT2 and CDBT7 inoculums

Preserved yeast strains CDBT2 (Gene Bank accession # MK910215) and CDBT7 (Gene Bank accession # MK910216) were used to develop inoculums. Inoculums were prepared by inoculating a loop-full of agar cultures of CDBT2 and CDBT7 strains into PYN (Peptone, Yeast extract and Nutrient) media (Peptone: 3.5 gm·L^{-1}, yeast extract: 3 gm·L^{-1}, KH_2PO_4: 2 gm·L^{-1}, MgSO4:1 gm·L^{-1}, and $(NH_4)_2SO_4$: 1 gm·L^{-1}) (Balakumar and Arasaratnam, 2012) supplemented with 5% glucose. They were cultured in orbital shaker for 18 h at 30°C and pH 5.0.

Construction of an electrochemical cell (ECC)

The anodic and cathodic compartment of ECC was assembled tightly using a rubber gasket inserted with nafion membrane that separates the two chambers (**Figure 1**). Working volume of the cathodic and anodic compartments were ∼300 mL each. Normal graphite felt (11 cm × 3 cm × 1 cm) was used as cathode and platinum wire (0.2 mm diameter, 1 m length) was used as anode. Each time 1.2 mL of respective inoculum, prepared above, was added with 300 mL PYN media in each case.

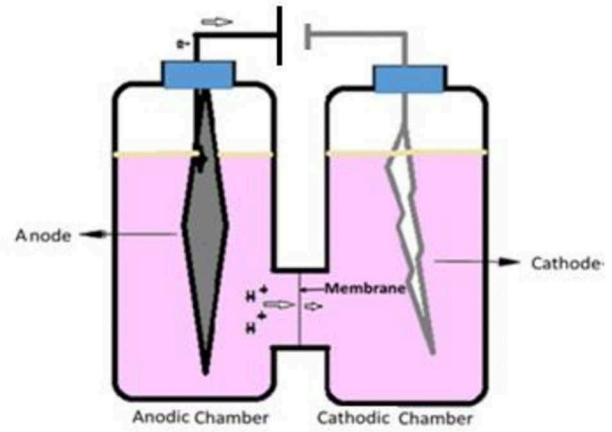

FIGURE 1 | The electrochemical cell (ECC): The ECC was assembled using the Pyrex glass fuel cell assembly as shown in the figure, separated by a nafion membrane using a leak-proof rubber gasket. The electrodes were inserted through small openings in each of the chamber caps and then connected to a power pack to supply external voltage.

Optimization of ethanol production in an ECC

The yeast strains CDBT2 and CDBT7 were cultured in ECC (**Figure 1**) and evaluated for ethanol production in the presence of carbohydrate sources, i.e., glucose (5%) and lignocellulosic biomass hydrolysate (with 3.3% reducing sugar). Lignocellulosic biomass hydrolysate was prepared by collecting the hydrolysate that was formed after pretreating *Saccharum spontaneum* biomass (250–500 μm size) with hot water at 100°C for 2 h followed by hydrolyzing with 0.5M HCl for 24 h. The 5% glucose or biomass hydrolysate acted as carbohydrate sources (Joshi et al., 2018). PYN media composition was added as supplements. The fermentation media in ECC without culture and the external source of voltage served as control. The two compartments of the ECC were filled with PYN media supplemented with glucose or lignocellulosic biomass hydrolysate, inoculated with yeast strains and allowed to produce ethanol in the presence and absence of applied voltage at an optimized pH 5.5 and 30°C (Joshi et al., 2014).

Ethanol production by yeast strains CDBT2 and CDBT7 under applied voltage

In the first fermentation reaction, the yeast strains CDBT2 and CDBT7 were cultured in cathodic and anodic chambers, respectively. In a second fermentation reaction, the yeast strains CDBT2 and CDBT7 were cultured in anodic and cathodic chambers, respectively. In each of the above reactions, the ECC was supplied with 4V constantly. Ethanol production by yeast strains CDBT2 and CDBT7 in ECC was monitored at intervals of 12 h as described by Seo et al. (2009). The sample broth (1 mL) collected from ECC was initially centrifuged at 4000 × g for 15 min to remove cell debris. The supernatant was then mixed with 1 mL tri n-butyl phosphate (TBP), vortexed for 15 min and centrifuged at 4000 × g for 15 min to separate layers. About 750 μL of upper TBP layer was transferred to another tube and mixed with equal amount of acidified 5% potassium dichromate reagent. The mixture was vortexed, centrifuged as above and lower green layer (potassium dichromate reagent layer) was separated and its absorbance was measured at 595 nm using spectrophotometer against blank. Cell growth was monitored by measuring turbidity of culture broth at 600 nm. The reduction in reducing sugar concentrations in the broth samples were measured by DNSA method (Miller, 1959).

Formation of film in graphite electrode by yeast

Biofilm formation was analyzed by Scanning Electron Microscopy (SEM). After completion of experiment in ECC, graphite electrodes kept as cathode with cultures of CDBT2 and CDBT7 were vacuum evaporated and packed in sterile plastic pouch. The samples were sent to Advanced Instrumental Lab, Jawaharlal Nehru University, New Delhi, India for SEM. The biofilm formation was confirmed from the micrograph.

Ethanol production by CDBT2 and CDBT7 at different voltage

To determine optimum supply of external voltage for ethanol production, the ECC voltage was varied between 0 and 5V (± 0.1 V), at an interval of 1V and ethanol production was measured as above.

Comparison of ethanol production by CDBT7 vs. several strains of S. cerevisiae

To compare the ethanol production efficiency of CDBT2 with other *S. cerevisiae*, ethanol production in the anodic compartment of ECC was monitored by culturing *S. cerevisiae* strains obtained from different sources. Yeast strains MKY09 (a laboratory yeast strain) and Ethanol Red (an industrial yeast strain) were kindly provided by Prof. Eckhard Bole, University of Frankfurt, Germany. Yeast strain MKY09 transformed with pGPD2 plasmid inserted with laccase gene (pGPD2/lac) was developed at Central Department of Biotechnology, Tribhuvan University, Nepal (Bishwakarma, 2017). The plasmid pGPD2/lac was constructed by cloning synthetic laccase gene of *Ganoderma lucidum* of size 1,576 bp in pGPD2 expression vector purchased from Addgene Company. The constructed plasmid was transformed into MKY09 strain. Yeast strain CDBT7 was cultured in cathodic compartment in all cases. The two chambers were separated by nafion membrane. The ethanol production was measured as described above.

Effect of different electron transport enhancing system in ECC

Production of ethanol was monitored in cathodic and anodic compartments by culturing yeast strains CDBT2 and CDBT7 in various combinations as follows. In reaction 1, yeast strain CDBT2 was cultured in both the compartments. In reaction 2, yeast strains CDBT2 and CDBT7 were cultured in anodic and cathodic compartments, respectively. In reaction 3, yeast strains CDBT2 and CDBT7 were co-cultured in both cathodic and anodic compartments. In all reactions, ethanol production was monitored as above. In the next set of reactions, the graphite felt (cathode) and platinum wire (anode) were coated with different electron transport enhancers and used as cathode and anode in ECC. In first case, the graphite electrode was immobilized with yeast cells using calcium alginate gel and used as cathode. Briefly, about 2.4 mL of 18 h culture of yeast strains were first centrifuged, the pellet mixed with 10 mL of 25 mM phosphate buffer (pH 7.0) containing 4% sodium alginate, and allowed to absorb into the graphite electrode for 30 min. The graphite electrode containing alginate and yeast cells was then soaked in a chilled 100 mM $CaCl_2$ solution for 30 min to induce calcium alginate coagulation and finally washed with 25 mM phosphate buffer. In the second case, the platinum electrode was coated with platinum nanoparticle electrochemically in anode. For this platinum wire was dipped in 10% hydrogen hexachloroplatinate (IV) hexahydrate solution in distilled water (Kanto Chemical Co.) with constant supply of 0.2 V using Hokuto Denko-151 potentiostat (Hokuto Denko Corporation, Japan) for 30 min. In the third case, the cathode was coated with neutral red as described by Jeon and Park (2010). Briefly, the graphite felt was first soaked in methanol, then dipped in 1% polyvinyl alcohol solution for 3 to 4 h and was dried in an oven at about 80°C for 24 h. The completely dried graphite felt was then soaked in pure chloroform containing 10% thionylchloride and 0.01% neutral red for 6 h. The graphite felt was then left for 12 h to air dry. It was then autoclaved and washed in running distilled water till color persists. Finally, it was dried at 60°C for 24 h and used as cathode. Best combination of electron transport system amongst was determined on the basis of higher ethanol production.

Ethanol Production by Lignocellulosic Biomass Hydrolysate as Carbohydrate Source

Ethanol production from hydrolysate

Lignocellulose biomass hydrolysate supplemented with PYN media was used for further fermentation to produce ethanol. The hydrolysates were kept in ECC chambers. After autoclaving, the chambers were inoculated with CDBT2 and CDBT7 yeast strains in anodic and cathodic chambers, respectively. The two chambers were separated by a nafion membrane. Ethanol production was measured as described above.

Comparison of ethanol production by nafion and cellulose acetate membrane

The experiments above were repeated in an ECC fitted with a cellulose acetate membrane to separate the two chambers. Ethanol production was measured as above and compared to those determined when the separating membrane was nafion membrane.

Statistical Analysis

All the data presented were the average of three redundant data. All graphs and statistical calculations were performed with Graph Pad Prism 8.0.1. Standard errors were represented in terms of ± standard deviation (±SD).

RESULTS

Optimization of Ethanol Production in an Electrochemical Cell (ECC)

The standard conditions under which fermentation was performed in the ECC (schematic of ECC assembly shown in **Figure 1**) using various yeast strains were pH 5.5, 30°C, PYN broth supplemented with 5% glucose and an external supply of 4V. The fermentation system in which CDBT2 strain was cultured in anodic compartment and CDBT7 strain in cathodic compartment was found to be most efficient for ethanol production than culturing CDBT2 strain in cathodic compartment and CDBT7 strain in anodic compartment (**Figures 2A,B**, **Table 1**). Scanning electron microscopic imaging showed the formation of a film of CDBT7 in graphite felt electrode (**Figure 3**). The fermentation efficiency was enhanced in both cathodic and anodic chamber cultures as compared to fermentation reactions carried out in the absence of applied voltage. There was observed faster and enhanced growth of CDBT2 in anodic compartment (**Figure 2C**). On the other hand, growth of CDBT2 strain when cultured in cathodic compartment was relatively limited. The CDBT7 strain when cultured in anodic compartment, showed relatively lower enhancement in ethanol production (**Table 1**). On application of external voltage in the range of 0 to 5V (± 0.1V), while

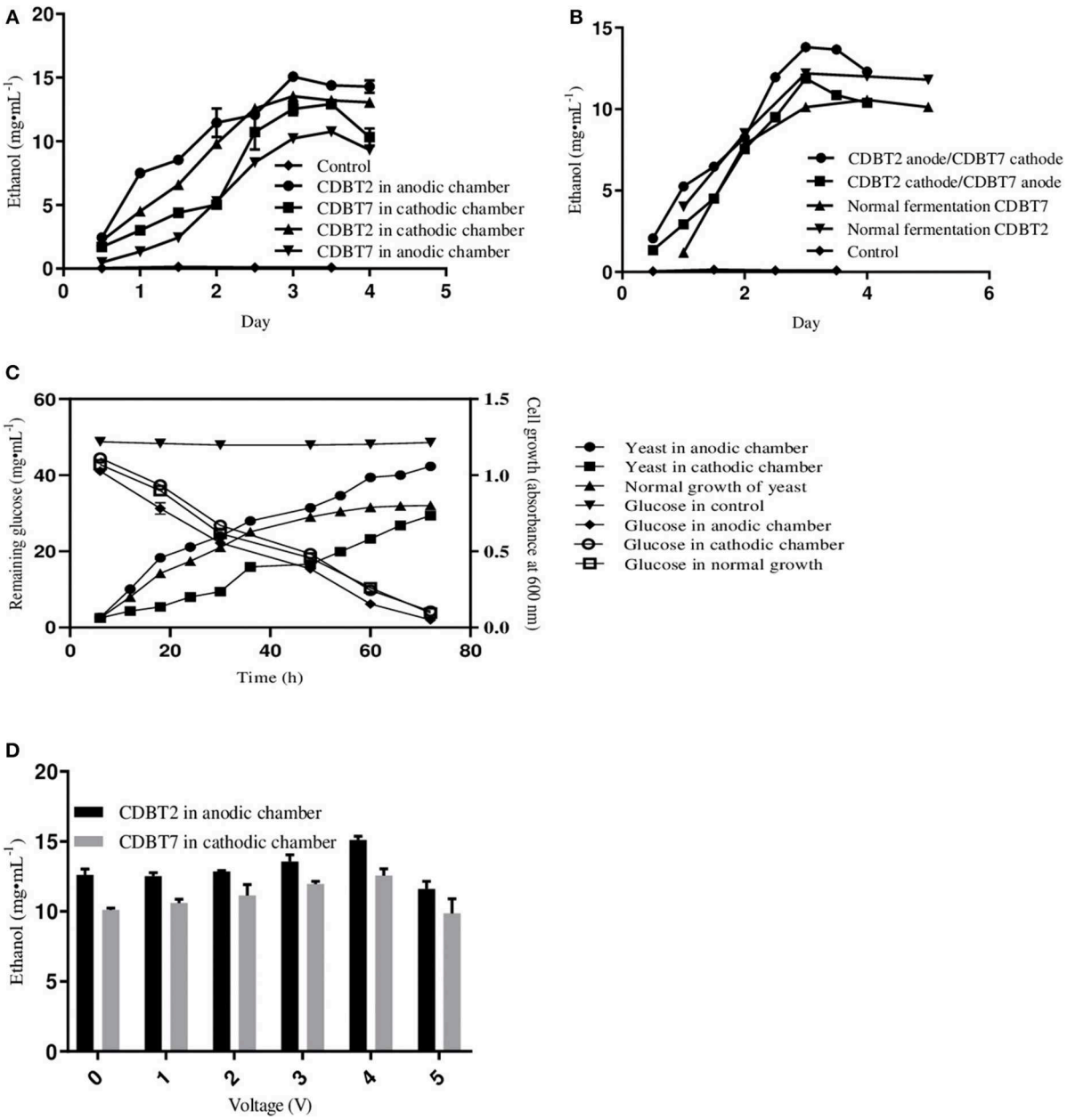

FIGURE 2 | Ethanol production in ECC by yeast strains CDBT2/CDBT7 with the supply of 4V externally. **(A)** Ethanol production in cathodic and anodic chambers by CDBT2 and CDBT7 individually. **(B)** Average of ethanol production in both chambers. **(C)** Cell growth and glucose utilization when CDBT2 cultured in anodic and cathodic chambers with and without applied external voltage (normal growth—without the supply of external voltage). **(D)** Effect of applied electrical current on ethanol production by CDBT2 and CDBT7. (Control: ECC w/o/yeast culture and w/o voltage supply; normal fermentation: ECC w/o voltage supply).

CDBT2 was cultured in the anodic compartment and CDBT7 cultured in cathodic compartment, application of 4V produced the highest amount of ethanol (**Figure 2D**). The enhancement of ethanol production observed was 19.4 ± 0.18% when CDBT2 was cultured in anodic compartment and 23.7 ± 0.51% when CDBT7 was cultured in cathodic compartment. Supply of external voltage through ECC in the absence of yeast inoculums (negative control) did not produce detectable levels of ethanol.

Comparison of Ethanol Production by Various *S. cerevisiae* Strains Cultured in Anodic Compartment Coupled With CDBT 7 Strain Cultured in Cathodic Compartment

To determine the efficiency of ethanol production using different *S. cerevisiae* strains in ECC, ethanol production was monitored by culturing CDBT2, ethanol red, MKY09, and MKY09-pGPD2/lac in anodic compartment against CDBT7 in cathodic

TABLE 1 | Ethanol produced by CDBT2 and CDBT7 cultured in different compartments.

S. No.	CDBT2 in AC	CDBT7 in CC	CDBT2 CC	CDBT7 in AC	CDBT2*	CDBT7*
Ethanol ($mg{\cdot}mL^{-1}$)	15.1 ± 0.28	12.5 ± 0.49	13.5 ± 0.0	10.2 ± 0.0	12.6 ± 0.42	10.1 ± 0.14
% increment	19.8 ± 0.50	23.7 ± 0.51	7.14 ± 0.64	1.00 ± 0.14		

AC, Anodic chamber; CC, Cathodic chamber.
**Fermentation under normal conditions (no external source of electricity).*

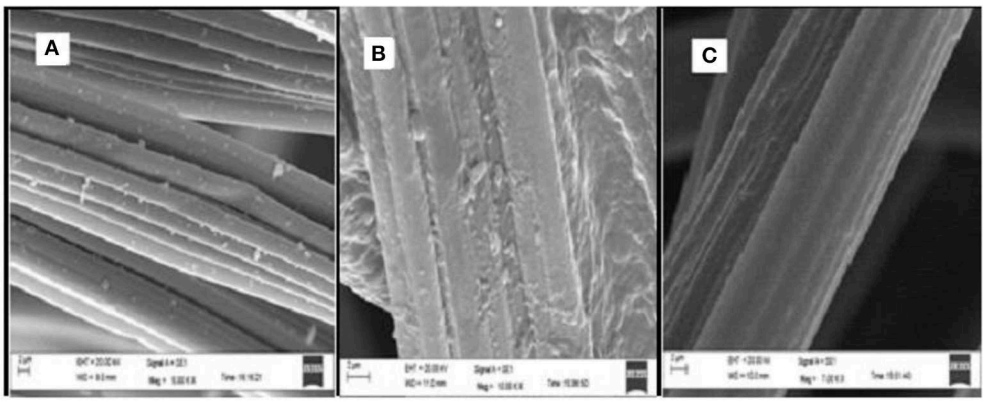

FIGURE 3 | Scanning electron microscopic images of graphite felt electrodes. **(A)** Plane graphite felt. **(B)** Graphite felt cathode post CDBT7 growth and ethanol production in the cathodic chamber. **(C)** Graphite felt cathode post CDBT2 growth and ethanol production in the cathodic chamber.

compartment. Once again, CDBT2 produced the highest amount of ethanol (**Figure 4A**) as compared to other *S. cerevisiae* strains. Further, genetic modification of MKY09 strain by transforming it with a laccase gene (MKY09-pGPD2/lac) did not affect ethanol production in ECC, rather both MKY09 and MKY09-pGPD2/lac strains produced similar amounts of ethanol. In addition, yeast strain CDBT2 cultured in anodic chamber, coupled to CDBT7 strain cultured in cathodic chamber showed enhancement of the ethanol production by CDBT7 (**Figure 4B**).

Effect of Different Electron Transport Systems

Effect of Yeast Cultures

To determine the effect of yeast cultures on electron transport systems, yeast strains CDBT2 and CDBT7 were cultured in ECC in the following combinations; (i) CDBT2/CDBT2 in anodic/cathodic compartments; (ii) CDBT2/CDBT7 in anodic and cathodic compartments and (iii) co-culture of CDBT2 and CDBT7 in both compartments. In combination of CDBT2/CDBT2, it was found that CDBT2 yeast strain produced more ethanol in the anodic compartment (15.5 ± 0.14 $mg{\cdot}mL^{-1}$) as compared to cathodic compartment (13.4 ± 0.07 $mg{\cdot}mL^{-1}$). The average ethanol production in this combination was 14.4 ± 0.15 $mg{\cdot}mL^{-1}$ (**Table 2**) and the increase in ethanol production was 27.5 ± 0.44%. In combination of CDBT2/CDBT7, CDBT2 strain again produced more ethanol in anodic chamber (15.10 ± 0.28 $mg{\cdot}mL^{-1}$) as compared to CDBT7 strain in cathodic compartment (12.5 ± 0.50 $mg{\cdot}mL^{-1}$). The average ethanol production in this combination was 13.8 ± 0.56 $mg{\cdot}mL^{-1}$ (**Figure 5A**, **Table 2**) and the increase in ethanol production was 21.5 ± 0.71%. When CDBT2 and CDBT7 strains were co-cultured in both compartments, ethanol production was significantly lower as compared to individual cultures.

Effect of Immobilization of Yeast

Yeast strain CDBT7 immobilized in presence of calcium alginate on cathode, when used for ethanol production in an ECC with CDBT2 strain in anodic compartment, produced 12.6 ± 0.42 $mg{\cdot}mL^{-1}$ and 4.95 ± 0.07 $mg{\cdot}mL^{-1}$ ethanol by CDBT2 and CDBT7 strain respectively without the applied voltage i.e., there was a significant decrease in ethanol production (**Figure 5B**). The same system when used in ECC with the application external voltage input (4V), the ethanol production was significantly enhanced. The ethanol production in the latter case were 16.1 ± 0.49 $mg{\cdot}mL^{-1}$ (CDBT2 in anodic compartment) and 7.75 ± 0.5 $mg{\cdot}mL^{-1}$ (CDBT7 strain in the cathodic compartment), respectively. The average ethanol production was 11.5 ± 0.70 $mg{\cdot}mL^{-1}$ and the increase in ethanol production was 36.2 ± 0.54% than without voltage supply. However, the average ethanol production in ECC was less than without immobilization of CDBT7 in cathode. In summary, immobilization did not show the better enhancement in ethanol production.

Effect of Electron Transport Enhancing Materials

Coating of platinum electrode with fine particles (nanoparticles) of platinum using hexachloroplatinate (IV) and graphite cathode with neutral red, and culturing CDBT2 strain in anodic

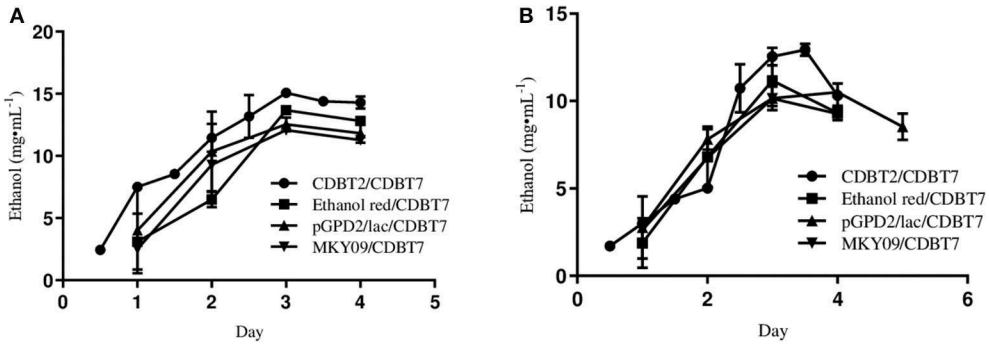

FIGURE 4 | Ethanol production by various *S. cerevisiae* strains cultured in anodic compartment of electrochemical cell with CDBT7 cultured in cathodic compartment: a comparative study. **(A)** Ethanol production in anodic compartment. **(B)** Ethanol production in cathodic compartment.

TABLE 2 | Ethanol production in an ECC with various combinations of anodic and cathodic systems for electron transport enhancement: summary.

S. no.	Culture types*	Ethanol in anodic chamber (mg·mL^{-1})	Ethanol cathodic chamber (mg·mL^{-1})	Average ethanol (mg·mL^{-1})	Average increase (%)
(A) YEAST COMBINATIONS					
1	CDBT2/CDBT7 Normal Fermentation with no Applied voltage	12.60 ± 0.42	10.10 ± 0.14	11.3 ± 0.44	
2	CDBT2/CDBT7 in ECC with 4V	15.1 ± 0.28	12.5 ± 0.49	13.8 ± 0.56	21.5 ± 0.71
3	CDBT2/CDBT2 in ECC with 4V	15.5 ± 0.14	13.4 ± 0.07	14.4 ± 0.15	27.5 ± 0.44
4	CDBT2+CDBT7 mixed/co-culture with 4V	13.2 ± 0.0	10.4 ± 0.71	11.8 ± 0.71	3.96 ±0.83
(B) IMMOBILIZED YEAST					
1	CDBT2/CDBT7 with CDBT7 Immobilized on Graphite Cathode without Applied Voltage	12.6 ± 0.42	4.95 ± 0.07	8.77 ± 0.42	
2	CDBT2/CDBT7 with CDBT7 immobilized on graphite cathode and 4V supply	16.1 ± 0.49	7.75 ± 0.50	11.9 ± 0.70	5.3 ± 0.82
(C) ELECTRON TRANSPORT SYSTEMS					
1	CDBT2/CDBT7 Pt coated Pt anode/graphite cathode	15.7 ± 0.16	14.0 ± 1.06	14.8 ± 1.07	30.9 ± 1.15
2	CDBT2/CDBT7 Pt anode and neutral red coated cathode	17.1 ± 0.07	15.7 ± 0.30	16.4 ± 0.30	44.6 ± 0.53
3	CDBT2/CDBT7 Pt coated Pt anode/neutral red coated cathode	17.5 ± 0.01	17.2 ± 0.01	17.3 ± 0.01	52.8 ± 0.44

**Normal fermentation: Yeast cultured in ECC without external voltage supply. The yeast strain listed first was used in the anodic compartment and the organism listed second was cultured in the cathodic compartment. Values reported are mean ± SD of 3 different independent experiments.*

compartment and CDBT7 strain in cathodic compartment produced 17.5 ± 0.01 mg·mL^{-1} and 17.2 ± 0.01 mg·mL^{-1} ethanol, respectively (**Figure 5C**). A significant increase in ethanol production (52.8 ± 0.44%) was observed than normal fermentation without voltage supply (**Table 2**).

Electrochemical Ethanol Production From *Saccharum spontaneum* Hydrolysate

When lignocellulosic (*Saccharum spontaneum)* hydrolysate with 3.3% reducing sugar was used as substrate for fermentation in ECC, there was significant enhancement in ethanol production in anodic (9.0 ± 0.1 mg·mL^{-1}; increase = 60.8 ± 0.10%) as well as in cathodic (11.9 ± 0.05 mg·mL^{-1}; increase = 63.0 ± 0.07%) compartments, with an average enhancement of 61.9 ± 0.12% than normal fermentation without voltage supply. Ethanol production by CDBT2 and CDBT7 without external voltage supply were 5.6 ± 0.03 and 7.3 ± 0.06 mg·mL^{-1}, respectively (**Figure 6**, **Table 3**). The increase in amount of ethanol produced, when the fermentation substrate was lignocellulosic hydrolysate, was much higher when compared to fermentation with glucose as substrate under identical conditions. In addition, when the membrane barrier was changed to cellulose acetate in place of nafion membrane, there was a further increase (6.30 ± 0.22%) in ethanol production (**Figure 7**, **Table 3**).

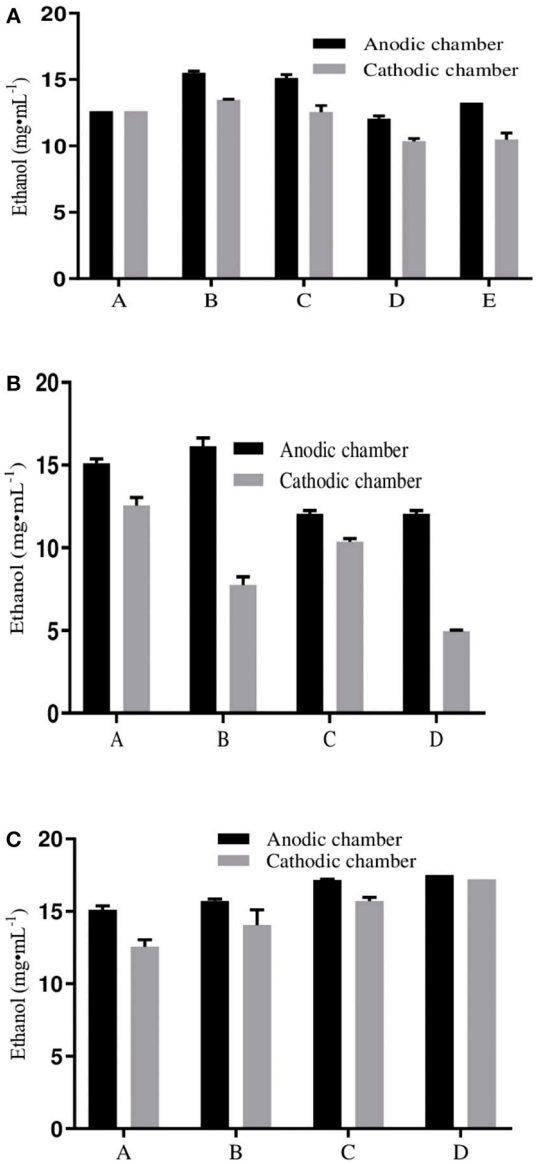

FIGURE 5 | Ethanol production with different electron transport enhancement systems. **(A)** Use of yeasts in various combinations in ECC (A: CDBT2 normal fermentation; B: CDBT2/CDBT2 in Electrochemical cell; C: CDBT2/CDBT7 in Electrochemical cell, D: CDBT2/CDBT7 normal fermentation, E: CDBT2/CDBT7 mixed culture). **(B)** Use of graphite electrode immobilized with CDBT7 yeast strain [A: Graphite cathode/Pt anode; B: Graphite cathode (immobilized with CDBT7)/Pt anode; C: Normal fermentation CDBT2/CDBT7; D: Normal fermentation CDBT2/CDBT7 immobilized in graphite]. **(C)** Use of electrodes coated with different electron transporters (A: Normal Platinum anode/graphite cathode; B: Platinum coated Platinum anode/graphite cathode; C: Neutral red coated graphite cathode/Platinum anode; D: Neutral red coated cathode/Pt coated anode).

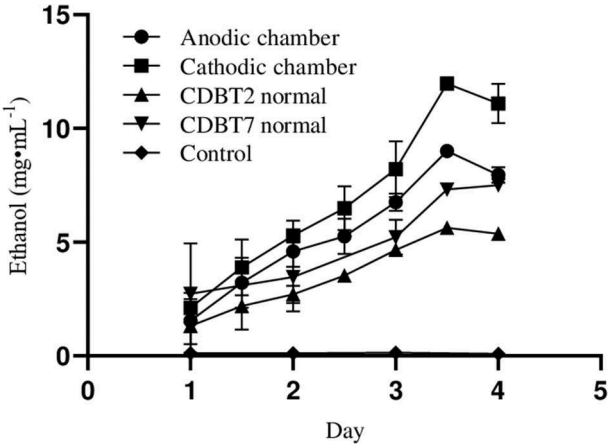

FIGURE 6 | Ethanol production from lignocellulosic hydrolysate (*S. spontaneum* pretreated with hot water for 2 h followed by 0.5M acid hydrolysis) in ECC with CDBT2 and CDBT7 strains cultured in anodic and cathodic compartments, respectively (Control: ECC without yeast culture and without external voltage supply. Normal: ECC with yeast culture and without external voltage supply).

DISCUSSION

S. cerevisiae CDBT2 and *W. anomalus* CDBT7 yeast strains were selected for the study because both are good ethanol producers and the later has been shown to be capable of converting xylose into ethanol. The pH optima for ethanol production using yeast strains CDBT2 and CDBT7 were pH 5.5 and temperature 30°C, respectively. The conditions were consistent with our previous experiments with optimization of yeast strains CDBT2 (Joshi et al., 2014). The ECC system with CDBT2 in anodic compartment and CDBT7 in cathodic compartment, produced the highest amount of ethanol as compared to reverse system tested. This may be because CDBT7 strain forms film on graphite cathode resulting in fast electron transport through cathode. This was further supported by the fact that (i) SEM images of cathode surface clearly show CDBT7 biofilm formation (**Figure 3**), and (ii) use of CDBT7 immobilized cathode resulted in significant fold increase in ethanol production when cultured in ECC (**Table 2**) (Toit and Pretorius, 2000). Further, the study by Mohamoud (2014) suggests that supply of external voltage enhances film redox potential and thus results in enhancing more electron transport and more ethanol production. According to that study there was 40% enhancement in film redox potential when electricity was passed to electrode with polyaniline/polyvinyl composite. Canelas et al. (2008) observed that ethanol formation requires the maintenance of NAD^+/NADH ratios. In healthy eukaryotes, NAD^+/NADH ratios usually are relatively high and the range varies widely (60–700). Canelas et al. (2008) also observed that the cytosolic free NAD^+/NADH ratio in *S. cerevisiae* under steady and highly dynamic state ranges between 101 ± 14 and 320 ± 45 where as whole cell NAD^+/NADH ratio was 7.5 ± 2.5. Further it was observed that in *S. cerevisiae* NAD^+/NADH ratio was reduced when there is presence of electron donor and the ratio was increased in the presence of electron acceptor. In our case, when yeast strain was cultured in cathodic compartment, there was increment in ethanol production because the cathode was the electron donor, thus resulting more conversion of NAD^+ to NADH

which has directed the conversion of pyruvate to ethanol. Reversibly when yeast strain cultured in anodic compartment which is electron acceptor, converted NADH to NAD^+ which had directed fast conversion of glucose to pyruvate so that we could see enhancement in growth and ethanol formation as well. In spite of the ratios reported above, eukaryotes could survive even when the NAD^+/NADH ratio was as low as 7–10 (Veech et al., 1972). The supplied external voltage input polarizes ions present in cytosol and as a result positively charged NAD^+ ion bound to cell membrane make the transfer of electrons from cathode easier and faster (Gunawardena et al., 2008; McGillivray and Gow, 2009) thus makes it easy to access for reduction of NAD^+ to NADH in cathode resulting more ethanol production. According to Yau et al. (2013), the applied voltage was believed to polarize ionic charges in yeast cells, which may lower the tunnel barrier for transferring electrons during glucose oxidation resulting more pyruvate and hence more cell growth and ethanol production.

The pyruvate formed during glycolysis is converted to (i) acetyl CoA under aerobic conditions in eukaryotes, (ii) lactate during homolactic fermentation in mammals, or (iii) ethanol during anaerobic fermentation in yeast and bacteria. When an external voltage was supplied, NAD^+ was directly converted to NADH, increasing the level of NADH. This is known to cause an imbalance in the growth of yeasts that favors production of ethanol by forcing the yeast to convert pyruvate to acetaldehyde and then to ethanol by consuming NADH. It has also been shown that increased NADH allosterically inhibits pyruvate dehydrogenase (Harris et al., 2002) and prevents conversion of pyruvate to acetyl coenzyme A. Accordingly, pyruvate can be diverted to ethanol formation. Song et al. (2014) have shown that external input of voltage can be used to control the kinetics of glucose metabolism in *S. cerevisiae* under both aerobic and anaerobic conditions. Here, intracellular electron carriers such as NAD^+, NADH and the transplasma membrane electron transfer (tPMET) system located in the plasma membrane plays important role for direct transport of electrons through cell membrane. tPMET system consists of cytochromes and various redox enzymes such as NADH oxidase which provides redox activity to the membrane at specific sites.

In reality, for reduction of NAD^+/NADH ratio, applied voltage requirement is around −0.33V (Veech et al., 1972). In our experiments, we can see that optimal ethanol production was obtained at 4V ± 0.1V. The higher voltage, we believe, was because of ohmic drop exerted by the designed ECC. Mathew et al. (2015) have reported the gradual increase in growth by 1.1 fold and ethanol production by 2 fold when *S. cerevisiae* was cultured with external voltage supply till 15V. In our study, increasing voltage beyond 4V reduces ethanol production. This may be because, increasing voltage might oxidize Platinum to Platinum dioxide which acted as insulator and decreased the activity of electrode (Wang et al., 2006). Similarly in cathode, there might be overproduction of hydrogen gas which might decrease the activity of graphite electrode (Hsu et al., 2008). Further, when mixed culture of yeast strains CDBT2 and CDBT7 were used, ethanol production was relatively low. This may be because when *S. cerevisiae* and *W. anomalous* were cultured together,

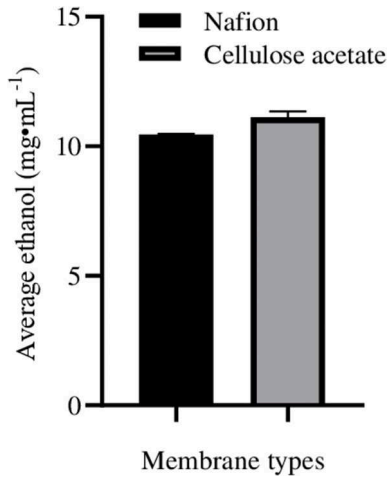

FIGURE 7 | Ethanol production from lignocellulosic hydrolysate (*S. spontaneum* pretreated hot water for 2 h followed by 0.5M acid hydrolysis) in ECC with CDBT2 and CDBT7 in anodic and cathodic compartments separated by nafion membrane or cellulose acetate membrane. Ethanol measurements in the cultures were determined after 3.5 days of fermentation.

growth of *W. anomalous* may have suppressed the growth of *S. cerevisiae* thus decreased the overall ethanol production (Ruyters et al., 2015).

Steinbusch et al. (2010) have reported an increase in more than 2 fold enhancement of ethanol production in the presence of an external source of electrical current when acetate was used as substrate for fermentation. He et al. (2016), have reported 60.3% enhancement in butanol production by *Clostridium spp*. when neutral red was used as electron transporter. He et al. have also demonstrated that neutral red increased the butanol production better than other electron transporters such as viologen dyes (dyes containing pyridine groups). Further neutral red can strongly bind to cell membranes (Park et al., 1999). It has a redox potential of about −0.325V which is similar to that of the redox potential of NADH (−0.32 V). Accordingly neutral red could interact with NADH and, thus, increase the level of NAD^+/NADH giving rise to more ethanol. The decrease in ethanol production in immobilized culture was because immobilization reduces substrate diffusion and hence ethanol production was less than in normal growth whereas it enhances fast electron transport at the intersection of the electrode.

The increase in ethanol production due to applied external source of voltage was further more when acid hydrolyzed *Saccharum spontaneum* hydrolysate was used as substrate. This may be because; the NaCl present in the neutralized hydrolysate may help in enhancement of ethanol production by decreasing resistance. In fact, Yang et al. (2015) have shown that when the concentrations of NaCl was increased from 5 to 30 $g{\cdot}L^{-1}$ in the fermentation media, the internal resistances of the system decreases from 2432.0 to 2328.4 Ω. Similarly, Kamcev et al. (2018) also observed that increasing salt concentration increases electrical conductivity hence increases electron flow and reduces resistance. Accordingly, the increased conductivity is likely

TABLE 3 | Ethanol produced by CDBT2 and CDBT7 cultured with lignocellulosic biomass hydrolysate.

S. no.	CDBT2 in AC	CDBT7 in CC	Average production	CDBT2*	CDBT7*
Ethanol ($mg{\cdot}mL^{-1}$)	9.01 ± 0.1	11.9 ± 0.05	10.4 ± 0.11	5.60 ± 0.03	7.30 ± 0.06
% Increase	60.8 ± 0.10	63.0 ± 0.07	61.9 ± 0.12		

AC, Anodic chamber; CC, Cathodic chamber.
**Fermentation under normal conditions (no external source of electricity).*

to promote ethanol production. The increased production of ethanol from lignocellulosic biomass could also be partly due to the presence of various natural products/substance present in the mixture that could promote growth of yeast strains. Alteration of cellulose acetate membrane in place of nafion membrane enhanced ethanol production. The latter could be due to transport of xylose across cellulose acetate membrane from anodic chamber to cathodic chamber, as well as decrease in internal resistance due to ion accumulation on the membrane surface (Tang et al., 2010).

CONCLUSION

In summary, a combination of yeast strains *S. cerevisiae* CDBT2 and *W. anomalous* CDBT7 effectively and efficiently produce ethanol from both glucose and lignocellulosic biomass hydrolysate. Use of CDBT2/CDBT7 strains in an ECC efficiently utilize reducing sugars as indicated by near complete utilization of reducing sugars. Ethanol production by CDBT2 and CDBT7 yeast strains can be enhanced by supplying low levels of external voltage. *S. cerevisiae* CDBT2 was most efficient at ethanol production in the anodic compartment, whereas *W. anomalous* CDBT7 yeast strain was most efficient in ethanol production in the cathodic compartment. Further enhancement of ethanol production was observed when ECC was operated with fine platinum nanoparticles coated on the platinum anode, and neutral red was deposited on graphite cathode. Hot water pretreated and mineral acid hydrolyzed lignocellulosic biomass (an economic method) can be used as substrate for fermentation in ECC with CDBT2 and CDBT7 strains. An additional advantage of using hydrolyzed lignocellulosic biomass was that it further enhances ethanol production in ECC. Given the data reported herein, yeast strain CDBT2 could serve as a potent industrial strain for genetic modification and ethanol production. One of the limitation of this study is to go for further scaled up. It is strongly believed that the scale up of this study is entirely feasible with the availability of large electrochemical fermentation cell and is next phase of our study.

DATA AVAILABILITY

All datasets generated for this study are included in the manuscript/supplementary files.

AUTHOR CONTRIBUTIONS

JJ performed laboratory work and prepared manuscript draft. TB, LS, and AY edited manuscript. PD, BP, PP, MY, MM, and RM helped in laboratory works. All the authors revised the manuscript and approved the submitted version.

ACKNOWLEDGMENTS

Mr. Sujan Bishwokarma, Central department of biotechnology, Tribhuvan University, Renewable Nepal funding program are highly acknowledged for their support.

REFERENCES

Balakumar, S., and Arasaratnam, V. (2012). Osmo-, thermo- and ethanol- tolerances of. *Braz. J. Microbiol.* 43, 157–166. doi: 10.1590/S1517-838220120001000017

Bishwakarma, S. (2017). *Heterologous expression of laccase gene of Ganoderma lucidum in Saccharomyces cerevisiae for degradation of lignocellulosic biomass* (M. Sc. Thesis). Tribhuvan University, Registration No.:5-1-48-301-2007.

Canelas, A. B., Van Gulik, W. M., and Heijnen, J. J. (2008). Determination of the cytosolic free NAD/NADH ratio in *Saccharomyces cerevisiae* under steady-state and highly dynamic conditions. *Biotechnol. Bioeng.* 100, 734–743. doi: 10.1002/bit.21813

Gunawardena, A., Fernando, S., and To, F. (2008). Performance of a yeast-mediated biological fuel cell. *Int. J. Mol. Sci.* 9, 1893–1907. doi: 10.3390/ijms9101893

Haque, M., and Epplin, F. M. (2012). Cost to produce switchgrass and cost to produce ethanol from switchgrass for several levels of biorefinery investment cost and biomass to ethanol conversion rates. *Biomass Bioenergy* 46, 517–530. doi: 10.1016/j.biombioe.2012.07.008

Harris, R. A., Bowker-kinley, M. M., and Huang, B. (2002). Regulation of the activity of the pyruvate dehydrogenase complex. *Adv. Enzyme Regul.* 42, 249–259.

He, A. Y., Yin, C. Y., Xu, H., Kong, X. P., Xue, J. W., Zhu, J., et al. (2016). Enhanced butanol production in a microbial electrolysis cell by *Clostridium beijerinckii* IB4. *Bioprocess Biosyst. Eng.* 39, 245–254. doi: 10.1007/s00449-015-1508-2

Hermosilla, E., Schalchli, H., Mutis, A., and Diez, M. C. (2017). Combined effect of enzyme inducers and nitrate on selective lignin degradation in wheat straw by *Ganoderma lobatum*. *Environ. Sci. Pollut. Res.* 24, 21984–21996. doi: 10.1007/s11356-017-9841-4

Hsu, P. C., Seol, S. K., Lo, T. N., Liu, C. J., Wang, C. L., Lin, C. S., et al. (2008). Hydrogen bubbles and the growth morphology of ramified zinc by electrodeposition. *J. Electrochem. Soc.* 155:D400. doi: 10.1149/1.2894189

Jeon, B. Y., and Park, D. H. (2010). Improvement of ethanol production by electrochemical redox combination of *Zymomonas mobilis* and *Saccharomyces cerevisiae*. *J. Microbiol. Biotechnol.* 20, 94–100. doi: 10.4014/jmb.0904.04029

Joshi, B., Bhatt, M. R., Sharma, D., Joshi, J., Malla, R., and Sreerama, L. (2011). Lignocellulosic ethanol production: current practices and recent

developments. *Biotechnol. Mol. Biol. Rev.* 6, 172–182. doi: 10.1111/j.1540-8159.2011.03289.x

Joshi, J., Bhattarai, T., and Sreerama, L. (2018). Efficient methods of pretreatment for the release of reducing sugars from lignocellulosic biomass native to Nepal and characterization of pretreated lignocellulosic biomass. *Int. J. Adv. Biotechnol. Res.* 9, 9–23.

Joshi, J., Shrestha, R., Manandhar, R., Manandhar, K., Sreerama, L., and Bhattarai, T. (2014). Improvement of ethanol production by electrochemical redox combination of yeast cells. *Int. J. Biol. Sci. Appl.* 1, 46–54. doi: 10.13140/RG.2.2.19735.06564

Kamcev, J., Sujanani, R., Jang, E. S., Yan, N., Moe, N., Paul, D. R., et al. (2018). Salt concentration dependence of ionic conductivity in ion exchange membranes. *J. Membrane Sci.* 547, 123–133. doi: 10.1016/j.memsci.2017.10.024

Khatiwada, D., and Silveira, S. (2011). Greenhouse gas balances of molasses based ethanol in Nepal. *J. Clean. Prod.* 19, 1471–1485. doi: 10.1016/j.jclepro.2011.04.012

Mathew, A. S., Wang, J., Luo, J., and Yau, S. T. (2015). Enhanced ethanol production via electrostatically accelerated fermentation of glucose using *Saccharomyces cerevisiae*. *Sci. Rep.* 5, 1–6. doi: 10.1038/srep15713

McGillivray, A. M., and Gow, N. A. R. (2009). Applied electrical fields polarize the growth of mycelial fungi. *Microbiology* 132, 2515–2525. doi: 10.1099/00221287-132-9-2515

Miller, G. L. (1959). Use of dinitrosalicylic acid reagent for determination of reducing sugar. *Anal. Chem.* 31, 426–428.

Mohamoud, M. A. (2014). Unexpected redox enhancement and electrochemical pseudo-capacitance performance of polyaniline/poly(vinyl alcohol) (PAn/PVA) composite films. *Electrochim. Acta* 139, 201–208. doi: 10.1016/j.electacta.2014.06.174

Moscoviz, R., Toledo-Alarcón, J., Trably, E., and Bernet, N. (2016). Electro-fermentation: how to drive fermentation using electrochemical systems. *Trends Biotechnol.* 34, 856–865. doi: 10.1016/j.tibtech.2016.04.009

Park, D. H., Laivenieks, M., Guettler, M. V., Jain, M. K., and Zeikus, J. G. (1999). Microbial utilization of electrically reduced neutral red as the sole electron donor for growth and metabolite production. *Appl. Environ. Microbiol.* 65, 2912–2917.

Rose, M., and Palkovits, R. (2011). Cellulose-based sustainable polymers: state of the art and future trends. *Macromol. Rapid Commun.* 32, 1299–1311. doi: 10.1002/marc.201100230

Ruyters, S., Mukherjee, V., Verstrepen, K. J., Thevelein, J. M., Willems, K. A., and Lievens, B. (2015). Assessing the potential of wild yeasts for bioethanol production. *J. Ind. Microbiol. Biotechnol.* 42, 39–48. doi: 10.1007/s10295-014-1544-y

Saisirirat, P., and Joommanee, B. (2017). Study on the performance of the micro direct ethanol fuel cell (Micro-DEFC) for applying with the portable electronic devices. *Energy Proc.* 138, 187–192. doi: 10.1016/j.egypro.2017.10.148

Schievano, A., Pepé Sciarria, T., Vanbroekhoven, K., De Wever, H., Puig, S., Andersen, S. J., et al. (2016). Electro-fermentation – merging electrochemistry with fermentation in industrial applications. *Trends Biotechnol.* 34, 866–878. doi: 10.1016/j.tibtech.2016.04.007

Seo, H. B., Kim, H. J., Lee, O. K., Ha, J. H., Lee, H. Y., and Jung, K. H. (2009). Measurement of ethanol concentration using solvent extraction and dichromate oxidation and its application to bioethanol production process. *J. Ind. Microbiol. Biotechnol.* 36, 285–292. doi: 10.1007/s10295-008-0497-4

Song, Y., Wang, J., and Yau, S. T. (2014). Controlled glucose consumption in yeast using a transistor-like device. *Sci. Rep.* 4, 1–7. doi: 10.1038/srep05429

Steinbusch, K. J., Hamelers, H. V., Schaap, J. D., Kampman, C., and Buisman, C. J. (2010). Bioelectrochemical ethanol production through mediated acetate reduction by mixed cultures. *Environ. Sci. Technol.* 44, 513–517. doi: 10.1021/es902371e

Tang, X., Guo, K., Li, H., Du, Z., and Tian, J. (2010). Microfiltration membrane performance in two-chamber microbial fuel cells. *Biochem. Eng. J.* 52, 194–198. doi: 10.1016/j.bej.2010.08.007

Toit, D. M., and Pretorius, I. S. (2000). Microbial spoilage and preservation of wine: using weapons from nature's own arsenal - a review. *S. Afr. J. Enol. Vitic.* 21, 74–96.

Veech, R. L., Guynn, R., and Veloso, D. (1972). The time-course of the effects of ethanol on the redox and phosphorylation states of rat liver. *Biochem. J.* 127, 387–397. doi: 10.1042/bj1270387

Wang, X., Kumar, R., and Myers, D. J. (2006). Effect of voltage on platinum dissolution. *Electrochem. Sol. State Lett.* 9, A225–A227. doi: 10.1149/1.2180536

Yang, E., Choi, M. J., Kim, K. Y., Chae, K. J., and Kim, I. S. (2015). Effect of initial salt concentrations on cell performance and distribution of internal resistance in microbial desalination cells. *Environ. Technol.* 36, 852–860. doi: 10.1080/09593330.2014.964333

Yau, S. T., Xu, Y., Song, Y., Feng, Y., and Wang, J. (2013). Voltage-controlled enzyme-catalyzed glucose-gluconolactone conversion using a field-effect enzymatic detector. *Phys. Chem. Chem. Phys.* 15, 20134–20139. doi: 10.1039/c3cp52004h

Conflict of Interest Statement: The authors declare that the research was conducted in the absence of any commercial or financial relationships that could be construed as a potential conflict of interest.

frontiers in Energy Research

ORIGINAL RESEARCH
published: 23 August 2019
doi: 10.3389/fenrg.2019.00079

Evolutionary Relationships Between Low Potential Ferredoxin and Flavodoxin Electron Carriers

Ian J. Campbell[1], *George N. Bennett*[2,3] *and Jonathan J. Silberg*[2,3,4]*

[1] Biochemistry and Cell Biology Graduate Program, Rice University, Houston, TX, United States, [2] Department of BioSciences, Rice University, Houston, TX, United States, [3] Department of Chemical and Biomolecular Engineering, Rice University, Houston, TX, United States, [4] Department of Bioengineering, Rice University, Houston, TX, United States

Proteins from the ferredoxin (Fd) and flavodoxin (Fld) families function as low potential electrical transfer hubs in cells, at times mediating electron transfer between overlapping sets of oxidoreductases. To better understand protein electron carrier (PEC) use across the domains of life, we evaluated the distribution of genes encoding [4Fe-4S] Fd, [2Fe-2S] Fd, and Fld electron carriers in over 7,000 organisms. Our analysis targeted genes encoding small PEC genes encoding proteins having ≤200 residues. We find that the average number of small PEC genes per Archaea (∼13), Bacteria (∼8), and Eukarya (∼3) genome varies, with some organisms containing as many as 54 total PEC genes. Organisms fall into three groups, including those lacking genes encoding low potential PECs (3%), specialists with a single PEC gene type (20%), and generalists that utilize multiple PEC types (77%). Mapping PEC gene usage onto an evolutionary tree highlights the prevalence of [4Fe-4S] Fds in ancient organisms that are deeply rooted, the expansion of [2Fe-2S] Fds with the advent of photosynthesis and a concomitant decrease in [4Fe-4S] Fds, and the expansion of Flds in organisms that inhabit low-iron host environments. Surprisingly, [4Fe-4S] Fds present a similar abundance in aerobes as [2Fe-2S] Fds. This bioinformatic study highlights understudied PECs whose structure, stability, and partner specificity should be further characterized.

Keywords: electron transfer, evolution, ferredoxin, flavin mononucleotide, flavodoxin, iron-sulfur cluster, oxidoreductase, oxidative stress

OPEN ACCESS

Edited by:
Jeffrey A. Gralnick, University of Minnesota Twin Cities, United States

Reviewed by:
Marcus Joseph Edwards, University of East Anglia, United Kingdom
Kyle Costa, University of Minnesota Twin Cities, United States

***Correspondence:**
Jonathan J. Silberg
joff@rice.edu

Specialty section:
This article was submitted to Bioenergy and Biofuels, a section of the journal Frontiers in Energy Research

Received: *03 June 2019*
Accepted: *25 July 2019*
Published: *23 August 2019*

Citation:
Campbell IJ, Bennett GN and Silberg JJ (2019) Evolutionary Relationships Between Low Potential Ferredoxin and Flavodoxin Electron Carriers. Front. Energy Res. 7:79. doi: 10.3389/fenrg.2019.00079

INTRODUCTION

Redox-active cofactors are essential components of metabolism, functioning as molecules that transfer electrons at various reduction potentials, according to metabolic need. These pools of small molecules (e.g., NADH, NADPH, FADH, FMN, riboflavin, and quinones) can couple their reducing power to a wide range of oxidoreductases in parallel. For example, the quinone that functions in aerobic respiration within *Escherichia coli* interacts with two dozen oxidoreductases, while NADH/NADPH are used by over one hundred oxidoreductases in this microbe (Orth et al., 2011). What these small molecules lack, however, is the ability to evolve structures that discriminate partner binding and tune their midpoint potentials. In contrast, protein electron carriers (PECs) can tune both reduction potential and partner binding by modifying their amino acid sequences (Hosseinzadeh and Lu, 2016; Kim et al., 2016). This tunability is thought to enable the evolution of protein-controlled, energy-conserving electron transfer (ET) pathways.

The Iron-Sulfur World Hypothesis, that life evolved within the cavities and capillaries of iron-sulfur enriched mounds, implicates ferredoxins (Fds) with [4Fe-4S] clusters as the earliest low potential PECs (Sousa et al., 2013). This idea is supported by the observations that these proteins represent the smallest PECs, having as few as 55 amino acids (Bertini et al., 1995), and the observation that iron and sulfur can readily combine to form iron-sulfur clusters under anaerobic conditions (Venkateswara Rao and Holm, 2004). With the advent of oxygenic photosynthesis and the Great Oxidation Event, the usage of O_2-sensitive [4Fe-4S] Fds may have been disincentivized relative to the more O_2-tolerant [2Fe-2S] Fds. Support for this idea comes from the observation that [4Fe-4S] clusters within canonical bacterial Fds have an exposed sulfido atom which can be attacked by O_2, resulting in the release of iron and destruction of the cluster (Imlay, 2006; Jagannathan and Golbeck, 2009). With a hydrophobic patch covering their metallocluster, [2Fe-2S] Fds are more shielded from this degradation (Pierella Karlusich et al., 2014), while still capable of presenting a similar range of midpoint potentials (Atkinson et al., 2016). As a result, [2Fe-2S] Fds are thought to have emerged as the favored electron acceptor for the O_2-evolving photosystem, proliferating in the new O_2-rich world. While it is clear that some [4Fe-4S] Fds are more sensitive to O_2 than [2Fe-2S] Fds, the extent to which these two Fd types are used across different environmental niches has not been well established.

The rise in global O_2 concentration created insoluble iron hydroxides, thereby lowering the amount of bioavailable iron (Ilbert and Bonnefoy, 2013; Pierella Karlusich et al., 2014). It was at this time that flavodoxins (Flds) are thought to have risen in popularity, especially as an iron limitation response for phytoplankton (Pierella Karlusich et al., 2014). Flds use flavin mononucleotide (FMN) as their redox cofactor and are able to substitute for [2Fe-2S] Fds in a wide range of ET reactions within phototrophs (Demuez et al., 2007; Goñi et al., 2008; Pierella Karlusich et al., 2014). Despite an increasing body of Fld research (Freigang et al., 2002; Demuez et al., 2007; Goñi et al., 2008; Pierella Karlusich et al., 2014; Mellor et al., 2017), we still do not know how prevalent Flds are across extant organisms and how they work with Fds to manage ET across different biochemical pathways.

Gene duplication events during evolution have led to the growth and diversification of PECs (Onda et al., 2000; Terauchi et al., 2009; Peden et al., 2013; Cassier-Chauvat and Chauvat, 2014; Pierella Karlusich et al., 2014; Atkinson et al., 2016; Mellor et al., 2017; Burkhart et al., 2019). Biochemical and cellular studies of [2Fe-2S] Fd paralog specialization have been performed in a hyperthermophilic Archaeon, *Thermococcus kodakarensis* (Burkhart et al., 2019), and three model photosynthetic organisms: *Synechocystic* sp. PCC6803, *Zea mays,* and *Chlamydomonas reinhardtii* (Onda et al., 2000; Terauchi et al., 2009; Cassier-Chauvat and Chauvat, 2014). These studies revealed variations in the pattern of expression as well as differences in partner binding. However, we still lack basic information on how these and other low potential PECs evolved and specialized across the tree of life. While we have some limited information on the number of Flds and [4Fe-4S] Fds in phototrophs, beyond these organisms estimates of PEC distribution are scarce. We know that Flds often replace [2Fe-2S] Fds under iron limited conditions, both in free-living organisms and host-associated organisms (Freigang et al., 2002; Goñi et al., 2008), but a quantitative description at the genomic level is lacking.

To gain a better understanding of how evolution has selected extant PECs, we report on the genome mining of 7,079 organisms for sequence motifs that are characteristic of three different low-potential PEC families, including the [4Fe-4S] Fds, [2Fe-2S] Fds, and Flds. We show that many organisms have large pools of small PEC genes, with 50% of our analyzed organisms possessing six or more small PEC genes, including members of all three PEC types. We find that PEC pools vary across genomes, with some organisms lacking small PEC genes and others having >50 total small PEC genes. We also report that PEC genes elongate in organisms having multiple PEC-encoding genes and under certain environmental conditions.

MATERIALS AND METHODS

Genome Mining

We harvested 7079 genomes from the Joint Genome Institute (JGI) with the "finished" sequencing status and scanned them for genes matching Interpro sequence signatures for Fld/nitric oxide synthase (IPR008254), [2Fe-2S] Fd-cluster binding domain (IPR001041), and [4Fe-4S] Fd-cluster binding domain (IPR017896) (Finn et al., 2017). Interpro annotation was chosen because it synthesizes signatures from multiple databases with complementary but distinct annotation strategies, such as Pfam and PROSITE, which match for proteins on the basis of Hidden Markov Models and shared alignment profiles, respectively (Finn et al., 2017). Genes with over 200 amino acids were excluded from the dataset to focus the analysis on small PECs. Metadata for each genome was also downloaded and used for environmental niche analysis. Sequences obtained from genome-mining were collected in a FASTA format and analyzed for Interpro (IPR) sequence signatures with InterProScan 5 (Jones et al., 2014). **Supplementary Dataset 1** contains a list of organisms with the number of genes having each IPR signature and metadata about ecosystem characteristics. It also contains a list of the individual PECs collected after genome mining, with their sequences and the metadata of their host organisms.

Analysis of PEC Structures

The protein data bank was used to compile structures of [4Fe-4S] Fds, [2Fe-2S] Fds, and Flds (Berman, 2000). For [4Fe-4S] Fds, we used PDB identifiers (IDs) 1DUR, 2FDN, 1CLF, 1FXD, 1VJW, 1FXR, 1SJ1, 4ID8, 1BC6, 1BWE, 1H98, 4KT0, 1RGV, 1JB0, 1IQZ, 1BLU, 2FGO, 2ZVS, 2VKR, 1XER, 2V2K, and 7FDR. For [2Fe-2S] Fds, we used PDB IDs 1L5P, 4ITK, 1WRI, 1AWD, 2MH7, 1FRR, 4ZHO, 3AV8, 1PFD, 1OFF, 5H57, 3AB5, 1ROE, 1A70, 4FXC, 3B2G, 3B2F, 1RFK, 1JQ4, 1IUE, 1FRD, 1CZP, 2WLB, 3LXF, 1B9R, 1UWM, 1PDX, 1M2D, 1I7H, 3AH7, 2MJD, 2MJ3, 2Y5C, 5FFI, 3P1M, 1E0Z, 1DOI, and 1AYF. For Flds, we used PDB IDs 2FZ5, 1FLD, 4HEQ, 2HNA, 2FX2, 3F6R, 3KAP, 5B3L,

4OXX, 1FUE, 2BMV, 2W5U, 1CZH, 1FLV, 1OBO, 2MT9, 2FCR, 1AG9, 1YOB, 2WC1, and 2ARK.

Pairwise Analysis of PEC Abundance

The gene counts for each PEC type were plotted against one another in heatmaps generated using the Matplotlib python package (Hunter, 2007). A log-scaled color gradient was used to illustrate the number of organism with each PEC count combination. For ternary plot analysis, organisms were binned on the basis of their relative PEC pool composition. For each organism, counts of each PEC family were normalized such that they summed to 100%. All combinations of PEC pools were divided into bins with step sizes of 10%. If an organism's PEC composition placed it at the boundary of two or more bins, it was randomly placed in one of the adjoining bins. The density of organisms in each bin were visualized using a viridis color gradient. Results were plotted using the python-ternary package (Harper et al., 2015).

PEC Phylogeny Mapping

Evolutionary analysis was performed using a previously described evolutionary tree derived from concatenated protein sequences (Hug et al., 2016). The tree was pruned down to the 351 organisms present in our dataset using the Environment for Tree Exploration (ETE) 3 python toolkit (Huerta-Cepas et al., 2016). The IPR-matching PEC gene counts were placed at each organisms leaf in the phylogenetic tree in a stacked bar graph. Data was visualized using the Interactive Tree of Life webservice (Letunic and Bork, 2016).

Environmental Niche Analysis

Organisms were sorted on the basis of their JGI metadata labels. Organisms labeled thermotolerant were placed into the thermophile bins, while those labeled psychrotolerant and psychrotrophic were placed in the psychrophile bin. A heatmap was generated by plotting the average PEC gene count for organisms at each O_2 niche and growth temperature bin. Average values were rounded to two significant figures. Average PEC counts for external pH values were calculated by dividing PEC counts by the number of organisms observed at each pH.

PEC Length Analysis

To generate plots showing PEC length distributions and abundances, organisms were divided into different categories (PEC gene count, O_2 requirement, growth temperature), and the length distributions in each category were smoothed using kernel density estimation via the Matplotlib package (Hunter, 2007).

Statistics

The weighted pH average of each PEC type was calculated, along with the weighted standard deviation, and the three distributions were compared using a paired, two-tail *t*-test calculated using NumPy (van der Walt et al., 2011).

RESULTS

Genome-Mining Strategy

To understand how low-potential PEC usage varies in nature, we downloaded 7079 genomes with the sequencing status "Finished" from the Integrated Microbial Genomes and Microbiomes database (Chen et al., 2019). A majority of the genomes were from Bacteria (n = 6,733), although Archaea (n = 275) and Eukaryotes (n = 71) were represented. We scanned each genome for genes having Fld, [2Fe-2S] Fd, and [4Fe-4S] Fd Interpro sequence signatures (Finn et al., 2017). We excluded all gene matches encoding proteins above 200 amino acids. This size cutoff was chosen because it is greater than the largest [4Fe-4S] Fd (106 residues: 7FDR), [2Fe-2S] Fds (128 residues: 1E0Z), and Flds (184 residues: 2ARK) reported in the PDB (Schipke et al., 1999; Marg et al., 2005). By using a size cutoff that exceeds the length of PECs with single domain structures in the PDB, we sought to evaluate how the size of these three PEC families varies beyond the family members that have already been studied. We applied the same size cutoff to all three PEC types, even though they differ in average size within the PDB. Their average sizes are 77 ([4Fe-4S] Fds), 111 ([2Fe-2S] Fds), and 160 (Flds) residues. By using this approach, our analysis allowed the comparison of PEC evolution across the same size range. Additionally, the use of a 200 amino acid cutoff minimized Fld false positives, as IPR008254 also identifies nitric oxide synthases, enzymes that can be >400 amino acids (Fischmann et al., 1999; Fedorov et al., 2003). Because sequence additions frequently do not abolish the function of the ancestral domain (Björklund et al., 2005), we posited that many of the gene sequences detected with our approach encode proteins capable of ET like known Fds and Flds.

Organisms Differ in Their PEC Gene Counts

Organisms were initially sorted by taxonomic domain to visualize how gene abundances vary. **Figure 1** shows that Archaea have the largest average number of PEC genes per organism ($\mu = 12.7 \pm 5.7$), heavily favoring genes with [4Fe-4S] Fd IPR signatures. This observation is in line with previous observations that archaeal metabolisms depend more heavily on non-heme iron-binding proteins than those of the other two domains (Andreini et al., 2007). Eukaryotes present the smallest number of PEC genes per organism ($\mu = 2.8 \pm 5.3$), utilizing genes with [2Fe-2S] Fd signatures to the greatest extent. Bacteria have an intermediate level of PEC genes ($\mu = 7.9 \pm 6.2$) and favor a more balanced composition.

We next quantified the abundances of genes encoding each PEC type within each genome. **Figure 2A** shows that [4Fe-4S] Fd genes occur with the greatest abundances, with more than 400 organisms having ten or more [4Fe-4S] Fd genes. In contrast, there are only 162 organisms with 10 or more [2Fe-2S] Fd genes (**Figure 2B**), and only one organism having more than 10 Fld genes (**Figure 2C**). The total counts of genes encoding all three PECs were also summed together for each organism (**Figure 2D**). This analysis reveals that 50% of all organisms analyzed have

6 or more PEC genes, and 3% of the organisms lack small PEC genes.

PECs can at times transfer electrons to overlapping sets of partner proteins, suggesting that some have evolved as interchangeable ET hubs. In some organisms, Fds are used for ET under iron-rich conditions, while Flds support ET among the same partner oxidoreductases under limiting iron conditions (Demuez et al., 2007; Goñi et al., 2008; Pierella Karlusich et al., 2014). To evaluate if the abundances of the different PEC gene types are proportional in some organisms or if there are differences in the relative abundances, we compared the pairwise counts of the different PEC types within each genome. All three pairwise comparisons presented a wide range of abundance combinations. In the case of the Fld and [2Fe-2S] Fd comparison (**Figure 3A**), most organisms have <4 genes encoding each PEC type (64%). A small fraction of organisms (3%) contain ≥4 genes encoding both PEC types, and the remainder have ≥4 of one PEC type and <4 of the other type (33%).

The pairwise relationships between [4Fe-4S] Fds and Flds (**Figure 3B**) and [4Fe-4S] and [2Fe-2S] Fds (**Figure 3C**) presented larger number of organisms with higher abundances of both PEC types. With the [4Fe-4S] Fd and Fld comparison, 17% of the organisms have ≥4 of both PEC types, while the [4Fe-4S] and [2Fe-2S] Fd comparison revealed that 12% of the organisms have ≥4 of each PEC type. With these comparisons, the organisms with the highest [4Fe-4S] Fd gene abundances frequently present three or fewer Fld or [2Fe-2S] Fd genes. Of the genomes analyzed, 26% of genomes possess ≥4 [4Fe-4S] Fd genes and <4 Fld genes, while the reverse composition is only observed in 3% of genomes. In addition, 31% possess ≥4 [4Fe-4S] Fd genes and <4 [2Fe-2S] Fd genes, while the reverse composition is only observed in 6% of genomes. These trends support the idea that [4Fe-4S] Fds arose early in evolution

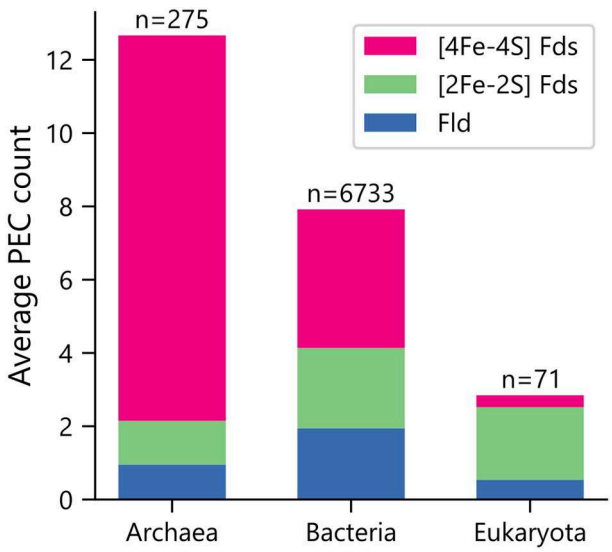

FIGURE 1 | Average PEC gene counts across the domains of life. The average number of PEC genes containing motifs that are characteristic of [4Fe-4S] Fds (red), [2Fe-2S] Fds (green), and Flds (blue) in each domain. The number of genomes analyzed within each domain is shown on top of each bar.

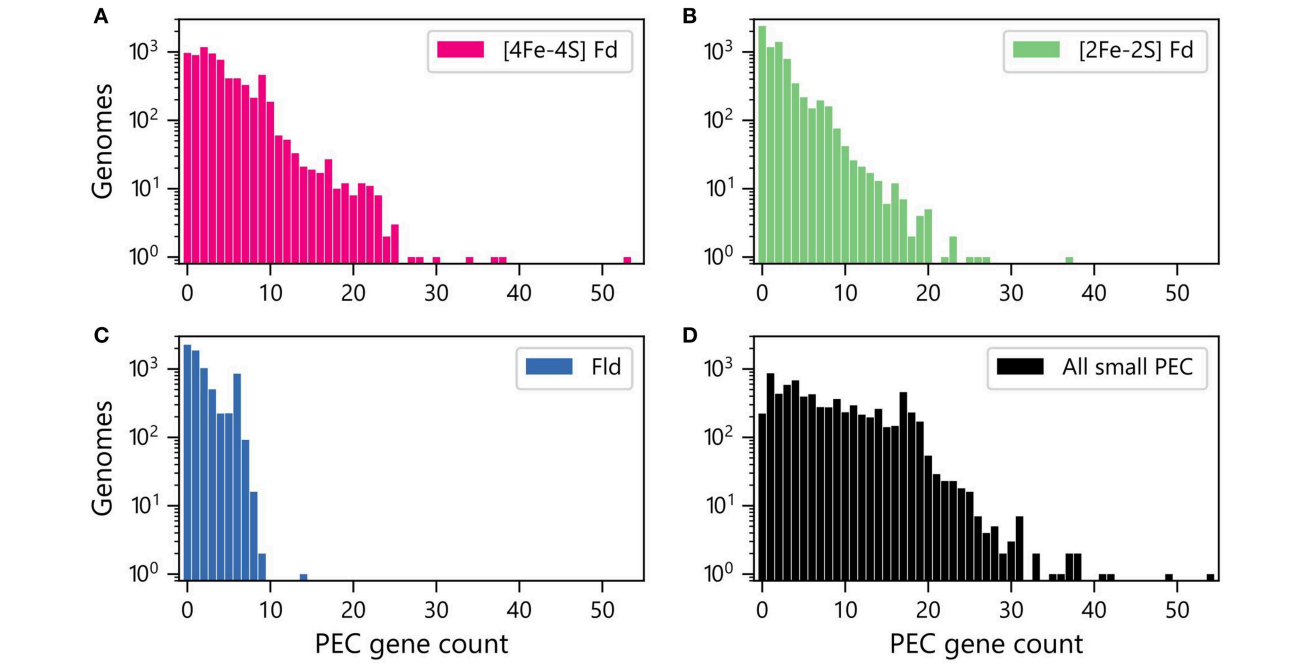

FIGURE 2 | Numbers of genomes having different abundances of PEC genes. Number of organisms with different **(A)** [4Fe-4S] Fd (red), **(B)** [2Fe-2S] Fd (green), and **(C)** Fld (blue) gene counts. **(D)** Number of organisms with different total numbers of PEC genes (black). The data shown was obtained by summing up the Fld, [2Fe-2S] Fd, and [4Fe-4S] Fd counts in each genome.

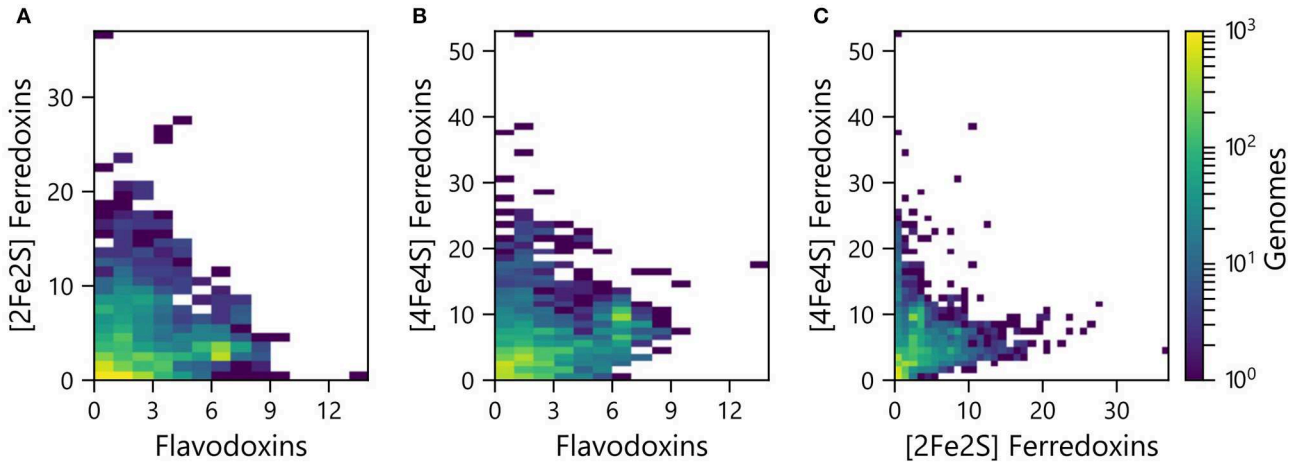

FIGURE 3 | Pairwise abundance of PEC genes within each genome. The abundances of **(A)** [2Fe-2S] Fd and Fld, **(B)** [4Fe-4S] Fd and Fld, and **(C)** [4Fe-4S] Fd and [2Fe-2S] Fd genes are plotted as heat maps. The density of organisms having each pairwise count is shown using a viridis color gradient.

and diversified through gene duplications, gaining critical metabolic functions before the widespread use of the [2Fe-2S] Fds and Flds.

We next calculated the abundance of genes encoding all three PEC types in each genome and visualized this data using a ternary plot (**Figure 4**). The values obtained for each organism were distributed into bins based on the relative percentages of each gene type. With this analysis, ∼20% of the organisms had only one type of PEC gene, a small subset lacked all three PEC types (3%), and the remainder of the organisms had two or three PEC types encoded in their genomes (77%). One of the most popular PEC gene pool makeups is near the middle of the ternary plot, representing organisms with 40–50% [4Fe-4S] Fd, 10–20% [2Fe-2S] Fd, and 30–40% Fld genes. This hotspot is attributed to the high number of proteobacteria in our data set, which dominate this makeup.

The ternary plot also reveals PEC combinations that are absent from the dataset organisms. For organisms that lack [4Fe-4S] Fd genes, only a subset of the possible [2Fe-2S] Fd and Fld gene mixtures are observed. Under this constraint, Fld and [2Fe-2S] Fd gene specialists are most common. This trend is consistent with the pairwise PEC comparisons that show organisms only possess large numbers of [2Fe-2S] Fd or Fld genes in cases where they also possess multiple [4Fe-4S] Fd genes. Taken together, these results indicate that genes encoding [4Fe-4S] Fds are widespread with a high degree of penetration in many genomes and provide further evidence that ancient organisms were likely dependent upon the [4Fe-4S] Fds family before the expansion of the other two families.

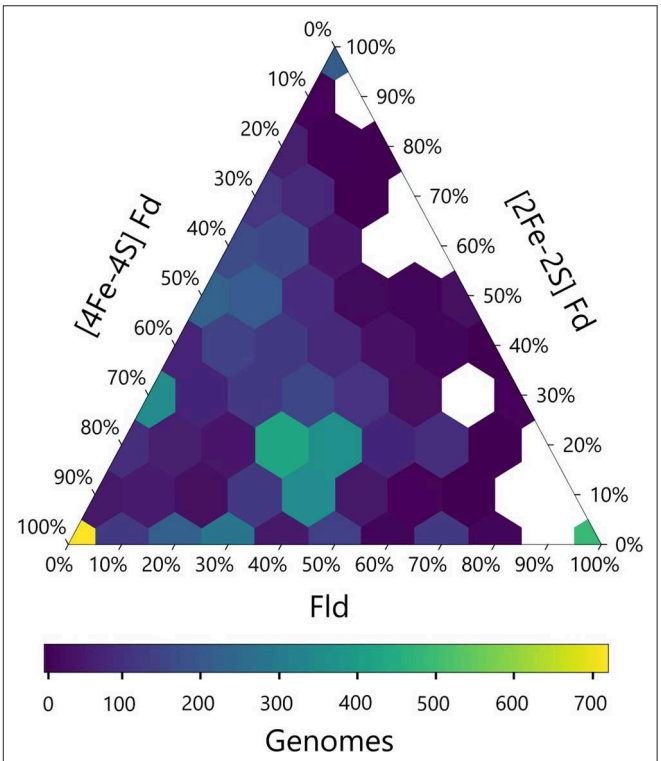

FIGURE 4 | Relative abundances of PEC specialist and generalists. The relative percentage of PEC gene counts for all three families are plotted with the density of organisms at each coordinate illustrated by a viridis color gradient. White hexagons represent combinations that were not observed.

PEC Gene Evolution

To understand how PEC gene counts vary across extant organisms, we mapped our data onto an evolutionary tree (Hug et al., 2016). For visualization, we pruned the phylogenetic tree down to those organisms represented in our data set (n = 351). We show the abundance for all 351 organisms in a bar graph at each of the leaves on a tree (**Figure 5**) and the average abundance in the major taxonomic groups (**Table 1**). From this analysis, it appears that evolution has selected for the expansion of homologs of all three PEC types more than once. The [4Fe-4S] Fds are most widespread in overall abundance, being dispersed through most organisms. However, this PEC type clearly spikes in average abundance (>10 paralogs) within the Archaea,

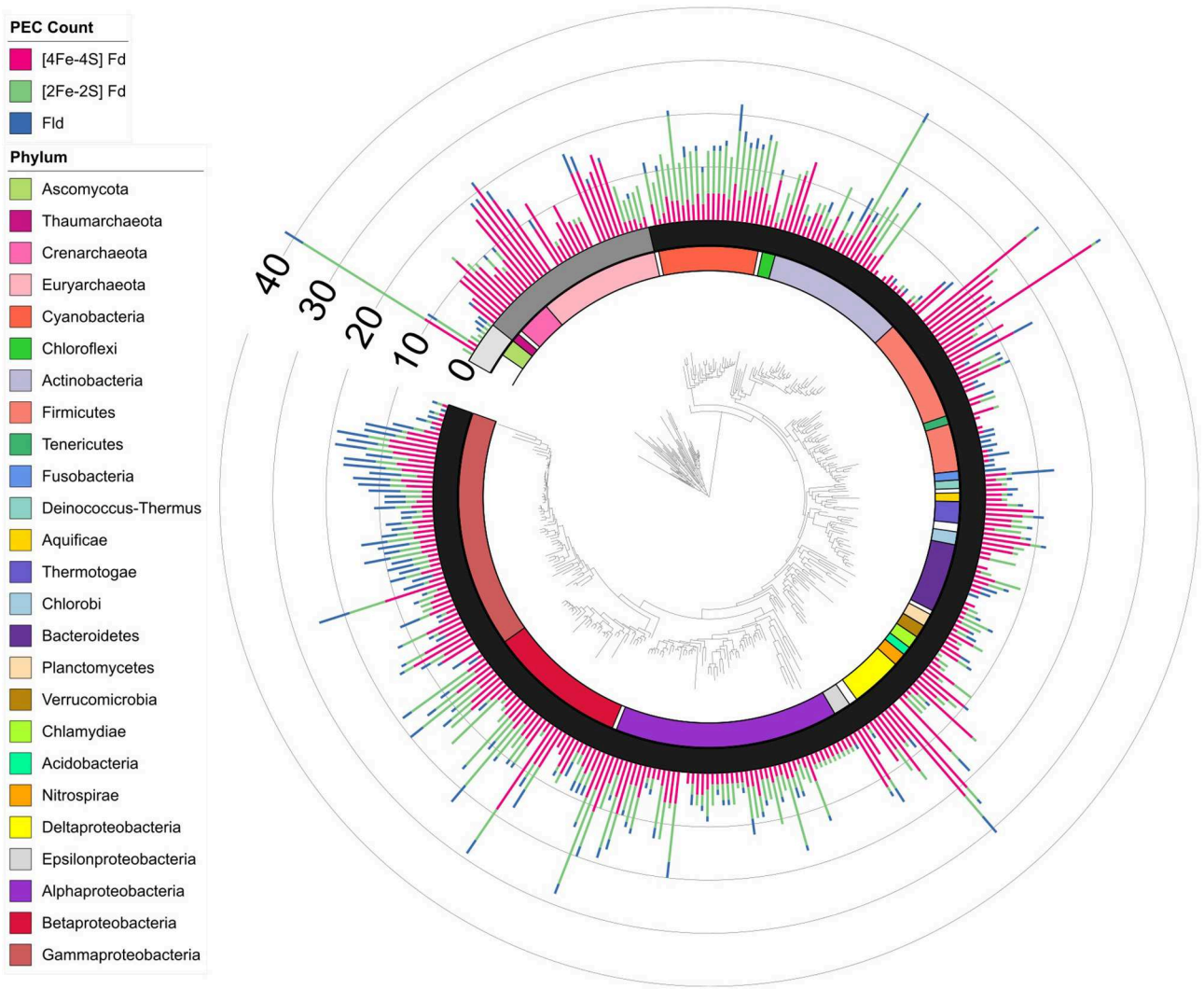

FIGURE 5 | PEC gene abundance mapped onto an evolutionary tree. Bars are used to illustrate the total PEC gene counts of the three different PEC families at the leaves in a stacked bar graph, including [4Fe-4S] Fds (red), [2Fe-2S] Fds (green), and Flds (blue). The domain for each organism is depicted by shading internal to the stacked bars: Eukaryotes (Light gray), Archaea (dark gray), and Bacteria (black). The major phyla and classes of organisms represented in the tree are visualized internal to the domains using the colored bars as noted in the key. Phyla with only one representative are labeled with white bars.

Firmicutes, Deltaproteobacteria, and Betaproteobacteria. The [2Fe-2S] Fds present the greatest abundances within phototrophs (plants, Cyanobacteria), Alphaproteobacteria, and Betaproteobacteria. The Flds are most abundant within a subset of the Firmicutes (Bacilli), Gammaproteobacteria, and in parasitic organisms. Below, we describe the trends in greater detail for individual taxonomic groups that are well represented in our data set.

Eukaryota

In our data set, this kingdom has the smallest number of genomes, including algae, a protozoan, a plant, fungi, and *Homo sapiens*. These organisms exhibit highly variable PEC compositions, although they all possess [2Fe-2S] Fds. Corn (*Zea mays*) possesses the largest number of PECs of any organism on the tree ($n = 42$) and the fourth most PEC genes of any organism in the dataset, utilizing a mix of all three types. This observation is consistent with an ancient plant duplication event and a high rate of retention of duplicate genes in plant genomes (Panchy et al., 2016). With the exception of the green algae *Ostreococcus lucimarinus*, which contains 11 PEC genes, all other organisms in this domain possess small numbers of PEC genes. *Homo sapiens* uses two [2Fe-2S] Fds (Sheftel et al., 2010), while fungi have incorporated one [2Fe-2S] Fd and up to two Flds. Both human Fds are nuclear-encoded and translocated to mitochondria (Sheftel et al., 2010). Additionally, the chloroplasts in phototrophs are hotbeds of PECs (Pierella Karlusich and Carrillo, 2017). Taken together, these observations support the idea that some organisms compartmentalize PECs within organelles that function in light

TABLE 1 | The average PEC gene counts for each phylum is displayed, including the number of [4Fe-4S] Fd, [2Fe-2S] Fd, and Fld genes, as well as the sum of all three types.

Phyla	< Protein electron carriers >			Total	Genomes
	[4Fe-4S]	[2Fe-2S]	Fld		
Streptophyta	6.50	18.50	2.00	27.00	2
Euryarchaeota	11.91	1.13	1.19	14.23	190
Deltaproteobacteria	10.71	1.77	0.76	13.24	79
Acidithiobacillia	7.50	4.50	1.00	13.00	4
Cyanobacteria	4.35	7.40	1.00	12.75	109
Gammaproteobacteria	5.75	2.62	4.18	12.55	2091
Synergistetes	7.22	3.11	0.67	11.00	9
Betaproteobacteria	3.87	5.62	1.05	10.54	557
Crenarchaeota	8.02	1.73	0.47	10.22	66
Candidatus Korarchaeota	10.00	0.00	0.00	10.00	1
Deferribacteres	8.80	0.20	1.00	10.00	5
Calditrichaeota	8.00	2.00	0.00	10.00	1
Nitrospirae	7.22	1.89	0.22	9.33	9
Chloroflexi	6.63	1.69	0.81	9.13	32
Caldiserica	6.00	3.00	0.00	9.00	1
Ignavibacteriae	7.50	1.00	0.50	9.00	2
Bacillariophyta	2.00	5.00	2.00	9.00	1
Lentisphaerae	6.33	1.67	1.00	9.00	3
Thermodesulfobacteria	8.75	0.00	0.00	8.75	4
Chlorophyta	1.50	6.00	1.00	8.50	2
Thermotogae	6.13	1.10	1.03	8.26	31
Alphaproteobacteria	3.47	3.90	0.66	8.03	566
Chlorobi	6.33	0.40	0.80	7.53	15
Acidobacteria	3.09	3.82	0.36	7.27	11
Chrysiogenetes	7.00	0.00	0.00	7.00	1
Dictyoglomi	4.50	0.00	2.50	7.00	2
Gemmatimonadetes	2.33	4.33	0.00	6.66	3
Aquificae	5.13	1.07	0.20	6.40	15
Thaumarchaeota	5.87	0.00	0.33	6.20	15
Oligoflexia	2.00	3.00	0.43	5.43	7
Fibrobacteres	4.40	0.00	0.80	5.20	5
Planctomycetes	3.35	1.06	0.65	5.06	17
Epsilonproteobacteria	3.90	0.06	1.07	5.03	272
Candidatus Cloacimonetes	3.50	1.50	0.00	5.00	2
Actinobacteria	2.91	1.61	0.41	4.93	700
Deinococcus-Thermus	2.88	1.33	0.46	4.67	24
Armatimonadetes	2.60	1.80	0.20	4.60	5
Fusobacteria	0.85	0.19	3.54	4.58	26
Chordata	0.50	4.00	0.00	4.50	2
Firmicutes	2.14	0.67	1.55	4.36	1401
Elusimicrobia	3.67	0.00	0.33	4.00	3
Bacteroidetes	2.16	1.28	0.48	3.92	248
Verrucomicrobia	2.38	0.50	0.56	3.44	16
unclassified	1.29	2.00	0.14	3.43	7
Spirochaetes	1.19	0.76	0.62	2.57	149
Apicomplexa	0.00	1.83	0.00	1.83	12
Ascomycota	0.03	0.95	0.75	1.73	40
Chlamydiae	0.03	1.03	0.00	1.06	148
Nanoarchaeota	1.00	0.00	0.00	1.00	2
Candidatus Micrarchaeota	1.00	0.00	0.00	1.00	1
Microsporidia	0.00	1.00	0.00	1.00	4
Nematoda	0.00	1.00	0.00	1.00	1
Basidiomycota	0.00	0.67	0.00	0.67	3
Tenericutes	0.18	0.02	0.12	0.32	155
Candidatus Saccharibacteria	0.00	0.00	0.00	0.00	2

(Continued)

TABLE 1 | Continued

The average PEC gene counts for each phylum is displayed, including the number of [4Fe-4S] Fd, [2Fe-2S] Fd, Fld genes, as well as the sum of all three types. Phyla are listed in descending order of total average PEC genes.

harvesting and energy production (Sheftel et al., 2010; Scheibe and Dietz, 2012).

Archaea

This domain has the highest average number of PEC genes per genome. The [4Fe-4S] Fds are the most popular PEC type in most Archaea represented. The exception to this trend is the Haloarchaea, which predominately uses [2Fe-2S] Fds. This class is noted for having many members that live aerobically and in extreme saline conditions (Sorokin et al., 2017). This observation is interesting because Haloarchaea are thought to have acquired >1,000 genes from methanogens in a single gene transfer event, and because methanogens are generally anaerobic and dominated by [4Fe-4S] Fds. It seems unlikely that Haloarchaea received large numbers of [2Fe-2S] Fds from this gene transfer event, although they received other oxidoreductases from methanogens, such as pyruvate:Fd oxidoreductase (Nelson-Sathi et al., 2012). Haloarchaea possess [2Fe-2S] Fds with a high-degree of similarity to plant-type Fds, with the exception of a ∼30 amino acid addition near the N-terminus, which has been hypothesized to have entered the organism through gene transfer from cyanobacteria (Pfeifer et al., 1993; Marg et al., 2005; Nelson-Sathi et al., 2012). Surprisingly, a few archaea lack genes with Fd and Fld IPR signatures. Two organisms in the phylogenetic tree (*Archaeoglobus fulgidus* DSM 8774 and *Palaeococcus pacificus* DY20341) lack PEC genes, although other organisms from their respective classes that are present in the genome mining dataset contain PEC encoding genes (**Supplementary Dataset 1**).

Cyanobacteria

The PEC gene distribution in these organisms most closely matches the Haloarchaea, with averages of 8.6 [2Fe-2S] Fd, 4.5 [4Fe-4S] Fd, and 1.0 Fld genes per genome. This trend makes this one of the richest phyla in terms of consistent, uniform abundance across all three PEC types. This representation is thought to arise in part because Cyanobacteria express Flds instead of [2Fe-2S] Fds under iron-limiting conditions (Pierella Karlusich et al., 2014). Rather than contributing to management

ET in chloroplasts, the [4Fe-4S] Fds in these organisms have been implicated in oxidative and metal stress response pathways (Cassier-Chauvat and Chauvat, 2014).

Chloroflexi

Some of these organisms have genes encoding all three PEC types like Cyanobacteria. However, this phylum has lower average PEC gene counts, and only a subset of Chloroflexi have Fld genes. This latter trend is thought to occur because the Chloroflexi in our tree have highly divergent life strategies, including the mesophilic anaerobic organohalide respirer *Dehalococcoides mccartyi* (Löffler et al., 2013), the aerobic predator *Herpetosiphon aurantiacus* (Kiss et al., 2011), and the aerobic thermophile *Thermomicrobium roseum* (Wu et al., 2009).

Actinobacteria

These Gram-positive bacteria vary in their PEC specialization, with some having 100% [4Fe-4S] Fd genes (e.g., *Adlercreutzia equolifaciens*) and others having 75% [2Fe-2S] Fd genes (e.g., *Saccharopolyspora erythraea*). Like Chloroflexi, only a subset of the genomes contain Fld genes. These organisms range widely in their total PEC gene counts, with some lacking PEC genes (*Dermacoccus nishinomiyaensis*) and others having 31 PEC genes (*Pseudonocardia dioxanivorans*). This wide variation appears to be the result of a split within the Actinobacteridae class, leaving one half PEC-rich and the other half PEC-scarce. Each half encompasses organisms with many life strategies. Two notable representatives of the PEC-rich organisms include the symbiotic nitrogen-fixing *Frankiaceae* and the antibiotic-producing *Mycobacteriaceae* (Ventura et al., 2007). The PEC-poor half harbors at least six bacterial families (Kineosporiaceae, Dermacoccaceae, Promicromonosporaceae, Actinomycetaceae, Bifidobacteriaceae, Microbacteriaceae) which include many soil bacteria, the gamma-radiation resistant *Kineococcus radiotolerans* (Phillips et al., 2002), and the gastrointestinal-tract inhabiting Bifidobacteriaceae (Ventura et al., 2007). The clustering of PEC-poor and PEC-rich organisms suggests that there has been evolutionary pressure for these trends, but the underlying cause of that pressure is not known.

Firmicutes

This phylum is split into two major branches: Clostridia and Bacilli. The Clostridia mirrors Archaea in their high total numbers of PEC genes and high [4Fe-4S] Fd abundances. Bacilli, in contrast, contain low total numbers of PEC genes. While different PEC gene types are observed in Bacilli, Flds are most common. In our dataset, Bacilli are largely represented by members of the Lactobacillales order. There are two reasons why these lactic acid bacteria may utilize few Fds. First, most lactic acid bacteria colonize iron-poor environments and have evolved metabolisms that support growth without iron (Duhutrel et al., 2010). Second, many lactic acid bacteria produce H_2O_2 in unusually large quantities as part of their metabolism (Imlay, 2019). The harmful Fenton chemistry that can arise from high H_2O_2 and iron may have selected for these bacteria to evolve pathways dependent on Flds rather than iron-containing Fds.

Bacteroidetes

These microbes have diverse PEC gene pools, with total gene counts that vary between zero and twelve. They are unique in possessing organisms that are PEC specialists, with individual members that contain genes encoding only [4Fe-4S] Fds or Flds. The Fld specialists are confined to the Bacteroidales order, which includes the Fld-specialist *Parabacteroides distasonis* and the PEC-generalist *Porphyromonas gingivalis*. Both of these species are commensal and pathogenic bacteria associated with the oral cavity (Naito et al., 2008; Kverka et al., 2011). The [4Fe-4S] Fd specialists include an endosymbiont of amoebas with a reduced genome and severely limited biosynthetic capabilities (*Candidatus Amoebophilus asiaticus*), and an aerobic gliding soil bacterium that digests cellulose (*Cytophaga hutchinsonii*) (Penz et al., 2010; Zhu and McBride, 2017).

Delta and Epsilon Proteobacteria

These organisms encode [4Fe-4S] Fd genes at higher levels in their genomes compared with the other two PEC types. The sulfur-reducing *Desulfobacula toluolica* is a standout member that exemplifies this trend. This organism possesses twenty-two [4Fe-4S] Fd, five [2Fe-2S] Fd, and four Fld genes. One unusual order in the Deltaproteobacteria class is Myxococcales. These strict aerobic organotrophs metabolize macromolecules like cellulose, and despite having some of the largest bacterial genomes which are 9 to 10 million nucleotides in length, the two Myxococcales species in the pruned phylogenetic tree possess only five PEC genes (Dawid, 2000). In comparison, another myxobactera, *Stigmatella aurantiaca* DW4/3-1, which is not present in the phylogenetic tree, has seven PEC encoding genes (**Supplementary Dataset 1**). Additionally, this order stands out from the rest of the Delta and Epsilon Proteobacteria because it has predominately [2Fe-2S] Fd genes.

Alphaproteobacteria

Organisms within this class range from having 0 to 28 PEC genes, with a majority having genomes with at least one [4Fe-4S] Fd and one [2Fe-2S] Fd gene; only half have a Fld gene. Alphaproteobacteria with the highest PEC abundance are in the nitrogen-fixing *Rhizobiales* order ($\mu = 10.6 \pm 7.1$). In these organisms, the most abundant PEC genes encode [2Fe-2S] Fds. For instance, *Bradyrhizobium japonicum* has genes encoding nineteen [2Fe-2S] Fds, seven [4Fe-4S] Fds, and two Flds. The two-stage life cycle of Rhizobia, which includes bacteroid and free-living cells, may explain this abundance of PEC genes. In the bacteroid stage, Rhizobia derive reducing equivalents from host roots and, as they are metabolically active but not growing, must often shunt a large portion of those reducing equivalents into lipogenic pathways to maintain redox balance (Terpolilli et al., 2016). This coupling enables nitrogen assimilation, a process which requires Fds for transfer of low potential electrons from central metabolism to nitrogenase (Terpolilli et al., 2016). In contrast, free-living Rhizobia often gain a competitive advantage by metabolizing the secondary products excreted by a bacteroid

of the same species, using oxidative pathways that are species-specific and require specialized PECs (Bahar et al., 2000).

One member of the Alphaproteobacteria (*Ensifer adhaerens* OV14) lacks PEC genes. As an opportunistic predator of the rhizosphere, *E. adhaerens* has recently generated interest as an alternative to *Agrobacterium tumefaciens* for the transformation of plants (Rudder et al., 2014). Often living in the nutrient-rich nodules of the rhizosphere, it is thought to depend upon the metabolisms of plants or other rhizosohere microbes to supplement the loss of some PEC-dependent pathways (Rudder et al., 2014).

Betaproteobacteria

These organisms also have a large variability in PEC gene numbers in each genome, with one organism having 29 PEC genes (*Azoarcus* sp. KH32C) and some containing only three PEC genes (*Nitrosomonas europaea, Candidatus Profftella armatura,* and *Candidatus Kinetoplastibacterium oncopeltii* TCC290E). One interesting order within this class, *Nitrosomonadales*, has genes encoding only [4Fe-4S] Fds. This observation can be contrasted with other Betaproteobacteria genomes, which frequently encode at least one [2Fe-2S] Fd and one Fld. Both of the organisms that are [4Fe-4S] specialists are notable wastewater bioremediators, *Nitrosomonas europaea* and *Nitrospira multiformis*, each of which oxidize ammonium to nitrite (Arp et al., 2002; Norton et al., 2008). How these organisms reduce [4Fe-4S] Fds is an open question. *N. europaea* grows autotrophically on NH_3, CO_2, and mineral salts alone (Arp et al., 2002), harvesting reducing power from NH_3 to produce NADH (Guo et al., 2013) which has a redox potential of–320 mV (Huang et al., 2012), well above the potential of many [4Fe-4S] Fds which can range from−280 mV to−650 mV (Atkinson et al., 2016). Measuring the reduction potential of [4Fe-4S] Fds in nitrifying organisms may reveal that they are shifted more positively than canonical Fds.

Gammaproteobacteria

Organisms in this class are highly balanced in their usage of all three PEC types. This trend may arise because this class contains many pathogens. Endosymbiotic organisms often struggle to scavenge sufficient iron from the host environment, so the substitution of Flds for iron-demanding Fds may have occurred to support fitness under iron-limiting conditions (Litwin and Calderwood, 1993). The *Enterobacteriales* order, which contains pathogens such as *Salmonella enterica* and *Yersinia pestis*, stands out as being highly populated by all three PEC types, presenting a high percentage (up to 50%) of Flds.

Additional Phyla

Members of Planctomycetes, Verrucomicrobia, Chlamydia, Acidobacteria, and Nitrospirae are represented within the tree, but only in low numbers. In these organisms, [4Fe-4S] Fds are most abundant, although all three PEC types are observed. Additionally, our tree contains small numbers of organisms from the Fusobacteria, Deinococcus, Aquificae, Thermotogae, and Chlorobi phyla. In Fusobacteria, Flds genes are most abundant among the three PEC types, although there are members of this phylum with mixed PEC usage. Many Fusobacteria participate in polymicrobial infections of the respiratory tract and other anaerobic mucosal surfaces (Bennett and Eley, 1993). In these niches, iron availability is predicted to be limited, so Fusobacteria may use Fld genes as part of an evolutionary pressure to be iron frugal. Deinococcus, Aquificae, Thermotogae, and Chlorobi are more dominated by [4Fe-4S] Fds and have mixed PEC usage.

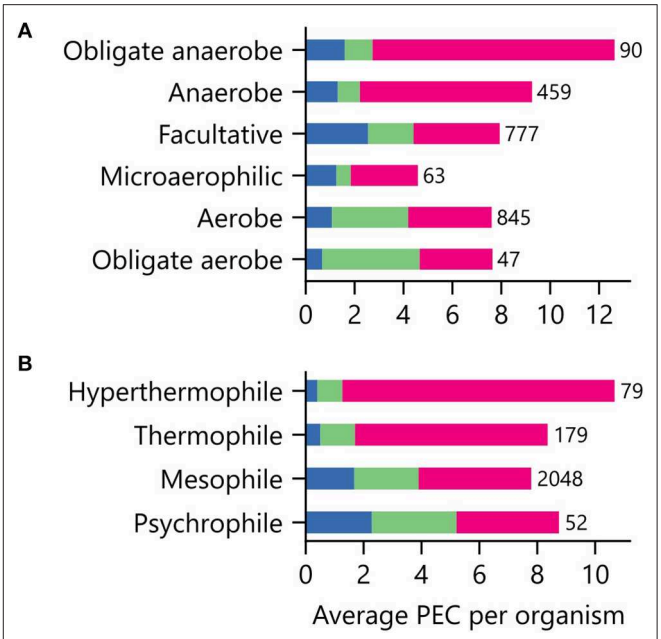

FIGURE 6 | Relationship between environmental niche and PEC use. The average PEC gene counts for organisms having different **(A)** O_2 requirements and **(B)** growth temperatures. Colors represent the counts of [4Fe-4S] Fd (red), [2Fe-2S] Fd (green), and Fld (blue) gene abundances. The number of genomes of each type is shown adjacent to the bars.

PEC Usage Varies With Environment Niche

Low potential PECs differ in their iron requirements and stabilities in the presence of atmospheric O_2 concentrations (Jagannathan et al., 2012; Pierella Karlusich et al., 2014; Holm and Lo, 2016). To determine if an organism's environmental niche correlates with PEC abundance, we evaluated how an organism's preferences for O_2, external pH, and temperature relate to the average number of PEC genes found in a genome. **Figure 6A** shows that organisms with distinct O_2 requirements differ in their PEC usage. The [4Fe-4S] Fds, whose cofactors can be damaged by O_2 (Hsueh et al., 2013), represent the majority of PECs within anaerobes and obligate anaerobes. As O_2 tolerance increases, Flds and [2Fe-2S] Fds increase in relative abundance, becoming the majority of PECs in aerobes and obligate aerobes. Interestingly, [4Fe-4S] Fd usage is not abolished in aerobes. This observation suggests that some [4Fe-4S] Fds have evolved strategies to protect their [4Fe-4S] clusters from oxidative damage.

Several mechanisms have been proposed to increase [4Fe-4S] stability, including: (1) an elongation that creates a sequence that shields the [4Fe-4S] cluster from O_2, (2) tight association

with partner proteins to achieve [4Fe-4S] shielding (Jagannathan and Golbeck, 2009), and (3) adoption of a [3Fe-4S] cluster as a redox cofactor rather than a [4Fe-4S] cluster (Tilley et al., 2001). Support for the last mechanism has come from successes in purifying Fds with [3Fe-4S] clusters that remain stable under aerobic conditions (Aono et al., 1989; Gomes et al., 1998; Ricagno et al., 2007). Additionally, some [4Fe-4S] clusters lose a single Fe atom when placed in an oxidizing atmosphere, rather than losing the entire cluster (Beinert et al., 1996; Tilley et al., 2001). These findings have led some to posit that Fds that bind one [3Fe-4S] cluster and one [4Fe-4S] cluster (*i.e.*, 7Fe Fds) evolved from ancestral Fds that coordinate two [4Fe-4S] clusters to tolerate O_2 (Iwasaki et al., 1994; Tilley et al., 2001).

To gain insight into the role that an aerobic atmosphere had on the evolution of 7Fe Fds, we used InterProScan software to analyze the distribution of [3Fe-4S] ferredoxins. For this analysis, we examined the abundance of genes with the IPR signature for 7Fe ferredoxins (IPR000813). This analysis revealed that the [4Fe-4S] Fd genes in obligate aerobes and aerobes matched the 7Fe Fd signature 30 and 27% of the time, respectively (**Supplementary Dataset 1**). Facultative microbes yielded matches with only 7.8% of the [4Fe-4S] Fd genes, while anaerobes and obligate anaerobes yielded even lower percentages. These trends provide support for the idea that Fds with a [3Fe-4S] metallocluster are more stable under aerobic conditions.

We next investigated how PEC usage relates to growth temperature (**Figure 6B**). Genes encoding [4Fe-4S] Fds were most prevalent in thermophilic and hyperthermophilic organisms, with abundances of 80% and 88% respectively. These thermotolerant organisms also use [2Fe-2S] Fds and Flds, with the [2Fe-2S] Fds being >2-fold more prevalent than Flds. As optimal growth temperature decreases, the [4Fe-4S] Fds are partially replaced by [2Fe-2S] Fds and Flds.

To investigate how PEC gene abundance relates to both growth temperature and O_2 preference, we generated heat maps that compare the average number of PEC genes for different combination of conditions. **Figure 7A** shows that organisms with the greatest abundances of [4Fe-4S] Fd genes live at high temperatures in the absence of O_2, and those with the lowest abundances live at lower temperatures in the presence of O_2. **Figure 7B** illustrates how the organisms with the highest [2Fe-2S] Fd gene counts are mesophiles and obligate aerobes. This analysis also shows that [2Fe-2S] Fds present the lowest abundances at extreme temperatures in the absence of O_2. **Figure 7C** shows that Fld genes are most abundant in psychrophiles that are facultative, and this comparison reveals that Flds present similar low abundance across thermotolerant microbes that live in the presence of different O_2 concentrations. The underlying cause of this trend is not known. However, the paucity of Flds at high temperatures could be caused by the accelerated degradation rates of free FMN cofactor at higher temperatures (Daniel and Cowan, 2000). **Figure 7D** shows the number of genomes used to analyze PEC abundance in each growth niche category.

Elevated pH can lead to the formation of iron hydroxides, which can decrease the concentration of accessible iron. To determine if organisms that grow in niches with high pH are enriched in PECs that use organic FMN rather than Fe-S clusters as cofactors, we compared PEC usage in organisms for which data was available on the pH of their ecological niche (n = 246). All three PEC types were found in organisms that grow optimally at the extreme ends of the pH scale (**Figure 8**). The [2Fe-2S] and [4Fe-4S] Fds are found in lower average external pH environments than Flds, although t-tests comparing the distributions found no significant difference in their mean values.

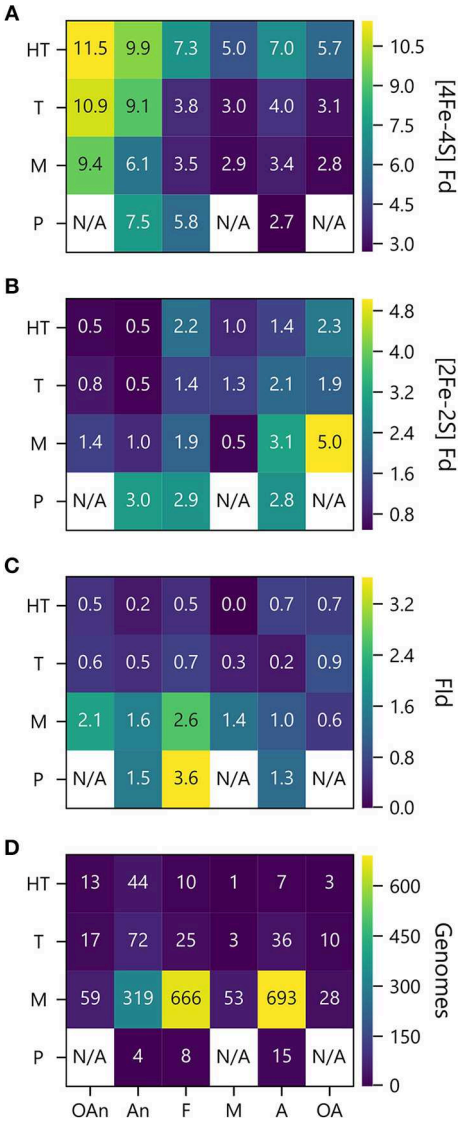

FIGURE 7 | PEC counts sorted by temperature and oxygen niche. The average numbers of **(A)** [4Fe-4S] Fd **(B)**, [2Fe-2S] Fd, and **(C)** Fld gene counts per genome are plotted as a function of O_2 requirement and optimal growth temperature. **(D)** Genome counts from each environmental niche are plotted as a function of O_2 requirement and optimal growth temperature. O_2 requirements shown on the x axis are abbreviated as obligate anaerobe (OAn), anaerobe (An), facultative (F), microaerophilic (M), aerobic (A), and obligate aerobic (OA). Growth temperatures shown on the y axis are abbreviated as hyperthermophile (H), thermophile (T), mesophile (M), and psychrophile (P). N/A denotes not applicable when organisms were not observed.

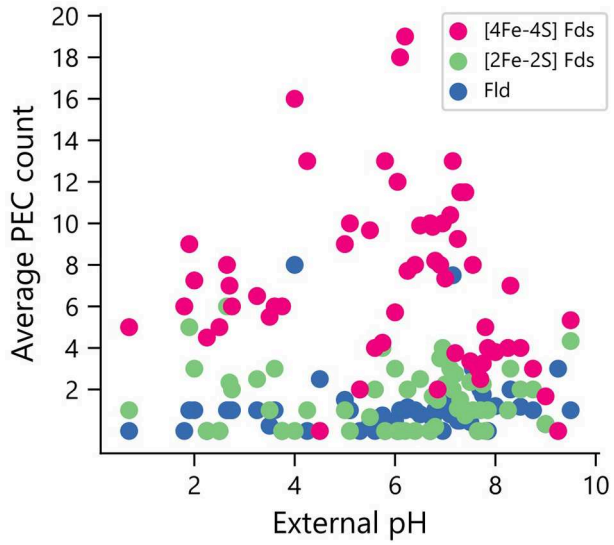

FIGURE 8 | Relationship between environmental pH and PEC gene counts. The distribution of PEC gene counts is normalized by the number of organisms found to grow at each pH value to obtain weighted averages of each PEC type. Analysis of the means revealed no significant pairwise differences using a paired two-tail *t*-test ($p = 0.126$ for [2Fe-2S] Fd and Fld comparison, $p = 0.163$ for [4Fe-4S] Fd and Fld comparison, and $p = 0.75$ for [2Fe-2S] and [4Fe-4S] Fd comparison).

PEC Length Distributions

In organisms with multiple PEC paralogs, studies have revealed that homologs can specialize and evolve partner specificity that allows individual PECs to transfer electrons efficiently to a subset of oxidoreductase partners in an insulated manner (Terauchi et al., 2009). Biochemical studies have shown that this specificity can be achieved by altering the physicochemical properties of the PEC surface to tune binding rates and affinities for specific partners (Akashi et al., 1999), using allosteric conformational changes upon partner binding to regulate ET rates (Tyson et al., 1972; Schlesier et al., 2016), and increasing protein length to create protrusions that sterically hinder binding to some partners (Aoki et al., 1998). With the last mechanism, one would expect that organisms having a single PEC would exhibit smaller average sizes than those family members found in organisms having multiple PECs. To investigate this idea, we sorted PECs by the total numbers of PEC-encoding genes within each genome, and we plotted the distribution of lengths for each PEC type against the total number of PEC genes within genomes.

Organisms having only one PEC gene presented smaller [2Fe-2S] and [4Fe-4S] Fds compared with organisms have two or more total PECs (**Figure 9**). Additionally, organisms with only one PEC gene presented a tighter distribution of Fld lengths compared to organisms possessing multiple PEC genes (**Figure 9**). For organisms with multiple PEC genes, different numbers of modes are observed for the size of each PEC. For Flds and [2Fe-2S] Fds, organisms having a single PEC display a single mode with average lengths of ∼150 and ∼90 residues, respectively. These "short-chain" Flds and [2Fe-2S] Fds are well represented in the Protein Data Bank, including *Desulfovibrio vulgaris* Fld (2FX2) (Watt et al., 1991), *Desulfovibrio desulfuricans* Fld (3KAP) (Romero et al., 1996), *Citrobacter braakii* Fld (4OXX) (Madrona et al., 2014), *Trichomonas vaginalis* Fd (1L5P) (Crossnoe et al., 2002), *Equisetum arvense* Fd (1WRI) (Kurisu et al., 2005), and *Scenedesmus fuscus* Fd (1AWD) (Bes et al., 1999). In contrast, organisms having a single [4Fe-4S] Fd display two distinct modes. These modes are centered around ∼80 and ∼105 residues, respectively. The first mode corresponds in size to di-cluster [4Fe-4S] Fds seen in the PDB and often associated with photosystem I, such as *Synechocystis sp. PCC 6803* Fd (4KT0) (Mazor et al., 2013), *Thauera aromatica* Fd (1RGV) (Unciuleac et al., 2004), and *Thermosynechococcus elongatus* Fd (1JB0) (Jordan et al., 2001). The second mode corresponds to the hybrid [3Fe-4S][4Fe-4S] Fds in the PDB, such as *Sulfolobus tokodaii* Fd (1XER) (Fujii et al., 1996), *Mycobacterium smegmatis* Fd (2V2K) (Ricagno et al., 2007), and *Azotobacter vinelandii* Fd (7FDR) (Schipke et al., 1999).

As the total number of PECs encoded in a genome increases, the average length of each PEC type increases, and the variance around each mode increases. In the case of [4Fe-4S] Fds, multiple distinct modes appear at total PEC abundances greater than two (**Figure 9A**). These are centered around ∼70, ∼110, and ∼170 residues. The relative abundance of each mode changes with total PEC abundance. At lower total PEC abundances (<10), the two smaller modes dominate and blur into a single continuous mode. As total PEC abundance increases from 10 to 20, the largest mode becomes dominant. At even higher PEC abundances, the lower two modes are most prevalent and appear as a single smear. The [4Fe-4S] Fds in the PDB have a distinct size distribution. Structurally-characterized [4Fe-4S] Fds have lengths ranging from 54 to 106 amino acids (**Figure 9B**). The protein data bank lacks family members above this length regime, like those in our dataset.

For [2Fe-2S] Fds (**Figure 9C**), a single mode is observed with organisms that have a single PEC, and two or three modes are observed in organisms having multiple PEC genes. These modes occur at ∼90, ∼110, and ∼160 residues. The size dispersion of the data around the longer modes is greater than that observed with smallest mode. To date, there have been extensive structural studies of [2Fe-2S] Fds with the shorter lengths, including 22 structures of [2Fe-2S] Fds having <100 amino acids and 16 structures of [2Fe-2S] Fds having lengths ranging from 103 to 128 amino acids (**Figure 9D**). However, analysis of the size distribution of structurally-characterized [2Fe-2S] Fds reveals that we lack structural information on Fds from the largest mode (∼150).

Flds (**Figure 9E**) clearly present two modes as the number of PECs in an organism exceeds ten, which are centered around 145 and 170 residues. This observation suggests that previously described short and long-chain Flds represent two distinct subtypes that are widespread in nature (López-Llano et al., 2004). In cells with even higher PEC abundances, a third Fld size appears having a mode near 200 amino acids. Conducting BLAST searches on these proteins reveals high similarity to the WrbA family of flavoproteins, which are distinct from short- and long-chain flavodoxins in their capacity to conduct two-electron

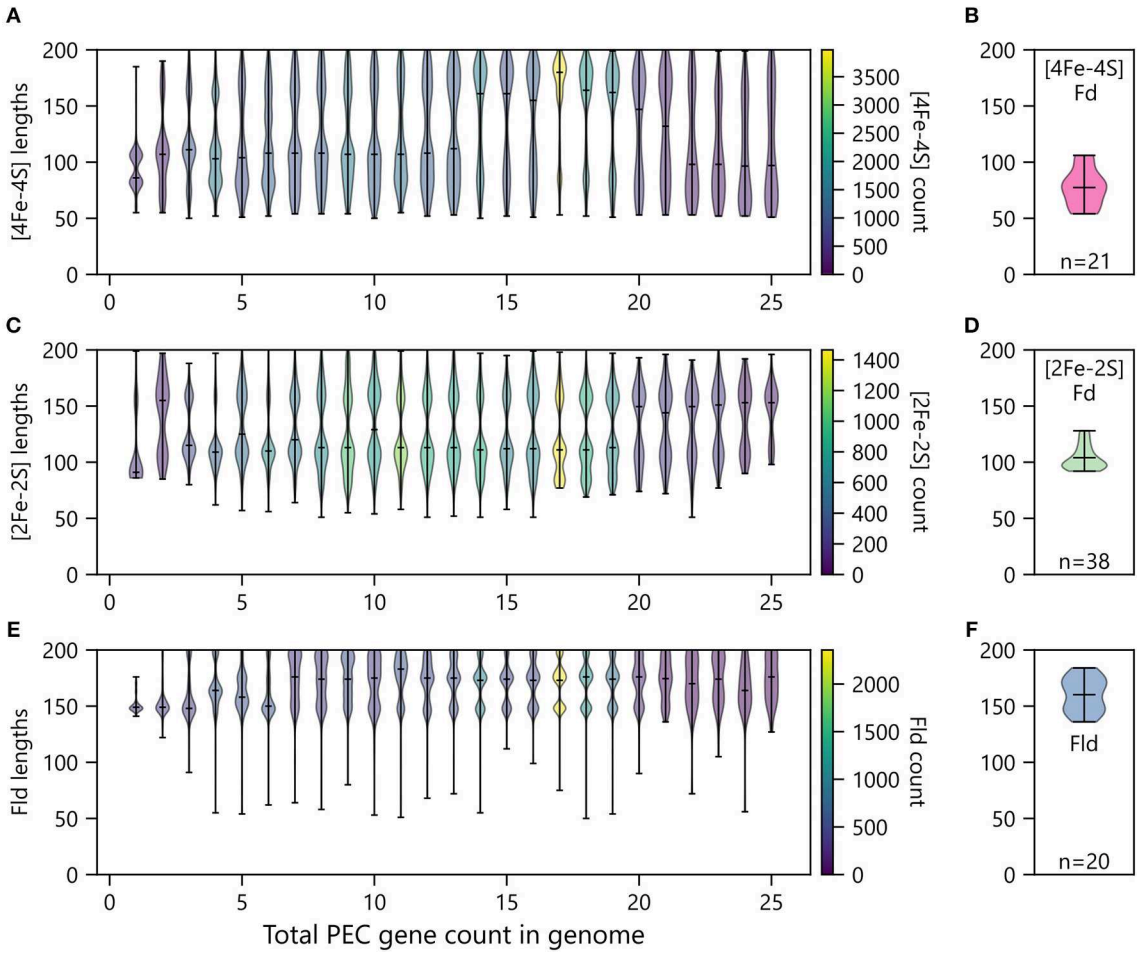

FIGURE 9 | Relationship between PEC length and number of PECs per organism. The abundances of **(A)** [4Fe-4S] Fds, **(C)** [2Fe-2S] Fds, and **(E)** Flds of different lengths encoded by genomes having different *total* numbers of PEC genes. Violin plots show the relative abundance of PECs having different sizes in each bin. The extrema are marked by horizontal edge lines at the ends of the vertical bars, and the average length is marked by an internal horizontal line. The number of genes within each violin plot is visualized using a viridis color gradient. For comparison, the lengths of **(B)** [4Fe-4S] Fd, **(D)** [2Fe-2S] Fd, and **(F)** Fld structures deposited in the Protein Data Bank (Berman, 2000). The number of structures used to generate these plots are noted at the bottom of each panel.

oxidation and reduction reactions which they utilize in their role as NAD(P)H:quinone oxidoreductases (Patridge and Ferry, 2006; Andrade et al., 2007). While it is clear that traditional Flds and previously studied WbrA proteins differ in their ET roles, we do not know if any natural variants exist that can promiscuously perform both functions. The similar structures of the two protein subfamilies suggests that WbrA homologs may be able to bind to natural Fld oxidoreductase partners, at least transiently. Future biochemical studies will be needed to test this idea. Indeed, analysis of the size distribution of structurally-characterized Flds reveals that only a handful (∼10) of each subtype have been studied (**Figure 9F**).

Oxidizing Conditions and PEC Size Distribution

To probe the relationship between O_2 growth requirements and PEC lengths within a genome, we binned organisms by ecological niche and evaluated the average size within the modes observed under each condition. With the [4Fe-4S] Fds (**Figure 10A**), most organisms presented two major modes. The protein length for the larger mode was centered near 170 residues in all cases. However, the average size for the smaller mode increases with the transition from low O_2 (obligate anaerobes) to high O_2 (obligate aerobes) conditions. The [4Fe-4S] Fds in aerobes have a length distribution that is devoid of [4Fe-4S] Fds with lengths ($\leq$60 residues) that are characteristic of the prototypical Clostridial Fds (Bertini et al., 1995; Atkinson et al., 2016). This finding suggests that only certain [4Fe-4S] Fds can support ET under the oxidizing conditions where these organisms grow optimally.

When examining [2Fe-2S] Fds length across different O_2 growth requirements, a distinct trend is observed from the [4Fe-4S] Fds (**Figure 10B**). The lengths of [2Fe-2S] Fds on the anaerobic end of the spectrum are distributed around a single mode that is centered near 155 residues. In organisms that tolerate and require O_2, additional modes appear, which are centered at ∼80 and 105 amino acids. The underlying cause of this trend is not known. In aerobic organisms, the greater abundance of small [2Fe-2S] Fds may arise to support ET that is challenging for [4Fe-4S] Fds, due to their sensitivity to oxidation.

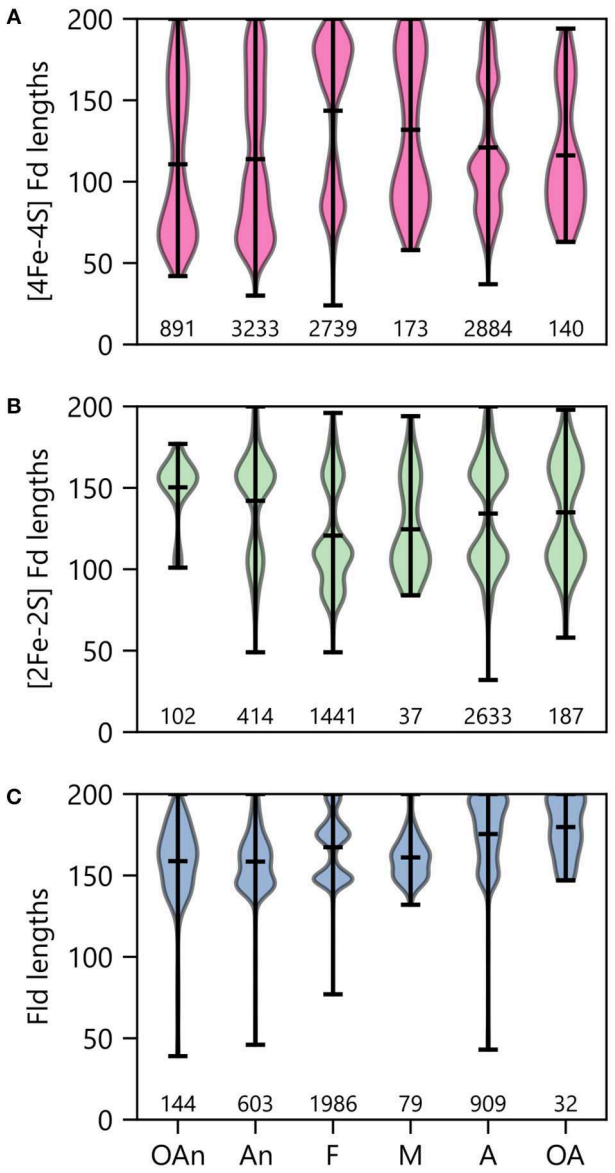

FIGURE 10 | PEC length distributions in organisms having different O_2 requirements. The lengths of **(A)** [4Fe-4S] Fd, **(B)** [2Fe-2S] Fd, and **(C)** Fld genes in organisms having distinct O_2 requirements. Growth requirements are abbreviated as obligate anaerobe (OAn), anaerobe (An), facultative (F), microaerophilic (M), aerobic (A), and obligate aerobic (OA). The extrema are marked by the horizontal bars at the edges of the vertical bars, and the average length is noted with an internal horizontal bar. The number of individual genes in each category is listed below each plot.

Interestingly, Flds become longer on average as O_2 growth requirements increase (**Figure 10C**). The average Fld length is ∼160 residues within obligate anaerobes and ∼180 residues in obligate aerobes. In most cases, the Fld lengths are diffusely distributed around their means, with the exception of facultative organisms, which present multiple modes with small variances. There appears to be three Fld lengths that are highly popular in facultative species. Notably, of all the O_2 requirement groups, we found the most Flds in facultative species (**Figure 10C**). These organisms are noted for being some of the most enthusiastic Fld adopters with an average percent incorporation of 32% (**Figure 6A**). Lastly, it is worth noting that in aerobes and obligate aerobes, the Fld length distributions seems to butt up against the ceiling of the 200 amino acid cut-off. This observation suggests that this size cutoff may miss some Flds and that the true length averages for aerobes and obligate aerobes are higher than shown.

Optimal Growth Temperature and PEC Size Distribution

To determine how optimal growth temperature relates to PEC gene lengths, we binned PEC types by growth temperature and evaluated the average size under each condition (**Figure 11**). Under thermophilic and hyperthermophillic conditions, genes encoding [2Fe-2S] Fds and Flds are longer on average than their mesophilic and psychrophilic counterparts. In contrast, there is marked shift toward smaller [4Fe-4S] Fds in thermotolerant organisms. This latter trend is consistent with the proposed emergence of [4Fe-4S] Fds before [2Fe-2S] Fds and Flds in ancient thermophilic archaea (Sousa et al., 2013).

DISCUSSION

Our bioinformatics analysis reveals that genes encoding low potential PECs are abundant within genomes from organisms across the tree of life. In the 56 phyla studied herein, we found 98% of them harbor at least one organism with a PEC gene. While kingdom level analysis revealed that the average number of PEC genes per organism decreases as one goes from Archaea (∼13) to Bacteria (∼8) and Eukarya (∼3), a large amount of variation was observed within each kingdom. For example, one bacterium contains as many as 54 total small PEC-encoding genes (*Desulfitobacterium hafniense* DCB-2), 53 of which match for [4Fe-4S] PEC genes, and one eukaryote presented 42 PEC genes (*Zea mays*). As one considers the individual protein families analyzed, over 500 organisms presented 10 or more paralogs from either the [4Fe-4S] or [2Fe-2S] Fd families. In contrast only one organism had 10 or more Fld paralogs. The reason why iron-sulfur cluster containing PECs evolved larger numbers of paralogs within extant organisms is not known.

Although many lifeforms maintain an extensive PEC gene pool, suggesting a need for distinct physiological roles for each paralog (Onda et al., 2000; Terauchi et al., 2009; Peden et al., 2013; Cassier-Chauvat and Chauvat, 2014; Atkinson et al., 2016; Mellor et al., 2017; Burkhart et al., 2019), some organisms in our dataset lack annotated genes encoding small (<200 amino acids) PECs. These organisms span over a dozen phyla and all three domains of life. Given the phylogenetic diversity of organisms that lack annotated PEC genes, these organisms are unlikely to share a common metabolism. Further investigation will be needed to determine if these organisms evolved a more extensive use of NAD/NADP-dependent oxidoreductases and/or if they utilize oxidoreductases that arose from the fusion of genes encoding small PECs and their partner oxidoreductase. Such fusion proteins would not have been detected by our 200 amino acid cutoff.

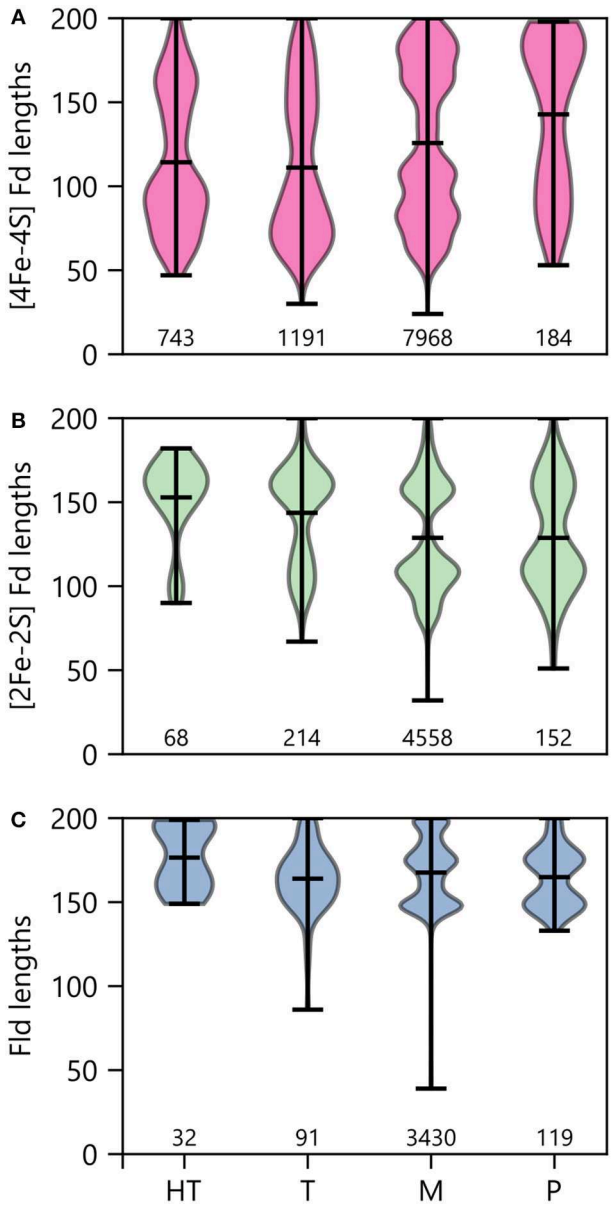

FIGURE 11 | PEC length distributions in organisms having different growth temperatures. The lengths of **(A)** [4Fe-4S] Fds, **(B)** [2Fe-2S] Fds, and **(C)** Flds found in organisms having different optimal growth temperatures is shown using violin plots. Optimal growth temperatures are abbreviated as hyperthermophile (H), thermophile (T), mesophile (M), and psychrophile (P). The extrema are noted with horizontal bars at the edges, and the average is noted with an internal horizontal bar. The number of individual genes in each category is listed below the plots.

Our size analysis revealed significant variation in PEC lengths. The average lengths of the [2Fe-2S] Fds, [4Fe-4S] Fds, and Flds were smallest in organisms containing a single PEC. This observation suggests that organisms with more than one PEC may require longer primary structures to support increased partner specificity, allowing organisms to discriminate which PEC is involved in an ET pathway (Onda et al., 2000; Terauchi et al., 2009; Duhutrel et al., 2010; Peden et al., 2013; Cassier-Chauvat and Chauvat, 2014; Atkinson et al., 2016; Burkhart et al., 2019). Our size analysis also revealed a large dispersion of gene lengths with multiple modes for each PEC type. For example, multiple modes were observed with the [4Fe-4S] Fds, which varied with the number of total small PECs encoded by genomes. While these modes occurred at different lengths, we observed family members with almost every possible size connecting these modes. This observation can be contrasted with the size distribution of structurally-characterized PECs. A narrower distribution of PEC sizes occurs in the structures within the PDB (Berman, 2000). This finding suggests that one way to obtain greater insight into PEC structural diversity would be to obtain structural data for PECs exhibiting a greater diversity of lengths.

To better understand the underlying reason for variation in PEC lengths, we evaluated how the primary structure of each PEC type changes with organismal growth requirements. We uncovered widespread variation in PEC structure and gene pool makeup that coincides with changes in an organism's O_2 requirement and tolerance. Previous research has found that Fd sequence extensions and partner protein binding can both enhance O_2 tolerance of [4Fe-4S] clusters through shielding (Jagannathan and Golbeck, 2009). In support of this observation, we detected the shortest [4Fe-4S] Fd lengths in anaerobic organisms and a shift toward longer [4Fe-4S] Fds in aerobic organisms, additionally observing that [4Fe-4S] Fds are restricted to fewer permissible lengths under aerobic conditions. Altering the cluster type of a [4Fe-4S] Fd to a [3Fe-4S] Fd by removing one of the Fe atoms has also been hypothesized as a strategy for increasing resistance to oxidative damage (Tilley et al., 2001). In support of this idea, we found that 7Fe Fd gene signatures are more prevalent in aerobic organisms. Furthermore, we observed that [2Fe-2S] Fd and Fld genes make up a larger portion of the gene pool in aerobic organisms, reinforcing the notion that these organisms have been enriched in O_2-tolerant [2Fe-2S] Fds and Flds. Our findings highlight the need for further *in vitro* studies examining how the O_2-tolerance of [4Fe-4S] Fds varies with primary structure.

Our bioinformatics analysis supports the idea that [4Fe-4S] Fds represent the most ancient low potential PEC family (Sousa et al., 2013). Organisms harboring [4Fe-4S] Fds were observed extensively across the tree of life, but they occurred with the greatest abundance in Archaea, which are deeply rooted (Sousa et al., 2013). Our pairwise analysis of PEC abundance provides additional evidence for this hypothesis. Organisms with five or more [2Fe-2S] Fds or Flds almost always contain [4Fe-4S] Fds (>99% of the time). However, as the numbers of [4Fe-4S] Fds increases, the abundances of [2Fe-2S] Fds and Flds decrease. Furthermore, it has been theorized that the most ancient organisms on Earth were thermophilic, anaerobic, and similar to modern day Archaea (Sousa et al., 2013). We found that organisms in all three of these categories are enriched in [4Fe-4S] Fds compared with the other PEC types. Taken together, these findings support the theory that [4Fe-4S] Fds enjoyed early adoption across the global microbiome before the Great

Oxidation Event and have been maintained in many lineages as [2Fe-2S] Fds and Flds grew in popularity.

One thing that is more challenging to discern is whether [2Fe-2S] Fds or Flds evolved first. Our comparison of the relative abundances of these PECs identified similar numbers of organisms that are [2Fe-2S] Fd and Fld specialists. Additionally, [2Fe-2S] Fds and Flds are both found in a range of organisms that are deeply rooted in the tree of life, including Archaea and Cyanobacteria. However, [2Fe-2S] Fds are most abundant within Cyanobacteria, suggesting that these PECs arose prior to Flds in this phylum to support photosynthesis and diversified through duplication and mutation prior to these organisms evolving Flds. One avenue to unraveling this question may be to examine the PEC "fossil record" from a structural perspective. A recent study using the structural database to study oxidoreductase evolution observed a modular origin of biological ET chains (Raanan et al., 2018). An additional way to elucidate this question is to use protein design to test ideas about ancestral PECs that are no longer observed in nature (Mutter et al., 2019).

In a small number of organisms, proteomic studies have provided evidence that cells differentially control the flow of electrons across metabolic pathways by diversifying their PEC pool. Our finding that PECs are abundant in many genomes across the tree of life illustrates the need to understand the rules that guide PEC partner specificity. Structural studies have provided some insight into the molecular interactions that mediate PEC interactions with partner oxidoreductases, including structures of PEC-partner complexes (Morales et al., 2000; Kurisu et al., 2001; Müller et al., 2001; Dai et al., 2007; Xu et al., 2008; Strushkevich et al., 2011). However, these studies are limited to a small number of protein complexes. Even for the best-characterized PECs, we lack rules for anticipating partner specificities and predicting the electron fluxome. Our understanding of sequence-structure-electrochemical properties further limits our ability to anticipate PEC-mediated control over electron flow in cells. Relatively few PECs have had their midpoint reduction potentials measured (Atkinson et al., 2016), and strategies for characterizing the electrochemical properties of PECs are low throughput due to the need for protein overexpression and purification prior to electrochemical characterization. Unfortunately, algorithms for predicting midpoint potentials from primary structure are not yet sufficiently accurate and robust to predict PEC midpoint potentials without the need for *in vitro* characterization (Perrin and Ichiye, 2013).

In the future, high-throughput methods for comparing the ET efficiencies of PECs with defined partner proteins could help develop rules that relate PEC sequence to partner specificities. Cellular assays that couple biomass production to PEC-mediated ET in synthetic pathways have been reported and utilized to study both natural and synthetic PECs (Barstow et al., 2011; Atkinson et al., 2016, 2019). Such methods could be leveraged to analyze the partner specificities of any PEC imaginable, since genes are cheap to synthesize. We posit that the best PECs to analyze in such assays will be those having divergent sequences, which can be identified using sequence similarity networks (Brown and Babbitt, 2012). It may also be possible to uncover PECs with strong partner interactions by identifying operons that colocalize PECs with their partner oxidoreductases (Gerlt, 2017). Further biochemical studies will be required to evaluate whether oxidoreductases colocalized with PECs exhibit greater specificity for one another compared with PECs encoded in more distal genomic regions. We hypothesize that the quickest way to obtain this information will be through high-throughput cellular assays that couple electron transfer between a PEC and its partner to cell growth (Atkinson et al., 2016). Large amounts of specificity data can be generated by expressing different PEC homologs in the presence of the same partner oxidoreductases and cataloging differences in growth that are observed with different PEC-partner combinations (Barstow et al., 2011; Atkinson et al., 2019). Since growth is proportional to electron transfer to a partner protein, the growth data obtained in such assays reflects the relative specificity of PECs for the same partner protein.

DATA AVAILABILITY

All datasets generated and analyzed in this study are included in the manuscript and the **Supplementary Files**.

AUTHOR CONTRIBUTIONS

IC, JS, and GB conceptualized the project. IC conducted genome mining, data processing, and visualization. IC and JS wrote the manuscript.

ACKNOWLEDGMENTS

This project was supported by DOE grant DE-SC0014462 and NASA NAI grant number 80NSSC18M0093. Additionally, IC was supported by a Lodieska Stockbridge Vaughn Fellowship. Consultations for statistics were provided by Rice University Data Science Consulting Clinic members Alex Aguilar, Daniel Bourgeois, Shannon Chen, Wendy Feng, Zhuowei Han, Gunny Liu, Minjie Wang, and James Warner.

SUPPLEMENTARY MATERIAL

The Supplementary Material for this article can be found online at: https://www.frontiersin.org/articles/10.3389/fenrg.2019.00079/full#supplementary-material

REFERENCES

Akashi, T., Matsumura, T., Ideguchi, T., Iwakiri, K., Kawakatsu, T., Taniguchi, I., et al. (1999). Comparison of the electrostatic binding sites on the surface of ferredoxin for two ferredoxin-dependent enzymes, ferredoxin-NADP(+) reductase and sulfite reductase. *J. Biol. Chem.* 274, 29399–29405. doi: 10.1074/jbc.274.41.29399

Andrade, S. L., Patridge, E. V., Ferry, J. G., and Einsle, O. (2007). Crystal Structure of the NADH:quinone oxidoreductase WrbA from *Escherichia coli*. *J. Bacteriol.* 189, 9101–9107. doi: 10.1128/JB.01336-07

Andreini, C., Banci, L., Bertini, I., Elmi, S., and Rosato, A. (2007). Non-heme iron through the three domains of life. *Proteins* 67, 317–324. doi: 10.1002/prot.21324

Aoki, M., Ishimori, K., and Morishima, I. (1998). Roles of negatively charged surface residues of putidaredoxin in interactions with redox partners in P450cam monooxygenase system. *Biochim. Biophys. Acta BBA-Protein Struct. Mol. Enzymol.* 1386, 157–167. doi: 10.1016/S0167-4838(98)00094-6

Aono, S., Bryant, F. O., and Adams, M. W. (1989). A novel and remarkably thermostable ferredoxin from the hyperthermophilic archaebacterium *Pyrococcus furiosus*. *J. Bacteriol.* 171, 3433–3439. doi: 10.1128/jb.171.6.3433-3439.1989

Arp, D. J., Sayavedra-Soto, L. A., and Hommes, N. G. (2002). Molecular biology and biochemistry of ammonia oxidation by *Nitrosomonas europaea*. *Arch. Microbiol.* 178, 250–255. doi: 10.1007/s00203-002-0452-0

Atkinson, J. T., Campbell, I., Bennett, G. N., and Silberg, J. J. (2016). Cellular assays for Ferredoxins: a strategy for understanding electron flow through protein carriers that link metabolic pathways. *Biochemistry* 55, 7047–7064. doi: 10.1021/acs.biochem.6b00831

Atkinson, J. T., Campbell, I. J., Thomas, E. E., Bonitatibus, S. C., Elliott, S. J., Bennett, G. N., et al. (2019). Metalloprotein switches that display chemical-dependent electron transfer in cells. *Nat. Chem. Biol.* 15, 189–195. doi: 10.1038/s41589-018-0192-3

Bahar, M., de Majnik, J., Saint, C. P., and Murphy, P. J. (2000). Conservation of a pseudomonad-like hydrocarbon degradative ferredoxin oxygenase complex involved in rhizopine catabolism in *Sinorhizobium meliloti* and *Rhizobium leguminosarum* bv. viciae. *J. Mol. Microbiol. Biotechnol.* 2, 257–259.

Barstow, B., Agapakis, C. M., Boyle, P. M., Grandl, G., Silver, P. A., and Wintermute, E. H. (2011). A synthetic system links FeFe-hydrogenases to essential *E. coli* sulfur metabolism. *J. Biol. Eng.* 5, 1–15. doi: 10.1186/1754-1611-5-7

Beinert, H., Kennedy, M. C., and Stout, C. D. (1996). Aconitase as iron–sulfur protein, enzyme, and iron-regulatory protein. *Chem. Rev.* 96, 2335–2374. doi: 10.1021/cr950040z

Bennett, K. W., and Eley, A. (1993). Fusobacteria: new taxonomy and related diseases. *J. Med. Microbiol.* 39, 246–254. doi: 10.1099/00222615-39-4-246

Berman, H. M. (2000). The protein data bank. *Nucleic Acids Res.* 28, 235–242. doi: 10.1093/nar/28.1.235

Bertini, I., Donaire, A., Feinberg, B. A., Luchinat, C., Piccioli, M., and Yuan, H. (1995). Solution structure of the oxidized 2[4Fe-4S] ferredoxin from *Clostridium pasteurianum*. *Eur. J. Biochem.* 232, 192–205. doi: 10.1111/j.1432-1033.1995.tb20799.x

Bes, M. T., Parisini, E., Inda, L. A., Saraiva, L. M., Peleato, M. L., and Sheldrick, G. M. (1999). Crystal structure determination at 1.4 A resolution of ferredoxin from the green alga *Chlorella fusca*. *Struct. Lond. Engl.* 7, 1201–1211. doi: 10.1016/S0969-2126(00)80054-4

Björklund, A. K., Ekman, D., Light, S., Frey-Skött, J., and Elofsson, A. (2005). Domain rearrangements in protein evolution. *J. Mol. Biol.* 353, 911–923. doi: 10.1016/j.jmb.2005.08.067

Brown, S. D., and Babbitt, P. C. (2012). Inference of functional properties from large-scale analysis of enzyme superfamilies. *J. Biol. Chem.* 287, 35–42. doi: 10.1074/jbc.R111.283408

Burkhart, B. W., Febvre, H. P., and Santangelo, T. J. (2019). Distinct physiological roles of the three ferredoxins encoded in the hyperthermophilic archaeon *Thermococcus kodakarensis*. *MBio* 10, e02807–e02818. doi: 10.1128/mBio.02807-18

Cassier-Chauvat, C., and Chauvat, F. (2014). Function and regulation of ferredoxins in the cyanobacterium, synechocystis PCC6803: recent advances. *Life* 4, 666–680. doi: 10.3390/life4040666

Chen, I. A., Chu, K., Palaniappan, K., Pillay, M., Ratner, A., Huang, J., et al. (2019). IMG/M v.5.0: an integrated data management and comparative analysis system for microbial genomes and microbiomes. *Nucleic Acids Res.* 47, D666–D677. doi: 10.1093/nar/gky901

Crossnoe, C. R., Germanas, J. P., LeMagueres, P., Mustata, G., and Krause, K. L. (2002). The crystal structure of *Trichomonas vaginalis* ferredoxin provides insight into metronidazole activation. *J. Mol. Biol.* 318, 503–518. doi: 10.1016/S0022-2836(02)00051-7

Dai, S., Friemann, R., Glauser, D. A., Bourquin, F., Manieri, W., Schürmann, P., et al. (2007). Structural snapshots along the reaction pathway of ferredoxin–thioredoxin reductase. *Nature* 448, 92–96. doi: 10.1038/nature05937

Daniel, R. M., and Cowan, D. A. (2000). Biomolecular stability and life at high temperatures. *Cell. Mol. Life Sci.* 57, 250–264. doi: 10.1007/PL00000688

Dawid, W. (2000). Biology and global distribution of myxobacteria in soils. *FEMS Microbiol. Rev.* 24, 403–427. doi: 10.1111/j.1574-6976.2000.tb00548.x

Demuez, M., Cournac, L., Guerrini, O., Soucaille, P., and Girbal, L. (2007). Complete activity profile of *Clostridium acetobutylicum* [FeFe]-hydrogenase and kinetic parameters for endogenous redox partners. *FEMS Microbiol. Lett.* 275, 113–121. doi: 10.1111/j.1574-6968.2007.00868.x

Duhutrel, P., Bordat, C., Wu, T.-D., Zagorec, M., Guerquin-Kern, J.-L., and Champomier-Vergès, M.-C. (2010). Iron sources used by the nonpathogenic lactic acid bacterium Lactobacillus sakei as revealed by electron energy loss spectroscopy and secondary-ion mass spectrometry. *Appl. Environ. Microbiol.* 76, 560–565. doi: 10.1128/AEM.02205-09

Fedorov, R., Hartmann, E., Ghosh, D. K., and Schlichting, I. (2003). Structural basis for the specificity of the nitric-oxide synthase inhibitors W1400 and Nomega-propyl-L-Arg for the inducible and neuronal isoforms. *J. Biol. Chem.* 278, 45818–45825. doi: 10.1074/jbc.M306030200

Finn, R. D., Attwood, T. K., Babbitt, P. C., Bateman, A., Bork, P., Bridge, A. J., et al. (2017). InterPro in 2017-beyond protein family and domain annotations. *Nucleic Acids Res.* 45, D190–D199. doi: 10.1093/nar/gkw1107

Fischmann, T. O., Hruza, A., Niu, X. D., Fossetta, J. D., Lunn, C. A., Dolphin, E., et al. (1999). Structural characterization of nitric oxide synthase isoforms reveals striking active-site conservation. *Nat. Struct. Biol.* 6, 233–242. doi: 10.1038/6675

Freigang, J., Diederichs, K., Schäfer, K. P., Welte, W., and Paul, R. (2002). Crystal structure of oxidized flavodoxin, an essential protein in *Helicobacter pylori*. *Protein Sci.* 11, 253–261. doi: 10.1110/ps.28602

Fujii, T., Hata, Y., Wakagi, T., Tanaka, N., and Oshima, T. (1996). Novel zinc-binding centre in thermoacidophilic archaeal ferredoxins. *Nat. Struct. Biol.* 3, 834–837. doi: 10.1038/nsb1096-834

Gerlt, J. A. (2017). Genomic enzymology: web tools for leveraging protein family sequence–function space and genome context to discover novel functions. *Biochemistry* 56, 4293–4308. doi: 10.1021/acs.biochem.7b00614

Gomes, C. M., Faria, A., Carita, J. C., Mendes, J., Regalla, M., Chicau, P., et al. (1998). Di-cluster, seven-iron ferredoxins from hyperthermophilic Sulfolobales. *J. Biol. Inorg. Chem.* 3, 499–507. doi: 10.1007/s007750050260

Goñi, G., Serrano, A., Frago, S., Hervás, M., Peregrina, J. R., De la Rosa, M. A., et al. (2008). Flavodoxin-mediated electron transfer from photosystem I to ferredoxin-$NADP^+$ reductase in *anabaena*: role of flavodoxin hydrophobic residues in protein–protein interactions. *Biochemistry* 47, 1207–1217. doi: 10.1021/bi7017392

Guo, J., Peng, Y., Wang, S., Ma, B., Ge, S., Wang, Z., et al. (2013). Pathways and organisms involved in ammonia oxidation and nitrous oxide emission. *Crit. Rev. Environ. Sci. Technol.* 43, 2213–2296. doi: 10.1080/10643389.2012.672072

Harper, M., Weinstein, B., Simon, C., Chebee7i, Swanson-Hysell, N., Badger, T. G., Greco, M., et al. (2015). *Python-Ternary: Ternary Plots in Python*. Zenodo. doi: 10.5281/zenodo.34938

Holm, R. H., and Lo, W. (2016). Structural conversions of synthetic and protein-bound iron–sulfur clusters. *Chem. Rev.* 116, 13685–13713. doi: 10.1021/acs.chemrev.6b00276

Hosseinzadeh, P., and Lu, Y. (2016). Design and fine-tuning redox potentials of metalloproteins involved in electron transfer in bioenergetics. *Biochim. Biophys. Acta BBA Bioenerg.* 1857, 557–581. doi: 10.1016/j.bbabio.2015.08.006

Hsueh, K.-L., Yu, L.-K., Chen, Y.-H., Cheng, Y.-H., Hsieh, Y.-C., Ke, S.-C., et al. (2013). FeoC from *Klebsiella pneumoniae* contains a [4Fe-4S] cluster. *J. Bacteriol.* 195, 4726–4734. doi: 10.1128/JB.00687-13

Huang, H., Wang, S., Moll, J., and Thauer, R. K. (2012). Electron bifurcation involved in the energy metabolism of the acetogenic bacterium *Moorella thermoacetica* growing on glucose or H_2 plus CO_2. *J. Bacteriol.* 194, 3689–3699. doi: 10.1128/JB.00385-12

Huerta-Cepas, J., Serra, F., and Bork, P. (2016). ETE 3: reconstruction, analysis, and visualization of phylogenomic data. *Mol. Biol. Evol.* 33, 1635–1638. doi: 10.1093/molbev/msw046

Hug, L. A., Baker, B. J., Anantharaman, K., Brown, C. T., Probst, A. J., Castelle, C. J., et al. (2016). A new view of the tree of life. *Nat. Microbiol.* 1:16048. doi: 10.1038/nmicrobiol.2016.48

Hunter, J. D. (2007). Matplotlib: a 2D graphics environment. *Comput. Sci. Eng.* 9, 90–95. doi: 10.1109/MCSE.2007.55

Ilbert, M., and Bonnefoy, V. (2013). Insight into the evolution of the iron oxidation pathways. *Biochim. Biophys. Acta BBA Bioenerg.* 1827, 161–175. doi: 10.1016/j.bbabio.2012.10.001

Imlay, J. A. (2006). Iron-sulphur clusters and the problem with oxygen. *Mol. Microbiol.* 59, 1073–1082. doi: 10.1111/j.1365-2958.2006.05028.x

Imlay, J. A. (2019). Where in the world do bacteria experience oxidative stress? Oxidative stress in natural environments. *Environ. Microbiol.* 21, 521–530. doi: 10.1111/1462-2920.14445

Iwasaki, T., Wakagi, T., Isogai, Y., Tanaka, K., Iizuka, T., and Oshima, T. (1994). Functional and evolutionary implications of a [3Fe-4S] cluster of the dicluster-type ferredoxin from the thermoacidophilic archaeon, *Sulfolobus* sp. strain 7. *J. Biol. Chem.* 269, 29444–29450.

Jagannathan, B., and Golbeck, J. H. (2009). Understanding of the binding interface between PsaC and the PsaA/PsaB heterodimer in photosystem I. *Biochemistry* 48, 5405–5416. doi: 10.1021/bi900243f

Jagannathan, B., Shen, G., and Golbeck, J. H. (2012). "The evolution of type I reaction centers: the response to oxygenic photosynthesis," in *Functional Genomics and Evolution of Photosynthetic Systems,* eds R. Burnap and W. Vermaas (Dordrecht: Springer), 285–316. doi: 10.1007/978-94-007-1533-2_12

Jones, P., Binns, D., Chang, H.-Y., Fraser, M., Li, W., McAnulla, C., et al. (2014). InterProScan 5: genome-scale protein function classification. *Bioinformatics* 30, 1236–1240. doi: 10.1093/bioinformatics/btu031

Jordan, P., Fromme, P., Witt, H. T., Klukas, O., Saenger, W., and Krauss, N. (2001). Three-dimensional structure of cyanobacterial photosystem I at 2.5 A resolution. *Nature* 411, 909–917. doi: 10.1038/35082000

Kim, J. Y., Nakayama, M., Toyota, H., Kurisu, G., and Hase, T. (2016). Structural and mutational studies of an electron transfer complex of maize sulfite reductase and ferredoxin. *J. Biochem.* 160, 101–109. doi: 10.1093/jb/mvw016

Kiss, H., Nett, M., Domin, N., Martin, K., Maresca, J. A., Copeland, A., et al. (2011). Complete genome sequence of the filamentous gliding predatory bacterium *Herpetosiphon aurantiacus* type strain (114-95(T)). *Stand. Genomic Sci.* 5, 356–370. doi: 10.4056/sigs.2194987

Kurisu, G., Kusunoki, M., Katoh, E., Yamazaki, T., Teshima, K., Onda, Y., et al. (2001). Structure of the electron transfer complex between ferredoxin and ferredoxin-NADP(+) reductase. *Nat. Struct. Biol.* 8, 117–121. doi: 10.1038/84097

Kurisu, G., Nishiyama, D., Kusunoki, M., Fujikawa, S., Katoh, M., Hanke, G. T., et al. (2005). A structural basis of *Equisetum arvense* ferredoxin isoform II producing an alternative electron transfer with ferredoxin-NADP+ reductase. *J. Biol. Chem.* 280, 2275–2281. doi: 10.1074/jbc.M408904200

Kverka, M., Zakostelska, Z., Klimesova, K., Sokol, D., Hudcovic, T., Hrncir, T., et al. (2011). Oral administration of *Parabacteroides distasonis* antigens attenuates experimental murine colitis through modulation of immunity and microbiota composition: bacterial components and experimental colitis. *Clin. Exp. Immunol.* 163, 250–259. doi: 10.1111/j.1365-2249.2010.04286.x

Letunic, I., and Bork, P. (2016). Interactive tree of life (iTOL) v3: an online tool for the display and annotation of phylogenetic and other trees. *Nucleic Acids Res.* 44, W242–W245. doi: 10.1093/nar/gkw290

Litwin, C. M., and Calderwood, S. B. (1993). Role of iron in regulation of virulence genes. *Clin. Microbiol. Rev.* 6, 137–149. doi: 10.1128/CMR.6.2.137

Löffler, F. E., Yan, J., Ritalahti, K. M., Adrian, L., Edwards, E. A., Konstantinidis, K. T., et al. (2013). Dehalococcoides mccartyi gen. nov., sp. nov., obligately organohalide-respiring anaerobic bacteria relevant to halogen cycling and bioremediation, belong to a novel bacterial class, *Dehalococcoidia classis* nov., order Dehalococcoidales ord. nov. and family *Dehalococcoidaceae* fam. nov., within the phylum *Chloroflexi*. *Int. J. Syst. Evol. Microbiol.* 63, 625–635. doi: 10.1099/ijs.0.034926-0

López-Llano, J., Maldonado, S., Bueno, M., Lostao, A., Ángeles-Jiménez, M., Lillo, M. P., et al. (2004). The long and short flavodoxins: I. The role of the differentiating loop in apoflavodoxin structure and fmn binding. *J. Biol. Chem.* 279, 47177–47183. doi: 10.1074/jbc.M405792200

Madrona, Y., Hollingsworth, S. A., Tripathi, S., Fields, J. B., Rwigema, J.-C., Tobias, D. J., et al. (2014). Crystal structure of cindoxin, the P450cin redox partner. *Biochemistry* 53, 1435–1446. doi: 10.1021/bi500010m

Marg, B.-L., Schweimer, K., Sticht, H., and Oesterhelt, D. (2005). A two-alpha-helix extra domain mediates the halophilic character of a plant-type ferredoxin from halophilic archaea. *Biochemistry* 44, 29–39. doi: 10.1021/bi0485169

Mazor, Y., Nataf, D., Toporik, H., and Nelson, N. (2013). Crystal structures of virus-like photosystem I complexes from the mesophilic cyanobacterium Synechocystis PCC 6803. *ELife* 3:e01496. doi: 10.7554/eLife.01496

Mellor, S. B., Vavitsas, K., Nielsen, A. Z., and Jensen, P. E. (2017). Photosynthetic fuel for heterologous enzymes: the role of electron carrier proteins. *Photosynth. Res.* 134, 329–342. doi: 10.1007/s11120-017-0364-0

Morales, R., Kachalova, G., Vellieux, F., Charon, M. H., and Frey, M. (2000). Crystallographic studies of the interaction between the ferredoxin-NADP+ reductase and ferredoxin from the cyanobacterium Anabaena: looking for the elusive ferredoxin molecule. *Acta Crystallogr. D Biol. Crystallogr.* 56, 1408–1412. doi: 10.1107/S0907444900010052

Müller, J. J., Lapko, A., Bourenkov, G., Ruckpaul, K., and Heinemann, U. (2001). Adrenodoxin reductase-adrenodoxin complex structure suggests electron transfer path in steroid biosynthesis. *J. Biol. Chem.* 276, 2786–2789. doi: 10.1074/jbc.M008501200

Mutter, A. C., Tyryshkin, A. M., Campbell, I. J., Poudel, S., Bennett, G. N., Silberg, J. J., et al. (2019). *De novo* design of symmetric ferredoxins that shuttle electrons *in vivo*. *Proc. Natl. Acad. Sci. U.S.A.* 116, 14557–14562. doi: 10.1073/pnas.1905643116

Naito, M., Hirakawa, H., Yamashita, A., Ohara, N., Shoji, M., Yukitake, H., et al. (2008). Determination of the genome sequence of *Porphyromonas gingivalis* strain ATCC 33277 and genomic comparison with strain W83 revealed extensive genome rearrangements in *P. gingivalis*. *DNA Res.* 15, 215–225. doi: 10.1093/dnares/dsn013

Nelson-Sathi, S., Dagan, T., Landan, G., Janssen, A., Steel, M., McInerney, J. O., et al. (2012). Acquisition of 1,000 eubacterial genes physiologically transformed a methanogen at the origin of Haloarchaea. *Proc. Natl. Acad. Sci. U.S.A.* 109, 20537–20542. doi: 10.1073/pnas.1209119109

Norton, J. M., Klotz, M. G., Stein, L. Y., Arp, D. J., Bottomley, P. J., Chain, P. S. G., et al. (2008). Complete genome sequence of *Nitrosospira multiformis*, an ammonia-oxidizing bacterium from the soil environment. *Appl. Environ. Microbiol.* 74, 3559–3572. doi: 10.1128/AEM.02722-07

Onda, Y., Matsumura, T., Kimata-Ariga, Y., Sakakibara, H., Sugiyama, T., and Hase, T. (2000). Differential interaction of maize root ferredoxin:NADP(+) oxidoreductase with photosynthetic and non-photosynthetic ferredoxin isoproteins. *Plant Physiol.* 123, 1037–1045. doi: 10.1104/pp.123.3.1037

Orth, J. D., Conrad, T. M., Na, J., Lerman, J. A., Nam, H., Feist, A. M., et al. (2011). A comprehensive genome-scale reconstruction of *Escherichia coli* metabolism—2011. *Mol. Syst. Biol.* 7, 535–535. doi: 10.1038/msb.2011.65

Panchy, N., Lehti-Shiu, M., and Shiu, S.-H. (2016). Evolution of gene duplication in plants. *Plant Physiol.* 171, 2294–2316. doi: 10.1104/pp.16.00523

Patridge, E. V., and Ferry, J. G. (2006). WrbA from *Escherichia coli* and *Archaeoglobus fulgidus* is an NAD(P)H:quinone oxidoreductase. *J. Bacteriol.* 188, 3498–3506. doi: 10.1128/JB.188.10.3498-3506.2006

Peden, E. A., Boehm, M., Mulder, D. W., Davis, R., Old, W. M., King, P. W., et al. (2013). Identification of global ferredoxin interaction networks in *Chlamydomonas reinhardtii*. *J. Biol. Chem.* 288, 35192–35209. doi: 10.1074/jbc.M113.483727

Penz, T., Horn, M., and Schmitz-Esser, S. (2010). The genome of the amoeba symbiont "Candidatus *Amoebophilus asiaticus*" encodes an afp-like prophage possibly used for protein secretion. *Virulence* 1, 541–545. doi: 10.4161/viru.1.6.13800

Perrin, B. S., and Ichiye, T. (2013). Identifying sequence determinants of reduction potentials of metalloproteins. *J. Biol. Inorg. Chem.* 18, 599–608. doi: 10.1007/s00775-013-1004-6

Pfeifer, F., Griffig, J., and Oesterhelt, D. (1993). The fdx gene encoding the [2Fe−2S] ferredoxin of *Halobacterium salinarium* (*H. halobium*). *Mol. Gen. Genet.* 239, 66–71.

Phillips, R. W., Wiegel, J., Berry, C. J., Fliermans, C., Peacock, A. D., White, D. C., et al. (2002). Kineococcus radiotolerans sp. nov., a radiation-resistant, gram-positive bacterium. *Int. J. Syst. Evol. Microbiol.* 52, 933–938. doi: 10.1099/00207713-52-3-933

Pierella Karlusich, J. J., and Carrillo, N. (2017). Evolution of the acceptor side of photosystem I: ferredoxin, flavodoxin, and ferredoxin-NADP+ oxidoreductase. *Photosynth. Res.* 134, 235–250. doi: 10.1007/s11120-017-0338-2

Pierella Karlusich, J. J., Lodeyro, A. F., and Carrillo, N. (2014). The long goodbye: the rise and fall of flavodoxin during plant evolution. *J. Exp. Bot.* 65, 5161–5178. doi: 10.1093/jxb/eru273

Raanan, H., Pike, D. H., Moore, E. K., Falkowski, P. G., and Nanda, V. (2018). Modular origins of biological electron transfer chains. *Proc. Natl. Acad. Sci. U.S.A.* 115, 1280–1285. doi: 10.1073/pnas.1714225115

Ricagno, S., de Rosa, M., Aliverti, A., Zanetti, G., and Bolognesi, M. (2007). The crystal structure of FdxA, a 7Fe ferredoxin from *Mycobacterium smegmatis*. *Biochem. Biophys. Res. Commun.* 360, 97–102. doi: 10.1016/j.bbrc.2007.06.013

Romero, A., Caldeira, J., Legall, J., Moura, I., Moura, J. J., and Romao, M. J. (1996). Crystal structure of flavodoxin from *Desulfovibrio desulfuricans* ATCC 27774 in two oxidation states. *Eur. J. Biochem.* 239, 190–196. doi: 10.1111/j.1432-1033.1996.0190u.x

Rudder, S., Doohan, F., Creevey, C. J., Wendt, T., and Mullins, E. (2014). Genome sequence of *Ensifer adhaerens* OV14 provides insights into its ability as a novel vector for the genetic transformation of plant genomes. *BMC Genomics* 15:268. doi: 10.1186/1471-2164-15-268

Scheibe, R., and Dietz, K.-J. (2012). Reduction-oxidation network for flexible adjustment of cellular metabolism in photoautotrophic cells: redox network for adjustment of cellular metabolism. *Plant Cell Environ.* 35, 202–216. doi: 10.1111/j.1365-3040.2011.02319.x

Schipke, C. G., Goodin, D. B., McRee, D. E., and Stout, C. D. (1999). Oxidized and reduced *Azotobacter vinelandii* ferredoxin I at 1.4 A resolution: conformational change of surface residues without significant change in the [3Fe-4S]+/0 cluster. *Biochemistry* 38, 8228–8239. doi: 10.1021/bi983008i

Schlesier, J., Rohde, M., Gerhardt, S., and Einsle, O. (2016). A conformational switch triggers nitrogenase protection from oxygen damage by shethna protein II (FeSII). *J. Am. Chem. Soc.* 138, 239–247. doi: 10.1021/jacs.5b10341

Sheftel, A. D., Stehling, O., Pierik, A. J., Elsässer, H.-P., Mühlenhoff, U., Webert, H., et al. (2010). Humans possess two mitochondrial ferredoxins, Fdx1 and Fdx2, with distinct roles in steroidogenesis, heme, and Fe/S cluster biosynthesis. *Proc. Natl. Acad. Sci. U.S.A.* 107, 11775–11780. doi: 10.1073/pnas.1004250107

Sorokin, D. Y., Messina, E., Smedile, F., Roman, P., Damsté, J. S. S., Ciordia, S., et al. (2017). Discovery of anaerobic lithoheterotrophic haloarchaea, ubiquitous in hypersaline habitats. *ISME J.* 11, 1245–1260. doi: 10.1038/ismej.2016.203

Sousa, F. L., Thiergart, T., Landan, G., Nelson-Sathi, S., Pereira, I. A., Allen, J. F., et al. (2013). Early bioenergetic evolution. *Philos. Trans. R. Soc. Lond. B. Biol. Sci.* 368:20130088. doi: 10.1098/rstb.2013.0088

Strushkevich, N., MacKenzie, F., Cherkesova, T., Grabovec, I., Usanov, S., and Park, H.-W. (2011). Structural basis for pregnenolone biosynthesis by the mitochondrial monooxygenase system. *Proc. Natl. Acad. Sci. U.S.A.* 108, 10139–10143. doi: 10.1073/pnas.1019441108

Terauchi, A. M., Lu, S., Zaffagnini, M., Tappa, S., Hirasawa, M., Tripathy, J. N., et al. (2009). Pattern of expression and substrate specificity of chloroplast ferredoxins from *Chlamydomonas reinhardtii*. *J. Biol. Chem.* 284, 25867–25878. doi: 10.1074/jbc.M109.023622

Terpolilli, J. J., Masakapalli, S. K., Karunakaran, R., Webb, I. U., Green, R., Watmough, N. J., et al. (2016). Lipogenesis and redox balance in nitrogen-fixing pea bacteroids. *J. Bacteriol.* 198, 2864–2875. doi: 10.1128/JB.00451-16

Tilley, G. J., Camba, R., Burgess, B. K., and Armstrong, F. A. (2001). Influence of electrochemical properties in determining the sensitivity of [4Fe-4S] clusters in proteins to oxidative damage. *Biochem. J.* 360, 717–726. doi: 10.1042/bj3600717

Tyson, C. A., Lipscomb, J. D., and Gunsalus, I.C. (1972). The role of putidaredoxin and $P450_{cam}$ in methylene hydroxylation. *J. Biol.* Chem. 247, 5777–5784.

Unciuleac, M., Boll, M., Warkentin, E., and Ermler, U. (2004). Crystallization of 4-hydroxybenzoyl-CoA reductase and the structure of its electron donor ferredoxin. *Acta Crystallogr. D Biol. Crystallogr.* 60, 388–391. doi: 10.1107/S0907444903028506

van der Walt, S., Colbert, S. C., and Varoquaux, G. (2011). The NumPy array: a structure for efficient numerical computation. *Comput. Sci. Eng.* 13, 22–30. doi: 10.1109/MCSE.2011.37

Venkateswara Rao, P., and Holm, R. H. (2004). Synthetic analogues of the active sites of iron-sulfur proteins. *Chem. Rev.* 104, 527–559. doi: 10.1021/cr020615+

Ventura, M., Canchaya, C., Tauch, A., Chandra, G., Fitzgerald, G. F., Chater, K. F., et al. (2007). Genomics of actinobacteria: tracing the evolutionary history of an ancient phylum. *Microbiol. Mol. Biol. Rev.* 71, 495–548. doi: 10.1128/MMBR.00005-07

Watt, W., Tulinsky, A., Swenson, R. P., and Watenpaugh, K. D. (1991). Comparison of the crystal structures of a flavodoxin in its three oxidation states at cryogenic temperatures. *J. Mol. Biol.* 218, 195–208. doi: 10.1016/0022-2836(91)90884-9

Wu, D., Raymond, J., Wu, M., Chatterji, S., Ren, Q., Graham, J. E., et al. (2009). Complete genome sequence of the aerobic CO-oxidizing thermophile *Thermomicrobium roseum*. *PLoS ONE* 4:e4207. doi: 10.1371/journal.pone.0004207

Xu, X., Reinle, W., Hannemann, F., Konarev, P. V., Svergun, D. I., Bernhardt, R., et al. (2008). Dynamics in a pure encounter complex of two proteins studied by solution scattering and paramagnetic NMR spectroscopy. *J. Am. Chem. Soc.* 130, 6395–6403. doi: 10.1021/ja7101357

Zhu, Y., and McBride, M. J. (2017). The unusual cellulose utilization system of the aerobic soil bacterium *Cytophaga hutchinsonii*. *Appl. Microbiol. Biotechnol.* 101, 7113–7127. doi: 10.1007/s00253-017-8467-2

Conflict of Interest Statement: The authors declare that the research was conducted in the absence of any commercial or financial relationships that could be construed as a potential conflict of interest.

frontiers in Energy Research

ORIGINAL RESEARCH
published: 27 August 2019
doi: 10.3389/fenrg.2019.00087

Surface-Induced Formation and Redox-Dependent Staining of Outer Membrane Extensions in *Shewanella oneidensis* MR-1

Grace W. Chong[1], *Sahand Pirbadian*[2] *and Mohamed Y. El-Naggar*[1,2,3]*

[1] Molecular and Computational Biology Section, Department of Biological Sciences, University of Southern California, Los Angeles, CA, United States, [2] Department of Physics and Astronomy, University of Southern California, Los Angeles, CA, United States, [3] Department of Chemistry, University of Southern California, Los Angeles, CA, United States

The metal-reducing bacterium *Shewanella oneidensis* MR-1 produces extensions of its outer membrane (OM) and periplasm that contain cytochromes responsible for extracellular electron transfer (EET) to external redox-active surfaces, including minerals and electrodes. While the role of multi-heme cytochromes in transporting electrons across the cell wall is well established, their distribution along *S. oneidensis* OM extensions is also thought to allow lateral electron transport along these filaments. These proposed bacterial nanowires, which can be several times the cell length, would thereby extend EET to more distant electron acceptors. However, it is still unclear why these extensions form, and to what extent they contribute to respiration in living cells. Here, we investigate physical contributors to their formation using *in vivo* fluorescence microscopy. While previous studies focused on the display of *S. oneidensis* outer membrane extensions (OMEs) as a response to oxygen limitation, we find that cell-to-surface contact is sufficient to trigger the production of OMEs, including some that reach >100 μm in length, irrespective of medium composition, agitation, or aeration. To visualize the extent of heme redox centers along OMEs, and help distinguish these structures from other extracellular filaments, we also performed histochemical redox-dependent staining with transmission electron microscopy on wild type and cytochrome-deficient strains. We demonstrate that redox-active components are limited to OMEs and not present on other extracellular appendages, such as pili and flagella. We also observed that the loss of 8 functional periplasmic and outer membrane cytochromes significantly decreased both the frequency and intensity of redox-dependent staining found widespread on OMEs. These results will improve our understanding of the environmental conditions that influence the formation of *S. oneidensis* OMEs, as well as the distribution and functionality of EET components along extracellular appendages.

Keywords: *Shewanella*, redox, extracellular electron transfer, bacterial nanowires, cytochromes

OPEN ACCESS

Edited by:
Uwe Schröder,
Technische Universitat Braunschweig, Germany

Reviewed by:
Johannes Gescher,
Karlsruhe Institute of Technology (KIT), Germany
Largus Angenent,
University of Tübingen, Germany

***Correspondence:**
Mohamed Y. El-Naggar
mnaggar@usc.edu

Specialty section:
This article was submitted to Bioenergy and Biofuels, a section of the journal Frontiers in Energy Research

Received: *25 June 2019*
Accepted: *13 August 2019*
Published: *27 August 2019*

Citation:
Chong GW, Pirbadian S and El-Naggar MY (2019) Surface-Induced Formation and Redox-Dependent Staining of Outer Membrane Extensions in Shewanella oneidensis MR-1. Front. Energy Res. 7:87. doi: 10.3389/fenrg.2019.00087

INTRODUCTION

Shewanella oneidensis MR-1 is a Gram-negative, facultative anaerobic heterotrophic bacterium with versatile respiratory capabilities: in its quest for energy, it can utilize an array of soluble and insoluble electron acceptors, from oxygen to extracellular solid surfaces such as minerals and electrodes. This ability to couple intracellular reactions to the respiration of

external surfaces, known as extracellular electron transfer (EET), allows microbial catalytic activity to be harnessed on the electrodes of bioelectrochemical technologies ranging from microbial fuel cells to microbial electrosynthesis (Nealson, 2017; Schröder and Harnisch, 2017). As an extensively studied model organism for EET, studies of *S. oneidensis* revealed the critical role of periplasmic and outer membrane multi-heme cytochromes in forming extracellular electron conduits that bridge the cell envelope (Beliaev et al., 2001; Myers and Myers, 2001; Richardson et al., 2012; Beblawy et al., 2018; Chong et al., 2018; Edwards et al., 2018). Specifically, the periplasmic decaheme cytochrome MtrA connects through the MtrB porin to the outer membrane decaheme cytochrome MtrC that, along with another decaheme cytochrome OmcA, function as the terminal reductases of external electron acceptors or soluble electron shuttles (Richardson et al., 2012). In addition to this well-established role in directing electron transfer across the cell envelope, the Mtr/Omc components have been recently shown to facilitate long-distance electron transport across the membranes of multiple cells via a redox conduction mechanism thought to arise from a combination of multistep hopping along cytochrome heme chains and cytochrome-cytochrome interactions (Xu et al., 2018).

S. oneidensis also forms extensions of the outer membrane and periplasm that include the Mtr/Omc multi-heme cytochromes responsible for EET (El-Naggar et al., 2010; Pirbadian et al., 2014; Subramanian et al., 2018). These outer membrane extensions (OMEs) are proposed to function as bacterial nanowires that also facilitate long-distance EET through redox conduction. However, in contrast to electrode-spanning cells measured by electrochemical gating (Xu et al., 2018), the cytochrome-dependent conductivity of these proposed bacterial nanowires has only been directly assessed under dry, chemically fixed conditions (El-Naggar et al., 2010; Leung et al., 2013). A full understanding of the role of *S. oneidensis* OMEs will therefore require challenging *in vivo* measurements of their specific impact on extracellular respiration and observations of the membrane protein dynamics that allow inter-cytochrome electron exchange and redox conduction (Zacharoff and El-Naggar, 2017).

Beyond the detailed mechanism of electron transport along these structures, additional questions remain regarding the physical and environmental conditions that trigger their formation. The *S. oneidensis* OMEs can extend to several times the cell length, and have been observed with a range of morphologies from chains of interconnected outer membrane vesicles to membrane tubes (Pirbadian et al., 2014). Since early reports suggested that they form in response to electron acceptor limitation, particularly oxygen limitation (Gorby et al., 2006), subsequent studies involving these OMEs have been performed in oxygen limiting conditions (El-Naggar et al., 2010; Pirbadian et al., 2014; Barchinger et al., 2016; Subramanian et al., 2018). However, while the increased expression and production of multi-heme cytochromes under oxygen limiting and anaerobic conditions is well established (Myers and Myers, 1992; Pirbadian et al., 2014; Barchinger et al., 2016), it is not clear if oxygen limitation is the sole contributor to the membrane extension phenotype in *S. oneidensis*. In fact, a recent gene expression study hinted at independent regulatory mechanisms for extending the membrane and localizing the EET proteins (Barchinger et al., 2016). Furthermore, membrane extensions have been reported in multiple organisms under a variety of growth conditions (Wanner et al., 2008; Dubey and Ben-Yehuda, 2011; Galkina et al., 2011; Shetty et al., 2011; McCaig et al., 2013; Benomar et al., 2015; Pande et al., 2015), including those in the form of vesicle chains (Pérez-Cruz et al., 2013; Remis et al., 2014; Wei et al., 2014; Dubey et al., 2016; Subramanian et al., 2018), as is the case for *S. oneidensis*.

It was previously shown that *S. oneidensis* membrane vesicles, which form the basis of OMEs, are redox-active, and that this activity likely stems from the cytochromes present on the purified vesicles (Gorby et al., 2008). The native-state characterization of cytochromes on the OMEs themselves is so far limited to microscopic observations ranging from immunofluorescence (Pirbadian et al., 2014) to electron cryotomography (Subramanian et al., 2018), rather than mapping the activity of the redox centers. The possible association of redox-active components with other extracellular filaments in *Shewanella*, beyond OMEs, also remains largely unexplored. Recent studies in both bacteria and archaea, however, have demonstrated that a combination of histochemical heme-reactive staining and electron microscopy can be used to visualize redox-dependent activity of cytochromes that enable functions ranging from mineral oxidation to interspecies electron transfer within methanotrophic consortia (McGlynn et al., 2015; Deng et al., 2018).

This study set out to address some of these outstanding questions regarding *S. oneidensis* OMEs. To determine the conditions underlying OME formation, we designed *in vivo* fluorescence microscopy experiments allowing us to examine the specific role of oxygen limitation and other physical conditions which might influence OME production in *S. oneidensis* MR-1. We find that cell-to-surface contact is sufficient to trigger the formation of *S. oneidensis* OMEs under a wide range of conditions. To assess the extent of cytochrome-dependent redox activity in these structures, we implemented heme-dependent staining with transmission electron microscopy to compare OMEs in wild type and cytochrome-deficient strains. In doing so, we also probed 3 types of extracellular filaments (OMEs, flagella, and pili) for these EET components. We find that periplasmic and outer membrane cytochromes are responsible for most of the redox activity detected using this assay, and that these components are limited to OMEs and do not associate with flagella or pili.

MATERIALS AND METHODS

Cell Cultivation

For experiments probing the conditions of OME formation with fluorescence microscopy, *S. oneidensis* MR-1 cells were grown aerobically from frozen (−80°C) stock in 50 mL LB broth overnight at 30°C and 150 rpm up to late logarithmic phase (OD_{600} 2.4–2.8). From this overnight culture, 5 mL of cells were collected by centrifugation at 4,226 × *g* for 5 min and washed twice in sterile defined medium (Pirbadian et al., 2014). Cells

were then introduced into a perfusion flow imaging platform described previously (Pirbadian et al., 2014) or the coverslip-bottom glass reactor described below after appropriate dilution to achieve a desirable cell density on the surface for fluorescence time-lapse imaging.

Heme staining and transmission electron microscopy were performed on anaerobic cultures of *S. oneidensis* MR-1 and JG1486 (ΔMtr/Δ*mtrB*/Δ*mtrE*) (Coursolle and Gralnick, 2012). For both strains, 5 mL of an aerobic overnight LB pre-culture was pelleted by centrifugation, washed in defined medium (Pirbadian et al., 2014), and used to inoculate 100 mL of anoxic defined medium in sealed serum bottles with 30 mM fumarate as the sole electron acceptor. After 24 h at 30°C and 150 rpm, at OD_{600} 0.28, this anaerobic culture was harvested by centrifugation at 7,142 × *g* for 10 min, washed by centrifugation (4,226 × *g* for 5 min), and resuspended in defined medium for a total volume of 10 mL. Cells were then injected into the perfusion flow imaging platform containing an electron microscopy grid, as described previously (Subramanian et al., 2018).

Fluorescence Microscopy

In all experiments, the membrane stains FM 4-64FX (Life Technologies; 0.25 μg/mL), FM 1-43FX (Life Technologies; 0.25 μg/mL), or TMA-DPH (Cayman Chemical Company; 10 μM) were used to visualize cells and OMEs on an inverted microscope (Nikon Eclipse Ti-E) using the TRITC, FITC, or DAPI channels (Nikon filter sets G-2E/C, B-2E/C, and UV-2E/C) with 500, 500, and 100 ms exposure times, respectively. FM 4-64FX was generally used as the membrane stain, except in experiments with no flow or agitation, as this concentration of dye faded more quickly over time in unmixed solutions.

Two experimental platforms were used for fluorescence imaging experiments: a perfusion flow setup used previously (Pirbadian et al., 2014; Subramanian et al., 2018) or a coverslip-bottom glass reactor constructed to allow gas injection and measurement of dissolved oxygen levels while visualizing cells. The reactor consisted of a clean glass tube (thickness 1.5 mm, interior diameter 24.7 mm, and length 50 mm) glued on to a clean 43 × 50 mm no. 1 thickness glass coverslip (Thermo Scientific) using waterproof silicone glue (General Electric). The autoclaved reactor was placed on the inverted microscope, and a peristaltic pump (Cole-Parmer Masterflex L/S Easy-Load II) was used to control injection of filtered air at a rate of 3.6 mL/min into the reactor. The air inlet (22G 3" sterile needle) was placed 1–2 mm from the coverslip bottom of the reactor so as to ensure oxygen availability and good mixing near the focal plane. Time-lapse imaging was started immediately following introduction of 10 mL of the cell-media mixture into the reactor and continued for 2 h with images acquired in 5 min increments. Oxygen levels in the reactor were measured by a dissolved oxygen probe (Milwaukee Instruments MW600) at various levels (e.g., 1 mm from bottom, middle, and 1 mm from top) over time after cells were added. To check whether the planktonic cells also displayed OMEs, imaging was stopped after the surface-attached cells produced OMEs, and 400 μL of the planktonic mixture (obtained within 1–2 mm from the top solution-air interface) was gently pipetted to a new clean coverslip, and immediately imaged for another 2 h.

Heme-Reactive Staining and Transmission Electron Microscopy

All heme staining experiments were performed on cells attached to electron microscopy grids recovered from the perfusion flow imaging platform after confirmation of OME production using fluorescence microscopy, as described previously (Subramanian et al., 2018). To accomplish this, an X-thick holey carbon-coated, R2/2, 200 mesh Au NH2 London finder Quantifoil EM grid was glued to the glass coverslip, with the carbon film-coated side facing away from the glass, before sealing the perfusion chamber. The chamber was filled with flow medium, then 400–600 μL of washed cells were injected for a surface density of 50–150 cells visible per 74 × 74 μm square in the 200 mesh grid. Cells were allowed to settle for 5–15 min on the grid before resuming perfusion flow at a volumetric flow rate of 6.1 ± 0.5 μL/s. Imaging continued for about 3.5 h in 5 min increments before medium flow was stopped and the chamber opened under sterile medium. The EM grid was then removed, chemically fixed, and prepared for electron microscopy visualization of heme iron, using a staining protocol adapted from McGlynn et al. (2015). First, the sample was fixed for 30 min in 2.5% glutaraldehyde (dissolved in 25 mM HEPES, pH 7.4, 17.5 g/L NaCl), washed 5 times by soaking 1 min each in buffer (50 mM HEPES, pH 7.4, 35 g/L NaCl), then incubated for 1 h or 2.5 h with the heme-reactive stain 3,3′-diaminobenzidine (DAB; 0.0015 g/mL, dissolved in 50 mM Tris HCl, pH 8) with or without 0.02% hydrogen peroxide (H_2O_2). After 5 washes (100 mM HEPES, pH 7.8), the sample was stained for 1 h in 1% osmium tetroxide, and washed again 5 times. The sample was negative stained in 1% uranyl acetate or 1% phosphotungstic acid for 2 min and air dried overnight. Dried samples were stored in a desiccator before transmission electron microscopy (TEM) imaging. TEM images were acquired on a JEOL JEM-2100F instrument operated at 200 kV, a FEI Morgagni 268 instrument operated at 80 kV, or a FEI Talos F200C instrument operated at 200 kV.

To determine and quantify the extent of cytochrome-reactive staining after treatment with DAB, ImageJ was used to measure the mean pixel intensity (arbitrary gray value units reflecting electron transmission) across an area in the interior of an extension (*A*), or an area in the background (*B*). For each image, a background threshold value (*C*) was generated by taking the mean background intensity (*B*) and subtracting its standard deviation (*D*); thus, $C = B–D$. If the mean intensity of an extension (*A*) was lower than this threshold (*C*), then it was categorized as stained. For each condition (wild type, mutant, and chemical control), the percentage of stained OMEs (*E*) was calculated. To calculate the staining intensity of a single OME (*F*), the mean pixel intensity of the extension (*A*) was subtracted from that of the background (*B*), giving $F = B–A$. A value of *F* was calculated for each of the OMEs assessed in each replicate experiment for each condition (wild type, mutant, and chemical control). For each condition, the mean of all *F* values was calculated, giving G_{WT}, G_{mutant}, and $G_{control}$. Then, G_{WT} and G_{mutant} were corrected by subtracting $G_{control}$, where $G_{WT}–G_{control} = H_{WT}$, and $G_{mutant}–G_{control} = H_{mutant}$. These values H_{WT} and

H_{mutant} represent mean staining intensities of all the OMEs in each strain, corrected for the contribution of negative staining ($G_{control}$). To calculate the fold difference in staining frequency between wild type and the mutant, the percentage of OMEs stained in the wild type (E_{WT}) was divided by that of the mutant (E_{mutant}). To calculate the fold difference in staining intensity between wild type and the mutant, the mean staining intensity of the wild type (H_{WT}) was divided by that of the mutant (H_{mutant}).

RESULTS AND DISCUSSION

Surface Contact Is Sufficient to Induce Production of Outer Membrane Extensions by *Shewanella oneidensis* MR-1

Production of OMEs by a majority of *S. oneidensis* cells was observed in the oxygen limiting perfusion flow platform, as previously described (Pirbadian et al., 2014; Subramanian et al., 2018) (**Figure 1**), but also in near-saturating oxygen conditions (6.5–7.5 ppm O_2) provided by a glass-bottomed reactor that allowed air injection during *in vivo* microscopy (**Figure 2**). Though it can take up to several hours for a majority of surface-attached cells to produce OMEs, we can observe production of OMEs as early as 10 min after cells contact the surface of a glass coverslip (**Figure 2**, **Figure S1**). To further examine the role of surface contact, planktonic cells from the bulk oxygenated reactor were sampled 2 h after the reactor was inoculated (∼1.5 h after OMEs started being produced by surface-attached cells) and transferred to clean coverslips for observation. These previously planktonic cells showed no evidence of OMEs at the time of sampling, but then also went on to begin to display OMEs within 35 min after contacting the surface (**Figure 2**). These observations were not limited to the defined minimal medium used, a particular surface chemistry, or mixing conditions; post-attachment OME production was also observed in rich (LB) medium or in buffer (PBS), on different surfaces (glass coverslips and carbon-coated electron microscopy grids), and regardless of liquid flow or agitation (**Figures S1**, **S2**). To ensure that the used cell density did not result in O_2-limiting conditions selectively at the surface, we also experimented with sparse coverage, down to 5–20 cells per field of view (112 × 112 μm) in a well-mixed and oxygenated reactor, and confirmed that these cells also produced OMEs (**Figure S2C**).

Taken collectively, these observations of OME production by surface-attached cells, but not by planktonic cells until subsequent attachment, and regardless of medium composition, surface type, and oxygen availability, point to surface contact as the primary determinant of OME production by *S. oneidensis*. Previous studies on the role of cytochrome-functionalized OMEs as bacterial nanowires primarily focused on the formation of these structures under O_2-limited conditions (Gorby et al., 2006; El-Naggar et al., 2010; Pirbadian et al., 2014; Subramanian et al., 2018). Previous works indicate that O_2 limitation is necessary for enhanced production of the multi-heme cytochromes required for EET (Myers and Myers, 1992; Rosenbaum et al., 2012; Barchinger et al., 2016), and that oxygen availability also impacts *S. oneidensis* performance and current production in bioelectrochemical systems (Rosenbaum et al., 2010; TerAvest et al., 2014). However, our observations suggest that the membrane extension phenotype is predominantly controlled by surface attachment. Our findings are consistent with a previous proposal based on transcriptome and mutant analyses (Barchinger et al., 2016) that independent pathways are responsible for producing the EET components and extending the outer membrane, while implicating surface contact in controlling the latter pathway.

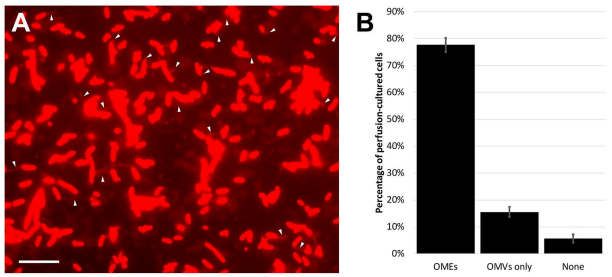

FIGURE 1 | Outer membrane extensions are commonly formed by surface-attached perfusion culture cells. **(A)** Time-lapse fluorescence microscopy snapshot of outer membrane extensions (OMEs, white arrows) produced by *S. oneidensis* MR-1 at a single timepoint in a 3.5-h perfusion flow imaging experiment. Cells and OMEs are visualized with the red membrane stain FM 4-64FX. **(B)** Statistics of OME production from over 5,400 cells in 4 replicate 3.5-h perfusion culture experiments illustrates that a majority (78%) of cells produce OMEs visible over time. The remaining cells were seen with only outer membrane vesicles (OMVs), or nothing at all. Error bars show mean ± SEM (Scale bar: 10 μm).

While our observations show that surface attachment is sufficient to induce OMEs, it is important to note that we do not rule out the influence of O_2 limitation on the frequency of OME production. In perfusion flow imaging, we are able to precisely define the percentage of OME-producing cells: observation of 5,400 cells over four replicate experiments revealed that 78% of surface-attached cells produced OMEs during 3.5 h of perfusion culture (**Figure 1**). This precise quantification is possible in perfusion flow imaging because the laminar flow helps to restrict the structures to the focal plane near the surface. However, this laminar flow establishes O_2 limitation as a result of cellular O_2 consumption and the no-slip condition at the surface-solution interface (Pirbadian et al., 2014). Thus, we could precisely determine the frequency of OME production only in O_2-limiting perfusion conditions, but not in oxygenated well-mixed reactors where the structures could fluctuate in and out of the focal plane.

It was previously shown that phage-induced cell lysis (particularly the release of extracellular DNA) promotes biofilm development in *S. oneidensis* (Gödeke et al., 2011), and that explosive cell lysis in actively growing *Pseudomonas aeruginosa* biofilms is accompanied by the release of extracellular DNA and the production of vesicles containing cytoplasmic content (Turnbull et al., 2016). However, lysis does not appear to play a role in the large fraction (∼78%) of *S. oneidensis* cells

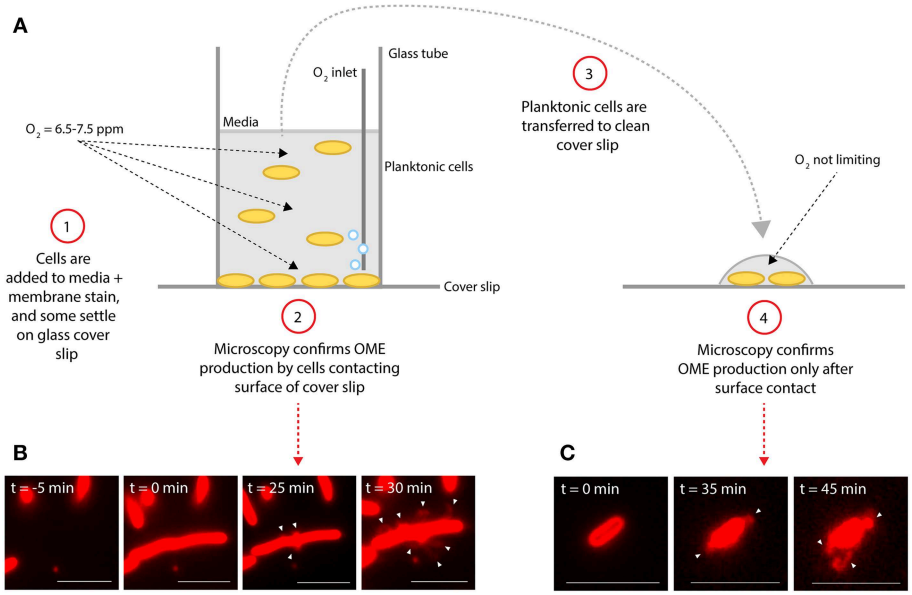

FIGURE 2 | Surface attachment is sufficient to induce production of outer membrane extensions. **(A)** Diagram illustrates experimental procedure. **(B,C)** Microscopy images of *S. oneidensis* MR-1 cells and membrane extensions (white arrows) labeled with the red membrane stain FM 4-64FX. Time (t = 0 min) indicates estimated time of cells contacting the glass surface. **(B)** Demonstrates production of outer membrane extensions (OMEs) by surface-attached cells in the aerated glass-bottomed reactor. **(C)** Demonstrates OME production by planktonic cells from the reactor which were transferred to a new coverslip surface after events in **(B)** were confirmed (Scale bars: 5 μm).

seen producing OMEs under our experimental conditions. Our *in vivo* fluorescence observations reported here (**Figures 1–3**, **Movie S1**), as well as correlative fluorescence and cryo-electron microscopy observations (Subramanian et al., 2018), capture the extension process from originating intact cells with no evidence for loss of cell integrity and eliminate the possibility that the OMEs are lysis products that subsequently attach to nearby cells. Moreover, we previously reported GFP-labeling observations where only periplasmic GFP, but not cytoplasmic GFP, localized to the extensions, demonstrating an intact cytoplasmic membrane during the OM extension process (Pirbadian et al., 2014). However, while we demonstrate that OMEs are not simply a consequence of cell lysis, we do not rule out that OM extension may be partially associated with an instability or change in membrane integrity.

Membrane extensions, including those formed as chains of membrane vesicles (MVs), are not limited to *S. oneidensis* (Wanner et al., 2008; Dubey and Ben-Yehuda, 2011; Galkina et al., 2011; Shetty et al., 2011; McCaig et al., 2013; Pérez-Cruz et al., 2013; Remis et al., 2014; Wei et al., 2014; Benomar et al., 2015; Pande et al., 2015; Dubey et al., 2016; Subramanian et al., 2018). The finding that surface contact plays an important role is consistent with prior observations of vesicle chains and OMEs produced by surface-attached cells of other bacteria, including *Shewanella vesiculosa* (Pérez-Cruz et al., 2013), *Bacillus subtilis* (Dubey et al., 2016), and biofilms of *Myxococcus xanthus* (Remis et al., 2014). In addition, another *M. xanthus* study noted that static, rather than shaken, conditions promote more OME production (Wei et al., 2014). However, while MVs are ubiquitous features of bacteria, the mechanisms behind MV and MV chain formation are still widely unknown (Gill et al., 2019; Toyofuku et al., 2019), but they do not appear to simply result from loss of membrane integrity (McBroom et al., 2006). The importance of surface-attached, biofilm, or static conditions may point to a generalized mechanism where MVs are successively produced and merged into long extensions rather than shed away under more dynamic (e.g., free-swimming or shaken culture) conditions. Once formed, these extensions may then enable a variety of functions ranging from facilitating cell-cell interactions (Dubey and Ben-Yehuda, 2011; Remis et al., 2014; Dubey et al., 2016) to the long-distance EET role proposed for *S. oneidensis* OMEs (Gorby et al., 2006; El-Naggar et al., 2010).

It was also previously proposed that MVs and OMEs can increase the likelihood of encountering neighboring cells and external redox-active surfaces by virtue of the significant change in surface area-to-volume ratio that these structures present (Pirbadian et al., 2014). Consistent with this proposal, we occasionally captured multiple extensions from single cells (**Figure S3**) as well as *in vivo* fluorescent observations of remarkably long OMEs, likely the longest observed to date. **Figure 3** and **Movie S1** captures a cell producing a >100 μm OME at a rate over 40 μm/h, at the same time that the cell surface area appeared to shrink by an amount consistent with the newly displayed OME.

Redox-Dependent Staining of Extracellular Filaments

The localization of the multi-heme cytochromes responsible for EET to OMEs has been previously demonstrated by immunofluorescence observations of MtrC and OmcA

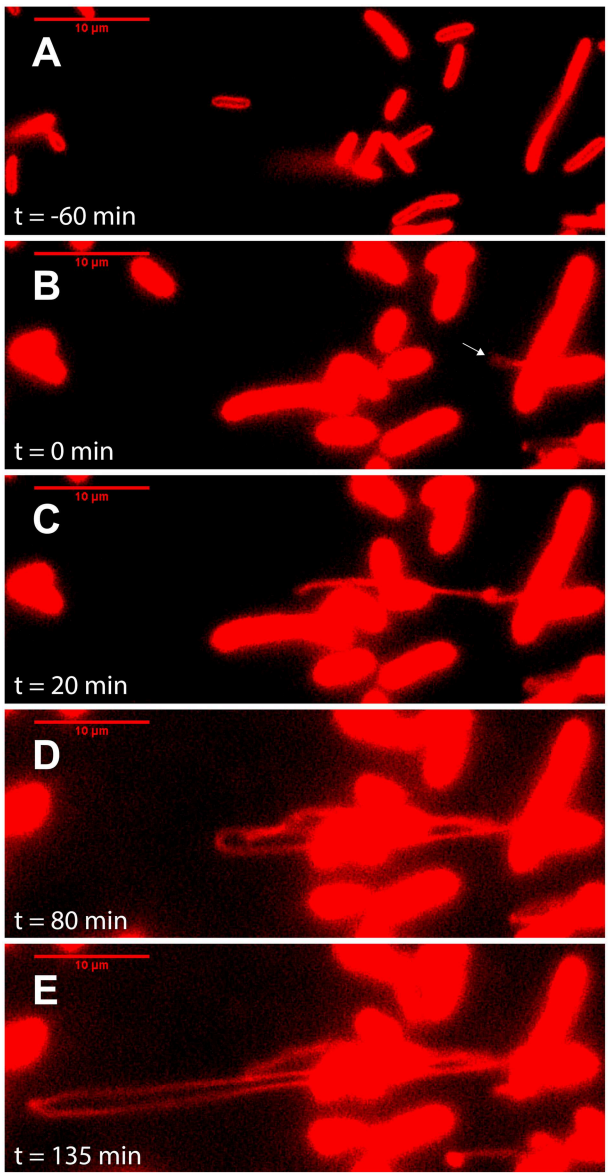

FIGURE 3 | Outer membrane extensions can reach a length of >100 µm, produced at a rate >40 µm/h. Image sequence from time-lapse fluorescence microscopy of surface-attached perfusion cultured *S. oneidensis* MR-1 ΔMtr/Δ*mtrB*/Δ*mtrE* cells. Cells and outer membrane extensions (OMEs) were visualized with the red membrane stain FM 4-64FX. Time ($t = 0$) marks time since OME production (white arrow). Images depict progression of events, such as **(A)** cell contacting surface, **(B)** OME first visible (white arrow), **(C)** OME elongates and begins to fold, **(D)** further OME elongation, **(E)** OME reaches longest point visible during this experiment (Scale bars: 10 µm).

(Pirbadian et al., 2014), as well as electron cryotomography observations of outer membrane and periplasmic electron densities consistent with cytochrome dimensions (Subramanian et al., 2018). To examine the distribution and activity of the heme iron redox centers along the OMEs, we applied the heme-reactive 3,3′-diaminobenzidine (DAB)-H_2O_2 staining procedure (McGlynn et al., 2015). Here, the iron centers in heme will catalyze the oxidation of DAB coupled to the reduction of H_2O_2. The oxidized DAB forms a localized dark precipitate that can be observed with the resolution of transmission electron microscopy (TEM). In our TEM experiments, we observed only 3 types of extracellular filaments: OMEs, pili, and flagella (**Figures 4**, **5**, **Figure S3**). As expected, the OMEs clearly stained for heme; with prolonged exposure to DAB (2.5 h DAB staining step) a noticeable <50 nm band of dark precipitate lined the vesicles that compose the entire structure (**Figure 4**). Staining was clearly limited to the OMEs and was absent from the other extracellular filaments observed, demonstrating that the cytochromes do not associate with pili and flagella (**Figure 4**). The absence of staining in these structures, even when observed in contact with the OMEs (**Figure 4**), also demonstrates that DAB precipitate does not diffuse to non-specifically stain nearby structures. Meanwhile, the <50 nm thickness of precipitate lining OMEs (i.e., precipitate expansion in the direction perpendicular to the surface of the OME) suggests <50 nm lateral distribution of heme redox centers on OMEs, consistent with the surface distribution of putative cytochromes on OMEs visualized by electron cryotomography (Subramanian et al., 2018). However, in general this technique cannot be used to localize specific cytochromes or to define their exact distribution on the membrane. For this reason, we also used image analysis (**Figure 5**) to compare overall staining displayed by many OMEs rather than focusing on discrete sites on a single structure.

In addition to chemical controls for staining (e.g., wild type experiments in which H_2O_2 was omitted), we systematically compared redox-dependent staining in OMEs from wild type *S. oneidensis* and a mutant lacking genes encoding eight functional periplasmic and outer membrane cytochromes (ΔMtr/Δ*mtrB*/Δ*mtrE*), including the entire Mtr/Omc pathway of decaheme cytochromes (Coursolle and Gralnick, 2012). This mutant is unable to perform EET (Coursolle and Gralnick, 2012; Xu et al., 2018; Wang et al., 2019) or support long-distance redox conduction across electrodes (Xu et al., 2018). We performed two replicate experiments for each of three conditions: wild type (**Figure 5A**), mutant (**Figures 5B,C**), and wild type chemical control with no H_2O_2 (**Figure 5D**), with a total of 45–60 OMEs analyzed per condition. Using image processing to compare OME staining to background intensities (see Materials and Methods), we found that the majority (92%) of wild type OMEs stained for heme, but none stained in the chemical control where H_2O_2 was omitted (**Figure 5E**). In contrast, a fraction (39%) of OMEs in the mutant strain exhibited heme staining, 2.4-fold less than in wild type ($p < 0.0001$, Pearson's chi-squared test; **Figure 5E**). While lacking all cytochromes necessary for EET, staining in the mutant OMEs is likely due to the additional periplasmic cytochromes, including the flavocytochrome FccA present that functioned as the terminal fumarate reductase to support respiration of fumarate in our anaerobic cultures. Consistent with this interpretation, staining intensity was 3.6-fold stronger in the wild type than in the mutant ($p < 0.0001$, Student's t-test, two-sample assuming equal variances; **Figure 5F**). Relative to the mutant control, the observed wild type increase in both staining frequency and

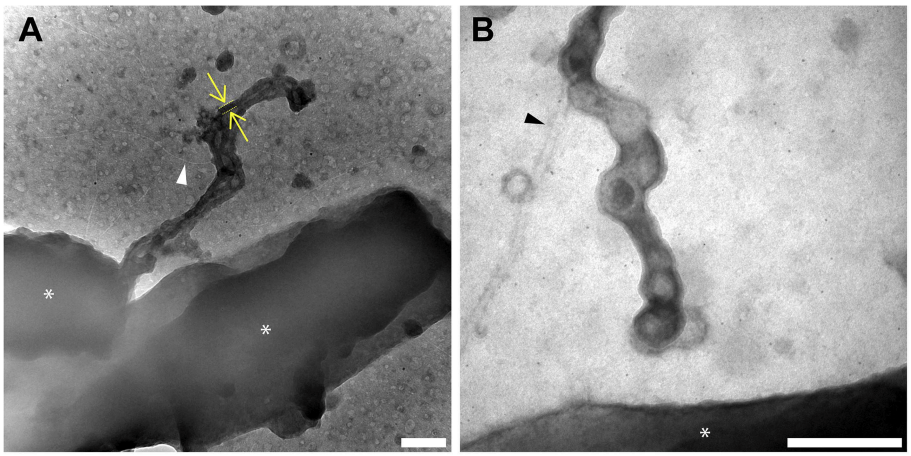

FIGURE 4 | Redox components are present only on outer membrane extensions, not pili or flagella. Histochemical redox-dependent staining with 3,3′-diaminobenzidine (2.5 h staining step) and transmission electron microscopy distinguishes between types of extracellular filaments in *S. oneidensis* MR-1. Images depict dark precipitate (yellow arrows and lines) labeling only outer membrane extensions, but not adjacent extracellular structures **(A)** pili (white arrow), and **(B)** flagella (black arrow). Cells are indicated by asterisk symbols (*) (Scale bars: 200 nm).

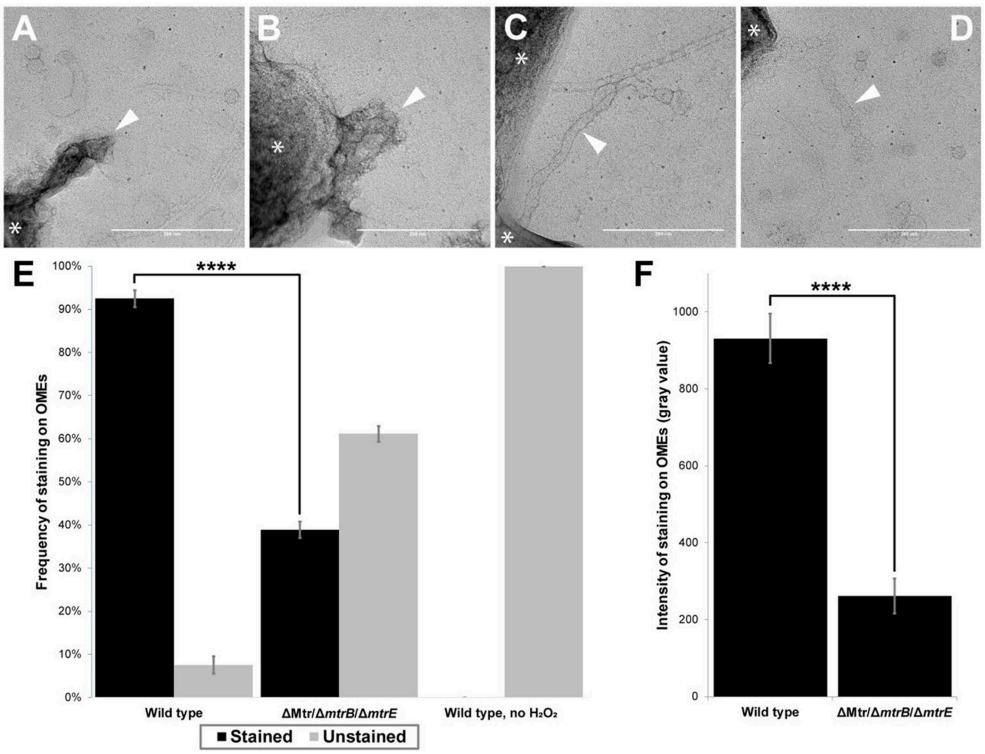

FIGURE 5 | Presence of multi-heme cytochromes important for extracellular electron transfer leads to significantly higher frequency and intensity of redox-dependent staining on outer membrane extensions. **(A–D)** Transmission electron microscopy images depict outer membrane extensions (OMEs, white arrows) stained by 3,3'-diaminobenzidine (DAB; 1 h staining step) in wild type and cytochrome-deficient (ΔMtr/Δ*mtrB*/Δ*mtrE*) *S. oneidensis* MR-1 cells. Cells are indicated by asterisk symbols (*). **(A)** Wild type OMEs are stained by DAB precipitate. **(B,C)** Mutant OMEs treated by DAB exhibit varying degrees of staining. **(D)** Wild type OMEs in chemical controls where H_2O_2 was omitted appear unstained aside from negative stain. **(E)** Frequency of staining displayed by OMEs in wild type, ΔMtr/Δ*mtrB*/Δ*mtrE* mutant, and wild type chemical control where H_2O_2 was omitted. 2.4-fold more OMEs were stained in wild type than in the mutant ($p < 0.0001$). Statistical significance was determined by *p*-value from Pearson's chi-squared test. **(F)** Intensity of staining displayed by OMEs is 3.6-fold higher in wild type than in ΔMtr/Δ*mtrB*/Δ*mtrE* mutant ($p < 0.0001$). Statistical significance was determined by two-tailed *p*-value from Student's *t*-test, two-sample assuming equal variances. Error bars show mean ± SEM (Scale bars: 200 nm).

intensity indicates that the periplasmic and outer membrane cytochromes necessary for EET contribute much of the redox capacity of the OMEs.

Given its ability to discriminate between cytochrome-containing and cytochrome-free extracellular filaments, and to examine the effect of specific mutations, this heme visualization strategy may hold promise for understanding the presence of redox centers in a variety of microbial systems. However, a detailed understanding of the extent to which these redox centers enable long-distance electron transport along OMEs requires: (i) applying electrochemical techniques, recently used to measure redox conduction in biofilms (Yates et al., 2016; Xu et al., 2018), specifically to OMEs or their MV constituents; and (ii) measurements of the diffusive dynamics of redox molecules along membranes, to test the hypothesis that these dynamics facilitate a collision-exchange mechanism of inter-protein electron transport over micrometer length scales (Subramanian et al., 2018). We are actively pursuing these electrochemical and dynamics measurements.

CONCLUSIONS

In summary, we investigated physical contributors to the production of OMEs by *Shewanella oneidensis* MR-1 and applied heme-reactive staining to examine the extent of the redox centers along the extensions. While previous studies focused on the role of oxygen limitation in triggering the formation of these structures, we demonstrated that surface contact is sufficient to trigger production of OMEs under a variety of medium, agitation, and aeration conditions. In addition, we show that the multi-heme cytochromes necessary for EET contribute much of the redox-dependent staining widespread on OMEs, and that these EET components do not associate with other extracellular filaments. In addition to describing some reproducible microscopic and histochemical techniques to observe redox-functionalized membrane extensions, these observations motivate additional studies to understand the extent to which *Shewanella oneidensis* OMEs can contribute to EET and long-distance redox conduction.

DATA AVAILABILITY

The datasets generated for this study are available on request to the corresponding author.

AUTHOR CONTRIBUTIONS

GC designed, performed, and analyzed experiments with guidance from SP and ME-N. GC and ME-N wrote and edited the manuscript, with revisions from SP.

FUNDING

GC is a National Science Foundation Graduate Fellow supported by NSF grant DGE1418060. This work was supported by the Air Force Office of Scientific Research Presidential Early Career Award for Scientists and Engineers (FA955014-1-0294, to ME-N).

ACKNOWLEDGMENTS

We are grateful to Professor Jeffrey A. Gralnick for providing the cytochrome mutant strain. Transmission electron microscopy at 200 kV was performed at the University of Southern California's Core Center of Excellence in Nano Imaging. We also thank Christopher Buser for imaging our electron microscopy samples at 80 kV at the Huntington Medical Research Institutes.

SUPPLEMENTARY MATERIAL

The Supplementary Material for this article can be found online at: https://www.frontiersin.org/articles/10.3389/fenrg.2019.00087/full#supplementary-material

REFERENCES

Barchinger, S. E., Pirbadian, S., Sambles, C., Baker, C. S., Leung, K. M., Burroughs, N. J., et al. (2016). Regulation of gene expression during electron acceptor limitation and bacterial nanowire formation in *Shewanella oneidensis* MR-1. *Appl. Environ. Microbiol.* 82, 5428–5443. doi: 10.1128/AEM.01615-16

Beblawy, S., Bursac, T., Paquete, C., Louro, R., Clarke, T. A., and Gescher, J. (2018). Extracellular reduction of solid electron acceptors by *Shewanella oneidensis*. *Mol. Microbiol.* 109, 571–583. doi: 10.1111/mmi.14067

Beliaev, A. S., Saffarini, D. A., McLaughlin, J. L., and Hunnicutt, D. (2001). MtrC, an outer membrane decahaem *c* cytochrome required for metal reduction in *Shewanella putrefaciens* MR-1. *Mol. Microbiol.* 39, 722–730. doi: 10.1046/j.1365-2958.2001.02257.x

Benomar, S., Ranava, D., Cárdenas, M. L., Trably, E., Rafrafi, Y., Ducret, A., et al. (2015). Nutritional stress induces exchange of cell material and energetic coupling between bacterial species. *Nat. Commun.* 6:6283. doi: 10.1038/ncomms7283

Chong, G. W., Karbelkar, A. A., and El-Naggar, M. Y. (2018). Nature's conductors: what can microbial multi-heme cytochromes teach us about electron transport and biological energy conversion? *Curr. Opin. Chem. Biol.* 47, 7–17. doi: 10.1016/j.cbpa.2018.06.007

Coursolle, D., and Gralnick, J. A. (2012). Reconstruction of extracellular respiratory pathways for iron(III) reduction in *Shewanella oneidensis* strain MR-1. *Front. Microbiol.* 3, 1–11. doi: 10.3389/fmicb.2012.00056

Deng, X., Dohmae, N., Nealson, K. H., Hashimoto, K., and Okamoto, A. (2018). Multi-heme cytochromes provide a pathway for survival in energy-limited environments. *Sci. Adv.* 4, 1–9. doi: 10.1126/sciadv.aao5682

Dubey, G. P., and Ben-Yehuda, S. (2011). Intercellular nanotubes mediate bacterial communication. *Cell* 144, 590–600. doi: 10.1016/j.cell.2011.01.015

Dubey, G. P., Malli Mohan, G. B., Dubrovsky, A., Amen, T., Tsipshtein, S., Rouvinski, A., et al. (2016). Architecture and characteristics of bacterial nanotubes. *Dev. Cell* 36, 453–461. doi: 10.1016/j.devcel.2016.01.013

Edwards, M. J., White, G. F., Lockwood, C. W., Lawes, M. C., Martel, A., Harris, G., et al. (2018). Structural modeling of an outer membrane electron conduit from a metal-reducing bacterium suggests electron transfer via periplasmic redox partners. *J. Biol. Chem.* 293, 8103–8112. doi: 10.1074/jbc.RA118.001850

El-Naggar, M. Y., Wanger, G., Leung, K. M., Yuzvinsky, T. D., Southam, G., Yang, J., et al. (2010). Electrical transport along bacterial nanowires from

Shewanella oneidensis MR-1. *Proc. Natl. Acad. Sci. U.S.A.* 107, 18127–18131. doi: 10.1073/pnas.1004880107

Galkina, S. I., Romanova, J. M., Bragina, E. E., Tiganova, I. G., Stadnichuk, V. I., Alekseeva, N. V., et al. (2011). Membrane tubules attach *Salmonella Typhimurium* to eukaryotic cells and bacteria. *FEMS Immunol. Med. Microbiol.* 61, 114–124. doi: 10.1111/j.1574-695X.2010.00754.x

Gill, S., Catchpole, R., and Forterre, P. (2019). Extracellular membrane vesicles in the three domains of life and beyond. *FEMS Microbiol. Rev.* 43, 273–303. doi: 10.1093/femsre/fuy042

Gödeke, J., Paul, K., Lassak, J., and Thormann, K. M. (2011). Phage-induced lysis enhances biofilm formation in *Shewanella oneidensis* MR-1. *ISME J.* 5, 613–626. doi: 10.1038/ismej.2010.153

Gorby, Y. A., McLean, J., Korenevsky, A., Rosso, K. M., El-Naggar, M. Y., and Beveridge, T. J. (2008). Redox-reactive membrane vesicles produced by *Shewanella*. *Geobiology* 6, 232–241. doi: 10.1111/j.1472-4669.2008.00158.x

Gorby, Y. A., Yanina, S., McLean, J. S., Rosso, K. M., Moyles, D., Dohnalkova, A. C., et al. (2006). Electrically conductive bacterial nanowires produced by *Shewanella oneidensis* strain MR-1 and other microorganisms. *Proc. Natl. Acad. Sci. U.S.A.* 103, 11358–11363. doi: 10.1073/pnas.0604517103

Leung, K. M., Wanger, G., El-Naggar, M. Y., Gorby, Y., Southam, G., Ming Lau, W., et al. (2013). *Shewanella oneidensis* MR-1 bacterial nanowires exhibit *p*-Type, tunable electronic behavior. *Nano Lett.* 13, 2407–2411. doi: 10.1021/nl400237p

McBroom, A. J., Johnson, A. P., Vemulapalli, S., and Kuehn, M. J. (2006). Outer membrane vesicle production by *Escherichia coli* is independent of membrane instability. *J. Bacteriol.* 188, 5385–5392. doi: 10.1128/JB.00498-06

McCaig, W. D., Koller, A., and Thanassi, D. G. (2013). Production of outer membrane vesicles and outer membrane tubes by *Francisella novicida*. *J. Bacteriol.* 195, 1120–1132. doi: 10.1128/JB.02007-12

McGlynn, S. E., Chadwick, G. L., Kempes, C. P., and Orphan, V. J. (2015). Single cell activity reveals direct electron transfer in methanotrophic consortia. *Nature* 526, 531–535. doi: 10.1038/nature15512

Myers, C. R., and Myers, J. M. (1992). Localization of cytochromes to the outer membrane of anaerobically grown *Shewanella putrefaciens* MR-1. *J. Bacteriol.* 174, 3429–3438. doi: 10.1128/jb.174.11.3429-3438.1992

Myers, J. M., and Myers, C. R. (2001). Role for outer membrane cytochromes OmcA and OmcB of *Shewanella putrefaciens* MR-1 in reduction of manganese dioxide. *Appl. Environ. Microbiol.* 67, 260–269. doi: 10.1128/AEM.67.1.260-269.2001

Nealson, K. H. (2017). Bioelectricity (electromicrobiology) and sustainability. *Microb. Biotechnol.* 10, 1114–1119. doi: 10.1111/1751-7915.12834

Pande, S., Shitut, S., Freund, L., Westermann, M., Bertels, F., Colesie, C., et al. (2015). Metabolic cross-feeding via intercellular nanotubes among bacteria. *Nat. Commun.* 6, 1–13. doi: 10.1038/ncomms7238

Pérez-Cruz, C., Carrión, O., Delgado, L., Martinez, G., López-Iglesias, C., and Mercade, E. (2013). New type of outer membrane vesicle produced by the gram-negative bacterium *Shewanella vesiculosa* M7T: implications for DNA content. *Appl. Environ. Microbiol.* 79, 1874–1881. doi: 10.1128/AEM.03657-12

Pirbadian, S., Barchinger, S. E., Leung, K. M., Byun, H. S., Jangir, Y., Bouhenni, R. A., et al. (2014). *Shewanella oneidensis* MR-1 nanowires are outer membrane and periplasmic extensions of the extracellular electron transport components. *Proc. Natl. Acad. Sci. U.S.A.* 111, 12883–12888. doi: 10.1073/pnas.1410551111

Remis, J. P., Wei, D., Gorur, A., Zemla, M., Haraga, J., Allen, S., et al. (2014). Bacterial social networks: structure and composition of *Myxococcus xanthus* outer membrane vesicle chains. *Environ. Microbiol.* 16, 598–610. doi: 10.1111/1462-2920.12187

Richardson, D. J., Butt, J. N., Fredrickson, J. K., Zachara, J. M., Shi, L., Edwards, M. J., et al. (2012). The "porin-cytochrome" model for microbe-to-mineral electron transfer. *Mol. Microbiol.* 85, 201–212. doi: 10.1111/j.1365-2958.2012.08088.x

Rosenbaum, M., Cotta, M. A., and Angenent, L. T. (2010). Aerated *Shewanella oneidensis* in continuously fed bioelectrochemical systems for power and hydrogen production. *Biotechnol. Bioeng.* 105, 880–888. doi: 10.1002/bit.22621

Rosenbaum, M. A., Bar, H. Y., Beg, Q. K., Segrè, D., Booth, J., Cotta, M. A., et al. (2012). Transcriptional Analysis of *Shewanella oneidensis* MR-1 with an electrode compared to Fe(III)citrate or oxygen as terminal electron acceptor. *PLoS ONE* 7:e30827. doi: 10.1371/journal.pone.0030827

Schröder, U., and Harnisch, F. (2017). Life electric—nature as a blueprint for the development of microbial electrochemical technologies. *Joule* 1, 244–252. doi: 10.1016/j.joule.2017.07.010

Shetty, A., Chen, S., Tocheva, E. I., Jensen, G. J., and Hickey, W. J. (2011). Nanopods: a new bacterial structure and mechanism for deployment of outer membrane vesicles. *PLoS ONE* 6:e20725. doi: 10.1371/journal.pone.0020725

Subramanian, P., Pirbadian, S., El-Naggar, M. Y., and Jensen, G. J. (2018). Ultrastructure of *Shewanella oneidensis* MR-1 nanowires revealed by electron cryotomography. *Proc. Natl. Acad. Sci. U.S.A.* 115:103242. doi: 10.1073/pnas.1718810115

TerAvest, M. A., Rosenbaum, M. A., Kotloski, N. J., Gralnick, J. A., and Angenent, L. T. (2014). Oxygen allows *Shewanella oneidensis* MR-1 to overcome mediator washout in a continuously fed bioelectrochemical system. *Biotechnol. Bioeng.* 111, 692–699. doi: 10.1002/bit.25128

Toyofuku, M., Nomura, N., and Eberl, L. (2019). Types and origins of bacterial membrane vesicles. *Nat. Rev. Microbiol.* 17, 13–24. doi: 10.1038/s41579-018-0112-2

Turnbull, L., Toyofuku, M., Hynen, A. L., Kurosawa, M., Pessi, G., Petty, N. K., et al. (2016). Explosive cell lysis as a mechanism for the biogenesis of bacterial membrane vesicles and biofilms. *Nat. Commun.* 7:11220. doi: 10.1038/ncomms11220

Wang, Q., Jones, A.-A. D., Gralnick, J. A., Lin, L., and Buie, C. R. (2019). Microfluidic dielectrophoresis illuminates the relationship between microbial cell envelope polarizability and electrochemical activity. *Sci. Adv.* 5:eaat5664. doi: 10.1126/sciadv.aat5664

Wanner, G., Vogl, K., and Overmann, J. (2008). Ultrastructural characterization of the prokaryotic symbiosis in "*Chlorochromatium aggregatum*." *J. Bacteriol.* 190, 3721–3730. doi: 10.1128/JB.00027-08

Wei, X., Vassallo, C. N., Pathak, D. T., and Wall, D. (2014). *Myxobacteria* produce outer membrane-enclosed tubes in unstructured environments. *J. Bacteriol.* 196, 1807–1814. doi: 10.1128/JB.00850-13

Xu, S., Barrozo, A., Tender, L. M., Krylov, A. I., and El-Naggar, M. Y. (2018). Multiheme cytochrome mediated redox conduction through shewanella oneidensis MR-1 cells. *J. Am. Chem. Soc.* 140, 10085–10089. doi: 10.1021/jacs.8b05104

Yates, M. D., Strycharz-Glaven, S. M., Golden, J. P., Roy, J. N., Tsoi, S., Erickson, J. S., et al. (2016). Measuring conductivity of living *Geobacter sulfurreducens* biofilms. *Nat. Nanotechnol.* 11, 910–913. doi: 10.1038/nnano.2016.186

Zacharoff, L. A., and El-Naggar, M. Y. (2017). Redox conduction in biofilms: From respiration to living electronics. *Curr. Opin. Electrochem.* 4, 182–189. doi: 10.1016/j.coelec.2017.09.003

Conflict of Interest Statement: The authors declare that the research was conducted in the absence of any commercial or financial relationships that could be construed as a potential conflict of interest.

frontiers in Energy Research

ORIGINAL RESEARCH
published: 06 September 2019
doi: 10.3389/fenrg.2019.00091

On Site Evaluation of a Tubular Microbial Fuel Cell Using an Anion Exchange Membrane for Sewage Water Treatment

Mari Sugioka[1†], *Naoko Yoshida*[1*†] *and Kazuki Iida*[2]

[1] Department of Civil Engineering, Nagoya Institute of Technology (Nitech), Nagoya, Japan, [2] Nippon Koei Co., Ltd., Tokyo, Japan

This study evaluated the performance of a tubular microbial fuel cell (MFC) having a core of air-chamber wrapped with an anion exchange membrane in sewage wastewater treatment. Three MFCs were vertically assembled into one module and floated in sewage water channels before and after treatments in the primary sedimentation tank. The two MFC-modules exhibited nearly similar electricity production in the range of 1.3–5.7 $Wh{\cdot}m^{-3}$-MFC while the bottom MFCs (60–90 cm) showed a decrease in electricity compared with the top (0–30 cm) and the middle MFCs (30–60 cm) due to the water leakage into air-cathode. One MFC module was then evaluated for its chemical oxygen demand (COD) removal efficiency with two external resistances of 27 and 3Ω in a chemostat reactor (MFC:reactor = 1:5, v/v) using three hydraulic retention times (HRTs), i.e., 3, 6, and 12 h. The best COD removal efficiency (COD-RE_{MFC}), 54 ± 14%, and BOD removal efficiency, 37 ± 17%, were observed with a resistance of 3Ω and a 12 h HRT, which resulted in 3.8 ± 2.0 $A{\cdot}m^{-3}$ of current recovery and 15 ± 7.5% of Coulombic efficiency. The electricity generation efficiency (EGE_{MFC}) was the best with a resistance of 27Ω and a 12 h HRT, accounting for 0.19 ± 0.12 $kWh{\cdot}kg\text{-}COD^{-1}$ with a 17 ± 6.4% COD-RE_{MFC} and 0.65 ± 0.10 $Wh{\cdot}m^{-3}$ electricity production. Based on calculations using the COD-RE_{MFC} and $EGE_{MFC,}$ the integration of MFC treatments prior to aeration can reduce wastewater treatment electricity consumption by 55%.

Keywords: microbial fuel cell, sewage water treatment, anion exchange membrane, organic matter reduction, energy balance

OPEN ACCESS

Edited by:
Eileen Hao Yu,
Newcastle University, United Kingdom

Reviewed by:
Xu Wang,
Wuhan University, China
Qaisar Mahmood,
COMSATS University, Islamabad Campus, Pakistan

***Correspondence:**
Naoko Yoshida
yoshida.naoko@nitech.ac.jp

†These authors have contributed equally to this work

Specialty section:
This article was submitted to Bioenergy and Biofuels, a section of the journal Frontiers in Energy Research

Received: *25 June 2019*
Accepted: *16 August 2019*
Published: *06 September 2019*

Citation:
Sugioka M, Yoshida N and Iida K (2019) On Site Evaluation of a Tubular Microbial Fuel Cell Using an Anion Exchange Membrane for Sewage Water Treatment. Front. Energy Res. 7:91. doi: 10.3389/fenrg.2019.00091

INTRODUCTION

Electricity consumption in sewage wastewater treatment accounts for 1–3% of domestic electricity consumption in developed countries (Maktabifard et al., 2018) while sewage potentially has much more bio-mass energy in itself (Shizas and Bagley, 2004). Anaerobic digestion of sewage sludge has received significant attention to neutralize this energy imbalance (Yan et al., 2017). In Japan, 1.5 × 10^{10} $m^3{\cdot}yr^{-1}$ of sewage water is treated in sewage wastewater treatment plants, which includes ~400 $mg{\cdot}L^{-1}$ of chemical oxygen demand (COD). Based on the assumption that all organic carbon is converted to CH_4, and, by extension, that all CH_4 is converted to electricity, the potential biomass energy in sewage water (PE_W) is as much as 2.1 × 10^{10} $kWh{\cdot}yr^{-1}$ (**Supplementary Information**). This PE_W is ~1.8-fold higher than that of sewage sludge (PE_S). The PE_W of sewage sludge can be

calculated as a product of the sewage sludge produced annually (2.2×10^9 kg-dry sludge (DS)·yr^{-1}) and its calorific value (4,500 kcal·kg-DS^{-1}). Theoretically, all electricity requirements for sewage treatment can be met via energy conversion of > 0.67 kWh·kg-COD^{-1} from sewage water or > 1.8 kWh·kg-DS^{-1} from sewage sludge. However, biogas production cannot be directly applied to sewage water due to its relatively lower carbon content compared with the carbon content in the same volume of sludge. Therefore, organic matter must be concentrated from sewage water prior to biogas production, which includes concentrations of the membrane bioreactor (Martinez-Sosa et al., 2011), aquatic weeds (Kaur et al., 2018), and algae (Arcila and Buitrón, 2016). An alternative technology that directly recovers energy from sewage water is the microbial fuel cell (MFC) (Liu et al., 2004; Li et al., 2014). The MFC is a promising technology that can be introduced into existing sewage treatment plants without large-scale construction projects.

MFC is a technology collecting the electrons emitted in the microbial oxidation of organic matter to an electrode (Logan et al., 2006). The representative configuration of an MFC includes a single chamber with an anode filled with wastewater, which is equipped with an oxygen-reducing cathode exposed to the atmosphere (Liu et al., 2004; Du et al., 2007). Theoretically, this type of MFC has the best cathodic potential due to the high electrode potential of O_2/H_2O. Tentatively, three key materials, i.e., an anode, separator, and cathode, determine the performance of the MFCs. Although electrode improvement and optimization is still ongoing (Li et al., 2017), carbon-based anodes, such as carbon brushes and felt (Logan et al., 2007), and cathode supporting carbon-catalysts, such as carbon black and activated carbon (Zhang et al., 2014a,b), are becoming increasingly popular due to their commercial availability and inexpensive cost.

For the application of MFCs in sewage water treatment at a large-scale, separation of air, and liquid phases while retaining the permeability of ions or oxygen is of great concern (Leong et al., 2013). An ion exchange membrane (IEM) (Kim et al., 2007; Leong et al., 2013) and PTFE layer (Cheng et al., 2006) have been used to separate the air and liquid phase, which allow ion and oxygen mobility, respectively. In particular, large-scale MFCs with greater depth favor IEMs, especially the cation exchange membrane (CEM), due to their commercial availability and physical toughness at a relatively inexpensive cost (Ge and He, 2016; Liang et al., 2018). However, the MFC that treats the wastewater contains higher concentrations of various cations, such as Na^+, Ca^{2+}, K^+, and NH^{3+}, in the anolyte, which compete with protons that attach to the negatively charged function groups in the CEM (Rozendal et al., 2006). This can cause reduction in electricity production after long-term operation (Ge and He, 2016; Liang et al., 2018).

An anion exchange membrane (AEM) is an alternative IEM and involves the movement of OH^- from air (cathode) to the sewage water in a single chambered MFC as illustrated in **Supplementary Figure 1**. Previous studies have shown that the AEM is characterized by improved electricity production in the MFC compared with the CEM in not only a dual chambered MFC (Kim et al., 2007; Fornero et al., 2008) but also in a single chambered MFC (Zhang et al., 2010). However, MFCs that use an AEM have never been evaluated for wastewater treatment over long-term operation, such as over 1 month. These facts motivated us to perform a preliminary evaluation of an MFC using an AEM to remove organic matter and recover electricity from the wastewater. Based on the assumption that OH^-, generated by oxygen reduction on the cathode, is the dominant anion in the AEM, its limitation can likely extend the lifetime of the MFC. The MFC used in this study was specially designed to be applicable to the existing sewage treatment tank. The MFC first ran in a sewage water channel for 140–230 days to test its electricity generation and lifetime, after which it was placed in a chemostat reactor to evaluate its ability to reduce organic matter.

MATERIALS AND METHODS

MFC Configuration

The single MFC used in this study was tubular in shape ($\phi 4.0 \times 33$ cm) with a core of the air chamber (**Supplementary Figure 1**). The air-core was tubular and made of stainless mesh surrounded by a cathode ($4\pi \times 33$ cm), separator ($4\pi \times 33$ cm), and anode ($4\pi \times 33$ cm) without spacing. The cathode was comprised of a carbon cloth (TOYOBO, Osaka, Japan) painted with

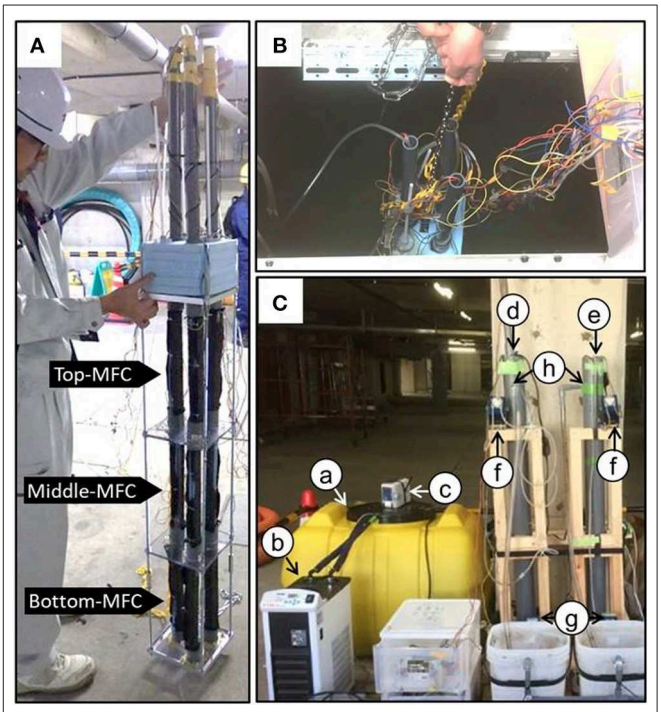

FIGURE 1 | The modularized microbial fuel cells used in this study **(A)** and the MFC modules floating in the sewage water channel **(B)** and chemostat reactors **(C)**. In **(C)**, the letters indicate the following components: (a) influent storage tank, (b) cooling water circulating system, (c) impeller for mixing the influent, (d) reactor with the MFC, (e) reactor without the MFC (NON), (f) circulation pump, (g) feeding pump, and (h) effluent outlet. The effluent was sampled from the outlet (h) to determine the COD concentration. The influent was also partially collected from the tube that connected the storage tank (a) to the reactors (d,e).

a mixture of 1.7 mg·cm^{-2} activated carbon (Wako, Tokyo, Japan), 1.1 mg·cm^{-2} of carbon black (Fuel Cell Earth, Woburn, MA, USA), 14 μL·cm^{-2} of isopropanol, 5.6 μL·cm^{-2} of 20% Poly (diallyldimethylammonium chloride) solution (SIGMA-ALDRICH, St. Louis, MO, USA), and 5.6 μL·cm^{-2} of 60% PTFE solution (SIGMA-ALDRICH). An AEM (ASTOM, Tokyo, Japan) was used as the separator while a graphite felt sheet, with a thickness of 0.5 cm, was used as the anode (Yoshida et al., 2016b). To collect electrons, a stainless steel mesh (Clever, Toyohashi, Japan) was used in both electrodes. The anode was immersed in a sewage sludge suspension as described in Yoshida et al. (2016c) prior to operation. Three units were vertically connected and assembled to form one MFC module (**Figure 1A**).

MFC Operation in Water Channels

Two sets of MFC modules were introduced in water channels for electricity production using the sewage water. The MFC module introduced into the water channel before its treatment in the primary sedimentation tank (PST) was termed IN-MFC while the module introduced into water after the PST-treatment was termed EF-MFC (**Figure 1B**). The MFC modules were fixed on a steel cage with a styrene foam floater on the top and a plummet at the bottom. The three sets of electrodes in the module were individually polarized with an external resistance of 120 (0–7 days) and 27 Ω (after 7 days). The voltage was measured every hour as described previously (Yoshida et al., 2016b).

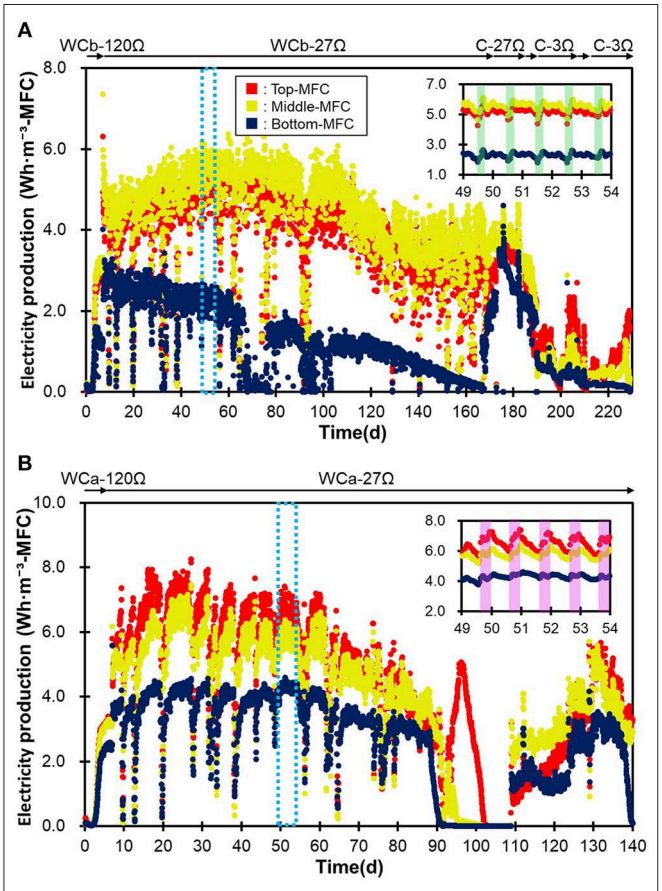

FIGURE 2 | The production of electricity by the three MFCs in the IN-MFC module **(A)** and EF-MFC module **(B)**. WCb and WCa show the MFCs that were operated in the water channel before and after treatment in the PST, respectively. C indicates the MFCs in a chemostat reactor polarized via resistances of 3 (C-3Ω) and 27Ω (C-27Ω). The green frame represents the morning (5:30–11:30) while the purple frame represents the daytime (8:30–17:30).

Linear Sweep Voltammetry

Linear sweep voltammetry (LSV) of the three MFCs in the IN-MFC module was performed using a potentio-galvanostat analyzer as described as described previously (Yoshida et al., 2016a). The cell current was measured when the anode was connected as the working electrode with the cathode connected to the reference and counter electrodes. When measuring the anodic and cathodic currents, Ag/AgCl (BAS Inc., Tokyo, Japan) was used as the reference electrode. To measure the anodic current, an anode, and cathode were connected as the working and counter electrodes, respectively, while the cathodic current was measured with the cathode as the working electrode and anode as the counter electrode. LSV was performed at a voltage from the open circuit potential to 0 V with a sweep rate of 0.5 mV·s^{-1}.

COD Removal Evaluation by the MFCs

The IN-MFC was removed from the water channel and re-set in a cylindrical chemostat reactor (ϕ7.7 × 130 cm) to evaluate the removal of COD (Nurmiyanto et al., 2017). The approximate volume ratio of MFC:reactor was set to 1:5 (v/v) (**Figure 1C**). For comparison, a similar cylindrical reactor without an MFC (NON) was also installed in parallel. The reactors were maintained under chemostat conditions to obtain 3, 6, and 12 h hydraulic retention times (HRTs) via a continuous supply of influent from the bottom of the reactor. For the influent, wastewater was taken from a water channel before treatment in the PST. The water was stored in a storage tank with a 300 L capacity, maintained at ∼15°C via a cooling water circulation system (AS ONE, Osaka Japan), and mixed continuously using an SMT-101 stirring blade (AS ONE). The temperature of the chemostat reactor was maintained at 30°C with continuous mixing using a magnetic stirrer and circulation via internal wastewater pumping. The three sets of electrodes were individually polarized with an external resistance of 27 and 3Ω. The reactors were maintained under six operational conditions with different combinations of HRTs and external resistances (**Supplementary Table 1**). The IN-MFC was stabilized under the given operational conditions for at least 12 h prior to the first sampling. The COD and BOD were analyzed for the influent and effluents from the MFC and NON reactors. The analyses were performed at the Environmental Research Center (Nagoya, Japan) as described previously (Goto and Yoshida, 2017). Sampling was repeated at least three times with an interval longer than the HRT under each operational condition.

RESULTS

Electricity Production in the Water Channels

The two MFC modules, i.e., the IN-MFC and EF-MFC, were individually installed and polarized in the water channels for the PST influent and effluent, respectively (**Figure 1**). In both modules, electricity production drastically increased within 4 days and then became relatively stable (**Figure 2**). The top and middle MFCs had similar electricity production while the bottom MFC had lower electricity production than the upper MFCs. This trend was observed for both modules.

In the IN-MFC, the top and middle MFCs were characterized by relatively stable electricity production from days 7–110, with an average of 4.7 ± 0.5 and 5.1 ± 0.6 $Wh{\cdot}m^{-3}$-MFC, respectively (**Figure 2**). The production gradually decreased between days 110 and 130 and then became stable again at 3.4 ± 0.62 $Wh{\cdot}m^{-3}$-MFC until the MFC was moved to the chemostat reactor on day 173. Meanwhile, the bottom MFC had a stable electricity production of 2.3 ± 0.33 $Wh{\cdot}m^{-3}$-MFC from days 7–66. However, this production declined due to water leakage into the cathodic chamber and stopped by day 76. Electricity production was then recovered on day 77 via the removal of water in the cathode chamber and fixing the leak. Electricity in the bottom MFC, however, decreased gradually thereafter until the end of the operation. Corrosion of the electric wire attached to the air-core stainless mesh due to wastewater leakage possibly caused this gradual decrease in the bottom MFC.

In the EF-MFC module, all MFCs had a relatively stable electricity production by day 88, which was 5.7 ± 1.2 (top), 5.1 ± 1.0 (middle), and 3.5 ± 0.68 (bottom) $Wh{\cdot}m^{-3}$-MFC. The electricity production decreased due to water leakage into the cathode chamber from day 89 and was then recovered on day 109 by fixing the water leak. However, production again decreased from day 131 and completely stopped on day 150 due to corrosion caused by leaking water.

The overall trend in electricity production for the two MFC modules was not significantly different despite a reduction of nearly half in the organic matter content via treatments in the PST. On the other hand, daily fluctuations in electricity production were observed at <1.0 $Wh{\cdot}m^{-3}$-MFC. Production was usually higher in the morning hours (5:00–10:00) in the water channel before PST and during the daytime (8:00–17:00) in the water channel after PST (**Figure 2**). These differences can possibly be attributed to the differences in wastewater qualities in COD concentration, conductivity and temperature (Hiegemann et al., 2016).

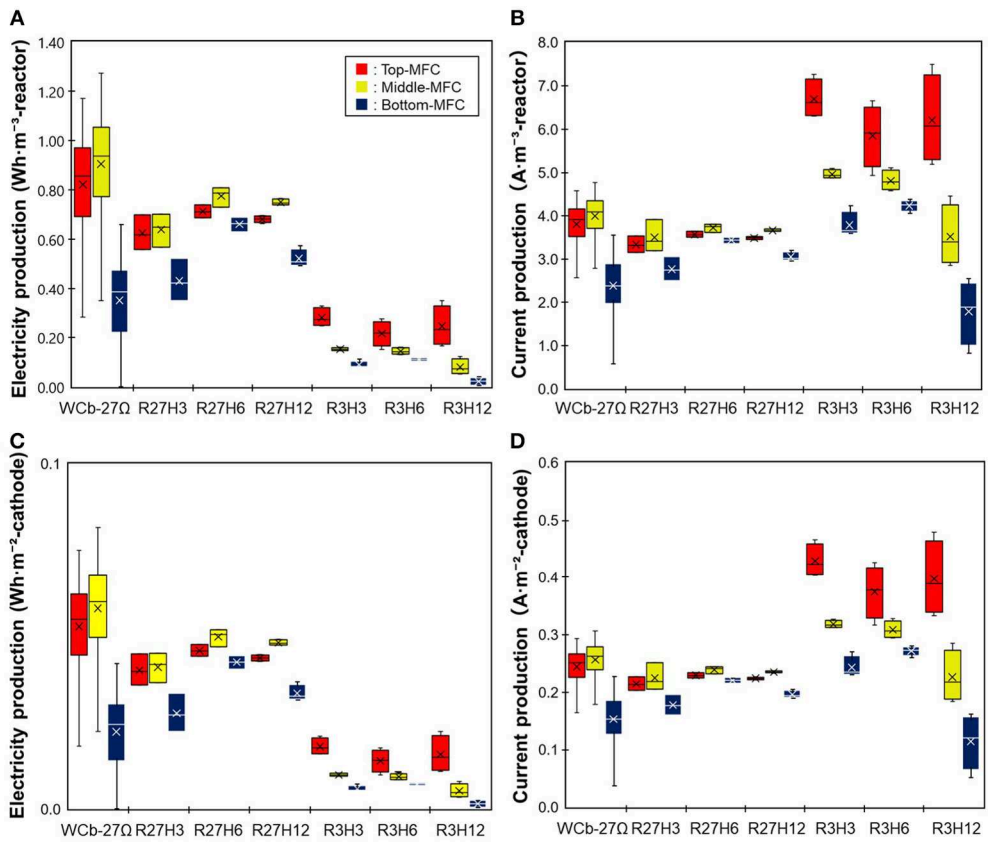

FIGURE 3 | A comparison of the electricity production by the MFCs operated under six different conditions. **(A,B)** indicate electricity and current production, respectively, normalized by the reactor volume. **(C,D)** indicate electricity and current production, respectively, normalized by the cathode area.

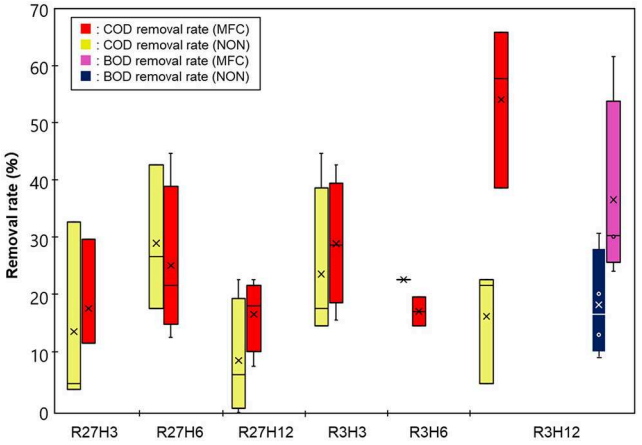

FIGURE 4 | The removal of organic matter by the MFCs operated under six different conditions.

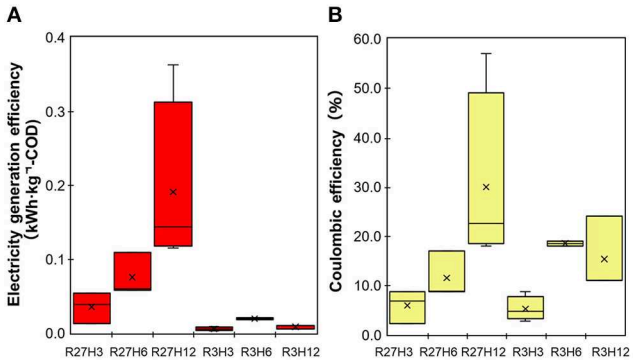

FIGURE 5 | The electricity generation efficiency **(A)** and Coulombic efficiency **(B)** for the MFCs operated under 6 different conditions.

LSV Analysis of the MFCs at Different Depths

Supplementary Figure 2 shows the LSV profiles of the three MFCs in the IN-MFC module. Maximum cell currents were approximately half the values of the cathodic and anodic currents in the top and middle MFCs. This suggests that ion mobility, rather than anodic and cathodic reactions, determined the electricity production in the two MFCs. In the bottom MFC, the cathodic current was lower than that in the top and middle MFCs and similar to the cell current. Corrosion or insufficient air in the air chamber possibly suppressed electricity production in the bottom MFC. Less anodic current in the top MFC as compared with current in the two lower MFCs suggests a competition between the anode and oxygen as an e^- acceptor at the water surface.

Electricity and Current Recovery From MFCs in the Chemostat Reactor

The IN-MFC that retained electricity production after 170 days of pre-operation in the water channel was moved to a chemostat reactor and sequentially maintained under a total of six operational conditions with different HRTs and external resistances (**Supplementary Table 1**). Although electricity production was normalized by the reactor volume hereafter, electricity production in the water channels was normalized by the MFC volume as shown in **Figure 2**.

Figure 3 shows the electricity and current production of the three MFCs in the reactor. Electricity production was higher at 27Ω than that at 3Ω while the current was higher at 3Ω. Under the six operation conditions, the electricity production was the highest under R27H6, which was 0.71 ± 0.026, 0.78 ± 0.040, and 0.66 ± 0.030 $Wh \cdot m^{-3}$-reactor for the top, middle, and bottom MFCs, respectively, while the current was highest under R3H3, with 6.7 ± 0.45, 5.0 ± 0.1, and 3.8 ± 0.30 $A \cdot m^{-3}$-reactor, for the top, middle, and bottom MFCs, respectively. Differences in the HRT did not affect the electricity and current production. A significant decrease in electricity and current production was observed in the bottom MFC under R3H12. This was possibly caused by the gradual deterioration of the bottom MFC, which experienced water leakage several times throughout the operation.

COD Removal via MFCs in the Chemostat Reactor

Figure 4 shows the results of COD removal by the IN-MFC in the chemostat reactor. Compared with the NON reactor, the COD significantly decreased only under R3H12 while no significant differences between the NON and MFC reactors were observed under the other conditions. Specifically, the average COD removal efficiency (COD-RE) was 54 ± 14% in the reactor with the MFC and 17 ± 10% without the MFC. Under the other conditions, the COD-RTs were in the range of 8.0–45%. For R3H12, the BOD also showed a significant decrease with the MFC reactor. The BOD removal efficiency in the MFC reactor was, on average, 37 ± 17%, which was higher than the BOD removal efficiency in the NON (19 ± 9.5%). The COD and BOD of the effluent from the MFC reactor under R3H12 were 210 ± 82 and 320 ± 98 $mg \cdot L^{-1}$, respectively.

MFC Energy Recovery Efficiency

Energy recovery was evaluated based on the electricity production and removal of COD in the chemostat reactor under the six operational conditions, which are indicated as the electricity generation efficiency (EGE, kWh·kg-COD^{-1}) and Coulomb efficiency (CE, %) (**Figure 5**). The values of both the EGE and CE increased with longer HRTs. The highest EGE_{MFC}, i.e., 0.19 ± 0.12 kWh·kg-COD^{-1}, was observed during R27H12, with a value that was 2.5- and 5.4-fold higher than the EGE_{MFC}s for the 6 and 3 h HRTs, respectively. The CE was also highest during R27H12h (30 ± 18%) but the value was not significantly different under R3H12 (15 ± 7.5%) and R3H6 (19 ± 0.7%). Representative data obtained in the MFC are summarized in **Table 1**.

Energy Balance Calculations of the MFC-Integrated Wastewater Treatment

Based on the COD-RE and EGE, we calculated the energy consumption for three wastewater treatment scenarios, i.e., aeration (Case-1), a combination of anaerobic degradation and

TABLE 1 | A summary of IN-MFC performance compared with other MFCs treating real wastewater.

Anode	Cathode	Separator	GDL[a]	CSSA[b] ($m^2 \cdot m^{-3}$)	$COD_{influent}$ ($mg \cdot L^{-1}$)	HRT (h)	COD-RE (%)	Power ($Wh \cdot m^{-2}$-cathode)	Current ($A \cdot m^{-2}$-cathode)	CE (%)	EGE (kwh·kg-COD^{-1})	References
GFB	Carbon cloth/Pt	WW	PTFE	8	330	143	79	0.058	0.22	3.0–5.0	0.065	Feng et al., 2014
GFB	Stainless steel/AC	WW	PTFE	0.6	820	72	85	0.17	0.56	19	0.081	Dong et al., 2015
GFB	Stainless steel/AC	WW	PTFE	0.6	3,300	144	88	0.15	0.55	8	0.033	Dong et al., 2015
GFB	Carbon cloth/Pt	WW	PTFE	11	120	22	24	0.082	–	25	0.36	Hiegemann et al., 2016
GF	CC/AC	AEM	–	22	450	12	17	0.042	0.22	30	0.19	This study (R27H12)
GF	CC/AC	AEM	–	22	450	12	54	0.0074	0.25	15	0.0086	This study (R3H12)

[a]*Gas diffusion layer.*
[b]*Cathode specific surface area.*

aeration (Case-2), and a combination of aeration and MFC under R27H12 (Case-3) and R3H12 (Case-4) (**Tables 1**, **2**). In Case-2, biomass energy was tentatively retrieved by CH_4 fermentation based on the calculations. The EGE via CH_4 fermentation (EGE_{CH4}) have never evaluated for sewage water. however, data for swine wastewaters, are in the range of 0.79–2.6 kWh·kg-COD^{-1}, with an average of 1.6 kWh·kg-COD^{-1} (Lo et al., 1994; Hill and Bolte, 2000; Song et al., 2010; Duda et al., 2015; **Supplementary Table 2**). The EGE in the MFC (EGE_{MFC}) was 0.19 ± 0.12 kWh·kg-COD^{-1} during R27H12 in Case-3 and 0.0086 ± 0.0025 kWh·kg^{-1}-COD during R3H12 in Case-4. The EGE_{MFC} was <15 and 1% of the EGE_{CH4} under R27H12 and R3H12, respectively. However, taken together with the energy consumption associated with the removal of COD via aeration, i.e., −0.6 kWh·kg-COD^{-1} (He, 2013; Maktabifard et al., 2018), the system integrated with an MFC operated under R3H12 is advantageous in comparison with systems integrated with CH_4-fermentation and an MFC polarized at 27Ω (**Table 2**). Although the MFC that operated under R27H12 consumed more energy than the CH_4-fermentation-integrated system, the MFC that operated under R3H12 can reduce the energy consumption by 55%, which was higher than that for the CH_4-fermentation-integrated system (48%). This calculation indicates that the removal of COD without aeration had more of an effect on the total energy balance as compared with the electricity production.

DISCUSSION

This is the first study to investigate the long-term operation of an MFC using an AEM in sewage water. The observed performance was compared with other MFCs that have a capacity >2.0 L and operate in real wastewater (**Table 1**). The best EGE_{MFC} and CE in the MFC were 0.19 ± 0.12 kWh·kg-COD^{-1} and 30%, respectively, which are comparable to previously reported MFCs (Feng et al., 2014; Dong et al., 2015; Hiegemann et al., 2016). Several strategies can be considered to increase the energy balance, i.e., an increase in the MFC filling rate (Park et al., 2018) and HRT (Hiegemann et al., 2016) or a decrease in the energy consumed by aeration via a combination with the anaerobic membrane reactor (Ren et al., 2014). However, these strategies do not have practical applications in sewage water treatment due to the two major functions of sewage water treatment plants, i.e., controlling the water quality, including the concentration of dissolved oxygen, and the drainage of storm water. Increases in the COD-RE, electricity recovery normalized by the electrode-area and cathode specific surface area are important factors as reported previously (Logan et al., 2015).

The MFC configuration used in this study was specially designed for its application to sewage treatment plants characterized by both a high influent volume and fluctuations in water levels due to rain water. Moreover, these treatment plants have been widely constructed in Japan. The tubular structure is physically tough, the floating structure can be adapted to changes in the water level, and the core-air chamber allows a simple installation into the existing sewage treatment plant without the construction of a reactor. However, a simple but

TABLE 2 | Energy reduction via the installation of the MFCs.

		COD ($mg \cdot L^{-1}$)	Energy recovery ($kWh \cdot kg\text{-}COD^{-1}$)	Total energy ($kWh \cdot m^{-3}$)
Case-1	Influent	450		
	Aeration		−0.6	−0.27
	Aeration effluent	4.0		
	Total			−0.27
Case-2	Influent	450		
	Anaerobic digestion		1.6	0.09
	Anaerobic digestion effluent	390		
	Aeration		−0.6	−0.23
	Aeration tank effluent	4.0		
	Total			−0.14
	Energy reduction (%)[a]			48
Case-3	Influent	450		
	MFC (R27H12)		0.19	0.01
	MFC effluent	370		
	Aeration		−0.6	−0.22
	Aeration tank effluent	4.0		
	Total			−0.21
	Energy reduction (%)			23
Case-4	Influent	450		
	MFC (R3H12)		0.0086	0.002
	MFC effluent	210		
	Aeration		−0.6	−0.12
	Aeration effluent	4.0		
	Total			−0.12
	Energy reduction (%)			55

[a] *Energy reduction in comparison with energy consumption in case-1.*

serious problem was encountered during the installation of the MFC in the sewage water channel. This was the leakage of sewage water into the air-chamber of the MFC at a depth of 1.0 m. The main reactor tank in the sewage water treatment plant generally has a depth of 3.0–5.0 m. However, the operation of single chamber-MFC at more than 1.0 m of water depth has never been reported, to the best of our knowledge, while many large-scale MFCs have been constructed (Ge and He, 2016; Hiegemann et al., 2016; Lu et al., 2017; Liang et al., 2018). Additionally, the MFC with water leakage showed a gradual decrease in electricity production, which was possibly caused by corrosion. On the other hand, the MFC units that did not experience water leakage, i.e., the top and middle MFCs in the IN-MFC module had nearly constant current production in 230 days of operation (**Supplementary Figure 3**), suggesting no deterioration of electrode and membrane in this duration. In our MFC configuration, AEM elasticity caused water leakage. These membranes shrink upon drying and expand in water. For the longer running MFCs using elastic separator at various depths, further improvement is required in the MFC configuration.

In conclusion, an AEM can be used in a single chamber MFC with a comparative level of electricity production that has been observed for other single chamber MFCs that use a CEM. Within 230 days of the experimental duration, deterioration was not observed in the MFCs did not experience water leakage. The application of the MFCs to wastewater treatment at depths >1.0 m requires technical advancements and further research. Preliminary calculation of energy balance of the system combined MFC and aeration, the MFC having more COD-removal rather than electricity production is advantageous in the total energy reduction.

DATA AVAILABILITY

The raw data supporting the conclusions of this manuscript will be made available by the authors, without undue reservation, to any qualified researcher.

AUTHOR CONTRIBUTIONS

MS performed MFC experiments and analyzed the data and described the draft of the manuscript. NY designed the experiments and revised the manuscript. KI designed the experiment.

FUNDING

This study received funding from the MEXT/JSPS KAKENHI (Grant number: 18K18876) and Hibi Science Foundation.

ACKNOWLEDGMENTS

We are grateful to Mitsuhiro Sakoda (Tamano Consultants Co., Ltd.), Hirokazu Matsubara (Nippon Koei Co., Ltd.), and Yoshinori Genda (Tamano Consultants Co., Ltd.) for their management of the on-site evaluation. We would like to show our appreciation to Dr. Yasushi Miyata (Nagoya Municipal Industrial Research Institute) for his advice regarding the use of the AEM as a separator in the MFC. We also thank Akihiro Iwata and Yoshimasa Suzuki for their extensive efforts in optimizing the procedure to manufacture the MFC and technical advice on fixing the AEM to the solid frame of the MFC. We also extend our gratitude to the staff of Nagoya City Waterworks & Sewerage Bureau for providing us a venue for the on-site evaluation.

SUPPLEMENTARY MATERIAL

The Supplementary Material for this article can be found online at: https://www.frontiersin.org/articles/10.3389/fenrg.2019.00091/full#supplementary-material

REFERENCES

Arcila, J. S., and Buitrón, G. (2016). Microalgae–bacteria aggregates: effect of the hydraulic retention time on the municipal wastewater treatment, biomass settle ability and methane potential. *J. Chem. Technol. Biotechnol.* 91, 2862–2870. doi: 10.1002/jctb.4901

Cheng, S., Liu, H., and Logan, B. E. (2006). Power densities using different cathode catalysts (Pt and CoTMPP) and polymer binders (Nafion and PTFE) in single chamber microbial fuel cells. *Environ. Sci. Technol.* 40, 364–369. doi: 10.1021/es0512071

Dong, Y., Qu, Y., He, W., Du, Y., Liu, J., Han, X., et al. (2015). A 90-liter stackable baffled microbial fuel cell for brewery wastewater treatment based on energy self-sufficient mode. *Bioresour. Technol.* 195, 66–72. doi: 10.1016/j.biortech.2015.06.026

Du, Z., Li, H., and Gu, T. (2007). A state of the art review on microbial fuel cells: a promising technology for wastewater treatment and bioenergy. *Biotechnol. Adv.* 25, 464–482. doi: 10.1016/j.biotechadv.2007.05.004

Duda, R. M., da Silva Vantini, J., Martins, L. S., de Mello Varani, A., Lemos, M. V. F., Ferro, M. I. T., et al. (2015). A balanced microbiota efficiently produces methane in a novel high-rate horizontal anaerobic reactor for the treatment of swine wastewater. *Bioresour. Technol.* 197, 152–160. doi: 10.1016/j.biortech.2015.08.004

Feng, Y., He, W., Liu, J., Wang, X., Qu, Y., and Ren, N. (2014). A horizontal plug flow and stackable pilot microbial fuel cell for municipal wastewater treatment. *Bioresour. Technol.* 156, 132–138. doi: 10.1016/j.biortech.2013.12.104

Fornero, J. J., Rosenbaum, M., Cotta, M. A., and Angenent, L. T. (2008). Microbial fuel cell performance with a pressurized cathode chamber. *Environ. Sci. Technol.* 42, 8578–8584. doi: 10.1021/es8015292

Ge, Z., and He, Z. (2016). Long-term performance of a 200 liter modularized microbial fuel cell system treating municipal wastewater: treatment, energy, and cost. *Environ. Sci. Water Res. Technol.* 2, 274–281. doi: 10.1039/c6ew00020g

Goto, Y., and Yoshida, N. (2017). Microbially reduced graphene oxide shows efficient electricity ecovery from artificial dialysis wastewater. *J. Gen. Appl. Microbiol.* 63, 165–171. doi: 10.2323/jgam.2016.10.001

He, Z. (2013). Microbial fuel cells: now let us talk about energy. *Environ. Sci. Technol.* 47, 332–333. doi: 10.1021/es304937e

Hiegemann, H., Herzer, D., Nettmann, E., Lübken, M., Schulte, P., Schmelz, K. G., et al. (2016). An integrated 45 L pilot microbial fuel cell system at a full-scale wastewater treatment plant. *Bioresour. Technol.* 218, 115–122. doi: 10.1016/j.biortech.2016.06.052

Hill, D. T., and Bolte, J. P. (2000). Methane production from low solid concentration liquid swine waste using conventional anaerobic fermentation. *Bioresour. Technol.* 74, 241–247. doi: 10.1016/S0960-8524(00)00008-0

Kaur, M., Kumar, M., Sachdeva, S., and Puri, S. K. (2018). Aquatic weeds as the next generation feedstock for sustainable bioenergy production. *Bioresour. Technol.* 251, 390–402. doi: 10.1016/j.biortech.2017.11.082

Kim, J. R., Cheng, S., Oh, S. E., and Logan, B. E. (2007). Power generation using different cation, anion, and ultrafiltration membranes in microbial fuel cells. *Environ. Sci. Technol.* 41, 1004–1009. doi: 10.1021/es062202m

Leong, J. X., Daud, W. R. W., Ghasemi, M., Liew, K. B., and Ismail, M. (2013). Ion exchange membranes as separators in microbial fuel cells for bioenergy conversion: a comprehensive review. *Renew. Sustain. Energy Rev.* 28, 575–587. doi: 10.1016/j.rser.2013.08.052

Li, S., Cheng, C., and Thomas, A. (2017). Carbon-based microbial-fuel-cell electrodes: from conductive supports to active catalysts. *Adv. Mater.* 29:1602547. doi: 10.1002/adma.201602547

Li, W. W., Yu, H. Q., and He, Z. (2014). Towards sustainable wastewater treatment by using microbial fuel cells-centered technologies. *Energy Environ. Sci.* 7, 911–924. doi: 10.1039/c3ee43106a

Liang, P., Duan, R., Jiang, Y., Zhang, X., Qiu, Y., and Huang, X. (2018). One-year operation of 1000-L modularized microbial fuel cell for municipal wastewater treatment. *Water Res.* 141, 1–8. doi: 10.1016/j.watres.2018.04.066

Liu, H., Ramnarayanan, R., and Logan, B. E. (2004). Production of electricity during wastewater treatment using a single chamber microbial fuel cell. *Environ. Sci. Technol.* 38, 2281–2285. doi: 10.1021/es034923g

Lo, K., Liao, E., and Gao, Y. (1994). Anaerobic treatment of swine wastewater using hybrid UASB reactors. *Bioresour. Technol.* 47, 153–157. doi: 10.1016/0960-8524(94)90114-7

Logan, B., Cheng, S., Watson, V., and Estadt, G. (2007). Graphite fiber brush anodes for increased power production in air-cathode microbial fuel cells. *Environ. Sci. Technol.* 41, 3341–3346. doi: 10.1021/es062644y

Logan, B. E., Hamelers, B., Rozendal, R., Schröder, U., Keller, J., Freguia, S., et al. (2006). Microbial fuel cells: methodology and technology. *Environ. Sci. Technol.* doi: 10.1021/es0605016

Logan, B. E., Wallack, M. J., Kim, K. Y., He, W., Feng, Y., and Saikaly, P. E. (2015). Assessment of microbial fuel cell configurations and power densities. *Environ. Sci. Technol. Lett.* 2, 206–214. doi: 10.1021/acs.estlett.5b00180

Lu, M., Chen, S., Babanova, S., Phadke, S., Salvacion, M., Mirhosseini, A., et al. (2017). Long-term performance of a 20-L continuous flow microbial fuel cell for treatment of brewery wastewater. *J. Power Sources* 356, 274–287. doi: 10.1016/j.jpowsour.2017.03.132

Maktabifard, M., Zaborowska, E., and Makinia, J. (2018). Achieving energy neutrality in wastewater treatment plants through energy savings and enhancing renewable energy production. *Rev. Environ. Sci. Biotechnol.* 17, 655–689. doi: 10.1007/s11157-018-9478-x

Martinez-Sosa, D., Helmreich, B., Netter, T., Paris, S., Bischof, F., and Horn, H. (2011). Anaerobic submerged membrane bioreactor (AnSMBR) for municipal wastewater treatment under mesophilic and psychrophilic temperature conditions. *Bioresour. Technol.* 102, 10377–10385. doi: 10.1016/j.biortech.2011.09.012

Nurmiyanto, A., Kodera, H., Kindaichi, T., Ozaki, N., Aoi, Y., and Ohashi, A. (2017). Dominant *Candidatus Accumulibacter phosphatis* enriched in response to phosphate concentrations in EBPR process. *Microbes Environ.* 32, 260–267. doi: 10.1264/jsme2.me17020

Park, Y., Nguyen, V. K., Park, S., Yu, J., and Lee, T. (2018). Effects of anode spacing and flow rate on energy recovery of flat-panel air-cathode microbial fuel cells using domestic wastewater. *Bioresour. Technol.* 258, 57–63. doi: 10.1016/j.biortech.2018.02.097

Ren, L., Ahn, Y., and Logan, B. E. (2014). A two-stage microbial fuel cell and anaerobic fluidized bed membrane bioreactor (MFC-AFMBR) system for effective domestic wastewater treatment. *Environ. Sci. Technol.* 48, 4199–4206. doi: 10.1021/es500737m

Rozendal, R. A., Hamelers, H. V. M., and Buisman, C. J. N. (2006). Effects of membrane cation transport on pH and microbial fuel cell performance. *Environ. Sci. Technol.* 40, 5206–5211. doi: 10.1021/es060387r

Shizas, I., and Bagley, D. M. (2004). Experimental determination of energy content of unknown organics in municipal wastewater streams. *J. Energy Eng.* 130, 45–53. doi: 10.1061/(ASCE)0733-9402(2004)130:2(45)

Song, M., Shin, S. G., and Hwang, S. (2010). Methanogenic population dynamics assessed by real-time quantitative PCR in sludge granule in upflow anaerobic sludge blanket treating swine wastewater. *Bioresour. Technol.* 101(Suppl. 1), S23–S28. doi: 10.1016/j.biortech.2009.03.054

Yan, P., Qin, R. C., Guo, J. S., Yu, Q., Li, Z., Chen, Y. P., et al. (2017). Net-zero-energy model for sustainable wastewater treatment. *Environ. Sci. Technol.* 51, 1017–1023. doi: 10.1021/acs.est.6b04735

Yoshida, N., Goto, Y., Miyata, Y., and Thakur, V. K. (2016c). Selective growth of and electricity production by marine exoelectrogenic bacteria in self-agregated hydrogel of microbially reduced graphene oxide. *J. Carbon. Res.* 2:15. doi: 10.3390/c2020015

Yoshida, N., Miyata, Y., Doi, K., Goto, Y., Nagao, Y., Tero, R., et al. (2016a). Graphene oxide-dependent growth and self-Aggregation into a hydrogel complex of exoelectrogenic bacteria. *Sci. Rep.* 6:21867. doi: 10.1038/srep21867

Yoshida, N., Miyata, Y., Mugita, A., and Iida, K. (2016b). Electricity recovery from municipal sewage wastewater using a hydrogel complex composed of microbially reduced graphene oxide and sludge. *Materials (Basel).* 9:742. doi: 10.3390/ma9090742

Zhang, X., Cheng, S., Huang, X., and Logan, B. E. (2010). Improved performance of single-chamber microbial fuel cells through control of membrane deformation. *Biosens. Bioelectron.* 25, 1825–1828. doi: 10.1016/j.bios.2009.11.018

Zhang, X., Pant, D., Zhang, F., Liu, J., He, W., and Logan, B. E. (2014a). Long-term performance of chemically and physically modified activated carbons in Air cathodes of microbial fuel cells. *ChemElectroChem* 1, 1859–1866. doi: 10.1002/celc.201402123

Zhang, X., Xia, X., Ivanov, I., Huang, X., and Logan, B. E. (2014b). Enhanced activated carbon cathode performance for microbial fuel cell by blending carbon black. *Environ. Sci. Technol.* 48, 2075–2081. doi: 10.1021/es405029y

Conflict of Interest Statement: This study was partially funded by Nippon Koei Co., Ltd. and Tamano Consultants Co., Ltd. KI was an employee of Nippon Koei Co., Ltd. We are currently applying for a patent for the MFC configuration reported in this study. All authors acknowledge the scientific fairness of the experimental design and interpretation of the results.

frontiers in Energy Research

ORIGINAL RESEARCH
published: 10 September 2019
doi: 10.3389/fenrg.2019.00093

High Performing Gas Diffusion Biocathode for Microbial Fuel Cells Using Acidophilic Iron Oxidizing Bacteria

Paniz Izadi[1†], *Jean-Marie Fontmorin*[1†], *Luis F. L. Fernández*[2], *Shaoan Cheng*[3], *Ian Head*[4] *and Eileen H. Yu*[1*]

[1] School of Engineering, Newcastle University, Newcastle upon Tyne, United Kingdom, [2] Departamento de Ingeniería Química, Universidad de Castilla-La-Mancha, Ciudad Real, Spain, [3] Department of Energy Engineering, Zhejiang University, Hangzhou, China, [4] School of Natural and Environmental Sciences, Newcastle University, Newcastle upon Tyne, United Kingdom

The development of a sustainable catalyst for the oxygen reduction reaction (ORR) is still a major bottleneck for the scale-up and commercialization of Microbial Fuel Cells (MFCs). In this work, we have studied the utilization of iron-oxidizing bacteria (IOB) enriched from natural environment and Fe^{2+} in MFCs equipped with gas diffusion electrodes (GDEs) as an alternative to traditional Pt-based catalysts. In half-cells systems, the oxidation of Fe^{2+} into Fe^{3+} by IOB and its regeneration at the cathode produced constant current densities close to 2 A m^{-2} for more than 45 days. In MFCs operated in batch mode, significant pH changes in both compartment led to the instability of the system. However, when operated in continuous mode, pH remained stable in both compartments and MFCs produced maximum power densities of 1.1 W m^{-2} were then reached, compared to 0.5 W m^{-2} for MFCs equipped with Pt catalyst. Diffusion of oxygen through the GDEs improved mass transport and the performance of the MFCs, and avoided the utilization of costly aeration system. This IOB GDE system also provides a reproducible and fast start-up for biocathode for MFCs.

Keywords: microbial fuel cell, biocathode, acidophile, gas diffusion electrode, oxygen reduction

OPEN ACCESS

Edited by:
Subba Rao Chaganti, University of Windsor, Canada

Reviewed by:
Deepak Pant, Flemish Institute for Technological Research, Belgium
Feng Zhao, Institute of Urban Environment (CAS), China

***Correspondence:**
Eileen H. Yu
eileen.yu@ncl.ac.uk

[†]*These authors have contributed equally to this work*

Specialty section:
This article was submitted to Bioenergy and Biofuels, a section of the journal Frontiers in Energy Research

Received: *18 June 2019*
Accepted: *21 August 2019*
Published: *10 September 2019*

Citation:
Izadi P, Fontmorin J-M, Fernández LFL, Cheng S, Head I and Yu EH (2019) High Performing Gas Diffusion Biocathode for Microbial Fuel Cells Using Acidophilic Iron Oxidizing Bacteria. Front. Energy Res. 7:93. doi: 10.3389/fenrg.2019.00093

INTRODUCTION

Microbial fuel cells (MFCs) are a promising technology with widespread applications such as wastewater treatment with the ability to generate power from wastes in order to decrease the energy consumption associated with these applications (Seelam et al., 2018). However, MFC technologies are still limited to laboratory scale mainly due to the low power outputs generated or the limitations associated with their scale up (Du et al., 2007; Rahimnejad et al., 2015). A conventional MFC consists of two compartments (anodic and cathodic) which can be separated by a membrane. At the anode, electrochemically-active microorganisms oxidize the organics from wastes and release electrons, carbon dioxide, and protons. At the cathode, reduction reaction occurs: oxygen is the preferred terminal electron acceptor due to its virtually inexhaustible availability and its high value of standard potential (E^0 = 1.229 V vs. Standard Hydrogen Electrode). However, kinetics of the oxygen reduction reaction (ORR) are sluggish, associated with high overpotentials which is why the ORR is still a bottleneck for the development of MFCs. Therefore, the cathode compartment is one

of the main factor limiting the MFC performance in power generation (Yu et al., 2007, 2012; Rabaey et al., 2008; Rismani-Yazdi et al., 2008). Different methods have been suggested to improve the reduction reaction at the cathode. Using different electron acceptors with high reduction potential such as permanganate or ferricyanide showed improvement in terms electricity generation (Oh et al., 2004; Kong et al., 2010; Oliveira et al., 2013). However, due to the irreversibility of these reactions, the catholyte should be replaced regularly. Therefore, this method is not economically favorable especially at larger scale. The utilization of chemical catalysts such as platinum (Pt), transition metal-based catalysts (Yu et al., 2007, 2009), or activated carbon has been extensively studied in the past (Burkitt et al., 2016). However, they have disadvantages such as high cost, lack of robustness, and sustainability. A promising and sustainable alternative is to replace chemical catalysts with biological catalysts. Biological catalysts offer several advantages, as they are cheaper, more stable in the long term, and environmentally sustainable (He and Angenent, 2006; Liew et al., 2014; Milner et al., 2014). In the past few years, several studies have focused on aerobic biocathodes using mixed cultures of microorganisms enriched from natural environments with various communities responsible for the ORR (Huang et al., 2011). In a previous study on aerobic biocathode using activated sludge as inoculum, it was shown that *Gammaproteobacteria* was mainly responsible for the ORR with direct electron uptake from the cathode, with the biofilm enriched at an applied potential of +0.2 V vs. Ag/AgCl (Milner et al., 2016). In spite of the ability of aerobic biocathodes to consume the electron directly from the cathode, the development of the biofilm associated with the ORR is a long process (usually at least 50 days). The utilization of a chemical mediator can help overcome this limitation as some bacteria can reduce oxygen by using mediators as electron donors. Previous studies have shown that the acidophilic iron oxidizing bacteria (IOB) *Acidithiobacillus ferrooxidans* are able to catalyze ORR at the cathode compartment at the acidic pH (Ter Heijne et al., 2006; Carbajosa et al., 2010). It was reported that IOB are able to derive energy directly from the cathode (Carbajosa et al., 2010), however the presence of ferrous ions (Fe^{2+}) as a mediator significantly improves the kinetics at the cathode and makes the biocathode much faster to develop. *Acidithiobacillus ferrooxidans* are autotrophs that use CO_2 as the carbon source, derive energy from the oxidation of Fe^{2+} and use oxygen as electron acceptor at low pH (typically around 3). Fe^{3+} produced from the biological oxidation is then regenerated at the cathode to Fe^{2+} (Lovley, 1991). Oxidizing ferrous iron and reducing oxygen by the iron oxidisers in an acidic condition yields almost 30 KJ/mole energy for their growth. Using Calvin cycle to fix CO_2, it has been estimated that *Acidithiobacillus ferrooxidans* oxidizes 71 mole Fe^{2+} to fix one mole CO_2 (Hedrich et al., 2011). Although at neutral pH, neutrophilic iron oxidisers are able to oxidize Fe^{2+}, the reduction of oxygen—and thus the energy gain for the bacteria—is more favorable at pH 2 than at pH 7 (Ferguson and Ingledew, 2008). A successful scaled-up MFC using acidophilic iron oxidisers at the cathode at pH 2 and acetate oxidation at the anode compartment by a bioanode biofilm resulted in a high power density of 2 $W.m^{-2}$ (Ter Heijne et al., 2011). However, in this study, expensive materials were used such as a biopolar membrane to overcome the pH shifts in both compartments as well as costly Pt- and Ir-coated electrodes.

It was proven that the performance of aerobic biocathodes can be limited by the oxygen mass transfer to the biofilm (Milner and Yu, 2018). To provide sufficient dissolved oxygen in the catholyte, aeration by air pump was used at different flow rates, showing that increasing the flow rate led to an increase in the dissolved oxygen concentration and consequently of the cathode and cell potentials (Milner and Yu, 2018). However, using air pump is not economically viable. Passive aeration using gas diffusion electrodes (GDEs) showed the appealing alternative to aeration by pump as it was proven that using GDEs for development of aerobic biocathodes could produce cell power comparable to that using Pt as the cathode catalyst (Xia et al., 2013). Despite the ability of GDE in overcoming the limitation of oxygen mass transfer, not many studies focused on using GDE for development of aerobic biocathodes. In this study, we developed a MFC using an aerobic biocathode with Fe^{2+} as a mediator in a dual chamber reactor equipped with GDE. *Acidithiobacillus ferrooxidans* was enriched from natural environment and used as biocatalyst. Reactors were started as a batch and later changed to continuous to overcome pH shifts-related limitations. The performance of the developed MFC was compared with a similar system equipped with a GDE coated with Pt catalyst.

MATERIALS AND METHODS

Enrichment of IOB

Inoculum for cathode compartment was collected from the iron-rich river sediment in Lake District, Cumbria, U.K. The sediment had an initial orange-brown color and a pH of 3.6. For the enrichment, 20 g L^{-1} $FeSO_4{\cdot}7H_2O$ was added to 100 mL of the environmental samples and kept in incubator at the temperature of 33°C and 170 rpm. One milliliter-samples were taken from the solution every 1–3 days to measure the pH and concentration of the Fe^{2+}/Fe^{3+} ions using the ferrozine method (Viollier et al., 2000). The control was composed of the exact same composition as the enrichment sample but was autoclaved to ensure no living bacteria was present. When pH of the solution dropped to 2.0, the color of the solution was dark red-orange, 20% of the samples were transferred to a fresh medium composed by 20 g L^{-1} $FeSO_4{\cdot}7H_2O$, 0.4 g L^{-1} $(NH_4)_2SO_4$, 0.4 g L^{-1} KH_2PO_4, and 0.4 g L^{-1} $MgSO_4$ (Fontmorin and Sillanpaa, 2015). After two more transfers, IOB were successfully enriched based on the color, pH, and the concentration of the Fe^{2+}/Fe^{3+} ions (Ter Heijne et al., 2007; Malki et al., 2008; Hedrich et al., 2011), and 20% of the solution was transferred to the cathode compartment of the MFC.

BES Setup and Operation

Dual chamber cells with GDEs as cathodes were used in this study. Cells were made of 3 Perspex pieces; two pieces were used as the anode and cathode compartments with a working volume of 60 mL each. The two compartments were separated by an anion exchange membrane (AEM, Fumasep FFA-3-PK-130, Fumatech, Germany). Carbon paper with gas diffusion layer (GDL) was purchased from Quintech (H2315 I2 C6, Göppingen,

Germany) and used as the GDE. Before the MFC operation, carbon paper was pre-treated to increase hydrophilicity by immersing the electrode in a mixture containing 20 mL of concentrated H_2SO_4 (98%) and 2 g of $KMnO_4$ at room temperature for 2 min, washing properly by deionized water and finally heating at 150°C for 2 h (Qiu et al., 2015). In MFCs equipped with platinized carbon paper (Pt-C) cathode, the same carbon paper was used and coated with 0.5 mg cm^{-2} Pt. The surface of the cathode was 12.5 cm^2 and a titanium sheet as a current collector. Carbon felt purchased from VWR (Cat. No. 43200.RR, Alfa Aesar, UK) was used as anode material. The carbon felt had dimensions of 2 × 3 cm and 0.5 cm thickness. Temperature was kept constant during the whole experiment at 30°C. MFCs were operated in duplicate for the both parts of the experiment.

Half-Cells

The first part was performed to investigate the development of acidophilic IOB biocathode and investigate its performance in terms of cathodic current consumption. During 47 days, BESs were operated in 3 electrode configuration (half-cells) with carbon paper GDEs as working electrodes at an applied potential of 200 mV vs. Ag/AgCl. Potential was controlled using a Quad Potentiostat (Whistonbrook Technologies, U.K.). Platinum mesh and Ag/AgCl (BASi, RE-5B) were used as counter and reference electrodes, respectively. Cathode medium consisted of the same chemicals used in the enrichment step (pH 2) but with lower concentration of 1 g/L $FeSO_4{\cdot}7H_2O$. 20% of the cathode medium was inoculated with IOB from the enrichment step. Anode medium was the same medium used in cathode compartment without $FeSO_4{\cdot}7H_2O$ and inoculum. A control was operated with the similar medium without IOB inoculum. All the potentials in this study are reported against Ag/AgCl, unless stated otherwise.

MFC Set Up and Operation

The second part of the experiment was carried out in full MFCs with external resistors of 200 Ω. **Figure 1** shows the MFC operated for this part of experiment. Cell voltages and anode potentials were recorded using a Pico Technology ADC-24 data logger (St Neots, U.K.). MFCs were first operated with Pt-C at the cathode in order to develop bioanodes. Graphite felts with the projected surface area of 4.9 cm^2 were used as the anode, using titanium sheet as current collector. Twenty percentage of the anode compartment was inoculated with the effluent of an MFC running in the laboratory over a year using glucose and acetate as carbon sources. The bacterial community of the inoculum was dominated by *Geobacter* (Spurr et al., 2018). Anode medium consisted of 50 mM phosphate buffer (PBS), 1 g L^{-1} of sodium acetate, 25 mL L^{-1} of macronutrients solution, 1 mL L^{-1} of micronutrients solution, and 0.5 mL L^{-1} of vitamins solution (see composition in **Table S1**).

The anolyte was replaced by fresh medium every 4 days after completion of one batch cycle (after the current generated would drop). After development of bioanodes, Pt-Cs were replaced with iron oxidizing biocathode developed in the half-cells and the same medium as used in half-cells was used. In continuous mode, 30 mL h^{-1} flow rate was used for both anolyte and catholyte using a dosing pump. The strategy for the BES operation in this study is summarized in **Table 1**.

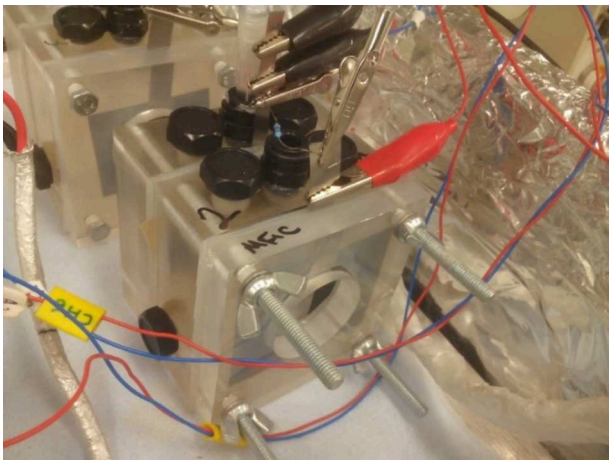

FIGURE 1 | MFC with GDE design operated for this experiment.

Analysis

Electrochemical Analysis

Cyclic voltammetry (CV) was performed using Metrohm Autolab potentiostat (Runcorn, U.K.). All the CVs were recorded at a scan rate of 2 mV s^{-1}.

Polarization Curves

After reaching the stable cell voltage in the MFC, polarization, and power density curves were recorded. The values of the external resistances used were: open circuit, 100 kΩ, 52.2 kΩ, 25.6 kΩ, 10.0 kΩ, 5.1 kΩ, 2.5 kΩ, 997 Ω, 505 Ω, 301 Ω, 103 Ω, 51 Ω, 12 Ω. The cell voltages and anode potentials for each resistance were recorded by data logger. The Ohm law was used to calculate the current values for each voltage and resistance.

RESULTS

Enrichment of IOB From Mixed Culture of Microorganisms

The enrichment of IOB was followed visually, with pH and iron speciation measurements. Environmental samples from Lake District (United Kingdom) were initially brown and turned to red-orange after 5 days of enrichment. The change in the color of the inoculated solutions was accompanied by a significant drop of pH (**Figure 2**). The pH of both inoculated and control solutions decreased from 3.5 to 2.7 on day 6, and to just under 2 on day 7, while the pH value of the control solution stayed stable circa 2.9. These observations can be associated with the faster and more advanced oxidation of Fe^{2+} into Fe^{3+} due to the presence and growth of IOB in the inoculated samples (Fontmorin and Sillanpaa, 2015).

In aerobic conditions, it is known that the oxidation of Fe^{2+} can occur chemically. The rate of this reaction (Equation 1)

TABLE 1 | BES operation strategy in this study.

	Half-cell (47 days)	Bioanode development in MFC (15 days)	MFC (12 days)
Cathode	Carbon paper	Pt-C	Carbon paper with the developed biocathode from the half-cell
Anode	Pt mesh	Graphite felt	Graphite felt with the bioanode after the bioanode development
Catholyte	1 g L^{-1} $FeSO_4 \cdot 7H_2O$ 0.4 g L^{-1} $(NH_4)_2SO_4$ 0.4 g L^{-1} KH_2PO_4 0.4 g L^{-1} $MgSO_4$ at pH 2 (adjusted by H_2SO_4) 20% inoculum (IOB from enrichment step)	50 mM PBS	1 g L^{-1} $FeSO_4 \cdot 7H_2O$ 0.4 g L^{-1} $(NH_4)_2SO_4$ 0.4 g L^{-1} KH_2PO_4 0.4 g L^{-1} $MgSO_4$ at pH 2 (adjusted by H_2SO_4) 20% inoculum (IOB from enrichment step)
Anolyte	0.4 g L^{-1} $(NH_4)_2SO_4$ 0.4 g L^{-1} KH_2PO_4 0.4 g L^{-1} $MgSO_4$ at pH 2 (adjusted by H_2SO_4)	50 mM PBS 1 g L^{-1} acetate 25 ml L^{-1} macronutrients solution 1 ml L^{-1} micronutrients solution 0.5 ml L^{-1} vitamins solution 20% inoculum (effluent of parent cell)	50 mM PBS 1 g L^{-1} Acetate 25 ml L^{-1} macronutrients solution 1 ml L^{-1} micronutrients solution 0.5 ml L^{-1} vitamins solution 20% inoculum (effluent of parent cell)

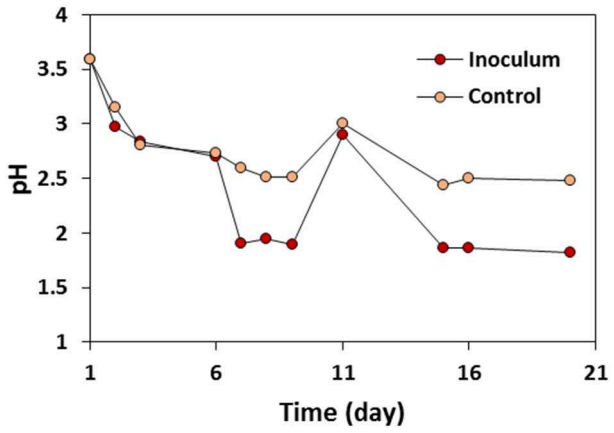

FIGURE 2 | pH of the inoculated and control solutions during the enrichment step.

depends on the environment conditions such as concentration of protons and dissolved oxygen (Stumm and Morgan, 1996):

$$-\frac{d\left[Fe^{2+}\right]}{dt} = k\left[O_2\right]\frac{\left[Fe^{2+}\right]}{\left[H^+\right]^2} \quad (1)$$

Where k is the rate constant of the reaction (3×10^{-12} mol L^{-1} min^{-1} at 20°C). Therefore, at pH 2, the spontaneous oxidation of ferrous ions by molecular oxygen is very limited. In addition, at such pH, the redox potential of the oxygen/water couple is about 0.3 V more positive than at pH 7, which makes the oxidation of iron and the utilization of oxygen as electron acceptor energetically favorable for IOB (Hedrich et al., 2011).

At day 11 (see **Figure 2**), 20% of the inoculum was transferred to the fresh medium containing 20 g L^{-1} $FeSO_4 \cdot 7H_2O$. Higher rate of the pH drop in the solution with inoculum compared to the control solution after the transfer and change in the color of the inoculated solution confirmed the biological conversion of Fe^{2+} to Fe^{3+} (Ter Heijne et al., 2007). The color of the control solution was orange-brown during the 20 days of the enrichment step. Fe^{2+} concentration was also measured during the enrichment step using ferrozine method (Viollier et al., 2000), indicating the decrease in the concentration of the Fe^{2+} in the inoculated solution while Fe^{2+} concentration was stable in the control solution (data not shown). The difference in color, pH, and Fe^{2+} concentration between the inoculated and control solutions indicated the successful enrichment of IOB in the inoculated solution which was used as the inoculum for the half-cells and MFCs experiments.

IOB as Biocatalyst and Fe^{2+} as a Mediator in Half-Cell Systems

Half-cells equipped with GDEs were operated at 0.2 V and inoculated with the enriched environmental sample. **Figure 3** shows the current density of one of the duplicate half-cells during the 47 days of half-cell experiment and the control without inoculum during the 17 days of the abiotic experiment. Similar current density was observed in the second half-cell (duplicate) as presented in **Figure S1**. Very low current density was measured over 17 days of the experiment in the control cell, therefore it was terminated after this period. Electron uptake was observed in the half-cells inoculated from the beginning of the experiment: current densities of 1 A m^{-2} were measured just after inoculation and about 2 A m^{-2} after day 5 and for more than 45 days of operation (**Figure 3**). The presence of Fe^{2+}/Fe^{3+} as a mediator with iron-oxidizing bacteria (IOB) as biocatalyst allows to avoid the long start-up usually associated with the development of biocathodes catalyzing the ORR. It was reported in previous studies that IOB such as *Acidithiobacillus ferrooxidans* can accept electrons directly from a cathode without the need for Fe^{2+} as a mediator (Carbajosa et al., 2010). However, in this case, the current generation only appeared after 22 days which corresponded to the time necessary for a biofilm to grow directly at the surface of the electrode. In addition, maximum current densities were measured at a potential of

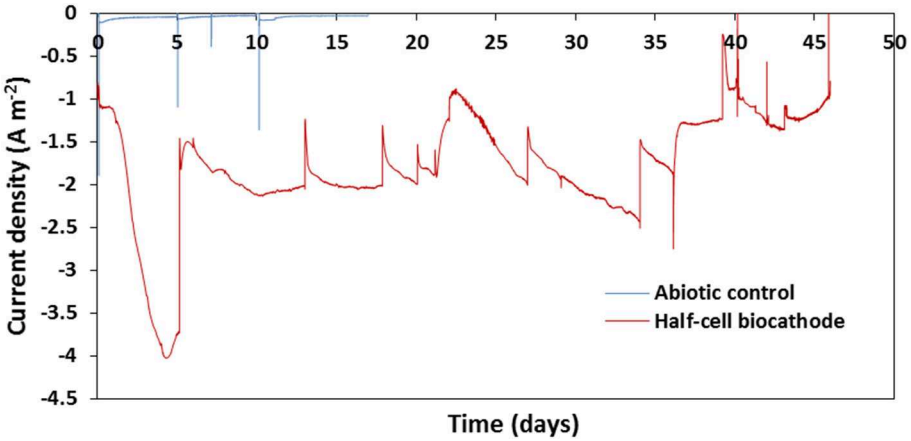

FIGURE 3 | Chronoamperometry of half-cell poised at 0.2 V and inoculated by enriched IOB during the 47 day experiment and control half-cell during the 17 days abiotic experiment.

0.05 V, potential corresponding to the catalysis of the ORR by the biofilm (Carbajosa et al., 2010).

In order to confirm the mechanism occurring in the system used in the study, CVs were recorded after 47 days of operation, and compared with these recorded on a Pt-C GDE (**Figure 4**). The voltammogram recorded on the Pt-C GDE (**Figure 4A**) shows a clear catalysis of the ORR with an onset potential around 0.4 V. It was reported that in absence of mediator, IOBs are able to accept electron directly from a cathode to catalyze the reduction of oxygen (Carbajosa et al., 2010). In our system using IOB and iron as mediator, however, there is no obvious shift of the onset potential of the ORR but the presence of a pseudo-reversible signal of $E^{0'}$ about 0.4 V which can be attributed to the Fe^{2+}/Fe^{3+} redox couple. In addition, the very little difference between the CVs recorded in presence and absence of oxygen (**Figure 4B**) suggests the limited impact of oxygen on the reaction occurring at the electrode. These observations would confirm a mediated electron transfer mechanism between the cathode and IOB and that in presence of iron in the medium there is no direct biological catalysis of the ORR occurring at the electrode, despite oxygen being used as a terminal electron acceptor by IOB.

The proposed mechanism occurring at the electrode is presented in **Figure 5**. After the cells were opened, a red-orange layer could be observed at the surface of the GDEs. This was most likely due to the deposition of layer of iron oxides/hydroxides. It can thus be expected that the cathode potential of the MFCs equipped with IOB as biocatalyst and Fe^{2+} as mediator will be close to the reduction potential of Fe^{3+} into Fe^{2+} observed in **Figure 4**, i.e., about 0.3 V.

IOB as Biocatalyst and Fe^{2+} as Mediator in MFCs Equipped With GDEs

Development of Bioanodes

Following the half-cells experiments, MFCs were set up with GDE cathodes equipped with either Pt-C or IOB. Bioanodes were first developed using Pt-C as cathodes. The effluent from a glucose/glutamic acid-fed parent MFC was used as inoculum. **Figure S2** shows the anode and MFC potentials during the bioanode development stage. As can be seen in **Figure S2A**, a quick start-up of the electricity generation after 1 day, reaching a cell potential of 0.3 V after 2 days. The other duplicate showed a very similar trend. To confirm the bioanode development, CVs were recorded on day 15 of MFC operation, after the 7th batch cycle, after acetate was depleted (**Figure S3**). Redox features appeared at potentials of −0.1, −0.30, −0.37 and −0.47 V which can be associated with the electron transfer between the biofilm and the electrode, as it was reported in previous studies involving bioanode formed by *G. sulfurreducens* (Fricke et al., 2008; Richter et al., 2009). In addition, polarization and power density curves of the cell showed maximum power production of 0.6 W m^{-2} and open circuit potential (OCP) of 0.74 V (**Figure S2B**). Similarly, MFC 2 reached power densities of 0.52 W m^{-2} and OCP of 0.73 V.

Performance of MFCs Equipped With GDE and IOB Using Fe^{2+} as Mediator

After the development of bioanodes, the platinized GDEs were replaced by the GDEs used in the half-cell experiment discussed in section IOB as Biocatalyst and Fe2+ as a Mediator in Half-Cell Systems. The objective was then to compare the performance of MFCs equipped with IOBs and iron at the cathode with the MFCs equipped with Pt-C catalyst. As demonstrated in **Figure 4**, the CVs recorded on the GDE with IOBs present a pseudo-reversible signal of $E^{0'}$ about 0.4 V. There is no apparent catalysis of the ORR and the expected potential of the cathode in the MFC is therefore the potential of reduction of Fe^{2+}/Fe^{3+} mediator, i.e., about 0.3 V.

Cell, anode, and cathode potentials after replacing the cathodes are reported in **Figure 6**. After switching cathodes, the cell potential decreased to 0.25 V after 1 h and to 0.04 V after 1 day, before reaching almost zero at the end of day 2. The drop of potential was associated with the significant drop in the anode potential, as depicted in **Figure 6**. After day 2, media of both compartments were replaced with fresh media, the cell potential

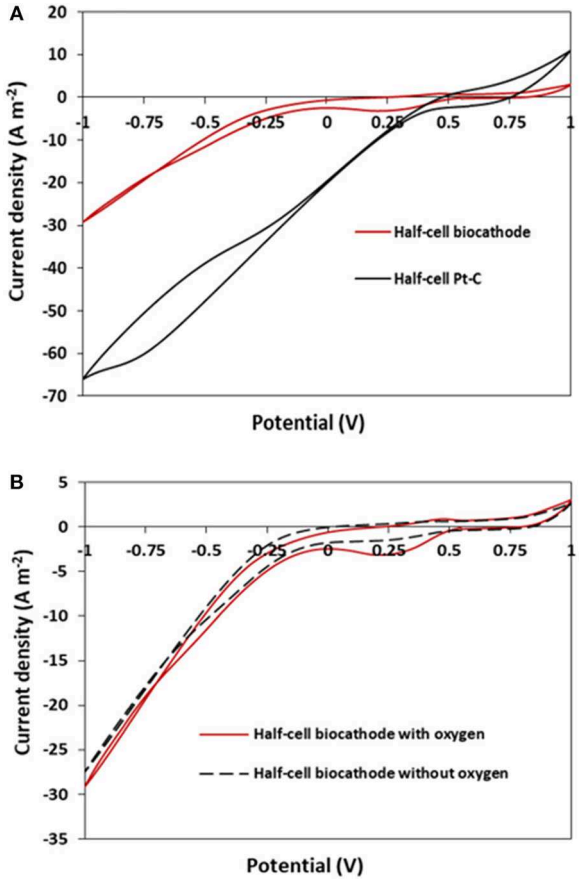

FIGURE 4 | (A) Voltammograms recorded in half-cell reactors equipped with GDEs with Pt-C (black) and IOB biocathode as catalysts (red); **(B)** voltammograms recorded in half-cells reactors equipped with GDEs and IOB biocathode as catalyst after 47 days of operation, in presence (red) and absence (dashed black) of oxygen. CVs recorded at a scan rate of 2 mV s^{-1}.

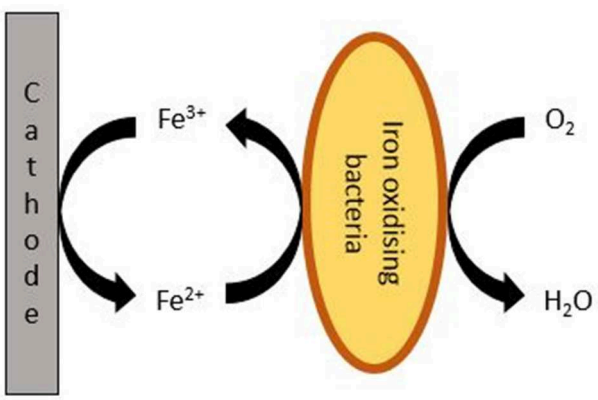

FIGURE 5 | Schematic of the suggested reaction occurring in the cathodic compartment.

reached 0.13 V and remained stable for almost 3 days before dropping back to zero on day 5. This drop was accompanied by significant changes in the pH of the anolyte and catholyte.

Despite using 50 mM phosphate buffer at pH 7 in the anode compartment, the pH dropped to 4 after 2 days due to the high difference between the pH of the anolyte (pH 7) and catholyte (pH 2) separated by AEM. Although daily media refreshment helped reaching cell potential of 0.2 V, such a potential could only be sustained for a few hours as the pH of the anolyte would rapidly decrease to 5. Similarly, a significant change was observed in the pH of the cathodic solution. Over the first 5 days after switching the cathodes, the pH of catholyte raised to about 5. The pH could be decreased to around 3 with regular medium replacement; however, it couldn't be stabilized at the initial and optimal pH of 2. The performance and pH of the duplicate MFC followed the similar trend, as presented in **Figure S4**. Polarization and power density curves of the MFCs equipped with IOBs as biocatalyst and iron as mediator were recorded and compared with the MFC equipped with Pt catalyst (**Figure S5** and also **Figure 8A**). As can be seen, the inability to control the pH had a big impact on the performance of the cells as the maximum power density achieved was 0.59 W m^{-2} for MFCs equipped with Pt compared to 0.12 W m^{-2} in the MFCs by IOB in batch mode, which was similar in duplicates. This change is also associated with higher internal resistance in the MFC, as suggested by the increase of the slope of the polarization curve. It is understood that pH of both anolyte and catholyte have a great impact on MFCs performance. It was shown that the optimal value of anolyte pH is between 7 and 8 and that a pH outside this range decreases the MFC performance (He et al., 2008). Previous studies reported that acidic anolyte (pH 5) affects the microbial activity of the biofilm which then led to lower current generation (Gil et al., 2003; Ren et al., 2007). Similarly, in the presence of IOBs and iron as catalyst and mediator, pH higher than 2 in the cathodic compartment results in iron precipitation which affects the performance of the biocathode (Ter Heijne et al., 2006). In addition, and as described in section Enrichment of IOB, pH of 2 provides optimal conditions for acidophilic IOB to produce ATP from the oxidation of Fe^{2+} and using molecular oxygen as terminal electron acceptor (Hedrich et al., 2011). Therefore, the pH of both the catholyte and anolyte needs be controlled to maintain the MFCs performance.

MFC Performance With IOB Biocathode Operated in Continuous Mode

In order to control the pH in both compartments and avoid using expensive bipolar membranes, the cell operation was converted from fed-batch to continuous mode using a dosing pump for both anolyte and catholyte with similar hydraulic retention times (HRTs) of 2.0 h. Such a low HRT helped stabilize pH in both compartments and significantly improved MFCs performance compared to fed-batch operation. Over the whole experiment in continuous mode, pH of the anode and cathode media remained stable around 6.8 and 2.0, respectively. Five hours after switching from fed-batch to continuous mode, the anode potential dropped to −0.4 V whereas the cathode potential increased to −0.1 V, resulting in a cell voltage of 0.3 V (**Figure 7**). The anode potential stabilized at −0.45 V and the cathode potential kept increasing slowly to reach −0.05 V after 65 h, for a corresponding cell potential of ∼0.4 V. In order to confirm that the oxygen mass

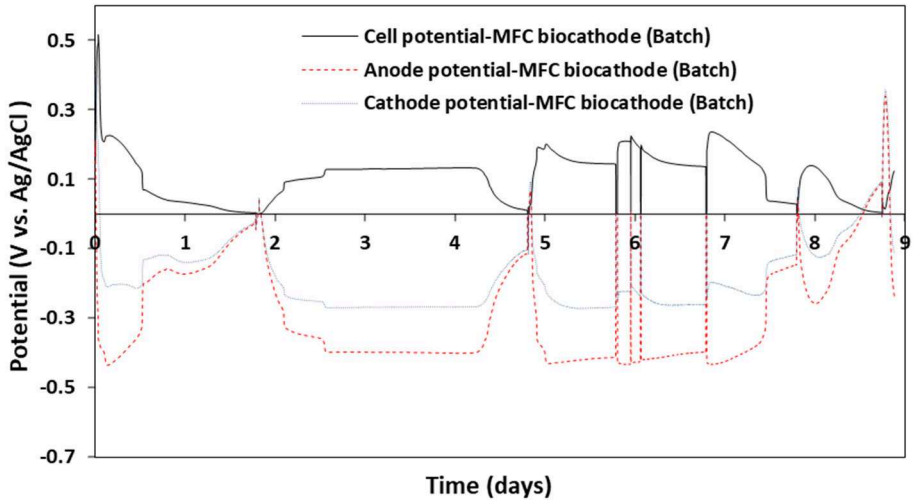

FIGURE 6 | Cell, anode, and cathode potentials of MFC equipped with GDE and IOB biocathode and operated in fed-batch mode.

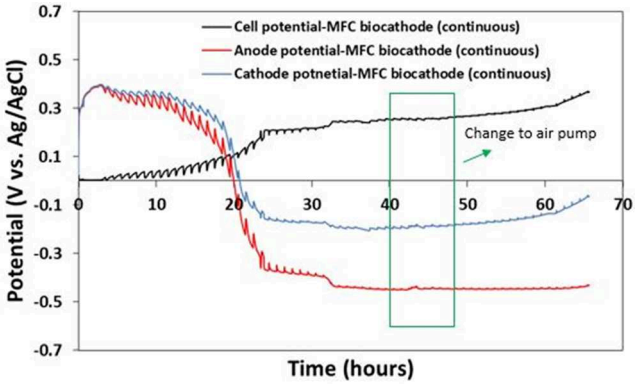

FIGURE 7 | Cell, anode, and cathode potentials of MFC with IOB biocathode operated in continuous mode. Green box shows the time between hours 40 and 48 that catholyte reservoir tank was aerated using an aquarium air pump.

transfer was not limiting the bio-electrochemical process, the catholyte reservoir tank was purged with air using an aquarium air pump for 8 h (between hours 40 and 48). As can be seen in **Figure 7**, no significant change in cathode potential nor in cell voltage was observed, showing that the passive diffusion of oxygen through the GDE is not a limitation to the performance of the MFCs. Therefore, such a design allows to avoid expensive aeration system which is not viable especially at larger scale.

Previously, GDEs were mainly used for abiotic cathodic reactions such as catalysis of the ORR. It was for example reported that air-cathode MFC with GDE modified with activated carbon produced a comparable power to the MFC operated with platinum as the cathode after 1 month of operation (Zhang et al., 2014). To date, only few studies focused on the utilization of GDEs for aerobic or anaerobic biocathodes formation. In previous research, GDE design was used for the diffusion of CO_2 through the GDL to provide sufficient CO_2 for the development of anaerobic biocathode (Bajracharya et al., 2016; Srikanth et al., 2018). It was reported in this study that mass transfer of carbon dioxide was higher than when purging directly in the catholyte, leading to the improvement of the BES performance in terms of CO_2 reduction and bio-production. Studies focusing on MFCs equipped with GDE for aerobic biocathodes are still scarce compared to systems with aeration, but the possibility to grow aerobic biofilms on such electrodes was already shown in the past (Wang et al., 2013; Xia et al., 2013; Montpart et al., 2018) However, the growth of such biofilms is time-consuming (usually at least 50 days), takes much longer time than the growth of bioanodes and is very challenging on non-porous materials such as carbon paper (Rimboud et al., 2015). Therefore, the combination of GDE with IOBs as biocatalyst and Fe^{2+} as mediator stands as a good alternative to classical Pt-based catalysts in aerated system.

Figure 8A shows the polarization and power density curves of the MFC after 65 h of continuous operation in comparison with the polarization and power density figures of the MFC in fed-batch mode using platinized carbon paper and biocathode. A maximum power density of 1.02 W m^{-2} was produced in continuous mode compared to 0.12 W m^{-2} in fed-batch mode using IOBs and 0.59 W m^{-2} using platinized carbon paper as cathode (see in **Table 2**). By stabilizing pH of both the anolyte and catholyte, continuous mode operation led to significant improvement of the MFC outputs, then outperforming the MFC equipped with Pt catalyst. It can however be observed that there is a "doubling back" of the power curve for current densities exceeding 1.7 A m^{-2} which is also known as "power overshoot" (Kim et al., 2017). Similar phenomenon was observed in MFCs equipped with aerobic biocathodes (Milner and Yu, 2018), which was further attributed to the impact of aeration and DO concentration in solution on the cathode and cell potentials as there was a sharp decrease on cathode potential. However, in the present study, the utilization of an air pump did not have any significant impact on the cell performance, showing that

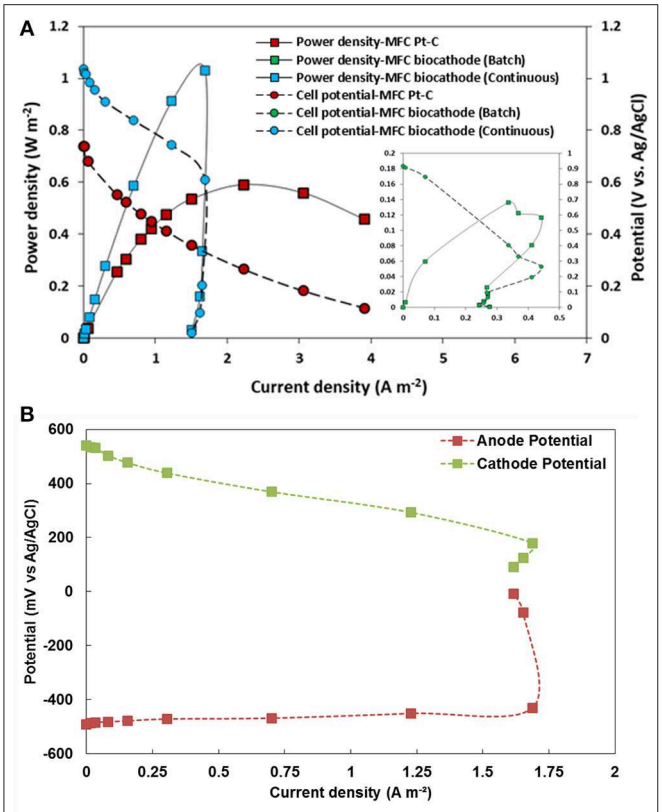

FIGURE 8 | (A) Polarization curve and power density of MFC equipped with different cathodes and operated in batch or continuous mode; **(B)** Anode and cathode potentials during the polarization of the MFC equipped with IOB biocathode and operated in continuous mode.

TABLE 2 | Summary of the performance achieved by the MFCs equipped with different cathodes.

	Pt	Fe^{2+}/IOB (Batch)	Fe^{2+}/IOB (Continuous)
Current density (A m^{-2})	2.1	0.12	1.02
Power density (W m^{-2})	0.59	0.34	1.7

the GDE configuration provided sufficient oxygen to the system. Therefore, the cause of sudden drop in performance in this study was due to different reason.

The doubling back observed in **Figure 8A** can be explained with the potential profiles of the anode and cathode recorded during the polarization and presented in **Figure 8B**. As can be seen, the anode potential is relatively stable between −0.45 and −0.4 V until the current density reached 1.68 A m^{-2}. At this current density, the cathode potential reaches ∼0.25 V which is the potential at which Fe^{3+} starts to be electrochemically reduced into Fe^{2+} (as shown in CVs presented in **Figures 5**, **7**). The current required by the cathode thus increases and exceeds what the bioanode can supply. At this stage, it can be assumed that the bioanode becomes limiting, thus explaining the drop of both the anode potential and the cell voltage. Although the cathode potential also decreased, it did not seem as significant as the drop of the anode potential. In MFCs using oxygen as terminal electron acceptor, the power output is usually limited by the performance of the cathode, whether the ORR is catalyzed by Pt or biocatalysts (Milner et al., 2016). Nevertheless, in the presence of IOBs as Fe^{2+} as mediator, and according to the potential profiles presented in **Figure 8B**, the bioanode appears to be limiting. This phenomenon was explained in a previous study showing that the power overshoot can occur when anodic kinetics are slower than cathodic kinetics, thus causing electrons depletion (Kim et al., 2017). In our specific case, this could be explained by the development of a non-mature biofilm due to a too short inoculation process at lower external resistances (Hong et al., 2011), or in other words by a biocathode outperforming the bioanode.

CONCLUSIONS

In this study, we demonstrated the feasibility of using IOB as biocatalyst and Fe^{2+} as a mediator as an alternative to Pt catalyst in MFCs equipped with GDEs. IOB were enriched from a natural environment sample and first used as an inoculum in half-cell reactors. Stable current densities of 2 A m^{-2} were produced during 45 days. Due to the presence of Fe^{2+} as mediator, no lag time was observed before such current densities were reached, thus avoiding the long start-up phase usually associated with aerobic biocathodes. Although the contribution of a direct electron transfer between the cathode and the bacteria cannot be totally ruled out, cyclic voltammogramms strongly suggest mediated electron transfer (by Fe^{2+}) as the main mechanism. In the second part of the study, when MFCs were operated in batch mode, the performances of the cells containing IOB as biocatalyst were comparable to these equipped with Pt. However, these performances could not be sustained due to the drop of pH in the anodic compartment and the increase of pH in the cathodic compartment. Operating MFCs in continuous mode helped stabilize pH in both compartments. Maximum power densities of 1.02 W m^{-2} were then reached, compared to 0.59 W m^{-2} for MFCs equipped with Pt catalyst. Finally, the passive diffusion of oxygen through the GDEs did not appear as a limiting factor to the performance of the MFCs, showing that the system studied represent or good alternative to both chemical catalysts and non-mediated aerobic biocathodes without the need for costly aeration systems.

DATA AVAILABILITY

The datasets generated for this study are available on request to the corresponding author.

AUTHOR CONTRIBUTIONS

All authors listed have made a substantial, direct and intellectual contribution to the work, and approved it for publication.

ACKNOWLEDGMENTS

The authors thank EPSRC LifesCO2R project (EP/N009746/1), EPSRC NECEM (EP EP/R021503/1) and NERC MeteoRR (NE/

NE/L014246/1). PI thanks the Doctoral Training Awards (SAgE DTA, 2015 cohort) from Faculty of Science, Agriculture and Engineering, Newcastle University for supporting her PhD study. The authors thank William Foxall for his contribution in preliminary experiments.

SUPPLEMENTARY MATERIAL

The Supplementary Material for this article can be found online at: https://www.frontiersin.org/articles/10.3389/fenrg.2019.00093/full#supplementary-material

REFERENCES

Bajracharya, S., Vanbroekhoven, K., Buisman, C. J. N., Pant, D., and Strik, D. P. (2016). Application of gas diffusion biocathode in microbial electrosynthesis from carbon dioxide. *Environ. Sci. Pollut. Res.* 23, 22292–22308. doi: 10.1007/s11356-016-7196-x

Burkitt, R., Whiffen, T. R., and Yu, E. H. (2016). Iron phthalocyanine and MnOx composite catalysts for microbial fuel cell applications. *Appl. Catal. B Environ.* 181, 279–288. doi: 10.1016/j.apcatb.2015.07.010

Carbajosa, S., Malki, M., Caillard, R., Lopez, M. F., Palomares, F. J., Martin-Gago, J. A., et al. (2010). Electrochemical growth of *Acidithiobacillus ferrooxidans* on a graphite electrode for obtaining a biocathode for direct electrocatalytic reduction of oxygen. *Biosens. Bioelectron.* 26, 877–880. doi: 10.1016/j.bios.2010.07.037

Du, Z., Li, H., and Gu, T. (2007). A state of the art review on microbial fuel cells: a promising technology for wastewater treatment and bioenergy. *Biotechnol. Adv.* 25, 464–482. doi: 10.1016/j.biotechadv.2007.05.004

Ferguson, S. J., and Ingledew, W. J. (2008). Energetic problems faced by micro-organisms growing or surviving on parsimonious energy sources and at acidic pH: I. *Acidithiobacillus ferrooxidans* as a paradigm. *Biochim. Biophys. Acta.* 1777, 1471–1479. doi: 10.1016/j.bbabio.2008.08.012

Fontmorin, J. M., and Sillanpaa, M. (2015). Bioleaching and combined bioleaching/Fenton-like processes for the treatment of urban anaerobically digested sludge: removal of heavy metals and improvement of the sludge dewaterability. *Sep. Purif. Technol.* 156, 655–664. doi: 10.1016/j.seppur.2015.10.061

Fricke, K., Harnisch, F., and Schröder, U. (2008). On the use of cyclic voltammetry for the study of anodic electron transfer in microbial fuel cells. *Energy Environ. Sci.* 1, 144–147. doi: 10.1039/b802363h

Gil, G.-C., Chang, I.-S., Kim, B. H., Kim, M., Jang, J.-K., Park, H. S., et al. (2003). Operational parameters affecting the performannce of a mediator-less microbial fuel cell. *Biosens. Bioelectron.* 18, 327–334. doi: 10.1016/S0956-5663(02)00110-0

He, Z., and Angenent, L. T. (2006). Application of bacterial biocathodes in microbial fuel cells. *Electroanalysis* 18, 2009–2015. doi: 10.1002/elan.200603628

He, Z., Huang, Y., Manohar, A. K., and Mansfeld, F. (2008). Effect of electrolyte pH on the rate of the anodic and cathodic reactions in an air-cathode microbial fuel cell. *Bioelectrochemistry* 74, 78–82. doi: 10.1016/j.bioelechem.2008.07.007

Hedrich, S., Schlömann, M., and Barrie Johnson, D. (2011). The iron-oxidizing proteobacteria. *Microbiology* 157, 1551–1564. doi: 10.1099/mic.0.045344-0

Hong, Y. Y., Call, D. F., Werner, C. M., and Logan, B. E. (2011). Adaptation to high current using low external resistances eliminates power overshoot in microbial fuel cells. *Biosens. Bioelectron.* 28, 71–76. doi: 10.1016/j.bios.2011.06.045

Huang, L., Regan, J. M., and Quan, X. (2011). Electron transfer mechanisms, new applications, and performance of biocathode microbial fuel cells. *Biores. Technol.* 102, 316–323. doi: 10.1016/j.biortech.2010.06.096

Kim, B., An, J., and Chang, I. S. (2017). Elimination of power overshoot at bioanode through assistance current in microbial fuel cells. *Chemsuschem* 10, 612–617. doi: 10.1002/cssc.201601412

Kong, X., Sun, Y., Yuan, Z., Li, D., Li, L., and Li, Y. (2010). Effect of cathode electron-receiver on the performance of microbial fuel cells. *Int. J. Hydrog. Energy* 35, 7224–7227. doi: 10.1016/j.ijhydene.2010.03.106

Liew, K. B., Daud, W. R. W., Ghasemi, M., Leong, J. X., Lim, S. S., and Ismail, M. (2014). Non-Pt catalyst as oxygen reduction reaction in microbial fuel cells: a review. *Int. J. Hydrog. Energy* 39, 4870–4883. doi: 10.1016/j.ijhydene.2014.01.062

Lovley, D. R. (1991). Dissimilatory Fe (III) and Mn (IV) reduction. *Microbiol. Rev.* 55, 259–287. doi: 10.1007/978-3-642-30141-4_69

Malki, M., De Lacey, A. L., Rodríguez, N., Amils, R., and Fernandez, V. M. (2008). Preferential use of an anode as an electron acceptor by an acidophilic bacterium in the presence of oxygen. *Appl. Environ. Microbiol.* 74, 4472–4476. doi: 10.1128/AEM.00209-08

Milner, E., Scott, K., Head, I., Curtis, T., and Yu, E. (2014). "Electrochemical investigation of aerobic biocathodes at different poised potentials: evidence for mediated extracellular electron transfer. *Chem. Eng. Trans.* 41, 355–360. doi: 10.3303/CET1441060

Milner, E. M., Popescu, D., Curtis, T., Head, I. M., Scott, K., and Yu, E. H. (2016). Microbial fuel cells with highly active aerobic biocathodes. *J. Power Sources* 324, 8–16. doi: 10.1016/j.jpowsour.2016.05.055

Milner, E. M., and Yu, E. H. (2018). The effect of oxygen mass transfer on aerobic biocathode performance, biofilm growth and distribution in microbial fuel cells. *Fuel Cells* 18, 4–12. doi: 10.1002/fuce.201700172

Montpart, N., Rago, L., Baeza, J. A., and Guisasola, A. (2018). Oxygen barrier and catalytic effect of the cathodic biofilm in single chamber microbial fuel cells. *J. Chem. Technol. Biotechnol.* 93, 2199–2207. doi: 10.1002/jctb.5561

Oh, S., Min, B., and Logan, B. E. (2004). Cathode performance as a factor in electricity generation in microbial fuel cells. *Environ. Sci. Technol.* 38, 4900–4904. doi: 10.1021/es049422p

Oliveira, V. B., Simões, M., Melo, L. F., and Pinto, A. (2013). Overview on the developments of microbial fuel cells. *Biochem. Eng. J.* 73, 53–64. doi: 10.1016/j.bej.2013.01.012

Qiu, Y., Cheng, Z., Guo, B., Fan, H., Sun, S., Wu, T., et al. (2015). Preparation of activated carbon paper through a simple method and application as a supercapacitor. *J. Mater. Sci.* 50, 1586–1593. doi: 10.1007/s10853-014-8719-9

Rabaey, K., Read, S. T., Clauwaert, P., Freguia, S., Bond, P. L., Blackall, L. L., et al. (2008). Cathodic oxygen reduction catalyzed by bacteria in microbial fuel cells. *ISME J.* 2, 519–527. doi: 10.1038/ismej.2008.1

Rahimnejad, M., Adhami, A., Darvari, S., Zirepour, A., and Oh, S.-E. (2015). Microbial fuel cell as new technology for bioelectricity generation: a review. *Alex. Eng. J.* 54, 745–756. doi: 10.1016/j.aej.2015.03.031

Ren, Z., Ward, T. E., and Regan, J. M. (2007). Electricity production from cellulose in a microbial fuel cell using a defined binary culture. *Environ. Sci. Technol.* 41, 4781–4786. doi: 10.1021/es070577h

Richter, H., Nevin, K. P., Jia, H., Lowy, D. A., Lovley, D. R., and Tender, L. M. (2009). Cyclic voltammetry of biofilms of wild type and mutant Geobacter sulfurreducens on fuel cell anodes indicates possible roles of OmcB, OmcZ, type IV pili, and protons in extracellular electron transfer. *Energy Environ. Sci.* 2, 506–516. doi: 10.1039/b816647a

Rimboud, M., Desmond-Le Quemener, E., Erable, B., Bouchez, T., and Bergel, A. (2015). The current provided by oxygen-reducing microbial cathodes is related to the composition of their bacterial community. *Bioelectrochemistry* 102, 42–49. doi: 10.1016/j.bioelechem.2014.11.006

Rismani-Yazdi, H., Carver, S. M., Christy, A. D., and Tuovinen, O. H. (2008). Cathodic limitations in microbial fuel cells: an overview. *J. Power Sources* 180, 683–694. doi: 10.1016/j.jpowsour.2008.02.074

Seelam, J. S., Maesara, S. A., Mohanakrishna, G., Patil, S. A., Ter Heijne, A., and Pant, D. (2018). "Resource recovery from wastes and wastewaters using bioelectrochemical systems," in *Waste Biorefinery*, eds T. Bhaskar, A. Pandey, S. V. Mohan, D. J. Lee, and S. K. Khanal (Amsterdam: Elsevier), 535–570. doi: 10.1016/B978-0-444-63992-9.00018-5

Spurr, M. A., Yu, E. H., Scott, K., and Head, I. M. (2018). Extending the dynamic range of biochemical oxygen demand sensing with multi-stage microbial fuel cells. *Environ. Sci. Water Res. Technol.* 4, 2029–2014. doi: 10.1039/C8EW00497H

Srikanth, S., Singh, D., Vanbroekhoven, K., Pant, D., Kumar, M., Puri, S. K., et al. (2018). Electro-biocatalytic conversion of carbon dioxide

to alcohols using gas diffusion electrode. *Biores. Technol.* 265, 45–51. doi: 10.1016/j.biortech.2018.02.058

Stumm, W., and Morgan, J. J. (1996). *Aquatic Chemistry: Chemical Equilibria and Rates in Natural Waters* {*Environmental Science and Technology*}. Hoboken, NJ: Wiley.

Ter Heijne, A., Hamelers, H. V. M., and Buisman, C. J. N. (2007). Microbial fuel cell operation with continuous biological ferrous iron oxidation of the catholyte. *Environ. Sci. Technol.* 41, 4130–4134. doi: 10.1021/es0702824

Ter Heijne, A., Hamelers, H. V. M., De Wilde, V., Rozendal, R. A., and Buisman, C. J. N. (2006). A bipolar membrane combined with ferric iron reduction as an efficient cathode system in microbial fuel cells. *Environ. Sci. Technol.* 40, 5200–5205. doi: 10.1021/es0608545

Ter Heijne, A., Liu, F., Van Rijnsoever, L. S., Saakes, M., Hamelers, H. V. M., and Buisman, C. J. N. (2011). Performance of a scaled-up microbial fuel cell with iron reduction as the cathode reaction. *J. Power Sources* 196, 7572–7577. doi: 10.1016/j.jpowsour.2011.04.034

Viollier, E., Inglett, P. W., Hunter, K., Roychoudhury, A. N., and Van Cappellen, P. (2000). The ferrozine method revisited: Fe (II)/Fe (III) determination in natural waters. *Appl. Geochem.* 15, 785–790. doi: 10.1016/S0883-2927(99)00097-9

Wang, Z. J., Zheng, Y., Xiao, Y., Wu, S., Wu, Y. C., Yang, Z. H., et al. (2013). Analysis of oxygen reduction and microbial community of air-diffusion biocathode in microbial fuel cells. *Biores. Technol.* 144, 74–79. doi: 10.1016/j.biortech.2013.06.093

Xia, X., Tokash, J. C., Zhang, F., Liang, P., Huang, X., and Logan, B. E. (2013). Oxygen-reducing biocathodes operating with passive oxygen transfer in microbial fuel cells. *Environ. Sci. Technol.* 47, 2085–2091. doi: 10.1021/es3027659

Yu, E. H., Burkitt, R., Wang, X., and Scott, K. (2012). Application of anion exchange ionomer for oxygen reduction catalysts in microbial fuel cells. *Electrochem. Commun.* 21, 30–35. doi: 10.1016/j.elecom.2012.05.011

Yu, E. H., Cheng, S., Logan, B. E., and Scott, K. (2009). Electrochemical reduction of oxygen with iron phthalocyanine in neutral media. *J. Appl. Electrochem.* 39, 705–711. doi: 10.1007/s10800-008-9712-2

Yu, E. H., Cheng, S., Scott, K., and Logan, B. (2007). Microbial fuel cell performance with non-Pt cathode catalysts. *J. Power Sources* 171, 275–281. doi: 10.1016/j.jpowsour.2007.07.010

Zhang, X., Pant, D., Zhang, F., Liu, J., He, W., and Logan, B. E. (2014). Long-term performance of chemically and physically modified activated carbons in air cathodes of microbial fuel cells. *ChemElectroChem* 1, 1859–1866. doi: 10.1002/celc.201402123

Conflict of Interest Statement: The authors declare that the research was conducted in the absence of any commercial or financial relationships that could be construed as a potential conflict of interest.

frontiers in Energy Research

ORIGINAL RESEARCH
published: 11 September 2019
doi: 10.3389/fenrg.2019.00095

Preventing Hydrogen Disposal Increases Electrode Utilization Efficiency by *Shewanella oneidensis*

Komal Joshi[1†], *Aunica L. Kane*[1†], *Nicholas J. Kotloski*[1], *Jeffrey A. Gralnick*[1,2*] *and Daniel R. Bond*[1,2*]

[1] BioTechnology Institute, University of Minnesota-Twin Cities, St. Paul, MN, United States, [2] Department of Plant and Microbial Biology, University of Minnesota-Twin Cities, St. Paul, MN, United States

Many bacteria use hydrogen anaerobically as both a source and sink for electrons; consuming hydrogen when it is plentiful and producing it when concentrations are low enough to allow proton reduction. While this can increase an organism's competitiveness, hydrogen uptake, or excretion can also make it difficult to control electron flux to a specific product. For example, when *Shewanella oneidensis* strain MR-1 is used to oxidize organic molecules and recover electrons in microbial electrochemical devices, small changes in ambient hydrogen concentrations could dramatically alter the efficiency of electron capture at the anode due to this organism's respiratory flexibility. When new three-electrode reactor designs created to minimize oxygen intrusion during anodic growth were tested with lactate-oxidizing *S. oneidensis*, current production decreased significantly in reactors vented to remove hydrogen produced at the counter electrode, suggesting a role for hydrogen uptake or disposal when cells used electrodes as electron acceptors. A Δ*hydA*Δ*hyaB* mutant lacking both hydrogenases reversed this trend, and nearly doubled current production rates. This increase was shown to be due to the efficiency of lactate oxidation, as 90% of electrons were recovered as electricity in the Δ*hydA*Δ*hyaB* mutant compared to only 50% for wild type. Experiments with Fe(III) oxide provided additional evidence that *S. oneidensis* generates hydrogen reducing equivalents during reduction of insoluble electron acceptors, while experiments with cells incubated with Fe(III) citrate showed increased survival of wild-type compared to Δ*hydA*Δ*hyaB* in stationary phase. Together these data show how the multiple routes of electron disposal of *S. oneidensis*, while beneficial under changing conditions, limits the efficiency of electron recovery in electrochemical systems, and demonstrates a simple approach to increasing current production rates in systems where hydrogen is being captured as a product.

Keywords: extracellular electron transfer, hydrogen metabolism, coulombic efficiency, hydrogenase, *Shewanella*, microbial fuel cells

OPEN ACCESS

Edited by:
Daniel Puyol,
Rey Juan Carlos University, Spain

Reviewed by:
Jung Rae Kim,
Pusan National University, South Korea
Falk Harnisch,
Helmholtz Centre for Environmental Research (UFZ), Germany

***Correspondence:**
Jeffrey A. Gralnick
gralnick@umn.edu
Daniel R. Bond
dbond@umn.edu

[†]These authors have contributed equally to this work

Specialty section:
This article was submitted to Bioenergy and Biofuels, a section of the journal Frontiers in Energy Research

Received: *16 June 2019*
Accepted: *26 August 2019*
Published: *11 September 2019*

Citation:
Joshi K, Kane AL, Kotloski NJ, Gralnick JA and Bond DR (2019) Preventing Hydrogen Disposal Increases Electrode Utilization Efficiency by Shewanella oneidensis. Front. Energy Res. 7:95. doi: 10.3389/fenrg.2019.00095

INTRODUCTION

Life began, and continues to thrive today, in anaerobic ecosystems across the planet. A variety of metabolic strategies allow life to persist in anaerobic conditions within environments such as sediments, subsurface aquifers, stratified lakes, digestive tracts, wastewater treatment plants, and anaerobic digesters. For heterotrophic respiratory organisms, life under anaerobic conditions

is often constrained by the ability of cells to dispose of electrons generated during carbon compound oxidation; thus the availability of electron acceptors such as nitrate or Fe(III) controls the options for energy generation within a niche (Thauer et al., 1977). In all of these environments, hydrogenases represent a means to dispose of low-potential electrons via proton reduction, depending on ambient concentrations. Here, we explore the effect of this hydrogen disposal choice in a dissimilatory metal reducing bacterium, and show that while hydrogen production may benefit an organism in terms of electron balance, it significantly decreases the efficiency of electricity-generating devices due to diversion of electron flux away from the electrode.

Shewanella oneidensis strain MR-1 (hereafter referred to as MR-1) is a facultative anaerobe that thrives in redox-stratified environments due to its ability to utilize a wide range of terminal electron acceptors (Nealson and Scott, 2006; Hau and Gralnick, 2007). MR-1 is able to couple the oxidation of electron donors such as lactate, formate, and hydrogen, to reduction of over 20 organic and inorganic compounds including insoluble metal oxides (Nealson and Scott, 2006; Hau and Gralnick, 2007; Kane et al., 2016). The process of transferring electrons produced during anaerobic metabolism to insoluble terminal electron acceptors is termed extracellular electron transfer, and has been well-studied in MR-1 (Beblawy et al., 2018). During extracellular electron transfer, electrons flow from the quinone pool through a series of cytochromes known as the Mtr respiratory pathway to the exterior of the cell, where they are transferred to solid acceptors directly or with the aid of secreted flavin-based redox shuttles (Beblawy et al., 2018). The ability of MR-1 to couple organic carbon oxidation to reduction of insoluble metals is important in biogeochemical cycling, and in applications where electrodes within bioelectrochemical reactors serve as proxies for the metals used as terminal electron acceptors (Rabaey and Verstraete, 2005; Bretschger et al., 2007; Hau and Gralnick, 2007; Fredrickson et al., 2008; Coursolle et al., 2010). For example, when *Shewanella* is used to supply electrons to the anode in a device termed a "Microbial Electrolysis Cell," a small voltage can be applied to these electrons to produce valuable cathodic hydrogen at a counter electrode (Bretschger et al., 2007; Coursolle et al., 2010).

To better harness extracellular electron transfer in bioenergy and bioelectronic applications, knowing the fate of electrons generated during metabolic oxidation is essential. Coulombic efficiency is calculated by comparing the number of electrons released during oxidation of the donor to the electron equivalents recovered at the anode. Efficiency decreases when electrons are diverted to products or acceptors other than the anode. For example, experimental artifacts such as leakage of oxygen into electrode chambers in a two chambered bioreactor containing *Shewanella* supports higher cell density and synthesis of higher concentrations of flavins that enhance electron transfer, but at the expense of decreasing coulombic yield due to oxygen respiration and formation of biomass (Rosenbaum et al., 2010; TerAvest et al., 2014; Lu et al., 2017). Inefficient transfer of protons across chambers from membrane fouling as well leaking of substrates or oxygen from the cathode chamber into the anode chamber results in low coulombic efficiency. In single chamber devices where a counter electrode produces hydrogen, coulombic efficiency can appear to exceed 100% if cells re-uptake produced hydrogen, a process that wastes energy by applying energy to the same electron equivalents multiple times (Lee et al., 2009; Lee and Rittmann, 2010). Conversely, MR-1 can also produce hydrogen during lactate oxidation, representing a loss of energy and electrons (Pinchuk et al., 2011). Thus, due to the high affinity of MR-1 for oxygen, and the reversible nature of hydrogenases, very small alterations in experimental design can cause large changes in the performance of microbial electrochemical systems (Lee et al., 2009; Lee and Rittmann, 2010). It should be noted that these challenges are accentuated in single chamber three electrode bioreactors where a single organism is used. Hydrogen dynamics will differ substantially in membrane-separated systems and in mixed-culture systems.

The genome of MR-1 contains two hydrogenase gene clusters that contribute to hydrogen production and uptake. The cluster *hyaABCDE-hypF-hypBCDEA* (SO2089-2099) encodes a Group 1 [NiFe] hydrogenase and the *hy*drogenase *p*leitropy (*hyp*) maturation proteins, while *hydAB-fdhC-hydGXEF* (SO3920-3926) encodes an [FeFe] hydrogenase, maturation proteins, and a gene annotated as a formate dehydrogenase gamma subunit (Meshulam-Simon et al., 2007). The HydA hydrogenase functions primarily in hydrogen formation while HyaB is capable both of hydrogen production and uptake (Meshulam-Simon et al., 2007). Both hydrogenases are expressed during anaerobic growth, and hydrogen production has been observed in cultures following depletion of the electron acceptor fumarate (Meshulam-Simon et al., 2007; Kreuzer et al., 2014).

Here, we describe new electrochemical reactors capable of maintaining strictly anaerobic conditions to eliminate artifacts from aerobic growth, combined with modifications that prevent hydrogen recycling. These reactors allow investigation of the role of hydrogen and the HydA/HyaB systems in altering coulombic efficiency of bioelectrochemical reactions, revealing new insights into the anaerobic metabolic strategy of *Shewanella*. We demonstrate that deletion of *hydA* and *hyaB* in *Shewanella* results in higher current density and coulombic efficiency by diverting electron flux to the anode instead of to hydrogen disposal. Hydrogenase-containing cells are shown to produce a burst of reducing equivalents when exposed to another insoluble electron acceptor (Fe(III) oxide), and the presence of hydrogenases enhances survival when other electron donors are depleted during growth with Fe(III) citrate. This evidence suggests that hydrogen production provides *S. oneidensis* with an electron disposal mechanism, and that eliminating this ability to use protons as electron acceptors diverts oxidative metabolism to exclusive use of the Mtr respiratory pathway, allowing enhanced capture of electrons in electrochemical cells.

MATERIALS AND METHODS

Bacterial Strains and Culture Conditions

Strains and plasmids used in this study are listed in **Table 1**. *S. oneidensis* MR-1 has been described previously (Venkateswaran et al., 1999). *Escherichia coli* strains used for cloning (UQ950) and conjugal transfer (WM3064) were

TABLE 1 | Strains and plasmid used in this study.

Strain or plasmid	Characteristics	Reference/Source
S. oneidensis strain MR-1	Wild-type	Venkateswaran et al., 1999
Δ*hydA*Δ*hyaB*	*S. oneidensis* Δ*hydA*Δ*hyaB*	This study
E. coli WM3064	DAP auxotroph *E. coli* conjugal donor strain	Saltikov and Newman, 2003
E. coli UQ950	DH5α; cloning strain	Saltikov and Newman, 2003
pSMV3	9.1 kb suicide vector; *oriR6K*, mobRP4, *sacB*, Km^R	Saltikov and Newman, 2003

TABLE 2 | Primers used in this study.

Primer name	Sequence
Primers for *hydA* deletion:	
hydA-UF	GCATGGGCCCGCATTATCAATTCACCATAAACCC
hydA-UR	GCATACTAGTATTAATCTTGATCAGCCC
hydA-DF	GCATACTAGTGTGAAATCAGCCTCTGTC
hydA-DR	GCATGAGCTCTTTTGCTAGGCTGTCGTCCTTG
Primers for *hyaB* deletion:	
hyaB-UF	GCATGGGCCCGTGGCCGTTTTGATGCAG
hyaB-UR	GCATACTAGTTTTCAGTATGACTTCAATAAC
hyaB-DF	GCATACTAGTGATGCTGTCAATGCCCTG
hyaB-DR	GCATGAGCTCATGCGGGTTTCAGAATGG
Primers for sequencing:	
hydA-SP1	TTCGACTCTACCTATGAAGCAATTAC
hydA-SP2	GATGTGCACATCATAGGTTAGCTG
hyaB-SP1	GTCAGCAAACCCGTGATTAACTTAG
hyaB-SP2	GATCCAACCTTGTACTAATACATCCGT

maintained on lysogeny broth (LB) agar plates containing 50 μg/mL kanamycin and/or 250 μM 2,6-diaminopimelic acid as necessary at 37°C and have been described previously (Saltikov and Newman, 2003). *S. oneidensis* strains were maintained on LB agar plates at 30°C. *Shewanella* basal media (SBM) pH 7.2 was used where indicated and contained the following (per liter): 0.225 g K_2HPO_4, 0.225 g KH_2PO_4, 0.46 g NaCl, 0.225 g $(NH_4)_2SO_4$, 0.117 g $MgSO_4.7H_2O$, 5 mL vitamin mix, 5 ml of trace mineral mix, and 0.05% casamino acids (Hau et al., 2008). For growth assays, *S. oneidensis* strains were freshly streaked from −80°C glycerol stocks on LB plates and incubated for ∼16 h at 30°C. Single colonies from these plates were used to inoculate 5 mL of liquid LB medium shaken at 250 rpm at 30°C for 8 h and were then sub-cultured into 5 mL of SBM supplemented with 20 mM lactate for ∼16 h shaken at 250 rpm at 30°C. Cultures were then washed twice and added to SBM containing 20 mM lactate and 40 mM fumarate in tubes sealed with butyl rubber stoppers containing an argon headspace.

Reagents and Materials

Enzymes were purchased from New England Biolabs (Ipswich, MA). Kits for gel and plasmid purification were purchased from Invitrogen (Carlsbad, CA). All related reactions were carried out according to manufacturer instructions. Media components were purchased from Becton, Dickinson and Company (Sparks, MD), and chemicals including sodium DL-lactate and disodium fumarate were purchased from Sigma-Aldrich (St. Louis, MO).

Generation of Deletion Mutants

Oligonucleotide primers used to amplify regions of the MR-1 chromosome for deletion constructs are listed in **Table 2**. Regions of ∼500 base pairs both up and downstream of the target deletion region were amplified using primers hyaB-UF/hyaB-UR, hyaB-DF/hyaB-DR, hydA-UF/hydA-UR, and hydA-DF/hydA-DR with high fidelity polymerase Pfu Ultra (Agilent Technologies, Santa Clara, CA). Following restriction digest, up and downstream fragments were gel purified and cloned into the suicide vector pSMV3. Deletion constructs were introduced into MR-1 via conjugal transfer using *E. coli* donor strain WM3064 (Saltikov and Newman, 2003). In-frame gene deletions for *hydA* and *hyaB* were generated by homologous recombination as described previously (Saltikov and Newman, 2003). Plasmid constructs and deletion strains were sequence verified using primers hyaB-SP1/hyaB-SP-2 and hydA-SP1/hydA-SP2 at the University of Minnesota Genomics Center.

Anaerobic Bioreactors Vented to Remove Hydrogen

To eliminate intrusion of oxygen into bioelectrochemical reactors, a new sealed top mechanism was machined for 25 mL glass cones (Bioanalytical Systems, West Lafayette, IN), from PEEK (a polyether ether ketone thermoplastic polymer). PEEK is gas impermeable and mechanically robust, supporting a compression seal around openings and threaded ports for stainless steel fittings (McMaster-Carr). The bioreactor top has three ports at the center to house three electrodes (working, counter, and salt bridge for a reference electrode). The electrodes were fed through the top with the help of gaskets and a PEEK disc compressed by a threaded screw at the center (**Figure 1A**). Tightening of the center screw compresses the gasket, providing a seal on the glass tubing used for electrodes. Stainless steel screws mounted around the outer edge pull a ring from below, compressing the top of the reactor in a gasket within a groove. This design ensures that the distance between electrodes and the reference relative to the working and counter stays constant in every experiment, decreasing variability and increasing repeatability. **Supplementary Figure 1** is an overview of the reactor design, with detailed CAD file drawings and parts description list available here: https://github.com/komaljoshi-umn/Bond_lab_reactors.

At all stages of design and testing, oxygen levels were measured using a Series 3,000 Trace Oxygen Analyzer capable of detecting O_2 levels in the gas phase below 1 ppm (Alpha Omega, Lincoln RI). Anoxic conditions were maintained by slowly flushing reactors with argon purified of oxygen using a heated copper column, and oxygen in the headspace was measured to be below 2 ppm even at <1 ml/min flushing rate.

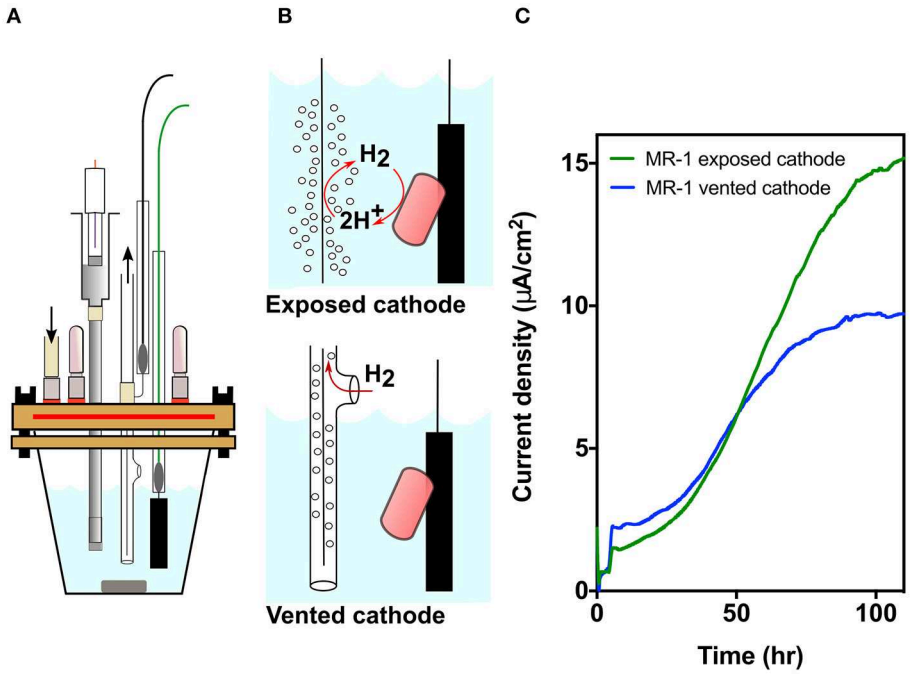

FIGURE 1 | MR-1 produces lower current density when cathodic hydrogen is vented. **(A)** Model of the new strictly anaerobic three electrode electrochemical cell. **(B)** Designs for exposed vs. vented cathodes to control release of cathodic hydrogen into the reactor. Hydrogen from the exposed cathode could suppress hydrogen disposal by bacteria, or serve as an electron donor if concentrations are high enough. **(C)** Current density over time for MR-1 cultures in new bioreactors containing exposed (green) and vented (blue) cathodes anodes poised at +0.240 V vs. SHE. Representative data from three independent experiments ($n = 3$) are shown.

Argon was bubbled through sealed vessels containing anoxic MilliQ water for humidification. When needed, flexible tubing for making connections was fresh Pharmed BPT tubing (Cole Parmer, Vernon Hills IL), as we found that after exposure to multiple (>5) rounds of autoclaving, 0.5 m of flexible tubing allowed in as much as 5 ppm O_2. The working electrode consisted of a graphitic carbon electrode measuring 0.5 cm × 3 cm × 1 mm connected to a platinum wire with a Teflon bolt (McMaster Carr, Elmhurst, IL). The working electrode was polished with 400 grit sandpaper, rinsed in 1 N HCl and cleaned by sonication in deionized water twice for 10 min prior to use. The reference consisted of a glass body Ag/AgCl electrode in 3M KCl connected to the system via a glass capillary tube filled with 1% agarose in a 0.1 M KCl solution and capped with a vycor frit. The counter electrode consisted of a platinum wire, and when indicated was contained within glass tubing that was vented from the reactor to eliminate introduction of hydrogen into the system. Bioreactors were maintained at 30°C using a water bath and were stirred continuously. Electrochemical data was monitored using a 16-channel VMP® potentiostat (Bio-Logic, Claix, France).

Bioreactor Preparation and Electrochemical Analysis

For bioreactor assays, single *S. oneidensis* colonies were used to inoculate LB medium incubated at 30°C, 250 rpm for ∼16 h. Strains were then sub-cultured in LB supplemented with 20 mM lactate and 40 mM fumarate under an argon headspace. When anaerobic LB cultures reached an optical density measured at 600 nm (OD_{600}) of 0.5–0.6, 1 mL of culture was added to bioreactors containing 14 mL of SBM medium containing 50 mM NaCl, 100 mM HEPES buffer, and 60 mM lactate, and 40 mM fumarate. After ∼5 h, the fumarate acceptor in these cultures is exhausted, and cells begin respiring electrodes (reflected in sudden jumps in current in **Figures 1**, **2**). Following inoculation, the working electrode was poised at +0.240 V vs. SHE (Standard Hydrogen Electrode), and current was monitored for ∼120 h until current plateaued. Reactors were then washed three times with SBM containing 50 mM NaCl but lacking electron donor or acceptor, and current was monitored until basal levels were reached indicating depletion of lactate. SBM containing 50 mM NaCl, 30 mM lactate, 1 μM riboflavin, and 10 mM arabinose (arabinose included as an internal HPLC standard not utilized as a carbon source by MR-1) was then added to reactors and current analysis was continued for 96 h (Rodionov et al., 2010; Golitsch et al., 2013). Supernatant was removed every 24 h for metabolite analysis by HPLC.

High Performance Liquid Chromatography (HPLC) and Coulombic Efficiency Calculations

Metabolites were quantified by HPLC using Shimadzu Scientific equipment including an SCL-10A system controller, LC-10AT

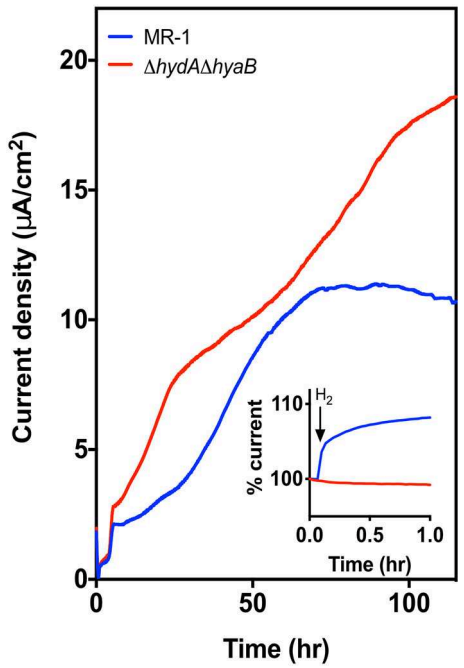

FIGURE 2 | Deletion of hydrogenases results in higher current density. Current density produced by MR-1 (blue) vs. Δ*hydA*Δ*hyaB* (red) in anaerobic bioreactors with vented cathodes. Lactate was supplied as the carbon source, and graphite carbon anodes were poised at +0.240 V vs. SHE. Data represents average current density produced in reactors run in triplicate. Inset figure shows the response in current production to addition of 1% exogenous hydrogen into the reactor headspace, with level of current at time of injection represented as 100%.

pump, SIL-10AF auto-injector, CTO-10A column oven, RID-10A refractive index detector (210 nm), and an SPD-10A UV-Vis detector. Mobile phase consisted of 15 mN H_2SO_4 set at a flow rate of 0.400 mL min^{-1}. Injection volumes of 50 μL were separated on an Aminex HPX-87H column maintained at 46°C. Reactor samples were compared to standard curves generated from known concentrations of each metabolite ($R^2 > 0.99$). These data were used to calculate coulombic efficiency, as Lactate→ Acetate + CO_2 + 4 e^-, and Coulombic efficiency (%) = (moles of electrons collected at the electrode) / (moles of electrons recovered as acetate × 4).

Fe(III) Oxide Reduction

Strains were streaked on LB agar plates from −80°C stocks at 30°C incubator overnight. Single colonies were inoculated into LB medium incubated at 30°C, 250 rpm for ∼16 h. Strains were then sub-cultured in anaerobic LB medium containing 20 mM lactate and 40 mM fumarate under anaerobic conditions. After the cultures reached an OD_{600nm} of 0.5–0.55, 1 mL of culture was inoculated into bioreactors containing 14 mL of SBM with 50 mM Fe(III) oxide, and 10 mM lactate. Platinum redox probes were included in the bioreactors to continuously measure the redox potential of the system. Bioreactors were maintained at 30°C using a water bath and were stirred continuously. Change in redox potential over time was measured using OCV (open circuit voltage) technique using a 16-channel VMP® potentiostat (Bio-Logic). Calibration redox probe measurements were also performed in the presence of Fe(III) oxide, except no cells were added and 10–1% hydrogen was added in the headspace.

Fe(III) Citrate Reduction Assay

Strains were streaked on LB agar plates from −80°C stocks as described for Fe(III) oxide experiments, and after subcultures reached an OD_{600nm} of 0.5–0.55, 1 mL of culture was inoculated into 14 mL of SBM with 50 mM Fe(III) citrate and 10 mM lactate. Following inoculation, 200 μL samples were taken using a degassed syringe at regular time intervals. Hundred microliter of sample was saved into 900 μL of 0.5 N HCl for the FerroZine assay and the remaining 100 μL was used to determine cell density. Fe(II) was measured in the samples using a modified FerroZine assay (Lovley and Phillips, 1987).

To determine cell density during Fe citrate reduction, 100 μL samples were removed at the time points indicated using a degassed syringe. Samples were then serially diluted, plated on LB agar, and colonies were counted after incubation overnight at 30°C.

RESULTS

Using a three-electrode potentiostat-poised system, a working electrode can be maintained at a constant potential, and respiration by bacteria capable of extracellular electron transfer can be monitored in real-time. In this case, the graphite electrode was poised at +0.24 V vs. SHE, allowing bacteria to oxidize lactate and utilize the anode as a terminal electron acceptor (Baron et al., 2009). Electron transfer efficiency to the electrode can be influenced due to oxygen acting as an alternative electron acceptor, by hydrogen produced by cells escaping into the headspace, or by hydrogen evolved from the counter electrode (cathode) serving as an additional electron donor. The design shown in **Figure 1A** (for detailed design, see **Supplementary Figure 1**) was optimized to eliminate all routes for oxygen entry, which then resulted in a device so well-sealed that gases produced in the medium could remain within the reactor (**Figure 1B**). To then isolate the effect of hydrogen, we modified reactors further by containing counter electrodes within tubing that vented produced hydrogen from the chamber, and compared the current density of strictly anaerobic MR-1 utilizing electrodes in vented vs. exposed designs.

Venting Cathodic Hydrogen Decreases Current Production by MR-1 in Three-Electrode Bioreactors

Cathodic hydrogen produced at exposed counter electrodes can raise hydrogen levels to concentrations that thermodynamically prevents hydrogen production by cells. At higher levels, hydrogen can act as an additional electron donor (Geelhoed and Stams, 2011; Schink and Stams, 2013) (**Figures 1A,B**). When cathodic hydrogen was vented from oxygen-free reactors operated in triplicate for each condition, current density by

MR-1 was significantly diminished compared to reactors with exposed cathodes (**Figure 1C**). Venting hydrogen out of the reactors decreased current density by 36.6 ± 4.5%, suggesting either that hydrogen inhibited electron flow out of MR-1, or that a significant portion of current density resulted from re-utilization of hydrogen (**Figure 1C**). To investigate this metabolic choice, mutants unable to produce or use hydrogen were constructed.

Hydrogenase Mutants Produce Higher Current Density in Single-Chamber, Three-Electrode Bioreactors

Electrons produced during anaerobic metabolism can either be transported from the quinone pool to external acceptors via the Mtr pathway, or, if their redox potential is low enough relative to the ambient hydrogen concentration, shunted to hydrogenases (Pinchuk et al., 2011). To quantify the role of hydrogen metabolism, marker-less in-frame deletions were constructed in the regions encoding both large subunits of the hydrogenases in the MR-1 genome (strain referred to as Δ*hydA*Δ*hyaB*). Deletion of both hydrogenases did not adversely affect growth rate or yield of Δ*hydA*Δ*hyaB* utilizing lactate as the donor and fumarate as the acceptor (**Supplementary Figure 2**).

In contrast, when triplicate MR-1 or Δ*hydA*Δ*hyaB* cultures were grown with lactate in anaerobic bioreactors with vented cathodes, maximum current densities for Δ*hydA*Δ*hyaB* were significantly higher compared to wild type (p-value < 0.0001) (**Figure 2**). The rate of current increase was also faster for all Δ*hydA*Δ*hyaB* reactors during the first 20 h following inoculation, and continued to increase for 60 h. MR-1 produced very little current over the first 20 h, and plateaued much sooner (**Figure 2**).

As the Δ*hydA*Δ*hyaB* mutant lacks options for electron flux out of the cell via hydrogenases, this improvement was consistent with a strict dependence on using the electrode. While MR-1 can only oxidize lactate to acetate under anaerobic conditions, under low cell density conditions in reactors lacking hydrogen, MR-1 could dispose of some electrons via hydrogen production and not be as dependent upon the electrode as its sole electron acceptor. To verify the presence or absence of hydrogenases under these conditions, 1% hydrogen was injected into the reactor headspace, causing current production to increase in MR-1 cultures for over 5 h, while no such increase was seen in mutant cultures (**Figure 2**, inset). This illustrated how sensitive MR-1 current production is to ambient hydrogen concentrations, and confirmed that the Δ*hydA*Δ*hyaB* mutant was insensitive to the presence of hydrogen.

Deletion of Hydrogenases Increases Efficiency of Electron Capture in Three-Electrode Bioreactors

After cultivating both strains for 120 h (**Figure 2**), all replicates of wild type and mutant cultures reached their maximum current density, with Δ*hydA*Δ*hyaB* cultures always producing more current than wild type. To test whether this increased current was due to diversion of more electrons per lactate to the electrode, the reactor medium was exchanged with fresh medium containing 30 mM lactate, 1 μM riboflavin, and 10 mM arabinose (included as an internal control for HPLC). Following medium replacement, Δ*hydA*Δ*hyaB* cultures sustained higher current densities, demonstrating nearly twice the rate of electron transfer to the anode as that of MR-1, and the attached biofilms maintained this constant plateau for over 4 days (**Figure 3A**, $n = 3$ for each strain). Samples were removed from triplicate reactors during these incubations and analyzed by HPLC to determine the fate of the lactate donor, which *S. oneidensis* typically oxidizes to acetate and four electrons under anaerobic conditions (Hunt et al., 2010; Pinchuk et al., 2011).

While Δ*hydA*Δ*hyaB* biofilms produced current nearly twice as fast as MR-1, acetate production rates from lactate were not as significantly different between the two strains: Δ*hydA*Δ*hyaB* produced 42 ± 3 μM acetate hr^{-1}, while MR-1 produced 38 ± 3 μM acetate hr^{-1} (**Figure 3B**). This was consistent with each culture consuming lactate at similar rates, while Δ*hydA*Δ*hyaB* biofilms diverted significantly more electrons to electrodes. When coulombic efficiencies were calculated by dividing the moles of electrons recovered at electrodes by the moles of lactate oxidized to acetate, nearly 90% of electrons were recovered as electricity in the Δ*hydA*Δ*hyaB* strain, while this ratio was only 52% for MR-1 under the same conditions (**Figure 3C**). Based on these results, when hydrogen concentrations are low, MR-1 can dispose of nearly half of its electrons via hydrogen production.

Evidence for Hydrogen Disposal During Reduction of Fe(III) Oxide

Shewanella cells need time to attach to solid acceptors such as Fe(III) oxides or electrodes, and electron transfer to these acceptors is accelerated by soluble shuttles. Thus, cells exposed to insoluble extracellular acceptors experience an excess of electrons. Hydrogen production should also be detectable in cultures exposed to metal oxides, if they represent a sustained bottleneck to electron disposal similar to what is observed with electrode-based acceptors.

For these experiments, MR-1 and the Δ*hydA*Δ*hyaB* strain were inoculated into medium with only particulate Fe(III) oxide as the electron acceptor, and a platinum redox probe was included to detect hydrogen. When MR-1 and the Δ*hydA*Δ*hyaB* were inoculated into Fe(III) oxide medium, the redox potential dropped in MR-1 cultures immediately after introduction of cells, while this change did not occur in Δ*hydA*Δ*hyaB* (**Figure 4A**). Very little Fe(II) was detected at this early stage (data not shown), suggesting that wild type cells experiencing excess donor and limited ability to access Fe(III) oxide as the acceptor produced a burst of hydrogen to dispose of excess electrons.

In control experiments, when hydrogen gas was added directly into the headspace of chambers containing Fe(III) oxide medium alone, a near instantaneous drop in redox potential was also observed, and the drop was proportional to hydrogen concentrations (**Figure 4B**). Within ∼30 min the redox potential returned to baseline if the headspace was flushed with argon. The drop in redox potential observed upon hydrogen addition mimics the observation in MR-1 cultures when particulate Fe(III) oxide is the electron acceptor.

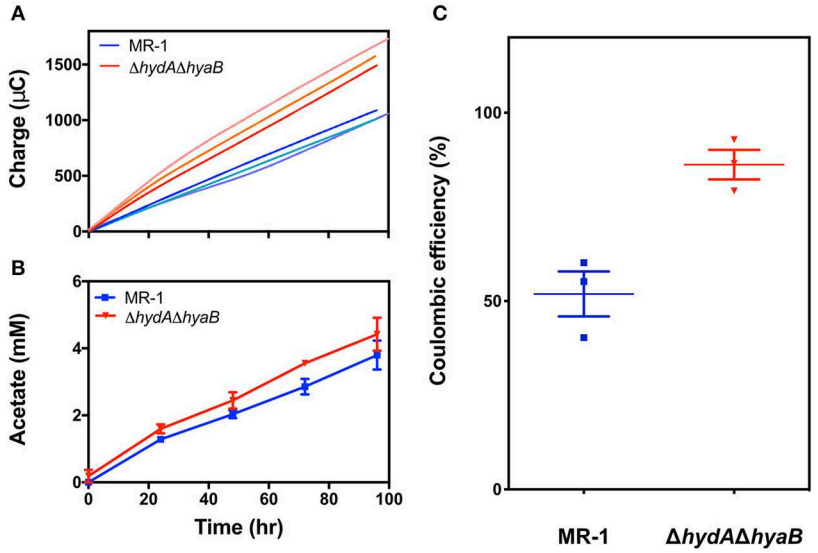

FIGURE 3 | Deletion of hydrogenases diverts electron flux toward the anode, increasing efficiency of electron recovery. **(A)** Recovered charge measured for reactors containing MR-1 (blue) as compared to Δ*hydA*Δ*hyaB* (red), reflecting the faster rate of current production by hydrogenase mutants. Each line represents one of three replicate reactors. **(B)** Acetate production rates for MR-1 (blue) and Δ*hydA*Δ*hyaB* (red), revealing similar rates of electron donor consumption, measured by HPLC in triplicate reactors. Error is represented as SEM. Time on the x-axis reflects time since replacing the medium in reactors containing mature biofilms with fresh 30 mM lactate and 1 μM riboflavin. **(C)** Coulombic efficiency measured as mole equivalents of electrons transferred to the anode vs. mole equivalents of electrons produced by lactate oxidized to acetate in MR-1 (blue) and Δ*hydA*Δ*hyaB* (red) in reactors with vented cathodes. Three independent experiments are shown for each strain with error representing SEM.

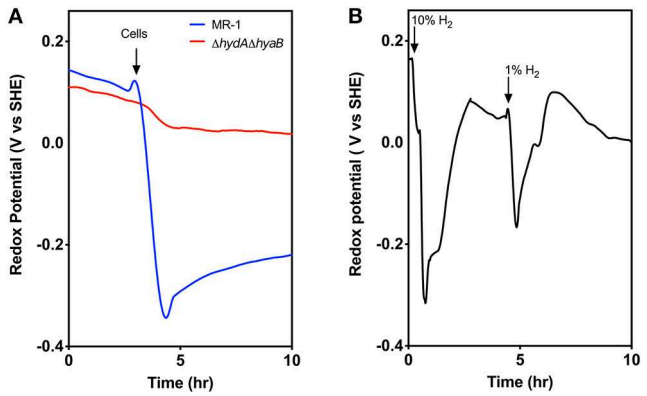

FIGURE 4 | Evidence for hydrogen disposal by MR-1 cells after transfer to Fe(III) oxide containing medium. **(A)** Redox probe based measurements detect a rapid decrease in redox potential when MR-1 cells with excess lactate are exposed to Fe(III) oxide as an electron acceptor. In contrast, Δ*hydA*Δ*hyaB* mutants do not lower redox potential, consistent with a burst of produced hydrogen by wild type cells experiencing donor-excess conditions. Fe(II) reduction at this early time point was minimal and similar by both strains (data not shown). **(B)** Abiotic control experiments showing similar rapid drop in redox potential in Fe(III) oxide medium in response to small additions of hydrogen to the headspace of reactors, and removal by flushing. Data is representative of three replicates.

Hydrogen Production Enhances Stationary Phase Survival

While deletion of hydrogenases diverted electrons to an electrode in a manner beneficial to the operation of a bioelectrochemical device, the presence of hydrogenases likely benefits the organism and aids survival under less steady-state conditions. To examine the effects of hydrogenases during starvation under conditions where cell viability could be easily determined, MR-1 and the Δ*hydA*Δ*hyaB* strain were grown with Fe(III) citrate as the sole terminal electron acceptor, which allowed the concentration of Fe(II) and cell density to be easily monitored over time. Reduction rates of Fe(III) citrate were not significantly different between MR-1 and the Δ*hydA*Δ*hyaB* strain (**Figure 5A**), and both reduced all available Fe(III) (**Supplementary Figure 3**). However, survival of MR-1 in stationary phase was greater than that of Δ*hydA*Δ*hyaB* (**Figure 5B**). A likely explanation for this phenotype is that disposal of hydrogen into the headspace by the wild type provided a route for a maintenance level of metabolism and enhanced survival.

DISCUSSION

Biochemically-derived hydrogen is generated during processes as diverse as fermentation and photosynthesis, is often a key molecule driving the thermodynamics of syntrophic partnerships (Stams and Plugge, 2009; Schink and Stams, 2013), and even affects virulence of *Salmonella* species in the gut (Spear et al., 2005; Maier et al., 2013). Particularly in anoxic environments, hydrogen concentrations are a controlling factor of microbial activity, and under steady state conditions can be used as an indicator of which terminal electron acceptor reactions are predominant (Lovley and Goodwin, 1988). The data presented here demonstrate how hydrogen is an important molecule in the ecophysiology of *Shewanella*, in particular within the engineered

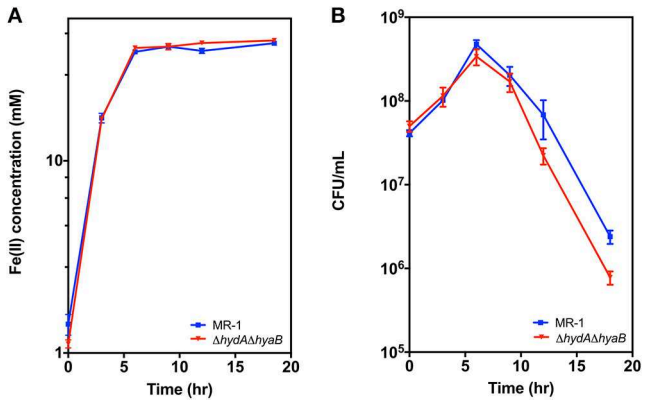

FIGURE 5 | Survival of MR-1 is enhanced compared to Δ*hydA*Δ*hyaB*. Strains were grown in vented bioreactors with Fe(III) citrate (50 mM) as the terminal electron acceptor and lactate (10 mM) as electron donor. Cultures were monitored over time for **(A)** Fe(II), and **(B)** cell density measured as colony forming units (CFU). Data represents three independent cultures with error reported as SEM.

environments of bioelectrochemical systems. *Shewanella* species thrive in a variety of environments because they encode multiple electron transport pathways enabling the use of a wide array of terminal electron acceptors, including protons, as they become available.

To study electron flux in *Shewanella*, it was essential to understand the fate of carbon sources and electron carriers as well as the efficiency of electron transfer to and from electrodes. Reported electron recovery calculations for MR-1 using a variety of reactor types in the literature range from 1.3–75%, with the majority between 10–20% (Ringeisen et al., 2006, 2007; Newton et al., 2009; Bretschger et al., 2010; Rosenbaum et al., 2010, 2011; Watson and Logan, 2010; Kouzuma et al., 2012; Wu et al., 2013; Kirchhofer et al., 2014; TerAvest and Angenent, 2014; Luo et al., 2016). Low recovery values indicate that most of the electrons generated from oxidation of lactate remained unaccounted for, even when the focus of the studies was electricity production. Transfer of electrons to oxygen due to oxygen-permeable materials can account for much of this electron loss. In our own experiments, even the simple act of flushing reactors with anaerobic gases can actually introduce oxygen to the system. For example, preliminary experiments conducted while redesigning reactors found that tubing that has been autoclaved multiple times becomes permeable enough to increase the O_2 in a reactor, as does introduction of a plastic membrane filter in the gas line. If the headspace contains even 10 ppm O_2, *S. oneidensis* cells respiring at rates shown in **Figure 2** could easily divert ∼50% of lactate oxidation to aerobic respiration over a 7-day incubation. The modified bioreactor system reported here was optimized to maintain oxygen levels below 2 ppm, and to minimize flushing of the headspace to limit delivery of further oxygen into the system.

Kozuma et al. attempted to limit oxygen losses by deleting the three terminal oxidases in MR-1, but the triple mutant was unable to produce current, likely due to oxygen toxicity caused by earlier reactor designs (Kouzuma et al., 2012). Higher coulombic efficiency (84 ± 7%) has been reported for MR-1 exposed to the conjugated oligoelectrolyte $DSSN^+$ that intercalates in membranes (Kirchhofer et al., 2014), possibly via inhibition of hydrogenases. Here we report a coulombic efficiency of 86.2 ± 6.8% in bioreactors through redesign of reactor components, and by diverting electron flux away from hydrogen production toward electrode reduction through deletion of the hydrogenase subunits *hydA* and *hyaB*, in *S. oneidensis* (**Figure 3C**).

Removing the hydrogenases from *S. oneidensis* shuts down a "leaky" pathway for electron disposal in electrochemical reactors, but we find evidence that this pathway may prove important in environments when terminal electron acceptors are limited. Conversion of protons to molecular hydrogen by hydrogenases is a relatively simple reaction, but it is limited by thermodynamic constraints due to its low standard redox potential (−414 mV) (Thauer et al., 1977). As hydrogen concentrations rise, continued hydrogen production becomes thermodynamically unfavorable from standard electron carriers with more positive redox potentials such as NADH (−320 mV) (Thauer et al., 1977; Stams and Plugge, 2009). Especially as the first step of lactate oxidation to pyruvate has a formal midpoint potential of −190 mV, even small amounts of ambient hydrogen prevents complete electron disposal via this pathway.

The new reactor design and double mutant allowed us to show that when utilizing an electrode as the terminal electron acceptor, MR-1 normally diverts some electron flux toward molecular hydrogen production. The small population size on an electrode, and low hydrogen concentration in these reactors further eases the thermodynamic constraints on hydrogen production as an electron disposal mechanism. As reduction rates of Fe(III) citrate were similar for both strains, soluble Fe(III) doesn't create the same bottleneck to electron transfer as an insoluble substrate. However, the increased survival of MR-1 containing hydrogenases indicates that maintenance of hydrogenases in a population provides a competitive advantage, at least in stationary phase conditions. As a respiratory generalist, *Shewanella* have been selected to dispose of electrons via any means available. This allows them to grow in a variety of environments or participate in syntrophic partnerships that consume their produced hydrogen (Nealson and Scott, 2006; Hau and Gralnick, 2007). However, under the more defined conditions of electrochemical systems, it may be necessary to remove some of this respiratory flexibility, to direct electron flow to electrodes and increase the efficiency of electron capture.

DATA AVAILABILITY

The datasets generated for this study will not be made publicly available. There are no datasets.

AUTHOR CONTRIBUTIONS

KJ and DB designed the bioreactor described here. KJ, AK, NK, JG, and DB designed experiments. KJ, AK, and NK performed experiments.

FUNDING

This work was supported by the Office of Naval Research (Award #N00014-12-1-0309 and #N00014-13-1-0552 to JG and Award #N00014-18-1-2632 to JG and DB).

ACKNOWLEDGMENTS

We would like to thank Geoff Harms (University of Minnesota) for help in constructing modified parts for bioreactors. This work is dedicated in fond memory of Ethan Johnson (1972–2010) who began these studies on hydrogenase mutants in *S. oneidensis*. We also thank members of the Gralnick and Bond Laboratories for helpful discussions throughout the project.

SUPPLEMENTARY MATERIAL

The Supplementary Material for this article can be found online at: https://www.frontiersin.org/articles/10.3389/fenrg.2019.00095/full#supplementary-material

REFERENCES

Baron, D., LaBelle, E., Coursolle, D., Gralnick, J. A., and Bond, D. R. (2009). Electrochemical measurement of electron transfer kinetics by *Shewanella oneidensis* MR-1. *J. Biol. Chem.* 284, 28865–28873. doi: 10.1074/jbc.M109.043455

Beblawy, S., Bursac, T., Paquete, C., Louro, R., Clarke, T. A., and Gescher, J. (2018). Extracellular reduction of solid electron acceptors by *Shewanella oneidensis*. *Mol. Microbiol.* 109, 571–583. doi: 10.1111/mmi.14067

Bretschger, O., Cheung, A. C. M., Mansfeld, F., and Nealson, K. H. (2010). Comparative microbial fuel cell evaluations of *Shewanella* spp. *Electroanalysis* 22, 883–894. doi: 10.1002/elan.200800016

Bretschger, O., Obraztsova, A., Sturm, C. A., Chang, I. S., Gorby, Y. A., Reed, S. B., et al. (2007). Current production and metal oxide reduction by *Shewanella oneidensis* MR-1 wild type and mutants. *Appl. Environ. Microbiol.* 73, 7003–7012. doi: 10.1128/AEM.01087-07

Coursolle, D., Baron, D. B., Bond, D. R., and Gralnick, J. A. (2010). The Mtr respiratory pathway is essential for reducing flavins and electrodes in *Shewanella oneidensis*. *J. Bacteriol.* 192, 467–474. doi: 10.1128/JB.00925-09

Fredrickson, J. K., Romine, M. F., Beliaev, A. S., Auchtung, J. M., Driscoll, M. E., Gardner, T. S., et al. (2008). Towards environmental systems biology of *Shewanella*. *Nat. Rev. Microbiol.* 6, 592–603. doi: 10.1038/nrmicro1947

Geelhoed, J. S., and Stams, A. J. M. (2011). Electricity-assisted biological hydrogen production from acetate by *Geobacter sulfurreducens*. *Environ. Sci. Technol.* 45, 815–820. doi: 10.1021/es102842p

Golitsch, F., Bücking, C., and Gescher, J. (2013). Proof of principle for an engineered microbial biosensor based on *Shewanella oneidensis* outer membrane protein complexes. *Biosens. Bioelectron.* 47, 285–291. doi: 10.1016/j.bios.2013.03.010

Hau, H. H., Gilbert, A., Coursolle, D., and Gralnick, J. A. (2008). Mechanism and consequences of anaerobic respiration of cobalt by *Shewanella oneidensis* Strain MR-1. *Appl. Environ. Microbiol.* 74, 6880–6886. doi: 10.1128/AEM.00840-08

Hau, H. H., and Gralnick, J. A. (2007). Ecology and biotechnology of the genus *Shewanella*. *Annu. Rev. Microbiol.* 61, 237–258. doi: 10.1146/annurev.micro.61.080706.093257

Hunt, K. A., Flynn, J. M., Naranjo, B., Shikhare, I. D., and Gralnick, J. A. (2010). Substrate-level phosphorylation is the primary source of energy conservation during anaerobic respiration of *Shewanella oneidensis* strain MR-1. *J. Bacteriol.* 192, 3345–3351. doi: 10.1128/JB.00090-10

Kane, A. L., Brutinel, E. D., Joo, H., Maysonet, R., VanDrisse, C. M., Kotloski, N. J., et al. (2016). Formate metabolism in *Shewanella oneidensis* generates proton motive force and prevents growth without an electron acceptor. *J. Bacteriol.* 198, 1337–1346. doi: 10.1128/JB.00927-15

Kirchhofer, N. D., Chen, X., Marsili, E., Sumner, J. J., Dahlquist, F. W., and Bazan, G. C. (2014). The conjugated oligoelectrolyte DSSN+ enables exceptional coulombic efficiency via direct electron transfer for anode-respiring *Shewanella oneidensis* MR-1—a mechanistic study. *Phys. Chem. Chem. Phys.* 16, 20436–20443. doi: 10.1039/C4CP03197K

Kouzuma, A., Hashimoto, K., and Watanabe, K. (2012). Influences of aerobic respiration on current generation by *Shewanella oneidensis* MR-1 in single-chamber microbial fuel cells. *Biosci. Biotechnol. Biochem.* 76, 270–275. doi: 10.1271/bbb.110633

Kreuzer, H. W., Hill, E. A., Moran, J. J., Bartholomew, R. A., Yang, H., and Hegg, E. L. (2014). Contributions of the [NiFe]- and [FeFe]-hydrogenase to H_2 production in *Shewanella oneidensis* MR-1 as revealed by isotope ratio analysis of evolved H_2. *FEMS Microbiol. Lett.* 352, 18–24. doi: 10.1111/1574-6968.12361

Lee, H.-S., and Rittmann, B. E. (2010). Significance of biological hydrogen oxidation in a continuous single-chamber microbial electrolysis cell. *Environ. Sci. Technol.* 44, 948–954. doi: 10.1021/es9025358

Lee, H.-S., Torres, C. I., Parameswaran, P., and Rittmann, B. E. (2009). Fate of H_2 in an upflow single-chamber microbial electrolysis cell using a metal-catalyst-free cathode. *Environ. Sci. Technol.* 43, 7971–7976. doi: 10.1021/es900204j

Lovley, D. R., and Goodwin, S. (1988). Hydrogen concentrations as an indicator of the predominant terminal electron-accepting reactions in aquatic sediments. *Geochim. Cosmochim. Acta* 52, 2993–3003. doi: 10.1016/0016-7037(88)90163-9

Lovley, D. R., and Phillips, E. J. P. (1987). Rapid assay for microbially reducible ferric iron in aquatic sediments. *Appl. Environ. Microbiol.* 53, 1536–1540.

Lu, M., Chan, S., Babanova, S., and Bretschger, O. (2017). Effect of oxygen on the per-cell extracellular electron transfer rate of *Shewanella oneidensis* MR-1 explored in bioelectrochemical systems. *Biotechnol. Bioeng.* 114, 96–105. doi: 10.1002/bit.26046

Luo, S., Guo, W., H., Nealson, K., and Feng, X., He, Z. (2016). ^{13}C pathway analysis for the role of formate in electricity generation by *Shewanella Oneidensis* MR-1 using lactate in microbial fuel cells. *Sci. Rep.* 6:20941. doi: 10.1038/srep20941

Maier, L., Vyas, R., Cordova, C. D., Lindsay, H., Schmidt, T. S. B., Brugiroux, S., et al. (2013). Microbiota-derived hydrogen fuels *Salmonella typhimurium* invasion of the gut ecosystem. *Cell Host Microbe* 14, 641–651. doi: 10.1016/j.chom.2013.11.002

Meshulam-Simon, G., Behrens, S., Choo, A. D., and Spormann, A. M. (2007). Hydrogen metabolism in *Shewanella oneidensis* MR-1. *Appl. Environ. Microbiol.* 73, 1153–1165. doi: 10.1128/AEM.01588-06

Nealson, K. H., and Scott, J. (2006). "Ecophysiology of the genus *Shewanella*," in *The Prokaryotes*, eds M. Dworkin, S. Falkow, E. Rosenberg, K.-H. Schleifer, and E. Stackebrandt (New York, NY: Springer), 1133–1151. doi: 10.1007/0-387-30746-X_45

Newton, G. J., Mori, S., Nakamura, R., Hashimoto, K., and Watanabe, K. (2009). Analyses of current-generating mechanisms of *Shewanella loihica* PV-4 and *Shewanella oneidensis* MR-1 in microbial fuel cells. *Appl. Environ. Microbiol.* 75, 7674–7681. doi: 10.1128/AEM.01142-09

Pinchuk, G. E., Geydebrekht, O. V., Hill, E. A., Reed, J. L., Konopka, A. E., Beliaev, A. S., et al. (2011). Pyruvate and lactate metabolism by *Shewanella oneidensis* MR-1 under fermentation, oxygen limitation, and fumarate respiration conditions. *Appl. Environ. Microbiol.* 77, 8234–8240. doi: 10.1128/AEM.05382-11

Rabaey, K., and Verstraete, W. (2005). Microbial fuel cells: novel biotechnology for energy generation. *Trends Biotechnol.* 23, 291–298. doi: 10.1016/j.tibtech.2005.04.008

Ringeisen, B. R., Henderson, E., Wu, P. K., Pietron, J., Ray, R., Little, B., et al. (2006). High power density from a miniature microbial fuel cell using *Shewanella oneidensis* DSP10. *Environ. Sci. Technol.* 40, 2629–2634. doi: 10.1021/es052254w

Ringeisen, B. R., Ray, R., and Little, B. (2007). A miniature microbial fuel cell operating with an aerobic anode chamber. *J. Power Sources* 165, 591–597. doi: 10.1016/j.jpowsour.2006.10.026

Rodionov, D. A., Yang, C., Li, X., Rodionova, I. A., Wang, Y., Obraztsova, A. Y., et al. (2010). Genomic encyclopedia of sugar utilization pathways in the *Shewanella* genus. *BMC Genomics* 11:494. doi: 10.1186/1471-2164-11-494

Rosenbaum, M., Cotta, M. A., and Angenent, L. T. (2010). Aerated *Shewanella oneidensis* in continuously fed bioelectrochemical systems for power and hydrogen production. *Biotechnol. Bioeng.* 105, 880–888. doi: 10.1002/bit.22621

Rosenbaum, M. A., Bar, H. Y., Beg, Q. K., Segrè, D., Booth, J., Cotta, M. A., et al. (2011). *Shewanella oneidensis* in a lactate-fed pure-culture and a glucose-fed co-culture with *Lactococcus lactis* with an electrode as electron acceptor. *Bioresour. Technol.* 102, 2623–2628. doi: 10.1016/j.biortech.2010.10.033

Saltikov, C. W., and Newman, D. K. (2003). Genetic identification of a respiratory arsenate reductase. *Proc. Natl. Acad. Sci. U.S.A.* 100, 10983–10988. doi: 10.1073/pnas.1834303100

Schink, B., and Stams, A. J. M. (2013). "Syntrophism among prokaryotes," in *The Prokaryotes: Prokaryotic Communities and Ecophysiology,* eds E. Rosenberg, E. F. DeLong, S. Lory, E. Stackebrandt, and F. Thompson (Berlin; Heidelberg: Springer Berlin Heidelberg), 471–493. doi: 10.1007/978-3-642-30123-0_59

Spear, J. R., Walker, J. J., McCollom, T. M., and Pace, N. R. (2005). Hydrogen and bioenergetics in the Yellowstone geothermal ecosystem. *Proc. Natl. Acad. Sci. U.S.A.* 102, 2555–2560. doi: 10.1073/pnas.0409574102

Stams, A. J. M., and Plugge, C. M. (2009). Electron transfer in syntrophic communities of anaerobic bacteria and archaea. *Nat. Rev. Microbiol.* 7, 568–577. doi: 10.1038/nrmicro2166

TerAvest, M. A., and Angenent, L. T. (2014). Oxidizing electrode potentials decrease current production and coulombic efficiency through cytochrome *c* inactivation in *Shewanella oneidensis* MR-1. *ChemElectroChem* 1, 2000–2006. doi: 10.1002/celc.201402128

TerAvest, M. A., Rosenbaum, M. A., Kotloski, N. J., Gralnick, J. A., and Angenent, L. T. (2014). Oxygen allows *Shewanella oneidensis* MR-1 to overcome mediator washout in a continuously fed bioelectrochemical system. *Biotechnol. Bioeng.* 111, 692–699. doi: 10.1002/bit.25128

Thauer, R. K., Jungermann, K., and Decker, K. (1977). Energy conservation in chemotrophic anaerobic bacteria. *Bacteriol. Rev.* 41, 100–180.

Venkateswaran, K., Moser, D. P., Dollhopf, M. E., Lies, D. P., Saffarini, D. A., MacGregor, B. J., et al. (1999). Polyphasic taxonomy of the genus *Shewanella* and description of *Shewanella oneidensis* sp. nov. *Int. J. Syst. Bacteriol.* 49(Pt 2), 705–724. doi: 10.1099/00207713-49-2-705

Watson, V. J., and Logan, B. E. (2010). Power production in MFCs inoculated with *Shewanella oneidensis* MR-1 or mixed cultures. *Biotechnol. Bioeng.* 105, 489–498. doi: 10.1002/bit.22556

Wu, D., Xing, D., Lu, L., Wei, M., Liu, B., and Ren, N. (2013). Ferric iron enhances electricity generation by *Shewanella oneidensis* MR-1 in MFCs. *Bioresour. Technol.* 135, 630–634. doi: 10.1016/j.biortech.2012.09.106

Conflict of Interest Statement: The authors declare that the research was conducted in the absence of any commercial or financial relationships that could be construed as a potential conflict of interest.

frontiers in Energy Research

ORIGINAL RESEARCH
published: 12 September 2019
doi: 10.3389/fenrg.2019.00100

Rational Selection of Carbon Fiber Properties for High-Performance Textile Electrodes in Bioelectrochemical Systems

*Liesa Pötschke[1], Philipp Huber[2], Sascha Schriever[2], Valentina Rizzotto[3], Thomas Gries[2], Lars M. Blank[1] and Miriam A. Rosenbaum[4,5]**

[1] Institute of Applied Microbiology, Aachen Biology and Biotechnology, RWTH Aachen University, Aachen, Germany, [2] Institut für Textiltechnik, RWTH Aachen University, Aachen, Germany, [3] Institute of Inorganic Chemistry, RWTH Aachen University, Aachen, Germany, [4] Bio Pilot Plant, Leibniz Institute for Natural Product Research and Infection Biology, Hans-Knöll-Institut, Jena, Germany, [5] Faculty of Biological Sciences, Friedrich-Schiller-University, Jena, Germany

Novel applications of bioelectrochemical systems (BES) are emerging constantly, but the majority still lacks economic viability. Especially the use of electrochemical system components without adaptation to BES requirements causes poor exploitation of the potential system performance. The electrode material is one central component that determines BES performance. While commercial carbon fiber (CF) fabrics are commonly used, their customizability as two- or three-dimensional electrode material for BES is rarely investigated. Using pure cultures of *S. oneidensis* MR-1, we identified CF properties impacting bacterial current generation: (1) The removal of the sizing (protective coating) is of great importance for all the fibers studied, as it acts as an electrical insulator. By desizing, the maximum current density (j_{max}) is increased by up to 40-fold. (2) Alteration of the filament surface chemistry results in an accelerated initial development of current generation, but the maximum current density (j_{max}) is hardly affected. (3) A specific yarn structure, the stretch-broken yarn, supports exceptionally high current densities. The good electrode performance is correlated to the presence of free filament ends (responsible for 41% current increase), which are characteristic for this yarn. (4) Moreover, a combination of these free filament ends with a high degree of graphitization enhances electrode performance of a commercial fabric by 100%. The results demonstrate that the CF selection can greatly influence the achievable electrode performance of CF fabrics, and thereby contributes to rational engineering of CF based electrodes that can be tailored for the many BES applications envisaged.

Keywords: carbon fiber electrode, carbon fabric, *S. oneidensis* MR-1, microbial fuel cells, chemical surface activation, desizing, electrical conductivity

OPEN ACCESS

Edited by:
Uwe Schröder, Technische Universitat Braunschweig, Germany

Reviewed by:
Annemiek Ter Heijne, Wageningen University & Research, Netherlands
Benjamin Erable, Centre National de la Recherche Scientifique (CNRS), France

****Correspondence:***
Miriam A. Rosenbaum
miriam.rosenbaum@leibniz-hki.de

Specialty section:
This article was submitted to Bioenergy and Biofuels, a section of the journal Frontiers in Energy Research

Received: *25 June 2019*
Accepted: *30 August 2019*
Published: *12 September 2019*

Citation:
Pötschke L, Huber P, Schriever S, Rizzotto V, Gries T, Blank LM and Rosenbaum MA (2019) Rational Selection of Carbon Fiber Properties for High-Performance Textile Electrodes in Bioelectrochemical Systems. Front. Energy Res. 7:100. doi: 10.3389/fenrg.2019.00100

INTRODUCTION

Bioelectrochemical systems (BES) unlock novel bioeconomic technologies by utilizing the microbial ability of extracellular electron transfer to a solid electrode (Santoro et al., 2017). Remarkably, the transition from lab to full-scale is not yet accomplished for most BES applications. A closer look suggests that recent successful implementations of BES are restricted to special

and niche applications in which the BES has no or few competing technologies or provides an added ecological value (reviewed by Gajda et al., 2018). This can be a combined waste treatment with electricity generation in areas of low infrastructure (Ieropoulos et al., 2016; Walter et al., 2018) or avoiding costly maintenance in the case of benthic fuel cells powering remote sensors (Tender et al., 2008; Donovan et al., 2013; Ewing et al., 2017). In such cases, a full exploitation of the microbial potential is not necessary and low-cost standard commercial materials (carbon felts, ceramic separators) perform satisfactorily. In contrast, large scale wastewater/remediation applications (Hiegemann et al., 2016; Lu et al., 2017b; Wang et al., 2017) or high-tech applications such as the production of specialty chemicals (Raes et al., 2016; Streeck et al., 2018) are not yet ready for marketing, because here, high efficiencies are mandatory for economic operation and competitiveness with established technologies.

Considerable effort has been put into the engineering of BES toward various enhanced performance parameters, which have been extensively reviewed elsewhere (Janicek et al., 2014; Santoro et al., 2017). Especially, the core element bioanode is in the focus of research and development. Independent from the electrode material, chemical and physical modifications have been applied successfully to increase electrode performances in BES (He et al., 2011; Guo et al., 2013; Kipf et al., 2013; Artyushkova et al., 2015; Baudler et al., 2015; Champigneux et al., 2018; Pierra et al., 2018; Moß et al., 2019).

In our preliminary work, we identified carbon fiber (CF) based textile electrodes as all-rounder electrode material, since they combine all preferred features for large scale applications, i.e., large specific surface area in the (m^2/g) range, good mechanical and chemical stability, customizable flexibility and porosity at µm up to cm scale; all of which enable high electrode packing densities (Morgan, 2005). Own previous pure culture screening showed a broad range of bioelectrochemical activity for different commercial carbon fiber materials (**Figure S1**). Although CF fabrics are widely used in lab-scale BES studies, they are usually not favored for large-scale BES, because they are considered too costly in manufacturing (Wang et al., 2009; Santoro et al., 2017). However, authors rarely acknowledge the extremely wide variety within the types of textile materials and especially the CF. Usually, the exact properties of the used materials are not reported, comparing e.g., just "carbon cloth" or "carbon mesh" without mentioning the underlying fiber (Wang et al., 2009; Blanchet et al., 2016). In contrast, the numerous high-tech applications of CF in fiber reinforced plastics, such as light-weight construction in aerospace, automobile, or reinforcement of sports and medical equipment, have created a worldwide industry with well-established processing technologies and customizable products.

CF are derived from organic precursors with preferably high carbon yield (i.e., low amount of non-C atoms that will vanish during carbonization). The most common precursors are polyacrylonitrile (PAN) and pitch with a market share of 96 and 3%, respectively (Das et al., 2016), and a substantial difference in application and especially price (typically around 20 €/kg for PAN and around 100 €/kg for pitch based CF). Pitch CF generally exhibit lower specific electrical resistivities than PAN CF, but the ranges are not far from overlapping (ρ_{fiber} = 0.3–0.8 vs. 1–2 mΩ·cm, own preliminary market screening, data not shown). The focus of this study was on PAN CF due to their advantages regarding price and availability.

The simplified standard production processes for PAN CF woven fabrics are depicted in **Figure 1**. Under tensile stress, the fibers are stabilized in air at 200–300°C (cyclization and increasing density of the polymer = oxidized PAN, PANOX), and subsequently carbonized by means of high temperature (1,000–1,700°C) in an inert atmosphere. The resulting CF are bundles of thousands of parallel filaments with diameters of 5–7 µm (Morgan, 2005). This structure provides the large specific surface area [m^2/g], which makes CF fabrics such popular electrode materials. The most common fiber type is the continuous multifilament roving (CM), which contains parallel, endless filaments with little to no twist. CM are also referred to as tows and classified by their tow size (xK = x,000 filaments). A CM may be converted into the less common stretch-broken yarn (SB). The result is a twisted bundle of filaments with an approximately length in the order of magnitude of 10 cm. The stretch-breaking process can be either applied to the carbonized CM or to the stabilized fiber, which is then carbonized at fabric level. Here, we consider only the latter type of SB fabrics (production route 2, **Figure 1**), which are usually referred to as PANOX fabrics.

The electrical properties of a carbon filament are determined by the purity and orientation of their basal planes, i.e., carbon grids along which electrons are conducted. The planes are stacked onto each other and electrons flow best in-plane, i.e., in-filament direction (Dutta, 1953; Windhorst and Blount, 1997). During carbonization, tensile stress and process temperature regulate CF electrical properties. CF carbonized at 1,000–1,700°C contain 92–98% atomic carbon (at.%). Higher temperatures above 2,000°C achieve graphitized fibers with a carbon content over 99 at.% (Morgan, 2005). After carbonization (graphitization), CF are stiff and brittle. Unlike SB, which are carbonized as a whole fabric, CM need to be subjected to a finishing step prior to textile processing. This includes a chemical surface activation and the subsequent application of a protective coating (sizing). Surface activation enhances the adhesion of the sizing via introduction of foreign atoms and residues into the carbon grid (Kozlowski and Sherwood, 1986; Alexander and Jones, 1996; Severini et al., 2002). The sizing itself is based on polymers like epoxy resins, polyurethanes, and others, which are able to reduce friction and wear on the fibers during the textile processing and enable the fiber-matrix adhesion in the production of CF reinforced plastics. On the other hand, the sizing usually acts as an electrical insulator, which is why this coating needs to be removed before CM can be employed as BES electrode material. Finally, a second round of chemical surface activation may be applied in order to enhance the fiber-bacteria interaction of the CF electrode (the first surface activation is usually not sufficiently stable, see Jones and Sammann, 1989). The introduction of polar and charged functional groups will mainly increase the initially poor

Abbreviations: BES, bioelectrochemical system; CE, coulombic efficiency; CF, carbon fiber; CM, continuous multifilament roving; MFC, microbial fuel cell; PAN, polyacrylonitrile; SB, stretch-broken yarn; TGA, thermogravimetric analysis; XPS, X-ray photoelectron spectroscopy.

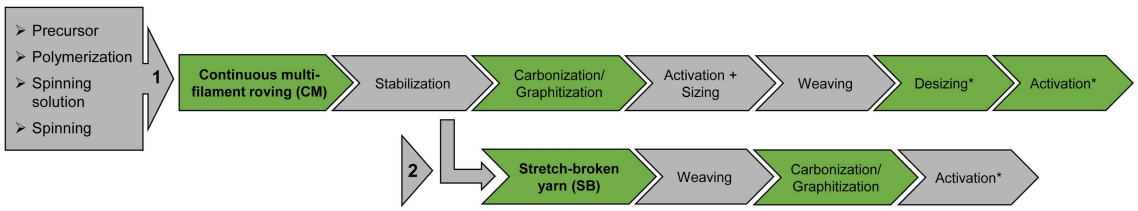

FIGURE 1 | Simplified general production process of woven CF fabrics (PAN based) made from either continuous multifilament rovings (1) or stretch-broken yarns (2). Stars mark the steps that are added especially for the application in BES. The parameters investigated in this study are highlighted in green (fiber type, degree of graphitization, desizing, and 2nd chemical surface activation).

TABLE 1 | Properties of commercial PAN CF used in this study.

Abbreviation	Feature of interest	Manufacturer	Product name	Tow size
HTS40	Good performance in previous BES fiber screening	TT	Tenax® E HTS40-F13	12K
CT50	Equivalent product to HTS40, but different processing	SGL	C T50-4.0/240-E100	50K
T300	Standard fiber and sizing	TO	Torayca® T300-40B	3K

SGL, SGL Carbon, Germany; TO, Toray Industries, Inc., Japan; TT, Teijin Carbon Europe GmbH (previously Toho Tenax), Japan/Germany.

wettability of the fiber surface (Qian et al., 2010), thus enhancing its accessibility.

With this study, we aimed at laying the foundation for a comprehensive customized engineering of CF woven electrodes for BES. With respect to the production process chain, we investigated possibly relevant parameters, such as yarn macrostructure (CM or SB), the filament conductivity, desizing, and 2nd surface activation, and evaluated their influence on electrode performance. To minimize biological variability during this comparative evaluation of material properties, we utilized the robust anodic electroactivity of *S. oneidensis* MR-1 for this work. One step beyond these crucial fiber and fabric materials properties, also the 3D fabric architecture will be an important parameter for successful CF electrode utilization in diverse BES applications. However, since this would overload the scope of the presented work, it will be followed up in subsequent publications.

MATERIALS AND METHODS

All textile products were denominated following international terminology standards (ASTM D123).

Preparation and Physical Characterization of Carbon Fiber and Fabric Samples

Fibers were subjected to a preparative physical characterization prior to evaluation as BES electrodes. The workflow was electrical resistivity measurement (**Table S1**), tribological characterization and/or artificial introduction of filament breaks (Tribology Test Rig), desizing (Desizing), and chemical surface activation (Chemical Surface Activation of Carbon Fibers), if applicable. Fabrics were desized (Desizing), and physical characteristics were obtained from manufacturer's datasheets. All materials were based on PAN precursor. An overview of the relevant properties of all included CF is given in **Table 1**, extended technical properties of these fibers are given in **Table S1**. **Table 2** introduces commercial and modified fabrics used in this study, extended technical properties can be found in **Table S2**. SIGRATEX® fabrics were especially selected for chapter Effect of Filament Conductivity and Fiber Type on Bacterial Current Generation, since both their carbonized and graphitized equivalents are commercially available. For the SB fabrics, technical details about fibers cannot be provided, since the carbonization process occurs on fabric level (**Figure 1**). High tenacity CM (like CT50 and HTS40, **Table 1**) were used for the production of SIGRATEX® CM fabrics.

The electrical resistivities of CF fabrics are in the same order of magnitude as the respective single CF. However, reliable standardized measurement methods do not exist on fabric level and the measurement errors tend to be high, which is why specific fabric resistivities are not given in **Table 2**.

Tribology Test Rig

For the introduction of intended breaks (damaged multifilament rovings, results Effect of Fiber Type on Bacterial Current Generation), a customized indenter with sharpened grooves was fabricated in-house. Fiber strengths were assessed according to ASTM D3108 (registered method to characterize to what extent fibers are prone to filament breakage) using an in-house test rig with the following operational parameters: looping angle 180°; 5 m/min yarn throughput, test interval 5 min (tested fiber length 25 m), initial load of filament break sensors before/after indenter 5 N/12 N. The resulting fiber damage is expressed as statistical average amount of broken filaments in a random cross-section of the roving [% of x K filaments]. Fibers with filament damage exceeding 10% could not be processed further since they disassembled in the non-twisted configuration. The obtained

TABLE 2 | CF fabrics used in this study.

Abbrevation	Feature of interest	Manufacturer	Product name	Fiber type
SB_{low}	Low C-content	SGL	SIGRATEX® C W270-TW2/2/CA	SB
$SB_{moderate}$	Moderate C-content	SGL	SIGRATEX® C W230-TW2/2/GR	SB
SB_{high}	High C-content	SGL	SIGRATEX® C W230-TW2/2/GR (graphitized at 2,800°C)	SB
CM_{low}	Low C-content	SGL	SIGRATEX® C W245-TW2/2	CM, 3K
$CM_{moderate}$	Moderate C-content	SGL	SIGRATEX® C W230-TW2/2/GR	CM, 3K
CM_{high}	High C-content	SGL	SIGRATEX® C W230-TW2/2/GR (graphitized at 2,800°C)	CM, 3K
T300 fabric[a]	Not surface activated during production, standard fiber and sizing	CT	CT200L-200	CM, 3K

SGL, SGL Carbon, Germany; CT, CARBO-TEX, Germany; SB, stretch-broken yarn; CM, multifilament roving. Except for SB (do not contain sizing), all fabrics were pyrolytically desized (N_2 atmosphere). SB_{high} and CM_{high} are not commercially available and were obtained from $SB_{moderate}$ and $CM_{moderate}$ by further graphitization in a muffle furnace under argon atmosphere at 2,800°C, 30 min holding time.

[a] The T300 standard fabric was fabricated from fiber Torayca® T300-40B and was mainly used to develop and evaluate a suitable desizing methodology.

range of fiber damage was 2.4–7.2%. Damaged fibers are referred to as "Dx" hereafter.

Desizing

In parallel to the screening of commercial CF for suitable material properties, a desizing method was established to be applicable to all CF based electrodes. Tested desizing methods were industrial washing agents (used according to manufacturer's protocols), Soxhlet extraction (removal of sizing by organic solvents) with acetone/20 cycles, as well as pyrolysis (burning off the sizing). Pyrolysis was identified as final method of choice and subsequently applied for all CF electrodes presented here. An inert process gas was chosen, since desizing under air may alter the CF surface (Morgan, 2005). This can lead to either negative effects when the fiber conductivity is affected, or positive effects when the surface chemistry is modified to be more hydrophilic. All fabrics were desized in a muffle furnace under N_2 atmosphere at 500°C, 20 min holding time. For single fibers, a continuous operation tube furnace (N_2 atmosphere) was used, which required differing operational parameters: 700°C with a retention time of 2–4 min depending on the fiber thickness. Quantitative control of desizing quality was performed via thermogravimetric analysis (TGA) in a TGA/DSC 1, Mettler Toledo, Germany. Samples were heated under N_2 atmosphere to 550°C within 110 min and the resulting weight loss was recorded. Qualitative control of desizing was performed via SEM (LEO 1450VP, Zeiss, Germany) with 15 kV accelerating voltage.

Chemical Surface Activation of Carbon Fibers

The two CM used for surface activation experiments were C T50-4.0/240-E100 (hereafter CT50) and Tenax® E HTS40-F13 (hereafter HTS40) from two different manufacturers. The material specifications of both fibers were comparable (**Table S1**), only the filament numbers resulted in different electrode fiber lengths (27 and 114 mm for CT50 and HTS40) to achieve a fixed filament surface area (300 cm^2) as a standardization parameter. The resulting electrical resistances of the fiber electrodes were 1.2 and 1.3 Ω for CT50 and HTS40, respectively. Desized fibers were activated by electrolysis or plasma treatment, both methods having industrial relevance regarding ease of process chain integration and scale-up. Operational parameters for electrolysis were 18% NH_3HCO_3, fiber connected to an external power supply as anode, graphite plate as counter electrode, applying 3 A/24 V for 240 s at 22°C. Plasma treatments were kindly conducted by Diener electronic GmbH & Co. KG, Germany; parameters were $3 \cdot 10^{-4}$ bar, continuous gas flow 30 sccm, 15 min using either oxygen, ammonia, or ambient air as process gas.

HTS40 fibers had shown a good performance in previous electrode screenings (single fiber BES, not shown). Therefore, they were selected as model fibers and were further characterized by contact angle and X-ray photoelectron spectroscopy (XPS) analysis. The contact angle measurement was conducted with a K100 SF (Krüss GmbH, Germany), which is designed for single carbon fibers (the fiber is pulled out from a wetting liquid and the contact angle is calculated from the resulting force). XPS survey spectra were recorded at a pass energy of 60 eV using a Phoibos 100 analyzer with a CCD detector (SPECS Surface Nano Analysis GmbH, Germany). High-resolution spectra of the C 1s, O 1s, and N 1s peaks were recorded at a pass energy of 20 eV.

General BES Setup and Analyses

For the preculture, *Shewanella oneidensis* MR-1 (ATCC® 700550™) was cultivated overnight in LB medium (LB Lennox, Carl Roth, Germany) at 30°C. For the bioelectrochemical experiments, the modified M4 medium (pH 6.8, solution conductivity 19 mS/cm) contained per liter: K_2HPO_4 2.21 g; KH_2PO_4 0.99 g; $NaHCO_3$ 0.168 g; $(NH_4)SO_4$ 1.189 g; NaCl 7.305 g; HEPES buffer 1.192 g; yeast extract 0.5 g; tryptone 0.5 g; $CaCl_2 \cdot H_2O$ 0.071305 g; 100x mineral mix stock as in Beg et al. (2012) 10 ml. 18 mM sodium D/L-lactate (60%$_{w/w}$ syrup, Sigma Aldrich, Germany) was used as carbon source and was added after autoclavation. Experiments were conducted at room temperature (recorded fluctuation 23.5–26°C). All potentials were controlled (potentiostats: VMP-3,

BioLogic Science Instruments, France; Ivium-n-Stat, Ivium Technologies, Netherlands; in-house designed handheld potentiostats controlled via the software tool Labview, Texas Instruments, TX, USA) at + 0.2 V against a $Ag/AgCl_{sat.KCl}$ reference electrode that was freshly prepared in-house prior to each experiment. Maximum electrical current density j_{max} was determined from one complete batch in single fiber BES. For fabric BES, up to 3 batches were run until the current generation did not increase any further, and j_{max} was determined considering all batches.

The optical density at 600 nm (OD_{600}), pH and concentrations of lactate and acetate (HPLC on Metab-AAC column, 300 × 7.8 mm, Isera GmbH, Germany; in 5 mM H_2SO_4 mobile phase, 0.6 ml/min, 30°C) were tracked for the whole experimental duration. Furthermore, selected bioelectrode samples were cut out and analyzed by scanning electron microscopy (SEM) with 10 kV accelerating voltage on a Zeiss DSM 982 Gemini microscope (Zeiss, Germany). The sample preparation procedure included fixation in 2.5% glutaraldehyde, storage in ethanol, and drying by hexamethyldisilazane, and sputtering with a 20 nm gold layer. Where reported, riboflavin concentrations of filtered (0.2 µm pore size) samples were analyzed spectrophotometrically in reference to a riboflavin standard (Carl Roth GmbH & Co. KG, Germany), excitation/emission 450/530 nm as reported in Lu et al. (2017a). Coulombic efficiencies (CEs) were calculated based on the incomplete lactate oxidation to acetate, yielding 4 electrons per molecule of consumed lactate, which *S. oneidensis* MR-1 performs stoichiometrically under anoxic conditions (Pinchuk et al., 2011).

Single Fiber BES

Single carbon rovings were configured in a loop-like structure and attached to graphite rods (grade EDM-3 (specific electrical resistivity 1.56 mΩ·cm), Ø 30 mm, Novotec, Germany) using conductive carbon cement (Leit-C, Sciences Services GmbH, Germany). Common adhesive tape delimited the desired immersed fiber length that performed as working electrode. The fiber length was normalized to a theoretical BET surface area of ∼300 cm^2 (calculated by considering single filaments as perfect solid cylinders), assuming that the available electrode surface area is the most crucial parameter for bacterial interaction (Chen et al., 2011; He et al., 2011). A longer graphite rod (grade EDM-3, Ø 30 mm, Novotec, Germany, immersed length 50 mm) was used as counter electrode. The reactors consisted of laboratory glass bottles of 100 ml working volume. Instead of a lid, a 3 mm thick butyl rubber served as septum for sampling and held the electrodes in place. PTFE tape was applied at the electrode-rubber contact points for additional sealing. The complete reactors were sterilized by standard wet autoclavation (1 bar, 121°C for min. 20 min) with exception for surface activated fibers, which were sterilized separately from the reactor by applying 70% ethanol (including the untreated controls). All reactors were filled with N_2-degassed medium in an anaerobic chamber to minimize the initial oxygen content in the system. These single fiber BES were run in triplicates or duplicates.

In deviation to the standard setup, fragile fibers of the filament break experiments (chapter Effect of Fiber Type on Bacterial Current Generation) were configured straight and stabilized by tooth picks as shown in **Figure 4**. In this case, the total fiber length of 12 cm (317 cm^2 filament surface) was split into two to fit in the reactor. The counter electrode was wrapped in a separator (0.2 µm Supor®-200 PES filter membrane, Pall Corporation, NY, USA) to prevent short-circuits between electrodes. T0 describes non-twisted fiber electrodes, while Tx fibers contain 12 twists of 180°. This way, T0 yielded an open electrode structure with freely floating single filaments, while Tx yielded a tight packing of the filaments and displayed a structure that was comparable to a commercial twisted yarn (**Figure 4**). The working volume was increased to 200 ml to fit the straight electrode and stirred at 100 rpm (50 mm magnetic stir bar) to enhance chemical species transport through the separator. An exemplary setup is shown in **Figure S2B**. The CEs of single fiber experiments were lower than in the plate reactors (chapter Fabric BES), around 26 ± 13% (n = 27) for the original setup and 7 ± 2% (n = 24) in the modified setup for broken fibers. The reduced CE was due to the lower electrode packing density—especially in the modified setup—and consequently electron loss to oxygen that slowly intruded into the headspace (**Figure S2A**). However, this oxygen was scavenged by a biofilm formed at the liquid-headspace interface (**Figure S2C**). This way, the single fiber setup still yielded filament current densities of one magnitude higher than comparable setups (∼1 vs. 0.13 $\mu A/cm^2_{filament}$ at the same poised potential in Lu et al., 2017a) and was appropriate for the investigation of fiber material properties independently from fabric level parameters such as weave density. However, overall biomass or mediator production could not be meaningfully connected with bacterial current generation. The modified single fiber BES were run in 6 biological replicates to compensate for possible influences by the low packing density.

Fabric BES

The working electrodes were constructed from 45 × 120 mm carbon fiber fabrics that were attached to graphite clamps. A graphite rod (grade EDM-3, Ø 30 mm, Novotec, Germany, immersed length 145 mm) was used as counter electrode. The flat-plate-type reactor consisted of two rectangular PEEK frames (10 × 148 × 55 mm) with glass walls that were pressed together along with a synthetic rubber gasket (EPDM Ø 6 mm, Hug Industrietechnik, Germany). Each of the frames held working/counter electrode and the reference electrode (**Figure S3**). A total working volume of 400 ml was recirculated at 20 ml/min between the reactor (net liquid volume 120 ml) and an external stirred recirculation bottle which allowed for mixing and continuous nitrogen sparging (∼0.5 L/min) of the electrolyte. All tubings were of low gas permeability and appropriate wall thickness (connection tubes: Norprene® A-60-G and pump tubes: Tygon® F-40-40-A, both ProLiquid GmbH, Germany; inner diameter 1.6/0.51 mm; wall thickness 1.6/0.9 mm; permeability for O_2 is 200/22 $cm^3/([cm\ Hg]\cdot 10^{-10})$ at 25°C, respectively]. CEs ranged around 43 ± 23% (n = 19), which are high for *S. oneidensis* based BES (literature values range from 10 to 40%; Watson and Logan, 2009; Rosenbaum et al., 2011; Kipf et al., 2013; Engel et al., 2019). Fabric BES were run in biological triplicates or duplicates.

TABLE 3 | Degrees of desizing after application of varying desizing methods for woven fabrics made from CF T300 (initial sizing amount 0.992%$_{w/w}$).

Desizing method	Process medium	Degree of desizing [%]
None	–	0
Pyrolysis	N_2	83.3
Soxhlet extraction	Acetone	73.8
	Ethanol	51.4
	Petroleum ether	16.0
Washing agents	Rucogen DFL-200 (Rudolf Group, Germany)	62.7
	Sulfaton D (Bozzetto GmbH, Germany)	57.5
	Tanaterge® Advance (Tanatex Chemicals, Netherlands)	70.7
	Propetal140/Sulfetal 4105 (mix) (Zschimmer & Schwarz, Germany)	44.8

Parameters were: Pyrolysis 500°C, 20 min; Soxhlet extraction 20 cycles; washing agents according to manufacturer's protocol. Degree of desizing expresses weight loss of a desized CF compared to the weight loss of the non-desized control as determined by TGA.

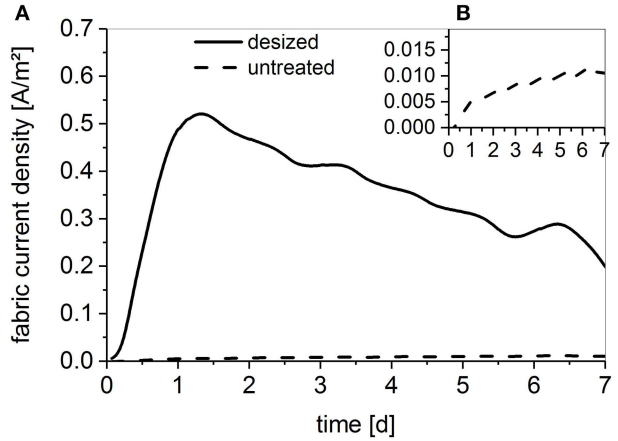

FIGURE 2 | (A) Bacterial current generation on T300 plain woven fabrics (average from $n = 2$); straight lines, pyrolytically desized (N_2 atmosphere); dashed lines, untreated (with intact sizing). Insert **(B)** shows untreated fabrics with smaller y-axis scale.

TABLE 4 | Physical characterization of surface activated HTS40 fibers.

Treatment	Contact angle [°]	O [at.%]	N [at.%]	C [at.%]
Not activated	76.53	5.46	1.81	92.73
NH_3 plasma	42.46	5.88	5.92	88.21
Electrolysis	15.68	15.27	6.64	78.09
Air plasma	9.26	12.63	3.06	84.31
O_2 plasma	8.52	18.11	1.77	80.13

All fibers were desized prior to surface activation. Contact angles were measured on a Krüss K100 SF (Wilhelmy method), atom contents via XPS. Other foreign atoms than O and N were not analyzed.

RESULTS

Establishing a Reliable Desizing Method for CF Electrodes

Standard T300 fabrics (**Table 2**) were used to establish a suitable desizing method for CF fabrics at the beginning of the project. The underlying fibers Torayca® T300-40B (**Table 1**) contain a common sizing type, i.e., epoxy resin or similar, but the exact compositions are company secrets (datasheet: "epoxy and phenolic compatible"). The amounts of sizing as analyzed by TGA were 0.992%$_{w/w}$ (percent weight of total CF + sizing weight), which matches the manufacturer's specifications (1%). The tested methods were pyrolysis under inert atmosphere, industrial washing agents, and Soxhlet extraction. All desizing methods were compared by means of their achieved degree of desizing (%), i.e., the weight loss of a desized CF compared to the weight loss of the non-desized control as determined by TGA (**Table 3**).

Desizing by pyrolysis achieved the highest degree of desizing. Regarding the electrode performance in BES, the pyrolytic removal of the sizing accounted to an ∼45-fold increase of j_{max} for a desized T300 fabric (**Figure 2**). The result was confirmed on single fiber level (∼10-fold increase of j_{max} by desizing, $n = 1$, not shown). One other method, Soxhlet extraction with acetone, achieved similarly high degrees of desizing as N_2 pyrolysis and was able to compete with the respective performance gain in the BES (not shown). However, Soxhlet extraction produces solvent waste and is more complicated for industrial scale-up. The washing agents were clearly inferior to pyrolysis and Soxhlet extraction, since the desized electrodes performed unsatisfactorily in the BES (not shown). The degrees of desizing were mainly consistent for another fiber type with epoxy-compatible resin (**Tables S1**, **S3**). We consequently applied N_2 pyrolysis as the desizing method of choice for all other CF (fabrics) in this work. Process parameters (e.g., retention time) were adapted, where necessary, in order to ensure a complete sizing removal.

Effect of Chemical Surface Activation of CF on Bacterial Current Generation

The two equivalent commercial PAN-based carbon fibers CT50 and HTS40 (**Table 1** and **Table S1**) were used for surface activation experiments. HTS40 fibers served as model fibers, which were additionally subjected to surface characterization by contact angle and XPS measurements.

Physical and Chemical Characterization of Surface Activated CF

All surface activation methods achieved a decrease in contact angle, i.e., increase in wettability, and introduced foreign atoms into the HTS40 fiber surface (**Table 4**).

Oxygen containing functional groups were introduced into the carbon surface by all methods. In NH_3 plasma treated samples, this amount was small and is unlikely related to the high-purity process gas. It was rather related to previously adsorbed atmospheric O_2, which appeared mainly as C-O bonds

TABLE 5 | High-resolution XPS spectra analysis of surface activated HTS40 fibers.

	C 1s				N 1s			O 1s		
Treatment	**C-C**	**C-O**	**O-C=O**	**C=O**	**N-C**	**N-?**	**N-O**	**O=C**	**O-C**	**O-N**
Not activated	75.73	13.14	–	3.86	1.4	0.41	–	2.83	2.83	–
NH_3 plasma	66.77	15.95	–	5.49	5.92	–	–	0.69	4.51	0.68
Electrolysis	57.45	12.61	–	8.03	5.74	–	0.9	4.97	10.3	–
Air plasma	60.22	13.55	4.03	6.51	2.64	0.42	–	10.35	2.28	–
O_2 plasma	52.62	13.05	7.04	7.42	1.77	–	–	7.41	10.7	–

Values are given in [%] of the C 1s, N 1s, and O 1s peaks, respectively. N-? refers to other atoms than C and O, which have not been analyzed in more detail.

(hydroxyl groups, since no O-C=O was observed) and, in small portions, in N-O bonds (e.g., imine-N-oxide) in the high-resolution spectra (**Table 5**). All other treatment methods preferably introduced O in the form of C=O or O-C=O (carboxyl/carbonyl groups). Nitrogen containing groups were introduced in lower quantities than oxygen containing groups. This was achieved by all treatments but the O_2 plasma treatment, which even removed a small portion of N from the original fiber surface. Both NH_3 plasma and electrolysis were similarly effective at introducing N as N-C (e.g., amine, imine, pyridone) and in small portions also N-O bonds (e.g., imine-N-oxide).

Characterization of Surface Activated CF in Single Fiber BES

Figure 3 shows the summarized results from single fiber BES (unstirred 100 mL setup, combined filament surface fixed at 300 cm^2). The total number of biological replicates was $n = 3$ for all treatments, except for electrolysis with $n = 2$. Besides j_{max}, the startup current density j_{12h} is given, which assesses effects on the initial bacteria-electrode interaction. The latter is expressed as current density after 12 h, since the initial current increase for the used BES varied in its characteristics, e.g., linear or exponential increase, and the calculation of a specific rate was not possible. A high standard deviation was observed for the activated fiber electrodes. This variation might be connected to the presumable short-term stability of introduced foreign atoms and residues in the carbon filament surface. Although empirical values are not collected in industry due to limited necessity (fibers are sized immediately after surface activation), chemical alterations of the introduced residues is expected by professionals within in the range of several hours to days (Jones and Sammann, 1989). This time frame is short compared to the preparation of the BES setup which takes at least 1.5 days from fiber activation until the start of the experiment. As a consequence, the variances of the samples are probably unequal; and the Welch corrected *t*-test was therefore chosen for statistical significance analysis (significance level < 0.05).

Untreated CT50 and HTS40 achieved similar j_{max} (**Figures 3C,D**), which is in correspondence with their equivalent electrode surfaces and material properties (**Table 1** and **Table S1**), but j_{12h} was higher with HTS40. For HTS40 (**Figures 3B,D**), neither j_{12h} nor j_{max} were significantly altered by any of the activation methods, although air plasma and electrolysis showed some promising trend regarding j_{max} and j_{12h}, which might have been just masked by the high variance of the replicate values.

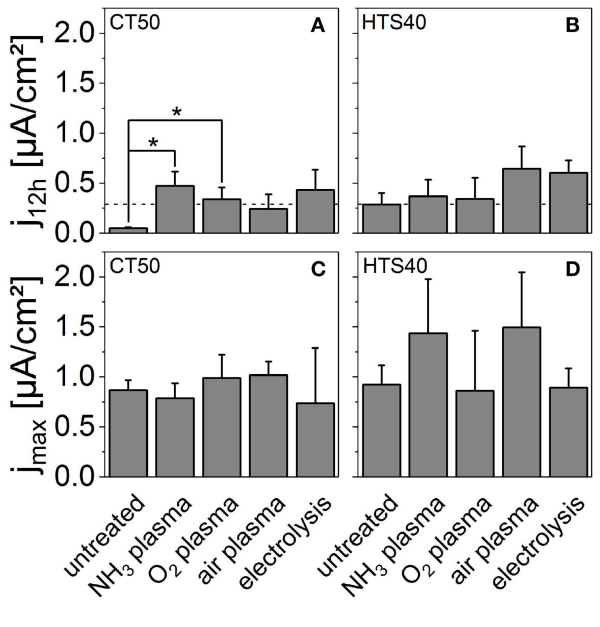

FIGURE 3 | Performances of single carbon fiber electrodes CT50 **(A,C)** and HTS40 **(B,D)**; influence of different surface activation methods on startup current density **(A,B)** and maximum current density **(C,D)**, both normalized to filament surface area (300 cm^2). Non-activated controls are only desized. The j_{12h} level of the untreated HTS40 control is indicated by the dashed horizontal line. Asterisks mark significance levels with $p < 0.05$ (Welch corrected two-sampled *t*-test).

For CT50 (**Figures 3A,C**), j_{12h} was significantly enhanced after surface activation for NH_3 and O_2 plasma ($p < 0.05$) and reached the level of the untreated HTS40. Also for the other two methods all single values were higher than those of untreated fibers, but *P*-values were above 0.05. However, we considered all activation methods capable of enhancing j_{12h} in CT50. Due to the high variance within replicates, quantitative comparisons between the methods were not possible.

Elucidating the High Performance of Stretch-Broken Yarn Based Electrodes

The two features that distinguish the less common SB from the classic CM are free filament ends (**Figure S4**) and a yarn twist.

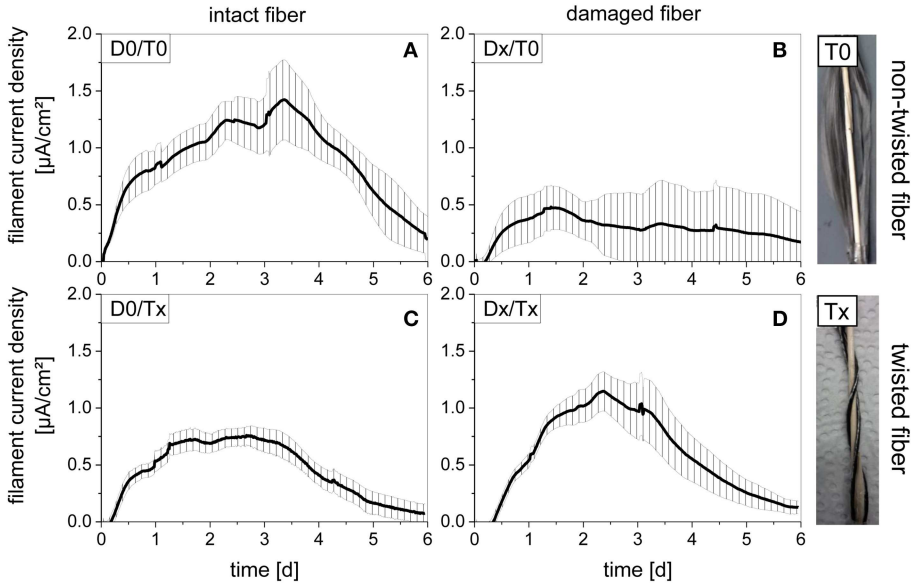

FIGURE 4 | Current density normalized to combined filament surface in single fiber BES (HTS40 CM); **(A,C)** intact fibers and **(B,D)** fibers with introduced breaks. Legend: D0, intact; Dx, damaged; T0, non-twisted **(A,B)**; Tx, twisted yarn **(C,D)**. One electrode consists of two 6 cm fiber pieces. Shown are average values and standard deviations from 6 replicates. Photographs (taken by F. Schmitz) show a representative fiber electrode for non-twisted yarns T0, i.e., open display of filaments, and twisted yarns Tx, which resemble commercial twisted yarns.

SB fabrics had yielded outstanding current densities and material utilization efficiencies in a previous screening (**Figure S1**). We aimed at systematically investigating the influence of the fiber macrostructure (SB vs. CM) on the performance of CF based electrodes in BES.

Effect of Fiber Type on Bacterial Current Generation

Free filament ends and yarn twist were introduced into HTS40 fibers (12K CM) at lab scale in order to reconstruct the industrial production of stretch-broken yarns from multifilaments. Identical CM without tribological treatment served as intact control electrodes. **Figure 4** shows the resulting current generation for all four D/T combinations (D0, intact; Dx, damaged; T0, non-twisted; Tx, twisted CM). In the open fiber structure of T0, the introduced filament breaks reduced current production by 58% (average). In tightly twisted fibers Tx, filament breaks enhanced j_{max} by an average of 41% compared to the intact (twisted) control (Dx/Tx vs. D0/Tx). The twist also resulted in a substantially increased j_{max} (by 93%) and decreased standard deviation compared to the untwisted damaged fibers Dx/Tx vs. Dx/T0. In the intact control, however, the introduction of a twist led to a reduced j_{max} by ∼43% (D0/Tx vs. D0/T0).

For a deeper understanding of the link between free filament ends and bacterial current generation, confocal scanning laser microscopy (CSLM) imaging of different fiber electrodes was performed (see **Supplementary Information**). However, it turned out challenging to find free filament ends in the bulk multifilament and only few were analyzed. The biofilm formation seemed uniform over the filament surface including free ends (**Figure S5**). The single fiber BES setup was not optimized for investigations of the mediated electron transfer due to side reactions with headspace oxygen (**Figure S2A**) and we rather went on to elucidate these mechanisms on fabric level.

Effect of Filament Conductivity and Fiber Type on Bacterial Current Generation

A set of related commercial fabric types was selected in order to verify the role of free filament ends in stretch-broken yarns and elucidate the mechanisms behind their good performance. Besides the filament macrostructure, we selected fabrics with different carbon atom content C [at.%] to vary filament conductivity, which was not possible to study at fiber level because of mechanical instability of graphitized fibers. The model electrodes were commercial SIGRATEX® fabrics made from CM or SB along with their equivalent graphitized products (**Table 2** and **Table S2**, all SGL Carbon, Germany). The samples will be referenced to as SB_{low} and $SB_{moderate}$ (SB = stretch-broken) and CM_{low} and $CM_{moderate}$ (CM = continuous multifilament); with the subscripts expressing the difference in carbon content. Additionally, both $SB_{moderate}$ and $CM_{moderate}$ fabrics were subjected to further graphitization at a higher temperature of 2,800°C, since highly graphitized versions of these fabric were not commercially available. These fabrics were referred to as SB_{high} and CM_{high}. Consequently, we obtained samples with ∼92, > 99, and > 99.9 C at.%. Note that CM and SB fabrics cannot be directly compared, since they differ in their material characteristics (precursor fiber, manufacturing process, filament diameter, and fabric areal weight). **Figure 5** summarizes the results for maximum OD_{600}, maximum current density j_{max} and start-up current density j_{12h} of SB fabrics. The

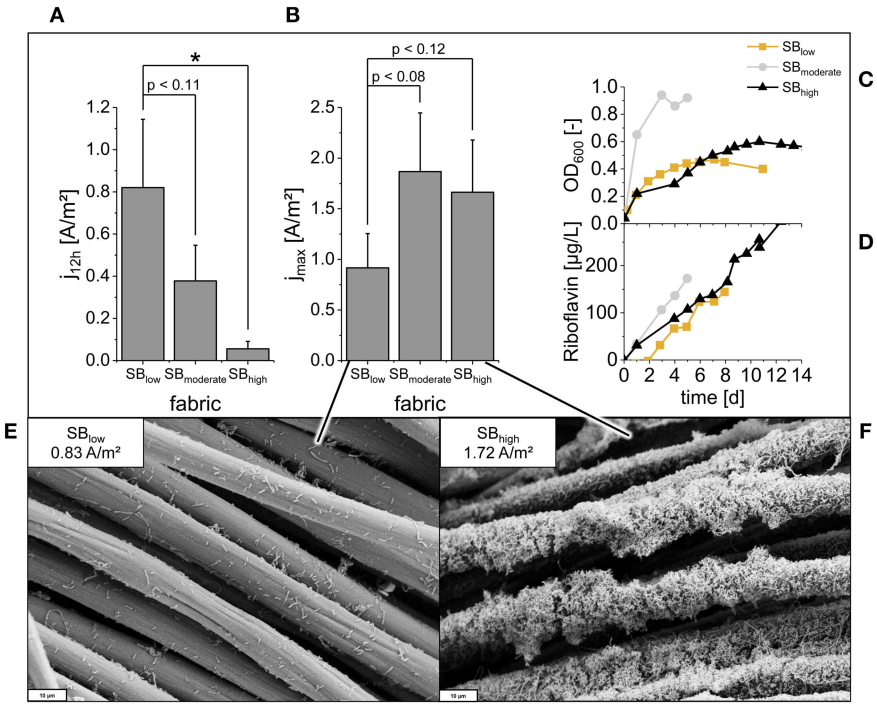

FIGURE 5 | (A) Maximum current densities j_{max}, **(B)** startup current density j_{12h} (both normalized to 2D projected surface area), **(C)** examples for planktonic growth, and **(D)** riboflavin production achieved with fabric electrodes made from stretch-broken yarn (SB) with increasing carbon contents (low, moderate, high). **(A,B)** Are average values and standard deviations from triplicates **(C,D)**, are representative single experiments. Asterisks mark significance levels of $p < 0.05$ (two-sampled *t*-test), other *p*-values lower than 0.12 are also given. **(E,F)**: SEM images of example fabrics SB_{low}/SB_{high}, which were taken after 15 days from reactors sharing identical inocula; scale bars = 10 µm. Current density values displayed in images **(E,F)** correspond to the sampling time point (end of experiment).

same overview is given for CM fabrics in **Figure 6**. Example full electrochemical datasets for both fabric types are given in **Figures S6**, **S7**, respectively.

In the case of stretch-broken fabrics, a substantial increase in maximum current density j_{max} (by average of 100%) and $OD_{600-max}$ (by average of 60%) was linked to an increased filament conductivity from SB_{low} to $SB_{moderate}$ (**Figure 5B**). With the second graphitization step from $SB_{moderate}$ to SB_{high}, j_{max} stayed at similar levels as $SB_{moderate}$ and the $OD_{600-max}$ even fell back to levels of SB_{low} (**Figure 5C**). In total, the increased carbon content from SB_{low} to SB_{high} came along with a progressive limitation on initial current generation (reduction of j_{12h} by ∼50 and 90% for $SB_{moderate}$ and SB_{high}, respectively, **Figure 5A**). This clear trend was not correlated with planktonic growth, which was similar for SB_{low} and SB_{high}, but much enhanced—both regarding growth rate and $OD_{600-max}$ – for $SB_{moderate}$ (**Figure 5C**). The production of the electron mediator riboflavin was similar in SB of all carbon contents, and only slightly enhanced in $SB_{moderate}$ (**Figure 5D**).

Two electrode samples, which were taken from reactors sharing identical inoculum and identical starting time points, were selected for SEM imaging. The carbonized SB_{low} (**Figure 5E**) displayed the typical thin biofilm (isolated single cells) of *S. oneidensis* on carbon based electrodes under anaerobic conditions, which has been observed in our lab and elsewhere (Rosenbaum et al., 2010). In contrast, the final biomass was exceptionally dense on the highly graphitized SB_{high} fabric (**Figure 5F**), displaying multiple cell layers. The cells were tightly packed in the biofilm and by this, formed continuous connections between individual filaments. Intruding oxygen can be responsible for an increased biomass on the electrode as well as planktonic growth and flavin production (TerAvest et al., 2014). However, the CE for the respective SB_{high} reactor was 44%, which is higher than results from other studies that claim close to anaerobic conditions (Rosenbaum et al., 2011; Engel et al., 2019), and it was also very close to the average CE of the plate reactor setup. We consequently consider the extraordinary biofilm on SB_{high} to be truly related to the electrode properties.

In CM fabrics, increased filament conductivity is not boosting j_{max}, and even has an adverse effect in the case of $CM_{moderate}$ fabrics (**Figure 6B**). The latter was in accordance with a slightly reduced number of cells on $CM_{moderate}$ compared to CM_{low} samples (**Figures 6E,F**). In this case, the handling of the graphitized fabric might have introduced some unintended breaks in the brittle filaments, which increased the fabric resistivity. In general, a reduced startup current production with increasing carbon content was observed, the decrease being especially strong between CM_{low} and the first graphitization step $CM_{moderate}$ (**Figure 6A**, reduction of j_{12h} by ∼85 and 93% for $CM_{moderate}$ and CM_{high}, respectively). This is also

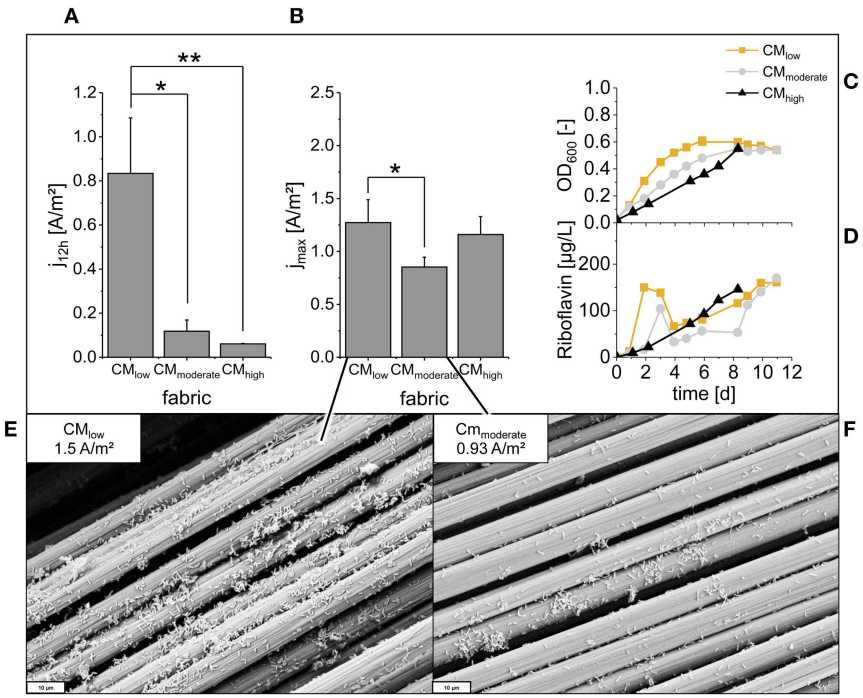

FIGURE 6 | (A) Startup current density j_{12h} **(B)**, maximum current densities j_{max} (both normalized to 2D projected surface area) **(C)**, planktonic growth, and **(D)** riboflavin production achieved with fabric electrodes made from continuous multifilament (CM) with increasing carbon contents (low, moderate, high). **(A,B)** Are average values and standard deviations from triplicates (duplicates for CM_{high}), **(C,D)** are representative single experiments. Single/double asterisks mark significance levels of $p < 0.05$ and $p < 0.01$ (two-sampled *t*-test). **(E,F)**: SEM images of the of CM_{low}/$CM_{moderate}$ electrodes, which were taken after 13 days from reactors sharing identical inocula; scale bars = 10 µm. Current density values displayed in images **(E,F)** correspond to the sampling time point (end of experiment).

correlated to a faster initial planktonic growth in the CM_{low} reactor compared to the other two reactors, while the final OD_{600} was not affected and reached similar values in all CM levels (**Figure 6C**). The fast current generation of CM_{low} was also accompanied by a fast initial increase in riboflavin concentration. After j_{max} was reached with CM_{low}, riboflavin levels dropped sharply in all 3 replicates, to continue with a slower increase after the drop (**Figure 6D**). $CM_{moderate}$ showed a similar trend of increase-drop-increase of riboflavin levels, but less pronounced. In CM_{high}, the riboflavin levels increased continuously corresponding to the OD_{600} increase.

DISCUSSION

CF based textile fabrics are a popular electrode material for BES, primarily because they offer a large surface area for bacteria-electrode interactions. However, the growing CF market and new applications have created a broad spectrum of many more tunable material characteristics. Growing production capacities result in dropping prices, which may soon allow for economic electrode designs for BES (Morgan, 2005; Das et al., 2016). In order to assess the specific effect of characteristics like the specific electrical resistance of a CF type on the final electrode performance in BES, suitable single fiber and fabric samples were selected and/or modified to enable a systematic investigation.

Pure cultures of the electroactive model organism *S. oneidensis* MR-1 were used for the performance screening of CF electrodes. The multiple, consecutive experiments performed in this work require a reliable inoculum performance over a certain period of time. While electroactive mixed cultures require an advanced level of practical experience in order to maintain a stable inoculum, the use of pure cultures provides a straightforward approach. *S. oneidensis* was chosen over other electroactive bacteria like e.g., *G. sulfurreducens* for its comparatively fast growth, easy handling and robust anodic electroactivity even in the presence of oxygen leaking into the system; all of which reduced the complexity and time-consumption of the experimental setups presented here. The inherent low current densities of *S. oneidensis* (Kipf et al., 2014) do not affect the main purpose of the tests to compare electrode materials against each other.

Desizing Is an Important Step in the Production of Carbon Fiber Based Electrodes

While SB fabrics get their sizing removed before the last production step, CM fabrics are always coated by a sizing (**Figure 1**). Our investigations highlight the importance of proper desizing for standard and cheap commercial CM fabrics. The impact of the electrically insulating sizing on the electrode

performance is especially great for large and voluminous carbon fiber based electrodes. Here, the desizing method has to be adapted (e.g., by prolonging process times) and complete removal of the sizing has to be ensured via e.g., TGA, as demonstrated here. Our results are supported by the work of other authors, who mentioned necessary "pretreatment" methods in order to turn "carbon mesh" (presumably a CM fabric) into electrochemically active anodes for power production in MFCs (Wang et al., 2009). The authors used TGA to follow the effect of their pretreatment and recorded a weight loss. The described thermal and solvent-based (acetone) cleaning procedures represent common industrial desizing methods and were all able to drastically increase the MFC performance over MFCs with an untreated "carbon mesh" on short term operation (17 days). The other material, which is referred to as "carbon cloth," did not have to be "pretreated" (presumably a PANOX SB fabric, but unfortunately no material specifications were provided).

Among the presented options, we recommend the use of thermal desizing as a waste-free method. Furthermore, the gaseous process medium leaves a clean fabric surface without the need for extensive washing steps. The thermal desizing can easily be scaled and implemented into existing process chains (technically, it is not much different from the equipment for carbonization). In a broader context, the thermal method could be used for a combined desizing and chemical surface activation by simply adapting the process gas. This can be O_2 or ambient air, or as shown by Wang et al. (2009), also ammonia modifies the carbon surface. In these cases, however, a strict process control is mandatory in order to only modify the filament surface and maintain good mechanical and electrical properties of the carbon fibers.

Chemical Modification of the Carbon Surface May Enhance Electrode Performance in Certain Cases

According to our results, the effect of surface activation cannot be generalized and depends on the fiber. This is not surprising in the light of the great spectrum of commercial products and their material properties. Although identical treatments were applied to the almost equivalent fibers HTS40 and CT50, the effects were only marginal in HTS40, but strong in CT50 CF. In this case, the increase of j_{12h} for pre-treated fibers could be correlated with an increase in hydrophilicity. The same effects on fiber surface and j_{12h} were achieved by increasing the C-content (**Figures 5A**, **6A**). Furthermore, slightly elevated arithmetic means of j_{12h} of air plasma and electrolytically activated HTS40 CF compared to others were observed, which fit to high amounts of both N and O containing functional residues introduced by these treatments. A higher diversity of functional residues probably offers more options for bacterial cells and biochemical molecules to interact with the filament surfaces in the beginning of the experiment.

The relationship between enhanced BES startup and a hydrophilic electrode surface has also been observed by Guo et al. (2013), who attributed a faster startup of mixed culture bioanodes to increased surface hydrophilicity of activated glassy carbon. In their case, the final current densities were also altered and high currents have been related to an increased selectivity of the activated surfaces for electroactive microorganisms. In other studies, hydrophilicity and positive charged N and O containing functional groups always enhanced the startup of the BES (and hydrophobic surfaces prolonged startup) (Flexer et al., 2013; Guo et al., 2013, 2014; Li et al., 2014; Liu et al., 2014; Santoro et al., 2014; Cornejo et al., 2015), but only in few cases, a long-term enhancement on j_{max} was observed, and if so, only for mixed culture derived systems (Guo et al., 2013, 2014; Liu et al., 2014). In this work, a pure culture of electroactive microorganisms was used. Hence, the lack of competitiveness between microorganisms might be the reason for lacking effect of surface activation on j_{max}. Consequently, the additional surface activation is not expected to improve the overall performance of pure culture BES. The only benefit is the faster startup of freshly inoculated electrodes, which is mainly relevant for batch operation.

Finally, a closer look reveals that j_{12h} of the CT50 was promoted to the level of an untreated HTS40 after surface activation (**Figures 3A,B**). We postulated that the cause for the difference has to originate in the production process parameters, which certainly differ between manufacturers. These may generate e.g., activated surfaces (prior to sizing, **Figure 1**) that even stay chemically stable during the desizing treatment applied for our BES experiments. We conclude that a thorough selection of commercial fibers and close communication with the manufacturers may possibly replace the second surface activation that we intended to add to the general production chain of carbon fibers.

Synergistic Effect of High Filament Conductivity and Free Filament Ends Boosts Bacterial Current Generation

In a perfect graphite crystal, the electrical conductivity along the planes is 10^4 fold higher than perpendicular to the planes (Dutta, 1953). In CF, the anisotropy is weaker, since the graphitic planes are only close to parallel and below 100 C at.%. However, the electrical conductivity may still exceed one order of magnitude in-filament direction compared to through-filament direction (Windhorst and Blount, 1997). The discrepancy is higher in graphitized fibers, which are closer to a perfect graphitic structure. In the most common type of carbon fibers, the multifilament roving (CM), only the longitudinal filament surface is available for bacterial interaction, whereas stretch-broken yarns (SB) allow for a better accessibility of the filament conductivity at the cross sections. We have demonstrated that these free filament ends are able to enhance bacterial current generation when introduced into CM single fiber electrodes (configuration Tx/Dx, chapter Effect of Fiber Type on Bacterial Current Generation).

Moving from single fiber to fabric level, we could further elaborate on the role of free filament ends in SB (chapter Effect of Filament Conductivity and Fiber Type on Bacterial Current Generation). With this yarn type, an increased filament conductivity was responded by an enhanced bacterial current generation (**Figure 5B**). In CM fabrics, which lack free filament

ends, such an effect was consequently not observed (**Figure 6B**). Likewise to our findings in SB fabrics, Baudler et al. (2015) have shown that the current generation of electroactive biofilms can be enhanced by using highly conductive materials like silver and copper instead of carbon (given that electrode potentials are low enough to prevent corrosion). Hence, the electron discharge to the electrode surface does represent a bottle neck in bacterial current generation despite their low turnover rates compared to e.g., metal electrocatalysts. It is still remarkable, though, to which high extent (∼+ 100%) the negligible surface area of free filament ends influenced the overall electrode performance compared to the current increase of about 40% for switching from a graphite to a copper electrode reported by Baudler et al. (2015). The μm-scale roughness of SB is not considered to be responsible for the high current generation, since the scale is not substantially different from the biofilm thickness (Moß et al., 2019). The beneficial effects of (1) free filament ends, and (2) elevated filament conductivity are probably synergistic, making graphitized SB fabrics an excellent electron sink, which triggers an efficient extracellular electron transfer.

This consideration is supported by a fast initial planktonic growth compared to a slower current increase in the moderately graphitized fabric $SB_{moderate}$ (**Figure S6**). It is known that both planktonic cells and biofilms of *S. oneidensis* MR-1 rely on soluble electron mediators for their extracellular electron transfer (Marsili et al., 2008). The soluble riboflavin in $SB_{moderate}$ was only slightly enhanced over SB_{low}, but the concentration in the biofilm was possibly very high. Furthermore, the high amount of planktonic cells (**Figure 5C**) that can discharge electrons to these flavins might already explain high j_{max} in $SB_{moderate}$. When $SB_{moderate}$ was further graphitized to SB_{high}, the role of the planktonic biomass decreased but instead, a multilayer biofilm was observed (**Figure 5F**). The link between high current densities and thick biofilms has been also observed in mixed culture biofilms (Santoro et al., 2014; Baudler et al., 2015), but it is unusual for anaerobically grown *S. oneidensis* (Rosenbaum et al., 2010). With the electrode being the main electron acceptor in this system, the thick biofilm on SB_{high} could only be sustained by an efficient interaction of the bacteria with the electrode. Since we have not analyzed the direct electron transfer via membrane-bound c-type cytochromes, the exact mechanism remains unclear. A high mediator concentration in the biofilm with probably enhanced electron discharge toward the electrode surface might serve as explanation. The presence of long cell bodies (visible in the bottom right section of **Figure 5F**) is also a hint that *S. oneidensis* cells formed efficient links between each other to fully exploit the free filament ends. Furthermore, the membrane-nanowires of *S. oneidensis* can exceed several cell lengths and might have added up to the inter-cell connections (Pirbadian et al., 2014).

Despite the high j_{max} of graphitized SB fabrics, the adverse effect of elevated C-content on startup current j_{12h} cannot be neglected. Since the effect was independent of the fiber type, it can be related to the increased purity of the CF surface, i.e., its increased hydrophobicity (**Figures 5A**, **6A**). This even seemed to affect j_{max} as observed in the graphitized $CM_{moderate}$ fabrics (**Figure 6B**). In SB fabrics, hydrophobicity probably counteracted increased filament conductivity, and consequently a higher graphitization (SB_{high}) than the commercial level ($SB_{moderate}$) did not further push j_{max}. One might argue that the prolonged startup time will not be critical for the actual applications or only relevant for batch operations, since the final OD_{600} was not significantly affected (**Figure 5C**). However, there are more indications in literature that a hydrophobic electrode surface could reduce final current densities due to reduced selectivity for electroactive microorganisms from mixed culture inocula (Guo et al., 2013). A surface activation of graphitized SB fabrics might be a technical solution, since it can reduce the startup time (chapter Characterization of Surface Activated CF in Single Fiber BES), but the additional process steps would clearly add up to the electrode cost. In summary, we propose (moderately) graphitized SB fabrics as a viable electrode material mainly for pure culture BES, especially when continuously operated. The configuration in a woven fabric allows for further engineering of highly porous, yet mechanically stable electrodes, which are useful for good mass transfer in stirred reactors. For large-scale mixed culture BES applications, however, CM fabrics might be a more economic choice. But also for CM, we show that the configuration of the fabric determines whether the full potential of the fibers can be exploited. The best configuration in the single fiber BES was the open configuration D0/T0 (**Figure 4**), which allows for an optimized accessibility of single filaments, but is impractical for most applications. Fabrics that come closest to conserve this configuration are thin unidirectional non-wovens or woven fabrics of low yarn input.

SUMMARY AND OUTLOOK

Carbon fiber woven fabrics are a versatile electrode material that can be customized with a high reproducibility. Their excellent trade-off between good mechanical stability, flexibility, electrical conductivity, and material exploitation makes them suitable materials for the wide variety of novel BES applications. This study shows that the potential of carbon fiber fabrics can be comprehensively exploited and there are several factors to be customized for the specific BES application. In the light of the diversity of CF and thereof derived products, we recommend that BES studies using such electrodes report the specific CF material properties and the applied treatments such as desizing and surface activation. This way, research results may be translated to a comprehensive adaptation of process parameters and push forward the industrial implementation of BES-oriented CF product lines. With the above results, we focused on identifying the relevant fiber material properties and found graphitized, stretch-broken fiber based woven fabrics to be interesting for stirred pure culture BES. For low-tech applications in highly competitive technological fields, such as wastewater treatment, the use of less costly fabrics based on continuous multifilament rovings is recommended. For these fabrics, we point out that a proper removal of the sizing is crucial for efficient bacteria-electrode interaction and should be verified by, e.g., TGA analysis. We also looked into different chemical surface activation methods in order to increase the biocompatibility of

the carbon fiber surface. The most suitable methods are such that introduce both nitrogen and oxygen containing residues and increase the hydrophilicity of the carbon surface. We could not confirm an impact of surface activation on maximum current density, but only on the reduction of startup time. However, the effect depended strongly on the fiber and we found that there are commercial fibers that already come with sufficiently biocompatible surfaces. We concluded that a surface activation is of limited use for pure culture BES lacking microbial competition during startup. Nevertheless, it may be useful for mixed culture BES to enhance selection of highly electroactive biofilm members.

DATA AVAILABILITY

All relevant data are included in this manuscript and the corresponding **Supplementary Material**.

AUTHOR CONTRIBUTIONS

LP coordinated the study, designed, conducted and analyzed all BES experiments, and prepared the manuscript. PH coordinated and performed the fiber and fabric material selection, supervised and analyzed their physical characterization experiments, and co-prepared the manuscript. SS coordinated and supervised the desizing, surface activation experiments and revised the manuscript. VR conducted SEM sample preparation and analyses in chapter Effect of Filament Conductivity and Fiber Type on Bacterial Current Generation and Revised the Manuscript. TG advised on all CF work, discussed results, and revised the manuscript. LB discussed the work and revised the manuscript. MR conceived the work, advised on the experimental plan, discussed experiments, and revised the manuscript.

FUNDING

The IGF research project (IGF Grant No. 19047 N) of the research association Forschungskuratorium Textil e.V., Reinhardtstraße 14-16, 10117 Berlin was funded via the AiF within the program for supporting the industrial Collective Research (IGF) from funds of the Federal Ministry of Economic Affairs and Energy (BMWi). Further funding was provided by the German Federal Ministry of Education and Research (BMBF) under Grant No. 031B0087A.

ACKNOWLEDGMENTS

We are very thankful to Almut Schwenke (SGL Carbon, Germany), who provided CF materials, discussed their properties, provided graphitization services, and revised the manuscript. We are also grateful to Sebastian Wittig (Diener electronic GmbH & Co. KG, Germany) for providing plasma activation services and expertise regarding surface activation. Furthermore, we wish to thank Myong-Hun Jung, Tobias Bolz, and Felicitas Schmitz for their great contribution to the experimental work. We also thank Jürgen Klimke (CARBO-TEX GmbH, Germany), who provided T300 fabrics and was always available for helpful advice.

SUPPLEMENTARY MATERIAL

The Supplementary Material for this article can be found online at: https://www.frontiersin.org/articles/10.3389/fenrg.2019.00100/full#supplementary-material

REFERENCES

Alexander, M. R., and Jones, F. R. (1996). Effect of electrolytic oxidation upon the surface chemistry of type A carbon fibres: III. Chemical state, source and location of surface nitrogen. *Carbon* 34, 1093–1102. doi: 10.1016/0008-6223(96)00061-9

Artyushkova, K., Cornejo, J. A., Ista, L. K., Babanova, S., Santoro, C., and Atanassov, P. (2015). Relationship between surface chemistry, biofilm structure, and electron transfer in *Shewanella* anodes. *Biointerphases* 10:019013. doi: 10.1116/1.4913783

Baudler, A., Schmidt, I., Langner, M., Greiner, A., and Schröder, U. (2015). Does it have to be carbon? Metal anodes in microbial fuel cells and related bioelectrochemical systems. *Energy Environ. Sci.* 8, 2048–2055. doi: 10.1039/C5EE00866B

Beg, Q. K., Zampieri, M., Klitgord, N., Collins, S. B., Altafini, C., Serres, M. H., et al. (2012). Detection of transcriptional triggers in the dynamics of microbial growth: application to the respiratorily versatile bacterium *Shewanella oneidensis*. *Nucleic Acids Res.* 40, 7132–7149. doi: 10.1093/nar/gks467

Blanchet, E., Erable, B., De Solan, M.-L., and Bergel, A. (2016). Two-dimensional carbon cloth and three-dimensional carbon felt perform similarly to form bioanode fed with food waste. *Electrochem. Commun.* 66, 38–41. doi: 10.1016/j.elecom.2016.02.017

Champigneux, P., Renault-Sentenac, C., Bourrier, D., Rossi, C., Delia, M.-L., and Bergel, A. (2018). Effect of surface nano/micro-structuring on the early formation of microbial anodes with *Geobacter sulfurreducens*: experimental and theoretical approaches. *Bioelectrochemistry* 121, 191–200. doi: 10.1016/j.bioelechem.2018.02.005

Chen, S., Hou, H., Harnisch, F., Patil, S. A., Carmona-Martinez, A. A., Agarwal, S., et al. (2011). Electrospun and solution blown three-dimensional carbon fiber non-wovens for application as electrodes in microbial fuel cells. *Energy Environ. Sci.* 4, 1417–1421. doi: 10.1039/c0ee00446d

Cornejo, J. A., Jopez, C., Babanova, S., Santoro, C., Artyushkova, K., Ista, L., et al. (2015). Surface modification for enhanced biofilm formation and electron transport in *Shewanella* anodes. *J. Electrochem. Soc.* 162, H597–H603. doi: 10.1149/2.0271509jes

Das, S., Warren, J., West, D., and Schexnayder, S. M. (2016). *Gobal Carbon Fiber Composites Supply Chain Competitiveness Analysis*. Energy Transportation Science Division, Oak Ridge National Laboratory. doi: 10.2172/1254094

Donovan, C., Dewan, A., Heo, D., Lewandowski, Z., and Beyenal, H. (2013). Sediment microbial fuel cell powering a submersible ultrasonic receiver: new approach to remote monitoring. *J. Power Sources* 233, 79–85. doi: 10.1016/j.jpowsour.2012.12.112

Dutta, A. K. (1953). Electrical conductivity of single crystals of graphite. *Phys. Rev.* 90, 187–192. doi: 10.1103/PhysRev.90.187

Engel, C., Schattenberg, F., Dohnt, K., Schröder, U., Müller, S., and Krull, R. (2019). Long-term behavior of defined mixed cultures of *Geobacter sulfurreducens* and *Shewanella oneidensis* in bioelectrochemical systems. *Front. Bioengineer. Biotechnol.* 7:60. doi: 10.3389/fbioe.2019.00060

Ewing, T., Ha, P. T., and Beyenal, H. (2017). Evaluation of long-term performance of sediment microbial fuel cells and the role of natural

resources. *Appl. Energy* 192, 490–497. doi: 10.1016/j.apenergy.2016.08.177

Flexer, V., Marque, M., Donose, B. C., Virdis, B., and Keller, J. (2013). Plasma treatment of electrodes significantly enhances the development of anodic electrochemically active biofilms. *Electrochim. Acta* 108, 566–574. doi: 10.1016/j.electacta.2013.06.145

Gajda, I., Greenman, J., and Ieropoulos, I. A. (2018). Recent advancements in real-world microbial fuel cell applications. *Curr. Opin. Electrochem.* 11, 78–83. doi: 10.1016/j.coelec.2018.09.006

Guo, K., Freguia, S., Dennis, P. G., Chin, X., Donose, B. C., Keller, J., et al. (2013). Effects of surface charge and hydrophobicity on anodic biofilm formation, community composition, and current generation in bioelectrochemical systems. *Environ. Sci. Technol.* 47, 7563–7570. doi: 10.1021/es400901u

Guo, K., Soeriyadi, A. H., Patil, S. A., Prévoteau, A., Freguia, S., Gooding, J. J., et al. (2014). Surfactant treatment of carbon felt enhances anodic microbial electrocatalysis in bioelectrochemical systems. *Electrochem. Commun.* 39, 1–4. doi: 10.1016/j.elecom.2013.12.001

He, G., Gu, A., He, S., Schröder, U., Chen, S., and Hou, H. (2011). Effect of fiber diameter on the behavior of biofilm and anodic performance of fiber electrodes in microbial fuel cells. *Bioresour. Technol.* 102, 10763–10766. doi: 10.1016/j.biortech.2011.09.006

Hiegemann, H., Herzer, D., Nettmann, E., Lübken, M., Schulte, P., Schmelt, K.-G., et al. (2016). An integrated 45 L pilot microbial fuel cell system at a full-scale wastewater treatment plant. *Bioresour. Technol.* 218, 115–122. doi: 10.1016/j.biortech.2016.06.052

Ieropoulos, I. A., Stinchcombe, A., Gajda, I., Forbes, S., Merino-Jimenez, I., Pasternak, G., et al. (2016). Pee power urinal—microbial fuel cell technology field trials in the context of sanitation. *Environ. Sci.* 2, 336–343. doi: 10.1039/C5EW00270B

Janicek, A., Fan, Y., and Liu, H. (2014). Design of microbial fuel cells for practical application: a review and analysis of scale-up studies. *Biofuels* 5, 79–92. doi: 10.4155/bfs.13.69

Jones, C., and Sammann, E. (1989). *The Effect of Low Power Plasmas on Carbon Fibre Surfaces, ONR-URI Composites Program Technical Report No. 16*. National Center for Composite Material Research at University of Illinois (Champaign, IL). doi: 10.21236/ADA234184

Kipf, E., Koch, J., Geiger, B., Erben, J., Richter, K., Gescher, J., et al. (2013). Systematic screening of carbon-based anode materials for microbial fuel cells with *Shewanella oneidensis* MR-1. *Bioresour. Technol.* 146, 386–392. doi: 10.1016/j.biortech.2013.07.076

Kipf, E., Zengerle, R., Gescher, J., and Kerzenmacher, S. (2014). How does the choice of anode material influence electrical performance? A comparison of two microbial fuel cell model organisms. *ChemElectroChem*. 1, 1849–1853. doi: 10.1002/celc.201402036

Kozlowski, C., and Sherwood, P. M. A. (1986). X-ray photoelectron spectroscopic studies of carbon fibre surfaces vii-electrochemical treatment in ammonium salt electrolytes. *Carbon.* 24, 357–363. doi: 10.1016/0008-6223(86)90238-1

Li, B., Zhou, J., Zhou, X., Wang, X., Li, B., Santoro, C., et al. (2014). Surface modification of microbial fuel cells anodes: approaches to practical design. *Electrochim. Acta* 134, 116–126. doi: 10.1016/j.electacta.2014.04.136

Liu, J., Liu, J., He, W., Qu, Y., Ren, N., and Feng, Y. (2014). Enhanced electricity generation for microbial fuel cell by using electrochemical oxidation to modify carbon cloth anode. *J. Power Sources* 265, 391–396. doi: 10.1016/j.jpowsour.2014.04.005

Lu, M., Chan, S., Babanova, S., and Bretschger, O. (2017a). Effect of oxygen on the per-cell extracellular electron transfer rate of *Shewanella oneidensis* MR-1 explored in bioelectrochemical systems. *Biotechnol. Bioeng.* 114, 96–105. doi: 10.1002/bit.26046

Lu, M., Chen, S., Babanova, S., Phadke, S., Salvacion, M., Mirhosseini, A., et al. (2017b). Long-term performance of a 20-L continuous flow microbial fuel cell for treatment of brewery wastewater. *J. Power Sources* 356, 274–287. doi: 10.1016/j.jpowsour.2017.03.132

Marsili, E., Baron, D. B., Shikhare, I. D., Coursolle, D., Gralnick, J. A., and Bond, D. R. (2008). *Shewanella* secrets flavins that mediate extracellular electron transfer. *PNAS* 105, 3968–3973. doi: 10.1073/pnas.0710525105

Morgan, P. (2005). *Carbon Fibers and Their Composites*. Boca Raton, FL: CRC Press, Taylor and Francis Group. doi: 10.1201/9781420028744

Moß, C., Patil, S. A., and Schröder, U. (2019). Scratching the surface—how decisive are microscopic surface structures on growth and performance of electrochemically active bacteria? *Front. Energy Res.* 7:18. doi: 10.3389/fenrg.2019.00018

Pierra, M., Golozar, M., Zhang, X., Prévoteau, A., Volder, M. D., Reynaerts, D., et al. (2018). Growth and current production of mixed culture anodic biofilms remain unaffected by sub-microscale surface roughness. *Bioelectrochemistry* 122, 213–220. doi: 10.1016/j.bioelechem.2018.04.002

Pinchuk, G. E., Geydebrekht, O. V., Hill, E. A., Reed, J. L., Konopka, A. E., Beliaev, A. S., et al. (2011). Pyruvate and lactate metabolism by *Shewanella oneidensis* MR-1 under fermentation, oxygen limitation, and fumarate respiration conditions. *Appl. Environ. Microbiol.* 77, 8234–8240. doi: 10.1128/AEM.05382-11

Pirbadian, S., Barchinger, S. E., Leung, M. L., Suk Byun, H. K., Jangir, Y., Bouhenni, R. A., et al. (2014). *Shewanella oneidensis* MR-1 nanowires are outer membrane and periplasmic extensions of the extracellular electron transport components. *PNAS* 111, 12883–12888. doi: 10.1073/pnas.1410551111

Qian, H., Bismarck, A., Greenhalgh, E. S., and Shaffer, M. S. P. (2010). Carbon nanotube grafted carbon fibres: a study of wetting and fibre fragmentation. *Compos. Part A Appl. Sci. Manuf.* 41, 1107–1114. doi: 10.1016/j.compositesa.2010.04.004

Raes, S. M. T., Jourdin, L., Buisman, C. J. N., and Strik, D. P. B. T.B. (2016). Continuous long-term bioelectrochemical chain elongation to butyrate. *ChemElectroChem* 4:386. doi: 10.1002/celc.201600587

Rosenbaum, M., Cotta, M. A., and Angenent, L. T. (2010). Aerated *Shewanella oneidensis* in continuously fed bioelectrochemical systems for power and hydrogen production. *Biotechnol. Bioeng.* 105, 880–888. doi: 10.1002/bit.22621

Rosenbaum, M. A., Bar, H. Y., Beg, Q. K., Segrè, D., Booth, J., Cotta, M. A., et al. (2011). *Shewanella oneidensis* in a lactate-fed pure-culture and a glucose-fed co-culture with *Lactococcus lactis* with an electrode as electron acceptor. *Bioresour. Technol.* 102, 2623–2628. doi: 10.1016/j.biortech.2010.10.033

Santoro, C., Arbizzani, C., Erable, B., and Ieropoulos, I. (2017). Microbial fuel cells: from fundamentals to applications. A review. *J. Power Sour.* 356, 225–244. doi: 10.1016/j.jpowsour.2017.03.109

Santoro, C., Guilizzoni, M., Correa Baena, J. P., Pasaogullari, U., Casalegno, A., Li, B., et al. (2014). The effects of carbon electrode surface properties on bacteria attachment and start up time of microbial fuel cells. *Carbon.* 67, 128–139. doi: 10.1016/j.carbon.2013.09.071

Severini, F., Formaro, L., Pegoraro, M., and Posca, L. (2002). Chemical modification of carbon fiber surfaces. *Carbon.* 40, 735–741. doi: 10.1016/S0008-6223(01)00180-4

Streeck, J., Hank, C., Neuner, M., Gil-Carrera, L., Kokko, M., Pauliuk, S., et al. (2018). Bio-electrochemical conversion of industrial wastewater combined with downstream methanol synthesis—an economic- and life cycle assessment. *Green Chem.* 20, 2742–2762. doi: 10.1039/C8GC00543E

Tender, L. M., Gray, S. A., Groveman, E., Lowy, D. A., Kauffman, P., Melhado, J., et al. (2008). The first demonstration of a microbial fuel cell as a viable power supply: powering a meteorological buoy. *J. Power Sources* 179, 571–575. doi: 10.1016/j.jpowsour.2007.12.123

TerAvest, M. A., Rosenbaum, M. A., Kotloski, N. J., Gralnick, J. A., and Angenent, L. T. (2014). Oxygen allows *Shewanella oneidensis* MR-1 to overcome mediator washout in a continuously fed bioelectrochemical system. *Biotechnol. Bioeng.* 111, 692–699. doi: 10.1002/bit.25128

Walter, X. A., Merino-Jiménez, I., Greenman, J., and Ieropoulos, I. (2018). PEE POWER® urinal II—Urinal scale-up with microbial fuel cell scale-down for improved lighting. *J. Power Sources* 392, 150–158. doi: 10.1016/j.jpowsour.2018.02.047

Wang, X., Cheng, S., Feng, Y., Merrill, M. D., Saito, T., and Logan, B. E. (2009). Use of carbon mesh anodes and the effect of different pretreatment methods on power production in microbial fuel cells. *Environ. Sci. Technol.* 43, 6870–6874. doi: 10.1021/es900997w

Wang, Y., Zhao, Y., Xu, L., Wang, W., Doherty, L., Tang, C., et al. (2017). Constructed wetland integrated microbial fuel cell system: looking back, moving forward. *Water Sci. Technol.* 76, 471–477. doi: 10.2166/wst.2017.190

Watson, V. J., and Logan, B. E. (2009). Power production in MFCs inoculated with *Shewanella oneidensis* MR-1 or mixed cultures. *Biotechnol. Bioeng.* 105, 489–498. doi: 10.1002/bit.22556

Windhorst, T., and Blount, G. (1997). Carbon-carbon composites: a summary of recent developments and applications. *Mater. Design* 18, 11–15. doi: 10.1016/S0261-3069(97)00024-1

Conflict of Interest Statement: The authors declare that the research was conducted in the absence of any commercial or financial relationships that could be construed as a potential conflict of interest.

frontiers in Energy Research

ORIGINAL RESEARCH
published: 12 September 2019
doi: 10.3389/fenrg.2019.00094

Living Architecture: Toward Energy Generating Buildings Powered by Microbial Fuel Cells

Jiseon You[1]*, *Gimi A. Rimbu*[1,2], *Lauren Wallis*[1], *John Greenman*[1] and *Ioannis Ieropoulos*[1]*

[1] Bristol BioEnergy Centre, University of the West of England, Bristol, United Kingdom, [2] National Institute for R&D in Electrical Engineering ICPE-CA, Bucharest, Romania

In this study, possibilities of integrating microbial fuel cell (MFC) technology and buildings were investigated. Three kinds of conventional house bricks from two different locations were tested as MFC reactors and their electrochemical characteristics were analysed. European standard off-the-shelf house bricks generated a maximum power of 1.2 mW (13.5 mW m^{-2}) when fed with human urine. Ugandan house air bricks produced a maximum power of 2.7 mW (32.8 mW m^{-2}), again with human urine. Different cathode types made by surface modifications using two kinds of carbon compounds and two PTFE based binders were tested in both wet and dry cathode conditions. The effects of both anode and cathode sizes, electrode connection, electrode configuration, and feedstock on brick MFC power generation were also studied. Water absorption test results showed higher porosity for the Ugandan air bricks than European engineering bricks, which contributed to its higher performance. This study suggests that the idea of converting existing and future buildings to micro-power stations and micro-treatment plants with the help of integrated MFCs and other renewable technologies is achievable, which will be a step closer to a truly sustainable life.

Keywords: microbial fuel cell (MFC), living architecture, building brick, nearly zero-energy building, self-sustainable system

OPEN ACCESS

Edited by:
Uwe Schröder, Technische Universitat Braunschweig, Germany

Reviewed by:
Mohanakrishna Gunda, Qatar University, Qatar
Xu Wang, Wuhan University, China

***Correspondence:**
Jiseon You
jiseon.you@uwe.ac.uk
Ioannis Ieropoulos
ioannis.ieropoulos@brl.ac.uk

Specialty section:
This article was submitted to Bioenergy and Biofuels, a section of the journal Frontiers in Energy Research

Received: *25 June 2019*
Accepted: *22 August 2019*
Published: *12 September 2019*

Citation:
You J, Rimbu GA, Wallis L, Greenman J and Ieropoulos I (2019) Living Architecture: Toward Energy Generating Buildings Powered by Microbial Fuel Cells. Front. Energy Res. 7:94. doi: 10.3389/fenrg.2019.00094

INTRODUCTION

Increasing global greenhouse gas emission through burning fossil fuels causes climate change. In spite of rapidly growing global energy demands, on the other hand, nearly 1.1 billion people still have no access to electricity (WEO-2017 Special Report: Energy Access Outlook, 2017). Therefore, there is no doubt that implementing a shift in where we obtain our energy from must be made in order to face global energy challenges (World Energy Scenarios 2016 - the Grand Transition, 2016). Sustainable energy portfolios with reliable energy supplies should consist of various renewable energy sources, since there is no clear winner among the renewable energy technologies in terms of power density and geological availability.

Although global urbanisation is a major trend, there is an increasing interest in distributed generation also known as on-site generation. Unlike conventional power stations which are usually large-scale and centralised, and are often required to cover large supply areas, resulting in long distance of energy transmission, distributed, or decentralised generation systems are more flexible in terms of available energy generating/storage technologies and locations. A shift to microgrid

systems accompanying distributed energy resources (DERs) has already begun and is reaching commercial markets. This is driven by technological developments and growing recognition of their benefits such as energy security improvement, economic benefits, and lowering environmental impact (Hirsch et al., 2018).

In DER systems, various technologies can be used and should preferably be used to generate energy. In this context, existing and future buildings are expected to play a crucial role. According to the recast of the Energy Performance of Buildings Directive (Directive 2010/31/EU), all new buildings in the EU should consume nearly zero-energy by the end of 2020. Not only are buildings the largest energy end-use sector (about 40% of total final energy use in the EU-28 and USA) (Bosseboeuf et al., 2015; EIA, 2019), buildings can also be sources of energy generation with the help of renewable energy technologies.

Microbial fuel cells (MFCs) are one of the emerging renewable energy technologies, producing electricity from organic matter including waste, using microorganisms. The dual-utility aspect of the technology, i.e., energy recovery from waste whilst cleaning the waste, makes it stand out among other renewable energy technologies. Energy density of an individual MFC unit is relatively low however, thus it is necessary to scale-up to gain a meaningful power output for practical applications. To scale-up, physical stacking and electrical connections of multiple MFC units have been suggested (Ieropoulos et al., 2008; Asensio et al., 2017). Recent studies have proven that various porous materials can be used as an MFC separator with comparable performance at a much lower cost compared to ion selective membranes (Zhang et al., 2010; Moon et al., 2015; Kim et al., 2016; Winfield et al., 2016). In this way, a building brick might be able to serve as an MFC separator as well as a chassis.

The idea of integrating MFC technology and buildings is very fascinating as buildings will be able to generate the power they need on site. This integrated approach can be widely implemented in both developing countries as well as developed countries, since bricks are ubiquitous. This is a paradigm shift for conventional building concepts, from energy consumer to energy provider. Moreover, this on-site energy generation can lessen the load of central waste treatment systems.

However, as recently shown, achieving a decent level of power output as well as waste treatment efficiency from an individual module can be challenging, as this requires rigorous design and optimisation (Walter et al., 2016). Therefore, this study is focused on how the integration of various MFC elements can be achieved in the context of a "living wall" and optimised based on the understanding of processes and current available materials. For this work, three types of conventional house bricks from two different locations were tested as MFC reactors and their electrochemical characteristics analysed. More specifically, different cathode types, the size of both anode and cathode, electrode connection, electrode configuration, and potential feedstock were tested. A material characteristic analysis of a test brick was also performed and the prospects of the integration have been presented.

MATERIALS AND METHODS

Test Bricks

Three types of real building bricks from two locations were obtained for this study. The first two bricks (Type 1) are essentially standard off-the-shelf house bricks purchased from the same manufacturer (Wienerberger, Cheshire, UK). These are commonly used house bricks in the UK. Both have the same dimension of 215 × 102 × 65 mm (W × D × H). Brick B (product name: Avenue smooth black), has six holes, each being 28.6 mL (10 × 44 × 65 mm), whereas brick R (product name: Staffordshire smooth crimson) has five holes which are bigger than brick B's (66.3 mL each, 17 × 60 × 65 mm). The distance between each compartment is 21 and 18.5 mm for brick B and brick R, respectively. Technical specification of brick B and brick R is presented in the **Supplementary Material**.

As an additional test with real house bricks, air bricks handmade by a local potter in Uganda was selected as the final test brick (named as brick O, Type 2). It was sourced during one of the Bristol Bioenergy Center field trials of the Pee Power® urinal (funded by the Bill & Melinda Gates Foundation grant no. OPP1149065), as an example of a local airbrick. The original size of the brick was 220 × 35 × 80 mm (W × D × H) with grooves of 2–3 mm depth on each side. Two different electrode configurations were tested with this brick, and for one configuration (external cathodes and internal anodes) these grooves were removed by cutting the sides off by 3 mm. It has six holes, with a volume of about 13 ml (13 × 13 × 80 mm) each.

Brick MFC Assembly and Operation

Type 1 Brick MFCs

Without any structural modifications to the brick, brick "B" and brick "R" were used to build a Type 1 MFC. These type of brick MFCs used perforations as anode or cathode chambers, which were arranged alternately. Since the two bricks had a different number of holes (six for brick B and five for brick R) each with a different volume, brick B MFCs had three anodes and three cathodes (**Figure 1A**), whereas brick R MFCs had three anodes and two cathodes (**Figure 1B**). For the anode, plain carbon fibre veil (20 g m^{-2} carbon loading; PRF Composite Materials Poole, Dorset, UK) was cut into different sizes and then folded in order to fit into the chambers. Using these type of brick MFCs, several tests were carried out, to investigate the effect of cathode type, electrode size, feedstock, and cathode surface modification on the MFC power performance. For cathode tests, cathodes were operated in two conditions; either dry or wet. Air was circulated at 189 ml hr^{-1} using a peristaltic pump (205U, Watson Marlow, Falmouth, UK) for dry cathodes, whereas wet cathodes were flooded with recirculated synthetic saline water (3.5% NaCl in deionized water) at a flow rate of 189 ml hr^{-1}. Two types of feedstock were tested; municipal wastewater collected from a local wastewater treatment plant (Wessex Water, Saltford, UK) and human urine donated from consenting adults. Feedstock was supplied continuously at a flow rate of 95 ml hr^{-1} for both brick B and brick R. The tested cathode surface modification is described in the section below.

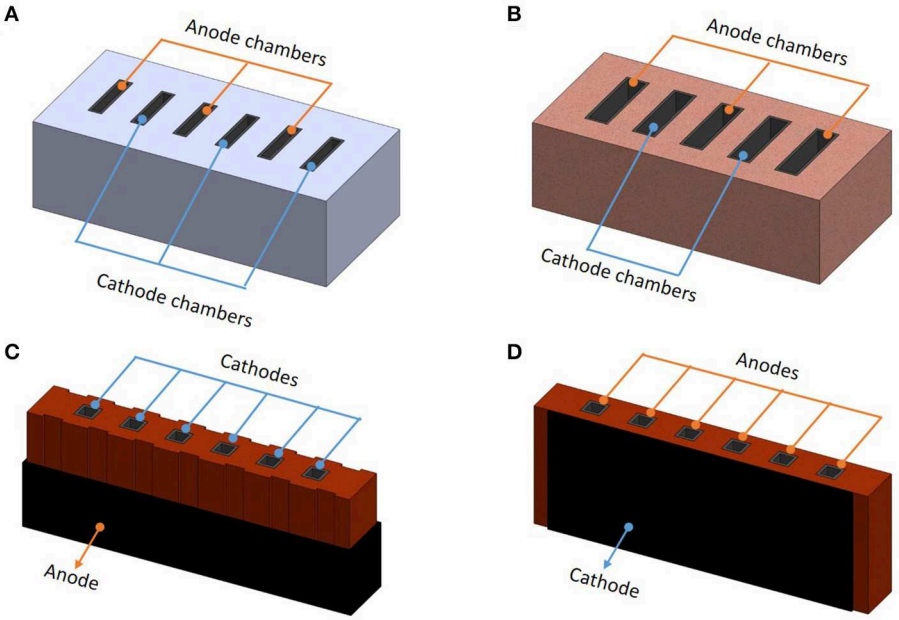

FIGURE 1 | Schematic diagrams of the tested brick MFCs: **(A)** Type 1 brick B MFC with three anode chambers and three cathode chambers. **(B)** Type 1 brick R MFC with three anode chambers and two cathode chambers. **(C)** Type 2 brick O MFC with one external anode and six internal cathodes. **(D)** Type 2 brick O MFC with two external cathodes and six internal anodes.

Type 2 Brick MFCs

For the anode/cathode configuration test, brick "O" was used to build the Type 2 brick MFCs. All six perforations of brick O, each with a volume of about 13 ml, were used as either anode or cathode chambers. For the original shaped brick O (internal cathode and external anode version), six 21 cm^2 (3 × 7 cm) size cathodes were placed inside the perforations. The bottom of the cathode chambers were sealed with an acrylic sheet and the top was left open to air. Cathodes were hot-pressed with activated carbon onto stainless steel mesh (Walter et al., 2018) and all six cathodes were electrically connected through a 0.3 mm Ni-Cr wire. A plain carbon veil anode of 810 cm^2 was wrapped outside of the brick (**Figure 1C**). This MFC was then placed in a plastic container containing 2.4 L human urine as the anode feedstock. MFCs were fed in batches; 500 ml of feedstock was replaced twice a week. For the other electrode configuration, structural modification was done to smoothen both sides of brick O (internal anode and external cathode version) in order to improve the physical contact between the cathodes and the body of the brick. Six internal anodes made of plain carbon veils with a total surface area of 810 cm^2 (135 cm^2 each), were put inside perforations and electrically connected. The internal anode brick MFC holds a 78 ml anolyte volume in total. Two cathodes (total surface area of 160 cm^2 each), made of the same hot-pressed activated carbon, were placed outside of the brick (**Figure 1D**) and also electrically connected. These internal anode-version brick MFCs were fed human urine continuously at a flow rate of 15 ml hr^{-1}.

Both Type 1 and 2 MFCs were inoculated with activated sludge (pH 7.8) (Wessex Water Scientific Laboratory, Saltford, UK) enriched with 1% tryptone and 0.5% yeast extract. Various external loads were used throughout the work, based on polarisation runs.

Figure 1 shows a schematic diagrams of the tested brick MFCs. Photos of experimental set-up for each brick MFC are presented in the **Supplementary Material**.

Cathode Surface Modification of Type 1 MFCs

A total of four types of cathodes were tested in Type 1 MFCs, three of which were modified. As a control, a plain carbon veil sheet (same as the anode material) without any modification was used only on brick R MFCs (named as R_plain). Another control was prepared as previously described (You et al., 2015); hot pressing activated carbon onto the plain carbon veil sheet using 20% PTFE (polytetrafluoroethylene) as a binder (carbon loading: 60 mg cm^{-2}). This PTFE also provides hydrophobicity to the cathode. The other two types of cathode modifications were made by mixing activated carbon (G. Baldwin & Co., London, UK) or carbon black (Vulcan XC 72R, Cabot Corporation, Georgia, USA) with 5% Nafion (Nafion 117, Sigma-Aldrich, Dorset, UK), then painting this mixture onto the plain carbon veil sheet. Both modifications resulted in additional carbon loading of 2 mg cm^{-2}. All these modifications were prepared in ambient conditions without a heating process.

Details of each test MFC are presented in **Table 1**.

Data Logging and Performance Analysis

Power output of the MFCs was monitored in real time in volts (V) against time using a multi-channel Agilent 34972A DAQ

TABLE 1 | Details of test brick MFCs.

Type	1		2	
Used brick	**Brick B**	**Brick R**	**Brick O**	**Brick O (both sides smoothened)**
Anode material	Carbon veil			
Anode size (mm)	432 × 48	610 × 48	900 × 90	150 × 90
Total number of anodes in one brick	3	3	1	6
Each anode chamber volume (mL)	28.6	66.3	2,400	13
Cathode material	2 modified cathodes	3 modified cathodes, 1 unmodified plain cathode	Hot pressed activated carbon	
Cathode size (mm)	108 × 48	152 × 48	70 × 30	200 × 80
Total number of cathodes in one brick	3	2	6	2
Each cathode chamber volume (mL)	28.6 (open to air for dry cathode)	66.3 (open to air for dry cathode)	Open to air	
Separator thickness (mm, distance between anode and cathode)	21	18.5	11	8-9
Feedstock	Municipal wastewater Human urine		Human urine	
Feeding mode	Continuous feeding (flow rate: 95 mL hr^{-1})		Batch-fed	Continuous feeding (flow rate: 15 mL hr^{-1})

unit (Agilent Technologies, California, USA) every 5 min. For polarisation sweeps, various external resistances ranging from 38 kΩ to 1 Ω were loaded every 5 min and the potential between the anode and cathode was recorded every 30 s. All experiments were carried out in a temperature-controlled environment, at 22 ± 2°C.

Water Absorption Measurement

To measure the water absorption of test bricks, brick samples were dried in a ventilated oven at a temperature of 110°C until they attained a substantially constant mass. Samples were then cooled to room temperature to be weighed (M_1). Dry samples were immersed completely in deionized water at room temperature for 24 h. After taking out the samples, any trace of water was wiped out with damp cloth and samples were weighed within 3 min after they had been removed from water (M_2). Water absorption is calculated as follows;

$$Water\ absorption = \frac{(M_2 - M_1)}{M_1} \times 100 \qquad (1)$$

RESULTS AND DISCUSSION

Cathode Comparison

Two types of carbon (activated carbon and carbon black) and binder (Nafion and PTFE) were used to modify the plain carbon veil cathode surface. The additional carbon increased the electrode surface area and both Nafion and PTFE served as a binder, as well as rendering the carbon veil based cathode more hydrophobic, which can be more suitable for an efficient cathode reaction (Li et al., 2010; Chi et al., 2018). A total of four types of cathodes including one control (unmodified plain carbon veil cathode) were tested in two running conditions, dry and wet.

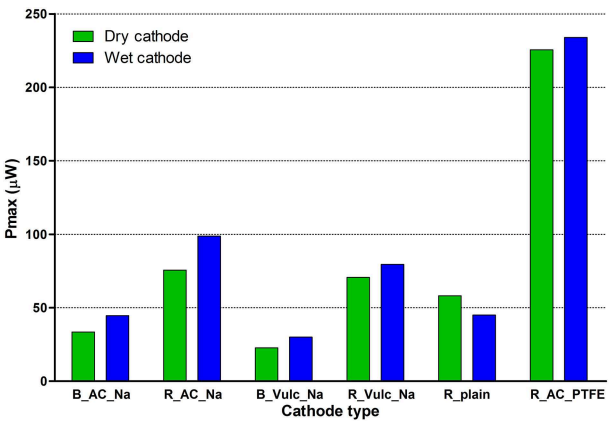

FIGURE 2 | Maximum power output from polarisation measurements of the test cathode types of Type 1 test bricks. Polarisation was performed between single anode and cathode of each brick.

Figure 2 shows the maximum power outputs from polarisation sweeps running on brick MFCs with these cathodes.

When electrons, protons and oxygen from free air react in the cathode to 'close the circuit' (when electricity is generated), water is formed on the cathode (Equation 2). Unlike some very conductive metals, such as silver, gold, and copper, conductivity of carbon-based electrode materials are comparatively low. For example, measured resistivity of plain carbon veil used in this study was $4.6 \times 10^{-4}\ \Omega \cdot m$ (at 20°C) (You et al., 2014). For this kind of air breathing cathodes (dry cathodes), water formation on the cathode is beneficial as it maintains the electrode wet thereby facilitating the continuous flow of cations from the anode. However, too much water formation

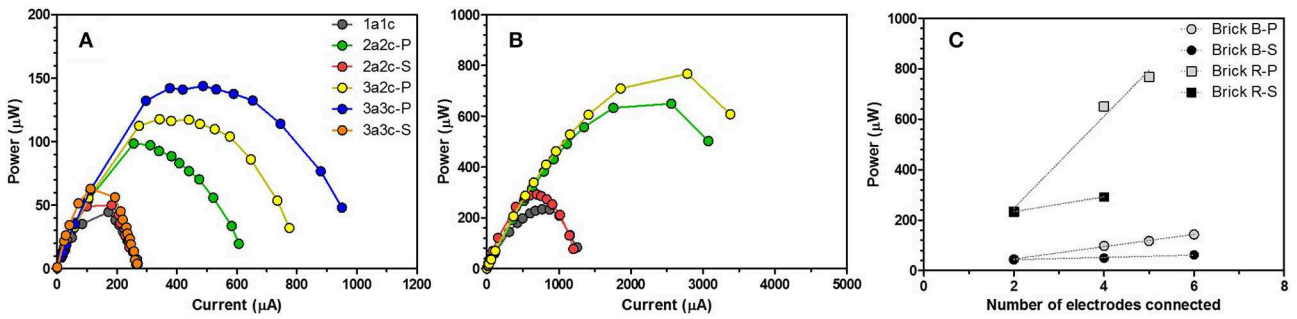

FIGURE 3 | Power curves of the best cathode of each tested Type 1 brick and maximum power output of each polarisation sweep. **(A)** B_AC_Na wet cathode **(B)** R_AC_PTFE wet cathode **(C)** maximum power output of each configuration in relation to the total number of electrodes (both anode and cathode) connected. In the legend, figures indicate the number of anodes or cathodes connected, letters "a," "c," "P," and "S" represent anode electrode, cathode electrode, parallel connection and serial connection, respectively.

hinders the electricity generation by covering reactive sites and lowering conductivity. This is known as "cathode flooding" (Yu et al., 2009; You et al., 2015). Therefore, it was thought that maintaining a dry condition and subsequently preventing cathode flooding by the constant supply of air could enhance the cathode performance.

$$O_2 + 4H^+ + 4e^- \rightarrow 2H_2O\,(E^0 = 1.23\,V) \qquad (2)$$

In general, dry cathodes produced 4–25% less power outputs than wet cathodes of the same kind, except for the plain cathode used in brick R (R_plain). This is thought to be due to excessive amounts of air blown into the cathodes, which evaporated moisture from the cathodes, thus lowering their conductivity. Whereas, for plain carbon veil material, supplying air to keep it less "wet" helped its current generation. Unlike modified cathodes which are more hydrophobic, once plain carbon veil becomes wet, it holds water well. Thus, cathode running in a dry condition by a continuous supply of air seems like a better option for this material. On the other hand, all of the modified cathodes, which are more hydrophobic, benefited from 3.5% saline water, since it provided sufficient moisture as well as higher conductivity.

In terms of modification components, a mixture of activated carbon and PTFE outperformed all other combinations. The best combination, activated carbon and PTFE modified cathode, produced 233.9 μW (wet R_AC_PTFE cathode), which is 2.4 times higher than the second-best cathode modified with activated carbon and Nafion (98.8 μW; wet R_AC_Na cathode). The lowest output was produced from a carbon black and Nafion combination (79.5 μW; wet R_Vulc_Na cathode) and the same order of cathode performance regarding the modification combination was also observed in brick B.

When comparing the two test bricks, brick R showed better performance than brick B. Although the total surface area of all cathodes placed in brick B was larger (155.5 cm^2) than brick R (145.9 cm^2), the distance between the anode and cathode chambers was longer for brick B (21.0 mm) than for brick R (18.5 mm). According to previous studies (Winfield et al., 2013; Pasternak et al., 2016), thickness of the ceramic separator plays a crucial role in the MFC power generation. In this case, brick R benefits from its thinner internal brick walls.

Electrode Configuration

Holes in bricks allow the bricks to dry faster, require less material to build, make them weigh less and provide space for mortar to lock the bricks together. In this study, these holes were used as either anode or cathode chambers without major alterations to the original brick structure. For Type 1 bricks, anodes and cathodes were placed in the holes alternately, resulting in brick MFCs with multiple electrodes. Since these electrodes were separate, different ways of connecting them electronically and corresponding power performance were investigated.

Figure 3 illustrates power curves of brick B and brick R with their best performing cathodes, AC_Na and AC_PTFE, respectively. For both brick MFCs, parallel connection of all available electrodes was the best option, in terms of power output. When connecting all three anodes and cathodes of brick B in parallel, the maximum power output (P_{MAX}) was 143.8 μW which was 2.3 times higher than P_{MAX} of the same electrodes connected in series (62.8 μW). This was possible due to fluid cross over between chambers, either because of material porosity or sealing between the perforations, which provided an alternative electron path that was opposing the electron flow through the connecting wires. For both parallel and series connections, maximum power output levels increased when additional electrodes were connected. This is easily predictable since a higher number of electrodes provide a more reactive surface, resulting in powers adding up. However, the degree of increment was more significant for parallel connection than serial connection (**Figure 3C**), perhaps for the same reasons mentioned above.

Feedstock Comparison

Following the electrode connection investigation, two kinds of feedstock were tested in the brick MFCs with all anodes and cathodes connected in parallel. Neat human urine and municipal wastewater enriched with extra nutrients (1% tryptone, 0.5 % yeast extract and 5 mm sodium acetate) were chosen for this

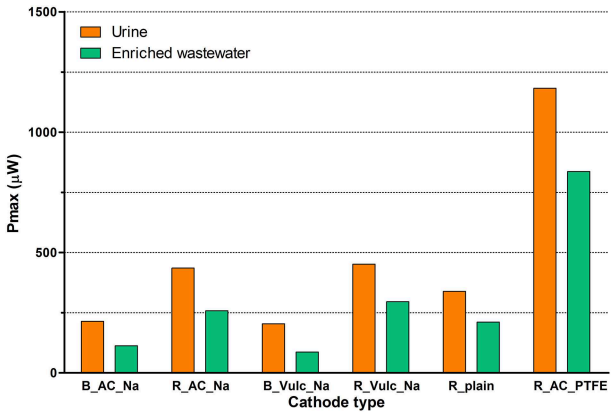

FIGURE 4 | Maximum power outputs of different feedstock tested in Type 1 brick MFCs. P_{MAX} was calculated from power curves. All anodes and cathodes in a single brick connected in parallel.

set of tests, since these can be easily supplied from residential building environments. Both types of feedstock were supplied continuously at a flow rate of 95 ml hr^{-1}, which resulted in hydraulic retention time (HRT) of 0.3 and 0.7 h for brick B and brick R, respectively. Once power outputs from brick MFCs running on each feedstock stabilised, polarisation tests were performed. The P_{MAX} of each test brick MFC is shown in **Figure 4**.

Despite varying degrees of difference (41–136%), urine outperformed wastewater, as a feedstock, in terms of power output in all cases. The best performing cathode type, R_AC_PTFE, generated 1182.4 μW when fed with urine. This was 41% higher than wastewater which produced 837.0 μW. Despite the relatively small portion of readily available carbon compounds presented in urine, it has proven to be a better fuel for MFC power generation (Ieropoulos et al., 2012, 2013). Its high conductivity, neutral-to-alkali pH, and a good combination of nitrogen, phosphorous, and potassium (all essential building blocks for new biomass, for which microbes have high affinity) are thought to contribute to its high conversion rate to electrical current output; more studies are required to further elucidate how urine works in MFCs.

In the scenario of integrating MFC technology into buildings, such as domestic dwellings or offices, wastewater produced onsite can be used as a feedstock for the MFCs. In a domestic setting, greywater include streams from different sources such as the bathroom, kitchen, dishwasher or laundry, in addition to blackwater. Given that urine is an excellent fuel for MFCs, such systems in buildings can be fed with urine only or toilet flush water from source separating toilets, resulting in diluted urine. Greywater can be used for flushing toilets to save water consumption in buildings and provide an extra carbon source to MFCs.

Electrode Position and Analysis of Brick Characteristics for Type 2 MFCs

Following the tests with European off-the-shelf bricks, as part of a wider campaign, bricks and brick materials from our trial site in Uganda were sourced and tested with the better performing urine feedstock. This section describes the test results and material characteristic analysis carried out with the additional test bricks (brick O-Type 2 bricks).

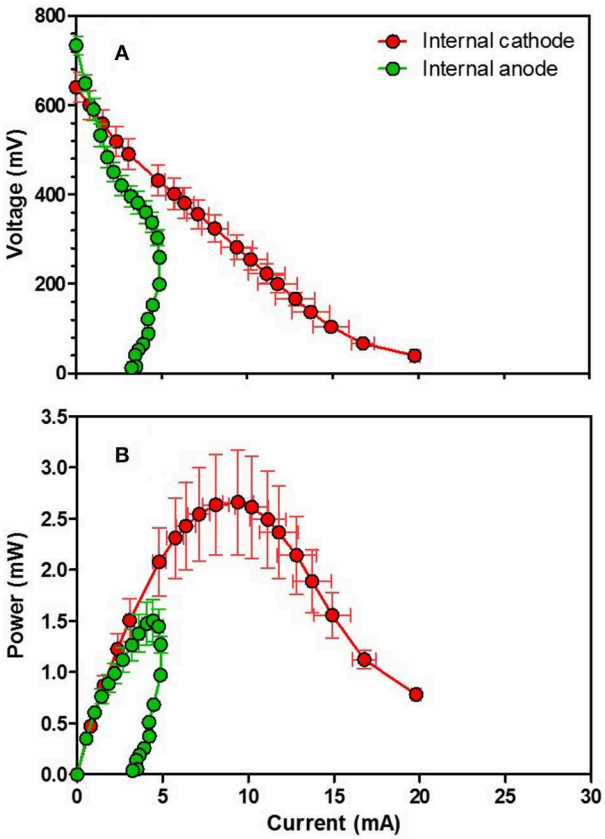

FIGURE 5 | Polarisation **(A)** and power curves **(B)** of Type 2 brick MFCs. Data points are average values of triplicates.

First, instead of using brick holes as cathode and anode chambers alternately, different electrode configurations were investigated by changing the position of electrodes either internally or externally (**Figures 1C,D**). This is another way of using the brick holes as chambers, and in this configuration, the wall between a hole and the outer brick acts as a separator between the anode and cathode. The thickness of this wall is 11–13 mm.

Figure 5 depicts polarisation and power curves of both internal cathode and internal anode version MFCs. Internal cathode version MFCs showed maximum power output of 2.7 ± 0.5 mW and maximum current over 20 mA. Open circuit voltage was 639.7 ± 33.0 mV. Internal anode version MFCs presented lower performance with a maximum power output of 1.5 ± 0.2 mW. It should be noted that since these two kinds of MFCs (internal cathode or internal anode version) had different sizes of both electrodes and volume of anolytes, direct comparison between the two kinds was not intended. These tests were performed to explore possibilities of using real house bricks as MFC reactors with minimum structural alterations.

TABLE 2 | Power outputs of test brick MFCs.

	Brick B	Brick R	Brick O (Internal cathode)	Brick O (Internal anode)
Absolute power (mW) max.	0.2	1.2	2.7	1.5
Power density-anolyte (W m^{-3})	2.5	5.9	1.1	19.2
Power density-anode (mW m^{-2})	3.4	13.5	32.8	18.5
Power density-cathode (mW m^{-2})	13.8	81.0	211.2	46.9

Despite the relatively thick brick wall still acting as a separator, these levels of power outputs are quite encouraging, especially those from the internal cathode version MFCs, in comparison to Type 1 MFCs. This is thought to be mainly due to the thinner wall separator and higher specific porosity of the Type 2 bricks. Water absorption measurement results indicate that Type 2 bricks can absorb at least 2.7 and 1.6 times more water than brick B (<6%) and brick R (<10%) of Type 1 can, respectively, implying that Type 2 bricks are more porous compared to off-the-shelf standard European engineering bricks.

Power output levels of all test brick MFCs in their best conditions, based on absolute power, are presented in **Table 2**.

CONCLUSIONS

Commercially available standard house bricks demonstrated feasibility as MFC reactors without significant structural alterations, generating P_{MAX} of 1.2 mW (13.5 mW m^{-2} normalised by total anode surface area, value from R_AC_PTFE). More porous air bricks (Type 2 brick MFCs) sourced from Uganda performed even better, with a P_{MAX} of 2.7 mW (32.8 mW m^{-2}). Although the power output levels produced from these brick MFCs were relatively low in comparison to recently reported work (Wang et al., 2017; Palanisamy et al., 2019), considering that no high-cost catalysts were used and that these bricks were not optimised as MFC systems, this work shows a high potential for self-sustainable systems. Type 2 brick MFC results are particularly encouraging, since they demonstrate the direct accessibility of MFC technology. It is possible to build MFC systems with locally available building materials, which could help the local economy of economically developing countries.

This study presents exemplar ways of utilising existing off-the-shelf bricks as MFCs. More bricks with different compositions, manufacturing processes, and designs can be further explored. Moreover, new designs and architectural concepts that can increase the functionality of bricks beyond simply load-bearing structures of buildings, and integrating MFC technology, should be investigated. The work presented herein is part of the Living Architecture project, which investigates the integration of MFCs, as well as other technologies in the "fabric" of buildings, to render these into self-sustainable habitats; further information can be found on the project website (https://livingarchitecture-h2020.eu).

The idea of converting existing and future buildings to micro-power stations as well as micro-treatment plants, with the help of MFCs and other potential renewable technologies, is definitely worth pursuing. In this way, zero-energy buildings are conceivable, which will be a step closer to a truly sustainable life.

DATA AVAILABILITY

The datasets generated for this study are available on request to the corresponding authors.

AUTHOR CONTRIBUTIONS

II and JG conceived the original idea and along with JY, GR, and LW designed the experiments of this study. JY and GR carried out the laboratory work. JY and GR organised the database and performed the statistical analysis. JY wrote the first draft of the manuscript. All authors contributed to manuscript revision, read, and approved the submitted version.

FUNDING

The work has been supported by the European Commission Horizon 2020 FET-OPEN Living Architecture Project, grant number 686585 and the open access publication has been supported by the European Commission 2020 FET-OPEN "Active Living Infrastructure: Controlled Environment" project, grant number 851246.

SUPPLEMENTARY MATERIAL

The Supplementary Material for this article can be found online at: https://www.frontiersin.org/articles/10.3389/fenrg.2019.00094/full#supplementary-material

REFERENCES

Asensio, Y., Mansilla, E., Fernandez-Marchante, C. M., Lobato, J., Cañizares, P., and Rodrigo, M. A. (2017). Towards the scale-up of bioelectrogenic technology: stacking microbial fuel cells to produce larger amounts of electricity. *J. Appl. Electrochem.* 47, 1115–1125. doi: 10.1007/s10800-017-1101-2

Bosseboeuf, D., Gynther, L., Lapillonne, B., and Pollier, K. (2015). *Energy Efficiency Trends and Policies in the Household and Tertiary Sectors.* Available online at: http://www.odyssee-mure.eu/publications/br/energy-efficiency-trends-policies-buildings.pdf (accessed June 20, 2019).

Chi, B., Hou, S., Liu, G., Deng, Y., Zeng, J., Song, H., et al. (2018). Tuning hydrophobic-hydrophilic balance of cathode catalyst layer to improve cell performance of proton exchange membrane fuel cell (PEMFC) by mixing polytetrafluoroethylene (PTFE). *Electrochim. Acta* 277, 110–115. doi: 10.1016/j.electacta.2018.04.213

EIA (2019). *How Much Energy Is Consumed in U.S. Residential and Commercial Buildings?* US Energy Inf. Assoc. Available online at: https://www.eia.gov/tools/faqs/faq.php?id=86&t=1.

Hirsch, A., Parag, Y., and Guerrero, J. (2018). Microgrids: a review of technologies, key drivers, and outstanding issues. *Renew. Sustain. Energy Rev.* 90, 402–411. doi: 10.1016/j.rser.2018.03.040

Ieropoulos, I., Gajda, I., You, J., and Greenman, J. (2013). Urine—waste or resource? The economic and social aspects. *Rev. Adv. Sci. Eng.* 2, 192–199. doi: 10.1166/rase.2013.1033

Ieropoulos, I., Greenman, J., and Melhuish, C. (2008). Microbial fuel cells based on carbon veil electrodes: stack configuration and scalability. *Int. J. Energy Res.* 32, 1228–1240. doi: 10.1002/er.1419

Ieropoulos, I., Greenman, J., and Melhuish, C. (2012). Urine utilization by microbial fuel cells; energy fuel for the future. *Phys. Chem. Chem. Phys.* 14, 94–8. doi: 10.1039/C1CP23213D

Kim, T., Kang, S., Sung, H., Kang, K., Kim, Y. H., and Jang, J. K. (2016). Characterization of polyester cloth as an alternative separator to Nafion membrane in microbial fuel cells for bioelectricity generation using swine wastewater. *J. Microbiol. Biotechnol.* 26, 2171–2178. doi: 10.4014/jmb.1608.08040

Li, A., Han, M., Chan, S. H., and Nguyen, N. (2010). Effects of hydrophobicity of the cathode catalyst layer on the performance of a PEM fuel cell. *Electrochim. Acta* 55, 2706–2711. doi: 10.1016/j.electacta.2009.12.048

Moon, J. M., Kondaveeti, S., and Min, B. (2015). Evaluation of low-cost separators for increased power generation in single chamber microbial fuel cells with membrane electrode assembly. *Fuel Cells* 15, 230–238. doi: 10.1002/fuce.201400036

Palanisamy, G., Jung, H.-Y., Sadhasivam, T., Kurkuri, M. D., Kim, S. C., and Roh, S.-H. (2019). A comprehensive review on microbial fuel cell technologies: Processes, utilization, and advanced developments in electrodes and membranes. *J. Clean. Prod.* 221, 598–621. doi: 10.1016/j.jclepro.2019.02.172

Pasternak, G., Greenman, J., and Ieropoulos, I. (2016). Comprehensive study on ceramic membranes for low-cost microbial fuel cells. *ChemSusChem* 9, 88–96. doi: 10.1002/cssc.201501320

Walter, X. A., Greenman, J., and Ieropoulos, I. (2018). Binder materials for the cathodes applied to self-stratifying membraneless microbial fuel cell. *Bioelectrochemistry* 123, 119–124. doi: 10.1016/j.bioelechem.2018.04.011

Walter, X. A., Stinchcombe, A., Greenman, J., and Ieropoulos, I. (2016). Urine transduction to usable energy: a modular MFC approach for smartphone and remote system charging. *Appl. Energy* 192, 575–581. doi: 10.1016/j.apenergy.2016.06.006

Wang, Z., Mahadevan, G. D., Wu, Y., and Zhao, F. (2017). Progress of air-breathing cathode in microbial fuel cells. *J. Power Sources* 356, 245–255. doi: 10.1016/j.jpowsour.2017.02.004

WEO-2017 Special Report: Energy Access Outlook (2017).

Winfield, J., Gajda, I., Greenman, J., and Ieropoulos, I. (2016). A review into the use of ceramics in microbial fuel cells. *Bioresour. Technol.* 215, 296–303. doi: 10.1016/j.biortech.2016.03.135

Winfield, J., Greenman, J., Huson, D., and Ieropoulos, I. (2013). Comparing terracotta and earthenware for multiple functionalities in microbial fuel cells. *Bioprocess Biosyst. Eng.* 36, 1913–1921. doi: 10.1007/s00449-013-0967-6

World Energy Scenarios 2016 - the Grand Transition (2016).

You, J., Santoro, C., Greenman, J., Melhuish, C., Cristiani, P., Li, B., et al. (2014). Micro-porous layer (MPL)-based anode for microbial fuel cells. *Int. J. Hydrogen Energy* 39, 21811–21818. doi: 10.1016/j.ijhydene.2014.07.136

You, J., Walter, X. A., Greenman, J., Melhuish, C., and Ieropoulos, I. (2015). Stability and reliability of anodic biofilms under different feedstock conditions: towards microbial fuel cell sensors. *Sens. Bio-Sens. Res.* 6, 43–50. doi: 10.1016/j.sbsr.2015.11.007

Yu, L., Chen, W., Qin, M., and Ren, G. (2009). Experimental research on water management in proton exchange membrane fuel cells. *J. Power Sources* 189, 882–887. doi: 10.1016/j.jpowsour.2009.01.037

Zhang, X., Cheng, S., Huang, X., and Logan, B. E. (2010). The use of nylon and glass fiber filter separators with different pore sizes in air-cathode single-chamber microbial fuel cells. *Energy Environ. Sci.* 3, 659–664. doi: 10.1039/b927151a

Conflict of Interest Statement: The authors declare that the research was conducted in the absence of any commercial or financial relationships that could be construed as a potential conflict of interest.

frontiers in Energy Research

ORIGINAL RESEARCH
published: 13 September 2019
doi: 10.3389/fenrg.2019.00098

Integrating Electrochemistry Into Bioreactors: Effect of the Upgrade Kit on Mass Transfer, Mixing Time and Sterilizability

Luis F. M. Rosa[1], *Steffi Hunger*[2], *Tom Zschernitz*[1], *Beate Strehlitz*[2] *and Falk Harnisch*[1]*

[1] Department of Environmental Microbiology, Helmholtz-Centre for Environmental Research, Leipzig, Germany, [2] Department Centre for Environmental Biotechnology, Helmholtz-Centre for Environmental Research, Leipzig, Germany

Microbial electrosynthesis (MES) is an exciting and dynamic research area at the nexus of microbiology and electrochemistry. To pave the way of MES to application, reactor infrastructure is needed that meets the requirements of both biological, and electrochemical engineering. Recently we presented an upgrade kit facilitating turning commercial bioreactors based on batch stirred tank reactors (BSTR) into electrobioreactors that can be scaled and benchmarked. The upgrade kit comprises electrodes and an inlay with membrane, separating the BSTR chamber into anode and cathode compartments. The obtained electrobioreactors enable seizing the existing infrastructure for monitoring and controlling the bioprocess while being complemented by electrochemical control and measurement. Here the effect of the upgrade kit on mass transfer was investigated in a 1 L electrobioreactor using experimental approaches and modeling of fluid dynamics. It is shown that the fluid dynamics in the BSTR are changed dramatically, impacting the integral parameters volumetric mass transfer coefficient, k_La, and mixing time, θ. The influences of the inlay chamber and electrodes as well as stirrer position and geometry are described. Additionally, the sterilizability of the inlay, housing the polymer-based membrane of the electrobioreactor, which is needed for operating two-chamber MES based on microbial pure cultures, are demonstrated.

Keywords: bioelectrochemical engineering, bioelectrosynthesis, bioelectrotechnology, electrobioreactor characterization, fluid dynamics, microbial electrosynthesis

OPEN ACCESS

Edited by:
Eileen Hao Yu,
Newcastle University, United Kingdom

Reviewed by:
Lars Regestein,
Leibniz Institute for Natural Product Research and Infection Biology, Germany
Jean-Marie Fontmorin,
University of Rennes 1, France

***Correspondence:**
Falk Harnisch
falk.harnisch@ufz.de

Specialty section:
This article was submitted to Bioenergy and Biofuels, a section of the journal Frontiers in Energy Research

Received: *10 June 2019*
Accepted: *29 August 2019*
Published: *13 September 2019*

Citation:
Rosa LFM, Hunger S, Zschernitz T, Strehlitz B and Harnisch F (2019) Integrating Electrochemistry Into Bioreactors: Effect of the Upgrade Kit on Mass Transfer, Mixing Time and Sterilizability. Front. Energy Res. 7:98. doi: 10.3389/fenrg.2019.00098

INTRODUCTION

Microbial electrosynthesis (MES) is a field of microbial electrochemical technologies (MET) that is defined as the execution of microbially catalyzed electrochemical reactions to transform a substance into a desired product (or a mixture of products) (Schröder et al., 2015). MES has gained increasing attention as it promises to use renewable (electric) energy and biogenic feedstock for a bio-based economy. For paving the way of MES from its current technology readiness level

(TRL[1]) of maximum 4–5 to a production technology, an adequate reactor infrastructure is required (Holtmann and Harnisch, 2019). These reactors must allow balancing the necessities related to the exploitation of microorganisms with the requirements for electrochemical reactions taking place. These are requirements that also need to be met by reactors for other applications in the field of MET, including its archetype the microbial fuel cell (MFC), and microbial desalination cells (MDC). MFC are designed for operating open, non-sterile cultures usually derived from wastewaters, where the electrochemically active organisms are mainly forming biofilms. Thus, design concepts and lessons learned during MFC engineering can be very well-adapted for MES using open cultures as well. Examples are the production of hydrogen in microbial electrolysis cells (MEC) or gaining carboxylates from CO_2 using microbial mixed cultures. However, this adaptation of design concepts is not possible when it comes to MES using defined co-cultures and (genetically modified) pure cultures. In this line of research substantial progress has been made in the last years, e.g., using *E. coli* for the production of acetoin from glucose (Sturm-Richter et al., 2015), and chiral alcohols from ketones (Mayr et al., 2019), or using *P. putida* for production of detergents (Schmitz et al., 2015). These studies exploited until now mostly distinct lab scale reactors, with custom made designs. The reactors are usually bottle-type reactors made with laboratory flasks with one or two chambers and electrodes inserted in the flasks using adapted lids. A two-chamber system–allowing separating the anode and cathode compartments–is implemented often by using H-cells based on tailored glass flasks that are separated by an ion exchange membrane (Nevin et al., 2010, 2011). Alternatively, for two-chamber systems an insertion of a (smaller) counter electrode chamber in the bigger (bottle-like) working electrode chamber is realized (Xu et al., 2014). The counter-electrode chamber often consists of a glass tube equipped with a membrane at one end. In all cases the membrane is essential for keeping the anode and cathode chambers physically separated, but ionically connected. Thus, the generated products or off-gas streams can be harvested with higher purities and (electro) chemical short circuits can be avoided. This results in improved characterization of MES, e.g., in terms of coulombic efficiency (CE) or product yield. However, from a bioprocess engineering perspective these reactors are not only poorly characterized but are also hardly suitable for process development and scaling. Further, an adequate benchmarking—meaning comparison of MES to biosynthesis not using electric power—seems impossible. To circumvent these limitations and enable knowledge-driven process development, we recently introduced an upgrade kit that allows (reversibly) transforming existing bioreactor infrastructure into electrobioreactors (Rosa et al., 2017). This upgrade kit makes the application of conventional bioreactors used for bioprocess engineering possible, including their infrastructure for process monitoring, and control for investigating MES. The resulting reactors are denominated as electrobioreactors. Using the upgrade kit, two-chamber 1 L electrobioreactors based on batch stirred tank reactors (BSTR) were achieved (see **Figure 1** and **Figure SI 1**). We demonstrated that the material and design of electrodes and other components of the 1 L electrobioreactors can be achieved allowing research on several pure cultures of electroactive microorganisms, e.g., *Gluconobacter oxidans* (Gimkiewicz et al., 2016), *Clostridium kluyveri* (Koch et al., 2017), *Shewanella oneidensis* (Rosa et al., 2017), and genetically modified *E. coli* (Mayr et al., 2019). However, to what extent the insertion of electrodes, an inlay creating two chambers, and the use of an adapted stirrer as well as removal of chicanes resulted in change of fluid dynamics remained unclear, and is addressed within this study.

For reactor engineering and scaling the description of a given reactor system in terms of geometry, flow fields and hydrodynamic conditions using standardized data representation are necessary. Reactor design parameters include dimensionless numbers like the Reynolds number (Re) or Newton number (Ne) for the description of the flow field or mixing environment (Harnisch and Holtmann, 2019), and when electrochemical performance is to be appraised, the Wagner number (Wa) (Ibl, 1981) must be taken into account in the scaling process. This means that the complex interplay of biotechnological, fluid-dynamic, and electrochemical processes must be investigated in an electrobiorector to reveal correlations between those that may allow subsequent engineering (Zlokarnik, 2006). Characterizations of a two-chamber BSTR were carried out with the determination of the common parameters for mass transfer and flow field: k_La and θ. The k_La is a value that comprises the volumetric interfacial gaseous-liquid surface area, a, and the mass transfer coefficient, k_L, measured as their product. The k_La is used for the characterization and design of bioreactors in order to compare different systems regarding mass-transfer limitations at the gas-liquid interface, and it is used as an important scale-up factor of processes in geometrically similar reactors (Moutafchieva et al., 2013). Most industrial productions are based on aerobic cultivation, often at high cell densities, characterized by a quick depletion of oxygen from the liquid phase, which can only be resupplied by forced dissolution from gas streams. Consequently, the k_La is usually assessed for oxygen transfer, but it can be measured for other gases that are relevant for a given process, like CO_2, as well (Enzmann et al., 2019). Generally, care must be taken to ensure that the response time of the sensors used for detecting the respective dissolved gas in solution is fast enough, otherwise it could be limiting, which leads to wrong k_La calculation (Meusel et al., 2016). The k_La depends heavily on the internal geometries of the reactors and its components, which determine the convective movement inside (vessel height to diameter ratios, number and geometry of chicanes and baffles, stirrers, stirring speeds and power), and on the properties of the liquid medium (density, viscosity, surface tension, and coalescence properties) (Van't Riet, 1979). Thus, the k_La is an excellent measure for the overall mass transfer capacity of a specific reactor system. In fact, one of the strategies for upscaling aerobic bioprocesses from laboratory scale to industrial scale is by keeping the k_La constant (Garcia-Ochoa and Gomez, 2009). Although most MES processes are operated anaerobically or

[1]https://ec.europa.eu/research/participants/data/ref/h2020/wp/2014_2015/annexes/h2020-wp1415-annex-g-trl_en.pdf

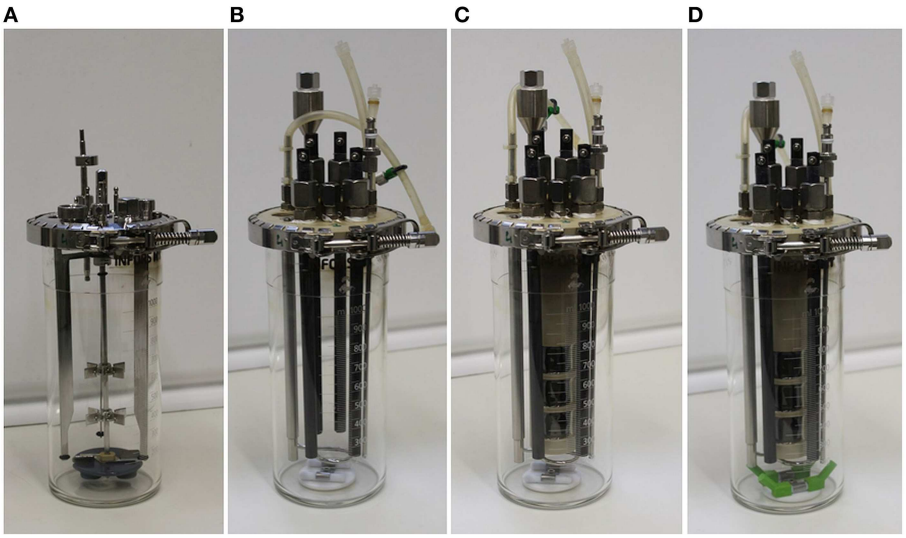

FIGURE 1 | Pictures of the different experimental setups described in the text in detail. **(A)** Bioreactor of the manufacturer (setup 1); **(B)** upgrade kit for bioreactors including working and counter electrodes, without chamber inlay, and with the standard upgrade kit stirrer (setup 2); **(C)** upgrade kit for bioreactors complete with membrane chamber inlay (setup 3); **(D)** upgrade kit for bioreactors complete with membrane inlay and a modified stirrer with extensions (setup 4).

microaerobically, here the k_La was measured using oxygen from air, as the gained numbers are highly suitable for mass transfer benchmarking.

In standard bioreactors, concentration and temperature gradients must be prevented in order to avoid unfavorable impact on cell growth and product formation (Kraume, 2004). Mixing efficiency affects both performance and scale-up in a bioreactor. Homogenization (mixing) is characterized by the mixing quality to be achieved and the mixing time necessary (Kraume, 2004). The mixing quality represents a pre-selected value (for example, macro-mixing, fine mixing, or mixing up to molecular dimensions) (Kaiser et al., 2011). The parameter mixing time, θ, is an excellent measure for the overall mass transfer in the liquid phase. Mixing time can be calculated for a reactor and different reactor running conditions. It is dependent on the bioreactor geometry, the used stirrer type and size, the specific power input (convective conditions established in the reactor), as well as the liquid properties, especially on the diffusivity of the compounds of interest in the bulk medium used, and the bulk medium liquid properties (Kaiser et al., 2011).

The aim of our investigations was to continue our line of reactor engineering to generate and characterize an electrobioreactor that fulfills the legal and factual requirements to be used in industrial and white biotechnology. In this study, following our previous work (Rosa et al., 2017), we investigated the influences of upgrade kit elements on the fluid dynamics in a 1 L reactor. Starting with the "conventional bioreactor" (setup 1–see section Materials and Methods for details)—which is the bioreactor without the upgrade kit, which is not applicable for MES—stirrer, electrodes and chamber were inserted consecutively, and k_La as well as θ were determined. Further, computational fluid dynamics (CFD) analysis of the reactors was performed. In conjunction, the results lead to the suggestion of new stirrer designs for the improvement of the mixing. Additionally, the sterilizability of the electrobioreactor needs to fulfill the regulatory standards in biotechnology. Therefore, the very first sterilization tests on the inlay housing the polymer membranes for 1 L electrobioreactor were carried out (GMP-Berater, 2018).

MATERIALS AND METHODS

Chemicals

All chemicals were of at least analytical grade and were obtained from Sigma-Aldrich (Deisenhofen, Germany), Carl-Roth GmbH & Co. KG (Karlsruhe, Germany), or VWR International GmbH (Darmstadt, Germany). For preparation of all solutions, deionized water (Millipore, Darmstadt, Germany) was used. Tap water, distilled water, and deionized water were used for the investigations of sterilization conditions for the membrane as indicated.

Reactor Setups

Four different experimental setups were used throughout this study (**Figure 1**), all based on the 1 L bioreactor vessel (Infors Multifors, Infors AG, Bottmingen, Switzerland):

Setup 1: Bioreactor of the manufacturer, with a stainless steel lid, three metal chicanes and one central shaft with two Rushton turbines evenly spaced, driven from the bottom of the reactor using magnetic coupling (**Figure 1A**).

Setup 2: Partial installation of the upgrade kit in the bioreactor (**Figure 1B**). This includes removing all the parts shown in **Figure 1A** (stainless steel lid, three metal chicanes, magnetic

stirrer shaft with two Rushton turbines, and magnetic coupling), and introducing a custom-made reactor lid made of polyetheretherketon (PEEK) equipped with four graphite rods (10 mm diameter and 250 mm long, CP-2200 quality, CP-Handels GmbH, Wachtberg, Germany), with two rods serving as working electrodes (WEs), and two rods serving as counter electrodes, a reference electrode (Ag/AgCl Sat. KCl, SE11, with 6 mm diameter, and 100 mm length, Xylem Analytics, Meinsberg, Germany), and a custom made magnetic stirrer composed of two 7 mm diameter, 40 mm long Teflon-covered magnets in the bottom of the vessel.

Setup 3: Based on setup 2, a membrane inlay is added. The inlay of the upgrade kit is also made of PEEK and contains three side openings (i.e., "windows") with an active membrane size of 716 mm^2 each (**Figure 1C**). A cation exchange membrane (fumasep FKE, FuMA-Tech GmbH, Bietigheim-Bissingen, Germany) is used to maintain the physical separation but to allow ionic connection of the two reactor chambers. The membrane is mounted on the inner side of the inlay and glued in the gaps with a two-component epoxy adhesive (Loctite Hysol 3430, Henkel, Düsseldorf, Germany). Inside the inlay, two graphite rods serving as counter-electrodes are installed. The 150 mL compartment formed by the inlay reduced the working volume of the working electrode chamber to 850 mL, comprising the complete upgrade kit for bioreactors (**Figure SI 1**).

Setup 4: An identical bioelectroreactor as for setup 3 was used, but with improved stirrer geometry. Therefore, 3D printed (Ultimaker 2+, Geldermalsen, The Netherlands) poly-lactic acid extensions (PLA, Innofil3D, Emmen, The Netherlands) were built to elongate the stirrer paddles by 2 cm at an angle of 45° (**Figure 1D**).

Experimental Determination of the Volumetric Mass-Transfer Coefficient k_La

The volumetric mass transfer coefficient, k_La, comprises the volumetric interfacial gas-liquid surface area, a, and the mass transfer coefficient, k_L, being both measured as their product (Garcia-Ochoa et al., 2010). Different methods for the experimental determination of k_La are available (Van't Riet, 1979; Garcia-Ochoa and Gomez, 2009), here the gassing-out method was used (Meusel et al., 2016). This method is based on the measurement of oxygen saturation of the electrolyte solution (Van't Riet, 1979). For all setups, different gassing [0.5, 1, and 2 standard liter per minute (sLpm)], and stirring conditions (200, 500, 650, and 1,000 rpm) were assessed using oxygen sensors (see below) in M4-mineral medium [1.27 mM K_2HPO_4, 0.73 mM KH_2PO_4, 5 mM HEPES, 125 mM NaCl, 9 mM $(NH_4)_2SO_4$], supplemented with trace elements (1 mM $MgSO_4$, 100 µM $CaCl_2$, 5 µM $CoCl_2$, 0.2 µM $CuSO_4$, 57 µM H_3BO_3, 5.4 µM $FeCl_2$, 1.3 µM $MnSO_4$, 67.2 µM Na_2EDTA, 3.9 µM Na_2MoO_4, 1.5 µM Na_2SeO_4, 5 µM $NiCl_2$, and 1 µM $ZnSO_4$). All values were obtained at 30 ± 0.5°C (Schütz et al., 2011).

The oxygen sensors were Clark-type electrodes (OxyFerm170, Hamilton Bonaduz AG, Bonaduz Switzerland) with response times of 25 to 30 s ($t_{63\%}$ response times, measured) that were left to polarize for at least 6 h before the measurements. Sensors were calibrated using the two-point calibration procedure: 100% dissolved oxygen tension (DOT) when a stable reading was obtained while sparging air at 2 sLpm and stirring at 1,000 rpm, and 0% DOT when a stable reading was obtained while sparging with N_2, using the designated stirring and sparging conditions. After calibration, oxygen saturation curves were obtained as four independent replicates ($n = 4$) for each aeration/stirring combination. The k_La values were calculated as the slope of a linear regression, obtained by fitting the ln[100-DOT(t)] vs. time, by means of the least square differences. DOT(t) is the normalized dissolved oxygen data at a certain time, obtained for each trial, fitted between 10 and 90% of saturation (Meusel et al., 2016).

Experimental Determination of the Mixing Time

The mixing time, θ, was experimentally determined using the conductivity meter sensor method (Meusel et al., 2016). In brief, 750 mL of de-ionized water was added to the reactor setups, and the conductivity was measured, using a conductivity meter with a 1 s response time (SevenExcellence™ S700, Mettler-Toledo, Greifensee, Switzerland). After adding 1 mL of a 4 M KCl, while stirring at 200, 500, 650, and 1,000 rpm, at 30°C, data collection was continued until a steady final conductivity was measured for at least 30 s. The measurements were repeated independently 10 times ($n = 10$) for each setup. The mixing time of each replicate was considered as the first time at which the measured conductivity (normalized from 0 to 100%) was stable in an interval 100 ± 5% of the measured average final conductivity of the last 30 measurements. Due to experimental limitations, we could only measure this parameter using different stirring rates without the use of gas sparging. Sparging can affect θ in both negative and positive ways (Vasconcelos et al., 1998), so its influence at this scale should be determined experimentally. The gas bubbles interfered severely with the signal of the conductivity meter used, resulting in very high fluctuations of the signal, which impeded appropriate signal treatment. Additionally, the conductivity meter used was limited to measuring intervals of a minimum of 1 s, so we consider the results to have an error of ±1 s.

Sterilization of the Inlay With Membrane

In general, the polymer-based ion exchange membrane (fumasep FKE, FuMA-Tech GmbH, Bietigheim-Bissingen, Germany) was glued using a two-component epoxy adhesive on the inner side of the inlay, as described above and shown in **Figure 2** (Gimkiewicz et al., 2016). Three different methodologies were used to study the sterilization of the inlay with the glued membrane and to test the stability of membrane material and gluing.

Sterilization 1: Sterilization with damp heat [steam sterilization: saturated steam 205 kPa, 121°C (GMP-Berater, 2018)]: The inlay was sterilized in an autoclave (Tuttnauer 2540, Tuttnauer Europe B.V., Breda, Netherlands) for 20 min in a 1 L beaker filled with 0.750 L demineralized water or tap water. The inlay was poured with 0.100 L demineralized water

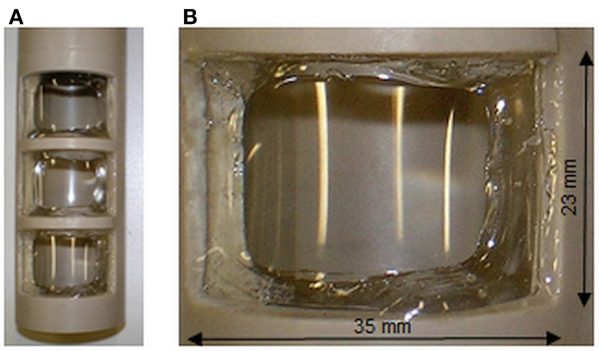

FIGURE 2 | Detailed views on the inlay **(A)** and on one window **(B)** with the glued membrane. Dimensions provided refer to the window opening; the active membrane surface is diminished by glue edges to 716 mm^2.

or tap water. The reference flask for the temperature sensor was 1 L tap water.

Sterilization 2: Sterilization with dry heat [hot air sterilization: temperature ≥160°C, 120 min (GMP-Berater, 2018)]: The drying oven (Heraeus UT 6120, Heraeus Holding GmbH, Hanau, Germany) was preheated to 180°C. The inlays were equipped with adhesive temperature measuring stripes (Testo SE & Co. KGaA, Lenzkirch, Germany) with visual display showing the maximum temperature of exposure (details see **Supplementary Information 1.1** and **Figure SI 5**) and were put in the drying oven. After the temperature on the measuring stripes exceeded 160°C, the timer of the oven was set to 120 min to start the process.

Sterilization 3: γ-sterilization: The inlay with the glued membrane was sterilized using γ-radiation to adsorb 25 kGy (GMP-Berater, 2018) at subcontractor (Synergy Health Radeberg GmbH, Radeberg, Germany).

For sterilization 1, additional study was performed. Membrane sections equal in size were placed each on a petri dish (made of glass) and filled with 30 ml distilled water, deionized water, tap water or 5 wt-% NaCl solution. The petri dishes were unsealed closed and autoclaved for 20 min and 121°C with a reference flask filled with 30 mL tap water (Autoclave: Tuttnauer 2540, Tuttnauer Europe B.V., Breda, Netherlands).

Statistics

All experimentally derived data (k_La, θ) were measured as independent replicates as detailed above; confidence intervals (CI) at 95% confidence ($p = 0.05$) were calculated using the standard deviation and Student-t probability distributions (Miller and Miller, 1988). Linear correlations were obtained using the minimization of the sum of the squares of errors.

Modeling Using Finite Element Method

Geometry and Mesh

The finite element method (FEM) numerical solving program, COMSOL Multiphysics (Comsol Multiphysics GmbH, Göttingen, Germany), was used to solve Navier-Stokes (NS) partial differential equations (PDEs) (Yang et al., 2014) to assess the velocity fields of setups 2 to 4. The different geometries of the setups are represented in **Figure 3**. **Figure 3A** shows the geometry of setup 2, **Figure 3B** depicts the geometry of setup 3, which includes all the accessories from geometry 3A plus the solid inlay with the ion exchange membrane window, which physically separates the working electrode chamber from the counter electrode chamber (being here not modeled). **Figure 3C** resembles the geometry and stirrer addition of setup 4. The CAD geometry dimensions were measured from the physical parts with an accuracy of 0.1 mm.

The meshing of the geometries was done using the default "Fine" settings. This created a static polyhedral mesh with adequate size and number for the chosen physics (time-dependent Rotating machinery NS), and also created an additional "sliding mesh" which is dynamic in time, for defining the boundaries around the moving stirrer. The mesh statistics for each of the studied geometries are described in **Table SI 1**, and a visual example of the mesh can be seen in **Figure SI 2**.

Modeling and Boundary Conditions

The geometries were modeled assuming the liquid phase was water ($\rho = 1{,}000\,kg\,m^{-3}$, $\mu = 0.001\,Pa\,s$, $T = 293.15\,K$). All the walls and internal static surfaces (vessel walls, electrodes, inlay, and membrane) were attributed to the boundary condition "no-slip," which assumes Newtonian behavior of the liquid, setting the velocity of the liquid at these surfaces to 0. The magnetic stirrer surfaces were modeled as a "rotating wall," which also sets surface velocity to 0, but inside a rotating domain. The stirrer was modeled encased in a rotating domain; this is a cylinder-shaped volume that contained the stirrer. The walls of this cylinder were modeled with "continuity" in order for the momentum forces generated to be passed to the exterior domain, i.e., the remaining liquid phase in the reactor.

The stirring speed was modeled with an incremental time-dependent s-shaped step function so that it was increased in time from 0 rpm to 1,000 rpm (**Figure SI 3**). With the time-dependent study being computed from time 0 s to time 0.6 s with 0.001 s of increment the rpm were increasing up to ≈0.45 s of modeled time, where it then became constant for the next 0.15 s. This means the model results will include 0.15 s of rotation at 1,000 rpm, from 0.45 to 0.6 s, yielding in total only three complete rotations at full speed. Although this can hardly be considered as "steady state conditions" we used the gained values. We are confident that this approach is more faithful to the physics than the Coriolis frozen rotor approach[2], which is not suitable, when introducing obstacles in the flow field, as is needed in this case. The time-dependent solver was used at the default settings.

[2]https://knowledge.autodesk.com/support/cfd/learn-explore/caas/CloudHelp/cloudhelp/2019/ENU/SimCFD-UsersGuide/files/GUID-81E86432-7979-41AF-A7C2-9123144FC6F9-htm.html

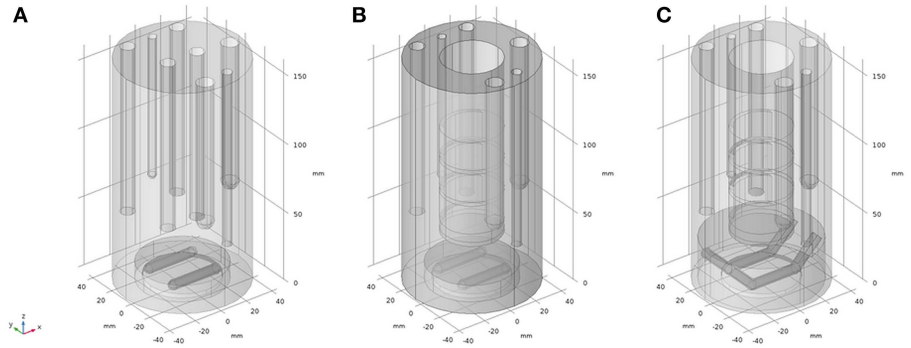

FIGURE 3 | CAD geometry representations of the reactor setups used for finite element modeling; **(A)** model used for representation of setup 2; **(B)** model used for representation of setup 3; **(C)** model used for representation of setup 4.

RESULTS AND DISCUSSION

Determination of the Volumetric Mass-Transfer Coefficient k_La

As introduced above, the volumetric mass transfer coefficient, k_La, is a critical parameter for determining the gas transfer rate across the liquid-gaseous interface in biotechnological processes and a key parameter in estimating reactor mass transfer performance. Thus, k_La is an excellent reference point for assessing changes in mass transfer. The k_La of a standard bioreactor (setup 1) and several modifications of the same vessel (setups 2 to 4) when installing the bioelectrochemical upgrade kit (Rosa et al., 2017) were assessed for different stirring speeds (200, 500, and 1,000 rpm) and fixed volumetric aeration rates with air (0.5, 1, and 2 sLpm).

Results obtained for the measurement of k_La are shown in **Figure 4**. In the original reactor setup 1, k_La varies almost linearly from low to high stirring speeds, independently of the aeration rate (**Figure 4A**). Maximum k_La is obtained for highest stirring speed and gassing, at 225.73 ± 26.72 h^{-1}, whereas the minimum k_La is obtained, as expected, for minimum stirring and gassing (20.49 ± 1.85 h^{-1}). Setup 2 is characterized by a different dependency of k_La (**Figure 4B**). For lower stirring speeds, i.e., between 200 and 500 rpm, the value of k_La is almost not increasing for all aeration rates (12.32 ± 0.73 h^{-1} to 22.55 ± 2.78 h^{-1} and 35.75 ± 4.23 h^{-1} at 200 rpm to 17.25 ± 0.63, 35.35 ± 2.16 and 46.03 ± 4.36 h^{-1} at 500 rpm at 0.5, 1, and 2 sLpm, respectively). Yet, it increases dramatically, from 500 to 1,000 rpm (from 17.25 ± 0.63, 35.35 ± 2.16 and 46.03 ± 4.36 h^{-1} at 500 rpm to 134.31 ± 6.52, 152.86 ± 3.33 and 152.67 ± 12.09 h^{-1} at 1,000 rpm at 0.5, 1, and 2 sLpm, respectively). These k_La values are still inferior to the ones obtained with setup 1. This can be explained by two major changes of setup 2 in the reactor geometry relatively to setup 1: the removal of the three metal baffles (chicanes) and the replacement of the two Rushton turbine stirrers evenly spaced in the liquid column by one single custom-made magnetic stirrer placed on the bottom of the reactor vessel. The removal of the baffles as a static element that countered the circular liquid movement inside the vessel diameter promoted mixing and turbulence, and the removal of the two Rushton turbines implies clearly that then only the one stirrer has to propel the complete liquid column. One may further assume that this led to a less even distribution of the liquid movement than using the original pair of Rushton turbines. The influence of these alterations is very remarkable, as evidenced by the k_La values as well as the modeling (*vide infra*). The further introduction of the inlay membrane (setup 3) brings the replacement of some of the stirred liquid volume by a static cylindrical solid element, centered in the reactor vessel. The resulting k_La values measured for setup 3 (**Figure 4C**) yield a mixed behavior compared to the k_La values of setup 1 and setup 2 as follows. For the lower aeration rate of 0.5 sLpm, there is a non-linearity of k_La from low to high stirring speeds, from 16.03 ± 2.01 h^{-1} to 33.98 ± 6.91 h^{-1} and then to 131.07 ± 5.94 h^{-1} at 200, 500, and 1,000 rpm, respectively, but as the aeration rate increases, k_La resumes an almost linear behavior with stirring speed (26.08 ± 0.79 h^{-1}, 56.18 ± 5.04 h^{-1} and 140.35 ± 2.59 h^{-1} at 1 sLpm and 54.35 ± 5.42, 82.43 ± 1.68 and 156.20 ± 9.87 h^{-1} at 2 sLpm, at 200, 500, and 1,000 rpm, respectively). In this case, the aeration regime has a clear effect on the k_La with increasing stirring rate in comparison to setup 2. We suspect this is due to the decreased liquid volume of the system from 1,000 mL (in setup 1 and 2) to 850 mL (in setup 3 and 4). The effective ratio of gassing rate to liquid volume is changed, i.e., a lower liquid volume to the same gassing rate, which brings a slight increase in the k_La, at least for the higher gassing regimes. Still, as expected, the k_La of setup 3 is inferior to the k_La of setup 1. The k_La of the electrobioreactor can be improved when using advanced stirrer geometry (setup 4). The detailed k_La results obtained for setups 3 and 4 are discussed in the following section, together with the results obtained for the respective modeling.

Modeling

The model geometries depicting the bioelectroreactor setups 2, 3, and 4 (**Figure 3**) were successfully solved. The results represent a numerical approximation of the velocity magnitude of the liquid

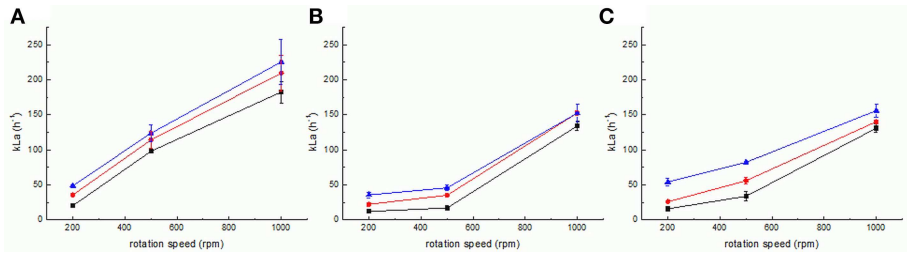

FIGURE 4 | Measurement of k_La for setups 1 **(A)**, 2 **(B)**, and 3 **(C)** at various gassing rates (0.5 sLpm–squares, 1 sLpm–circles and 2 sLpm–triangles). Error bars represent the confidence interval at 95% confidence calculated from at least 5 independent measurements ($n \geq 5$).

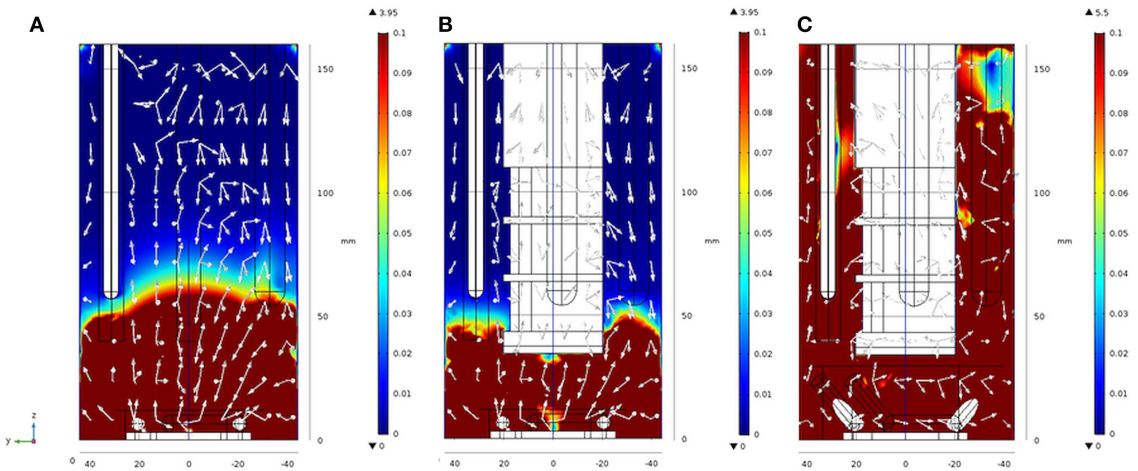

FIGURE 5 | Results from finite element modeling: velocity magnitude fields obtained for $t = 0.6$ s, 1,000 rpm in setups 2 **(A)**, 3 **(B)**, and 4 **(C)** in y-z cut planes of the geometry. White arrows are normalized and only serve to indicate the main direction of the velocity magnitude. 3D views of the same Figures are found in **Figure SI 4A–C**. For further details see also **Figure SI 4**.

inside the electrobioreactors, discretized in space and also in time, from 0 to 0.6 s of model time (with a resolution of 0.006 s), where from approximately 0.45 to 0.6 s at least 3 full rotations of the stirrer at maximum stirring rate (1,000 rpm) were modeled. The velocity magnitudes obtained for the different geometries at a fixed time of 0.6 s were analyzed (**Figure 5** and **Figure SI 4**).

From the images presented in **Figure SI 4** and taking into consideration the behavior of Newtonian fluids stirred by a Rushton turbine in a baffled reactor (see Zadravec et al., 2007), it is evident that different geometries in setups 2 to 4 have severe impact on the fluid flow inside the reactor as can be expected (Yang et al., 2014). **Figure 5A** shows that setup 2 is characterized by a clear and distinct separation of the velocity fields into two zones. One zone where velocity magnitudes vary from extremely high, 3.95 m s^{-1} down to 0.1 m s^{-1}, situated between reactor heights of 50 and 60 mm, and one zone where the magnitudes are considerably lower, from 0.1 to 0.001 m s^{-1}, above the reactor height of 60 mm. One should note that this is the zone at around 50–60 mm in the electrobioreactor, where most of the electrodes have their end tips. From this height upwards, the electrodes inside the reactors also serve as chicanes to the flow, hence breaking the high velocity fields. In setup 3 (**Figure 5B**), an additional large element (the inlay with the membrane) is included. The inlay tip is at 40 mm height from the bottom, and this brings the cut-line between high and low velocity zones 10 mm lower, to around 40 to 50 mm. Based on these modeling results and considering the associated k_La measurements, an improved stirrer (**Figure 3C**) finally leading to setup 4 (**Figure 1D**) was suggested. The stirrer in setup 4 consists in extending the magnetic stirrer cylinders (the "paddles" of the stirrer), generating a double anchor-like stirrer with a larger overall diameter, for which the tips sit higher in the liquid column. The model results for this geometry (setup 4) are presented in **Figure 5C**, where two major outcomes are visible: (i) the increase in the maximum velocity within the geometry (from 3.95 m s^{-1} for setups 2 and 3, to 5.5 m s^{-1} for setup 4), due to the increase in the stirrer diameter, and (ii) the disappearing of the zone delimited by velocity magnitudes inferior to 0.1 m s^{-1} due to the stirrer geometry.

Following the modeling results of the advanced stirrer geometry, it was also experimentally realized (**Figure 1D**), and the k_La of the derived setup 4 was measured (**Figure 6**). Due to the increased diameter of the stirrer (implying a higher power input for the same rpm), the magnetic coupling of the stirrer

magnets with the turning motor magnets was lost for rates >650 rpm. Consequently, the k_La could not be measured for the same rpm range as for the other setups. Remarkably, the k_La values measured for setup 4 at rates ≤650 rpm were in the same range as the k_La values obtained with the original bioreactor (setup 1) with a maximum k_La value obtained for 650 rpm and 2 sLpm gassing rate of 249.07 ± 5.02 h^{-1}. This illustrates that in electrobioreactors, k_La values can be reached that are comparable to shaking flasks with chicanes and that are needed for cultivations of usual cell densities.

Mixing Time

In order to further compare the two stirrer designs, the mixing time, θ, was measured using the conductivity meter sensor method. Setup 1 yielded mixing times between 18 and 3 s (for 200 and 1,000 rpm, respectively). The results obtained for setups 3 and 4 are shown in **Figure 7**. In both cases, θ decreased markedly, with the increase in the stirring rate from 19 to 7 s at 200 rpm and from 7 to 5 s at 500 rpm (for setup 3 and setup 4, respectively). The lowest θ obtained were 6 s for setup 3 at 1,000 rpm, and 4 s for setup 4 at 650 rpm. Once again, these values show that the introduction of a stirrer of higher diameter with tips elevated at a higher position in the reactor liquid column increases the convective mixing significantly.

Sterilization of the Inlay With Membrane

For MES using pure cultures, sterile conditions need to be assured. Thus, the sterilization of the upgrade kit as well as of the other parts not present in the conventional bioreactor need to be demonstrated. Preliminary considerations about sterilizable materials and sterilization procedures can already be found (Gimkiewicz et al., 2016; Enzmann et al., 2019), and recently sterilizability of electrodes for a secondary MES was demonstrated (Hegner et al., 2019). Here we focused on the sterilizability of the inlay of the upgrade kit housing the ion exchange membrane. This can be considered as the technological heart of the upgrade kit, as it allows operation in a two-chamber system with physical separation of anodic oxidation and cathodic reduction. As polmyer-based membranes are commonly applied as separators in MES, the sterilization procedure was exemplified using a widely utilized cation exchange membrane (fumasep FKE) (e.g., Rozendal et al., 2008; Sevda et al., 2013; Jiang et al., 2017; Rosa et al., 2017; James et al., 2018). For preliminary tests in non-sterile conditions, it was shown that mechanical mounting of the membrane was sufficient. But depending on the culture medium, different behavior of the membrane, and of its mounting was observed leading to leaking. This is due to differences in swelling, expansion, and wrinkling of the

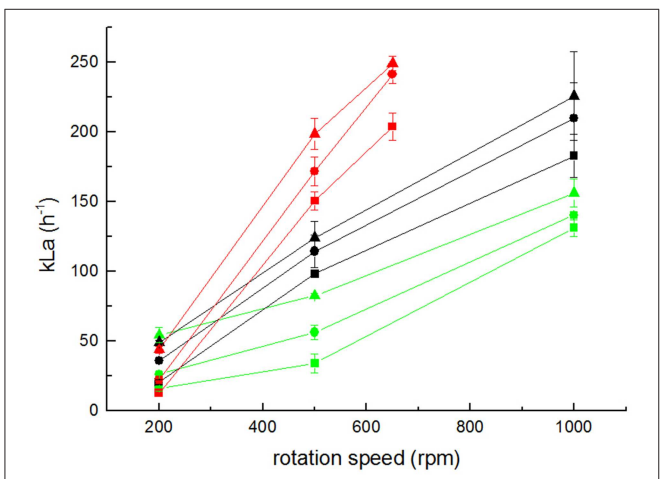

FIGURE 6 | Measurement of k_La values for setups 1 (black), 3 (green), and 4 (red) at various gassing rates (triangles 0.5 sLpm; circles 1 sLpm; and squares 2 sLpm). Error bars represent the confidence interval at 95% confidence calculated from at least 5 independent measurements ($n \geq 5$).

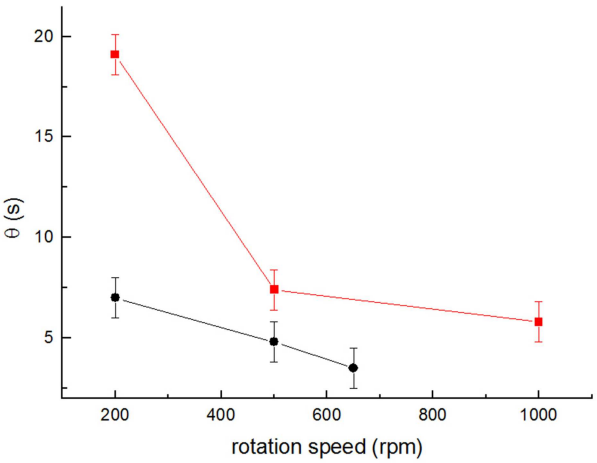

FIGURE 7 | Average values of mixing times θ obtained for the different stirring speeds for setup 3 (squares) and setup 4 (circles) for at least 3 independent determinations ($n \geq 3$). Error bars represent the time resolution of the conductivity meter (±1 s).

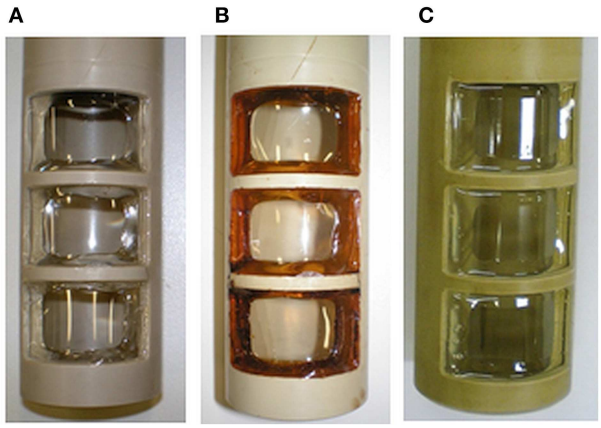

FIGURE 8 | Glued membrane before **(A)** and after sterilization with dry heat **(B)** and γ-radiation **(C)**.

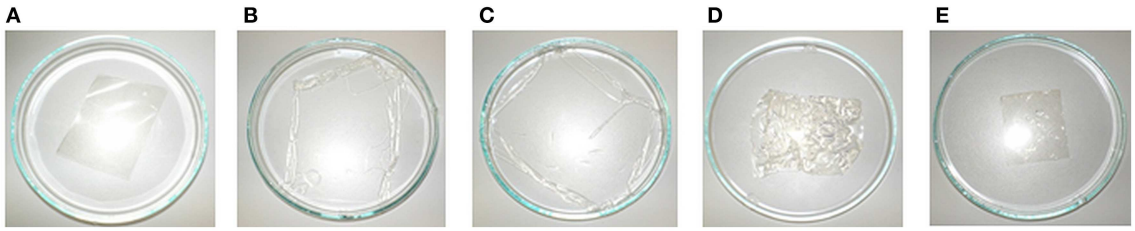

FIGURE 9 | Photographs of membrane before **(A)** and after autoclaving in distilled water **(B)**, deionized water **(C)**, tap water **(D)**, and 5 wt-% NaCl solution **(E)**.

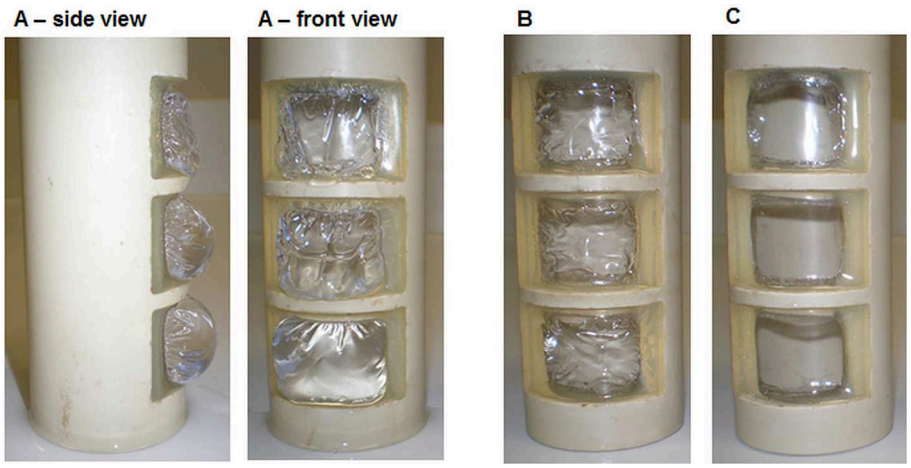

FIGURE 10 | Membrane after autoclaving in de-ionized water **(A)**, tap water **(B)**, and subsequent drying after autoclaving in tap water **(C)**.

membrane during pretreatment, conditioning and storage in liquid as already described. To exclude leakages of the inlay due to the mounting, a suitable gluing method was developed (details see section Materials and Methods). The inlay with the successfully glued membrane was systematically tested for sterilizability according to the technical conditions described in GMP-Berater (2018) for pure-culture processes using three state-of-the art sterilization methods. The visual characterization of the inlay and the glued membrane after sterilization with dry heat (**Figure 8B**) and γ-sterilization (**Figure 8C**) shows yellow coloration of the membrane and gluing surface. The coloration after sterilization with dry heat was more intense than with γ-radiation. The glue especially shows an increased optical response. Nevertheless, the connection between the membrane and the PEEK-inlay was reliable; the membranes did not show any visible damages and were not melted or leaky.

The sterilization with damp heat (Sterilization 1) exposes the membrane to liquid and supersaturated steam at a temperature of 121°C for 20 min. First, the behavior of the membrane itself was tested. **Figure 9** shows the enlargement of the membrane sheet after autoclaving in distilled (**Figure 9B**) and de-ionized water (**Figure 9C**), while the use of tap water (**Figure 9D**), and 5 wt-% NaCl solution (**Figure 9E**) does not result in a change of size. None of the membranes were damaged or melted, but structural changes of the membranes were observed after swelling (B and C had become soft and sensitive). The use of tap water did not result in a change of the stability of the membrane but led to wrinkles (D). Autoclaving using a 5 wt-% NaCl solution seemingly did not influence the structural integrity of the membrane (E).

For investigations using the glued membrane, the inlays were autoclaved in de-ionized water and tap water. The glued bonding was stable, and the membranes did not show any damages and were not melted. However, distinct structural changes of the membrane were observed after swelling. The membranes autoclaved in de-ionized water lost physical stability (**Figure 10A**) and were more sensitive to shear stress. Using tap water, the membranes were slightly wrinkled after autoclaving (**Figure 10B**) but could achieve their initial state after drying (**Figure 10C**). The glue was visually unchanged and kept the membrane in shape. These very first results demonstrate that the membranes tolerate the sterilization conditions but suffer some changes in their physical properties after the pretreatment with demineralized water.

Specifically, for the two-chamber electrobioreactor (setups 3 and 4), the variation of the window size, the use of window grills and further membrane developments are required. Subsequent investigations with several adhesives and the development

of possible mechanical or thermal connection between the membrane and the inlay are absolutely necessary. As alternatives to polymer-based membranes, other (porous) materials can be applied. Here, the uses of ceramic or porous glass seem to be the materials of choice for the harsh sterilization conditions, but they have limitations in selectivity, and permeability (Krieg et al., 2019).

CONCLUSIONS

Electrobioreactors were created by introducing an upgrade kit into a 1 L BSTR. The upgrade kit severely changes the fluid dynamics in the reactor, as characterized by the volumetric mass transfer coefficient k_La and mixing time θ, and as shown by CFD modeling. Derived by model-based predictions, small changes in the stirrer geometry (advanced stirrer) were realized experimentally. This resulted in considerably improved mass transfer performance in terms of increase of the velocity magnitude to up to 5.5 m s^{-1} and in removal of "dead zones" (i.e., volumes with velocity magnitudes <0.1 m s^{-1}) of the electrobioreactor (setup 4), being k_La, and θ values better than in "conventional" bioreactors (setup 1). The sterilizability of the inlay, being an assembly of polymer-based membrane glued to the PEEK-based cylinder, was demonstrated. The scale-up of a sterilizable two-chamber BSTR-based electrobioreactor might very likely be developed from an autoclavable to an *in-situ* sterilizable system. Consequently, the steam sterilization is an essential step in this development. This will require in-depth investigations concerning mechanical stability and functionality of the potential membrane materials. Although *in-situ* sterilization is preferred, the *ex-situ* sterilization using dry heat or γ-radiation is a temporarily acceptable solution, demanding an aseptic working environment which allows sterile transfer of the extern sterilized inlay into the bioreactor. Furthermore, the operational reliability of all sterilized components of the upgrade kit (inlay chamber, membrane, working-, counter- and reference electrode) must be tested. Microbial and electrochemical methods for surveying functionality in *modus operandi* should be established and integrated into the monitoring technology of electrobioreactors, e.g., electrochemical impedance spectroscopy (Koók et al., 2019).

DATA AVAILABILITY

The datasets generated for this study are available on request to the corresponding author.

AUTHOR CONTRIBUTIONS

FH, LR, and SH contributed the conception and design of the study. LR performed all modeling experiments, analyzed the modeling, and experimental data, performed the statistical analysis, prepared figures, and wrote sections of the manuscript. SH constructed the upgrade kit, performed the sterilization experiments, analyzed data, prepared figures, and wrote sections of the manuscript. TZ performed experiments for k_La and θ determination and analyzed the respective data. BS provided guidance on data analysis and manuscript preparation, discussed the data, and wrote sections of the manuscript. FH conceived of the study, advised and provided guidance on all experiments, obtained funding, and wrote the manuscript. All authors contributed to manuscript revision, read and approved the submitted version.

FUNDING

FH acknowledges support by the BMBF (Research Award Next generation biotechnological processes–Biotechnology 2020+) and the Helmholtz-Association (Young Investigators Group). This work was supported by the Helmholtz-Association within the Research Programme Renewable Energies.

ACKNOWLEDGMENTS

Peter Portius and co-workers from the workshop of the UFZ Leipzig are acknowledged for their excellent service for building the upgrade kits.

SUPPLEMENTARY MATERIAL

The Supplementary Material for this article can be found online at: https://www.frontiersin.org/articles/10.3389/fenrg.2019.00098/full#supplementary-material

REFERENCES

Enzmann, F., Mayer, F., Stöckl, M., Mangold, K.-M., Hommel, R., and Holtmann, D. (2019). Transferring bioelectrochemical processes from H-cells to a scalable bubble column reactor. *Chem. Eng. Sci.* 193, 133–143. doi: 10.1016/j.ces.2018.08.056

Garcia-Ochoa, F., and Gomez, E. (2009). Bioreactor scale-up and oxygen transfer rate in microbial processes: an overview. *Biotechnol. Adv.* 27, 153–176. doi: 10.1016/j.biotechadv.2008.10.006

Garcia-Ochoa, F., Gomez, E., Santos, V. E., and Merchuk, J. C. (2010). Oxygen uptake rate in microbial processes: an overview. *Biochem. Eng. J.* 49, 289–307. doi: 10.1016/j.bej.2010.01.011

Gimkiewicz, C., Hunger, S., and Harnisch, F. (2016). Evaluating the feasibility of microbial electrosynthesis based on gluconobacter oxydans. *Chemelectrochem* 3, 1337–1346. doi: 10.1002/celc.201600175

GMP-Berater (2018). "Band 4; Chapter 12: D Sterilisationsverfahren," in *Nachschlagewerk für Pharmaindustrie und Lieferanten,* eds B. Peither, T. Peither, and M. P. Ag (Schopfheim: Maas & Peither AG - GMP-Verlag), 1–38.

Harnisch, F., and Holtmann, D. (2019). "Electrification of biotechnology: status quo," in *Bioelectrosynthesis,* eds F. Harnisch and D. Holtmann (Cham: Springer International Publishing), 1–14. doi: 10.1007/10_2017_41

Hegner, R., Neubert, K., Rosa, L. F., and Harnisch, F. (2019). Engineering the electrochemical CO2 reduction to formate at bioprocess-compatible conditions to bioreactor scale. *ChemElectroChem* 6, 3731–3735. doi: 10.1002/celc.201900526

Holtmann, D., and Harnisch, F. (2019). "Electrification of biotechnology: quo vadis?," in *Bioelectrosynthesis,* eds. F. Harnisch and D. Holtmann. (Cham: Springer International Publishing), 395–411. doi: 10.1007/10_2018_75

Ibl, N. (1981). Nomenclature for transport phenomena in electrolytic systems. *Pure Appl. Chem.* 53:1827. doi: 10.1351/pac198153101827

James, O. O., Sauter, W., and Schröder, U. (2018). Towards selective electrochemical conversion of glycerol to 1,3-propanediol. *RSC Adv.* 8, 10818–10827. doi: 10.1039/C8RA00711J

Jiang, B. L., Muddemann, T., Kunz, U., Bormann, H., Niedermeiser, M., Haupt, D., et al. (2017). Evaluation of microbial fuel cells with graphite plus MnO_2 and MoS_2 paints as oxygen reduction cathode catalyst. *J. Electrochem. Soc.* 164, H3083–H3090. doi: 10.1149/2.0131703jes

Kaiser, S. C., Löffelholz, C., Werner, S., and Eibl, D. (2011). "CFD for characterizing standard and single-use stirred cell culture bioreactors," in *Computational Fluid Dynamics Technologies and Applications*, eds. I. V. Minin and O. V. Minin (London: InTechOpen), 97–122.

Koch, C., Kuchenbuch, A., Kracke, F., Bernhardt, P. V., Kromer, J., and Harnisch, F. (2017). Predicting and experimental evaluating bio-electrochemical synthesis - a case study with *Clostridium kluyveri*. *Bioelectrochemistry* 118, 114–122. doi: 10.1016/j.bioelechem.2017.07.009

Koók, L., Bakonyi, P., Harnisch, F., Kretzschmar, J., Chae, K.-J., Zhen, G., et al. (2019). Biofouling of membranes in microbial electrochemical technologies: causes, characterization methods and mitigation strategies. *Bioresour. Technol.* 279, 327–338. doi: 10.1016/j.biortech.2019.02.001

Kraume, M. (2004). *Transportvorgänge in der Verfahrenstechnik. Grundlagen und apparative Umsetzungen*. (Heidelberg: Springer-Verlag).

Krieg, T., Madjarov, J., Rosa, L. F. M., Enzmann, F., Harnisch, F., Holtmann, D., et al. (2019). "Reactors for microbial electrobiotechnology," in *Bioelectrosynthesis,* eds F. Harnisch and D. Holtmann. (Cham: Springer International Publishing), 231–271. doi: 10.1007/10_2017_40

Mayr, J., Grosch, J.-H., Hartmann, L., Rosa, L. F. M., Spiess, A. C., and Harnisch, F. (2019). Resting *Escherichia coli* as chassis for microbial electrosynthesis: production of chiral alcohols. *ChemSusChem* 12, 1631–1634. doi: 10.1002/cssc.201900413

Meusel, W., Löffelholz, C., Husemann, U., Dreher, T., Greller, G., Kauling, J., et al. (2016). *Recommendations for Process Engineering Characterisation of Single-Use Bioreactors and Mixing Systems by Using Experimental Methods*. Frankfurt: DECHEMA Gesellschaft für Chemische Technik und Biotechnologie e.V.

Miller, J. C., and Miller, J. N. (1988). Basic statistical methods for analytical chemistry. part I. statistics of repeated measurements. *Rev. Anal.* 113, 1351–1356. doi: 10.1039/an9881301351

Moutafchieva, D., Popova, D., Dimitrova, M., and Tchaoushev, S. (2013). Experimental determination of the volumetric mass transfer coefficient. *J. Chem. Technol. Metal.* 48, 351–356.

Nevin, K. P., Hensley, S. A., Franks, A. E., Summers, Z. M., Ou, J., Woodard, T. L., et al. (2011). Electrosynthesis of organic compounds from carbon dioxide is catalyzed by a diversity of acetogenic microorganisms. *Appl. Environ. Microbiol.* 77, 2882–2886. doi: 10.1128/AEM.02642-10

Nevin, K. P., Woodard, T. L., Franks, A. E., Summers, Z. M., and Lovley, D. R. (2010). Microbial electrosynthesis: feeding microbes electricity to convert carbon dioxide and water to multicarbon extracellular organic compounds. *mBio* 1:e00103–10. doi: 10.1128/mBio.00103-10

Rosa, L. F. M., Hunger, S., Gimkiewicz, C., Zehnsdorf, A., and Harnisch, F. (2017). Paving the way for bioelectrotechnology: integrating electrochemistry into bioreactors. *Eng. Life Sci.* 17, 77–85. doi: 10.1002/elsc.201600105

Rozendal, R. A., Jeremiasse, A. W., Hamelers, H. V. M., and Buisman, C. J. N. (2008). Hydrogen production with a microbial biocathode. *Environ. Sci. Technol.* 42, 629–634. doi: 10.1021/es071720+

Schmitz, S., Nies, S., Wierckx, N., Blank, L. M., and Rosenbaum, M. A. (2015). Engineering mediator-based electroactivity in the obligate aerobic bacterium *Pseudomonas putida* KT2440. *Front. Microbiol.* 6:284. doi: 10.3389/fmicb.2015.00284

Schröder, U., Harnisch, F., and Angenent, L. T. (2015). Microbial electrochemistry and technology: terminology and classification. *Energy Environ. Sci.* 8, 513–519. doi: 10.1039/C4EE03359K

Schütz, B., Seidel, J., Sturm, G., Einsle, O., and Gescher, J. (2011). Investigation of the electron transport chain to and the catalytic activity of the diheme cytochrome c peroxidase ccpA of *Shewanella oneidensis*. *Appl. Environ. Microbiol.* 77, 6172–6180. doi: 10.1128/AEM.00606-11

Sevda, S., Dominguez-Benetton, X., Vanbroekhoven, K., Sreekrishnan, T. R., and Pant, D. (2013). Characterization and comparison of the performance of two different separator types in air–cathode microbial fuel cell treating synthetic wastewater. *Chem. Eng. J.* 228, 1–11. doi: 10.1016/j.cej.2013.05.014

Sturm-Richter, K., Golitsch, F., Sturm, G., Kipf, E., Dittrich, A., Beblawy, S., et al. (2015). Unbalanced fermentation of glycerol in *Escherichia coli* via heterologous production of an electron transport chain and electrode interaction in microbial electrochemical cells. *Bioresour. Technol.* 186, 89–96. doi: 10.1016/j.biortech.2015.02.116

Van't Riet, K. (1979). Review of measuring methods and results in nonviscous gas-liquid mass transfer in stirred vessels. *Indust. Eng. Chem. Proc. Design Develop.* 18, 357–364. doi: 10.1021/i260071a001

Vasconcelos, J. M. T., Alves, S. S., Nienow, A. W., and Bujalsk, W. (1998). Scale-up of mixing in gassed multi-turbine agitated vessel. *Can. J. Chem. Eng.* 76, 398–404. doi: 10.1002/cjce.5450760308

Xu, H., Wang, K. J., and Holmes, D. E. (2014). Bioelectrochemical removal of carbon dioxide (CO2): an innovative method for biogas upgrading. *Bioresour. Technol.* 173, 392–398. doi: 10.1016/j.biortech.2014.09.127

Yang, Z. H., Wu, Z., Zeng, G. M., Huang, J., Xu, H. Y., Feng, J., et al. (2014). Assessing the effect of flow fields on flocculation of kaolin suspension using microbial flocculant GA1. *RSC Adv.* 4, 40464–40473. doi: 10.1039/C4RA04101A

Zadravec, M., Basic, S., and Hribersek, M. (2007). The influence of rotating domain size in a rotating frame of reference approach for simulation of rotating impeller in a mixing vessel. *J. Eng. Sci. Technol.* 2, 126–138.

Zlokarnik, M. (2006). *Scale-up: Modellübertragung in der Verfahrenstechnik*. Weinheim: Wiley-VCH Verlag GmbH & Co. KGaA.

Conflict of Interest Statement: The authors declare that the research was conducted in the absence of any commercial or financial relationships that could be construed as a potential conflict of interest.

frontiers in Energy Research

ORIGINAL RESEARCH
published: 18 September 2019
doi: 10.3389/fenrg.2019.00101

Degradation of Azo Dye (Acid Orange 7) in a Microbial Fuel Cell: Comparison Between Anodic Microbial-Mediated Reduction and Cathodic Laccase-Mediated Oxidation

Priyadharshini Mani[1], V. T. Fidal[2], Kyle Bowman[1], Mark Breheny[1], T. S. Chandra[2], Taj Keshavarz[1] and Godfrey Kyazze[1]**

[1] School of Life Sciences, University of Westminster, London, United Kingdom, [2] Department of Biotechnology, Indian Institute of Technology Madras, Chennai, India

OPEN ACCESS

Edited by:
Uwe Schröder, Technische Universitat Braunschweig, Germany

Reviewed by:
S. Venkata Mohan, Indian Institute of Chemical Technology (CSIR), India
Federico Aulenta, Water Research Institute (IRSA), Italy

***Correspondence:**
Priyadharshini Mani
Priyadharshini.Mani@my.westminster.ac.uk
Godfrey Kyazze
G.Kyazze@westminster.ac.uk

Specialty section:
This article was submitted to Bioenergy and Biofuels, a section of the journal Frontiers in Energy Research

Received: *25 June 2019*
Accepted: *02 September 2019*
Published: *18 September 2019*

Citation:
Mani P, Fidal VT, Bowman K, Breheny M, Chandra TS, Keshavarz T and Kyazze G (2019) Degradation of Azo Dye (Acid Orange 7) in a Microbial Fuel Cell: Comparison Between Anodic Microbial-Mediated Reduction and Cathodic Laccase-Mediated Oxidation. Front. Energy Res. 7:101. doi: 10.3389/fenrg.2019.00101

More than 80% of wastewater from industries is discharged into receiving water bodies without any pollution control. Microbial fuel cells (MFCs) are a promising technology for the simultaneous treatment of wastewater and electricity production. With regard to azo-dye containing wastewater (e.g., from textile manufacturing), the dye may be fed via the anode chamber containing electrochemically active bacteria or via the cathode chamber containing laccase enzyme as catalyst for oxygen reduction. This study investigated which of the two approaches is the best with regard to rate of decolourization of the dye (Acid orange 7), COD reduction and electricity production. The power density was higher for the $MFC_{Dye\ Cathode}$ (50 ± 4 mW m^{-2}, COD reduction 80.4 ± 1.2%) compared with 42.5 ± 2.6 mW m^{-2} (COD reduction 69 ± 2%) for $MFC_{Dye\ Anode}$. The time required for decolourization was longer in the $MFC_{Dye\ Anode}$ (*Shewanella oneidensis*) where only 20% decolourization was obtained after 24 h compared to 80% for the $MFC_{Dye\ Cathode}$. The anodic dye degradation products were unstable when exposed to air resulting in regaining of color. In case of degradation by laccase in the cathode chamber, the decolourization products were stable and simpler in chemical structure as determined by GC-MS. This work suggests that feeding azo dyes in cathode chambers of MFCs containing laccase is a better way of treating the dyes compared to the commonly used approach of feeding the dye in the anode chamber provided enzyme activity can be sustained.

Keywords: azo dyes, laccase, microbial fuel cells, decolourization, degradation

INTRODUCTION

Azo dyes are the most common type of synthetic dyes used in the textile industry. These dyes are known to be xenobiotic compounds that possess electron withdrawing groups that generates electron deficiency thereby making them resistant to degradation (Singh et al., 2014). The dyes go through activated sludge systems unchanged and while there are physical-chemical processes like

advanced oxidation, coagulation/flocculation and membrane filtration, these processes are costly and produce a sludge waste which creates a disposal problem.

Microbial fuel cells (MFCs) are extensively explored for treatment of dye containing wastewater and simultaneous electricity production. The major advantages of MFC compared to the conventional wastewater treatment methods are (1) Potential for power production rather than power consumption (2) Low sludge yield (3) Operates at mild temperatures and atmospheric pressure (4) MFCs offer the possibility of carrying out either anodic oxidation or cathodic reduction of the dyes.

In a MFC there are two modes of dye decolourization i.e., at anode and at cathode. At the anode under anaerobic conditions the -N=N- bond is cleaved in the presence of microorganisms to form aromatic amines (**Figure 1**; Fernando et al., 2014; Mani et al., 2017).

Some researchers have also reported that the reduction is mediated by reduced compounds e.g., sulfides, or by redox mediators or the dye itself that act as a terminal electron acceptor with electron transfer being aided by cytochromes and ultimately to the azoreductase on the outside of the membrane (Russ et al., 2000; Pandey et al., 2007). The aromatic amines produced during anode dye decolourization are recalcitrant in nature and do not undergo further degradation in that environment. They can be further reduced to less toxic products in the aerobic stage.

Laccase has been widely used for various types of dye decolourization studies (Daâssi et al., 2013; Ramírez-Montoya et al., 2015; Iark et al., 2019). The major advantage of laccase is that it degrades the dye by non-specific free radical mechanism to form phenolic products thereby avoiding the formation of aromatic amines (Chivukula and Renganathan, 1995). In MFC, laccase and its fungal source was employed at cathode for oxygen reduction reaction (ORR) and dye degradation by Savizi et al. (2012), Simões et al. (2019). The aerobic degradation by laccase yielded products that are less toxic than the original dye.

There are various studies that have investigated azo dye decolourization in the anode and others in the cathode (Huang et al., 2017; Lai et al., 2017; Mani et al., 2018). It is not clear which approach is the best as different studies used different organisms, operating conditions, cathode catalyst etc., making a direct comparison of decolourization rates for each system difficult (**Table 1**). This is the first study to understand the mechanism of dye decolourization in both the processes (anode & cathode), and the nature of products formed, while operating under the same conditions.

This study compared the performance of MFCs treating Acid Orange 7 under anaerobic condition in the presence of bacteria at the anode of MFC and in aerobic condition in the presence of laccase enzyme at the cathode of MFC. The rate of dye decolourization, power density, COD reduction, degradation products and their toxicity were used as performance indicators.

MATERIALS AND METHODS

Experimental Design

The MFCs used in the study were the 'H'-type reactors with a working volume of 200 ml in each chamber. The electrodes were constructed from carbon fiber (non-woven) with a surface area of 25 cm^2. The anolyte consisted of minimal salts medium containing (per liter): 0.46 g NH_4Cl, 0.22 g $(NH)_2SO_4$, 0.117 g $MgSO_4$, 7.7 g $Na_2HPO_4.7H_2O$, 2.87 g NaH_2PO_4 along with 1% (v/v) trace minerals as described by Marsili et al. (2008) and 1% (v/v) vitamin mix as described by Wolin et al. (1963). The carbon source was pyruvate at a concentration of 1 g L^{-1} and casein hydrolysate was added at 500 mg L^{-1}. The pH of the anode solution was adjusted to 7. pH and ionic strength were measured using a calibrated benchtop combined pH and ionic strength meter (pH/CON 700 meter, Cole-Parmer, UK). The concentration of Acid orange 7 dye used was 100 mg L^{-1}.

Three MFC systems were setup. System 1 was dye in the anode with *Shewanella oneidensis* MR1, and laccase enzyme in the cathode, subsequently to be referred to as "MFC $_{\text{Dye Anode}}$." System 2 was with *S. oneidensis* in the anode and laccase in the presence of dye in cathode, subsequently to be referred to as "MFC $_{\text{Dye Cathode}}$" and System 3 with absence of dye in both chambers known as "$MFC_{Control}$" (**Supplementary Figure 1**). Crude commercial laccase enzyme (*T. versicolor*, 10 Units mg^{-1}) obtained from Enzyme India Pvt. Ltd, Chennai was used at an activity of 0.3 U ml^{-1} freely suspended in 200 ml of 100 mM acetate buffer (pH 4.5).

Operating Conditions

The anode and cathode electrodes were connected to a resistor of 2 kΩ. The anode was inoculated with 10% v/v *S. oneidensis* MR-1 culture previously grown in Luria Bertani broth to log phase (OD: 0.4). The anode chamber was sparged for 10 min with nitrogen gas to remove any dissolved oxygen and maintain an anaerobic environment.

The cathode chamber was maintained in aerobic conditions by supplying air through an air stone at a rate of 200 ml air per min. Experiments were conducted at a temperature of 30°C. All experiments were performed in triplicates.

Analytical Procedures

Acid Orange 7 Decolourization

The decolourization of AO7 was measured at various time intervals using a UV-visible spectrophotometer at a wavelength of 484 nm which is the maximum absorption wavelength for AO7. The decolourization efficiency (DE) was calculated by

$$\text{DE}(\%) = \frac{\mathbf{Ao} - \mathbf{A_t}}{\mathbf{Ao}} \times \mathbf{100}$$

Ao and At are the absorbance units at the initial and each time point, respectively. A time series was plotted for the absorbance values measured.

Electrochemical Analysis

The voltage across the system was recorded every 10 min using a data acquisition system Picolog (Pico Technology, UK). The current through the unit was calculated using Ohm's Law:

$$\textit{Current}\ \ (\boldsymbol{I}) = \frac{\textit{Voltage}\,(\boldsymbol{V})}{\textit{Resistance}\,(\Omega)}$$

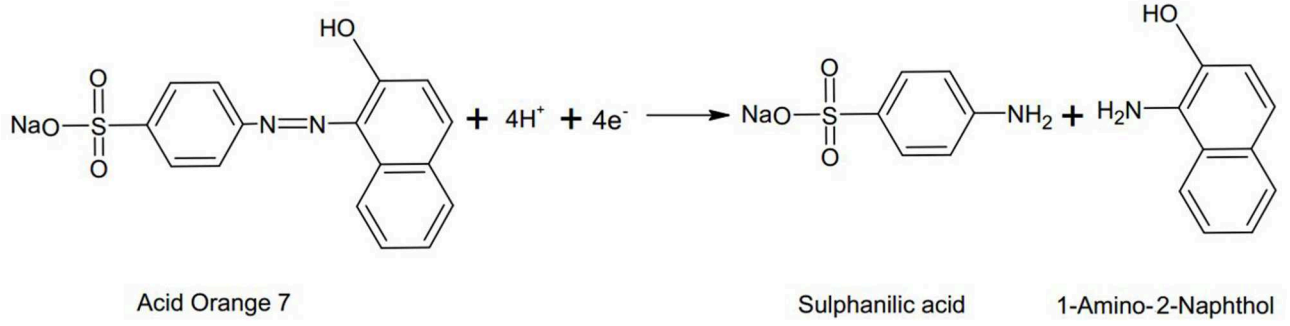

FIGURE 1 | An example illustrating the anaerobic reductive cleavage of azo bond in Acid orange 7 dye (Fernando, 2014).

TABLE 1 | Features of dye degradation in the anode vs. cathode of MFCs.

Anode dye degradation	Cathode dye degradation
I. Microbially mediated II. Reductive process forming aromatic amines III. Mechanism not clear- Azo reductase or reduction by exogenous mediators or reduction by sulfides IV. Microbes can be inhibited by parent dye or the dye degradation products. V. Complete mineralization of dye is unlikely.	I. Electrochemically mediated if the dye possesses a high redox potential or applying external power to the system II. Can involve oxidation of dye by laccase or other enzymes with oxygen as the terminal electron acceptor III. Dye or contaminants in wastewater may inhibit the enzyme activity IV. Complete mineralization of dye is possible.

The power produced was calculated using the following formula:

$$\mathbf{P = I \times V}$$

where P is power in Watts, I is current in amperes and V is the electric potential in volts.

The power and current per surface area of electrode (25 cm^2) was used to calculate the power and current density. To carry out polarization tests, each MFC unit was connected to various external resistances ranging from 10 Ω to 1 MΩ and the potential measured using a multimeter.

Coulombic Efficiency (CE)

The CE was calculated by the following formula (Logan et al., 2006):

$$\mathrm{CE}(\%) = \frac{M \int_0^t I\, dt}{b^* F^* V_{anode}{}^* \Delta COD}$$

where M is the molecular weight of oxygen (32), $\int_0^t I\, dt$ is the integration of current over the time period in an experiment (C), b number of electrons exchanged per mole of oxygen (4), F is Faraday constant (96485 C mol^{-1}), V_{anode} is working volume of anode and COD is change in COD over time (g L^{-1}).

Chemical Oxygen Demand (COD)

COD was measured by the standard closed reflux titrimetric method described by Environment Agency (UK), based on APHA method 5220D. The samples obtained from the MFCs were centrifuged at 4,000 g for 10 min and the supernatant was then filtered through 0.2 μm filter to remove suspended biomass. To 2 ml of appropriately diluted samples 4 ml of COD reagent-Ficodox (Fisher Scientific) containing sulphuric acid, $K_2Cr_2O_7$, Ag_2SO_4 was added and digested at 150°C for 2 h. The samples were then titrated against Ferrous Ammonium Sulfate (0.025 M) by adding 2 drops of Ferroin indicator to determine the residual $K_2Cr_2O_7$ present.

The COD was calculated by the following formula:

$$\mathrm{COD} = \frac{8000 * (Vb - Vs) * DF * M}{Volume\ of\ sample}$$

where, DF is the dilution factor, M is the molarity of FAS (0.025), V_b and Vs are the titrant volumes of FAS for blank and substrate.

Identification of Dye Degradation Metabolites by Gas Chromatography/Mass Spectrometry (GC-MS)

The dye degradation products from both the anode and cathode chamber were analyzed through GC-MS. The samples were extracted with dichloromethane (DCM) using liquid:liquid extraction at a combination of pHs (acidic, neutral, and basic). This modification of pH effectively neutralizes any charged compounds (e.g., phenolics, amines etc.) and allows a better partition into the organic solvent. For the extraction, 2 ml of sample (various pH) was added to 2 ml dichloromethane (DCM) to allow the compounds to separate from the aqueous phase to organic phase. The sample at pH 7 was best extracted into DCM. The extracted sample was introduced into the GC-MS (Agilent) equipped with Restek Rxi-5 ms (20 m × 180 μm × 0.18 μm) column. The initial temperature was held at 40°C for 1 min, and then ramped at 10°C min^{-1} until 340°C which was then held for 10 min. The interface temperature was 280°C. A 1 μl sample was injected on a pulsed splitless injection at 250°C. The flow rate of carrier gas helium was at 1.1 ml min^{-1}. Electron ionization (EI) was used with MS source temperature at 230°C and Quad temperature at 150°C. The m/z range selected was from 25 to 750 amu. The products were identified using NIST mass spectra database. Internal standards were injected in between the samples to validate the method used.

Microtox Toxicity Analysis

The toxicity of the samples were measured by the Microtox toxicity assay using the bioluminescence bacteria *Vibrio fischeri* (Hao et al., 1996).

The *Shewanella* decolourized products (anode); the autooxidation products of *Shewanella* sp. and laccase dye degradation (cathode) samples were centrifuged at 4000 g, the cells harvested, washed twice with sterile phosphate buffer (100 mM, pH 7.1) and suspended in 2% NaCl. Serial dilutions of the samples with 2% NaCl in the presence of the *V. fischeri* cell suspension was carried out in a 96 well-plate. The plate was incubated at 15°C for 10 min and the luminescence was measured using a Fluostar Optima plate reader. The absolute light units were recorded and IC_{50}, a concentration which inhibits 50% of light was calculated for each sample.

Cyclic Voltammetry (CV of Dye Degradation Products)

CV measurements were carried out for standards 1-Amino-2-Naphthol, sulfanilic acid, acid orange 7 dye and the dye degradation products. A three-electrode system with the working electrode as glassy carbon, platinum as the counter, and Ag/AgCl as reference electrode was used. The three standard compounds were prepared in deionized water at a concentration of 100 mg L^{-1}. The dye degradation products were filtered to remove any bacterial cells to prevent interference. CV was carried out using a potentiostat Keysight B2900A by cycling between potentials of −1 V to 1.5 V at 50 mV s^{-1}.

Statistical Analysis

All experimental data indicated in the text and graphs are the means of triplicate experiments unless otherwise stated. The error bars in the graphs and values in the text represent the standard deviation of the mean (SD).

RESULTS AND DISCUSSION

Power Generation and COD Reduction

The open circuit voltage (OCV) was highest for $MFC_{Control}$ with 1.3 V followed by $MFC_{Dye\ Cathode}$ with 950 and 930 mV for $MFC_{Dye\ Anode}$. The maximum power density obtained from $MFC_{Dye\ Anode}$ was 42.5 ± 2.6 mW m^{-2} and 50 ± 4 mW m^{-2} for $MFC_{Dye\ Cathode}$ and 57.8 ± 1.6 mW m^{-2} for $MFC_{Control}$ (**Figure 2A**). The lower power density in case of dye in the anode indicates that the presence of AO7 had a significant effect on the growth rate of *S. oneidensis*. One of the major reasons affecting the cell viability might be the accumulation of anaerobic degradation products of azo dyes such as aromatic amines which are known to be toxic to the bacteria. Moreover, it has been reported that the reduction of azo dyes by *S. oneidensis* under anaerobic condition is enhanced by mediators such as flavins and quinones (von Canstein et al., 2008; Le Laz et al., 2014). These flavins produced by *Shewanella* are also responsible for the extracellular electron transfer to the electrode at the anode (Marsili et al., 2008). The competition of electrons from the flavins between dye and electrode might result in lower power in the $MFC_{Dye\ Anode}$. Another possible mechanism for lower power is as suggested by Sun et al. (2013) that in biological decolourization of dyes in MFCs a portion of the available electrons are transported to electrode while another portion of electrons are used for reductive decolourization of dyes. The absence of dye in both chambers increased the power in $MFC_{Control}$ due to bacteria shuttling electrons to the electrode rather than the dye and at cathode the electrode is the sole electron donor to laccase. The internal resistance of $MFC_{Control}$ was lowest with 1.5 ± 0.07 kΩ followed by the $MFC_{Dye\ Anode}$ with 1.72 ± 0.11 kΩ and highest for $MFC_{Dye\ Cathode}$ with 1.9 ± 0.13 kΩ (**Figure 2B**).

There was 80.4 ± 1.2% reduction in COD for $MFC_{Dye\ Cathode}$ which was closely followed by the control system with 79.2 ± 1.3% reduction for $MFC_{Control}$ and finally 69 ± 2% for $MFC_{Dye\ Anode}$ on day 3 of the study. The Coulombic efficiency (CE) of the systems also followed the trend with 5% for $MFC_{Control}$, 4.7 and 3.6% for $MFC_{Dye\ Cathode}$ and $MFC_{Dye\ Anode}$, respectively. Overall, on comparing the voltage, CE, power density, and COD $MFC_{Control}$ performance was the best.

In the absence of dye at cathode, laccase accepts electrons from the electrode for oxygen reduction reaction. The redox potential of the dye (0.653 V vs. SHE) is lower than that of laccase at 0.78 V vs. SHE, therefore, in the system $MFC_{Dye\ Cathode}$ the dye is oxidized easily for electrons that are used for ORR. The lower power in $MFC_{Dye\ Cathode}$ than $MFC_{Control}$ might be due to the inhibition of the enzyme activity by the dye or its degradation products. Since the bacterial electron transfer is quite slow, the anode reaction acts as a rate limiting step in the MFC. As a result, whilst there is competition between the dye and electrode for electron transfer to laccase or inhibition of laccase by the dye, the power is not significantly affected by the cathode reaction (**Supplementary Figure 2**).

AO7 Dye Decolourization

The decolourization of Acid Orange 7 was measured at the maximum absorption wavelength for the dye (484 nm). The rate of decolourization was faster in the $MFC_{Dye\ Cathode}$ compared to $MFC_{Dye\ Anode}$. There was >80% decolourization within the first 24 h for laccase compared to 20% for $MFC_{Dye\ Anode}$ (**Figure 3**). The overall dye decolourization in 96 h was 97 ± 2% for $MFC_{Dye\ Anode}$ and 98 ± 3% for $MFC_{Dye\ Cathode}$. In $MFC_{Dye\ Anode}$, the bacteria have an initial lag phase (slower decolourization) followed by a log phase where there is an increased decolourization rate. Hence the time taken to reach maximum power density was also slower in case of dye in the anode as compared to the dye in the cathode.

Anaerobic treatment of azo dyes involves the reductive cleavage of the N=N to form colorless aromatic amines. In the anode, azo dye under anaerobic conditions is reduced by *Shewanella* via azoreductase enzyme or by the Mtr respiratory pathway. Initially an azo reductase enzyme was speculated to be responsible for degradation of azo dyes by *Shewanella*, but these enzymes were effective only with cell extracts and not with intact cells. Thus, establishing that decolourization is mainly an extracellular process (Brigé et al., 2008). Recent

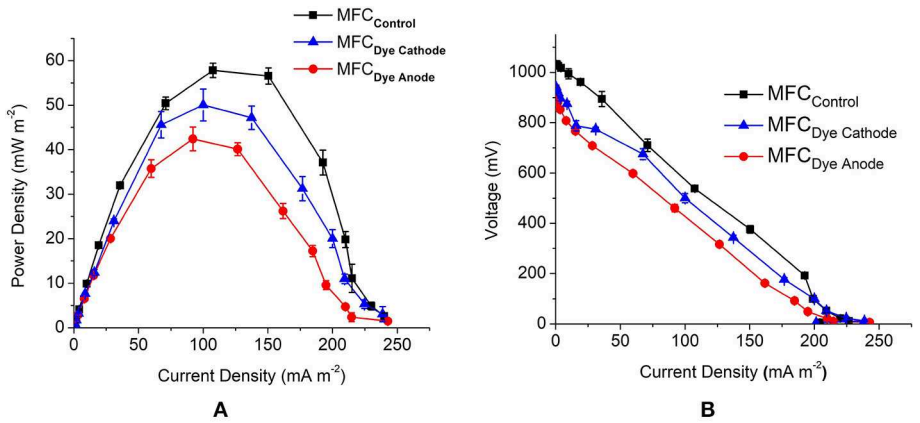

FIGURE 2 | (A) Comparison of MFC performance for all MFC systems obtained by varying the external circuit resistance (10 Ω-1 MΩ) **(B)** polarization curves for all the systems used in the study.

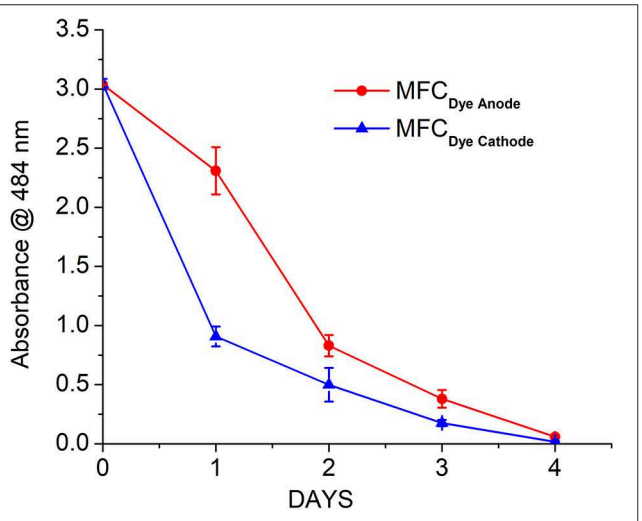

FIGURE 3 | Decolourization of AO7 in the anode (*Shewanella oneidensis*) and cathode (Laccase) of MFC over a period of 4 days.

studies have shown that Mtr respiratory pathway in *S. oneidensis* MR1 is responsible for azo dye reduction under anaerobic condition in which OmcA/MtrC plays the role of "azo reductase" (Hong and Gu, 2010). Flavins have been reported to aid and enhance the decolourization process (Cai et al., 2012). This is in concurrence with the lower power obtained for dye in anode due to the dye being the alternative electron acceptor to the electrode. Since azo dyes are large and usually charged, they are likely to be reduced extracellularly or with membrane bound enzymes.

The decolourization by laccase follows an entirely different mechanism than the bacteria. There is production of free radicals by laccase enzyme that carries out non-specific attack of the dye at various positions to yield a number of products. The dye decolourization was faster with enzyme due to the faster reaction kinetics of enzyme compared to the bacteria.

Electrochemical Analysis of Dye Degradation Products

The anode dye degradation products were analyzed using cyclic voltammetry for the presence of reduction end products. The CV was compared with the standard compounds viz. acid orange 7, sulfanilic acid (SA), and 1-amino-2-naphthol (1-A-2-N). Standard sulfanilic acid showed strong oxidation/reduction peaks at 0.94 V/0.811 V and a weak oxidation/reduction couple at 0.27 V/0.211 V vs. Ag/AgCl (**Figure 4**). The CV of initial AO7 dye produced a redox couple at 0.89 V/0.7 V and 0.11 V /−0.08 V vs. Ag/AgCl, respectively (**Figure 4A**). The shift in the peak potential is due to the presence of both SA and 1-A-2-N in the parent dye. The *S. oneidensis* degraded dye product showed a characteristic peak at 0.96 V indicating the presence of sulfanilic acid (**Figure 4B**). There was no peak observed for 1-A-2-N, which might be the result of limited solubility of the compound in water. Thus, it can be inferred that mechanism of dye degradation in anode is through the cleavage of the N=N azo bond separating the two rings. On the other hand, the laccase dye degradation at the cathode did not show any characteristic redox peaks indicating a completely different mechanism (**Figure 4B**). Since the redox peaks for both AO7 and sulfanilic acid were absent it can be presumed that the degradation involves a ring cleavage thus releasing the characteristic functional groups.

Auto-Oxidation of *S. oneidensis* (Anode) Decolourized Products

The anaerobic dye degradation products (colorless) on exposure to air regained color. This phenomenon of color formation from decolourized products was referred to as auto-oxidation (**Figure 5**).

To determine the possibility of auto-oxidation occurring in other azo dyes the anaerobic decolourization of Congo Red (CR), a diazo dye, was carried out in the presence of *S.oneidensis* to observe the stability of the decolourized products. Similar to AO7, the CR decolourized products were also auto-oxidized on exposure to air. Initially it was hypothesized the color formation

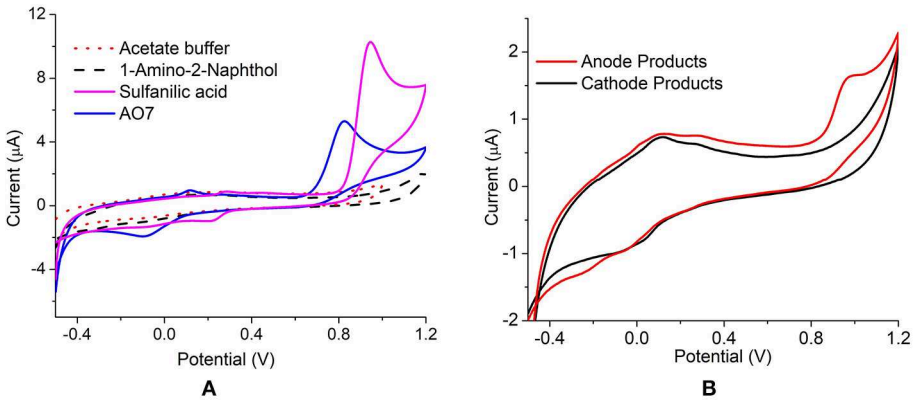

FIGURE 4 | Cyclic Voltammetry of **(A)** parent dye (AO7), standards SA and 1-A-2-N **(B)** anode and cathode decolourized products, at 50 mV s^{-1} vs. Ag/AgCl.

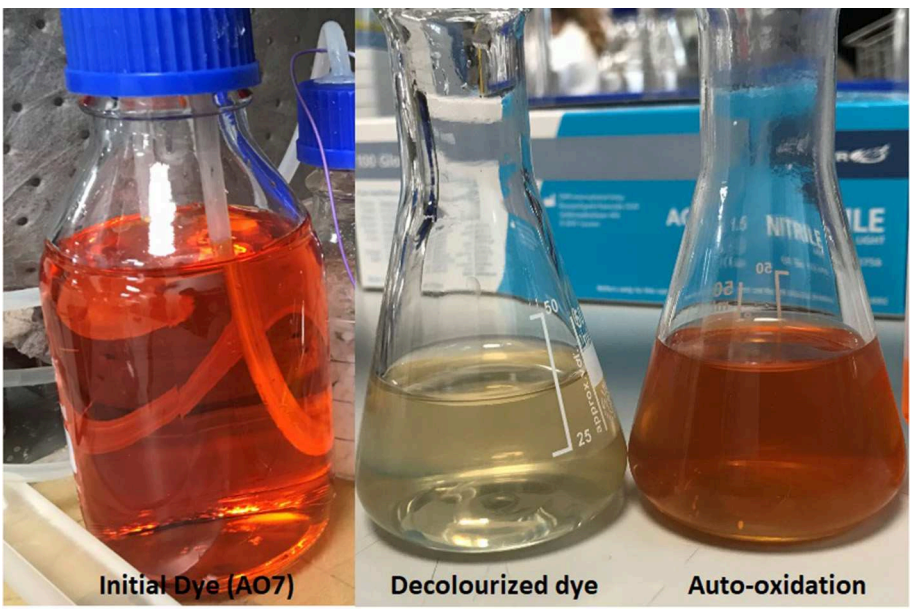

FIGURE 5 | The depiction of initial colored dye together with the decolourized products and the colored auto-oxidation products.

might be due to the diazotization (-N=N-) of the auto-oxidized products to form the initial dye. Therefore, a UV-scan of the decolourized products, auto-oxidized products, and the initial dye for both AO7 and CR was performed. The scan results revealed that the color was not due to the formation of -N=N- present in the initial dyes (**Figure 6**).

The auto-oxidation effect on anaerobic azo dye degradation products was first observed by Kudlich et al. (1999). They determined that mono and diazo sulfonated dyes that produced aminohydroxynaphthalenesulfonate (AHNS) by-products were unstable, sensitive to oxygen, and underwent dimerization to form colored products. The auto-catalysis of Acid Orange 7 (AO 7) studied by Carvalho et al. (2008) detected that 1-amino-2-naphthol, formed by reductive cleavage of the dye, when exposed to aerobic conditions yielded products that are brown in color.

The nature of auto-oxidation products of AO7 has not been discussed in literature thus far. A GC-MS analysis of these products was performed to identify and determine the pathway that leads to the formation of color.

GC-MS Analysis of Dye Degradation Products

Shewanella Oneidensis MR1 (Anode) Dye Degradation Products

The mechanism of the dye degradation analyzed by CV was further confirmed with GC-MS. Under anaerobic condition in $MFC_{Dye\ Anode}$, *S. oneidensis* was observed to symmetrically cleave the azo bond resulting in the formation of 1-amino-2-naphthalenol (1-A-2-N) ($M+H^+$ = 159, R_t: 18.13) and aminobenzene sulfonic acid (sulfanilic acid) (**Figure 7**). Sulfanilic

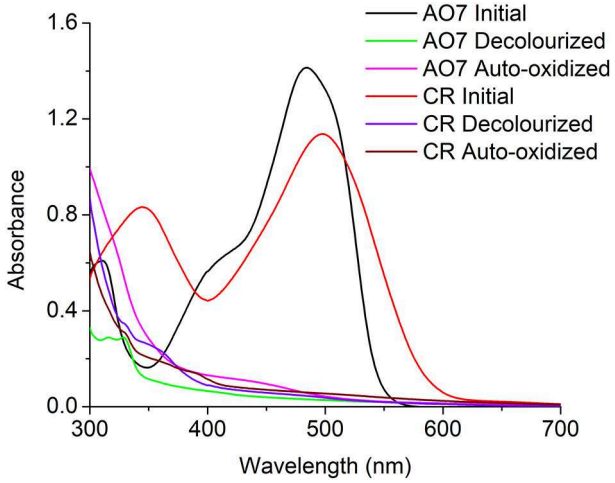

FIGURE 6 | UV-Scan of AO7 and CR initial dye, decolourized products, and Auto-oxidation products indicating the color in the auto-oxidation products was not a result of diazotization.

acid (SA) being highly polar molecule was not detected in GC-MS. 2-amino-1-naphthalenol ($M+H^+$ = 159, R_t: 18.49) was also present in the degradation products of *Shewanella* indicating the formation of various aromatic amine metabolites during the reductive decolourization of AO7 (**Figure 7**). The presence of aminobenzenes under anaerobic dye decolourization of AO7 was also observed by Fernando et al. (2012).

Auto-Oxidation Products and Mechanism

The initial products obtained were the same as in anode dye decolourized i.e., 1-amino-2-naphthalenol (1-A-2-N) ($M+H^+$ = 159, R_t: 18.13), aminobenzene sulfonic acid (sulfanilic acid), 2-amino-1-naphthalenol (2-A-1-N) ($M+H^+$ = 159, R_t: 18.49). On exposure to oxygen, 2-amino-1-naphthalenol was oxidized to 2-amino-1,4-naphthoquinone (2ANQ) ($M+H^+$ = 173, R_t: 15.75; **Figure 7**). The 2ANQ further underwent substitution reaction with carboxylic acids (acetate from bacterial metabolism) in the reaction medium to produce 2-methoxy-1,4-naphthoquinone (2MNQ) ($M+H^+$ = 188, R_t: 14.84) an orange colored product (**Figure 7**). 2MNQ is an orange color organic pigment originally derived from the soil (Lambert et al., 1971). The color formation in the auto-oxidized products might be due to the presence of the above pigment.

The other quinones observed in the GC-MS of auto-oxidation products were 4-quinolinecarboxyaldehyde ($M+H^+$ = 157, R_t:11.61) and 4-Thio-methyl-1,2-naphthoquinone ($M+H^+$ = 176, R_t:14.43) with 1,2- naphthoquinone being a product of 1-A-2-N oxidation (**Figure 7**). A clear mechanism of sulfanyl group (SO^{2-}) addition could not be further explained. Quinones are precursors for anthraquinone dyes and a number of these compounds have a chromophore moiety (Matsuoka, 1990). The production of quinone intermediates during anaerobic degradation of dyes is seen in number of mono and diazo dyes. In general, quinones possess redox mediating properties, and aid in azo dye decolourization by transferring electrons between dye and bacteria (Van der Zee et al., 2000).

The presence of a variety of quinone intermediates and their subsequent conversion products that yield a color clearly indicates the mechanism of color formation due to auto-oxidation.

This was also observed by Kudlich et al. (1999) in which the naphthalene derivatives of azo dye degradation underwent auto-oxidation to form dimers which resulted in color formation. In their study the oxidation of aminohydroxynaphthalenesulfonates (AHNS) to naphthoquinonesulfonates and their subsequent dimerization developed a colored product. The substitution reaction with carboxylic acid might be similar to that of 5-hydroxy-1,4-naphthoquinone when treated with acetic anhydride to form 5-hydroxy-3-methoxy-1,4-naphthoquinone (Blauenburg et al., 2012).

Laccase Dye Degradation Products and Mechanism

The first step in laccase degradation mechanism for system $MFC_{Dye\ Cathode}$ is the decolourization of the Acid Orange 7 dye by asymmetric cleavage of the -N=N- bond to form intermediates Naphthalen-2-ol and (4-sulfophenyl) diazenyl (**Figure 8**).

The intermediate Naphthalen-2-ol undergoes aromatic ring cleavage to produce 1,2-Benzenedicarboxylic acid (Phthalic acid) ($M+H^+$ = 149.1, R_t:9.50). Pthalic acid functional group is further oxidized to form benzoic acid ($M+H^+$ = 105, R_t: 7.89; **Figure 8**).

The other intermediate (4-sulfophenyl)diazenyl was subjected to oxidative desulfonation to form phenyldiazenyl. Phenyl diazene radical rapidly loses nitrogen (N_2) as gas molecule and the nucleophilic substitution of hydroxyl radical (OH^-) on the aromatic ring results in the formation of phenol. Phenols are the natural substrates for laccase therefore the oxidative ring cleavage of phenol ring was carried out to form fatty acid such as hexanoic acid ($M+H^+$ = 60, R_t: 4.95; **Figure 8**). Hexanoic acid is a non-toxic compound that is present in food products available for human consumption.

The benzoic acid pathway was also observed by Fernando et al. (2014) for aerobic degradation of AO7 suggesting that mono-oxygenase enzymes from bacteria were capable of the degradation pathway. Due to the slow bacterial metabolism, only the larger intermediate products were observed in their study. The rapid laccase reaction in this study led to the formation of smaller and simple products.

The symmetric and asymmetric cleavage depends on the dye structure and the type of enzyme used. It is suggested that bacterial laccase with low redox potential are not capable of cleaving the azo bond. Pereira et al. (2009) observed that laccase from *Bacillus subtilis* oxidized mono azo dye Sudan Orange G to produce oligomers and polymers by radical coupling reactions without the cleavage of the azo bond. Therefore, fungal laccase with high redox potential can effectively cleave the azo bonds to bring about decolourization.

Similar pathway was also observed for degradation of Remazol brilliant blue dye by *P. ostreatus* laccase with successive deamination, hydroxylation, oxidation followed by the ring cleavage (Zhuo et al., 2019). The formation of phenyl diazene radical and loss of N_2 was also observed by Chivukula and

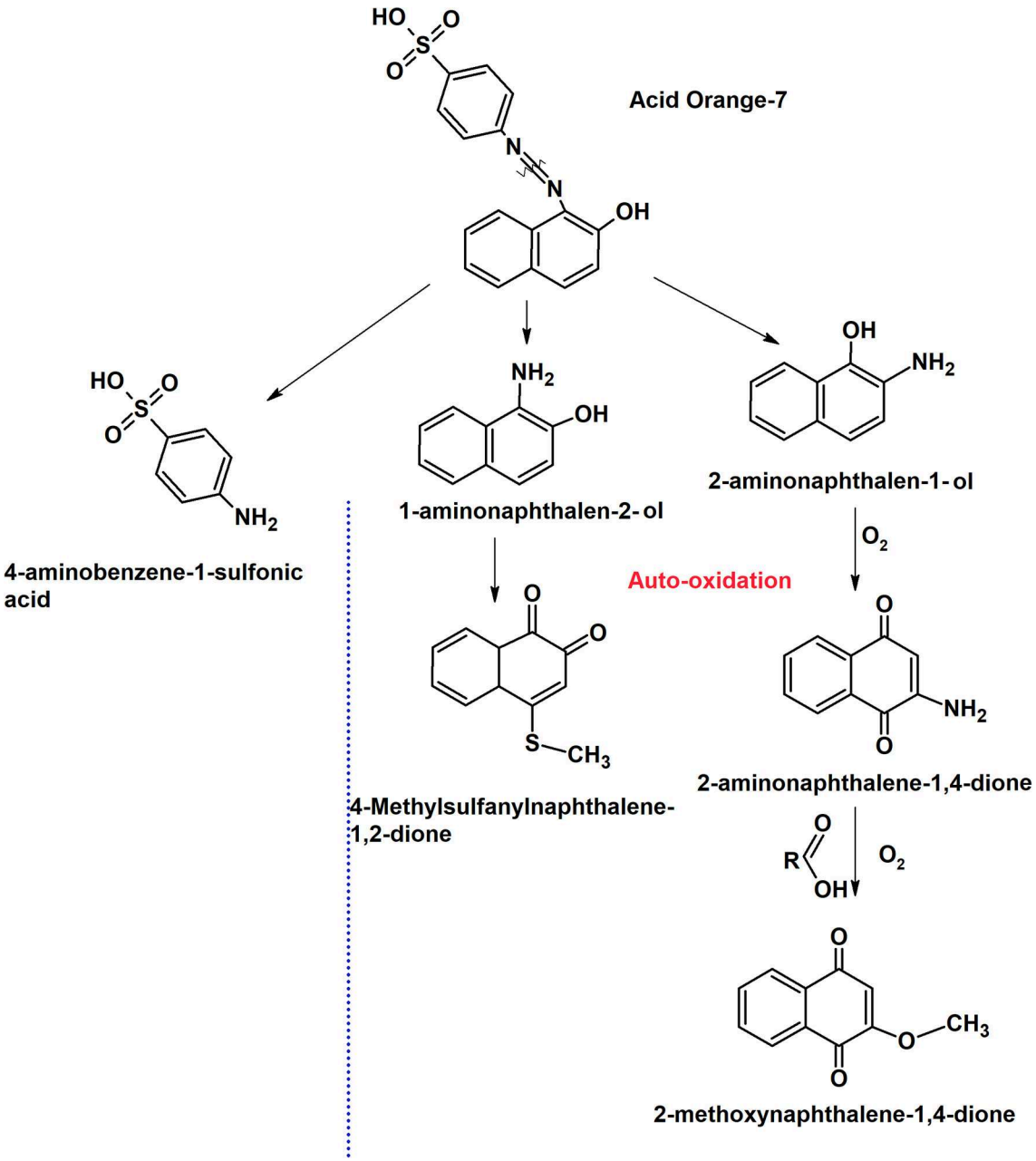

FIGURE 7 | Putative dye degradation pathway by *S. oneidensis* MR 1 at the anode and the auto-oxidation mechanism based on the intermediate products obtained from GC-MS analysis.

Renganathan (1995) for degradation of phenolic azo dyes by *P. oryzae* laccase. The attack of dioxygen on phenolic ring cleavage by laccase is widely seen in oxidation of lignin products and catechol (Crestini and Argyropoulos, 1998; Chen et al., 2017). Laccase oxidation of dye is through highly reactive free radicals that are involved in the above reactions and since they are non-specific a wide number of products are formed. This mechanism produces phenol-based products thereby avoiding the formation of toxic aromatic amines (**Figure 8**).

Toxicity Analysis

The toxicity of the samples was analyzed by *V. fischeri* toxicity assay to determine the percentage inhibition of the dye degradation products to the bacterial cells. The samples were subjected to dilutions and the corresponding inhibition values were plotted against each dilution (**Figure 9**).

It is evident that the auto-oxidation products have higher inhibition compared to anode ($MFC_{Dye\ Anode}$)

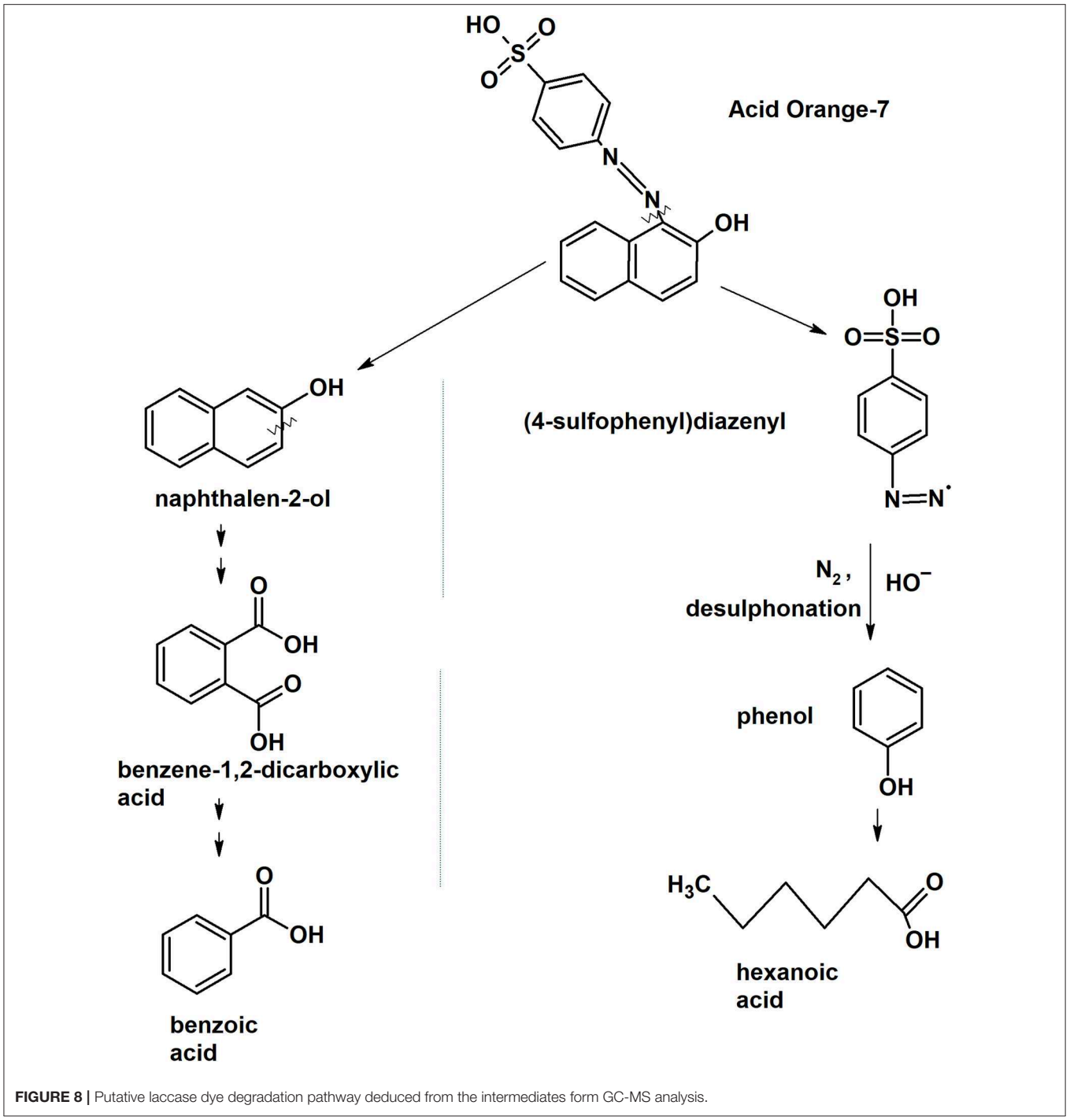

FIGURE 8 | Putative laccase dye degradation pathway deduced from the intermediates form GC-MS analysis.

and cathode ($MFC_{Dye\ Cathode}$) treated products. In the initial concentration, cathode treated products are comparatively more inhibitive than the anode products. As seen in the graph on increasing the concentration, the anode products have an upward trend while laccase products are quite constant throughout. As the concentration of the anode effluents increase the toxicity increases. Similar trend was observed for the auto-oxidation products.

Laccase degradation of dye is through a free radical mechanism that produces a huge number of products (phenol, benzoic acid, hexanoic acid) compared to *Shewanella* degradation. These products are monocyclic hydrocarbons that could be degraded readily in next stages of water treatment. The LD_{50} concentration of benzoic acid for mammalian cells is 2.3 gm/Kg (MSDS, Sigma Aldrich). The overall concentration of the dye is 100 mg/L in this study. Therefore, the concentration of dye breakdown would be

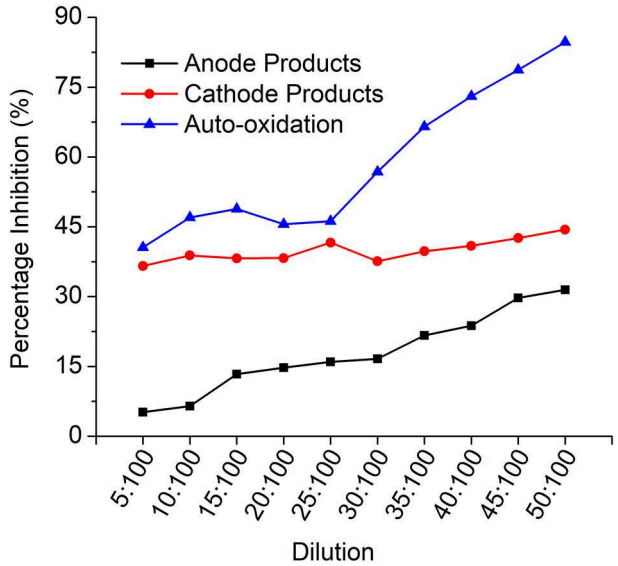

FIGURE 9 | *Vibrio fischeri* toxicity profile indicating the % inhibition for each dilution for all the products.

expected to be lower than 100 mg/L, which is a very low concentration to exhibit toxicity. The horizontal curve for cathode products might be due to the formation of phenol-based products by laccase that are toxic to the *V. fischeri* or the consumption of the dissolved oxygen by laccase enzyme that created anoxic conditions for the bacteria. *Vibrio fischeri* is a highly sensitive organism and it's EC_{50} for phenol is 23 mg L^{-1} (Fernando et al., 2014).

In contrast, 1-amino-2-napthalenol obtained from by reductive cleavage of the dye by *S. oneidensis* is known to be xenobiotic and are classified as possible human carcinogens by the International Agency for Research on Cancer (Group 1 or 2B) and the European Union (Category 1A or 1B). In Japan, 20% of workers involved in the production of aromatic amines developed uroepithelial cancer (Hamasaki et al., 1996). The auto-oxidation of these amines yielded products that are more toxic than the parent amines.

The auto-oxidation products showed highest toxicity to the *Vibrio* cells due to the presence of naphthoquinone intermediates (**Figure 7**). Naphthoquinones are highly reactive oxidative species that are known to cause cellular oxidative stress that affects the signaling pathway in the cells (Klotz et al., 2014). Quinones are used for medicinal purposes due to their anti-fungal, anti-bacterial and antioxidant properties. They are used in cancer drugs due their ability to form Reactive oxygen species (ROS) that attack and destroy the tumor cells (Verrax et al., 2011).

The toxicity measurements are a relative comparison between each system. There are various methods for testing the toxicity depending on the application of the discharged effluents. In this study, Microtox assay was utilized due to its high level of sensitivity compared to methods like MTT.

CONCLUSION

In the current study two different systems i.e., MFC with dye at the anode in presence of *S. oneidensis* and MFC with dye at cathode in the presence of laccase, were explored for AO7 degradation. The power density was higher in $MFC_{Dye\ Cathode}$ with 50 ± 4 mW m^{-2} compared to $MFC_{Dye\ Anode}$ with 42.5 ± 2.6 mW m^{-2}. The same trend was followed for CE (4.7 and 3.6% for $MFC_{Dye\ Cathode}$ and $MFC_{Dye\ Anode}$) and COD (80.4 ± 1.2% for $MFC_{Dye\ Cathode}$ and 69 ± 2% for $MFCD_{Dye\ Anode}$), respectively. The time required for decolourization was longer with bacteria (anode) where only 20% decolourization was obtained after 24 h whereas there was >80% for laccase during the same time. The anode decolourized products were found to be unstable when exposed to oxygen resulting in autooxidation and regaining of the color. GC-MS analysis revealed simpler compounds such as benzoic acid and hexanoic acid for laccase, whereas *S. oneidensis* produced aromatic amines. The color formation in auto-oxidation was likely due to the presence of quinones produced by oxidation of the aromatic amines. These auto oxidized products had higher toxicity than the initial anode and cathode dye degradation products. Therefore, from this study it was observed that laccase based MFC-dye decolourization systems are best suited for degradation and detoxification of azo dyes while producing good power output. Thus, the current study also provides an insight into the different mechanisms and pathways leading to maximal degradation of the azo dyes.

DATA AVAILABILITY

All datasets generated for this study are included in the manuscript/**Supplementary Files**.

AUTHOR CONTRIBUTIONS

GK, TC, and TK formulated the design of the experiments. PM, KB, and MB carried out the experiments. VF carried out the data analysis. PM wrote the first draft of the manuscript. GK edited the manuscript to the level at which it was submitted. All authors proof-read the draft.

FUNDING

This work was part of Newton-Mosharafa Institutional Links project fully funded by the Science and Technology Development Fund in Egypt (ID 27662) and British Council in UK (ID 261690585).

SUPPLEMENTARY MATERIAL

The Supplementary Material for this article can be found online at: https://www.frontiersin.org/articles/10.3389/fenrg.2019.00101/full#supplementary-material

Supplementary Figure 1 | Graphical representation of the study.

Supplementary Figure 2 | Relative enzyme activity of laccase in the absence and presence of the dye.

REFERENCES

Blauenburg, B., Metsä-Ketelä, M., and Klika, K. D. (2012). Formation of 5-hydroxy-3-methoxy-1,4-naphthoquinone and 8-Hydroxy-4-methoxy-1,2-naphthoquinone from Juglone. *ISRN Org. Chem.* 2012, 1–7. doi: 10.5402/2012/274980

Brigé, A., Motte, B., Borloo, J., Buysschaert, G., Devreese, B., and Van Beeumen, J. J. (2008). Bacterial decolorization of textile dyes is an extracellular process requiring a multicomponent electron transfer pathway. *Microb. Biotechnol.* 1, 40–52. doi: 10.1111/j.1751-7915.2007.00005.x

Cai, P. J., Xiao, X., He, Y. R., Li, W. W., Chu, J., Wu, C., et al. (2012). Anaerobic biodecolorization mechanism of methyl orange by *Shewanella oneidensis* MR-1. *Appl. Microbiol. Biotechnol.* 93, 1769–1776. doi: 10.1007/s00253-011-3508-8

Carvalho, M. C., Pereira, C., Gonçalves, I. C., Pinheiro, H. M., Santos, A. R., Lopes, A., et al. (2008). Assessment of the biodegradability of a monosulfonated azo dye and aromatic amines. *Int. Biodeter. Biodegr.* 62, 96–103. doi: 10.1016/j.ibiod.2007.12.008

Chen, M., Wang, L., Tan, T., Luo, X. C., Zheng, Z., Yin, R. C., et al. (2017). Radical mechanism of laccase-catalyzed catechol ring-opening. *Wuli Huaxue Xuebao/Acta Phys.* 33, 620–626. doi: 10.3866/PKU.WHXB201612011

Chivukula, M., and Renganathan, V. (1995). Phenolic azo dye oxidation by laccase from *Pyricularia oryzae*. *Appl. Environ. Microbiol.* 61, 4374–4377.

Crestini, C., and Argyropoulos, D. S. (1998). The early oxidative biodegradation steps of residual kraft lignin models with laccase. *Bioorg. Med. Chem.* 6, 2161–2169. doi: 10.1016/S0968-0896(98)00173-4

Daâssi, D., Zouari-Mechichi, H., Frikha, F., Martinez, M. J., Nasri, M., and Mechichi, T. (2013). Decolorization of the azo dye acid orange 51 by laccase produced in solid culture of a newly isolated *Trametes trogii* strain. *3 Biotech* 3, 115–125. doi: 10.1007/s13205-012-0076-2

Fernando, E. (2014). *Treatment of Azo Dyes in Industrial Wastewater Using Microbial Fuel Cells.* PhD thesis, Univ. Westminster, UK. Available online at: http://westminsterresearch.wmin.ac.uk/14330/

Fernando, E., Keshavarz, T., and Kyazze, G. (2012). Enhanced bio-decolourisation of acid orange 7 by *Shewanella oneidensis* through co-metabolism in a microbial fuel cell. *Int. Biodeterior. Biodegr.* 72, 1–9. doi: 10.1016/j.ibiod.2012.04.010

Fernando, E., Keshavarz, T., and Kyazze, G. (2014). Complete degradation of the azo dye Acid Orange-7 and bioelectricity generation in an integrated microbial fuel cell, aerobic two-stage bioreactor system in continuous flow mode at ambient temperature. *Bioresour. Technol.* 156, 155–162. doi: 10.1016/j.biortech.2014.01.036

Hamasaki, T., Aramaki, K., Hida, T., Inatomi, H., Fujimoto, N., Okamura, T., et al. (1996). [Clinical study of occupational uroepithelial cancer]. *J. UOEH* 18, 247–59. doi: 10.7888/juoeh.18.247

Hao, O. J., Chien-Jen, S., Chen-Fang, L., Fu-Tien, J., and Zen-Chyuan, C. (1996). Use of microtox tests for screening industrial wastewater toxicity. *Water Sci. Technol.* 34, 43–50. doi: 10.2166/wst.1996.0237

Hong, Y.-G., and Gu, J.-D. (2010). Physiology and biochemistry of reduction of azo compounds by *Shewanella* strains relevant to electron transport chain. *Appl. Microbiol. Biotechnol.* 88, 637–643. doi: 10.1007/s00253-010-2820-z

Huang, W., Chen, J., Hu, Y., Chen, J., Sun, J., and Zhang, L. (2017). Enhanced simultaneous decolorization of azo dye and electricity generation in microbial fuel cell (MFC) with redox mediator modified anode. *Int. J. Hydrogen Energy* 42, 2349–2359. doi: 10.1016/j.ijhydene.2016.09.216

Iark, D., Buzzo, A. J., Garcia, J. A. A., Côrrea, V. G., Helm, C. V., and Corrêa, R. C. G. (2019). Enzymatic degradation and detoxification of azo dye Congo red by a new laccase from *Oudemansiella canarii*. *Bioresour. Technol.* 289:121655. doi: 10.1016/j.biortech.2019.121655

Klotz, L. O., Hou, X., and Jacob, C. (2014). 1,4-naphthoquinones: from oxidative damage to cellular and inter-cellular signaling. *Molecules* 19, 14902–14918. doi: 10.3390/molecules190914902

Kudlich, M., Hetheridge, M. J., Knackmuss, H.-J., and Stolz, A. (1999). Autoxidation reactions of different aromatic *o*-aminohydroxynaphthalenes that are formed during the anaerobic reduction of sulfonated azo dyes. *Environ. Sci. Technol.* 33, 896–901. doi: 10.1021/es9808346

Lai, C. Y., Wu, C. H., Meng, C. T., and Lin, C. W. (2017). Decolorization of azo dye and generation of electricity by microbial fuel cell with laccase-producing white-rot fungus on cathode. *Appl. Energy* 188, 392–398. doi: 10.1016/j.apenergy.2016.12.044

Lambert, E. N., Seaforth, C. E., and Ahmad, N. (1971). The occurrence of 2-Methoxy-l,4-naphthoquinone in caribbean vertisols. *Soil Sci. Soc. Am. Proc.* 35, 7–8. doi: 10.2136/sssaj1971.03615995003500030037x

Le Laz, S., Kpebe, A., Lorquin, J., Brugna, M., and Rousset, M. (2014). H2-dependent azoreduction by *Shewanella oneidensis* MR-1: involvement of secreted flavins and both [Ni–Fe] and [Fe–Fe] hydrogenases. *Appl. Microbiol. Biotechnol.* 98, 2699–2707. doi: 10.1007/s00253-013-5208-z

Logan, B. E., Hamelers, B., Rozendal, R., Schroder, U., Keller, J., Freguia, S., et al. (2006). Microbial fuel cells: methodology and technology. *Environ. Sci. Technol.* 40, 5181–5192. doi: 10.1021/es0605016

Mani, P., Keshavarz, T., Chandra, T. S., and Kyazze, G. (2017). Decolourisation of Acid orange 7 in a microbial fuel cell with a laccase-based biocathode: influence of mitigating pH changes in the cathode chamber. *Enzyme Microb. Technol.* 96, 170–176. doi: 10.1016/j.enzmictec.2016.10.012

Mani, P., Kumar, V. T. F., Keshavarz, T., Chandra, T. S., Kyazze, G., Mani, P., et al. (2018). The role of natural laccase redox mediators in simultaneous dye decolorization and power production in microbial fuel cells. *Energies* 11:3455. doi: 10.3390/en11123455

Marsili, E., Baron, D. B., Shikhare, I. D., Coursolle, D., Gralnick, J. A., and Bond, D. R. (2008). *Shewanella* secretes flavins that mediate extracellular electron transfer. *PNAS* 105, 6–11. doi: 10.1073/pnas.0710525105

Matsuoka, M. (ed.). (1990). "Quinone Dyes," in *Infrared Absorbing Dyes* (Boston, MA: Springer), 35–43. doi: 10.1007/978-1-4899-2046-1_4

Pandey, A., Singh, P., and Iyengar, L. (2007). Bacterial decolorization and degradation of azo dyes. *Int. Biodeterior. Biodegrad.* 59, 73–84. doi: 10.1016/j.ibiod.2006.08.006

Pereira, L., Coelho, A. V., Viegas, C. A., Santos, M. M. C., dos Robalo, M. P., and Martins, L. O. (2009). Enzymatic biotransformation of the azo dye Sudan Orange G with bacterial CotA-laccase. *J. Biotechnol.* 139, 68–77. doi: 10.1016/j.jbiotec.2008.09.001

Ramírez-Montoya, L. A., Hernández-Montoya, V., Montes-Morán, M. A., Jáuregui-Rincón, J., and Cervantes, F. J. (2015). Decolorization of dyes with different molecular properties using free and immobilized laccases from *Trametes versicolor*. *J. Mol. Liq.* 212, 30–37. doi: 10.1016/j.molliq.2015.08.040

Russ, R., Rau, J., and Stolz, A. (2000). The function of cytoplasmic flavin reductases in the reduction of azo dyes by bacteria. *Appl. Environ. Microbiol.* 66, 1429–34. doi: 10.1128/AEM.66.4.1429-1434.2000

Savizi, I. S. P., Kariminia, H. R., and Bakhshian, S. (2012). Simultaneous decolorization and bioelectricity generation in a dual chamber microbial fuel cell using electropolymerized-enzymatic cathode. *Environ. Sci. Technol.* 46, 6584–6593. doi: 10.1021/es300367h

Simões, M. F., Maiorano, A. E., dos Santos, J. G., Peixoto, L., de Souza, R. F. B., Neto, A. O., et al. (2019). Microbial fuel cell-induced production of fungal laccase to degrade the anthraquinone dye Remazol Brilliant Blue R. *Environ. Chem. Lett.* 17, 1413–1420. doi: 10.1007/s10311-019-00876-y

Singh, R. P., Singh, P. K., and Singh, R. L. (2014). Bacterial decolorization of textile azo dye acid orange by *Staphylococcus hominis* RMLRT03. *Toxicol. Int.* 21, 160–166. doi: 10.4103/0971-6580.139797

Sun, J., Li, W., Li, Y., Hu, Y., and Zhang, Y. (2013). Redox mediator enhanced simultaneous decolorization of azo dye and bioelectricity generation in air-cathode microbial fuel cell. *Bioresour. Technol.* 142, 407–414. doi: 10.1016/j.biortech.2013.05.039

Van der Zee, F. P., Lettinga, G., and Field, J. A. (2000). The role of (auto)catalysis in the mechanism of an anaerobic azo reduction. *Water Sci. Technol.* 42, 301–308. doi: 10.2166/wst.2000.0528

Verrax, J., Beck, R., Dejeans, N., Glorieux, C., Sid, B., Pedrosa, R. C., et al. (2011). Redox-active quinones and ascorbate: an innovative cancer therapy that

exploits the vulnerability of cancer cells to oxidative stress. *Anticancer. Agents Med. Chem.* 11, 213–21. doi: 10.2174/187152011795255902

von Canstein, H., Ogawa, J., Shimizu, S., and Lloyd, J. R. (2008). Secretion of flavins by *Shewanella* species and their role in extracellular electron transfer. *Appl. Environ. Microbiol.* 74, 615–623. doi: 10.1128/AEM.01387-07

Wolin, E. A., Wolin, M. J., and Wolfe, R. S. (1963). Formation of methane by bacterial extracts. *J. Biol. Chem.* 238, 2882–6.

Zhuo, R., Zhang, J., Yu, H., Ma, F., and Zhang, X. (2019). The roles of *Pleurotus ostreatus* HAUCC 162 laccase isoenzymes in decolorization of synthetic dyes and the transformation pathways. *Chemosphere* 234, 733–745. doi: 10.1016/j.chemosphere.2019.06.113

Conflict of Interest Statement: The authors declare that the research was conducted in the absence of any commercial or financial relationships that could be construed as a potential conflict of interest.

frontiers in Energy Research

ORIGINAL RESEARCH
published: 19 September 2019
doi: 10.3389/fenrg.2019.00103

Electrochemical and Microbiological Characterization of Bioanode Communities Exhibiting Variable Levels of Startup Activity

*Juan F. Ortiz-Medina and Douglas F. Call**

Department of Civil, Construction, and Environmental Engineering, North Carolina State University, Raleigh, NC, United States

Microbial electrochemical technologies (METs) require the establishment of anode biofilms to generate electrical current. The factors driving bioanode formation and their variability during startup remain unclear, leading to a lack of effective strategies to initiate larger-scale systems. Accordingly, our objective was to characterize the electrochemical properties and microbial community structure of a large set of replicate bioanodes during their first cycle of current generation. To do this, we operated eight bioanode replicates at each of two fixed electrode potentials [−0.15 V and +0.15 V vs. standard hydrogen electrode (SHE)] for one fed-batch cycle. We found that startup time decreased and maximum current generation increased at +0.15 V compared to −0.15 V, but at both potentials the bioanode replicates clustered into three distinct activity levels based on when they initiated current. Despite a large variation in current generation across the eight +0.15 V bioanodes, bioanode resistance and abundance of *Geobacter* species remained quite similar, differing by only 10 and 12%, respectively. At −0.15 V, current production strongly followed *Geobacter* species abundance and bioanode resistance, wherein the largest abundance of *Geobacter* was associated with the lowest charge transfer resistance. Our findings show that startup variability occurs at both applied potentials, but the underlying electrochemical and microbial factors driving variability are dependent on the applied potential.

Keywords: microbial electrochemical technologies, bioanode, *Geobacter*, bioreactor start-up, bioenergy

OPEN ACCESS

Edited by:
Uwe Schröder, Technische Universitat Braunschweig, Germany

Reviewed by:
Benjamin Korth, Helmholtz Centre for Environmental Research (UFZ), Germany
Pascal E. Saikaly, King Abdullah University of Science and Technology, Saudi Arabia

****Correspondence:***
Douglas F. Call
dfcall@ncsu.edu

Specialty section:
This article was submitted to Bioenergy and Biofuels, a section of the journal Frontiers in Energy Research

Received: *17 June 2019*
Accepted: *04 September 2019*
Published: *19 September 2019*

Citation:
Ortiz-Medina JF and Call DF (2019) Electrochemical and Microbiological Characterization of Bioanode Communities Exhibiting Variable Levels of Startup Activity. Front. Energy Res. 7:103. doi: 10.3389/fenrg.2019.00103

INTRODUCTION

Microbial electrochemical technologies (METs) convert organic material, such as wastewater, into electricity, hydrogen gas, or commodity chemicals (Wang and Ren, 2013). Over the past few decades, these technologies have advanced from lab- to demonstration-scales (Janicek et al., 2014). A challenge facing larger-scale systems is the unpredictable and erratic behavior during the initiation of current or what is frequently referred to as reactor startup (Cusick et al., 2011; Paitier et al., 2017). Identifying the underlying reasons for this behavior and how to improve startup is therefore paramount for the success of these technologies.

Despite the important role that electricity-generating microorganisms, or exoelectrogens, play in initiating current, most of our knowledge of their function and composition comes from bioanodic communities operated over long time scales (Logan, 2009). The most common enrichment procedure used to study these communities is to operate them throughout several cycles (in a

batch system) until a stable current output is reached (Hutchinson et al., 2011; Paitier et al., 2017). Typically after at least 1 month of operation, bioanodes converge to similar electrochemical properties and community structure regardless of the inoculum source and operational conditions such as the anode potential (Yates et al., 2012; Zhu et al., 2014; Paitier et al., 2017). Most of these studies agree that exoelectrogens with efficient pathways of extracellular electron transfer (EET), such as members of the genus *Geobacter*, play a pivotal role in generating current and decreasing anode charge transfer resistance (Marsili et al., 2010; ter Heijne et al., 2015).

Bioanode properties during startup are less understood. Understanding startup behavior is important because many pilot-scale systems have reported significant delays (e.g., months) to initiate current (Cusick et al., 2011; Escapa et al., 2015; Hiegemann et al., 2016). It is frequently observed, but not discussed, in long-term studies that a high degree of variable electrochemical performance across replicates occurs during startup (Yates et al., 2012; Zhou et al., 2013), but the underlying factors driving the variation remain unclear. This can ultimately influence the predictability and reproducibility of bioanodes over the long term, as shown in several studies that observe this erratic behavior (Cusick et al., 2011; Zhang et al., 2013; Escapa et al., 2015; Yanuka-Golub et al., 2016). Insufficient replicates is an additional factor leading to this unpredictability, as it obscures a possible consensus on startup time, expected current, and influence of the microbial community. This causes conflicting results from which decisions about optimal electrochemical conditions for bioanode startup are determined, such as which fixed anode potential to choose (Finkelstein et al., 2006; Torres et al., 2009; Wagner et al., 2010; Zhu et al., 2014). The initial enrichment stage of bioanodes is further complicated by the fact that different outcomes during acclimation are influenced by both stochastic and deterministic factors, which are dictated by microbial community dynamics (Zhou et al., 2013).

The objective of this study was to characterize the electrochemical behavior and community structure of bioanode communities during startup as a function of anode potential. Two anode potentials were selected in order to create two different energy-harvesting conditions for the bioanodes. A lower anode potential of −0.15 V [vs. standard hydrogen electrode (SHE)] was chosen to impart a lower driving force for EET, and a higher potential of +0.15 V, which increases the EET rate, was selected to represent conditions under which the microorganisms could better exploit the available energy (Korth and Harnisch, 2019). Eight replicates at each anode potential were included in order to assess factors associated with startup variability, and all reactors were inoculated with the same enrichment culture (domestic wastewater) and electron donor (acetate). At the end of the first cycle, the bioanode electrochemical properties were measured using cyclic voltammetry and electrochemical impedance spectroscopy (EIS) and the community profile analyzed using high-throughput Illumina sequencing. Our findings show that startup variability occurs at both applied potentials, but the underlying electrochemical and microbial factors driving the variability are dependent on the applied potential.

MATERIALS AND METHODS

Reactor Assembly and Configuration

Microbial electrolysis cells (MECs) were based on a polycarbonate circular chamber design (28 mL empty volume) as previously described (Call and Logan, 2008). This configuration fixed the electrode spacing across the replicates (2.3 ± 0.1 cm between anode and cathode). We selected a single-chamber design for this study because compared to two-chamber designs using membrane separators, it lowers resistance and eliminates detrimental pH gradients. The electrodes and their pretreatment were based on previous methods (Call and Logan, 2011; Zhu et al., 2014). Briefly, the anodes were graphite plates (2 × 2 cm; GraphiteStore.com, Inc., Northbrook, IL) pretreated by polishing with sandpaper (grit type 400), soaked in a 1 M HCl solution overnight, and rinsed and stored in DI water until used. The cathodes were stainless steel mesh (4 cm diameter; Type 304, mesh size 50 × 50; McMaster-Carr, Elmhurst, IL). The current collectors were titanium wire (anode) and stainless steel wire (cathode). Each MEC was adjusted until the contact resistance between electrodes and current collectors was <0.7 Ω. To fix the anode potentials, Ag/AgCl reference electrodes (∼200 mV vs. SHE) were installed equidistant between the anode and cathode. All reference electrodes were checked against a calibrated saturated calomel electrode (SCE) to ensure that the difference in potential between them and the SCE was <1 mV.

Microbial Enrichment and Chronoamperometry

To perform the microbial enrichment, effluent from the primary clarifier of a domestic wastewater treatment plant (∼300 mg/L COD) was mixed in equal proportions with 100 mM phosphate buffer, 1 g/L sodium acetate (780 mg/L COD) as the electron donor, and 10 mL/L of both Wolfe's trace vitamin and mineral solutions (Call and Logan, 2011). The contribution of acetate and wastewater to the total COD was 84 and 16%, respectively. We amended our MECs with acetate to promote the growth of exoelectrogens and reduce diversion of electrons to other pathways, such as fermentation. Enhancing exoelectrogen growth allowed us to better understand differences across bioreactors that initiated current quickly, slowly, or not at all and is consistent with other lab-scale investigations (Torres et al., 2009; Liu et al., 2011; ter Heijne et al., 2015; Yanuka-Golub et al., 2016) and amendment practices in some larger-scale systems (Dekker et al., 2009; Cusick et al., 2011; Brown et al., 2014; Liang et al., 2018). Cathodically-generated H_2 gas may have been present and consumed as an electron donor as well by the microbial communities; thus, our design best represents applied systems operating without a membrane separator (e.g., MEC-amended anaerobic digesters) (Guo et al., 2013; Feng et al., 2015). The reactors were connected to a potentiostat (Bio-Logic Science Instruments, Knoxville, TN) and operated at different fixed anode potentials (E_{AN}): −0.15 V or +0.15 V (both vs. SHE) or open circuit voltage (OCV). These potentials were chosen because they provide different scenarios of energy harvesting by microorganisms based on EET kinetics. The lower potential (−0.15 V) represents a smaller driving force that yields slower

EET rates. The higher potential (+0.15 V) enables higher EET rates, and in turn more optimized energy harvesting from the available energy (Korth and Harnisch, 2019). Eight replicates for each of the three anode treatments were operated. Preliminary tests were conducted to assess when maximum current was reached for each E_{AN}. These values were 5.5 days for −0.15 V and 5.0 days for +0.15 V. Bioanodes at OCV were operated for 5.0 days. All reactors were operated at a constant 30°C.

Electrochemical Characterization

To characterize the electrochemical properties of the bioanodes, cyclic voltammograms (CVs) were collected at a scan rate of 1 mV/s, ranging from −0.3 to +0.5 V vs. SHE. A single CV cycle was performed to avoid a prolonged effect of varying the potential on the subsequent microbial community analysis. EIS was conducted to determine the total and component resistances of the bioanodes. The bioanodes were operated for 30 min at their respective enrichment E_{AN} (−0.15 or +0.15 V) and the frequency was varied from 0.1 to 10 mHz with a 10 mV perturbation amplitude. Both CVs and EIS were performed at the end of the chronoamperometry measurements. To initially characterize the reactors and ensure that all replicates agreed within 10%, both techniques were likewise performed at the start of the experiments with the reactors filled with 50 mM phosphate buffer and no inoculum. The same techniques were conducted in an identical manner on the OCV controls, but with the anode potential held at OCV during EIS instead of one of the two E_{AN}. Depending on the bioanode impedance behavior, data from the EIS tests were fitted using equivalent circuits similar to single and double-time constant models (**Figure S1**), which have been used previously (Srikanth et al., 2008; Martin et al., 2013). The resistances in the model were attributed to solution resistance (R_s) and charge transfer resistances (R_{ct}, $R_{ct,2}$). Model fitting was performed using the function Z-Fit on the EC-Lab software, version 11.10, by minimizing the Chi-Square values of each system.

Microbial Community Visualization and Analysis

After the electrochemical analyses were completed, the MECs were disassembled and the bioanodes processed for further analysis. To observe the extent of microbial colonization of the anodes, one piece of every electrode was visualized using scanning electron microscopy (SEM). The samples were placed in a 2.5% glutaraldehyde solution overnight, dehydrated in ethanol, and dried for 2 h at 30°C (Katuri et al., 2014). Before imaging, the samples were coated with a gold/palladium layer for 2 min at 12 mA under an argon atmosphere. The sample was visualized using a Hitachi S-3200N variable pressure scanning electron microscope (Hitachi High-Technologies, Japan) with an accelerating voltage of 5 kV and a working distance of 23 mm.

To analyze the microbial community composition and diversity, samples from the anodic biofilm and the suspension were obtained. Anodic biofilm was scraped using a sterile blade. For the suspension samples, 10 ml of reactor effluent was collected in 15 ml centrifuge tubes, then centrifuged at 4,000 rpm for 20 min. DNA from the biofilm and suspension pellets was extracted using a PowerSoil® DNA isolation kit (MO BIO Laboratories, Carlsbad, CA) following the manufacturer's instructions. The V3 and V4 regions of the 16S rRNA gene were amplified using the forward primer 5′ TCGTCGGCAG CGTCAGATGTGTATAAGAGACAGCCTACGGGNGGCWG CAG 3′ and the reverse primer 5′ GTCTCGTGGGCTCGG AGATGTGTATAAGAGACAGGACTACHVGGGTATCT AATCC 3′ for Illumina sequencing, using the protocol provided by the company (Illumina Inc., 2013). The samples were sequenced using the Illumina MiSeq platform (Illumina Inc., San Diego, CA), with a paired-end sequencing of 300 base pairs (bp) length. The sequencing data was deposited into the GenBank database of the National Center of Biotechnology Information (NCBI), under the BioProject accession number PRJNA559682.

To establish the composition and compare microbial communities, the software QIIME was utilized (Caporaso et al., 2010). After alignment, the samples were clustered into operational taxonomic units (OTUs) by performing open-reference picking with the UCLUST algorithm, using 97% sequence similarity as the threshold and following the default commands available at the developers' website (QIIME, 2015). After OTU classification at the genus level, the generated data was further processed in the R platform. Shannon (H) diversity indexes were calculated to assess the diversity of the studied samples, while Principal Component Analysis (PCA) plots were constructed to visualize the relationship between community composition and bioanode performance. Both were generated in R with the help of the vegan (Oksanen et al., 2017) and phyloseq packages (McMurdie and Holmes, 2013).

RESULTS AND DISCUSSION

Current Generation During Bioanode Initiation

We first examined current densities (I_A) over time during the startup period. Despite identical inoculum, reactor design, and operating conditions, I_A was highly variable across the eight replicates for each E_{AN} (**Figure 1**). To quantify variability, we defined startup time as the point when the bioanodes reached 0.1 A/m^2 [dashed line in **Figures 1A,B**; selected based on similar thresholds used in other MET startup studies (Liu et al., 2011; Commault et al., 2013)]. Bioanodes that did not reach this value after five (+0.15 V) or 5.5 days (−0.15 V) were defined as inactive. Based on this definition, three bioanodes were inactive at −0.15 V and one was inactive at +0.15 V. The remaining bioanodes clustered into two levels: (1) high-activity, which reached the 0.1 A/m^2 threshold the fastest, and (2) low-activity, which were the slowest to reach the threshold (**Figure 1B**).

Considering only the high- and low-activity bioanodes, there were appreciable differences during the startup period within and across each E_{AN}. At +0.15 V, the high-activity bioanodes required 3.91 ± 0.06 days and the low-activity bioanodes required 4.28 ± 0.10 days to reach the startup threshold. At −0.15 V, the high- and low-activity reactors took significantly longer to reach the threshold than those at +0.15 V (t-test, $p < 0.05$), requiring 4.60 ± 0.03 and 5.32 ± 0.16 days, respectively. Maximum I_A followed

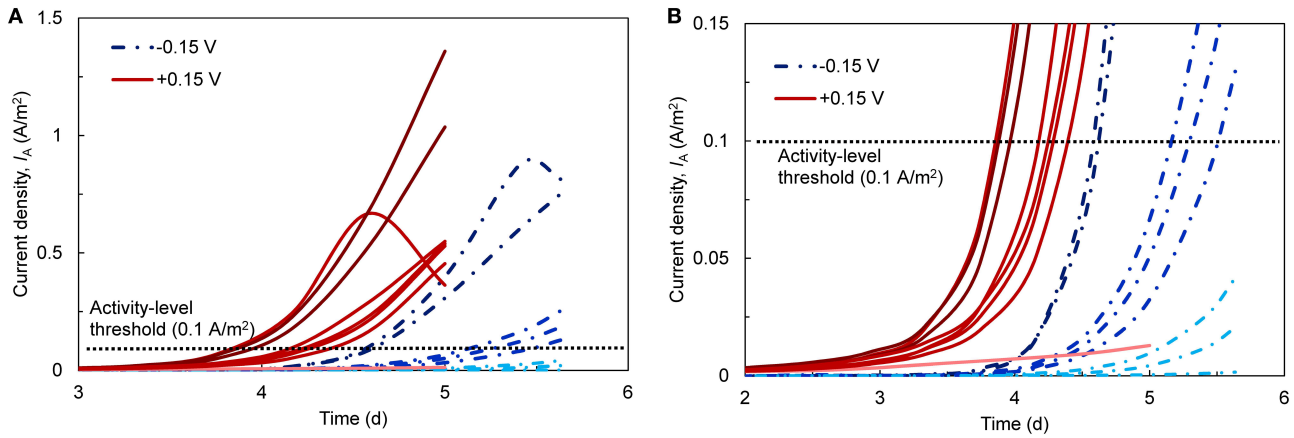

FIGURE 1 | (A) Current densities (I_A; normalized to anode surface area) over time during the startup phase of the bioanodes. Eight replicates (red lines) were started with an applied anode potential [E_{AN}; reported vs. the standard hydrogen electrode (SHE)] of +0.15 V and another eight (blue, segmented lines) were started at −0.15 V. The dark, medium, and light shading of the lines corresponds to high-, low-activity, and inactive bioanodes, respectively. The horizontal dotted line denotes the current density threshold (0.1 A/m^2) selected to define the bioanode activity level. **(B)** A closer view of the bioanode startup current densities with respect to the activity threshold.

a similar trend as the startup time, wherein bioanodes at +0.15 V reached higher maximum I_A than those at −0.15 V for all activity levels. Bioanode startup activity level largely agreed with the maximum current behavior. The exception was one bioanode at +0.15 V, which classified as high-activity with respect to startup time but did not reach the same I_A as the other high-activity bioanodes. This bioanode ended the cycle at the same level of current as the +0.15 V low-activity bioanodes.

The startup behavior of METs varies widely across the literature, and our results are consistent with some, but not all, prior reports. The high degree of startup variability that we observed is often not discussed (or reported) in other studies that use triplicate or duplicate reactors, even though there is a clear need to operate enough replicates to characterize possible outcomes (Yates et al., 2012). Zhou et al. (2013), which is one of the only studies to use more than triplicate reactors, reported a wide range of startup times (∼1–12 days) across 14 replicates, which is consistent with our findings. The effect of E_{AN} on startup varies across studies. Using a microbial fuel cell (MFC) with a cloth separator between the electrodes, Zhang et al. (2013) showed that wastewater-inoculated reactors at +0.2 V started up more quickly than those at −0.2 V. Faster startup at less negative potentials has been reported in other studies as well, in both single-chamber (Finkelstein et al., 2006) and double-chamber systems (Wang et al., 2009; Commault et al., 2013). While one explanation for this behavior is the higher energy harvested due to higher EET rates (Korth and Harnisch, 2019), a selection of exoelectrogens with more efficient EET mechanisms at higher potential has also been proposed (Commault et al., 2013). Conversely, Torres et al. (2009), using a double-chamber system with multiple anodes in one chamber, observed a faster startup and higher maximum current density at more negative anode potentials. They attributed this behavior to the selection of microorganisms (e.g., *Geobacter sulfurreducens*) that could harvest energy and transfer electrons efficiently at such negative potentials. However, it is unclear if their unique multi-anode configuration played a role in their findings. Kumar et al. (2013), comparing single- and double-chamber MECs with the same inoculum, medium, and under continuous operation, observed that the single-chamber MEC displayed a higher level of electrochemical activity at less negative potentials (0 V vs. SHE). Both configurations have inherent differences, such as cathodically-generated H_2 that can serve as an electron donor in single-chamber systems (Call et al., 2009; Lee and Rittmann, 2010) and pH gradients in double-chamber reactors (Rozendal et al., 2006) that may influence bioanode enrichment and startup time. Reactor configurations thus play an additional factor that needs to be considered during research on startup behavior.

Cyclic Voltammetry

To investigate the electrochemical properties of the bioanodes, we used cyclic voltammetry at the end of the startup cycle. Cyclic voltammetry reveals electron transfer kinetics between microorganisms and the electrode across a range of bioanode potentials, as well as possible electron transfer mechanisms (Fricke et al., 2008). The CVs clustered according to the activity levels defined above and had limiting currents ($i_{l,a}$) that were generally proportional to the maximum current densities recorded during startup (**Figure 2**). The CVs of bioanodes that did not reach the startup threshold closely followed the OCV control. All other bioanodes generated a sigmoidal shaped CV regardless of E_{AN}, which is indicative of a self-regenerating electron transfer process that is typical in mediatorless, exoelectrogenic biofilms (Katuri et al., 2010; Marsili et al., 2010; Zhang et al., 2013). These same bioanodes showed a similar midpoint potential ($E_{1/2}$) at −0.18 ± 0.01 V (dashed vertical line in **Figure 2**) and potential (E_p; *ca.* −0.1 V) where maximum oxidative current (i_p) was reached, which further

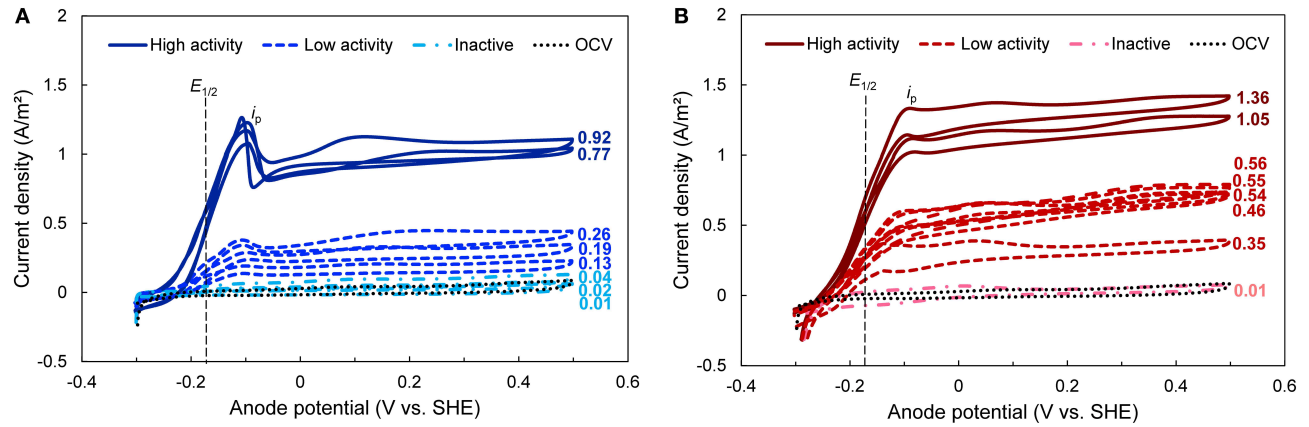

FIGURE 2 | Cyclic voltammograms (CVs) taken at the end of the startup period for bioanodes fixed at **(A)** $E_{AN} = -0.15$ V and **(B)** $E_{AN} = +0.15$ V. All curves in the same plot are replicates. High-, low-activity, and inactive bioanode levels are defined based on the time required to reach the startup current threshold (**Figure 1**). Numbers next to each curve represent the current density recorded at the end of the startup cycle. $E_{1/2}$, midpoint potential (vertical black dashed line); i_p, peak current obtained during the potential sweep; OCV, open circuit voltage (dotted black line).

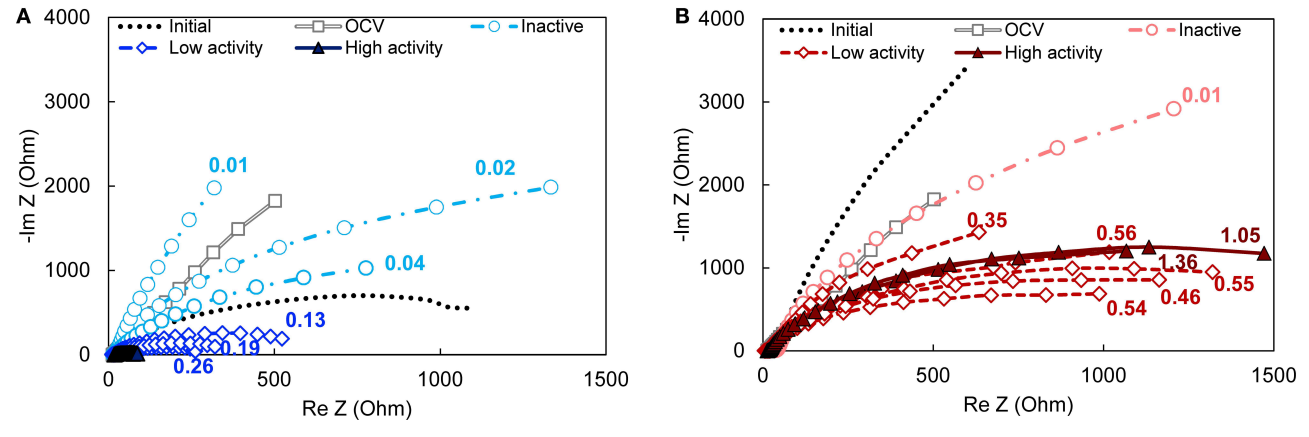

FIGURE 3 | Nyquist plots of bioanodes fixed at **(A)** $E_{AN} = -0.15$ V and **(B)** $E_{AN} = +0.15$ V taken at the end of the startup cycle. All curves in the same plot are replicates. The magnitude of impedance is lower when the ratio of the curve is lower, which translates into lower total resistance. High-, low-activity, and inactive bioanode levels are defined based on the time required to reach the startup current threshold (**Figure 1**). The numbers next to each curve are the current density recorded at the end of the startup period. OCV, open circuit voltage (gray double line with squares); Initial—prior to inoculation (dotted line).

confirms the presence of a primary electron transfer pathway utilized by the biofilm across E_{AN} and levels of activity. This behavior is frequently associated with bioanodes dominated by *Geobacter* spp., which normally show sigmoidal-shaped voltammograms and midpoint potentials between −0.16 and −0.22 V due to the outer membrane cytochromes expressed by these organisms (Marsili et al., 2008; Katuri et al., 2012; Zhu et al., 2014). This suggests that *Geobacter* spp. were primarily involved in EET on our bioanodes during startup.

The most notable effect of E_{AN} was observed in the CV behavior of the high-activity bioanodes. Although bioanodes at both E_{AN} showed similar sigmoidal curves and i_p values, after the sweeping potential increased beyond E_p, the current produced by the two high-activity bioanodes enriched at −0.15 V dropped sharply by ∼25% (**Figure 2A**). Current slightly increased with potential, but did not exceed i_p. In contrast, the bioanodes enriched at +0.15 V did not show the same drop in current; current remained similar to i_p after passing E_p (**Figure 2B**). Both behaviors at similar E_{AN} in other studies have been consistently observed in full grown biofilms (Marsili et al., 2010; Zhu et al., 2012, 2014; Commault et al., 2013). One explanation for this difference is that at +0.15 V, electron transfer rates operated near their maximum because this potential provided a larger driving force for electron flow through the cell (Korth and Harnisch, 2019). This is consistent with previous reports that at potentials beyond which i_p occurs, electron transfer rates do not increase substantially because they are kinetically limited by intracellular electron carriers (e.g., NAD^+/NADH) (Marsili et al., 2010; Wei et al., 2010; Korth and Harnisch, 2019). At −0.15 V, the bioanodes were subject to a lower driving force, and in turn lower electron turnover rates.

It is known that biofilms dominated by *Geobacter* spp. express different pathways, regulated by inner membrane cytochromes, to allow growth using electron acceptors at different potentials. This has been demonstrated by the presence of different oxidation peaks as a function of E_{AN} (Zhu et al., 2012; Peng et al., 2016). One electron transfer pathway, the CbcL-dependent pathway, operates at redox potentials below −0.10 V (Zacharoff et al., 2016), whereas at E_{AN} above this value, the ImcH-dependent pathway is expressed to harvest additional energy (Levar et al., 2017). The CbcL pathway has been reported to contribute significantly (at least 60%) to electron transfer, even in bioanodes formed at higher E_{AN} and its deletion shifts the midpoint potential to values around −0.1 V (Zacharoff et al., 2016). It is thus possible that the bioanodes at −0.15 V expressed a pathway that was not adapted to EET at more positive E_{AN}, which is consistent with the current drop after i_p. Differences in the expression and activity of these two pathways are therefore the likely reasons for the different CV profiles at −0.15 V and +0.15 V.

Electrochemical Impedance Spectroscopy

Bioanode impedance profiles, which characterize the biofilm-electrode interface in terms of resistance and capacitance elements, were dependent on activity level for the bioanodes enriched at −0.15 V, but not +0.15 V (**Figure 3**). The majority of the bioanode profiles (all except the high-activity −0.15 V bioanodes) reflected a single characteristic impedance semi-circle. Those profiles could be fitted to an equivalent circuit that considers the solution resistance (R_s) and a single charge transfer resistance (R_{ct}) circuit (Srikanth et al., 2008). For all bioanodes (both −0.15 and +0.15 V), R_s was 13 ± 4 Ω, which is low relative to the majority of the R_{ct} values. Other observable phenomena in the high frequency region of the semi-circle were perceived as too small (**Figure S2**) because including them during model fitting did not change the values of the other calculated resistances by more than 5%.

The impedance of the −0.15 V bioanodes decreased as the current recorded at the end of the startup period increased (**Figure 3A**). The corresponding R_{ct} ranged from 24 Ω to 3.4 $\times 10^4$ Ω between the bioanodes with the highest and the lowest current density, respectively. The high-activity bioanodes at −0.15 V had impedances that were up to 90% lower than the low-activity bioanodes (**Figure S3A**). They generated Nyquist plots with double semicircles (**Figure S4**) that can be attributed to two charge transfer processes (Ramasamy et al., 2009). Such processes can be better distinguished in the phase angle Bode plot as two local minimums that become one as activity decreases and impedance increases (**Figure S3B**). Relative to the abiotic controls (i.e., prior to introducing the microorganisms), impedance of the low-activity bioanodes was lower and the inactive bioanodes was higher. The latter result suggests that electron transfer to the anode was slowed or inhibited. This may have been caused by growth of non-conductive biofilms (Dheilly et al., 2008) or presence of substances such as polysaccharides (Kouzuma et al., 2010) that changed the anode surface conductivity. The similar impedance profile of these bioanodes and the OCV control (where microorganisms are present but not respiring on the anode) lends support for this hypothesis.

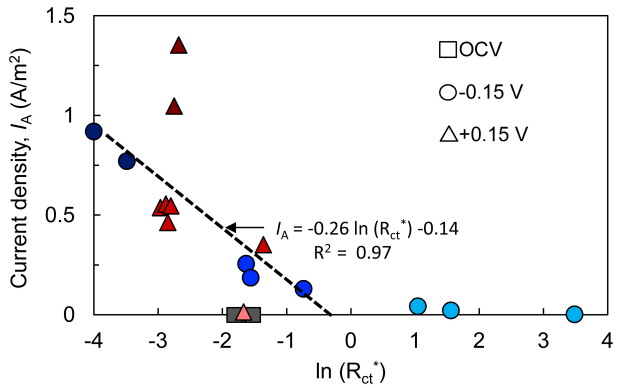

FIGURE 4 | Relationship between bioanode charge transfer resistance (R_{ct}^*; normalized to each bioanode's resistance prior to introducing microorganisms) and current density (I_A). Both metrics were recorded at the end of the startup cycle. Points with the same shape represent replicate bioanodes fixed at −0.15 V (circles) and +0.15 V (triangles). The points are shaded to reflect bioanode activity level (dark, high-activity; medium, low-activity; light, inactive). OCV, open circuit voltage bioanodes (squares). The linear regression of high- and low-activity bioanode points at −0.15 V is shown as a dashed line.

Bioanodes enriched at +0.15 V produced similar impedance profiles of single semi-circles, regardless of the startup current or the electrochemical activity reflected in the CVs (**Figure 3B**). Total impedance did not increase dramatically in the low frequency region as was observed for the bioanodes at −0.15 V (**Figure S3C**), and the phase angle only increased slightly relative to the initial response of the graphite anode (**Figure S3D**). The average charge transfer resistances (R_{ct}), calculated by the aforementioned model fitting, were 3,140 ± 330 and 2,140 ± 580 Ω for the high- and low-activity bioanodes, respectively. The differences in resistance cannot be explained by differences in the bioanode design, materials, connections, etc., because the impedance of each anode prior to inoculation was not related to the final activity obtained at both E_{AN} (**Figure S5**). Thus, higher current production at +0.15 V did not correlate with lower total resistance.

To better visualize the relationship between R_{ct} and bioanode activity level, R_{ct} of each bioanode was divided by the respective initial R_{ct} (calculated before inoculation). Plotting I_A against normalized charge transfer resistance (R_{ct}^*) yielded a linear relationship for the high- and low-activity ($R^2 = 97\%$) bioanodes at −0.15 V (**Figure 4**). Bioanodes at +0.15 V did not show a clear trend in terms of decrease in R_{ct}, and high-activity bioanodes had similar R_{ct}^* values as most of the low-activity bioanodes, but they had a much larger I_A (**Figure 4**). Their larger maximum current output in CVs indicates that despite appreciable resistance, these communities were highly efficient at transferring electrons to the anode.

Microbial Colonization of the Anodes

We visualized the bioanode surfaces to qualitatively assess relationships between the electrochemical characteristics described above and biofilm coverage. To do this, we captured

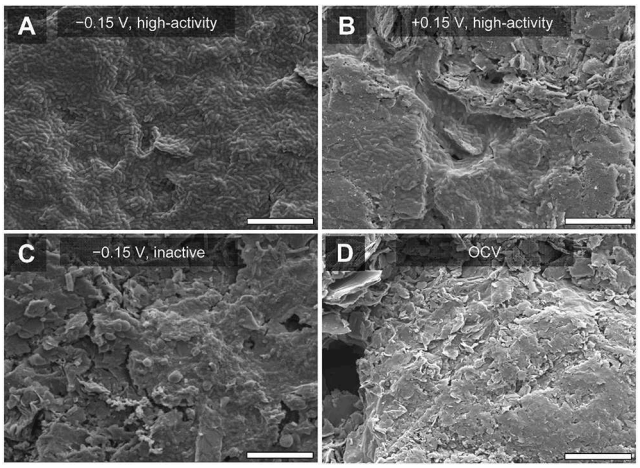

FIGURE 5 | Scanning electron microscopy (SEM) images of bioanodes at the end of the startup cycle. **(A)** High-activity bioanode at −0.15 V showing uniform and complete surface coverage of microorganisms, **(B)** high-activity bioanode at +0.15 V with similar cell morphology as **(A)**, but less surface coverage, **(C)** low-activity bioanode at −0.15 V, with mixed cell morphology and lower coverage relative to **(A)**, and **(D)** bioanode at open circuit voltage (OCV). White bar at the bottom of each figure represents a distance of 10 μm.

SEM images of the bioanodes at the end of the startup cycle. At −0.15 V, the high-activity bioanodes were fully covered with a homogenous layer of microorganisms (**Figure 5A**), and the low-activity bioanodes had little to no coverage (data not shown). At +0.15 V, biofilm coverage was patchy and heterogeneous (**Figure 5B**), with no clear difference between high- and low-activity bioanodes. Inactive bioanodes at both potentials showed a less defined colonization pattern (**Figure 5C**), which was similar to the OCV controls (**Figure 5D**).

Bioanode surface coverage was consistent with the EIS results. A more complete coverage of the anode minimizes charge transfer resistance (Marsili et al., 2008). This was observed in the high-activity bioanode impedance spectra at −0.15 V (**Figure 3**). Thin biofilms and limited surface coverage are associated with larger charge transfer resistance, which was observed in the high- and low-activity bioanodes at +0.15 V. This implies that even though bioanode resistance was larger at +0.15 V, the per-cell EET rates at that potential were greater than at −0.15 V. Improved kinetics and optimization of energy-harvesting pathways at more positive anode potentials support this observation (Ramasamy et al., 2009; Borole et al., 2010). Overall, these results show that bioanode growth and activity occur differently depending on E_{AN}.

Microbial Community Composition

Across low- and high-activity levels at both E_{AN}, sequences matching to *Geobacter* had the highest relative abundance in the biofilms (**Figure 6**). The relative abundance of this genus was generally higher in bioanodes that produced the highest I_A, which is more noticeable at −0.15 V (**Figure 6A**) than +0.15 V (**Figure 6B**). A similar trend was found in suspension samples obtained from the bioreactors, where *Geobacter* abundance was generally related to the maximum I_A (**Figure S6**). *Geobacter* species are frequently enriched in METs supplied acetate as the electron donor, regardless of E_{AN}, and consist of several known exoelectrogens (Zhu et al., 2014). The use of single chamber MECs in this study may have contributed to the enrichment of this genus, as some species are able to utilize hydrogen gas (H_2) produced at the cathode as an additional electron donor (Call et al., 2009; Lee and Rittmann, 2010). Several other genera were present in the bioanodes, some of which may have participated in current generation. Genera, including *Sedimentibacter*, *Fusibacter*, *Pseudomonas*, and an unknown genus of the family *Comamonadaceae*, were detected. While the latter were found in the OCV controls, both *Sedimentibacter* and *Fusibacter* were not highly abundant (**Figure S7A**). *Comamonadaceae* were present in the inoculum, although at a low abundance of around 2.5% (**Figure S7B**). In the high-activity bioanodes, there was a greater abundance of *Pseudomonas* species at +0.15 V than −0.15 V. Some *Pseudomonas* species are exoelectrogenic, producing current through the use of electron shuttles (Rabaey et al., 2004). A greater abundance of these bacteria at +0.15 V than −0.15 V is consistent with prior reports regarding the influence of E_{AN} on the thermodynamic favorability of electron transport mechanisms (Finkelstein et al., 2006; Wei et al., 2010).

To better visualize the relationship between community composition and bioanode performance, a PCA biplot was constructed (**Figure 7**). In this plot, genera are represented as vectors, and the points depict each bioanode and its corresponding current output at the end of the startup cycle. Points located along the axis of a vector contain a higher relative abundance of those respective genera, and the length of the vector indicates possible influence of the corresponding microorganism on the distribution of samples (Ramette, 2007). The genus *Geobacter* was the primary influence affecting bioanode activity level at both E_{AN}. Its vector aligns well with the horizontal axis that explains more than 90% of the observed variation. Bioanodes with the highest activity levels are closest to this vector. In contrast, samples corresponding to inactive bioanodes are located in the opposite direction of this vector, indicating a lower presence of *Geobacter* spp. The other enriched microorganisms, *Sedimentibacter* and *Fusibacter* spp., had a stronger influence on the low- and high-activity bioanodes at +0.15 V than −0.15 V. These microorganisms have been detected in METs exhibiting stable electrochemical performance (Lesnik and Liu, 2014). Although their function in an electrically conductive biofilm is unclear, their presence in early biofilm formation suggests a possible role during startup. In contrast, vectors of microorganisms such as *Comamonadaceae* and *Pseudomonas* spp. are directed toward inactive reactors and the OCV controls.

In all bioanodes, a higher abundance of *Geobacter* resulted in lower community diversity. By plotting the Shannon index (H), an indicator of microbial diversity, against the current density recorded at the end of the startup cycle, we found that diversity at both E_{AN} decreased as I_A increased (**Figure 8**); however, the rate of decrease was much faster at −0.15 V than +0.15 V. This result can be explained by the greater selection pressure at −0.15 V. The thermodynamic driving force for EET is lower at −0.15 V than +0.15 V; thus it favors

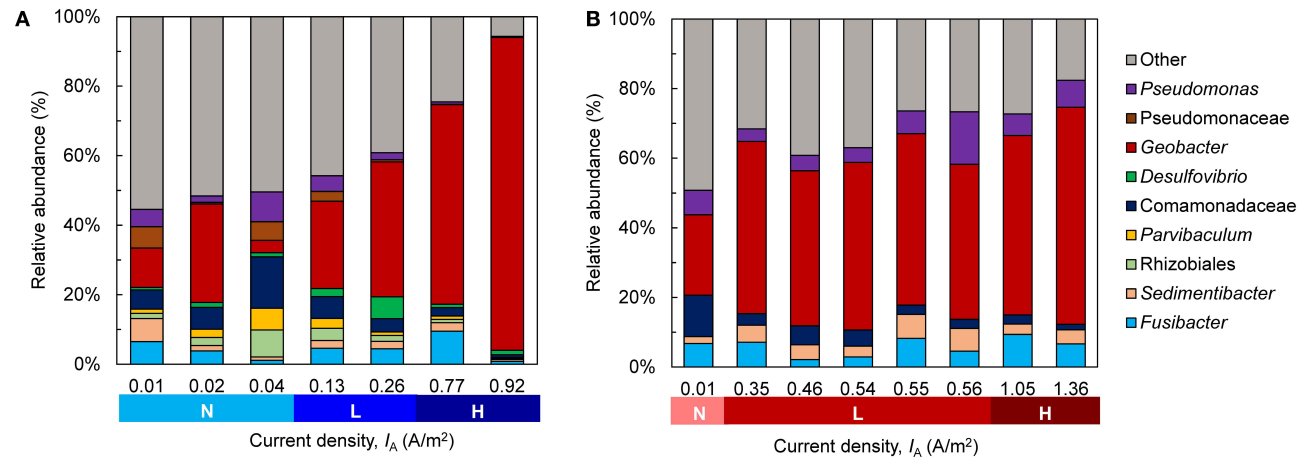

FIGURE 6 | Community composition of the bioanode biofilms fixed at **(A)** −0.15 V and **(B)** +0.15 V. The replicates for each anode potential are ordered from lowest to highest current density (I_A) recorded at the end of the startup cycle and are categorized according to their activity level during the startup cycle [Inactive (N), low-activity (L), high-activity (H)]. Genera with a relative abundance <5% are grouped into "Other".

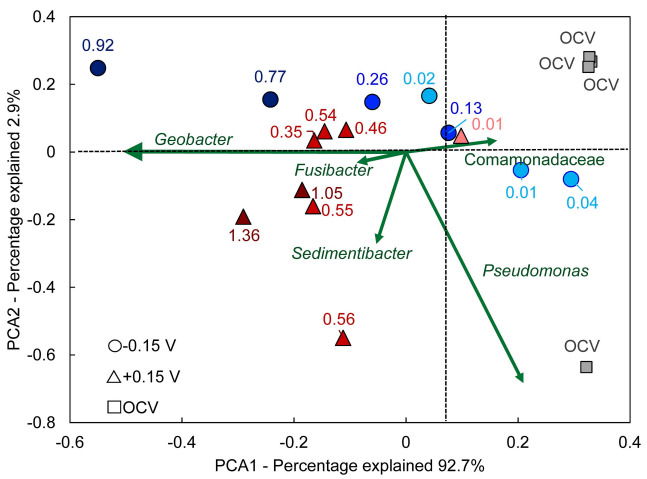

FIGURE 7 | Principal component analysis (PCA) biplot of anode biofilm microbial communities. Points with the same shape represent replicate bioanodes fixed at −0.15 V (circles) and +0.15 V (triangles). The points are shaded to reflect bioanode activity level (dark, high-activity; medium, low-activity; light, inactive). The numbers next to each curve are the current density recorded at the end of the startup period. Green vectors symbolize the eigenvector of the corresponding genus. Samples that are located in the direction of an eigenvector contain that particular genus, with an increased relative abundance the farther they are located from the center. OCV, open circuit voltage bioanodes (squares).

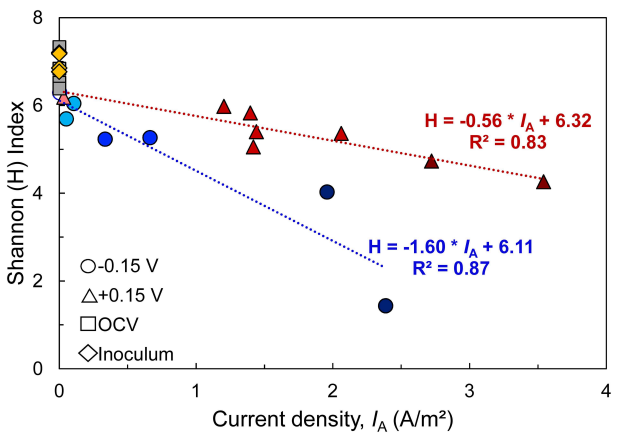

FIGURE 8 | Relationship between microbial diversity [estimated by the Shannon Diversity index (H)] and bioanode current density (I_A) recorded at the end of the startup cycle. A higher H index represents a more diverse microbial community. Linear regression of replicates from each fixed potential are represented by dotted lines (blue: −0.15 V, red: +0.15 V), along with regression equation and coefficient of determination (R^2). Points with the same shape represent replicate bioanodes fixed at −0.15 V (circles) and +0.15 V (triangles). The points are shaded to reflect bioanode activity level (dark, high-activity; medium, low activity; light, inactive). Communities from the wastewater inoculum are shown as yellow rhombi and the open circuit (OCV) controls are represented as gray squares.

microorganisms that can regulate electron transfer pathways to capture energy under challenging thermodynamic conditions (Korth and Harnisch, 2019). Microorganisms that use electron transport mechanisms, such as electron shuttles, that have more positive midpoint potentials than −0.15 V are limited by thermodynamic constraints (Torres et al., 2009). Comparatively, at +0.15 V, the thermodynamics are favorable for a wider range of microorganisms and/or electron transfer mechanisms (Torres et al., 2009).

The more selective nature of −0.15 V is one possible reason why there was a higher number of inactive bioanodes at −0.15 V. Since the driving force for energy harvesting is lower at −0.15 V than +0.15 V, external forces that influence bioanode colonization and respiration, such as alternative electron acceptors, may have a stronger impact on biofilm development than at +0.15 V. We hypothesize that under those conditions, competition of *Geobacter* spp. with other microorganisms that are able to use the same electron donor

and breathe on traces of other electron acceptors such as oxygen becomes more pronounced (Ren et al., 2014; Hasany et al., 2016). The relatively low abundance of *Geobacter* in inactive reactor bioanodes and suspension supports this hypothesis.

Coupling the microbial community data with the electrochemical properties described above, several interesting observations can be made. First, the relative abundance of *Geobacter* was closely linked with bioanode electrochemical behavior at −0.15 V, but not +0.15 V. From the low- to high-activity bioanodes at +0.15 V, the relative abundance of *Geobacter* deviated by only 12% and ranged from 44.5 to 62.3%. This trend matches well with the impedance data, wherein the total resistance across these same bioanodes varied by 10%. In contrast, at −0.15 V the relative abundance of *Geobacter* increased from 25.1 to 90.0% across these same activity levels, resulting in a total deviation of at least 53% compared to the average of all activity levels. Total bioanode resistance followed this pattern, with a 91% decrease in resistance between the low- to high-activity bioanodes. One possible explanation for why impedance did not vary with activity level for the +0.15 V bioanodes is that that potential selected for an EET pathway (i.e., from the terminal cytochrome to electrode) that was highly optimized for electron transfer to the anode. In that case, the rate of electron flow would depend on internal electron transfer processes (i.e., electron transport prior to EET) which would be a function of the "maturity," or activity level, of those internal pathways during startup.

CONCLUSIONS

Our overall objective was to determine the impact of two anode potentials on the electrochemical and microbial characteristics of bioanodes during the first cycle of current generation. Within this objective, we also assessed the variability in these characteristics across a large ($n = 8$) set of replicates for each potential. We found that the anode potential (E_{AN}; −0.15 V, +0.15 V vs. SHE) had a strong impact on the amount of time required to initiate current, the electrochemical properties [measured by cyclic voltammograms (CVs) and EIS], and the resulting microbial community composition. Even though variability across replicates was large, three distinct bioanode activity levels (defined based on the time required to reach a current density threshold) emerged within each E_{AN}. Bioanodes fixed at −0.15 V required more time to initiate current, and total resistance was closely related to the startup current and abundance of *Geobacter* species in the biofilm. Bioanodes at +0.15 V initiated current faster and had less variability in total resistance and *Geobacter* abundance across bioanode activity levels. SEM images of the bioanodes were consistent with the electrochemical profiles. Highly active bioanodes at −0.15 V had homogeneous biofilm coverage whereas sparse colonization at +0.15 V was consistent with the higher total resistance at that potential. A larger decrease in community diversity with current production at −0.15 V indicated that this potential was more selective for *Geobacter* spp., whereas the more favorable exploitation of energy at +0.15 V allowed for a greater diversity of other microorganisms. Further studies are needed in order to gain a deeper insight of microbial dynamics within the community that forms during the startup phase as a function of E_{AN}. Filling this knowledge gap may allow the design of more robust and predictable METs for practical applications.

DATA AVAILABILITY

Sequencing data was deposited into the GenBank database of the National Center of Biotechnology Information (NCBI), under the BioProject accession number PRJNA559682. Other generated datasets are available upon request to the corresponding author.

AUTHOR CONTRIBUTIONS

JO-M designed the experiments, collected and analyzed the data. DC and JO-M wrote the manuscript.

ACKNOWLEDGMENTS

This work was performed in part at the Analytical Instrumentation Facility (AIF) at North Carolina State University, which was supported by the State of North Carolina and the National Science Foundation (award number ECCS-1542015). The AIF is a member of the North Carolina Research Triangle Nanotechnology Network (RTNN), a site in the National Nanotechnology Coordinated Infrastructure (NNCI). Next Generation (Illumina) sequencing of microbial communities was performed by the Genomic Sciences Laboratory at North Carolina State University. Special thanks to Ling Wang and Chuck Mooney for their help during sequencing analysis and SEM visualization, respectively. This work was supported by funding from North Carolina State University.

SUPPLEMENTARY MATERIAL

The Supplementary Material for this article can be found online at: https://www.frontiersin.org/articles/10.3389/fenrg.2019.00103/full#supplementary-material

REFERENCES

Borole, A. P., Aaron, D., Hamilton, C. Y., and Tsouris, C. (2010). Understanding long-term changes in microbial fuel cell performance using electrochemical impedance spectroscopy. *Environ. Sci. Technol.* 44, 2740–2745. doi: 10.1021/es9032937

Brown, R. K., Harnisch, F., Wirth, S., Wahlandt, H., Dockhorn, T., Dichtl, N., et al. (2014). Evaluating the effects of scaling up on the performance of bioelectrochemical systems using a technical scale microbial electrolysis cell. *Bioresour. Technol.* 163, 206–213. doi: 10.1016/j.biortech.2014.04.044

Call, D. F., and Logan, B. E. (2008). Hydrogen production in a single chamber microbial electrolysis cell lacking a membrane. *Environ. Sci. Technol.* 42, 3401–3401. doi: 10.1021/es8001822

Call, D. F., and Logan, B. E. (2011). A method for high throughput bioelectrochemical research based on small scale microbial electrolysis cells. *Biosens. Bioelectron.* 26, 4526–4531. doi: 10.1016/j.bios.2011.05.014

Call, D. F., Wagner, R. C., and Logan, B. E. (2009). Hydrogen production by *Geobacter* species and a mixed consortium in a microbial electrolysis cell. *Appl. Environ. Microbiol.* 75, 7579–7587. doi: 10.1128/AEM.01760-09

Caporaso, J. G., Kuczynski, J., Stombaugh, J., Bittinger, K., Bushman, F. D., Costello, E. K., et al. (2010). QIIME allows analysis of high-throughput community sequencing data. *Nat. Publ. Gr.* 7, 335–336. doi: 10.1038/nmeth.f.303

Commault, A. S., Lear, G., Packer, M. A., and Weld, R. J. (2013). Influence of anode potentials on selection of *Geobacter* strains in microbial electrolysis cells. *Bioresour. Technol.* 139, 226–234. doi: 10.1016/j.biortech.2013.04.047

Cusick, R. D., Bryan, B., Parker, D. S., Merrill, M. D., Mehanna, M., Kiely, P. D., et al. (2011). Performance of a pilot-scale continuous flow microbial electrolysis cell fed winery wastewater. *Appl. Microbiol. Biotechnol.* 89, 2053–2063. doi: 10.1007/s00253-011-3130-9

Dekker, A., Ter Heijne, A., Saakes, M., Hamelers, H. V. M., and Buisman, C. J. N. (2009). Analysis and improvement of a scaled-up and stacked microbial fuel cell. *Environ. Sci. Technol.* 43, 9038–9042. doi: 10.1021/es901939r

Dheilly, A., Linossier, I., Darchen, A., Hadjiev, D., Corbel, C., and Alonso, V. (2008). Monitoring of microbial adhesion and biofilm growth using electrochemical impedancemetry. *Appl. Microbiol. Biotechnol.* 79, 157–164. doi: 10.1007/s00253-008-1404-7

Escapa, A., San-Martín, M. I., Mateos, R., and Morán, A. (2015). Scaling-up of membraneless microbial electrolysis cells (MECs) for domestic wastewater treatment: bottlenecks and limitations. *Bioresour. Technol.* 180, 72–78. doi: 10.1016/j.biortech.2014.12.096

Feng, Y., Zhang, Y., Chen, S., and Quan, X. (2015). Enhanced production of methane from waste activated sludge by the combination of high-solid anaerobic digestion and microbial electrolysis cell with iron-graphite electrode. *Chem. Eng. J.* 259, 787–794. doi: 10.1016/j.cej.2014.08.048

Finkelstein, D. A., Tender, L. M., and Zeikus, J. G. (2006). Effect of electrode potential on electrode-reducing microbiota. *Environ. Sci. Technol.* 40, 6990–6995. doi: 10.1021/es061146m

Fricke, K., Harnisch, F., and Schröder, U. (2008). On the use of cyclic voltammetry for the study of anodic electron transfer in microbial fuel cells. *Energy Environ. Sci.* 1, 144–147. doi: 10.1039/b802363h

Guo, X., Liu, J., and Xiao, B. (2013). Bioelectrochemical enhancement of hydrogen and methane production from the anaerobic digestion of sewage sludge in single-chamber membrane-free microbial electrolysis cells. *Int. J. Hydrogen Energy* 38, 1342–1347. doi: 10.1016/j.ijhydene.2012.11.087

Hasany, M., Mardanpour, M. M., and Yaghmaei, S. (2016). Biocatalysts in microbial electrolysis cells: a review. *Int. J. Hydrogen Energy* 41, 1477–1493. doi: 10.1016/j.ijhydene.2015.10.097

Hiegemann, H., Herzer, D., Nettmann, E., Lübken, M., Schulte, P., Schmelz, K.-G., et al. (2016). An integrated 45 L pilot microbial fuel cell system at a full-scale wastewater treatment plant. *Bioresour. Technol.* 218, 115–122. doi: 10.1016/j.biortech.2016.06.052

Hutchinson, A. J., Tokash, J. C., and Logan, B. E. (2011). Analysis of carbon fiber brush loading in anodes on startup and performance of microbial fuel cells. *J. Power Sources* 196, 9213–9219. doi: 10.1016/j.jpowsour.2011.07.040

Illumina Inc. (2013). *16S Metagenomic Sequencing Library Preparation*, 1–28. Available online at: http://support.illumina.com/content/dam/illumina-support/documents/documentation/chemistry_documentation/16s/16s-metagenomic-library-prep-guide-15044223-b.pdf (accessed August 21, 2017).

Janicek, A., Fan, Y., and Liu, H. (2014). Design of microbial fuel cells for practical application: a review and analysis of scale-up studies. *Biofuels* 5, 79–92. doi: 10.4155/bfs.13.69

Katuri, K. P., Kavanagh, P., Rengaraj, S., and Leech, D. (2010). *Geobacter sulfurreducens* biofilms developed under different growth conditions on glassy carbon electrodes: insights using cyclic voltammetry. *Chem. Commun.* 46, 4758–4760. doi: 10.1039/c003342a

Katuri, K. P., Rengaraj, S., Kavanagh, P., O'Flaherty, V., and Leech, D. (2012). Charge transport through *Geobacter sulfurreducens* biofilms grown on graphite rods. *Langmuir* 28, 7904–7913. doi: 10.1021/la2047036

Katuri, K. P., Werner, C. M., Jimenez-Sandoval, R. J., Chen, W., Jeon, S., Logan, B. E., et al. (2014). A novel anaerobic electrochemical membrane bioreactor (AnEMBR) with conductive hollow-fiber membrane for treatment of low-organic strength solutions. *Environ. Sci. Technol.* 48, 12833–12841. doi: 10.1021/es504392n

Korth, B., and Harnisch, F. (2019). Spotlight on the energy harvest of electroactive microorganisms: the impact of the applied anode potential. *Front. Microbiol.* 10:1352. doi: 10.3389/fmicb.2019.01352

Kouzuma, A., Meng, X. Y., Kimura, N., Hashimoto, K., and Watanabe, K. (2010). Disruption of the putative cell surface polysaccharide biosynthesis Gene SO3177 in *Shewanella oneidensis* MR-1 enhances adhesion to electrodes and current generation in microbial fuel cells. *Appl. Environ. Microbiol.* 76, 4151–4157. doi: 10.1128/AEM.00117-10

Kumar, A., Leech, D., Siggins, A., Katuri, K., Mahony, T., O'Flaherty, V., et al. (2013). Catalytic response of microbial biofilms grown under fixed anode potentials depends on electrochemical cell configuration. *Chem. Eng. J.* 230, 532–536. doi: 10.1016/j.cej.2013.06.044

Lee, H. S., and Rittmann, B. E. (2010). Significance of biological hydrogen oxidation in a continuous single-chamber microbial electrolysis cell. *Environ. Sci. Technol.* 44, 948–954. doi: 10.1021/es9025358

Lesnik, K. L., and Liu, H. (2014). Establishing a core microbiome in acetate-fed microbial fuel cells. *Appl. Microbiol. Biotechnol.* 98, 4187–4196. doi: 10.1007/s00253-013-5502-9

Levar, C. E., Hoffman, C. L., Dunshee, A. J., Toner, B. M., and Bond, D. R. (2017). Redox potential as a master variable controlling pathways of metal reduction by *Geobacter sulfurreducens*. *ISME J.* 11, 741–752. doi: 10.1038/ismej.2016.146

Liang, P., Duan, R., Jiang, Y., Zhang, X., Qiu, Y., and Huang, X. (2018). One-year operation of 1000-L modularized microbial fuel cell for municipal wastewater treatment. *Water Res.* 141, 1–8. doi: 10.1016/j.watres.2018.04.066

Liu, G., Yates, M. D., Cheng, S., Call, D. F., Sun, D., and Logan, B. E. (2011). Examination of microbial fuel cell start-up times with domestic wastewater and additional amendments. *Bioresour. Technol.* 102, 7301–7306. doi: 10.1016/j.biortech.2011.04.087

Logan, B. E. (2009). Exoelectrogenic bacteria that power microbial fuel cells. *Nat. Rev. Microbiol.* 7, 375–381. doi: 10.1038/nrmicro2113

Marsili, E., Rollefson, J. B., Baron, D. B., Hozalski, R. M., and Bond, D. R. (2008). Microbial biofilm voltammetry: direct electrochemical characterization of catalytic electrode-attached biofilms. *Appl. Environ. Microbiol.* 74, 7329–7337. doi: 10.1128/AEM.00177-08

Marsili, E., Sun, J., and Bond, D. R. (2010). Voltammetry and growth physiology of *Geobacter sulfurreducens* biofilms as a function of growth stage and imposed electrode potential. *Electroanalysis* 22, 865–874. doi: 10.1002/elan.200800007

Martin, E., Savadogo, O., Guiot, S. R., and Tartakovsky, B. (2013). Electrochemical characterization of anodic biofilm development in a microbial fuel cell. *J. Appl. Electrochem.* 43, 533–540. doi: 10.1007/s10800-013-0537-2

McMurdie, P. J., and Holmes, S. (2013). Phyloseq: an R package for reproducible interactive analysis and graphics of microbiome census data. *PLoS ONE.* 8:e61217. doi: 10.1371/journal.pone.0061217

Oksanen, J., Blanchet, F. G., Friendly, M., Kindt, R., Legendre, P., McGlinn, D., et al. (2017). *Package "Vegan." Community Ecology Package*, 1–263.

Paitier, A., Godain, A., Lyon, D., Haddour, N., Vogel, T. M., and Monier, J. M. (2017). Microbial fuel cell anodic microbial population dynamics during MFC start-up. *Biosens. Bioelectron.* 92, 357–363. doi: 10.1016/j.bios.2016.10.096

Peng, L., Zhang, X. T., Yin, J., Xu, S. Y., Zhang, Y., Xie, D. T., et al. (2016). *Geobacter sulfurreducens* adapts to low electrode potential for extracellular electron transfer. *Electrochim. Acta* 191, 743–749. doi: 10.1016/j.electacta.2016.01.033

QIIME (2015). *pick_open_reference_otus.py - Perform Open-Reference OTU Picking.* Available online at: http://qiime.org/scripts/pick_open_reference_otus.html (accessed April 27, 2017).

Rabaey, K., Boon, N., Siciliano, S. D., Verhaege, M., and Verstraete, W. (2004). Biofuel cells select for microbial consortia that self-mediate electron transfer. *Appl. Environ. Microbiol.* 70, 5373–5382. doi: 10.1128/AEM.70.9.5373-5382.2004

Ramasamy, R. P., Gadhamshetty, V., Nadeau, L. J., and Johnson, G. R. (2009). Impedance spectroscopy as a tool for non-intrusive detection of extracellular mediators in microbial fuel cells. *Biotechnol. Bioeng.* 104, 882–891. doi: 10.1002/bit.22469

Ramette, A. (2007). Multivariate analyses in microbial ecology. *FEMS Microbiol. Ecol.* 62, 142–160. doi: 10.1111/j.1574-6941.2007.00375.x

Ren, L., Zhang, X., He, W., and Logan, B. E. (2014). High current densities enable exoelectrogens to outcompete aerobic heterotrophs for substrate. *Biotechnol. Bioeng.* 111, 2163–2169. doi: 10.1002/bit.25290

Rozendal, R. A., Hamelers, H. V. M., and Buisman, C. J. N. (2006). Effects of membrane cation transport on pH and microbial fuel cell performance. *Environ. Sci. Technol.* 40, 5206–5211. doi: 10.1021/es060387r

Srikanth, S., Marsili, E., Flickinger, M. C., and Bond, D. R. (2008). Electrochemical characterization of *Geobacter sulfurreducens* cells immobilized on graphite paper electrodes. *Biotechnol. Bioeng.* 99, 1065–1073. doi: 10.1002/bit.21671

ter Heijne, A., Schaetzle, O., Gimenez, S., Navarro, L., Hamelers, B., and Fabregat-Santiago, F. (2015). Analysis of bio-anode performance through electrochemical impedance spectroscopy. *Bioelectrochemistry* 106, 64–72. doi: 10.1016/j.bioelechem.2015.04.002

Torres, C. I., Krajmalnik-Brown, R., Parameswaran, P., Marcus, A. K., Wanger, G., Gorby, Y. A., et al. (2009). Selecting anode-respiring bacteria based on anode potential: phylogenetic, electrochemical, and microscopic characterization. *Environ. Sci. Technol.* 43, 9519–9524. doi: 10.1021/es902165y

Wagner, R. C., Call, D. F., and Logan, B. E. (2010). Optimal set anode potentials vary in bioelectrochemical systems. *Environ. Sci. Technol.* 44, 6036–6041. doi: 10.1021/es101013e

Wang, H., and Ren, Z. J. (2013). A comprehensive review of microbial electrochemical systems as a platform technology. *Biotechnol. Adv.* 31, 1796–1807. doi: 10.1016/j.biotechadv.2013.10.001

Wang, X., Feng, Y., Ren, N., Wang, H., Lee, H., Li, N., et al. (2009). Accelerated start-up of two-chambered microbial fuel cells: effect of anodic positive poised potential. *Electrochim. Acta* 54, 1109–1114. doi: 10.1016/j.electacta.2008.07.085

Wei, J., Liang, P., Cao, X., and Huang, X. (2010). A new insight into potential regulation on growth and power generation of *Geobacter sulfurreducens* in microbial fuel cells based on energy viewpoint. *Environ. Sci. Technol.* 44, 3187–3191. doi: 10.1021/es903758m

Yanuka-Golub, K., Reshef, L., Rishpon, J., and Gophna, U. (2016). Community structure dynamics during startup in microbial fuel cells - The effect of phosphate concentrations. *Bioresour. Technol.* 212, 151–159. doi: 10.1016/j.biortech.2016.04.016

Yates, M. D., Kiely, P. D., Call, D. F., Rismani-Yazdi, H., Bibby, K., Peccia, J., et al. (2012). Convergent development of anodic bacterial communities in microbial fuel cells. *ISME J.* 6, 2002–2013. doi: 10.1038/ismej.2012.42

Zacharoff, L., Chan, C. H., and Bond, D. R. (2016). Reduction of low potential electron acceptors requires the CbcL inner membrane cytochrome of *Geobacter sulfurreducens*. *Bioelectrochemistry* 107, 7–13. doi: 10.1016/j.bioelechem.2015.08.003

Zhang, F., Xia, X., Luo, Y., Sun, D., Call, D. F., and Logan, B. E. (2013). Improving startup performance with carbon mesh anodes in separator electrode assembly microbial fuel cells. *Bioresour. Technol.* 133, 74–81. doi: 10.1016/j.biortech.2013.01.036

Zhou, J., Liu, W., Deng, Y., Jiang, Y.-H., Xue, K., He, Z., et al. (2013). Stochastic assembly leads to alternative communities with distinct functions in a bioreactor microbial community. *MBio* 4, e00584–12. doi: 10.1128/mBio.00584-12

Zhu, X., Yates, M. D., Hatzell, M. C., Ananda Rao, H., Saikaly, P. E., and Logan, B. E. (2014). Microbial community composition is unaffected by anode potential. *Environ. Sci. Technol.* 48, 1352–1358. doi: 10.1021/es404690q

Zhu, X., Yates, M. D., and Logan, B. E. (2012). Set potential regulation reveals additional oxidation peaks of *Geobacter sulfurreducens* anodic biofilms. *Electrochem. commun.* 22, 116–119. doi: 10.1016/j.elecom.2012.06.013

Conflict of Interest Statement: The authors declare that the research was conducted in the absence of any commercial or financial relationships that could be construed as a potential conflict of interest.

frontiers in Energy Research

ORIGINAL RESEARCH
published: 09 October 2019
doi: 10.3389/fenrg.2019.00106

Benchmarking of Industrial Synthetic Graphite Grades, Carbon Felt, and Carbon Cloth as Cost-Efficient Bioanode Materials for Domestic Wastewater Fed Microbial Electrolysis Cells

Emma Roubaud[1], Rémy Lacroix[2], Serge Da Silva[2], Luc Etcheverry[1], Alain Bergel[1], Régine Basséguy[1] and Benjamin Erable[1]*

[1] Laboratoire de Génie Chimique, Université de Toulouse, CNRS, INPT, UPS, Toulouse, France, [2] 6T-MIC Ingénieries, Castanet-Tolosan, France

OPEN ACCESS

Edited by:
Uwe Schröder,
Technische Universitat Braunschweig, Germany

Reviewed by:
Feng Zhao,
Institute of Urban Environment (CAS), China
Robert Keith Brown,
Technische Universitat Braunschweig, Germany

***Correspondence:**
Emma Roubaud
emma.roubaud@ensiacet.fr

Specialty section:
This article was submitted to Bioenergy and Biofuels, a section of the journal Frontiers in Energy Research

Received: 19 June 2019
Accepted: 19 September 2019
Published: 09 October 2019

Citation:
Roubaud E, Lacroix R, Da Silva S, Etcheverry L, Bergel A, Basséguy R and Erable B (2019) Benchmarking of Industrial Synthetic Graphite Grades, Carbon Felt, and Carbon Cloth as Cost-Efficient Bioanode Materials for Domestic Wastewater Fed Microbial Electrolysis Cells. Front. Energy Res. 7:106. doi: 10.3389/fenrg.2019.00106

Anode material selection is crucial when it comes to building up-scaled microbial electrolysis cells (MEC), as it has a huge influence on the achievable current density and account for a large part of the MEC total investment cost. Graphite is a material that is perfectly suited to the creation of up-scaled bioanodes as it is conductive, chemically stable, biocompatible, and relatively cheap but there are a very large number of commercially available grades of industrial graphite. In this study, five grades of industrial synthetic graphite (named G1–G5) were bench tested to select the most suitable grade for future development of 3D bioanode for domestic wastewater (dWW) fed MEC application. The five grades of graphite have been selected with similar physico-chemical and surface properties (electrical resistivity, surface roughness, and hydrophobicity) theoretically appropriate for EA biofilm development. Nevertheless, significant current density disparities where observed with the five graphite grades, which can certainly be explained by the fabrication procedures of the respective material grades. With the graphite grade giving the most efficient anodes (G3), an average steady state current density of 2.3 A/m² was produced, outperforming the other grades by at least 15%. Even though all graphites had very close physico-chemical characteristics, the grade had a clear significant influence on the current densities produced. G3 graphite was finally compared to carbon felt (CF) and carbon cloth (CC) both in terms of bio-electrochemical current production and bacterial communities colonizing electrodes. G3 bioanodes outperformed CF and CC bioanodes by 50% in term of steady state current density. Biofilms microbial population analysis showed that the *Geobacter* species was present at 82% on G3 bioanodes, 39% on CF bioanodes, and 61% on CC bioanodes when it was only present at 0.06% in the activated sludge used as inoculum. This significant difference

in bacterial enrichment could come from the huge gap between materials resistivity, as graphite resistivity is 200-fold lower than CF and CC resistivities. The strongly hydrophilic surface of G3 graphite was also certainly beneficial for biofilm development compared to the hydrophobic surfaces of CF and CC.

Keywords: anodic biofilm, microbial population analysis, MEC, wastewater treatment, electrode material benchmarking, hydrogen

INTRODUCTION

Microbial electrolysis cells (MEC) allow combining wastewater treatment and production of hydrogen at low cost. They combine the ability of electroactive (EA) bacteria to oxidize organic matter, using the anode as an electron acceptor, with the hydrogen evolution reaction at the cathode (Liu et al., 2004; Gil-Carrera et al., 2013). The valorization of this hydrogen as an energy source reduces the environmental impact associated with the chemical oxygen demand (COD) removal during wastewater treatment (Gude, 2016).

The up-scaling of MEC reactors fed with real domestic wastewater (dWW) is a challenge that requires optimization of reactor geometry (Heidrich et al., 2013; Kadier et al., 2014), electrolyte composition (Roubaud et al., 2018), electrode material and design (Wei et al., 2011; Hou et al., 2015; Xie et al., 2015), microbial consortia management, inoculation strategy (Bridier et al., 2015; Kitching et al., 2017), and operating conditions (temperature, hydraulic retention time, initial COD-load, cell voltage) (Nam et al., 2014; Pannell et al., 2016). MEC up-scaling must also consider financial viability to make the MEC technology to be economically competitive with other hydrogen production and wastewater treatment processes. This first involves reducing the construction costs of MECs as much as possible without affecting their performance. Aiken et al. (2019) recently established that anodic materials represent up to 75% of the total material cost of a MEC at an industrial scale. In this context, the anode material must be carefully chosen to minimize its impact on investment costs and ensure its durability to guarantee a sustainable investment for the exploitation of the technology in the long term.

Graphite, in addition to offering many proven advantages as an anode material in MEC (conductive, chemically stable, biocompatible...), has a relatively low price (Wei et al., 2011; Zhou et al., 2011) and a mechanical resistance over time that has already proven to be successful in many industrial fields other than MECs (metallurgical industry, electrical and electronic industries, aerospace...). In addition, graphite can be machined and assembled to create three-dimensional geometries of customized electrodes, with a controlled pore size (Chong et al., 2019), which could offer compact electrodes with maximized oxidation kinetics in domestic wastewater in the near future.

There are two types of graphite used in the industry: natural graphite and synthetic or artificial graphite. Natural graphite is a natural element mainly used as a lubricant, carbon additive, and pencil lead. Synthetic graphite is a composite material synthesized from petroleum used in a variety of applications requiring properties superior to those of natural graphite. The problem is that there are several grades or qualities of synthetic graphite available on the market whose physical, chemical, and surface characteristics depend largely on their production process: extrusion, vibration molding, compression molding, and isostatic molding. Their price generally varies according to their mechanical strength and premium graphite grades can easily be twice as expensive as low cost graphite grades.

Despite the tremendous amount of work relating to the use of graphite electrodes in MECs and even more widely in all BESs, no one has yet taken a closer look at the consequences of the use of different synthetic graphite grades on the formation and performance of anode EA biofilms. This is what we investigated in this study, by comparing five industrial synthetic grades of graphite plates selected *a priori* to have similar physico-chemical parameters in terms of electrical resistivity, surface roughness and hydrophobicity, probably conditioned by material elaboration protocols. In addition, all five graphite grades were theoretically optimal for biofilm development since they displayed low electrical resistivity, hydrophilic surfaces, and average roughness above 0.8 μm (Flint et al., 2000; Santoro et al., 2014).

Bioanodes were formed with each graphite grade in real dWW collected from a sewage treatment plant with a standardized bio-electrochemical protocol i.e., fixed electrode potential and constant COD concentration. To interpret differences in the bio-electrochemical behavior, materials surface analysis was performed by SEM observation, and microbial communities from biofilms formed on the various electrodes were analyzed by 16S rRNA gene amplicon pyrosequencing. In the end, one graphite grade was selected by taking into account the steady state current densities produced by the bioanodes as well as the graphite price and mechanical resistance. The bio-electrochemical performance of the selected graphite grade were then compared with two other materials commonly used as bioanode supports: carbon cloth (CC) and carbon felt (CF) (Liu et al., 2010; Wei et al., 2011).

MATERIALS AND METHODS

Inoculum and dWW Supply

dWW from a local sewage treatment plant (Castanet-Tolosan, France) was used as electrolyte aqueous medium and COD source for the bioanodes. Activated sludge (AS) obtained from the same treatment plant was used as inoculum (5% v/v of AS in dWW).

The dWW COD was measured with commercial cuvette tests (LCK 514, Hach). For soluble COD, membrane filtration (0.2 μm, Minisart® PES, Sartorius) was performed before measurement.

Before being used as feeding medium, dWW was hydrolyzed for 7 days in hermetically sealed 2 L glass bottles flushed with N_2 for 15 min at a flow rate of 10 mL/s. This hydrolysis step allows increasing the soluble COD concentration that will stay constant during 7 supplementary days (see **Supplementary Figure 1**). The average soluble COD of hydrolyzed dWW is 380 mg/L and average total COD is 800 mg/L.

Bio-Electrochemical Setup and Protocol

Bioanodes were formed on five different grades of graphite plate (Graphitech, France) labeled G1–G5 in this study. **Table 1** displays the characteristics given by the supplier for each grade.

For the graphite grades comparison experiments, the electrodes were prepared by coating 2 × 2 × 0.5 cm graphite plates with insulating varnish and drilling a hole of 1 cm diameter in the center of the electrode (see **Supplementary Figure 2**), so that only the surface inside the hole (surface area = 1.57 cm^2) was electroactive. This has made possible to exclude the influence of any surface residue from the manufacturing process and ensured comparable surface states between the five grades of graphite.

Bioanodes were also formed on carbon felt (CF, RVG 4000, Mersen, France), and carbon cloth (CC, Paxitech, France) and the flat surface of the G3 graphite for comparison. In this case, the electrodes were 2 × 1 cm pieces of each material.

All the experiments were conducted with 3-electrode set-ups. Working electrodes (graphite, CF, or CF) were connected to a titanium rod that served as the current collector. The counter electrode was a 15 × 3 cm 316 L stainless steel grid arranged in a circular shape around the working electrode. The grid was connected to a 316 L SS wire that served as the current collector. The reference electrode was a saturated calomel electrode (SCE, Radiometer Analytical +0.24 V/SHE) and was placed as close as possible to the working electrode (around 2 cm).

The protocol was defined in order to perform strictly identical comparative tests with the different anode materials. The 600 mL bio-electrochemical reactors were initially filled with a mix of dWW and 5% v/v of AS and were continuously sparged with nitrogen gas flux (5 mL/s). The anodes were polarized at −0.1 V/SCE and the current was recorded every 10 min (Chronoamperometry, CA). Cyclic voltammetry (CV) was recorded at 1 mV/s in the −0.5 to +0.2 V/SCE range at the beginning and end of the experiments.

TABLE 1 | Characteristics of industrial synthetic graphite grades, given by the supplier.

	G1	G2	G3	G4	G5
Electric resistivity (μΩ.m)	10.4	8.4	12.0	14.0	13.0
Mechanical strength (compressive strength) (MPa)	32	37	90	150	170
Price/m^2 (€)	501.2	507.9	533.1	679.8	1090.9

The reactors spent 10 days in batch mode. Then, each reactor was connected to a 2 L tank of dWW that had previously been hydrolyzed for 7 days to reach a stable soluble COD concentration (see section Inoculum and dWW Supply). Then, the reactors were operated in recirculating mode for 14 more days thanks to a peristaltic pump with a flow rate of 1.5 mL/min (hydraulic retention time = 6.7 h). The tubes used for the hydraulic recirculation of dWW were oxygen-proof (Tygon, Masterflex).

The dWW tank was renewed with fresh hydrolyzed dWW every 7 days with the aim of maintaining a high and constant soluble COD concentration. The amount of soluble COD consumed by the bioanode was very low thanks to the small size of the bioanode. Here the analytical system was not designed to obtain high COD degradation ratios, but to maintain COD as constant as possible in order to compare the different electrode materials in identical and stable conditions.

Materials Surface Analysis

Scanning Electron Microscopy (SEM)

Biofilms were fixed on the electrode in phosphate buffer (400 mM, pH = 7.4) with 4% glutaraldehyde for 20 min. They were rinsed in phosphate buffer containing saccharose (0.4 M) and dehydrated by immersion in increasing concentrations of acetone (50, 70, 100%), then in acetone and hexamethyldisilazane (50:50), and in 100% hexamethyldisilazane (HMDS). The last batch of HMDS was air-dried until complete evaporation. Surfaces were observed with a LEO 435 VP scanning electron microscope.

For non-colonized anode materials, no treatment was performed before SEM observation.

Surface Roughness

Experimental measurements were performed on each grade of graphite. Surface roughness was measured with an optical microscope (S-Neox, Sensofar) with the focus variation method. This method combines the small focus depth of an optical system with vertical scanning to provide topographical information from the variation of focus[1].

Two roughness parameters were measured: the spatial arithmetic average height (S_a) and the spatial kurtosis (S_{ku}), which indicate if the peaks and valleys are smooth (low S_{ku}) or steep (high S_{ku}). The measurements were performed on 4 mm^2 surfaces and 5 different locations on the electrode.

Water Contact Angle

Water contact angle measurements were performed using a tensiometer (DSA 100, Krüss) with the captive bubble method. An air bubble was produced on the underside of a graphite plate which was immersed in water[2] (Drop Shape Analyzer—DSA100). The ADVANCE software was used to measure the

[1]Focus-Variation|Alicona—High-resolution optical 3D measurement Available online at: https://www.alicona.com/focus-variation/ (accessed August 29, 2018).

[2]Drop Shape Analyzer—DSA100 Available online at: https://www.kruss-scientific.com/products/contact-angle/dsa100/drop-shape-analyzer-dsa100/ (accessed August 29, 2018).

resulting contact angle. The measurements were performed on 5 different locations for each grade of graphite.

Bacterial Community Analysis

The bioanodes were put in plastic tubes with 50 mL of phosphate buffer and placed in an ultrasonic bath at 80 W for 30 min to detach the biofilm. Two 50 mL tubes were also prepared with dWW and AS samples.

The tubes were centrifuged for 15 min at 4,600 g at 6°C. The supernatant was discarded and a DNA extraction kit (DNeasy PowerBiofilm, Qiagen) was used on the pellets according to the manufacturer's recommendations. Full pellets (∼0.03 g) were used for the biofilm samples and ∼0.20 g pellets for the AS and dWW samples. The DNA concentrations were checked with absorbance at 260 nm as well as the possible contamination by protein and humic acid with absorbance at 280 and 230 nm, respectively. The DNA samples were sent to the Research and Testing Laboratory (RTL, Texas, USA) where the DNA were amplified by PCR and sequenced with the bacterial primers 28F (5′-GAG TTT GAT YMT GGC TC-3′) and 519R (5′-GWA TTA CCG CGG CKG CTG-3′) according to RTL protocols[3] (RTLGenomics). Subsequent data analyses with the DNA quality, DNA sequence alignment, clustering in operational taxonomic and the assignment were also performed by RTL according to their protocol.

RESULTS AND DISCUSSION

Physico-Chemical Surface Properties of the Different Grades of Graphite

Physico-chemical properties of the bioanode material such as surface roughness, hydrophobicity, and electrical resistance affect the formation of electroactive (EA) biofilm on its surface (Santoro et al., 2014).

Surface Roughness

The average roughness (S_a) of graphite surface was between 1.3 and 4.4 μm (**Table 2**). In general, surfaces with S_a lower than 0.8 μm are considered as "hygienic" surface and are not suitable for microbial growth (Flint et al., 2000). Moreover, S_a values in the range of 1–10 μm are ideal for biofilm adhesion (Pons et al., 2011; Kano et al., 2012; Santoro et al., 2014; Champigneux et al., 2018). Indeed, bacteria particularly prefer rough areas and surface deformations, which size range is of the same order of magnitude as the size of the bacteria, i.e., in the order of a few micrometers. The surface roughness measurements indicate that all selected graphite grades present a suitable surface roughness for biofilm development.

The kurtosis roughness (S_{ku}) represents the sharpness of the surface[4].

- if $S_{ku} < 3$: Height distribution is skewed above the mean plane.
- if $S_{ku} = 3$: Height distribution is normal (sharp portions and indented portions co-exist).
- if $S_{ku} > 3$: Height distribution is spiked (high peaks, large valleys).

Characklis (2009) has stated that surface roughness elements, such as peaks and valleys, can provide "shelter" from shear forces for bacteria and increase convective mass transport near the surface. Thus, S_{ku} is an interesting parameter to assess if a surface is favorable for bacterial adhesion.

Graphite surfaces can be divided in two categories: graphites with spiked surfaces (G1, G2, and G3; $S_{ku} >> 3$) and graphites with smooth surfaces (G4 and G5; S_{ku} close to 3). Biofilm bacteria growing on G4 and G5 would be less protected from shear forces, leading to more bacterial detachment with those graphite grades when compared with G1, G2, and G3 (Picioreanu et al., 2001).

Surface Hydrophobicity

Water contact angle measurements showed that all five graphite grades have hydrophilic surfaces (contact angle $<< 90°$). Contact angle values range from 33 to 36°, which means there is no significant difference between graphite grades hydrophobicity (**Table 3**).

Santoro et al. (2014) have compared the effect of hydrophilic and hydrophobic surfaces on bacterial attachment, current, and power output in microbial fuel cells. Bioanodes formed on hydrophilic surfaces showed the shortest start-up time, the highest current, and power densities and the fastest electron transfer rates among the materials investigated. Also, Guo et al. (2013) demonstrated that positively charged and hydrophilic surfaces were more selective to EA microbes (e.g., *Geobacter*) and more conducive for EA biofilm formation.

As a conclusion, all five grades of graphite have strongly hydrophilic surfaces, which would be beneficial for bacterial attachment according to the literature. However, the difference between the measured contact angles for the five grades of graphite is slight, material hydrophobicity will not be a differentiation factor for the bioanode performance.

Electrical Resistivity

Graphite resistivity was on average 11.6 μΩ.m for the 5 graphite grades (**Table 1**). These values are significantly higher than that of

TABLE 2 | Surfaces roughness (S_a and S_{ku}) experimentally measured on graphite grades.

		G1	G2	G3	G4	G5
Surface roughness	S_a (μm)	4.4 ± 0.5	4.2 ± 0.2	1.9 ± 0.1	2.6 ± 0.1	1.3 ± 0.1
	S_{ku}	48 ± 13	26 ± 2	17 ± 7	3.8 ± 0.1	4.9 ± 0.3

TABLE 3 | Water contact angle on graphite grades, measured experimentally.

	G1	G2	G3	G4	G5
Contact angle	35 ± 5°	35 ± 1°	36 ± 2°	33 ± 2°	34 ± 2°

[3]RTLGenomics. Available online at: https://rtlgenomics.com/ (accessed April 8, 2019).

[4]Sku (Kurtosis)|Area Roughness Parameters|Introduction To Roughness|KEYENCE America. Available online at: https://www.keyence.com/ss/products/microscope/roughness/surface/sku-kurtosis.jsp (accessed March 19, 2019).

metallic materials such as stainless steel (∼0.7 μΩ.m) (Peckner and Bernstein, 1977) or copper (0.02 μΩ.m). Despite their low resistivity, metallic materials are not an obvious choice as bioanode materials since they do not always fulfill the other criteria required (chemical stability and bio-compatibility). Nevertheless, remarkable current densities were obtained on stainless steel electrodes in MFC inoculated with compost leachate (Pocaznoi et al., 2012a; Ketep et al., 2014) or on copper and silver electrodes inoculated with dWW (Baudler et al., 2015).

For Wang et al. (2013), solid graphite resistivity is low enough and its impact on the ohmic losses of BES cells is negligible, even in up-scaled reactors, which is not the case for granular or fibrous carbon materials (Baudler et al., 2015). Graphite is about 200 times less resistant than CF and CC (González-García et al., 1999) which are widely used as bioanode materials and with which remarkable current densities were still obtained (Cercado-Quezada et al., 2013).

The resistivity range of materials used as EA biofilm support in the literature is truly broad. The resistivity range of the 5 graphite grades considered here (from 8.4 to 14.0 μΩ.m) is narrow enough not to affect current densities.

Comparison of Industrial Grades of Graphite as Bioanode Material

Bio-Electrochemical Experiments

The five grades of graphite were tested to generate bioanodes from real dWW (protocol described in section Materials Surface Analysis). As discussed above, all five grades have suitable physico-chemical properties to allow biofilm growth on the surface: average surface roughness above 0.8 μm, hydrophilic surface and low electrical resistivity.

The current densities recorded during the 24 days of the CA are displayed on **Figure 1**.

In the initial batch period, current rise happened in the first 3–4 days for graphite grades G2, G3, and G4 as well as one G1 duplicate. For the other G1 and both G5 duplicates, the current rise happened later, after the 5th day. Maximum current density was reached during the batch period for G2 and G4 and during the recirculation period for G1, G3, and G5. Setting up the recirculation had little effect for G2 and G4 but triggered a current growth for G1, G3, and G5. During the recirculation period, with a stationary concentration of 380 $mg_{solubleCOD}/L$, steady state current was obtained from day 10 for G4, from day 11 for G1 and G2, from day 13 for G3, and from day 14 for G5.

As the current densities achieved stability at different points in time for each graphite grade, the steady state current density value was evaluated on both duplicates by averaging the current density values recorded from the first day of current generation stability to the end of the experiment (**Table 4**).

Steady state current densities ranged from 1.1 to 2.3 A/m^2. The lowest was obtained with G5, then G1, G4, G2, and the highest was obtained with G3. The steady state current generated by the G3 based electrodes was 15% higher than G2 (second best performing graphite grade) and 110% higher than G5 (least performing graphite grade).

To sum up, efficient EA biofilms developed on the five graphite grades. Significant current densities disparities were observed from one graphite grade to another despite them having similar hydrophilia and electrical resistance. The main differences between grades was the surface roughness (S_a and S_{ku}) but no obvious correlation was found between roughness parameters and steady state current densities. In conclusion, even when the major physico-chemical parameters are restricted to narrow ranges, the grade of industrial graphites reveals here to affect significantly the current provided by the bioanodes formed on the different materials. It is strongly suspected that these differences are mainly related to the production processes of the material grades. Experimental tests remain consequently necessary to check the capability of industrial graphite materials to drive the formation of efficient bioanodes.

Graphite Selection Considering Cost of Investment and Mechanical Strength

Apart from the physico-chemical characteristics of the materials, the investment cost of graphite is also an important indicator of the economic competitiveness of bioanodes applications.

In order to design an economically sustainable MEC, the anode material must be cheap and readily available. Wei et al. compared the bulk price for common electrode materials and stated that graphite was up to 50 times cheaper than CF or carbon fiber brushes (Wei et al., 2011).

Among the 5 grades of graphite tested, G1, G2, and G3 are the least expensive and are in the same range of price when G4 and G5 are significantly more expensive (up to twice as expensive for G5). Considering that anode materials account for 75% of an up-scaled MEC total material cost (Aiken et al., 2019), using a low-end graphite such as G1, G2, or G3 with a price twice as low as G5 would decrease up-scaled MECs investment costs by almost 40%. A case study about investment costs for the implementation of MECs in domestic wastewater treatment plants by Escapa et al. (2012) proposes a scenario in which a 108,300 m^2 bioanode produces a current density of 2.5 A/m^2, which is the same order of magnitude of the average current densities produced by the G3 bioanodes. As an example, in this scenario, using an electrode material costing about 50 €/m^2 instead of 100 €/m^2 would reduce the anode material cost by about 5 million euros.

Considering steady state current density and price, G2 and G3 have the best price-performance ratio. The main difference between those two graphite grades is their production process, which influences their mechanical strength. G3 graphite is produced through isostatic pressure as opposed to G2 that is produced through extruding. The isostatic pressure technique allows producing graphite with higher mechanical strength, making G3 compressive strength almost 1.5 times higher than G2. Overall, G3 is the most suited graphite grade to use as bioanode material in the context of an up-scaled MEC as its performance/price ratio is excellent and its mechanic strength is the highest among all graphite grades in the same price range.

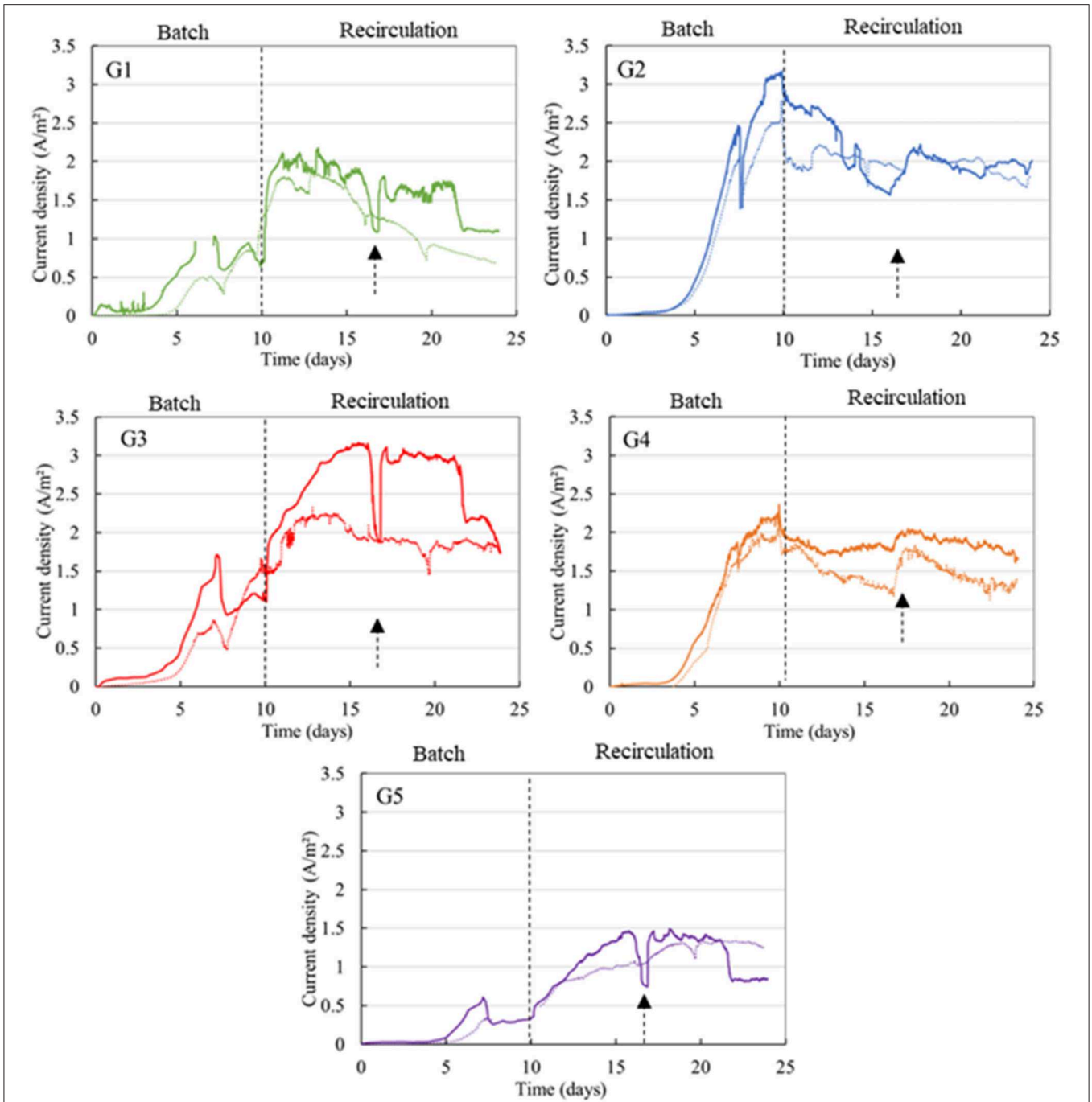

FIGURE 1 | Chronoamperometries (CA) for dWW-fed graphite bioanodes. The reactors were initially conducted in batch mode for 10 days and were then switched to recirculating mode (dashed line) in closed loop with a 2 L tank of hydrolyzed dWW that is renewed at day 17 (dashed arrow). Duplicates were conducted for each electrode graphite grade.

TABLE 4 | Steady state current densities and maximal current densities obtained with the 5 grades of graphite.

			G1	G2	G3	G4	G5
Steady state current density (A/m²)	Run 1	Run 2	1.7 ± 0.3	1.3 ± 0.4	2.0 ± 0.3	1.9 ± 0.2	2.8 ± 0.4	1.9 ± 0.2	1.8 ± 0.2	1.5 ± 0.2	1.2 ± 0.3	1.1 ± 0.2
	Mean value		1.5		2.0		2.3		1.6		1.1	

The current values are given for each run and the mean value is calculated on the line underneath.

Comparison of the G3 Grade of Graphite With Classical CF and CC Electrodes

Bio-Electrochemical Experiments

CF and CC are among the most commonly used anode materials in bioelectrochemical systems (Santoro et al., 2017; Yu et al., 2017) because they offer a porous 3-dimensional structures that can lead to efficient bioanodes in environments with low suspended solids and poor COD load. In order to validate the selection of G3 graphite grade, this material was compared to CC and CF in term of steady state current density. Bioanodes were formed in duplicates with G3 graphite plates, CF, and CC at the same time and using the same batch of AS and dWW to ensure strictly comparable results. The current densities recorded during the 24 days of the CA are displayed on **Figure 2** (left).

In the batch period, graphite and felt electrodes had similar behaviors with a current rise happening around the 5th−7th day. With the CC electrodes, no significant current rise was observed during the batch period.

When recirculation was started, the current kept rising for around 5 days with graphite and started to stabilize with CF. The current started to rise with CC. A steady state was achieved on the 13th day for graphite and CF and on the 18th day for CC. The current density value for the stationary phase was evaluated in the same way as in section Physico-Chemical Surface Properties of the Different Grades of Graphite. The values obtained are displayed in the **Table 5**. CF gave the most reproducible CAs, with an equal steady state current value on both runs (<3% difference between runs based on the average steady state current density value given in the **Table 5**). Difference between the two runs with the G3 graphite grade is 23%. CC was the less reproducible with 33% difference when steady state current density was reached.

The G3 graphite grade gave the highest steady state current with an average of 3.1 A/m². It is about 50% higher than steady state current densities obtained with CF and CC, which were 2.0 and 2.1 A/m², respectively.

When the steady state current was established on the different bioanodes (day 24), turnover CV were recorded with stable soluble COD concentrations (**Figure 2**, right). The shape of the turnover CV is characteristic of bioanodes oxidizing volatile fatty acids present in soluble COD (mainly acetate, formate, butyrate and propionate (Barker et al., 1999), at neutral pH (Pocaznoi et al., 2012b; Cercado-Quezada et al., 2013). The half-wave potentials are in the range of −0.4 to −0.3 V/SCE for G3 graphite, −0.22 V/SCE for CF, and in the range of −0.35 to −0.2 V/SCE for CC.

Current density showed a plateau value of 2.4 A/m² for CF, 3.2 A/m² for graphite, and 2.2 A/m² for CC, very similar to steady state current densities recorded on the CAs.

Microbial Electrode Colonization

Figure 3 displays the SEM observation of the 3 bioanode materials before and after biofilm colonization, i.e., at day 0 and after day 24 of the bioanode formation.

Before colonization (**Figure 3**, 1a), G3 graphite surface topography is not smooth and present some topographic peaks and valleys, in accordance with the roughness measurements (**Table 2**). The CF structure seems quite open, with a fiber diameter of about 20 μm (**Figure 3**, 1b). Inter-fiber spaces are variable between 10 and 500 μm. The fiber diameter of CC is about 10 μm (half the size of CF fibers). The fibers are tightly woven which makes inter-fiber spaces difficult to evaluate. On a bacterial scale, cloth porosity is almost non-existent.

After 24 days, a continuous biofilm with homogeneous visual appearance has developed on the G3 graphite surface (**Figure 3**, 2a). This biofilm seemed thicker than those developed on CF and CC because no more peaks or valleys can be observed by SEM on the graphite surface. On CF, biofilm was mainly located on the external fibers and did not cover the whole surface of the fibers nor all the volume of porosity between the fibers (**Figure 3**, 2b). The biofilm established on the CC electrode had fully covered the surface area of the electrode (**Figure 3**, 3b). However, its thickness was estimated at only 15 μm, because visually the topography of the CC under the biofilm layer was still visible.

Overall, the biofilm colonization is important on the three materials, with however a seemingly smaller biofilm density on CF. This certainly explains why the current densities obtained are in the same range. Theoretically, CF has a higher specific surface area than CC and the G3 graphite. The current densities should consequently have been higher on this material. Nevertheless, the biofilm only developed on the external fibers and did not penetrate inside the felt. Felt did not perform better than 2D materials such as cloth or graphite in real dWW. The poor infiltration of EA biofilm into the macro porosity of CF has already been highlighted (Blanchet et al., 2016).

Bacterial Population Ecology of EA Biofilms

Microbial population analysis was performed on the biofilms removed from the three types of electrodes as well as on dWW and AS used, respectively, as electrolyte and inoculum to form the bioanodes.

The three biofilms showed similar bacterial classes, with some variation in the relative abundance rate (**Figure 4**). On the one hand, the class of *Deltaproteobacteria* was systematically enriched in all biofilms formed on the electrodes (82% on G3 graphite, 39% on CF, and 61% on CC) regardless of the nature of the electrode material while this class of bacteria was only present at 0.06% in activated sludge and even not detected in dWW. On the other hand, a higher percentage of *Betaproteobacteria* is present on CF (11%) and CC (9%) than on graphite (<1%). This bacterial class is largely represented in AS and dWW but is depleted to the benefit of *Betaproteobacteria* on the graphite electrode.

For Mateo et al. (2018) biofilms grown on various carbon materials (carbon paper, carbon foam, and carbon cloth) showed the same microbial population. The performance gap between the electrodes came from the variation of specific surface area between the materials.

The proportion of *Deltaproteobacteria* in biofilms coincided well with the current density generated, i.e., the more efficient the bioanodes are, the higher the relative abundance of *Deltaproteobacteria*. At the family level, 99% of those *Deltaproteobacteria* belong to *Geobacteracae*. Many studies conducted on bioanodes inoculated with soils, activated sludge or marine sediments come to the same conclusion that EA biofilms

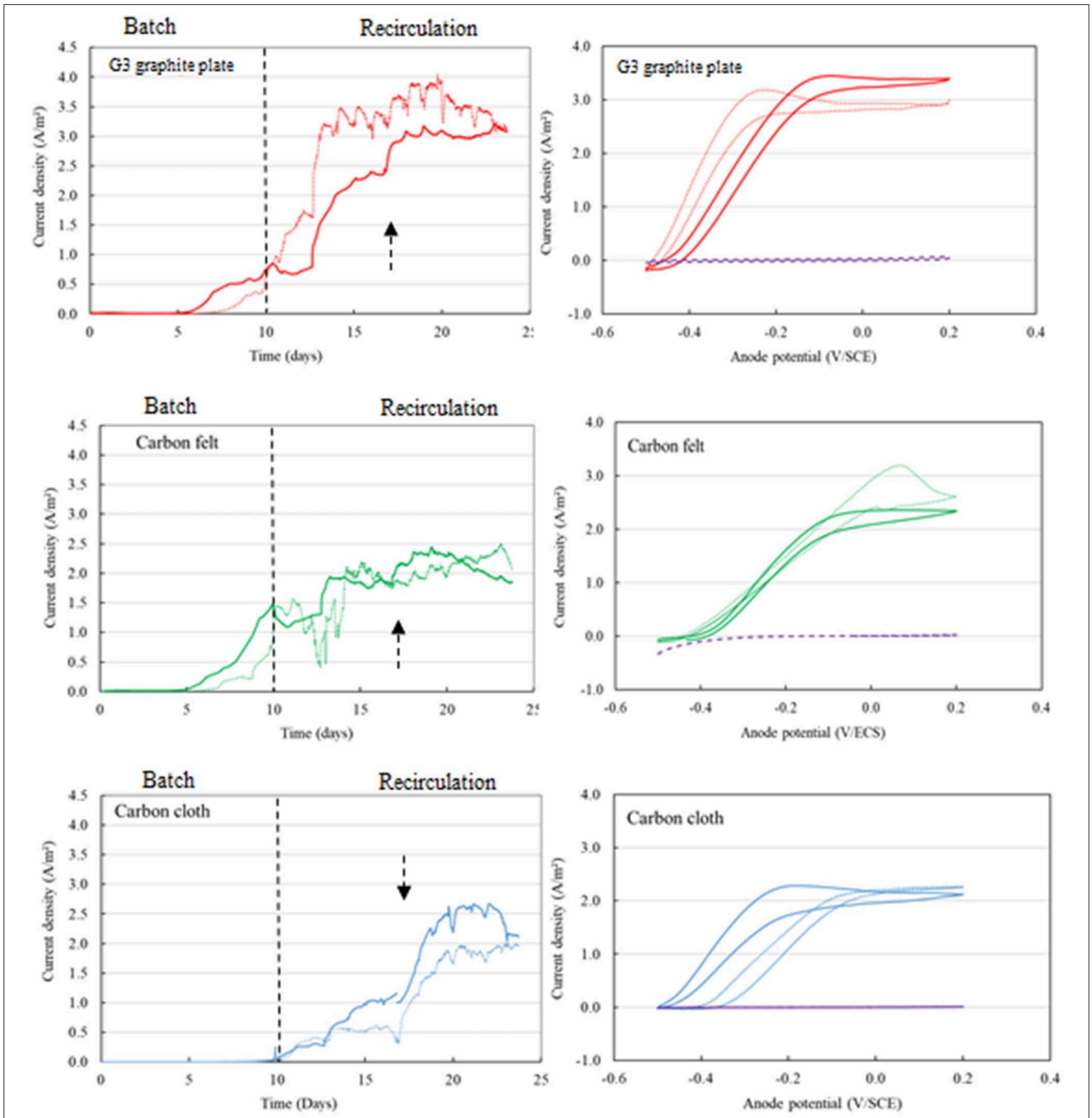

FIGURE 2 | (Left) Chronoamperometries for dWW-fed bioanodes formed on G3 graphite, CF, and CC electrodes. For the first 10 days the reactors are conducted in batch mode and are then switched to recirculating mode (dashed line) with a 2 L tank of hydrolyzed dWW that is renewed at day 17 (dashed arrow). **(Right)** Cyclic voltammetries performed in dWW with a stable COD concentration under turnover conditions at 1 mV/s, at the beginning of the experiment (dashed line) and after 24 days of experiment (full and dotted lines). Duplicates were conducted for each electrode material.

are especially enriched in species from the *Geobacteraceae* family (Bond et al., 2002; Cercado-Quezada et al., 2013; Blanchet et al., 2015). Among *Geobacteraceae*, some species have been isolated (*sulfureducens, metallireduscens*, and others…) (Koch and Harnisch, 2016), which are now used as model EA bacteria (Reguera et al., 2005; Kumar et al., 2016).

To conclude, G3 graphite out-performed the two other materials by 50% in term of steady state current density.

TABLE 5 | Average current density obtained in steady state on CF, CC, and G3 graphite.

			G3 graphite		Felt		Cloth	
Steady state current density (A/m²)	Run 1	Run 2	2.7 ± 0.5	3.4 ± 0.2	2.0 ± 0.2	2.0 ± 0.3	2.4 ± 0.2	1.7 ± 0.2
	Average		3.1		2.0		2.1	

Given for each replicate and averaged on both replicates.

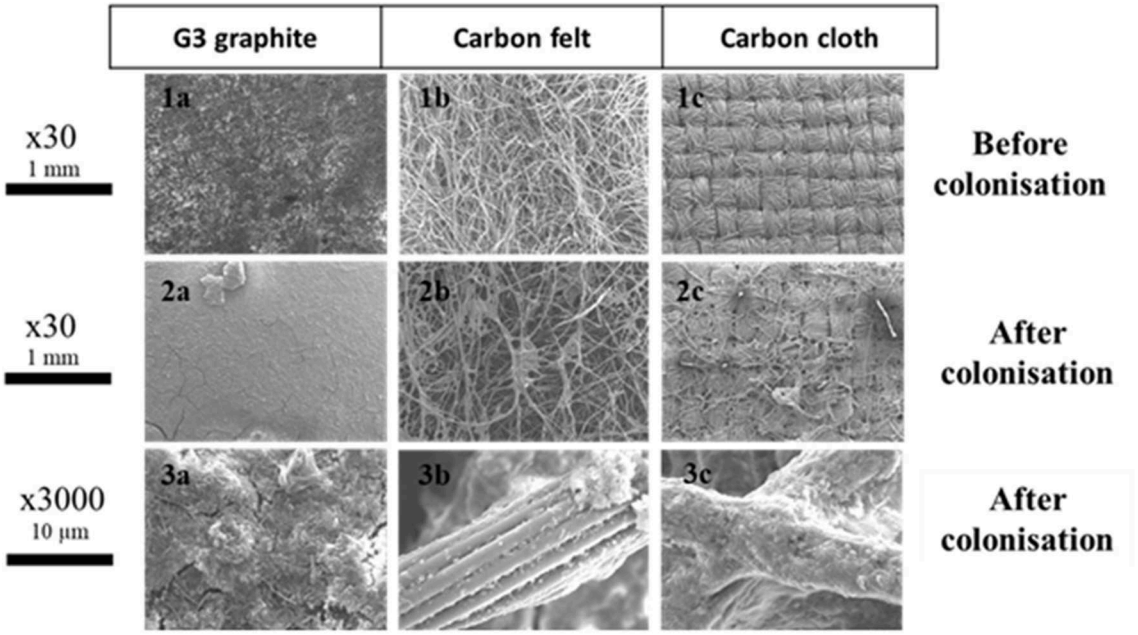

FIGURE 3 | SEM images of G3 graphite, CF, and CC electrode materials before and after biofilm colonization in a dWW-fed reactor.

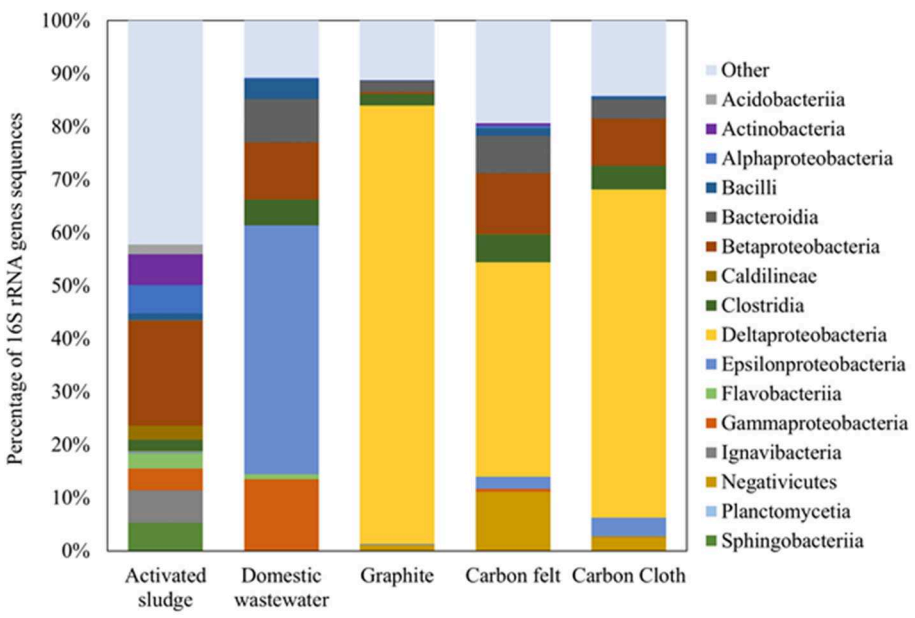

FIGURE 4 | Relative abundance of major bacterial classes identified in the activated sludge, the domestic wastewater and in biofilms developed after 24 days on G3, CF, and CC.

This performance gap could be justified by two factors. On the one hand, graphite resistivity is about 200 times lower than those of felt and cloth (González-García et al., 1999). This possibly led to more EA bacteria, especially the *Geobacteracae* family, colonizing the electrode and greater current density obtained with G3 graphite. To our knowledge, the direct correlation between extracellular electron transfer (EET) efficiency and support material electrical resistivity has yet to be demonstrated. This is mainly because producing materials with different resistivities but otherwise identical characteristics is challenging. Nevertheless, many studies have stated that a low electrical resistivity for the support material is necessary to obtain high current densities from bioanodes (Yu et al., 2017; Zhang et al., 2018).

3D pictures of EA biofilms revealed that anchoring to the surface seemed to be constituted of dispersed "pillars," the whole biofilm not being in direct contact with the electrode (Erable and Bergel, 2009). It has also been suggested that EA biofilm formed with *Geobacter sulfurreducens* transfer electrons to the electrode not uniformly through the whole surface area but through patches where pioneering adherent cells play the role of "electrochemical gate" between the biofilm and the electrode surface (Dumas et al., 2008). Pons et al. (2011) stated that extremely high current densities (up to 280 A/m^2) could be achieved locally in EA biofilms, especially with isolated bacteria and small colonies, when dense microbial colonies provided lower current densities. All these observations converge toward an electron transfer model that relies on the passage of high local current density through small patches rather than the passage of the average current density through the entire surface. Those high current points are the main EET zones, which means a large quantity of electrons is transferred through a small surface area. In such a context, the resistivity of the electrode could be a major rate-limiting cause because the higher is the local current, the higher is the potential drop opposed to the current.

On the other hand, CF and CC have hydrophobic surfaces (water contact angles, respectively 120 and 110°; Wang et al., 2007; Guo et al., 2014) while G3 graphite has a strongly hydrophilic surface (contact angle 50°). As discussed in section Electrical Resistivity, hydrophilic surfaces are beneficial for EA biofilms and the current density differences observed between CF, CC, and G3 graphite might also be linked to the significant difference between their hydrophilic properties.

CONCLUSION

Even if the five grades of graphite tested all had close properties in term of electrical resistivity, surface roughness and hydrophobicity, the grade of the synthetic graphite really makes a strong impact on the current densities obtained. Among the graphite grades tested, G3 produced the highest steady state current (2.3 A/m^2), giving it the best performance/mechanical strength/price ratio of all the graphite grades tested. The differences exist, they are self-evident. But the reasons why one grade more than another is able to initiate the formation of a high-performance bioanode are still unclear and are undoubtedly conditioned by the elaboration protocols of synthetic graphite grades. The main fact to keep in mind is that the grade of graphite is something significantly impacting and that we can no longer talk about a synthetic graphite electrode as a common, universally comparable material. The predictions or observations made today on the basis of graphite bioanodes cannot be generalized to all graphite electrodes. Even at this detailed stage of graphite grade, the use of an electrode material and its comparison with another material inevitably requires experimental tests.

Steady state current density obtained with G3 was 50% higher than with CF and CC, which are commonly used 3D carbon materials for bioanodes. Bacterial communities and surface colonization were roughly similar on the G3 graphite grade, CF and CC, with a high enrichment in EA bacteria of the genus *Geobacter* even more important on G3. The electrical resistivity of G3, 200 times lower than those of CC and CF plus its strongly hydrophilic surface, could explain an intensification of the EET within the biofilm and the improved current densities obtained with G3. The influence of anode material resistivity on EA bacterial communities, EET mechanisms, and the physical structure of biofilms on electrodes will be an interesting research path for the future, especially considering very intense local electrons flow (current) as discussed with the example of "electron transfer gates."

For the future, the standardized bio-electrochemical test protocol described in this study for the anodic materials comparison can be greatly useful to benchmark other materials as potential efficient dWW-fed bioanode support materials.

DATA AVAILABILITY STATEMENT

The datasets generated for this study are available on request to the corresponding author.

AUTHOR CONTRIBUTIONS

ER, AB, RB, and BE: study design and article writing. ER and LE: experiments. ER, RL, SD, LE, AB, RB, and BE: data analysis.

FUNDING

This work was funded by the French ANR within the framework of the WE-MET project (ERANETMED 2015 European call).

SUPPLEMENTARY MATERIAL

The Supplementary Material for this article can be found online at: https://www.frontiersin.org/articles/10.3389/fenrg.2019.00106/full#supplementary-material

REFERENCES

Aiken, D. C., Curtis, T. P., and Heidrich, E. S. (2019). Avenues to the financial viability of microbial electrolysis cells [MEC] for domestic wastewater treatment and hydrogen production. *Int. J. Hydrogen Energy* 44, 2426–2434. doi: 10.1016/j.ijhydene.2018.12.029

Barker, D. J., Mannucchi, G. A., Salvi, S. M. L., and Stuckey, D. C. (1999). Characterisation of soluble residual chemical oxygen demand (COD) in anaerobic wastewater treatment effluents. *Water Res.* 33, 2499–2510. doi: 10.1016/S0043-1354(98)00489-8

Baudler, A., Schmidt, I., Langner, M., Greiner, A., and Schröder, U. (2015). Does it have to be carbon? Metal anodes in microbial fuel cells and related bioelectrochemical systems. *Energy Environ. Sci.* 8, 2048–2055. doi: 10.1039/C5EE00866B

Blanchet, E., Desmond-Le Quemener, E., Erable, B., Bridier, A., Bouchez, T., and Bergel, A. (2015). Comparison of synthetic medium and wastewater used as dilution medium to design scalable microbial anodes: application to food waste treatment. *Bioresour. Technol.* 185, 106–115. doi: 10.1016/j.biortech.2015.02.097

Blanchet, E., Erable, B., De Solan, M. L., and Bergel, A. (2016). Two-dimensional carbon cloth and three-dimensional carbon felt perform similarly to form bioanode fed with food waste. *Electrochem. Commun.* 66, 38–41. doi: 10.1016/j.elecom.2016.02.017

Bond, D. R., Holmes, D. E., Tender, L. M., and Lovley, D. R. (2002). Electrode-reducing microorganisms that harvest from marine sediments. *Science* 295, 483–485. doi: 10.1126/science.1066771

Bridier, A., Desmond-Le Quemener, E., Bureau, C., Champigneux, P., Renvoise, L., Audic, J. M., et al. (2015). Successive bioanode regenerations to maintain efficient current production from biowaste. *Bioelectrochemistry* 106, 133–140. doi: 10.1016/j.bioelechem.2015.05.007

Cercado-Quezada, B., Byrne, N., Bertrand, M., Pocaznoi, D., Rimboud, M., Achouak, W., et al. (2013). Garden compost inoculum leads to microbial bioanodes with potential-independent characteristics. *Bioresour. Technol.* 134, 276–284. doi: 10.1016/j.biortech.2013.01.123

Champigneux, P., Delia, M. L., and Bergel, A. (2018). Impact of electrode micro- and nano-scale topography on the formation and performance of microbial electrodes. *Biosens. Bioelectron.* 118, 231–246. doi: 10.1016/j.bios.2018.06.059

Characklis, W. G. (2009). Bioengineering report: fouling biofilm development: a process analysis. *Biotechnol. Bioeng.* 102, 309–347. doi: 10.1002/bit.22227

Chong, P., Erable, B., and Bergel, A. (2019). Effect of pore size on the current produced by 3-dimensional porous microbial anodes: a critical review. *Bioresour. Technol.* 289:121641. doi: 10.1016/j.biortech.2019.121641

Dumas, C., Basseguy, R., and Bergel, A. (2008). Electrochemical activity of *Geobacter sulfurreducens* biofilms on stainless steel anodes. *Electrochim. Acta* 53, 5235–5241. doi: 10.1016/j.electacta.2008.02.056

Erable, B., and Bergel, A. (2009). First air-tolerant effective stainless steel microbial anode obtained from a natural marine biofilm. *Bioresour. Technol.* 100, 3302–3307. doi: 10.1016/j.biortech.2009.02.025

Escapa, A., Gómez, X., Tartakovsky, B., and Morán, A. (2012). Estimating microbial electrolysis cell (MEC) investment costs in wastewater treatment plants: case study. *Int. J. Hydrogen Energy* 37, 18641–18653. doi: 10.1016/j.ijhydene.2012.09.157

Flint, S. H., Brooks, J. D., and Bremer, P. J. (2000). Properties of the stainless steel substrate, influencing the adhesion of thermo-resistance Streptococci. *J. Food Eng.* 43, 235–242. doi: 10.1016/S0260-8774(99)00157-0

Gil-Carrera, L., Escapa, A., Moreno, R., and Morán, A. (2013). Reduced energy consumption during low strength domestic wastewater treatment in a semi-pilot tubular microbial electrolysis cell. *J. Environ. Manage.* 122, 1–7. doi: 10.1016/j.jenvman.2013.03.001

González-García, J., Bonete, P., Expósito, E., Montiel, V., Aldaz, A., and Torregrosa-Maciá, R. (1999). Characterization of a carbon felt electrode: structural and physical properties. *J. Mater. Chem.* 9, 419–426. doi: 10.1039/a805823g

Gude, V. G. (2016). Wastewater treatment in microbial fuel cells - an overview. *J. Clean. Prod.* 122, 287–307. doi: 10.1016/j.jclepro.2016.02.022

Guo, K., Freguia, S., Dennis, P. G., Chen, X., Donose, B. C., Keller, J., et al. (2013). Effects of surface charge and hydrophobicity on anodic biofilm formation, community composition, and current generation in bioelectrochemical systems. *Environ. Sci. Technol.* 47, 7563–7570. doi: 10.1021/es400901u

Guo, K., Soeriyadi, A. H., Patil, S. A., Prévoteau, A., Freguia, S., Gooding, J. J., et al. (2014). Surfactant treatment of carbon felt enhances anodic microbial electrocatalysis in bioelectrochemical systems. *Electrochem. Commun.* 39, 1–4. doi: 10.1016/j.elecom.2013.12.001

Heidrich, E. S., Dolfing, J., Scott, K., Edwards, S. R., Jones, C., and Curtis, T. P. (2013). Production of hydrogen from domestic wastewater in a pilot-scale microbial electrolysis cell. *Appl. Microbiol. Biotechnol.* 97, 6979–6989. doi: 10.1007/s00253-012-4456-7

Hou, Y., Zhang, R., Luo, H., Liu, G., Kim, Y., Yu, S., et al. (2015). Microbial electrolysis cell with spiral wound electrode for wastewater treatment and methane production. *Process Biochem.* 50, 1103–1109. doi: 10.1016/j.procbio.2015.04.001

Kadier, A., Simayi, Y., Abdeshahian, P., Azman, N. F., Chandrasekhar, K., and Kalil, M. S. (2014). A comprehensive review of microbial electrolysis cells (MEC) reactor designs and configurations for sustainable hydrogen gas production. *Alexandria Eng. J.* 55, 427–443. doi: 10.1016/j.aej.2015.10.008

Kano, T., Suito, E., Hishida, K., and Miki, N. (2012). Effect of microscale surface geometry of electrodes on performance of microbial fuel cells micromachined microbial and photosynthetic fuel cells. *Jpn. J. Appl. Phys.* 51, 6–4. doi: 10.7567/JJAP.51.06FK04

Ketep, S. F., Bergel, A., Calmet, A., and Erable, B. (2014). Stainless steel foam increases the current produced by microbial bioanodes in bioelectrochemical systems. *Energy Environ. Sci.* 7, 1633–1637. doi: 10.1039/C3EE44114H

Kitching, M., Butler, R., and Marsili, E. (2017). Microbial bioelectrosynthesis of hydrogen: current challenges and scale-up. *Enzyme Microb. Technol.* 96, 1–13. doi: 10.1016/j.enzmictec.2016.09.002

Koch, C., and Harnisch, F. (2016). Is there a specific ecological niche for electroactive microorganisms? *ChemElectroChem* 3, 1282–1295. doi: 10.1002/celc.201600079

Kumar, R., Singh, L., and Zularisam, A. W. (2016). Exoelectrogens: recent advances in molecular drivers involved in extracellular electron transfer and strategies used to improve it for microbial fuel cell applications. *Renew. Sustain. Energy Rev.* 56, 1322–1336. doi: 10.1016/j.rser.2015.12.029

Liu, H., Hu, H., Chignell, J., and Fan, Y. (2010). Microbial electrolysis: novel technology for hydrogen production from biomass. *Biofuels* 1, 129–142. doi: 10.4155/bfs.09.9

Liu, H., Ramnarayanan, R., and Logan, B. E. (2004). Production of electricity during wastewater treatment using a single chamber microbial fuel cell. *Environ. Sci. Technol.* 38, 2281–2285. doi: 10.1021/es034923g

Mateo, S., Cañizares, P., Rodrigo, M. A., and Fernandez-Morales, F. J. (2018). Biofilm and planktonic population distribution. Key aspects in carbonaceous anodes for microbial fuel cells. *J. Chem. Technol. Biotechnol.* 93, 3436–3443. doi: 10.1002/jctb.5701

Nam, J. Y., Yates, M. D., Zaybak, Z., and Logan, B. E. (2014). Examination of protein degradation in continuous flow, microbial electrolysis cells treating fermentation wastewater. *Bioresour. Technol.* 171, 182–186. doi: 10.1016/j.biortech.2014.08.065

Pannell, T. C., Goud, R. K., Schell, D. J., and Borole, A. P. (2016). Effect of fed-batch vs. continuous mode of operation on microbial fuel cell performance treating biorefinery wastewater. *Biochem. Eng. J.* 116, 85–94. doi: 10.1016/j.bej.2016.04.029

Peckner, D., and Bernstein, I. M. (1977). *Handbook of Stainless Steels*. New York, NY: McGraw Hill.

Picioreanu, C., Van Loosdrecht, M. C. M., and Heijnen, J. J. (2001). Two-dimensional model of biofilm detachment caused by internal stress from liquid flow. *Biotechnol. Bioeng.* 72, 205–218. doi: 10.1002/1097-0290(20000120)72:2<205::AID-BIT9>3.0.CO;2-L

Pocaznoi, D., Calmet, A., Etcheverry, L., Erable, B., and Bergel, A. (2012a). Stainless steel is a promising electrode material for anodes of microbial fuel cells. *Energy Environ. Sci.* 5:9645. doi: 10.1039/c2ee22429a

Pocaznoi, D., Erable, B., Etcheverry, L., Delia, M.-L., and Bergel, A. (2012b). Forming microbial anodes under delayed polarisation modifies the electron transfer network and decreases the polarisation time required. *Bioresour. Technol.* 114, 334–341. doi: 10.1016/j.biortech.2012.03.042

Pons, L., Délia, M. L., and Bergel, A. (2011). Effect of surface roughness, biofilm coverage and biofilm structure on the electrochemical efficiency of microbial cathodes. *Bioresour. Technol.* 102, 2678–2683. doi: 10.1016/j.biortech.2010.10.138

Reguera, G., McCarthy, K. D., Mehta, T., Nicoll, J. S., Tuominen, M. T., and Lovley, D. R. (2005). Extracellular electron transfer via microbial nanowires. *Nature* 435, 1098–1101. doi: 10.1038/nature03661

Roubaud, E., Lacroix, R., Da Silva, S., Bergel, A., Basséguy, R., and Erable, B. (2018). Catalysis of the hydrogen evolution reaction by hydrogen carbonate to decrease the voltage of microbial electrolysis cell fed with domestic wastewater. *Electrochim. Acta* 275, 32–39. doi: 10.1016/j.electacta.2018.04.135

Santoro, C., Arbizzani, C., Erable, B., and Ieropoulos, I. (2017). Microbial fuel cells: from fundamentals to applications. A review. *J. Power Sources* 356, 225–244. doi: 10.1016/j.jpowsour.2017.03.109

Santoro, C., Guilizzoni, M., Correa Baena, J. P., Pasaogullari, U., Casalegno, A., Li, B., et al. (2014). The effects of carbon electrode surface properties on bacteria attachment and start up time of microbial fuel cells. *Carbon N. Y.* 67, 128–139. doi: 10.1016/j.carbon.2013.09.071

Wang, H., Wang, G., Ling, Y., Qian, F., Song, Y., Lu, X., et al. (2013). High power density microbial fuel cell with flexible 3D graphene-nickel foam as anode. *Nanoscale* 5, 10283–10290. doi: 10.1039/c3nr03487a

Wang, Y., Wang, C. Y., and Chen, K. S. (2007). Elucidating differences between carbon paper and carbon cloth in polymer electrolyte fuel cells. *Electrochim. Acta* 52, 3965–3975. doi: 10.1016/j.electacta.2006.11.012

Wei, J., Liang, P., and Huang, X. (2011). Recent progress in electrodes for microbial fuel cells. *Bioresour. Technol.* 102, 9335–9344. doi: 10.1016/j.biortech.2011.07.019

Xie, X., Criddle, C., and Cui, Y. (2015). Design and fabrication of bioelectrodes for microbial bioelectrochemical systems. *Energy Environ. Sci.* 8, 3418–3441. doi: 10.1039/C5EE01862E

Yu, Y. Y., Zhai, D. D., Si, R. W., Sun, J. Z., Liu, X., and Yong, Y. C. (2017). Three-dimensional electrodes for high-performance bioelectrochemical systems. *Int. J. Mol. Sci.* 18:E90. doi: 10.3390/ijms18010090

Zhang, L., He, W., Yang, J., Sun, J., Li, H., Han, B., et al. (2018). Bread-derived 3D macroporous carbon foams as high performance free-standing anode in microbial fuel cells. *Biosens. Bioelectron.* 122, 217–223. doi: 10.1016/j.bios.2018.09.005

Zhou, M., Chi, M., Luo, J., He, H., and Jin, T. (2011). An overview of electrode materials in microbial fuel cells. *J. Power Sources* 196, 4427–4435. doi: 10.1016/j.jpowsour.2011.01.012

Conflict of Interest: RL is employed as research engineer by company 6T-MIC. SD is CEO of company 6T-MIC.

The remaining authors declare that the research was conducted in the absence of any commercial or financial relationships that could be construed as a potential conflict of interest.

frontiers in Energy Research

ORIGINAL RESEARCH
published: 09 October 2019
doi: 10.3389/fenrg.2019.00105

Effect of Electrode Properties on the Performance of a Photosynthetic Microbial Fuel Cell for Atrazine Detection

Lola Gonzalez Olias[1,2], *Petra J. Cameron*[3] *and Mirella Di Lorenzo*[1]*

[1] Centre for Biosensors, Bioelectronics and Biodevices (C3Bio) and Department of Chemical Engineering, University of Bath, Bath, United Kingdom, [2] Water Innovation Research Centre, University of Bath, Bath, United Kingdom, [3] Department of Chemistry, University of Bath, Bath, United Kingdom

The growing use of herbicides in agriculture poses increasing concerns on the pollution of water systems worldwide. To be able to assess the presence of these compounds in waters and limit their impact on human health and ecosystems, the development of effective *in-situ* monitoring tools is key. Yet, many existing sensing technologies are not suitable for *in-situ* and remote applications, due to challenges in portability, durability, cost, and power requirements. In this study, we explore for the first time the use of an algae-assisted cathode in a photosynthetic microbial fuel cell (p-MFC) as a self-powered dissolved oxygen probe for herbicides detection in water. The cathode is enriched with the alga *Scenedesmus obliquus* and two different electrode materials are tested, graphite felt and indium tin oxide, which differ in porosity, surface roughness, and transparency. Despite the much larger specific surface area of graphite felt compared to indium tin oxide, the current generated under light was only 10 times larger (109 ± 2 μA vs. 10.5 ± 0.6 μA) and eight times larger in the dark (37 ± 5 vs. 4.2 ± 0.6 μA). By generating a current output that correlates with the dissolved oxygen in the catholyte, the resulting p-MFCs could detect the EU legal atrazine concentration limit of 0.1 μg L^{-1}. The use of graphite felt led to shorter response times and better sensitivity, as a result of the greater current baseline. In both cases, the current baseline was recovered after exposure of the sensor to frequent toxic events, thus showing the resilience of the cathodic biofilm and the potential of the p-MFCs for early warnings of herbicides pollution in water.

Keywords: photosynthetic microbial fuel cell, biosensor, water quality, algae, atrazine, ITO, graphite felt

OPEN ACCESS

Edited by:
Uwe Schröder,
Technische Universitat Braunschweig, Germany

Reviewed by:
Sunil A. Patil,
Indian Institute of Science Education and Research Mohali, India
Mohanakrishna Gunda,
Qatar University, Qatar

***Correspondence:**
Mirella Di Lorenzo
m.di.lorenzo@bath.ac.uk

Specialty section:
This article was submitted to Bioenergy and Biofuels, a section of the journal Frontiers in Energy Research

Received: *06 July 2019*
Accepted: *19 September 2019*
Published: *09 October 2019*

Citation:
Gonzalez Olias L, Cameron PJ and Di Lorenzo M (2019) Effect of Electrode Properties on the Performance of a Photosynthetic Microbial Fuel Cell for Atrazine Detection. Front. Energy Res. 7:105. doi: 10.3389/fenrg.2019.00105

INTRODUCTION

Agricultural pollution is one of the major causes of degradation of water systems worldwide. Population growth, and the consequent increase in food demand, has led to an intensified use of pesticides and chemical fertilizers in agriculture that contaminate waters, posing serious risks to aquatic ecosystems and human health (FAO). In the EU, different directives, such as the Ground Water Directive, the Drinking Water Directive and the Water Framework Directive, regulate the maximum concentrations of individual pesticides and their degradation products in waters. To

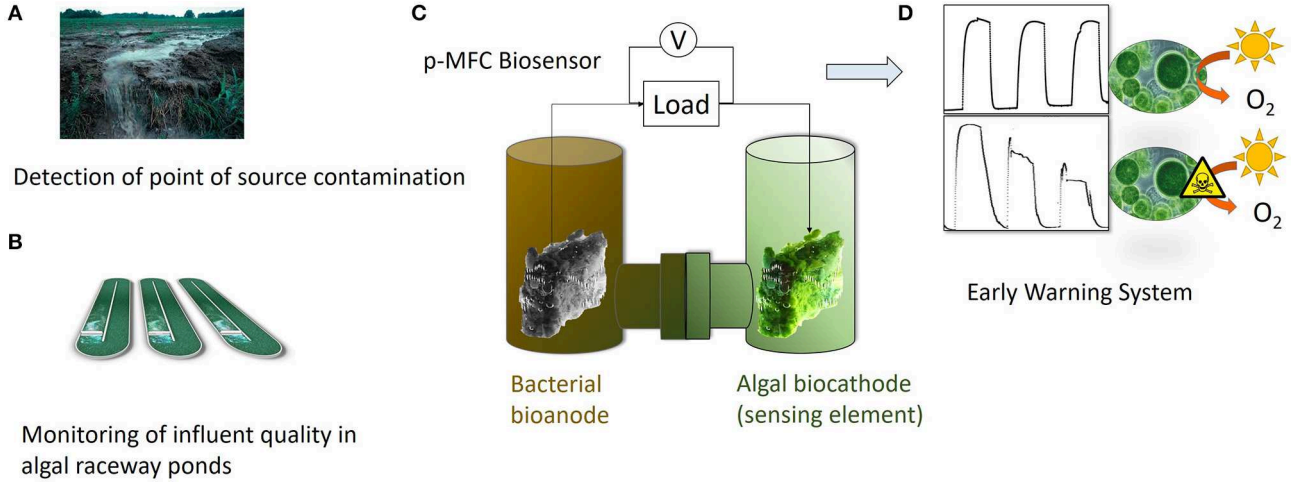

GRAPHICAL ABSTRACT | The photosynthetic MFC (p-MFC) presented in this work could target either point source contamination **(A)** or help monitoring the quality of influents in algal raceway ponds **(B)**. A two-chamber configuration is proposed, in which the algae-assisted cathode acts as a DO probe **(C)**. The presence of a bioactive compound in the catholyte, such as atrazine, will cause a drop in the DO, which is translated into a change in the output signal generated by the p-MFC **(D)**. Therefore, the p-MFC acts as a self-powered early warning tool.

enforce these directives, reliable analytical methods for *in situ* monitoring of chemical pollutants in water are required (Lepom et al., 2009).

Whole cell electrochemical biosensors represent a promising technology for water quality monitoring, leading to affordable technologies that can be used also in the most remote and poorest areas of the world, while moving away from the need of centralized analytical laboratories and the requirement of specialized personnel (Chouler et al., 2019). Particularly attractive is Microbial Fuel Cell (MFC) technology, which has also the potential benefit of self-powered operations (Labro et al., 2017).

Recently, the use of algae as the biorecognition element in photosynthetic MFC (p-MFC) based sensors has been reported (Chouler et al., 2019). Algae bring the benefits of great susceptibility toward a wide range of pollutants, but are particularly interesting for herbicide detection, as these compounds specifically disrupt the activity of photosynthetic cells. In p-MFCs algae can be used at the anode or at the cathode and act, respectively, as the electron donor or as a source of electron acceptor. In the case of an algae-assisted anode, the presence of a pollutant interferes with the electrons generated, thus causing a change in the baseline current. On this basis, the detection of the herbicide atrazine (Chouler et al., 2019), as well as other pollutants such as Zn, Cu, Ta (Labro et al., 2017), and formaldehyde (Chouler et al., 2019) was recently demonstrated. In these systems, however, the stability of the signal output is greatly influenced by changes in pH and BOD, which challenges their practical applications in field. An algae-assisted cathode as sensing element would instead generate a more resilient signal to operational disturbances, with the result of a more reliable sensor (Jiang et al., 2017). In this case, the pollutant would cause a change in the photosynthetic generation of oxygen at the cathode, thus affecting the oxidation reduction reaction, and consequently the signal output (Zhang and Angelidaki, 2012). As such, in this study we test for the first time the use of an algae-assisted cathode in a p-MFC based sensor for herbicide detection in water. We also investigate the role that the electrode properties have on the performance of the p-MFCs. In particular, two electrode materials, Graphite Felt (GF) and Indium Tin Oxide coated on Polyethylene Terephthalate (ITO/PET), are tested, which differ for surface area, roughness, and transparency. ITO/PET is widely used in Clark based electrochemical biosensors (Shitanda et al., 2005; Brayner et al., 2011), where photosynthetic oxygen is transduced into current, yet, to the best of our knowledge, its use at the cathode in photosynthetic microbial fuel cells has not been investigated yet.

The electrode properties can play an important role in the reliability and sensitivity of the resulting sensor. The porosity and surface roughness would influence the distribution, thickness and stability of the cathodic biofilm (Schneider et al., 2016). On a porous electrode the biofilm is more resilient to detachment, however mass transport limitations may be introduced. Conversely, the biofilm that develops on a smooth planar surface is homogeneously exposed to bulk conditions, but it is more prone to detachment due to shear forces (Li et al., 2019).

In this study, the cathode is inoculated with the microalgae *Scenedesmus obliquus*. This is a common eukaryotic alga, typically used for tertiary treatment in wastewater treatment plants, which has been previously tested for herbicide detection (Mofeed and Mosleh, 2013). Atrazine is used as the model herbicide, given its widespread use worldwide and the concerns about its high toxicity to aquatic life (Singh et al., 2018). The electrochemical performance of the resulting systems is

presented, and their ability to detect atrazine in water, due to changes in the dissolved oxygen, assessed.

MATERIALS AND METHODS

Materials

All reagents were purchased from Sigma Aldrich, unless otherwise specified.

Bold Basal Medium (BBM) was prepared by adding in 1 L of distilled water (Kakarla and Min, 2014): 0.25 g L^{-1} $NaNO_3$; 0.075 g L^{-1} $MgSO_4{\cdot}7H_2O$; 0.025 g L^{-1} NaCl; 0.075 g L^{-1} K_2HPO_4; 0.175 g L^{-1} KH_2PO_4; 0.025 g L^{-1} $CaCl_2{\cdot}2H_2O$; 0.011 g L^{-1} H_3BO_3; 1.0 mL of a trace elements solution (8.82 g L^{-1} $ZnSO_4{\cdot}7H_2O$, 1.44 g L^{-1} $MnCl_2{\cdot}4H_2O$, 0.71 g L^{-1} MoO_3, 1.57 g L^{-1} $CuSO_4{\cdot}5H_2O$, 0.49 g L^{-1} $Co(NO_3)2{\cdot}6H_2O$); a 1.0 mL EDTA solution (Na_2 5.0 g, KOH 3.1 g in 1 L of distilled water); and a 1.0 mL Fe solution (4.98 g $FeSO_4{\cdot}7H_2O$, 0.33 mL concentrated H_2SO_4 in 1 L of distilled water). The BBM was autoclaved (121°C, 1 bar, 15 min) prior to use. The final pH of the BBM solution was 6.75 ± 0.28 and the conductivity 0.97 ± 0.15 mS cm^{-1}.

Anaerobic sludge was provided by Wessex Water from a wastewater treatment plant in Avonmouth, UK. Artificial wastewater (AWW) was prepared as previously described (Chouler et al., 2017) (pH = 7.56 ± 0.21, conductivity 1.46 ± 0.35 mS cm^{-1}), with potassium acetate (9.8 g L^{-1}) as the carbon source, and autoclaved prior to use.

All aqueous solutions were prepared with reverse osmosis purified water.

The pH was measured with a pH-meter (Thermo Scientific Orion ROSS Ultra pH/ATC Triode, USA). Conductivity was measured with a conductivity benchtop cell (Orion, Thermo Scientific). The dissolved oxygen, DO, of the electrolytes was measured with a DO portable meter (RDO Orion 7003, Singapore). The COD was determined by using a commercial reagent for high range samples (0–14000 ppm, HANNA Instruments HI 839800 COD reactor).

Algal Culture

Scenedesmus obliquus (Dept. of Biology and Biochemistry, University of Bath, UK) was grown in 100 mL of autoclaved BBM, in triplicate, with no additional carbon source, in an incubator at 25°C and a 12/12 h light/dark cycle, on white light (5 lm m^{-1}). The cultures were inoculated at a seeding concentration of $3.8{\cdot}10^5$ cells mL^{-1} and maintained within the exponential phase (**Figure S1**) by discontinuous dilution with BBM. Algal cell biomass was determined by flow cytometry (Guava Easy Cyte, Millipore) and the optical density (OD) by spectroscopy (Spectronic 200, Thermo Scientific) at 750 nm.

Configuration and Operation of the Photo-Microbial Fuel Cell Sensor (p-MFC)

The photo-microbial fuel cell (p-MFC) consisted of a standard H-cell configuration made in glass. Each chamber had a total volume of 26 mL. The two chambers were separated by a Nafion 115 membrane, with an exposed area of 1.13 cm^2, and the two electrodes were kept at a fixed distance of 4 cm.

Carbon graphite felt (GF, Online Furnace Services Ltd.) was used as both the anode and cathode electrode, with a projected surface area of 13.6 cm^2 (2 × 2 × 0.7 cm). Prior to be used, the GF electrodes were acid treated to enhance both the hydrophilicity and the specific surface area of the graphite fibers, as previously described (Martinez and Di Lorenzo, 2019). For comparison, Indium Tin Oxide, coated with Polyethylene Terephthalate Film (ITO/PET, 60 Ω cm^{-1}, Sigma Aldrich), was also tested as cathode. The ITO/PET electrodes had a projected surface area of 5 cm^2 (5 × 1 cm). The p-MFC with GF cathode is hereafter named as p-MFC_{GF}, while the device with ITO/PET as p-MFC_{ITO}.

The anode and cathode were connected with Ti wire (25 mm, Advent Research Materials, Oxford, UK) to an external resistance (R_{ext}) of 510 Ohms to polarize the cells and to a data logger (PicoLog High Resolution Data Logger, Pico Technology) to monitor the voltage over time. The voltage (V) across the electrode terminals was measured every minute during normal operation and every 15 s during the toxic events.

The anolyte consisted of a 20% v/v AWW, inoculated with anaerobic sludge for a total COD of 7.41 ± 0.76 mg L^{-1} (n = 3). The solution was purged for 10 min with N_2 prior to use. After the enrichment period (∼25 days), the anode was fed only on with AWW and no bacteria, which was replaced on a 4 day basis. During the operation, the anode chamber was sealed with a rubber septum to ensure anaerobic conditions and covered with aluminum foil to prevent the growth of photosynthetic microorganisms.

The catholyte consisted on the algae inoculum in BBM, prepared as detailed above, at a concentration of 4.4×10^5 cells mL^{-1}. The initial conditions of the catholyte were: pH = 7.22; Conductivity = 0.871 mS cm^{-1}; Abs_{750} = 0.176; DO = 8.45 mg L^{-1}. The cathode chamber was open to air and operated under light/dark cycles of 12/12 h with LEDs lights (light intensity 1 mW cm^{-1}, 4.8 W m^{-3} warm white, 6,000 K, Lighting Ever, UK.), placed at ∼5 cm distance from the cathodes (**Figure S2**).

After the initial algal inoculation, tap water was added every 2 days to compensate for the evaporation losses. The catholyte was replaced by fresh algae (in the same seeding conditions) after 20 days of operation. After the toxic event, to allow the recovery of the biocathode, the catholyte was replaced by BBM.

The p-MFC cells were operated in batch mode, thus allowing the pH and DO of the catholyte to rise along with the planktonic growth of algae, to mimic the conditions of stagnant eutrophic waters and raceway ponds. Dissolved oxygen, conductivity and pH were monitored during the start-up period. The temperature during operation was 23.9 ± 2.3°C.

The current (I) was calculated according to Ohm's Law ($I = V/R_{ext}$) and power (P) was calculated as $P = I \times V$. The internal resistance was calculated from the slope of the middle section of the polarization curves, as previously described (Verstraete and Rabaey, 2006). Maximum power output was obtained from the power curve. For comparison with other studies, power density was normalized by the cathode projected surface area.

Polarization tests were conducted by using a resistance box (RS Components, UK), from Open Circuit Voltage (OCV) to short-circuit across a loading range of 10 MΩ to 500 Ω, and a benchtop multi-meter (RS PRO RS-14 Digital Multimeter).

Single electrode potentials were measured against an Ag/AgCl reference electrode (EDAQ, USA), which was placed inside the chamber of the electrode to be tested. Cyclic Voltammetry (CV) measurements were performed in a three-electrode system by using a potentiostat (Autolab Metrohm Potstat 126N AUT85001). In these tests, the anode or the cathode served as the working electrode, a Pt wire (0.5 mm diameter) was used as the counter electrode and Ag/AgCl as the reference electrode. The CVs were carried out at a scan rate of 1 mV s^{-1}, swiping from 0.3 to −0.8 V when the cathode was investigated and from 0.6 to −0.8 V when the anode was tested, with 10 s of stabilization.

Scanning electron microscopy (SEM) was performed as previously described (Chouler et al., 2017) to visualize the biofilm on the electrodes. The resulting images were digitized using a JEOL SEM6480LV scanning electron microscope (JEOL, UK).

Simulating the Toxic Event

Atrazine was used as model substance for the toxic event because of its well-known inhibitory effects on algal photosynthetic activity (Tucci et al., 2019). This was simulated by adding the toxicant to the catholyte for a final concentration ranging from 0.1 μg L^{-1} up to 10 mg L^{-1}, under agitation (45 rpm). The volume of toxicant injected was small enough to avoid significant changes of conductivity or pH (**Figure S3**). All experiments were performed in duplicate, unless otherwise specified, and at room temperature.

The sensors' response to atrazine was assessed in terms of response time, t_r, and recovery time, t_{rec}, calculated as:

$$t_{rec} = t_D - t_r \quad (1)$$

Where: t_r (h) is the response time, when the current output has reached 95% of its steady state (point C) response after exposure to the pollutants; t_D (h) is the time when the initial baseline current is re-established and it is assumed that the p-MFC has recovered from the toxicant event.

The rate of reduction of the signal, *SR*, in $(\mu A\ h^{-1})$ was calculated as Feng et al. (2013):

$$SR = \frac{I_b - I_r}{t_r - t_A} \quad (2)$$

Where I_b is the current baseline under light before the event (μA); I_r is the current at t_r; *and* t_A is the time of injection of the toxicant.

The response was also assessed in terms of inhibition ratio (%) in both the short and long term, which was calculated as:

$$IR_{short\ term} = \frac{I_{nb} - I_b}{I_{nb}} \times 100 \quad (3)$$

$$IR_{long\ term} = \frac{I_{nb(long\ term)} - I_b}{I_{nb}(long\ term)} \times 100 \quad (4)$$

Where I_{nb} (μA) is the current baseline established after the toxic event, either in the short or long term. A graphic description of these parameters is provided in **Figure S4**.

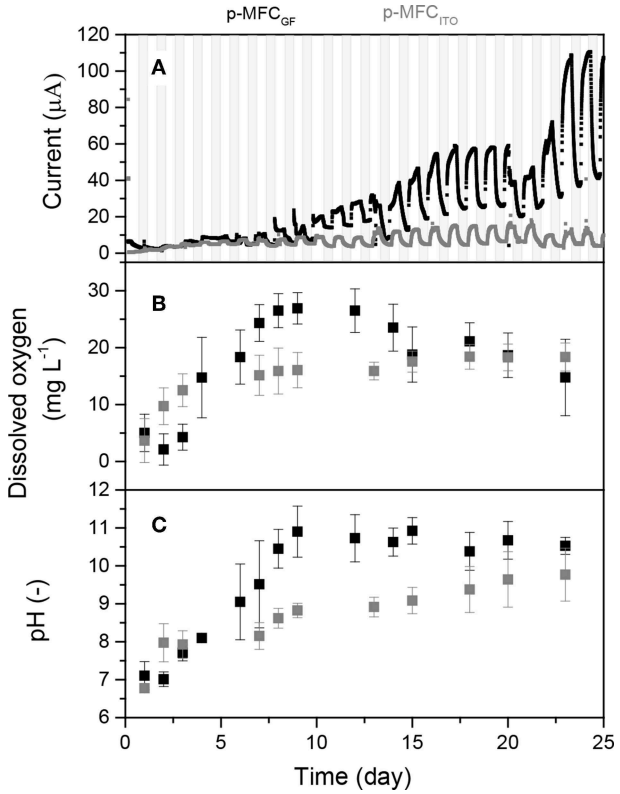

FIGURE 1 | (A) Output current over time generated by the p-MFCs during the first 25 days of operation (start-up period). Data is the average of six replicates. Shadowed areas indicate the operation during the dark cycle. **Figure S5** shows data with error bars and data normalized by projected surface area. **(B)** Dissolved oxygen in the catholyte during the start-up period. **(C)** pH and conductivity evolution of the catholytes during start-up. In all the graphs, data related to p-MFC$_{ITO}$ are reported in gray and data related to p-MFC$_{GF}$ are in black.

RESULTS AND DISCUSSION

Electrochemical Performance of the p-MFCs

This study explores the use of a photosynthetic cathode as the sensing element in a photo microbial fuel cell (p-MFC) sensor for atrazine in water *via* the detection of dissolved oxygen changes in the catholyte. To evaluate the effect that the electrode porosity and transparency have on the sensing performance, two electrode materials were tested at the cathode: graphite felt (GF), used in p-MFC$_{GF}$; and ITO/PET (from here on simply referred to as ITO), used in p-MFC$_{ITO}$.

Firstly, the anode and cathode were enriched, respectively, with bacteria and algae. **Figure 1A** shows the current trend over time for the two p-MFCs. As shown, for the case of p-MFC$_{ITO}$, after only 3 days of operation, a photosynthetic pattern in the output current was observed, which was characterized by current increase under light and current decrease under dark conditions. In the case of p-MFC$_{GF}$, this light/dark current cycle started after 7 days. This result suggests that that on the ITO electrode the cell attachment and biofilm formation is much more rapid than on

GF, which could be a consequence of the higher hydrophilicity and lower porosity of ITO compared to GF (Bombelli et al., 2012; Li et al., 2019).

In both systems the formation of a green biofilm on the cathode surface was observed after the first week of operation. With p-MFC_{GF}, a current growth curve, typical for anodic biofilm enrichment in microbial fuel cells (Lobato et al., 2013), is observed during a period of over 20 days. After that, the catholyte was replaced with a fresh algal solution. This caused a drop in the current output followed by an increase until reaching a higher steady-state current output (**Figure 1A**). As shown in **Figures 1B,C**, pH and DO of the catholyte was quickly recovered after this change. For the case of p-MFC_{ITO}, the catholyte replacement on day 20 did not cause marked changed in the current output.

The exponential current increase is not as obvious for p-MFC_{ITO}, which suggests that in this system the cathode limits the reaction also at early stages of the enrichment, due to the lower surface area.

After 13 days, a steady-state current was reached for p-MFC_{ITO}, while for p-MFC_{GF} 23 days were necessary. The longer time required for p-MFC_{GF} may be the result of the much larger specific surface area available for cell attachment in the case of GF (3D electrode) compared to ITO (2D electrode) (Li et al., 2019). Despite the great difference in the specific surface area, the current obtained with p-MFC_{GF} was, however, only 10 times larger than p-MFC_{ITO} under light (109.4 ± 2.6 vs. 10.47 ± 0.63 μA) and eight times larger under dark (36.8 ± 4.9 vs. 4.24 ± 0.57 μA). Similarly, the charge produced by p-MFC_{GF} during the first 24 days of operation was only 2.7 times larger than p-MFC_{ITO} (156 and 57 mC, respectively). This result indicates that, for this particular system, ITO is much more efficient than GF as cathodic material for energy production. Nevertheless, maximizing the power performance of the p-MFC would not necessarily lead to better sensing performance or better long term stability.

During the dark cycle, the current baseline generated by p-MFC_{GF} increases over time, probably as a consequence of the increasing oxygen produced and accumulated during the day. As shown in **Figure 1B**, the DO in the catholyte increases during the first days, to stabilize at a value of 16.4 ± 5.4 mg L^{-1} once a steady-state light/dark output current trend is reached and an algal biofilm is developed at the cathode (Commault et al., 2014; Colombo et al., 2017). The DO of the catholyte is influenced by multiple factors, i.e., light intensity (Zhao et al., 2013), temperature (Mowjood and Kasubuchi, 1998), algae concentration (Hou et al., 2016), and pH (Colombo et al., 2017). Following the DO trend, the pH of the catholyte also increases with time to reach a value of 10.1 ± 0.5 at steady state (**Figure 1C**). The increase in the catholyte pH during operation, with respect to the control in which no electrochemical reactions occur (**Figure S6**), suggests that hydroxide is being produced (Ge et al., 2015). This high value of pH may be the reason why the levels of DO reported in this study are higher than previously observed in other p-MFCs (**Table S1**). Alkaline conditions at the cathode would prevent the growth of heterotrophic bacteria, which, although tolerating pH values up to 10, grow optimally at neutral pH (He et al., 2008). Consequently, high pH would limit the risk of oxygen consumption in the catholyte not associated to electricity generation (Rago et al., 2017). There is in fact a good correlation between DO and pH of the catholyte ($R^2 = 0.8$), with an increase of 0.144 mg L^{-1} of DO per unit of pH for both materials. On the other hand, the high pH of the catholyte could be the reason for the relative low power output obtained in this study (**Figure S7**) compared to similar studies (**Table S1**), because it affects the cathode potential (Zhang et al., 2017).

In alkaline conditions, the theoretical OCV is 0.45 mV, in agreement with the value obtained in our study and other similar studies on GF (**Table S1**).

The electrochemical performance of the p-MFCs was assessed by polarization tests and cyclic voltammetry. In order to investigate whether the cathode is the limiting electrode under external load, polarization studies were performed not only on the fuel cell but also on the individual electrodes. Since in this study the cathode is the sensing probe, it should be the limiting electrode, and in order to obtain a direct correlation between DO in the catholyte and current, the limiting reaction should be the cathodic oxygen uptake. To minimize any influence of DO variations, the polarization tests were carried out once the current output reached a steady value during the light cycle (5 h after the start of the light cycle). **Figure 2A** reports the results obtained for both p-MFC configurations tested. Assuming that the rate of variation of the individual electrode potentials is an indicator for the limiting electrode (Babauta et al., 2012), it can be concluded that in p-MFC_{ITO} the cathode limits the reaction in the whole potential window. This result is expected if the relative surface areas of the anode and cathode electrodes are considered. Moreover, SEM images of the cathodes in the two p-MFC configurations (**Figure S8**) show a much denser biofilm onto the ITO electrode surface, which may lead to greater oxygen diffusion limitations compared to GF. The open structure of the latter could facilitate oxygen transport through the fibers.

In p-MFC_{GF} both the anode and the cathode contribute to the overpotential (**Figure 2B**), which may be a consequence of the fact that the two electrodes are made of the same material and have the same projected area. Future studies should therefore assess the impact of a relatively larger anode area on the performance of this system.

The analysis by cyclic voltammetry of the GF cathode (**Figure S9**) reveals a mass transport limited process with an onset potential for oxygen reduction at −0.21 V vs. Ag/AgCl and a maximum peak of current at around −0.5 V vs. Ag/AgCl, in agreement with previous studies (Darus et al., 2015; Rimboud et al., 2015). Such a negative potential is due to the high pH of the catholyte (Zhang et al., 2017). The onset potential on the ITO electrode is around 0.3 V vs. Ag/AgCl, suggesting a lower overpotential for the ORR at the ITO, or an alternative electron reduction pathway. The maximum current achieved is lower than for GF under similar DO concentration (around 10 mg L^{-1}) and the diffusion limitations was not as obvious in the CV of the ITO electrode which also suggests that the reduction reaction at the ITO cathode could be due to other mechanisms rather than the ORR.

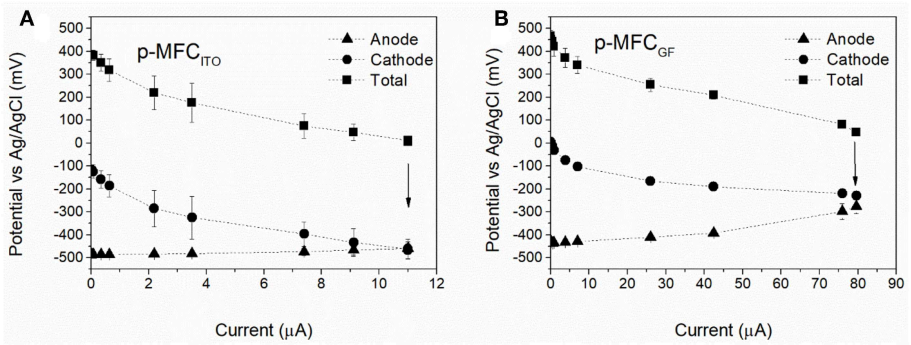

FIGURE 2 | Electrochemical characterization of the p-MFCs by polarization studies performed after 30 days of operation. **(A)** p-MFC$_{ITO}$, **(B)** p-MFC$_{GF}$. The fuel cells were left in OCV for 2 h before the polarization studies. These were carried out after 5 h from the beginning of the light cycle, when the current reaches a steady value. Arrows indicate the potential and current value under the external resistance of 510 Ω.

The external load of 510 Ω used in this work, leads to higher current baselines (point indicated with the arrow in **Figure 2**), which would benefit both sensitivity and range of detection of the p-MFCs used as sensor (Stein et al., 2012), while maximizing the rate of oxygen consumption. Low resistances increase the rate of the ORR, which could alter the oxygen concentration on the surface of the electrode (Zhang and Angelidaki, 2012). Due to the high concentration of DO in our system we assume that the diffusion gradient is sufficient to maintain a homogeneous profile of DO from the electrode to the bulk. The current output obtained at 510 Ω corresponds to the maximum current output for p-MFC$_{ITO}$ and p-MFC$_{GF}$ as determined by the polarization test (∼11 and 80 μA).

p-MFCs Performance During the Light Cycle, Influence of the DO on Current Output

Several studies have correlated the power generated by photosynthetic MFCs with the DO in the catholyte (**Table S1**), however sensitivity values usually are not reported. The energy performance of our system appears to be low. The lack of catalyst at the cathode electrode, oxygen crossover to the anode, due to high values of DO reached in the catholyte, low conductivity of the electrolytes, and high cathodic pH are the most likely reasons for the higher internal resistance and hence, poorer performance of our system. On the other hand, for sensing purposes, stability, and robustness of the electrodes used are more important than power output. Therefore, the use of a catalyst that may leach or deactivate over time is not advised. Likewise, if from one hand the high pH and relative low conductivity typical of algal systems are detrimental for power production, these operational conditions are important to assess the suitability of the biosensor performance in real scenarios.

To assess the performance of the p-MFCs as DO sensor, the DO was monitored hourly over a 12 h light cycle and its value was correlated to the current generated.

As shown in **Figure 3**, during the light cycle, the current output increases until a steady state value and then rapidly decreases once the light is off. In the case of p-MFC$_{GF}$, this trend is followed by the DO. The current output generated during the 12 h of light correlates well with the catholyte DO ($R^2 = 0.96$, **Figure S10**), with a sensitivity of 3.66 ± 0.35 μA L mg_{DO}^{-1} within the DO range 15–25 mg L^{-1} (**Figure 3B**).

In the case of p-MFC$_{ITO}$, there is no apparent correlation between current generated and DO (**Figure 3B**). This result could be either caused by the ITO saturation at lower concentrations of DO, due to the lower electrode area, or by the presence of other reduction mechanisms at the cathode *via* direct or mediated electron transfer from the biofilm (Wang et al., 2010), involving CO_2 reduction (Cao et al., 2009). The latter would occur when oxygen availability is limited at the electrode surface, as may be the case for the ITO electrode. The dense electrode coverage by the cathodic biofilm, observed from the SEM images, may in fact limit the access of bulk reactants to the electrode surface (**Figure S8**).

Response of the p-MFCs to Atrazine

Atrazine, an herbicide commonly used to control grassy leaves and broadleaf weeds in crops, was tested as the model toxicant in this study. Concentrations of atrazine and its metabolites in groundwater and surface water rarely exceed 2 μg L^{-1} and are commonly below 0.1 μg L^{-1}, although concentrations may be higher in agricultural areas where large amounts of pesticides are used (WHO, 2010). In Europe, the Water Framework Directive (WFD) limits the level of atrazine to 0.1 μg L^{-1} in environmental waters.

Since its mode of action toward freshwater algae is well-understood, atrazine is frequently used as a model pollutant for the development of algal biosensors (Shitanda et al., 2005). It binds specifically the Q_b site of the PSII within the photosynthetic electron transport chain of algae. The result is an inhibition of the light-induced oxygen produced by the algal cells (Jeuken, 2016). In the p-MFCs, the presence of atrazine in the catholyte would produce a change in the current output caused by a drop in the photosynthetic oxygen (Shitanda et al., 2005). Several studies report the inhibition of pesticides, including atrazine, on the oxygen production by *Sc. obliquus* (Mofeed and Mosleh, 2013; Chalifour et al., 2016; Zhu et al., 2016).

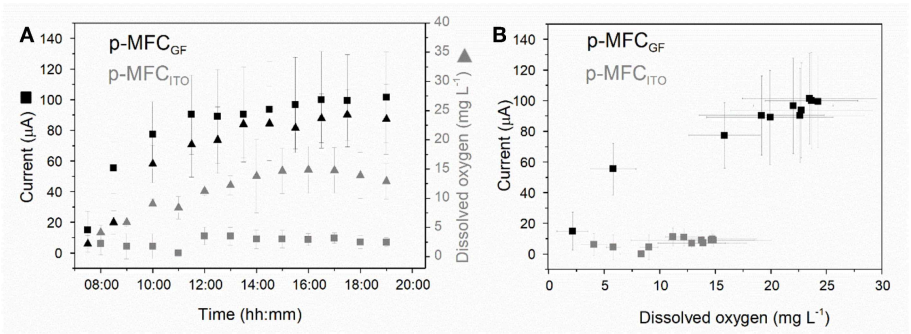

FIGURE 3 | Investigating the relationship between dissolved oxygen in the catholyte and current generated by the p-MFCs under light. **(A)** Dissolved oxygen (triangles) and current (squares) evolution with time over the 12 h of light for p-MFC$_{GF}$ (black) and p-MFC$_{ITO}$ (gray) **(B)** Correlation between the catholyte DO and the current, derived from **(A)**. Data is the average of six replicates.

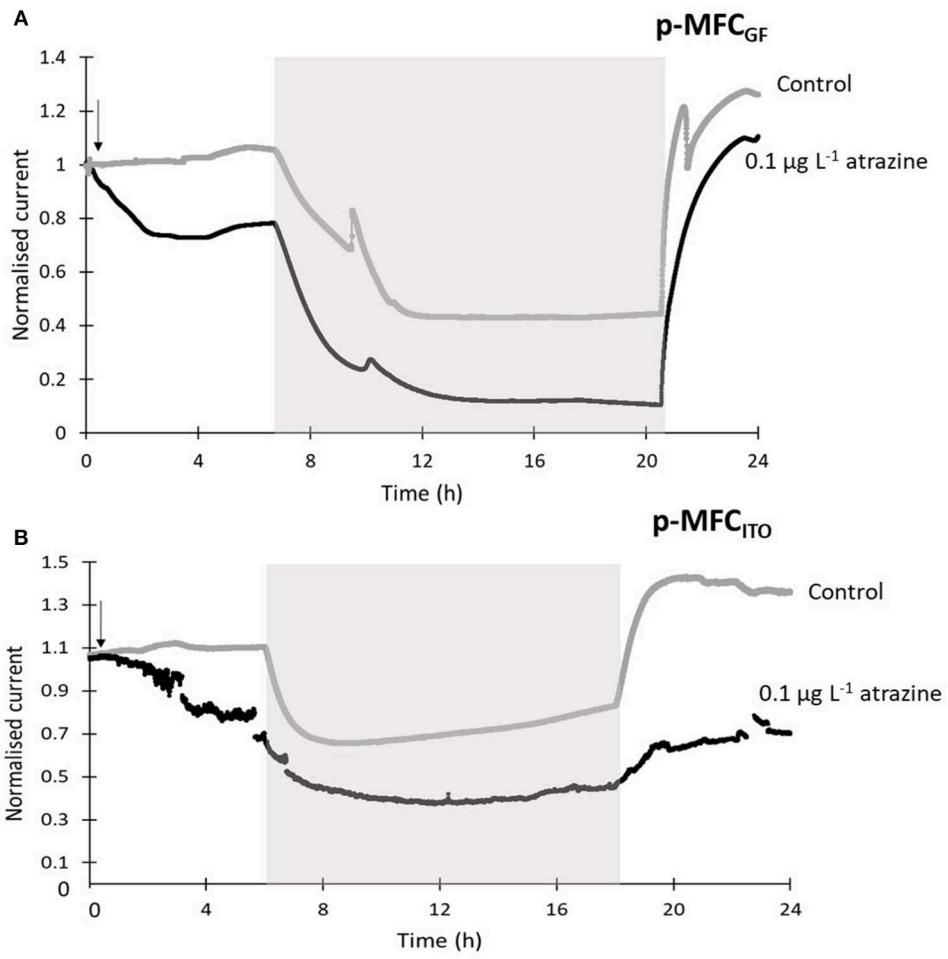

FIGURE 4 | Sensors response to 0.1 μg L^{-1} of atrazine for p-MFC$_{GF}$ **(A)** and p-MFC$_{ITO}$ **(B)** during the first 24 h after intoxication. The current output was normalized by the baseline current before the injection, I_b. Black lines correspond to the fuel cells exposed to atrazine and gray lines correspond to the control p-MFCs. The arrow indicates the point of atrazine injection. Error bars (referring to two replicates) are presented in **Figure S12**. Shadowed areas indicate the operation during the dark cycle.

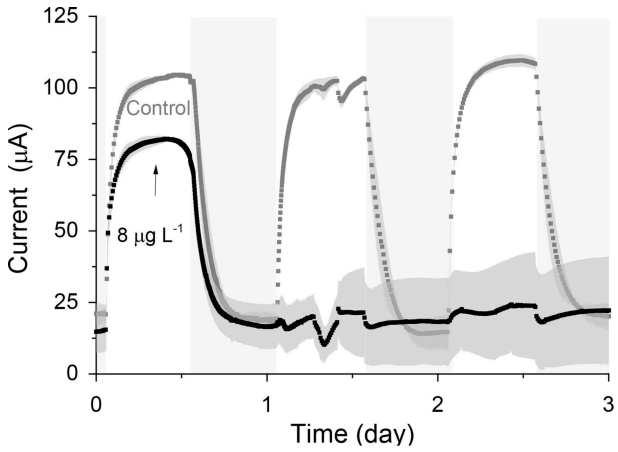

FIGURE 5 | Response of p-MFC$_{GF}$ to 8 μg L^{-1} of atrazine. The arrow indicates the point of atrazine injection. Shadowed areas indicate the operation during the dark cycle. Data is the average of two replicates. Error bars represent the absolute error between the two replicates.

Initially, the p-MFCs were exposed to a concentration of 0.1 μg L^{-1} to assess the suitability of the sensor to detect the threshold legal limit. Since point of source and groundwater concentrations are likely to be higher (Manamsa et al., 2016), concentrations up to 10 mg L^{-1} were also tested. The performance of the p-MFCs as sensor for atrazine detection was assessed in terms of rate of reduction, reproducibility, inhibition ratio, response time, and recovery of the baseline signal over time.

Cyclic voltammetry tests at the anode before and after atrazine injection confirmed that the electrode performance was unaffected by the toxic event, and, therefore, that the response was caused by changes at the cathode only (**Figure S11**).

When the sensors were exposed to a concentration of 0.1 μg L^{-1} of atrazine (**Figure 4**), an IR$_{short-term}$ of 25.5% (p-MFC$_{GF}$, **Figure S12A**) and 23.2% (p-MFC$_{ITO}$, **Figure 4B**), with a response time of 2.6 h (p-MFC$_{GF}$) and 3.6 h (p-MFC$_{ITO}$) was observed. The rate of reduction, SR, of p-MFC$_{GF}$ to atrazine was superior to p-MFC$_{ITO}$: 66.2 vs. 0.6 μA h^{-1} (**Figure S12**). The larger current drop obtained with p-MFC$_{GF}$ is also associated to a larger drop in the DO of the catholyte. In this case, in fact, the DO dropped from 17.5 to 7.7 mg L^{-1} when exposed to 0.1 μg L^{-1} of atrazine, while in p-MFC$_{ITO}$ it only dropped from 15.1 to 13 mg L^{-1}. p-MFC$_{GF}$, however, gave a much poorer reproducibility than p-MFC$_{ITO}$, as demonstrated by the larger error bars obtained (**Figure S12B**), which is probably due to trapped oxygen within the GF porous structure. Interestingly, when p-MFC$_{GF}$ was exposed to 8 μg L^{-1} (**Figure 5**), the photosynthetic pattern was lost on the next cycle showing the potential of the pMFC as shock sensor.

Both p-MFC devices showed a response to atrazine concentrations in the mg L^{-1} range. When the systems were exposed to 0.5 mg L^{-1} an immediate drop in the signal was observed (**Figures 6**, **7**). p-MFC$_{GF}$ showed a higher SR rate (23.54 μA h^{-1}) compared to p-MFC$_{ITO}$ (0.715 μA h^{-1}), with IR$_{short-term}$ of 53% (**Figure 6A**) and 27.3% (**Figure 7A**). Subsequent additions of atrazine in the cathode chamber caused further decreases in the current output, however, the IR$_{short-term}$ did not correlate with the concentration. Moreover, the extent of the current decay depended on the history of the sensor. For example, when p-MFC$_{ITO}$ was firstly exposed to 10 mg L^{-1} (**Figure 7B**) an IR$_{short-term}$ of 52% was observed. Nonetheless, an IR$_{short-term}$ of only 8% to the same concentration was recorded with device previously exposed to the pollutant (**Figure 7A**), thus suggesting that the biofilm may develop resistance to the toxicant (Patil et al., 2010). The acclimation of the biofilm to the toxic event means that a dose-response curve could not be representative of the performance of this type of sensor. The current drop was however correlated with a concomitant drop in the DO of the catholyte thus, the low reproducibility of the sensor is due to an uneven response of the algae to the toxicant. The anodic potential influences the sensitivity of the p-MFC sensor to the DO in the catholyte. The lower the anodic potential, the higher the current generated by the p-MFC and the higher the level of DO that saturates the sensor amperometric response.

The response time of the p-MFCs to atrazine was in the range of hours, instead of minutes as reported for other algae biosensors (Shitanda et al., 2005; Tahirbegi et al., 2016). Mass transfer limitations, especially within the porous structure of the GF cathode, and low electrode surface-area-to-volume-ratio, may be a reason for this (Rimboud et al., 2017).

Recovery of the Sensors After the Toxic Event

After exposure to 0.1 μg L^{-1} of atrazine, the baseline current generated by p-MFC$_{GF}$ recovered during the next dark/light cycle (**Figure 4A**). In the case of p-MFC$_{ITO}$, this recovery did not occur and a 36% decay in the current baseline was observed (**Figure 4B**). This result suggests that the p-MFC can be used as an early warning system to detect the limit concentration imposed by law. When p-MFC$_{GF}$ was exposed to higher concentrations of atrazine, however, the baseline current signal did not recover (**Figure 6B**), while p-MFC$_{ITO}$ (**Figures 7C,D**) recovered the baseline current in the next cycles without changing the electrolyte. The denser biofilm developed onto the ITO electrode (**Figure S8**) may protect it from the atrazine action. On the other hand, the uneven biofilm distribution on the GF electrode would facilitate atrazine access also to the cells closer to the electrode surface. In addition, atrazine could be adsorbed on the GF structure and released also after the completion of the simulated toxic event.

The SEM images (**Figures S8C,D**) suggest that the cathodes exposed to atrazine may be contaminated by fungi (Lopez-Llorca and Hernandez, 1996; Lopez-Llorca et al., 1999). The toxic effect of atrazine toward photosynthetic species would allow pathogens and opportunistic species to thrive and change the consortia within the biofilm. Not only is this detrimental for the health of the bioreceptor, but also for the stability of the baseline over time.

Maintaining sterile conditions at the cathode, would probably minimize baseline fluctuations over time and lead to a more stable sensor. Nevertheless, this approach is

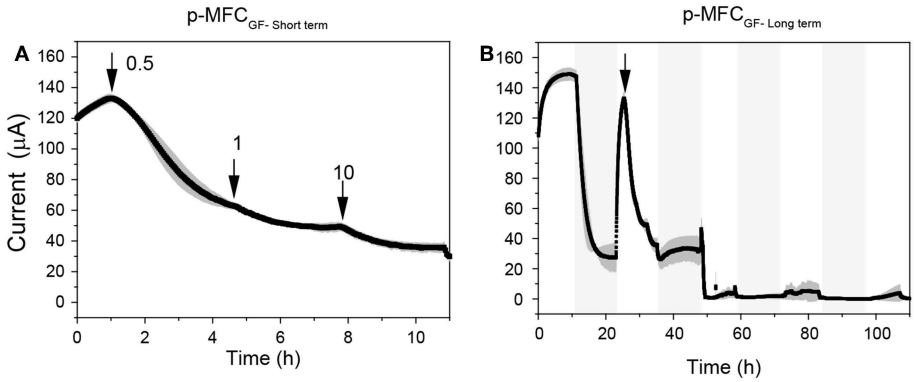

FIGURE 6 | Response of p-MFC$_{GF}$ to atrazine injection in the mg L^{-1} range. **(A)** Short term response. **(B)** Long term response. The arrows indicate the point of atrazine injection. Shadowed areas indicate the operation during the dark cycle.

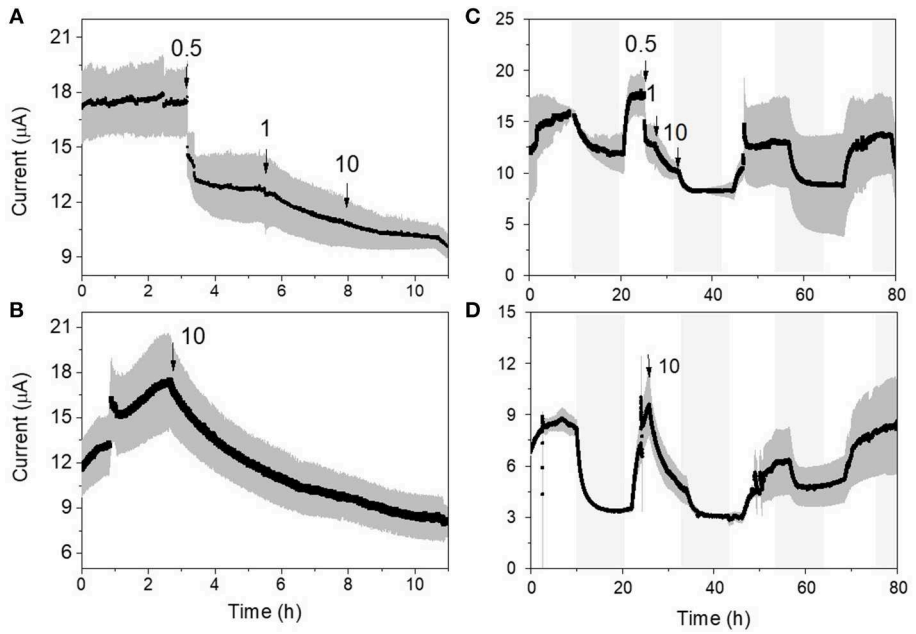

FIGURE 7 | Response of the p-MFC$_{ITO}$ sensor to atrazine. **(A)** and **(C)** response to subsequent injections of atrazine for concentrations ranging between 0.5 and 10 mg L^{-1}. **(B)** and **(D)** response to a single atrazine injection of 10 mg L^{-1}. **(A,B)** show the short-term response (i.e., up to 10 h), while **(C,D)** the response up to 80 h. Shadowed areas indicate the operation during the dark cycle.

incompatible with practical applications, where the cathodic probe would be exposed to the water samples to be analyzed. Future studies should include in-depth analyses of the microbial and algal communities at the cathode to try and relate the sensor performance over time with the cathodic biofilm evolution.

CONCLUSIONS

Algae are the ideal bioreceptors for the development of herbicides biosensors, given their high sensitivity to these compounds. Yet, their practical use is still limited by the development of reliable and portable systems for effective *in situ* operations. In this work, we investigated for the first time the use of photosynthetic microbial fuel cells, with algae-assisted cathodes, for the detection of atrazine in water systems. Two cathode materials were tested, graphite felt and ITO to investigate the effect of the electrode properties on performance, and long-term exposure studies with this technology were reported. When both devices were exposed to the limiting concentration imposed by the Water Framework Directive of 0.1 μg L^{-1}, a detectable change in the photosynthetic pattern was obtained. In the case of p-MFC$_{GF}$, higher concentration of atrazine, however, highly affected the current generation light/dark cycle permanently, while p-MFC$_{ITO}$ recovered the day/night cycle after the toxic events, for all concentrations tested.

The electrode porosity allows the built-up of a 3D cathodic biofilm, but the accumulation of oxygen within the fibers slows down the response time and affects the reproducibility of the sensor. On the other hand, the high cell density biofilm generated by the ITO surface prevents oxygen access to the electrode, which leads to a low sensitivity to DO changes in water.

Based on our results, both p-MFCs could be used for point of source detection of a toxic event or as early warning system to avoid contamination in algal raceway ponds fed with wastewater.

Further studies are required to investigate the effect of environmental factors (i.e., temperature, pH, light intensity, flow rate) and particularly the cathode potential on the sensitivity, detection limit, and range of application of the p-MFC system as DO sensor for environmental monitoring. The sensor performance in the co-presence of several other pesticides along with atrazine should be tested in future studies.

DATA AVAILABILITY STATEMENT

The datasets generated for this study are available on request to the corresponding author.

AUTHOR CONTRIBUTIONS

LG performed the experiments and wrote the manuscript. MD and PC provided guidance and supervision on the experiment design and results interpretations, and wrote the article.

ACKNOWLEDGMENTS

The authors thanks the Water Informatics, Science and Engineering (WISE) Center for Doctoral Training (CDT), funded by the UK Engineering and Physical Sciences Research Council (EP/L016214/1) to support LG's Ph.D. Scholarship; Aidan Barry from the Department of Biology, University of Bath for supplying the algae strain and assisting with the culture growth.

SUPPLEMENTARY MATERIAL

The Supplementary Material for this article can be found online at: https://www.frontiersin.org/articles/10.3389/fenrg.2019.00105/full#supplementary-material

REFERENCES

Babauta, J., Renslow, R., Lewandowski, Z., and Beyenal, H. (2012). Electrochemically active biofilms: Facts and fiction. A review. *Biofouling*. 28, 789–812. doi: 10.1080/08927014.2012.710324

Bombelli, P., Zarrouati, M., Thorne, R. J., Schneider, K., Rowden, S. J., Ali, A., et al. (2012). Surface morphology and surface energy of anode materials influence power outputs in a multi-channel mediatorless bio-photovoltaic (BPV) system. *Phys. Chem. Chem. Phys.* 14, 12221–12229. doi: 10.1039/c2cp42526b

Brayner, R., Couté, A., Livage, J., Perrette, C., and Sicard, C. (2011). Micro-algal biosensors. *Anal. Bioanal. Chem.* 401, 581–579. doi: 10.1007/s00216-011-5107-z

Cao, X., Huang, X., Boon, N., Liang, P., Fan, M., Zhang, L., et al. (2009). A completely anoxic microbial fuel cell using a photo-biocathode for cathodic carbon dioxide reduction. *Energy Environ. Sci.* 2, 1754–5692. doi: 10.1039/b901069f

Chalifour, A., LeBlanc, A., Sleno, L., and Juneau, P. (2016). Sensitivity of *Scenedesmus obliquus* and *Microcystis aeruginosa* to atrazine: effects of acclimation and mixed cultures, and their removal ability. *Ecotoxicology* 25, 1822–1831. doi: 10.1007/s10646-016-1728-5

Chouler, J., Bentley, I., Vaz, F., O'Fee, A., Cameron, P. J., and Di Lorenzo, M. (2017). Exploring the use of cost-effective membrane materials for Microbial Fuel Cell based sensors. *Electrochim. Acta*. 231, 319–326. doi: 10.1016/j.electacta.2017.01.195

Chouler, J., Monti, M. D., Morgan, W. J., Cameron, P. J., and Di Lorenzo, M. (2019). A photosynthetic toxicity biosensor for water. *Electrochim. Acta* 309, 392–401. doi: 10.1016/j.electacta.2019.04.061

Colombo, A., Marzorati, S., Lucchini, G., Cristiani, P., Pant, D., and Schievano, A. (2017). Assisting cultivation of photosynthetic microorganisms by microbial fuel cells to enhance nutrients recovery from wastewater. *Bioresour. Technol.* 237, 240–248. doi: 10.1016/j.biortech.2017.03.038

Commault, S., Lear, G., Novis, P., and Weld, R. J. (2014). Photosynthetic biocathode enhances the power output of a sediment-type microbial fuel cell. *N. Zeal. J. Bot.* 52, 48–59. doi: 10.1080/0028825X.2013.870217

Darus, L., Lu, Y., Ledezma, P., Keller, J., and Freguia, S. (2015). Fully reversible current driven by a dual marine photosynthetic microbial community. *Bioresour. Technol.* 195, 248–253. doi: 10.1016/j.biortech.2015.06.055

Feng, Y., Kayode, O., and Harper, W. F. (2013). Using microbial fuel cell output metrics and nonlinear modeling techniques for smart biosensing. *Sci. Total Environ.* 449, 223–228. doi: 10.1016/j.scitotenv.2013.01.004

Ge, X., Sumboja, A., Wuu, D., An, T., Li, B., Goh, F. W. T., et al. (2015). Oxygen reduction in alkaline media: from mechanisms to recent advances of catalysts. *ACS Catal.* 5, 4643–4667. doi: 10.1021/acscatal.5b00524

He, Z., Huang, Y., Manohar, A. K., and Mansfeld, F. (2008). Effect of electrolyte pH on the rate of the anodic and cathodic reactions in an air-cathode microbial fuel cell. *Bioelectrochemistry*. 74, 78–82. doi: 10.1016/j.bioelechem.2008.07.007

Hou, Q., Pei, H., Hu, W., Jiang, L., and Yu, Z. (2016). Mutual facilitations of food waste treatment, microbial fuel cell bioelectricity generation and *Chlorella vulgaris* lipid production. *Bioresour. Technol.* 203, 50–55. doi: 10.1016/j.biortech.2015.12.049

Jeuken, L. J. C. (ed.). (2016). *Biophotoelectrochemistry: From Bioelectrochemistry to Biophotovoltaics*, Vol. 158. Leeds, UK: Springer Nature. doi: 10.1007/978-3-319-50667-8

Jiang, Y., Liang, P., Liu, P., Wang, D., Miao, B., and Huang, X. (2017). Biosensors and Bioelectronics a novel microbial fuel cell sensor with biocathode sensing element. *Biosens. Bioelectron.* 94, 344–350. doi: 10.1016/j.bios.2017.02.052

Kakarla, R., and Min, B. (2014). Photoautotrophic microalgae *Scenedesmus obliquus* attached on a cathode as oxygen producers for microbial fuel cell (MFC) operation. *Int. Hydrogen Energy J.* 39, 1027–10283. doi: 10.1016/j.ijhydene.2014.04.158

Labro, J., Craig, T., Wood, S. A., and Packer, M. A. (2017). Demonstration of the use of a photosynthetic microbial fuel cell as an environmental biosensor. *Int. J. Nanotechnol.* 14, 213. doi: 10.1504/IJNT.2017.082467

Lepom, P., Brown, B., Hanke, G., Loos, R., Quevauviller, P., and Wollgast, J. (2009). Needs for reliable analytical methods for monitoring chemical pollutants in surface water under the European Water Framework Directive. *J. Chromatogr. A* 1216, 302–315. doi: 10.1016/j.chroma.2008.06.017

Li, J., Hu, J., Yang, C., Pu, W., Hou, H., Xu, J. K., et al. (2019). Enhanced detection of toxicity in wastewater using a 2D smooth anode based microbial fuel cell toxicity sensor. *RSC Adv.* 9, 8700–8706. doi: 10.1039/C8RA10337B

Lobato, J., González Del Campo, A., Fernández, F. J., Cañizares, P., and Rodrigo, M. A. (2013). Lagooning microbial fuel cells: a first approach by coupling electricity-producing microorganisms and algae. *Appl. Energy*. 110, 220–226. doi: 10.1016/j.apenergy.2013.04.010

Lopez-Llorca, L. V., Carbonell, T., and Salinas, J. (1999). Colonization of plant waste substrate by entomopathogenic and mycoparasitic fungi - A SEM study. *Micron* 30, 325–333. doi: 10.1016/S0968-4328(99)00031-1

Lopez-Llorca, L. V., and Hernandez, P. (1996). Infection of the green alga Oocystis lacustris chod with the chytrid fungus Diplochytridium deltanum (Masters) Karling. An SEM study. *Micron* 27, 355–358. doi: 10.1016/S0968-4328(96)00037-6

Manamsa, K., Crane, E., Stuart, M., Talbot, J., Lapworth, D., and Hart, A. (2016). A national-scale assessment of micro-organic contaminants in groundwater of England and Wales. *Sci. Total Environ.* 568, 712–726. doi: 10.1016/j.scitotenv.2016.03.017

Martinez, S. M., and Di Lorenzo, M. (2019). Electricity generation from untreated fresh digestate with a cost-effective array of floating microbial fuel cells. *Chem. Eng. Sci.* 198, 108–116. doi: 10.1016/j.ces.2018.12.039

Mofeed, J., and Mosleh, Y. Y. (2013). Toxic responses and antioxidative enzymes activity of Scenedesmus obliquus exposed to fenhexamid and atrazine, alone and in mixture. *Ecotoxicol. Environ. Saf.* 95, 234–240. doi: 10.1016/j.ecoenv.2013.05.023

Mowjood, M. I. M., and Kasubuchi, T. (1998). Dynamics of dissolved oxygen (DO) in ponded water of a paddy field. *Soil Sci. Plant Nutr.* 44, 405–413. doi: 10.1080/00380768.1998.10414462

Patil, S., Harnisch, F., and Schröder, U. (2010). Toxicity response of electroactive microbial biofilms-a decisive feature for potential biosensor and power source applications. *ChemPhysChem*. 11, 2834–2837. doi: 10.1002/cphc.201000218

Rago, L., Cristiani, P., Villa, F., Zecchin, S., Colombo, A., Cavalca, L., et al. (2017). Influences of dissolved oxygen concentration on biocathodic microbial communities in microbial fuel cells. *Bioelectrochemistry*. 116, 39–51. doi: 10.1016/j.bioelechem.2017.04.001

Rimboud, M., Barakat, M., Bergel, A., and Erable, B. (2017). Different methods used to form oxygen reducing biocathodes lead to different biomass quantities, bacterial communities, and electrochemical kinetics. *Bioelectrochemistry* 116, 24–32. doi: 10.1016/j.bioelechem.2017.03.001

Rimboud, M., Desmond-Le Quemener, E., Erable, B., Bouchez, T., and Bergel, A. (2015). The current provided by oxygen-reducing microbial cathodes is related to the composition of their bacterial community. *Bioelectrochemistry*. 102, 42–49. doi: 10.1016/j.bioelechem.2014.11.006

Schneider, K., Thorne, R. J., and Cameron, P. J. (2016). An investigation of anode and cathode materials in photomicrobial fuel cells an investigation of anode and cathode materials in photomicrobial fuel cells. *Philos. Trans. R. Soc. A Math. Phys. Eng. Sci.* 374, 1–22. doi: 10.1098/rsta.2015.0080

Shitanda, I., Takada, K., Sakai, Y., and Tatsuma, T. (2005). Compact amperometric algal biosensors for the evaluation of water toxicity. *Anal. Chim. Acta*. 530, 191–197. doi: 10.1016/j.aca.2004.09.073

Singh, S., Kumar, V., Chauhan, A., Datta, S., Wani, A. B., Singh, N., et al. (2018). Toxicity, degradation and analysis of the herbicide atrazine. *Environ. Chem. Lett.* 16, 211–237. doi: 10.1007/s10311-017-0665-8

Stein, N. E., Hamelers, H. V. M., and Buisman, C. N. J. (2012). Influence of membrane type, current and potential on the response to chemical toxicants of a microbial fuel cell based biosensor. *Sensors Actuators B Chem.* 163, 1–7. doi: 10.1016/j.snb.2011.10.060

Tahirbegi, I. B., Ehgartner, J., Sulzer, P., Zieger, S., Kasjanow, A., Paradiso, M., et al. (2016). Fast pesticide detection inside microfluidic device with integrated optical pH, oxygen sensors and algal fluorescence. *Biosens. Bioelectron.* 88, 188–195. doi: 10.1016/j.bios.2016.08.014

Tucci, M., Grattieri, M., Schievano, A., Cristiani, P., and Minteer, S. D. (2019). Microbial amperometric biosensor for online herbicide detection: Photocurrent inhibition of *Anabaena variabilis*. *Electrochim. Acta*. 302, 102–108. doi: 10.1016/j.electacta.2019.02.007

Verstraete, W., and Rabaey, K. (2006). Critical Review Microbial Fuel Cells: Methodology and Technology. *Environ Sci Technol.* 40, 5181–5192. doi: 10.1021/es0605016

Wang, X., Feng, Y., Liu, J., Lee, H., Li, C., Li, N., et al. (2010). Sequestration of CO2 discharged from anode by algal cathode in microbial carbon capture cells (MCCs). *Biosens. Bioelectron.* 25, 2639–2643. doi: 10.1016/j.bios.2010.04.036

WHO (2010). *Atrazine and Its Metabolites in Drinking-water; Background Document For Development of WHO Guidelines For Drinking-Water Quality*. WHO/HSE/WSH/10.01/11.

Zhang, H., Lin, C., Sepunaru, L., Batchelor-McAuley, C., and Compton, R. G. (2017). Oxygen reduction in alkaline solution at glassy carbon surfaces and the role of adsorbed intermediates. *J. Electroanal. Chem.* 799, 53–60. doi: 10.1016/j.jelechem.2017.05.037

Zhang, Y., and Angelidaki, I. (2012). A simple and rapid method for monitoring dissolved oxygen in water with a submersible microbial fuel cell (SBMFC). *Biosens. Bioelectron.* 38, 189–194. doi: 10.1016/j.bios.2012.05.032

Zhao, F., Zheng, Y., Wang, Z., Yang, Z., Xiao, Y., and Wu, Y. (2013). Light intensity affects the performance of photo microbial fuel cells with *Desmodesmus* sp. A8 as cathodic microorganism. *Appl. Energy*. 116, 86–90. doi: 10.1016/j.apenergy.2013.11.066

Zhu, X., Sun, Y., Zhang, X., Heng, H., Nan, H., Zhang, L., et al. (2016). Herbicides interfere with antigrazer defenses in *Scenedesmus obliquus*. *Chemosphere* 162, 243–251. doi: 10.1016/j.chemosphere.2016.07.087

Conflict of Interest: The authors declare that the research was conducted in the absence of any commercial or financial relationships that could be construed as a potential conflict of interest.

frontiers in Energy Research

ORIGINAL RESEARCH
published: 24 October 2019
doi: 10.3389/fenrg.2019.00116

Shewanella oneidensis NADH Dehydrogenase Mutants Exhibit an Amino Acid Synthesis Defect

*Kody L. Duhl and Michaela A. TerAvest**

Department of Biochemistry and Molecular Biology, Michigan State University, East Lansing, MI, United States

Shewanella oneidensis MR-1 is a dissimilatory metal reducing bacterium with a highly branched respiratory electron transport chain. The *S. oneidensis* MR-1 genome encodes four NADH dehydrogenases, any of which may be used during respiration. We previously determined that a double-knockout of two NADH dehydrogenases, Nuo and Nqr1, eliminated aerobic growth in minimal medium. However, the double-knockout strain was able to grow aerobically in rich medium. Here, we determined that amino acid supplementation rescued growth of the mutant strain in oxic minimal medium. To determine the mechanism of the growth defect, we monitored growth, metabolism, and total NAD(H) pools in *S. oneidensis* MR-1 and the NADH dehydrogenase knockout strain. We also used a genetically encoded redox sensing system and determined that NADH/NAD^+ was higher in the mutant strain than in the wild-type. We observed that the double-knockout strain was able to metabolize D,L-lactate and N-acetylglucosamine when supplemented with tryptone, but excreted high concentrations of pyruvate and acetate. The requirement for amino acid supplementation, combined with an apparent inability of the mutant strain to oxidize pyruvate or acetate suggests that TCA cycle activity was inhibited in the mutant strain by a high NADH/NAD^+.

Keywords: *Shewanella oneidensis* MR-1, NADH dehydrogenase, redox state, TCA cycle, amino acids

OPEN ACCESS

Edited by:
Jeffrey A. Gralnick, University of Minnesota Twin Cities, United States

Reviewed by:
Annette Ruth Rowe, University of Cincinnati, United States
Kai Thormann, University of Giessen, Germany

****Correspondence:***
Michaela A. TerAvest
teraves2@msu.edu

Specialty section:
This article was submitted to Bioenergy and Biofuels, a section of the journal Frontiers in Energy Research

Received: *21 June 2019*
Accepted: *04 October 2019*
Published: *24 October 2019*

Citation:
Duhl KL and TerAvest MA (2019) Shewanella oneidensis NADH Dehydrogenase Mutants Exhibit an Amino Acid Synthesis Defect. Front. Energy Res. 7:116. doi: 10.3389/fenrg.2019.00116

INTRODUCTION

Shewanella oneidensis MR-1 is a model organism studied for its ability to respire with a variety of terminal electron acceptors, including oxygen, nitrate, TMAO, metal oxides, and electrodes (Beliaev et al., 2005; Gralnick et al., 2006; Meshulam-Simon et al., 2007; Pinchuk et al., 2011; Coursolle and Gralnick, 2012; TerAvest and Angenent, 2014; Duhl et al., 2018). Underlying the respiratory versatility of *S. oneidensis* MR-1 is a highly branched electron transport chain, including four NADH dehydrogenases and 3 aerobic terminal oxidases, along with specialized terminal oxidases for a variety of electron acceptors (Heidelberg et al., 2002; Pinchuk et al., 2010; Deutschbauer et al., 2011). Even within use of a single electron acceptor, *S. oneidensis* MR-1 can remodel its electron transport chain depending on environmental conditions. For example, the cbb_3 cytochrome oxidase and the *bd* quinol oxidase are regulated in response to oxygen concentration, with the *bd* oxidase being upregulated under microaerobic conditions (Zhou et al., 2013). A third aerobic terminal oxidase, the caa_3 cytochrome oxidase, is rarely expressed in *S. oneidensis* MR-1 and has only been observed under high oxygen, low organic carbon conditions (Le Laz et al., 2016). The variety of respiratory complexes and their differential regulation may allow *S. oneidensis* MR-1 to optimize metabolic flux and energy conservation under the wide range of redox conditions it experiences in the environment.

Differential expression of respiratory complexes has wide-ranging effects on physiology because the electron transport chain is essential to maintaining redox balance and generating ion-motive forces by translocating H^+ or Na^+ across the inner cell membrane. The ion-motive forces generated by the electron transport chain power ATP synthesis, transport, and flagellar rotation, making them essential to the growth and maintenance of the cell (Senior, 1988; Paulick et al., 2009, 2015). Differential regulation of electron transport chain complexes will affect cellular energetics because the complexes vary kinetically and in their efficiencies of energy conservation. For example, the NADH dehydrogenases range from pumping 4 H^+ per electron pair (Nuo), to 2 Na^+ per electron pair (Nqr1 and Nqr2, $2Na^+/2e^-$), to 0 ions per electron pair (Ndh) (Pinchuk et al., 2010). By upregulating Nuo, *S. oneidensis* can gain the maximum ion-motive force for each NADH oxidized, whereas by upregulating Ndh, it can maintain a homeostatic redox state ($NADH/NAD^+$) even when the demand for ion-motive forces is low.

Evidence of electron transport chain remodeling at the NADH dehydrogenase step has previously been found in *Bacillus subtilis*. The type II NADH dehydrogenase, Ndh, is directly linked to a regulatory loop driven by $NADH/NAD^+$ within the cell. As NADH levels increase, Ndh is upregulated to ensure large fluctuations in $NADH/NAD^+$ do not occur (Gyan et al., 2006). *Escherichia coli* has also alters the ratio of its type I and type II NADH dehydrogenases depending on growth conditions (Matsushita et al., 1987; Yagi, 1991; Tran et al., 1997). With four NADH dehydrogenases encoded in the genome, it appears likely that remodeling of the electron transport chain for energy conservation and redox maintenance also occurs in *S. oneidensis* MR-1. To better understand the *S. oneidensis* MR-1 electron transport chain, we have begun to characterize the roles of NADH dehydrogenases in physiological processes, such as redox homeostasis and energy conservation.

We previously found that the presence of either Nuo or Nqr1 is required for growth under oxic conditions in minimal medium with D,L-lactate or N-acetylglucosamine (NAG) as the substrate (Duhl et al., 2018). However, we did not determine whether the growth defect was caused by an inability to maintain sufficient ion-motive force across the membrane or lack of capacity to re-oxidize NADH. We hypothesized that the growth defect in a Nuo/Nqr1 double knockout strain was due to an inability to re-oxidize NADH, rather than lack of ion-motive forces, because *S. oneidensis* is capable of aerobic growth without ATP synthesis via the F_0F_1-ATP synthase (Hunt et al., 2010). To test this hypothesis, we monitored growth, substrate utilization, product formation, redox state, and NAD(H) pools in the mutant strain. We analyzed redox state in real-time using a genetically encoded redox sensing system based on a transcriptional regulator, Rex, from *Bacillus subtilis* (Liu et al., 2019). We observed broad metabolic disruption in the double mutant strain. Growth was rescued by amino acid supplementation, suggesting that the growth defect was caused by an inability to synthesize amino acids because of TCA cycle inhibition.

RESULTS

S. oneidensis NADH Dehydrogenase Mutant Requires Amino Acid Supplementation

We previously developed NADH dehydrogenase knockout strains of *S. oneidensis* MR-1 and found a severe growth defect for a strain lacking Nuo and Nqr1 (Δ*nuoN*Δ*nqrF1*). The Δ*nuoN*Δ*nqrF1* strain was able to grow in lysogeny broth (LB) but not in M5 minimal medium under oxic conditions (Duhl et al., 2018). To determine which components of LB enabled growth, we grew the double-knockout strain in M5 minimal medium supplemented with the major components of LB; 0.5 and 1.0% (w/v) tryptone, or 0.25 and 0.5% (w/v) yeast extract. Both tryptone and yeast extract stimulated growth of Δ*nuoN*Δ*nqrF1*, but tryptone had a much greater effect than yeast extract. Addition of 1% tryptone enabled growth rates and final densities similar to the double-knockout in LB medium albeit with a prolonged lag phase (**Figure 1**).

To investigate why tryptone addition rescued growth of Δ*nuoN*Δ*nqrF1*, we grew the strain in M5 supplemented with 0.1% tryptone and 20 mM D,L-lactate or 10 mM NAG. To minimize the influence of tryptone as a carbon and energy source, 0.1% (w/v) tryptone was used instead of 0.5 or 1.0%. WT and Δ*nuoN*Δ*nqrF1* were grown for 48 h in 24-well plates in the semi-minimal medium with or without an additional carbon source to determine if Δ*nuoN*Δ*nqrF1* used either D,L-lactate or NAG in the presence of tryptone. The presence of 20 mM D,L-lactate increased growth of WT and Δ*nuoN*Δ*nqrF1* compared with 0.1% tryptone alone, suggesting that the mutant strain was capable of metabolizing D,L-lactate in the presence of tryptone (**Figure 2A**). HPLC analysis confirmed that after the 48-h incubation period, WT used 100% and Δ*nuoN*Δ*nqrF1* used ∼75% of the D,L-lactate (**Table 1**). The same results were observed with NAG as the substrate. Both WT and Δ*nuoN*Δ*nqrF1* grew to a higher OD_{600} with NAG and used 100 and ∼70% of the NAG, respectively (**Figure 2B** and **Table 1**). The growth rate of Δ*nuoN*Δ*nqrF1* was decreased compared to WT with both D,L-lactate and NAG, indicating a growth defect even in the presence of 0.1% tryptone ($p \leq 0.001$). To determine whether the effect of the tryptone was due to amino acid supplementation, we also compared growth of the wild-type and mutant supplemented with 0.5% casamino acids or a defined mixture of amino acids and 20 mM D,L-lactate or 10 mM NAG. WT grew with the casamino acids and the defined amino acid mixture, but Δ*nuoN*Δ*nqrF1* was unable to grow, suggesting that peptides may be a better amino acid source for *S. oneidensis* than free amino acids, as observed previously (Serres and Riley, 2006).

Analysis of Growth, Metabolism, and NAD(H) in Δ*nuoN*Δ*nqrF1*

To clarify the effects of knocking out both Nqr1 and Nuo from *S. oneidensis* MR-1, growth experiments were repeated in 250-mL Erlenmeyer flasks in 50-mL culture volumes. Prior to these experiments, growth was only monitored in 24-well plates in 1-mL culture volumes. Scaling up to 50 mL culture

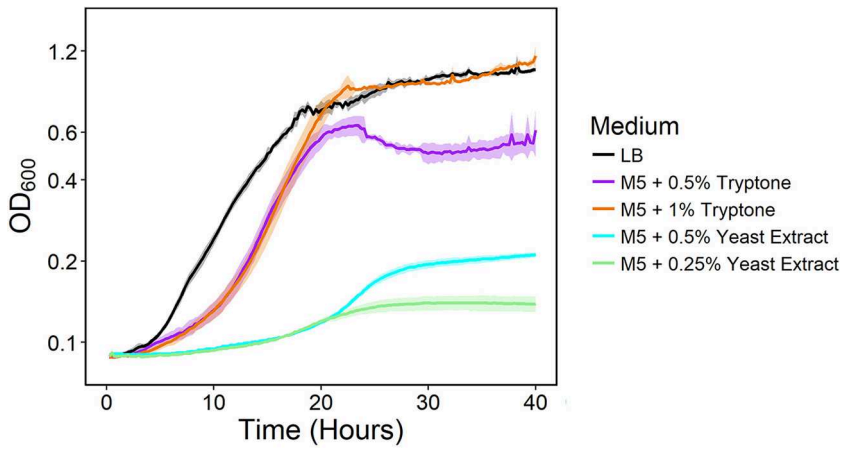

FIGURE 1 | Growth of the Δ*nuoN*Δ*nqrF1* strain in LB (black) or M5 medium supplemented with 0.5% (w/v) (purple) and 1.0% (w/v) (orange) tryptone, and 0.5% (w/v) (cyan) and 0.25% (w/v) (light green) yeast extract in 1-mL volumes in 24-well plates at 30°C with shaking.

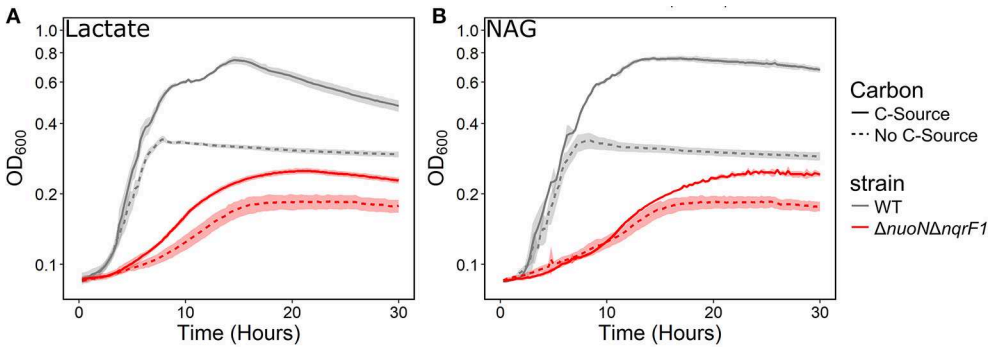

FIGURE 2 | Growth of WT (gray) and Δ*nuoN*Δ*nqrF1* (red) in M5 minimal medium supplemented with 0.1% tryptone, with (solid line) or without (dashed line) **(A)** 20 mM DL-lactate or **(B)** 10 mM NAG as a carbon source. Growth in 1 mL medium in 24-well plates at 30°C with shaking.

volumes allowed us to sample multiple times throughout growth to monitor metabolic products, and internal redox state ($NADH/NAD^+$). When grown in this culture format in M5 supplemented with 0.1% tryptone and 20 mM D,L-lactate as a carbon source, Δ*nuoN*Δ*nqrF1* again exhibited a severe growth defect compared to WT (**Figure 3A**). The doubling times for WT and Δ*nuoN*Δ*nqrF1* were 0.524 ± 0.053 h and 1.300 ± 0.083 h, respectively ($p \leq 0.001$). Further, Δ*nuoN*Δ*nqrF1* did not fully deplete the D,L-lactate, while WT consumed all available D,L-lactate by 12 h (**Figure 3B**). WT cultures briefly accumulated small amounts of pyruvate and acetate between hours 6 and 14 of growth, but both were completely consumed by 14 h. In contrast, Δ*nuoN*Δ*nqrF1* cultures accumulated large amounts of pyruvate and acetate, i.e., >50% of lactate was converted to these products and excreted (**Figures 3C,D**). Pyruvate and acetate accumulation in the Δ*nuoN*Δ*nqrF1* cultures remained high through the end of the experiment and it appeared that the mutant strain could not utilize these excreted products. To determine if knocking out Nqr1 and Nuo affected redox state in Δ*nuoN*Δ*nqrF1*, we conducted a colorimetric NADH and NAD^+ assay. We investigated $NADH/NAD^+$ and total NAD(H) pools. Overall, we did not find consistent differences in $NADH/NAD^+$ between WT and the mutant, which was unexpected, considering that two NADH dehydrogenases were deleted. However, the total NAD(H) pool of Δ*nuoN*Δ*nqrF1* was 1.75-fold higher than that of WT (**Table 2**).

In 50-mL cultures of M5 supplemented with 0.1% (w/v) tryptone and NAG, Δ*nuoN*Δ*nqrF1* also exhibited a growth defect compared to WT (**Figure 4A**). The doubling times for WT and Δ*nuoN*Δ*nqrF1* were 0.838 ± 0.065 and 1.823 ± 0.118 h, respectively ($p \leq 0.001$). The ability to utilize NAG as a carbon source was also hindered compared to WT (**Figure 4B**). Similar to what we observed in D,L-lactate, WT cultures accumulated little pyruvate and acetate, while the mutant cultures accumulated high concentrations of these products (>50% of NAG was converted to these products, **Figures 4C,D**). In this condition, the redox quantification assay data showed inconsistent $NADH/NAD^+$ ratios at the time points sampled. Again, the total NAD(H) pool of Δ*nuoN*Δ*nqrF1* was 2-fold larger than that of WT at $OD_{600} = 0.2$ (**Table 2**).

Altogether, our measurements of $NADH/NAD^+$ ratios were not consistently different between the two strains. This was

TABLE 1 | Growth and endpoint HLPC analysis of carbon source utilization from 24-well plate experiments after 48-h runtime in M5 supplemented with 0.1% tryptone and 20 mM D,L-lactate or 10 mM NAG from **Figure 2**.

Strain	Carbon source	C-source remaining (mM)	[Acetate] (mM)	OD_{MAX}	Growth rate (h^{-1})
WT	D,L-lactate	0	0	0.747 ± 0.03	0.896 ± 0.036
Δ*nuoN*Δ*nqrF1*	D,L-lactate	5.13 ± 0.24	28.7 ± 0.96	0.252 ± 0.01	0.448 ± 0.021
WT	NAG	0	0	0.765 ± 0.02	0.618 ± 0.033
Δ*nuoN*Δ*nqrF1*	NAG	2.96 ± 0.23	25.1 ± 1.05	0.259 ± 0.01	0.342 ± 0.014

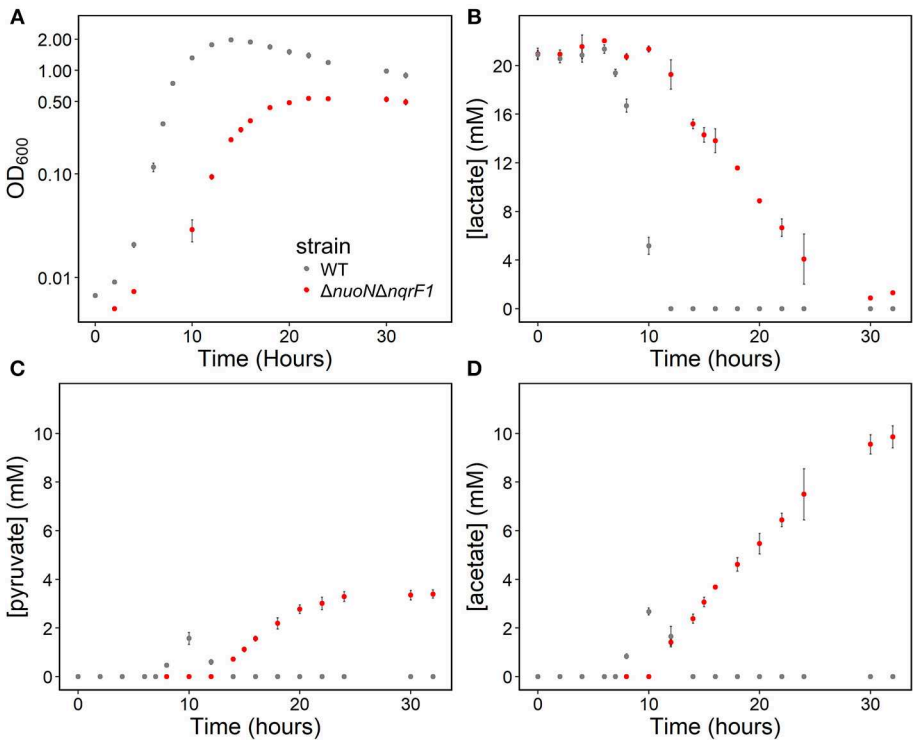

FIGURE 3 | (A) Growth of WT (gray) and Δ*nuoN*Δ*nqrF1* (red) in 50-mL culture volumes of M5 minimal medium supplemented with 0.1% tryptone and 20 mM D,L-lactate. **(B)** D,L-lactate utilization by WT and Δ*nuoN*Δ*nqrF1*. **(C)** Pyruvate and **(D)** acetate concentrations in culture supernatants.

unexpected, because the deletion of NADH dehydrogenases, combined with the accumulation of pyruvate and acetate suggest an accumulation of NADH in the mutant strain. We hypothesized that the sampling procedure for the redox assay may have biased the results because it included a 10-min centrifugation step during which the redox state of the cells could change. To determine whether oxygen levels may have influenced redox state during the centrifugation step, we measured oxygen consumption in centrifuge tubes. We transferred 25 mL of shaking cultures to a 50 mL conical tube and measured dissolved oxygen concentrations over time. We found that WT and Δ*nuoN*Δ*nqrF1* consumed oxygen at rates of 0.068 ± 0.004 and 0.058 ± 0.008 mg/L s^{-1} (normalized to OD_{600}), respectively. At these rates, both strains depleted all dissolved oxygen in the culture samples in 5 min or less (**Figure S1**).

We also measured the oxygen consumption rates of both strains in a custom device and found that it was 2.273 ± 0.152 μM/s for WT and 0.936 ± 0.134 μM/s for Δ*nuoN*Δ*nqrF1* at OD_{600} = 0.2. During the NADH/NAD^+ extraction process, assuming the initial oxygen concentration in the medium is saturated at 8 mg/L (250 μM) and that no additional oxygen dissolves into the liquid during the centrifugation step, all oxygen in the samples would be consumed within the first 2–4 min of the centrifugation. These calculations are complicated by the possibilities that oxygen in the headspace (10 mL) could dissolve into the sample and that as the cells pellet in the centrifuge, they could create a local environment with even less dissolved oxygen. However, these calculations do suggest that oxygen limitation occurs for both strains during the centrifugation step, thereby causing equalization of the NADH/NAD^+ ratios of the two strains. This helps to explain

why we did not observe consistent differences between redox state and only observed differences in the total NAD(H) pool sizes.

Analyzing NADH Dehydrogenase Knockouts Using a Genetically-Encoded Sensor

Because sampling cells for the enzymatic NADH/NAD$^+$ assay likely biased our results, we monitored redox state in real-time with a transcriptionally regulated redox sensor (Liu et al., 2019).

TABLE 2 | Comparison of NAD(H) pools and NADH/NAD$^+$ ratios of WT and Δ*nuoN*Δ*nqrF1* when grown in 50 mL cultures of M5 supplemented with 0.1% tryptone and either 20 mM D,L-lactate or 10 mM NAG.

Carbon source	OD_{600}	Strain	NAD(H) pool size (μmol/g protein)	NADH/NAD$^+$
D,L-lactate	0.1	WT	27.9 ± 3.8	0.28 ± 0.11
		Δ*nuoN*Δ*nqrF1*	48.9 ± 5.5	0.17 ± 0.02
	0.3	WT	51.4 ± 9.5	0.16 ± 0.03
		Δ*nuoN*Δ*nqrF1*	49.5 ± 5.5	0.20 ± 0.04
NAG	0.1	WT	4.84 ± 0.4	0.23 ± 0.08
		Δ*nuoN*Δ*nqrF1*	7.65 ± 2.7	0.37 ± 0.02
	0.2	WT	12.3 ± 0.8	0.20 ± 0.01
		Δ*nuoN*Δ*nqrF1*	26.9 ± 4.5	0.19 ± 0.03

The sensor is based on the transcriptional repressor Rex from *B. subtilis* (Liu et al., 2019). This redox sensor results in increased green fluorescent protein (GFP) production when NADH/NAD$^+$ increases. We introduced the sensor into *S. oneidensis* MR-1 and the NADH dehydrogenase knockout strain, Δ*nuoN*Δ*nqrF1*. To determine whether the redox sensor was functional in *S. oneidensis* MR-1, we monitored reporter fluorescence during an aerobic to anaerobic transition. Two sets of triplicate 50-mL WT (with redox sensor) cultures were grown aerobically for 6 h. After incubating under oxic conditions, one of the triplicate sets was incubated on the benchtop without shaking for 2 h, then transferred to an anoxic environment and given 50 mM fumarate as a terminal electron acceptor. We expected the reporter output to increase in cultures that were moved to an anaerobic environment because limitation of available terminal electron acceptor will increase intracellular NADH/NAD$^+$. Increased NADH accumulation has previously been observed in *E. coli* cultures in anaerobic conditions vs. aerobic conditions (de Graef et al., 1999). As predicted, fluorescence output from *S. oneidensis* with the Rex-based sensor increased in cultures that were transitioned from an aerobic to an anaerobic environment compared to the cultures that remained aerobic (**Figure 5**). These results suggest that the sensor functions as expected in *S. oneidensis* MR-1 and responds to increased NADH/NAD$^+$.

We conducted growth experiments and monitored OD_{600} and reporter fluorescence in *S. oneidensis* MR-1 and Δ*nuoN*Δ*nqrF1* in 24-well plates. Fluorescence per OD_{600} was higher in

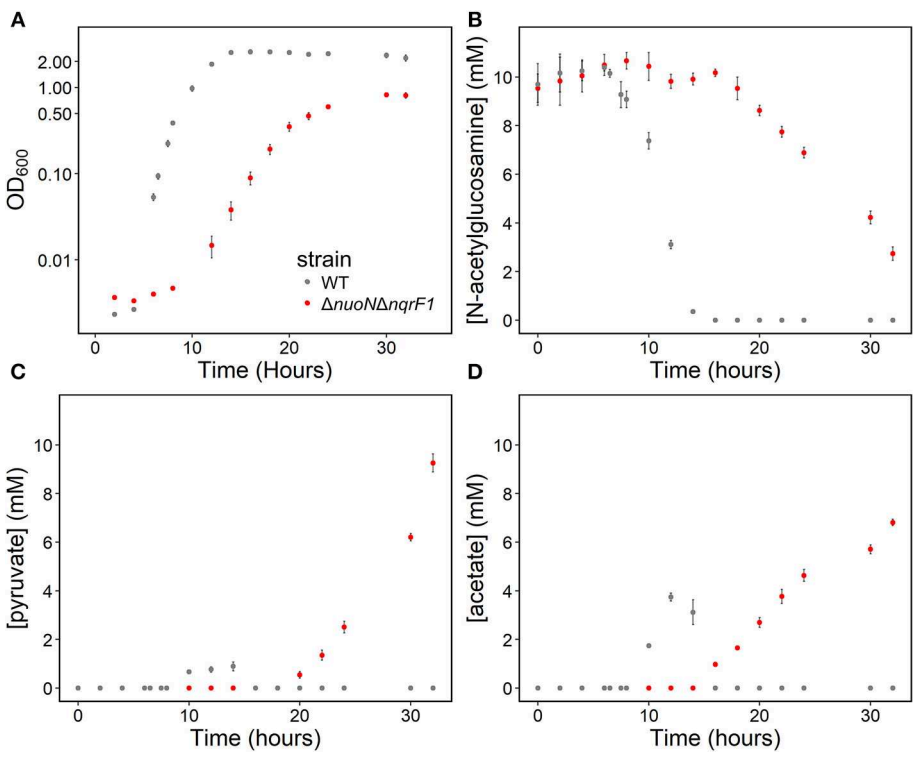

FIGURE 4 | (A) Growth of WT (gray) and Δ*nuoN*Δ*nqrF1* (red) in 50-mL culture volumes of M5 minimal medium supplemented with 0.1% tryptone and 10 mM N-acetylglucosamine (NAG). **(B)** NAG utilization by WT and Δ*nuoN*Δ*nqrF1*. **(C)** Pyruvate and **(D)** acetate concentrations in culture supernatants.

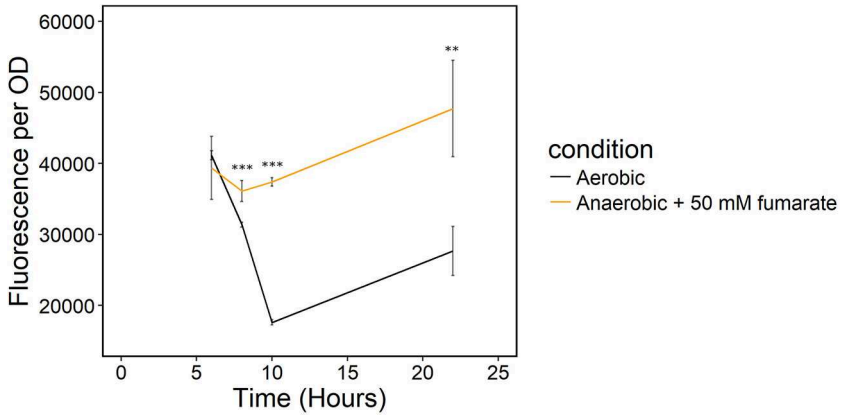

FIGURE 5 | Transition of *S. oneidensis* MR-1 with the Rex redox sensor growing in triplicate 50-mL cultures of LB from an oxic to an anoxic environment. The aerobic set (black) remained oxic and shaking and the anaerobic set (orange) of triplicates was given 50 mM fumarate as a terminal electron acceptor when moved to an anoxic environment. $^{**}p \leq 0.01$ and $^{***}p \leq 0.001$ denote significance of difference from the aerobic culture.

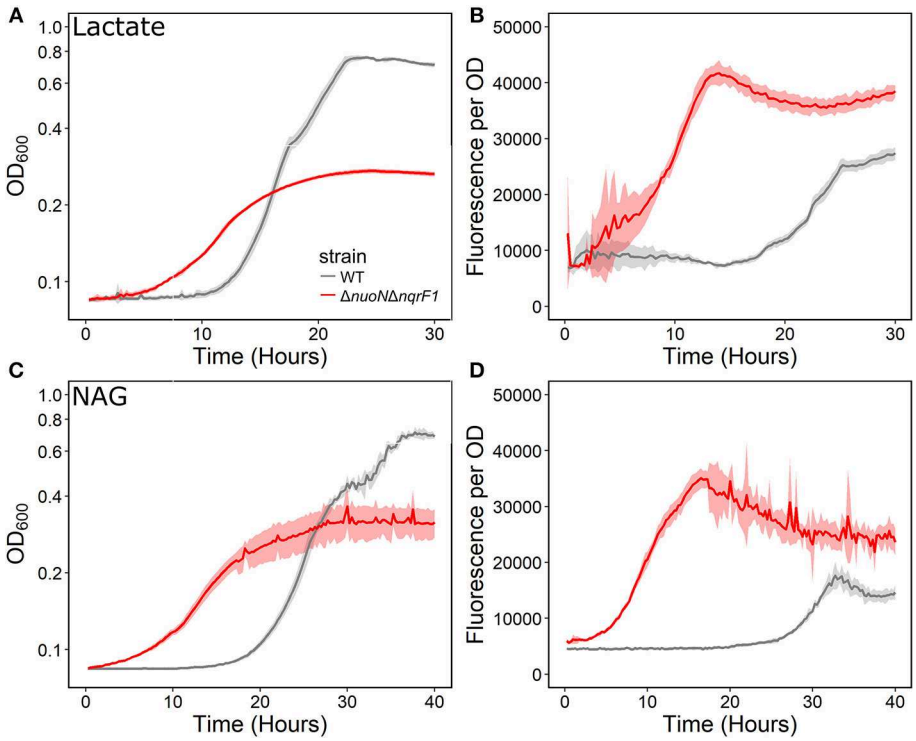

FIGURE 6 | (A) Analysis of growth of the WT and Δ*nuoN*Δ*nqrF1* strains that contain the Rex sensor in 1-mL culture volumes of M5 supplemented with 0.1% tryptone and 20 mM D,L-lactate while at 30°C with shaking. **(B)** Fluorescence output normalized to OD_{600} with D,L-lactate as the substrate. **(C)** Analysis of growth of the WT and Δ*nuoN*Δ*nqrF1* strains that contain the Rex sensor in 1-mL culture volumes of M5 supplemented with 0.1% tryptone and 10 mM NAG. **(D)** Fluorescence output normalized to OD_{600} with NAG as the substrate.

Δ*nuoN*Δ*nqrF1* than WT during log-phase and early stationary phase for both carbon sources, suggesting that the mutant strain exhibits increased NADH/NAD^+ during growth (**Figure 6**). However, it is important to note that the redox sensor altered growth of the strains. Therefore, we conducted a side-by-side comparison between strains with and without the sensor. We observed that the presence of the Rex-based redox sensor delayed growth of WT by about 14 h with D,L-lactate and 18 h with NAG (**Figure 7**). Lag times varied somewhat between experiments (**Figures 6**, **7**), possibly due to small differences in the growth phase of the overnight cultures used for inoculum. However, we consistently observed an extended lag phase in WT containing

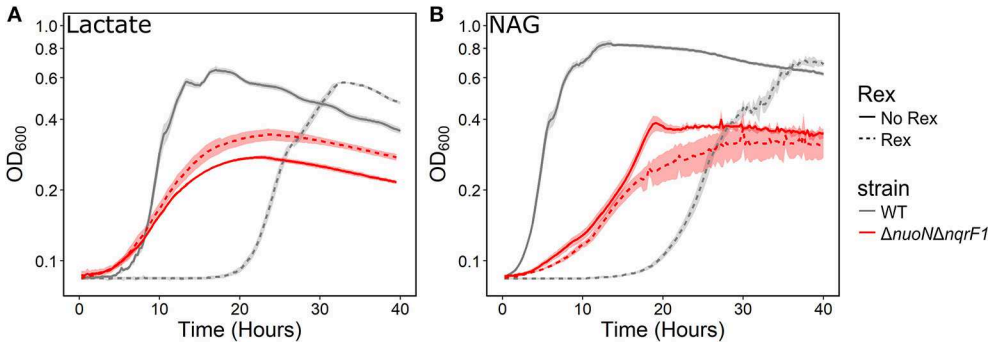

FIGURE 7 | Comparison of growth of WT (gray) and Δ*nuoN*Δ*nqrF1* (red) strains with (solid line) and without (dashed line) the Rex redox sensor in M5 supplemented with 0.1% tryptone and **(A)** 20 mM D,L-lactate or **(B)** 10 mM NAG. Growth conditions were done in 1-mL culture volumes in 24-well plates at 30°C with shaking.

TABLE 3 | Comparison of growth rates of WT and Δ*nuoN*Δ*nqrF1* with and without the Rex sensor growing in M5 supplemented with 0.1% tryptone and either 20 mM D,L-lactate or 10 mM NAG from **Figure 7**.

Strain	Growth rate in D,L-lactate (h^{-1})	Growth rate in NAG (h^{-1})
WT Rex	0.597 ± 0.024	0.305 ± 0.018
Δ*nuoN*Δ*nqrF1* Rex	0.380 ± 0.012	0.275 ± 0.041
WT	1.00 ± 0.029	0.899 ± 0.024
Δ*nuoN*Δ*nqrF1*	0.416 ± 0.015	0.513 ± 0.020

TABLE 4 | Endpoint HLPC analysis of carbon source utilization from 24-well plate experiments with WT and Δ*nuoN*Δ*nqrF1* containing the Rex redox sensor after 48-h runtime in M5 supplemented with 0.1% tryptone and 20 mM D,L-lactate or 10 mM NAG.

Strain	Carbon source	C-source remaining (mM)	[Pyruvate] (mM)	[Acetate] (mM)
WT	D,L-lactate	0	0	0
Δ*nuoN*Δ*nqrF1*	D,L-lactate	2.15 ± 0.54	0.16 ± 0.03	4.74 ± 1.2
WT	NAG	0	0	0
Δ*nuoN*Δ*nqrF1*	NAG	0.24 ± 0.22	0.63 ± 0.09	6.99 ± 1.2

the Rex sensor. The sensor also affected the growth rates of both strains with either D,L-lactate or NAG as the substrate, although the growth rate of the mutant was still lower than WT in all cases (**Table 3**). We conducted HPLC analysis of metabolites generated by the strains containing the Rex sensor. Similar to strains without the sensor, WT was able to deplete all initial carbon source, while the mutant was not (**Table 4**). Also in line with results without the sensor, the mutant strain produced significant amounts of acetate and pyruvate, while WT did not.

DISCUSSION

As observed in our previous work, Δ*nuoN*Δ*nqrF1* was unable to grow under oxic conditions in M5 minimal medium with either D,L-lactate or NAG as the substrate (Duhl et al., 2018). However, we have now observed that addition of 0.1% (w/v) tryptone to the medium allowed Δ*nuoN*Δ*nqrF1* to grow. The major component of tryptone is free amino acids and peptides, suggesting that the mutant strain requires amino acid supplementation and cannot make sufficient amino acids *de novo* to support growth. Together with accumulation of acetate and pyruvate the requirement for tryptone suggests reduced TCA cycle activity because some TCA reactions are required for *de novo* amino acid synthesis (Kanehisa and Goto, 2000). However, there are caveats to using tryptone because it is an undefined tryptic digest of casein and could contain other nutrients. We observed that other sources of amino acids, including casamino acids (acid-hydrolyzed casein) or defined amino acids did not rescue growth of the mutant. However, we propose that the rescue was caused by peptides in the tryptone, not by other nutrients. While there are minor differences in carbohydrate and mineral content between tryptone and casamino acids, these differences are small in comparison to the total mineral and carbohydrate content of the overall medium recipe (BD Biosciences, 2006). Further, previous work indicated that *S. oneidensis* MR-1 is incapable of using individual amino acids as carbon sources but is capable a wide variety of defined dipeptides (Serres and Riley, 2006). This suggests that *S. oneidensis* MR-1 is much more efficient in peptide uptake than free amino acid uptake, which would explain why tryptone rescues growth of the mutant, while casamino acids do not.

Along with the growth defect observed in the NADH dehydrogenase knockout strain, another finding of this study was that total NAD(H) pool sizes differed significantly between WT and Δ*nuoN*Δ*nqrF1*. With either D,L-lactate or NAG as carbon sources, we observed roughly 2-fold increases in the total NAD(H) pools. We hypothesize that the increased NAD(H) pool size is caused by NAD^+ synthesis to counteract the increase in [NADH] within the cell caused by the limitation of NADH dehydrogenase activity. In *S. oneidensis* MR-1, NAD^+ synthesis is regulated by the repressor NrtR. When [NAD^+] decreases, NrtR is released from promotors to allow expression of NAD^+ synthesis related genes (Rodionov et al., 2008). Because we observed increased NAD(H) pool sizes in the Δ*nuoN*Δ*nqrF1* mutant strain, we propose that excess [NADH]

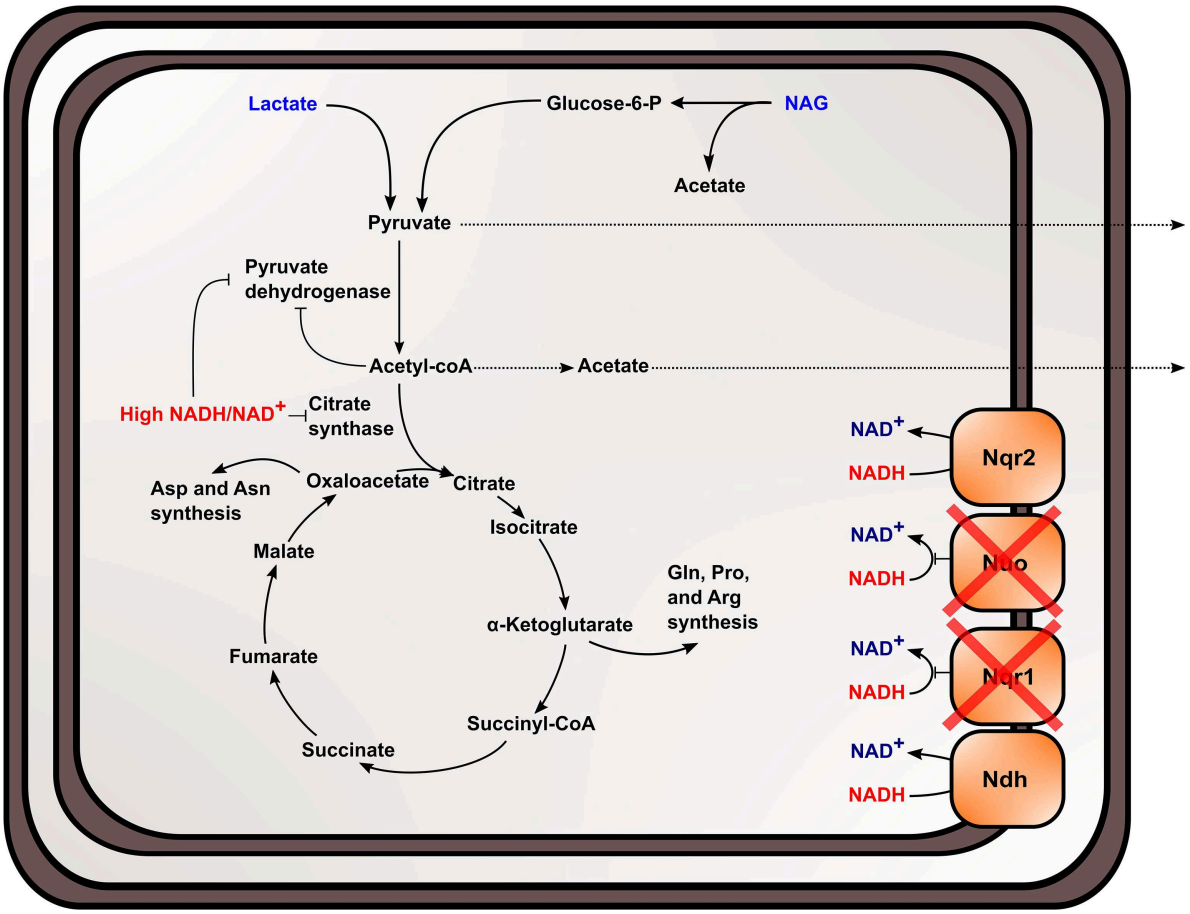

FIGURE 8 | Proposed effect of knocking out NADH dehydrogenases in *S. oneidensis* MR-1 and the subsequent effects on NADH oxidation, redox state, and TCA cycle inhibition within the cell.

and limited [NAD^+] led to overexpression of genes involved in NAD^+ synthesis.

The TCA cycle and upstream reactions are also affected by changes in internal redox state and NAD(H) pool size. NADH is an inhibitor of citrate synthase, which converts acetyl-CoA and oxaloacetate to citrate to bring carbon into the TCA cycle (Weitzman and Jones, 1968; Stokell et al., 2003). This suggests that increased NADH/NAD^+ may inhibit TCA cycle function by affecting citrate synthase activity. Furthermore, reactions upstream of the TCA cycle maybe affected, because pyruvate dehydrogenase (Pdh) activity is also regulated by NADH/NAD^+ and acetyl-CoA concentrations in *S. oneidensis* MR-1 (Pinchuk et al., 2011; Novichkov et al., 2013). Reduced citrate synthase activity would increase acetyl-CoA concentrations, which may inhibit Pdh function, together with increased NADH/NAD^+. It also has been previously shown that Pdh activity can be affected by both NADH/NAD^+ and NAD(H) pool size (Shen and Atkinson, 1970), meaning activity is slowed when NADH/NAD^+ ratios within the cell increase. Metabolic analysis of the mutant strain supports the hypothesis that pyruvate oxidation and TCA cycle activity were inhibited in Δ*nuoN*Δ*nqrF1* and further explains previous data observed in single-knockouts of Nqr1 and Nuo (Duhl et al., 2018). We observed excretion of high levels of pyruvate and acetate by Δ*nuoN*Δ*nqrF1*, which would be expected if flux through the TCA cycle is blocked (**Figure 8**). It is also important to note that all four of the NADH dehydrogenases have not been knocked out of *S. oneidensis* MR-1 in this study. This study sought to understand the roles of the two aerobically expressed NADH dehydrogenases (Pinchuk et al., 2010; Duhl et al., 2018), even though the other NADH dehydrogenases may play a role in redox state regulation in the Δ*nuoN*Δ*nqrF1* mutant strain.

To better understand the effects of NADH dehydrogenase knockouts on the physiological redox state in *S. oneidensis* MR-1 throughout growth, we used the Rex-based redox sensing system developed by Liu et al. (2019). One of the major limitations to standard NADH and NAD^+ quantification assays is the need to remove the bacteria from their growth environment to conduct extractions. We found that the cell harvest and extraction procedure may cause shifts in the cells' redox state. Prior to quenching with acid or base solution in the protocol, shaking of the cultures is ceased and samples are transferred to 15 mL conical tubes (Kern et al., 2014), likely leading to oxygen limitation. We have shown that the cells likely deplete all oxygen

within the medium during the centrifugation step, creating an oxygen limited environment that can influence and equalize redox state in both *S. oneidensis* strains. Conversely, the Rex-based redox sensor directly interacts with intracellular NADH and NAD^+ and allows real-time, qualitative measurements of NADH/NAD^+ via fluorescent reporter output (Liu et al., 2019). This allowed us to assess NADH/NAD^+ without processing the cells in a way that would influence redox state. Our data show that the sensor works as expected in *S. oneidensis* and that Δ*nuoN*Δ*nqrF1* exhibits increased fluorescence output compared to WT.

While the sensor did influence growth of the strains, we were still able to gain qualitative measurements of the internal redox state. It is not clear why the addition of the Rex sensor influenced growth in *S. oneidensis* MR-1. In *E. coli*, the Rex sensor did not appear to influence growth (Liu et al., 2019). It is possible that the metabolic burden generated from carrying the redox sensing system caused the changes, and that use of different plasmid backbones or promoters would reduce the effects of the sensor. However, we believe that the output of the sensor is still a valuable source of information for this study for multiple reasons; the sensor generated the expected output for an aerobic to anaerobic transition and the overall phenotypes and differences between WT and the mutant remained similar with the sensor. I.e., the mutant strain still grew to a lower final OD_{600} and at a slower rate than the WT when the sensor was present (**Figure 6** and **Table 3**). Further, differences in substrate consumption and acetate and pyruvate accumulation remained similar when the sensor was present, with the mutant strain failing to utilize all available carbon source and accumulating acetate and pyruvate. WT with the sensor was able to consume all available substrate and did not accumulate acetate or pyruvate. Although the sensor appeared to affect WT more than the mutant, the general effect on both strains appears similar, and the essential phenotypes remain the same; therefore, we believe that the sensor output reflects real differences in intracellular NADH/NAD^+ between the strains.

Altogether, our data indicate that deletion of NADH dehydrogenases affected NAD(H) pool sizes, NADH/NAD^+, and upstream metabolic activities, specifically by inhibiting the TCA cycle and blocking amino acid synthesis. Because we have shown that deleting NADH dehydrogenases from *S. oneidensis* MR-1 led to increased NADH/NAD^+ levels, larger NAD(H) pool sizes, and metabolic shifts within the cell, NADH dehydrogenase knockouts may provide an avenue for metabolic engineering. When engineering pathways in bacteria to generate products that are redox cofactor-dependent, it is advantageous to make modifications to that organism to generate higher levels of NADH (Berrios-Rivera et al., 2002). If enzyme concentrations no longer limit the rate of product formation, then the availability of redox cofactors may become limiting (Berrios-Rivera et al., 2002; Balzer et al., 2013). For example, it was necessary to eliminate pathways that compete for NADH in *E. coli* to improve 1-butanol production (Atsumi et al., 2008). Increasing NADH generation has also been used to enhance electric current production by *S. oneidensis* MR-1 (Li et al., 2018). These studies show the importance of NADH availability when engineering redox cofactor-dependent pathways. We have shown that knocking out NADH dehydrogenases and eliminating a competing pathway for NADH in *S. oneidensis* MR-1 increases the availability of NADH, which provides a possible background strain for metabolic engineering in *S. oneidensis* MR-1. With additional NADH available in these NADH dehydrogenase mutant strains, we could direct NADH into synthetic pathways for product formation, even when oxygen is present, as indicated by the high levels of pyruvate and acetate accumulation by the mutant strain.

METHODS

Generating NADH Dehydrogenase Knockout Strains Containing the Rex Redox Sensor

Each single NADH dehydrogenase knockout and the Δ*nuoN*Δ*nqrF1* double-knockout strain were generated in a previous study and confirmed by complementation (Duhl et al., 2018). The Rex redox sensor plasmids were received from Dr. Vatsan Raman and Yang Liu at the University of Wisconsin—Madison) and were described in their recent publication (Liu et al., 2019). The two-plasmid system has one plasmid that constitutively expresses Rex and another that contains a fluorescent reporter under Rex regulation. The Rex-containing plasmid was transformed into chemically competent *E. coli* WM3064 cells. The plasmid was then transferred to *S. oneidensis* MR-1 and NADH dehydrogenase knockout strains via a conjugation protocol similar to Webster et al. (2014). The plasmid containing the fluorescent reporter was transformed into chemically competent *E. coli* Mach 1 cells via heat shock. The Mach 1 cells were grown at 37°C while shaking for 18 h in 5 mL cultures. The cultures were used to extract the reporter plasmid via the E.Z.N.A Plasmid DNA Mini Kit I (Omega Bio-tek, D6943-02). Extracted plasmid was then used to transform electrocompetent *S. oneidensis* MR-1 and NADH dehydrogenase strains containing the Rex plasmid via electroporation (Myers and Myers, 1997). The presence of both plasmids in each strain were confirmed with antibiotic resistance and PCR.

Growth Conditions

Strains were pre-cultured in LB medium for 18 h. Each pre-culture was normalized to $OD_{600} = 1.0$ and washed in M5 minimal medium three times by centrifugation and resuspension. Each growth experiment used the following M5 minimal medium recipe: 1.29 mM K_2HPO_4, 1.65 mM KH_2PO_4, 7.87 mM NaCl, 1.70 mM NH_4SO_4, 475 μM $MgSO_4{\cdot}7H_2O$, 10 mM HEPES, 0.01% (w/v) casamino acids, 0.1% tryptone (w/v), 1X Wolfe's mineral solution (aluminum was not included), and 1X Wolfe's vitamin solution (riboflavin was not included), pH adjusted to 7.2 with 1 M NaOH. Carbon donors, either NAG or D,L-lactate, were added to the M5 medium to final concentrations of 10 or 20 mM, respectively. The addition of 0.1% tryptone to the M5 minimal medium recipe was the only adjustment from our previous work (Duhl et al., 2018). To determine if amino acids were the key components required to rescue the growth of the double NADH dehydrogenase knockout, two different modifications to the M5 recipe were made: the addition of 0.5% (w/v) casamino acids, or

the addition of a defined amino acid mixture containing 20 mM L-arginine (Alfa Aesar, A15738), 20 mM D,L-aspartic acid (TCI, A0544), 20 mM L-glutamic acid (TCI, G0059), 20 mM L-leucine (VWR, 5811), 20 mM L-lysine monochloride (Acros Organics, 123221000), 20 mM L-proline (TCI P0481), D,L-serine (TCI, S0034), and 20 mM L-valine (V0014). After the amino acids were added to the M5 minimal medium, the pH was readjusted to 7.2 with 5 M NaOH and the medium was filter sterilized.

High-throughput growth experiments containing multiple strains were conducted in clear 24-well culture plates (Greiner Bio-One, 662165) in 1 mL culture volumes of M5 medium, with four replicates per strain. Each well was inoculated with 10 μL of normalized pre-culture (OD_{600} = 1.0) and monitored in a Synergy H1 plate reader (BioTek Instruments, Winooski, VT) with orbital shaking at 30°C for 48 h. For growth and fluorescence experiments involving the Rex redox sensor, growth was monitored at 600 nm and fluorescence output was monitored at an excitation wavelength of 475 nm, and emission wavelength of 509 nm.

Flask growth experiments were conducted in 50 mL culture volumes in 250-mL Erlenmeyer flasks. Experiments were performed in M5 medium supplemented with 0.1% tryptone and 10 mM NAG or 20 mM D,L-lactate. Flasks were inoculated with 50 μL of standardized pre-cultures and incubated in a floor shaker (New Brunswick Scientific, 12500) at 30°C while shaking at 275 rpm. Cultures were grown in triplicate and sampled by removing 1 mL and reading OD_{600} on a spectrophotometer (Eppendorf BioPhotometer, D30).

HPLC Analysis

HPLC analysis was conducted as previously described (Duhl et al., 2018).

NADH/NAD^+ Quantification Assay

The protocol for the NADH/NAD^+ quantification assay was adapted from a previously published method (Kern et al., 2014). Samples (5 mL) for both NADH and NAD^+ extractions were taken during early logarithmic growth from 50-mL cultures growing in M5 medium containing 20 mM D,L-lactate or 10 mM NAG. Each 5-mL sample was transferred to a sterile 15-mL conical tube (VWR, 89039-664) and centrifuged at 5,000 × g at 4°C in a Sorvall ST 8R centrifuge (Thermo Scientific) HIGHConic rotor (Thermo Scientific, 75005709) for 10 min. The supernatant was removed from each tube and the pellets were resuspended in 500 μL of 0.1 M HCl containing 500 mM NaCl or 0.1 M NaOH containing 500 mM NaCl for NAD^+ or NADH extractions, respectively. Each sample was transferred to a 1.5-mL microcentrifuge tube and incubated for 5 min at 95°C. After incubation, the samples were placed on ice to cool for 10 min and then were centrifuged for 5 min at 5,000 × g at 4°C in the Sorvall ST 8R centrifuge with the microcentrifuge rotor (Thermo Scientific, 75005715). After centrifugation, 300 μL of supernatant were transferred from each sample into new 1.5-mL microcentrifuge tubes and stored at −80°C until the colorimetric assay was conducted.

Each assay was conducted in clear 96-well microplates (Greiner Bio-One, 655101). Standards were prepared from 0.1 mM NAD^+ (NAD trihydrate, Amresco, 0455) and 0.1 mM NADH (NADH disodium trihydrate, Amresco, 0384) stocks. Each standard and sample were aliquoted into duplicate sets of wells in 20 μL volumes. To initiate the assay, 180 μL of master mix was added to each well and the plate is placed in the plate reader to orbitally shake and incubate at 30°C. The wells were monitored at 1-min intervals with the Synergy H1 plate reader measuring absorbance at 550 nm. The in-well master mix component concentrations are as follows: 0.1 M bicine (VWR, 0149) buffer pH 8.0, 4 mM EDTA disodium salt (Invitrogen, 15576), 1.66 mM phenazine ethosulfate (Sigma-Aldrich, P4544), 0.42 mM thiazolyl blue tetrazolium bromide (Beantown Chemical, 142015), 10% (v/v) ethanol, and 3.2 units/mL alcohol dehydrogenase (Sigma, A3262). NAD^+ and NADH concentrations are determined following the data analysis protocol set out by Kern et al. (2014). Because the extraction efficiencies of 0.1 M HCl and NaOH differed, [NAD^+] and [NADH] were normalized to total protein from each extraction determined by conducting the Pierce™ BCA Protein Assay Kit (Thermo Scientific, 23225).

Aerobic to Anaerobic Transition

Pre-cultures of *S. oneidensis* MR-1 normalized to and OD_{600} of 1.0 were used to inoculate two sets of triplicate 50-mL cultures of LB to an OD_{600} of 0.01. Each set was grown for 6 h under oxic conditions at 30°C while shaking at 275 rpm. After the 6-h incubation period each culture was sampled and the one sets that would be transitioned to an anoxic environment was placed at room temperature without shaking for 2 h. After 2 h, each culture was sampled and the anaerobic cultures were moved to an anaerobic chamber and given 50 mM fumarate as a terminal electron acceptor. Each culture set was incubated for another 12 h and samples were taken from each culture 2- and 12-h post-transition.

Oxygen Consumption Measurements

Oxygen consumption of WT and Δ*nuoN*Δ*nqrF1* was measured within a microfluidic system designed by Dr. Denis Proshlyakov and Nathan Franz (Michigan State University). Samples were added to the microfluidic system and spectroscopically monitored in a custom device. Each run was conducted in triplicate with cultures normalized to and OD_{600} of 0.2 that were shaken at 275 rpm for 10 min prior to testing to ensure total oxygen saturation of the medium. Further testing of oxygen consumption was tested in large batch cultures grown in 50 mL of M5 medium supplemented with 0.1% tryptone and 20 mM D,L-lactate. 25 mL of culture that had been continuously shaking at 30°C at 275 rpm were transferred quickly into a 50 mL conical tube. Oxygen consumption was measured by submerging an oxygen probe (Mettler Toledo InLab® OptiOx, 51344621) in the 25 mL of culture and monitoring [O_2] over time.

Data Analysis

Analysis of growth, fluorescence, and HPLC data was performed using Rstudio (R Studio Team, 2019) with following packages: ggplot2 (Wickham, 2009), reshape2 (Wickham, 2007), dplyr (Wickham and Francois, 2015), and TTR (Ulrich, 2017).

Growth rates were calculated using R package "growthcurver" using default values with background correction set to "min" (Sprouffske and Wagner, 2016). NADH/NAD^+ quantification, BCA assay data, and oxygen consumption data were analyzed in Microsoft Excel (2016).

DATA AVAILABILITY STATEMENT

The datasets generated for this study are available on request to the corresponding author.

AUTHOR CONTRIBUTIONS

KD designed and performed the experiments, analyzed and interpreted the data, and drafted the manuscript. MT designed the study, designed the experiments, analyzed and interpreted the data, and revised the manuscript.

FUNDING

This research was partially supported by a fellowship from Michigan State University under the Training Program in Plant Biotechnology for Health and Sustainability (T32-GM110523). This work was also supported by the USDA National Institute of Food and Agriculture, Hatch project 1009805.

ACKNOWLEDGMENTS

The authors thank Dr. Cecilia Martinez-Gomez (Michigan State University) for sharing the adapted redox assay protocol, Nicholas Tefft (Michigan State University) for reviewing the manuscript, and Dr. Vatsan Raman and Yang Liu (University of Wisconsin—Madison) for sharing the Rex-based redox sensor and for helpful comments on the manuscript. The authors would also like to thank Dr. Denis Proshlyakov and Nathan Frantz (Michigan State University) for allowing us to use their microfluidic system to measure oxygen consumption.

SUPPLEMENTARY MATERIAL

The Supplementary Material for this article can be found online at: https://www.frontiersin.org/articles/10.3389/fenrg.2019.00116/full#supplementary-material

REFERENCES

Atsumi, S., Cann, A. F., Connor, M. R., Shen, C. R., Smith, K. M., Brynildsen, M. P., et al. (2008). Metabolic engineering of *Escherichia coli* for 1-butanol production. *Metab. Eng.* 10, 305–311. doi: 10.1016/j.ymben.2007.08.003

Balzer, G. J., Thakker, C., Bennett, G. N., and San, K.-Y. (2013). Metabolic engineering of *Escherichia coli* to minimize byproduct formate and improving succinate productivity through increasing NADH availability by heterologous expression of NAD^+-dependent formate dehydrogenase. *Metab. Eng.* 20, 1–8. doi: 10.1016/j.ymben.2013.07.005

BD Biosciences (2006). *BD Bionutrients Technical Manual Advanced Bioprocessing*. Available online at: https://www.bdbiosciences.com/documents/bionutrients_tech_manual.pdf

Beliaev, A. S., Klingeman, D. M., Klappenbach, J. A., Wu, L., Romine, M. F., Tiedje, J. M., et al. (2005). Global transcriptome analysis of *Shewanella oneidensis* MR-1 exposed to different terminal electron acceptors. *J. Bacteriol.* 187, 7138–7145. doi: 10.1128/JB.187.20.7138-7145.2005

Berrios-Rivera, S. J., Bennett, G. N., and San, K.-Y. (2002). Metabolic engineering of *Escherichia coli*: increase of NADH availability by overexpressing an NAD^+-dependent formate dehydrogenase. *Metab. Eng.* 4, 217–229. doi: 10.1006/mben.2002.0227

Coursolle, D., and Gralnick, J. A. (2012). Reconstruction of extracellular respiratory pathways for iron(III) reduction in *Shewanella oneidensis* strain MR-1. *Front. Microbiol.* 3:56. doi: 10.3389/fmicb.2012.00056

de Graef, M. R., Alexeeva, S., Snoep, J. L., and Teixeira de Mattos, M. J. (1999). The steady-state internal redox state (NADH/NAD^+) reflects the external redox state and is correlated with catabolic adaptation in *Escherichia coli*. *J. Bacteriol.* 181, 2351–2357.

Deutschbauer, A., Price, M. N., Wetmore, K. M., Shao, W., Baumohl, J. K., Xu, Z., et al. (2011). Evidence-based annotation of gene function in *Shewanella oneidensis* MR-1 using genome-wide fitness profiling across 121 conditions. *PLoS Genet.* 7:e1002385. doi: 10.1371/journal.pgen.1002385

Duhl, K. L., Tefft, N. M., and TerAvest, M. A. (2018). *Shewanella oneidensis* MR-1 utilizes both sodium-and proton-pumping NADH dehydrogenases during aerobic growth. *Appl. Environ. Microbiol.* 84:e00415-18. doi: 10.1128/AEM.00415-18

Gralnick, J. A., Vali, H., Lies, D. P., and Newman, D. K. (2006). Extracellular respiration of dimethyl sulfoxide by *Shewanella oneidensis* strain MR-1. *Proc. Natl. Acad. Sci. U.S.A.* 103, 4669–4674. doi: 10.1073/pnas.0505959103

Gyan, S., Shiohira, Y., Sato, I., Takeuchi, M., and Sato, T. (2006). Regulatory loop between redox sensing of the NADH/NAD^+ ratio by rex (YdiH) and oxidation of NADH by NADH dehydrogenase Ndh in *Bacillus subtilis*. *J. Bacteriol.* 188, 7062–7071. doi: 10.1128/JB.00601-06

Heidelberg, J. F., Paulsen, I. T., Nelson, K. E., Gaidos, E. J., Nelson, W. C., Read, T. D., et al. (2002). Genome sequence of the dissimilatory metal ion-reducing bacterium *Shewanella oneidensis*. *Nat. Biotech.* 20, 1118–1123. doi: 10.1038/nbt749

Hunt, K. A., Flynn, J. M., Naranjo, B., Shikhare, I. D., and Gralnick, J. A. (2010). Substrate-level phosphorylation is the primary source of energy conservation during anaerobic respiration of *Shewanella oneidensis* strain MR-1. *J. Bacteriol.* 192, 3345–3351. doi: 10.1128/JB.00090-10

Kanehisa, M., and Goto, S. (2000). KEGG: kyoto encyclopedia of genes and genomes. *Nucleic Acids Res.* 28, 27–30. doi: 10.1093/nar/28.1.27

Kern, S. E., Price-Whelan, A., and Newman, D. K. (2014). Extraction and measurement of $NAD(P)^+$ and NAD(P)H. *Methods Mol. Biol.* 1149, 311–323. doi: 10.1007/978-1-4939-0473-0_26

Le Laz, S., Kpebe, A., Bauzan, M., Lignon, S., Rousset, M., and Brugna, M. (2016). Expression of terminal oxidases under nutrient-starved conditions in *Shewanella oneidensis*: detection of the A-type cytochrome *c* oxidase. *Sci. Rep.* 6:19726. doi: 10.1038/srep19726

Li, F., Li, Y., Sun, L., Chen, X., An, X., Yin, C., et al. (2018). Modular engineering intracellular NADH regeneration boosts extracellular electron transfer of *Shewanella oneidensis* MR-1. *ACS Synth. Biol.* 7, 885–895. doi: 10.1021/acssynbio.7b00390

Liu, Y., Landick, R., Raman, S., Landick, B., and Raman, S. (2019). A regulatory NADH/NAD^+ redox biosensor for bacteria. *ACS Synth. Biol.* 8, 264–273. doi: 10.1021/acssynbio.8b00485

Matsushita, K., Ohnishi, T., and Kaback, H. R. (1987). NADH-ubiquinone oxidoreductases of the *Escherichia coli* aerobic respiratory chain. *Biochemistry* 26, 7732–7737. doi: 10.1021/bi00398a029

Meshulam-Simon, G., Behrens, S., Choo, A. D., and Spormann, A. M. (2007). Hydrogen metabolism in *Shewanella oneidensis* MR-1. *Appl. Environ. Microbiol.* 73, 1153–1165. doi: 10.1128/AEM.01588-06

Myers, C. R., and Myers, J. M. (1997). Replication of plasmids with the p15A origin in *Shewanella putrefaciens* MR-1. *Lett. Appl. Microbiol.* 24, 221–225. doi: 10.1046/j.1472-765X.1997.00389.x

Novichkov, P. S., Kazakov, A. E., Ravcheev, D. A., Leyn, S. A., Kovaleva, G. Y., Sutormin, R. A., et al. (2013). RegPrecise 3.0–a resource for genome-scale exploration of transcriptional regulation in bacteria. *BMC Genomics* 14:745. doi: 10.1186/1471-2164-14-745

Paulick, A., Delalez, N. J., Brenzinger, S., Steel, B. C., Berry, R. M., Armitage, J. P., et al. (2015). Dual stator dynamics in the *Shewanella oneidensis* MR-1 flagellar motor. *Mol. Microbiol.* 96, 993–1001. doi: 10.1111/mmi.12984

Paulick, A., Koerdt, A., Lassak, J., Huntley, S., Wilms, I., Narberhaus, F., et al. (2009). Two different stator systems drive a single polar flagellum in *Shewanella oneidensis* MR-1. *Mol. Microbiol.* 71, 836–850. doi: 10.1111/j.1365-2958.2008.06570.x

Pinchuk, G. E., Geydebrekht, O. V., Hill, E. A., Reed, J. L., Konopka, A. E., Beliaev, A. S., et al. (2011). Pyruvate and lactate metabolism by *Shewanella oneidensis* MR-1 under fermentation, oxygen limitation, and fumarate respiration conditions. *Appl. Environ. Microbiol.* 77, 8234–8240. doi: 10.1128/AEM.05382-11

Pinchuk, G. E., Hill, E. A., Geydebrekht, O. V, De Ingeniis, J., Zhang, X., Osterman, A., et al. (2010). Constraint-based model of *Shewanella oneidensis* MR-1 metabolism: a tool for data analysis and hypothesis generation. *PLoS Comput. Biol.* 6:e1000822. doi: 10.1371/journal.pcbi.1000822

R Studio Team (2019). R Studio: Integrated Development for R. Boston, MA: RStudio, Inc. Available online at: http://www.rstudio.com/

Rodionov, D. A., De Ingeniis, J., Mancini, C., Cimadamore, F., Zhang, H., Osterman, A. L., et al. (2008). Transcriptional regulation of NAD metabolism in bacteria: NrtR family of Nudix-related regulators. *Nucleic Acids Res.* 36, 2047–2059. doi: 10.1093/nar/gkn047

Senior, A. E. (1988). ATP synthesis by oxidative phosphorylation. *Physiol. Rev.* 68, 177–231. doi: 10.1152/physrev.1988.68.1.177

Serres, M. H., and Riley, M. (2006). Genomic analysis of carbon source metabolism of *Shewanella oneidensis* MR-1: predictions versus experiments. *J. Bacteriol.* 188, 4601–4609. doi: 10.1128/JB.01787-05

Shen, L. C., and Atkinson, D. E. (1970). Regulation of pyruvate dehydrogenase from Escherichia coli interactions of adenylate energy charge and other regulatory parameters. *J. Biol. Chem.* 245, 5974–5978.

Sprouffske, K., and Wagner, A. (2016). Growthcurver: an R package for obtaining interpretable metrics from microbial growth curves. *BMC Bioinformatics* 17:172. doi: 10.1186/s12859-016-1016-7

Stokell, D. J., Donald, L. J., Maurus, R., Nguyen, N. T., Sadler, G., Choudhary, K., et al. (2003). Probing the roles of key residues in the unique regulatory NADH binding site of type II citrate synthase of *Escherichia coli*. *J. Biol. Chem.* 278, 35435–35443. doi: 10.1074/jbc.M302786200

TerAvest, M. A., and Angenent, L. T. (2014). Oxidizing electrode potentials decrease current production and coulombic efficiency through cytochrome *c* inactivation in *Shewanella oneidensis* MR-1. *ChemElectroChem* 1, 2000–2006. doi: 10.1002/celc.201402128

Tran, Q. H., Bongaerts, J., Vlad, D., and Unden, G. (1997). Requirement for the proton-pumping NADH dehydrogenase i of Escherichia coli in respiration of NADH to fumarate and its bioenergetic implications. *Eur. J. Biochem.* 244, 155–160. doi: 10.1111/j.1432-1033.1997.00155.x

Ulrich, J. (2017). *TTR: Technical Trading Rules*. R Package version 0.23-2.

Webster, D. P., TerAvest, M. A., Doud, D. F. R., Chakravorty, A., Holmes, E. C., Radens, C. M., et al. (2014). An arsenic-specific biosensor with genetically engineered *Shewanella oneidensis* in a bioelectrochemical system. *Biosens. Bioelectron.* 62, 320–324. doi: 10.1016/j.bios.2014.07.003

Weitzman, P. D. J., and Jones, D. (1968). Regulation of citrate synthase and microbial taxonomy. *Nature* 219:270. doi: 10.1038/219270a0

Wickham, H. (2007). Reshaping data with the reshape package. *J. Stat. Softw.* 21, 1–20. doi: 10.18637/jss.v021.i12

Wickham, H. (2009). *ggplot2 Elegant Graphics for Data Analysis*.

Wickham, H., and Francois, R. (2015). *dplyr: A Grammar of Data Manipulation*. R Package version 0.4.2., 3.

Yagi, T. (1991). Bacterial NADH-quinone oxidoreductases. *J. Bioenerg. Biomembr.* 23, 211–225. doi: 10.1007/BF00762218

Zhou, G., Yin, J., Chen, H., Hua, Y., Sun, L., and Gao, H. (2013). Combined effect of loss of the caa_3 oxidase and Crp regulation drives Shewanella to thrive in redox-stratified environments. *ISME J.* 7, 1752–1763. doi: 10.1038/ismej.2013.62

Conflict of Interest: The authors declare that the research was conducted in the absence of any commercial or financial relationships that could be construed as a potential conflict of interest.

frontiers in Energy Research

ORIGINAL RESEARCH
published: 01 November 2019
doi: 10.3389/fenrg.2019.00121

In situ Electrochemical Studies of the Terrestrial Deep Subsurface Biosphere at the Sanford Underground Research Facility, South Dakota, USA

*Yamini Jangir[1], Amruta A. Karbelkar[2], Nicole M. Beedle[3], Laura A. Zinke[4], Greg Wanger[4], Cynthia M. Anderson[5], Brandi Kiel Reese[6], Jan P. Amend[3,4] and Mohamed Y. El-Naggar[1,2,3]**

[1] Department of Physics and Astronomy, University of Southern California, Los Angeles, CA, United States, [2] Department of Chemistry, University of Southern California, Los Angeles, CA, United States, [3] Department of Biological Sciences, University of Southern California, Los Angeles, CA, United States, [4] Department of Earth Science, University of Southern California, Los Angeles, CA, United States, [5] Center for the Conservation of Biological Resources, Black Hills State University, Spearfish, SD, United States, [6] Department of Life Sciences, Texas A&M University, Corpus Christi, TX, United States

OPEN ACCESS

Edited by:
Chi Ho Chan,
University of Minnesota Twin Cities,
United States

Reviewed by:
Fabrizio Colosimo,
University of New Hampshire,
United States
Craig Lee Moyer,
Western Washington University,
United States
Jonathan P. Badalamenti,
University of Minnesota Twin Cities,
United States

***Correspondence:**
Mohamed Y. El-Naggar
mnaggar@usc.edu

Specialty section:
This article was submitted to Bioenergy and Biofuels, a section of the journal Frontiers in Energy Research

Received: 22 June 2019
Accepted: 17 October 2019
Published: 01 November 2019

Citation:
Jangir Y, Karbelkar AA, Beedle NM, Zinke LA, Wanger G, Anderson CM, Reese BK, Amend JP and El-Naggar MY (2019) In situ Electrochemical Studies of the Terrestrial Deep Subsurface Biosphere at the Sanford Underground Research Facility, South Dakota, USA. Front. Energy Res. 7:121. doi: 10.3389/fenrg.2019.00121

The terrestrial deep subsurface is host to significant and diverse microbial populations. However, these microbial populations remain poorly characterized, partially due to the inherent difficulty of sampling, *in situ* studies, and isolating of the *in situ* microbes. Motivated by the ability of microbes to gain energy from redox reactions at mineral interfaces, we here present *in situ* electrochemical colonization (ISEC) reactor as a method to directly study microbial electron transfer activity and to enable the capture and isolation of electrochemically active microbes. We installed a potentiostatically controlled ISEC reactor containing four working electrodes 1,500 m below the surface at the Sanford Underground Research Facility (SURF). The working electrodes were poised at different redox potentials to mimic energy-yielding mineral reducing and oxidizing reactions predicted to occur at this site. We present a 16S rRNA analysis of the *in situ* electrode-associated microbial communities, revealing the dominance of novel bacterial lineages under cathodic conditions. We also demonstrate that the *in situ* electrodes can be further used for downstream electrochemical laboratory enrichment and isolation of novel strains. Using this workflow, we isolated *Bacillus*, *Anaerospora*, *Comamonas*, *Cupriavidus*, and *Azonexus* strains from the electrode-attached biomass. Finally, the extracellular electron transfer (EET) activity of *Comamonas* strain (isolated at −0.19 V vs. SHE and designated WE1-1D1) and *Bacillus* strain (isolated at +0.53 V vs. SHE and designated WE4-1A1-BC) from and to a poised electrode, respectively, were confirmed in electrochemical reactors. Our study highlights the utility of *in situ* electrodes and electrochemical enrichment workflows to shed light on microbial activity in the deep terrestrial subsurface.

Keywords: microbial electrochemical cell, Sanford Underground Research Facility, *Bacillus*, *Comamonas*, *in situ* studies, extracellular electron transfer, electromicrobiology

INTRODUCTION

Minerals that contain redox active elements (e.g., S, Fe, Mn) are abundant in subsurface environments, and can support the growth of microorganisms by acting as electron acceptors for heterotrophic respiration or electron donors for lithotrophic, and often autotrophic, metabolism (Nealson et al., 2002; Bach and Edwards, 2003; Edwards et al., 2005; Fredrickson and Zachara, 2008; Orcutt et al., 2011; Southam, 2012; Shi et al., 2016). This process of extracellular electron transfer (EET) to or from minerals is best characterized in a handful of Fe-reducing bacteria, especially *Geobacter* and *Shewanella* species (Lovley and Phillips, 1988; Myers and Nealson, 1988; Shi et al., 2016). To overcome the hurdle of electron transfer across the otherwise electrically-insulating cell envelope, these bacteria rely on a number of mechanisms: multiheme cytochrome complexes that bridge the periplasm and outer membrane (Myers and Myers, 1992; Hartshorne et al., 2009; White et al., 2013), microbial nanowires that reach out to distant electron acceptors (Reguera et al., 2005; Gorby et al., 2006), and soluble redox shuttles that diffusively link cells to external surfaces (Marsili et al., 2008; Von Canstein et al., 2008). EET can be electrochemically mimicked on electrode surfaces that function as surrogate electron acceptors (anodes) or donors (cathodes) to support microbial metabolism, depending on the poised potentials of these electrodes (Bond and Lovley, 2003; Gregory et al., 2004; Ross et al., 2011; Carmona-Martínez et al., 2013; Rowe et al., 2017a; Hirose et al., 2018). As a result, electrochemical enrichments have been applied to microbial samples from a variety of environments (Bond et al., 2002; Tender et al., 2002; Holmes et al., 2004; Kim et al., 2004; Rabaey and Verstraete, 2005; Reimers et al., 2006; White et al., 2009; Bond, 2010; Meyer et al., 2016). When combined with surveys of microbial community structure, these electrochemical techniques greatly expanded our understanding of the phylogenetic diversity of microbes capable of colonizing electrodes and led to the isolation of novel microorganisms capable of EET to anodes (Wrighton et al., 2008; Xing et al., 2008; Fedorovich et al., 2009; Badalamenti et al., 2016; Jangir et al., 2016; Kawaichi et al., 2018). While our mechanistic understanding of the molecular pathways that underlie inward EET (i.e., electron transfer from rather than to surfaces) lags behind metal reduction pathways, electrode-based techniques have highlighted the diversity of microbes capable of electron uptake from cathodes: acetogens, methanogens, as well as iron- and sulfur-oxidizers (Nevin et al., 2011; Summers et al., 2013; Bose et al., 2014; Beese-Vasbender et al., 2015; Deutzmann et al., 2015; Ishii et al., 2015; Rowe et al., 2015, 2017b).

The Sanford Underground Research Facility (SURF), located in the Black Hills of South Dakota, USA is the site of the former Homestake Gold Mine. It is hosted in quartz-veined, sulfide-rich segments of an Early Proterozoic, carbonate-facies iron-formation (Caddey et al., 1991; Hart et al., 2014; Lesko, 2015). The facility's tunnels provide access, maximally 4,850 ft (1,478 m) below ground surface (bgs), to deep subsurface fluids through a network of manifolds. The residence times of the accessible fluids range from very recent in the shallowest levels to much older (>10,000 years) fluids reaching the deeper levels (Murdoch et al., 2012; Osburn et al., 2014). The mine was converted to a state-run science facility in 2011, with emphasis on rare-process physics (Heise, 2015), and this accessible infrastructure provided a remarkable portal for *in situ* studies of the deep terrestrial biosphere. Osburn et al. (2014) combined geochemical data, energetic modeling, and 16S rRNA gene sequences from different boreholes to both assess the *in situ* microbial communities and predict energy-yielding metabolisms for unknown physiotypes. Notably, abundant energy was predicted for microorganisms from a variety of reactions including sulfur oxidation, iron oxidation, and manganese reduction, which motivated us to apply electrode-based techniques to assess and enrich for microbes capable of EET.

Here we report the deployment and operation of an *in situ* electrochemical colonization (ISEC) reactor fed by a manifold at the 4,850 ft (1,478 m) level of SURF. The reactor contained four working electrodes, poised at potentials spanning lower to higher, to act as an inexhaustible source or sink of electrons for capture of potential mineral oxidizing and reducing bacteria, with emphasis on mimicking sulfur oxidation, iron oxidation, and manganese reduction predicted as energy-yielding reactions in this manifold (Osburn et al., 2014). We hypothesized that physical electrodes, when deployed *in situ*, can serve as electron donors and/or acceptors to capture important bacterial lineages capable of EET from the deep subsurface. Further, we utilized these *in situ* electrodes for subsequent laboratory enrichment and isolation of novel strains, and directly tested the electron uptake by *Comamonas* isolate and electron donation by *Bacillus* isolate via a poised electrodes. To our knowledge, this effort represents the first potentiostatically-controlled multi-electrode reactor deployed *in situ* in a deep subsurface environment.

MATERIALS AND METHODS

Field Measurements

The exploratory borehole (DUSEL 3A) studied is located at the 1,478 m (4,850 ft) below ground surface level close to the Yates shaft at SURF in Lead, South Dakota (USA). The 214 m-long borehole, drilled in 2009 intersects the Precambrian amphibolite metamorphic schists (Caddey et al., 1991; Hart et al., 2014) and has been capped with manifolds to prevent flooding. One year prior to this study, initial aqueous chemistry of DUSEL 3A fluid was obtained for thermodynamic modeling in February 2014 (Osburn et al., 2014). Further, detailed geochemical data were acquired during installation (December 2014) and conclusion (May 2015) of the ISEC reactor incubation. Aqueous chemistry (**Table 1**) was measured as described earlier (Osburn et al., 2014). Briefly, oxidation-reduction potential (ORP), conductivity, pH, temperature, and total dissolved solids (TDS) were measured *in situ* with an Ultrameter II 6PFCE (Myron L Company, Carlsbad, CA). The redox-sensitive species were measured using Hach DR/2400 portable field spectrophotometers and associated reaction kits (Hach Company, Loveland, CO). Major anions and cations were measured using ion chromatography with Metrohm column Metrosep A SUPP 150 and Metrosep C6−250/4.0, respectively (Metrohm, Fountain Valley, CA).

TABLE 1 | Chemical composition of fluid from DUSEL 3A at the 4,850 ft (1,478 mbsl) level, Sanford Underground Research Facility (SD, USA), after commissioning and decommissioning of *in situ* electrochemical colonization (ISEC) reactor.

	Dec 2014	May 2015
pH	7.08	7.75
Temperature (°C)	18.7	19.31
Conductance (μS/cm)	6514	7869
TDS (ppm)	3257	3929
ORP (mV)	59.2	−50
Dissolved constituents		
dO_2 (mg/L)	3.79	0
S^{2-} (mg/L)	17	17
Fe^{2+}(mg/L)	0.6	0.6
NO_3^-(mg/L)	0.4	0.2
NH_3 (mg/L)	0.11	0.07
SiO_2 (mg/L)	24.7	9.7
Mn^{2+} (mg/L)	0.4	0.9
PO_4^{3-} (mg/L)	1.24	1.09
NO_2^- (mg/L)	BDL	0.001
Br_2 (mg/L)	BDL	0.01
Li^+ (mg/L)	0.024	0.035
Na^+ (mg/L)	10.619	5.698
K^+ (mg/L)	0.229	0.751
Cl^- (mg/L)	0.316	0.385
SO_4^{2-} (mg/L)	14.049	46.696

In situ Electrochemical Colonization Reactor

Fluid from DUSEL 3A was pumped through the ISEC reactor (**Figure 1**) for 5 months via peristaltic pumps (MasterFlex L/S Digital Drive, EW-07522-20, Cole-Parmer, USA) at a flow rate of 1 mL/min, providing a dilution rate of 1 day^{-1}. Aqueous chemistry (ORP, conductivity, pH, and temperature) of the ISEC effluent was logged using a multiparameter HI9829 meter (Hanna Instruments, Woonsocket, RI). ISEC is a standard electrochemical half-cell design, custom fabricated from a 1 L spinner flask (CLS-1410, Chemglass Life Sciences, Vineland, NJ) to incorporate an Ag/AgCl reference electrode (3M NaCl, MF-2052, BASi, West Lafayette, IN) and a platinum counter electrode (CHI115, CH Instruments, Austin, TX). It holds a PTFE assembly of five threaded rods, each of which supported a working electrode (WE) composed of 6 × 7 cm carbon cloth (PW06, Zoltek, St. Louis, MO, USA). During enrichment, four working electrodes (WE1, WE2, WE3, and WE4) were poised at −0.19, +0.01, +0.26, and +0.53 V vs. SHE, respectively, using a four-channel potentiostat (EA164 Quadstat, EDaq, USA). Potentials were chosen to mimic conditions consistent with elemental sulfur oxidation (−0.19 V vs. SHE), iron oxidation (+0.01 V vs. SHE), and manganese reduction (+0.53 V vs. SHE), all predicted as putative energy-yielding metabolisms for the microbial community inhabiting the DUSEL 3A fluid (Osburn et al., 2014). Since the reduction potential of many cytochromes ranges from −0.5 to +0.3 V vs. SHE (Kracke et al., 2015) a fourth potential was also applied at +0.26 V vs. SHE. The reduction potentials were evaluated by: (1) converting the standard Gibbs free energy (G^0) to standard reduction potential (E^0_{red}) of the reaction via $G^0 = -nFE^0_{red}$ (where: n refers to the number of electron transferred and F stands for the Faraday constant), and (2) using the geochemical data (specifically pH, temperature, and the concentration of SO_4^{2-}, S^{2-}, Mn^{2+}, Fe^{2+}) of DUSEL 3A liquid (from Dec 2014) to evaluate *in situ* reduction potential (E_{red}) via the Nernst Equation $E_{red} = E^0_{red} - \frac{RT}{nF} \ln Q_r$ (where R refers to the gas constant, T denotes the temperature in kelvin, n refers to the number of electron transferred and F stands for the Faraday constant and Q_r represents the reaction quotient of the cell reaction). All electrical connections were made using titanium insulated wire (KeegoTech, Menlo Park, CA, USA). The complete set-up was autoclaved along with the working and the counter electrodes. The reference electrode was ethanol-sterilized before it was inserted. Applied redox potentials and current production were controlled and recorded via the eCorder eCHART software (eDAQ Inc., Colorado Springs, CO). Before the deployment of the ISEC reactor in December 2014, the SURF facility made modifications to the manifold's design, which could potentially lead to backflow of fluid from a dehumidifier into the reactor. To avert this contamination, in December 2014, a check valve was installed upstream of the solenoid valve as shown in the schematic diagram of ISEC reactor (**Figure 1**). The reactor was incubated with a continuous flow of DUSEL 3A fluid for 5 months beginning December 2014, monitored monthly for proper operation, and finally retrieved in May 2015. During decommission, small sections of carbon cloth from each potential were collected for microscopy, active microbial community analysis, and further laboratory electrochemical enrichments as described below.

Secondary Laboratory Electrochemical Enrichment

At the conclusion of ISEC deployment, the carbon cloth working electrodes (3 × 6 cm) were placed into autoclaved 125 mL serum bottles containing filtered (0.22 μm) DUSEL 3A fluid filled to capacity and sealed with sterile butyl rubber stoppers and aluminum seals (Chemglass Life Sciences, USA). The serum bottles were stored in vacuum-sealed Mylar bags (ShieldPro, USA) with oxygen absorbers (OxyFree, USA) to minimize oxygen exposure during transportation. In the laboratory, secondary electrochemical enrichments were performed using the poised carbon cloth from the reactor in four separate three-electrode electrochemical cells (50 mL total volume). A standard three-electrode glass cell comprised of: (1) working electrode (WE): a carbon cloth with dimensions 1 × 1 cm; (2) counter electrode (CE): a platinum wire (CHI115, CH Instruments, USA), and (3) a reference electrode (RE): 1 M KCl Ag/AgCl reference electrode (CHI111, CH Instruments, USA). Specialty media was designed to mimic the *in situ* aqueous chemistry of DUSEL 3A at SURF, which included basal salts (L^{-1}): NaCl (0.029 g), KH_2PO_4 (0.041 g), NH_4Cl (0.160 g), $FeSO_4.7H_2O$ (0.042 g), Na_2SO_4 (0.014 g), and amended with yeast extract

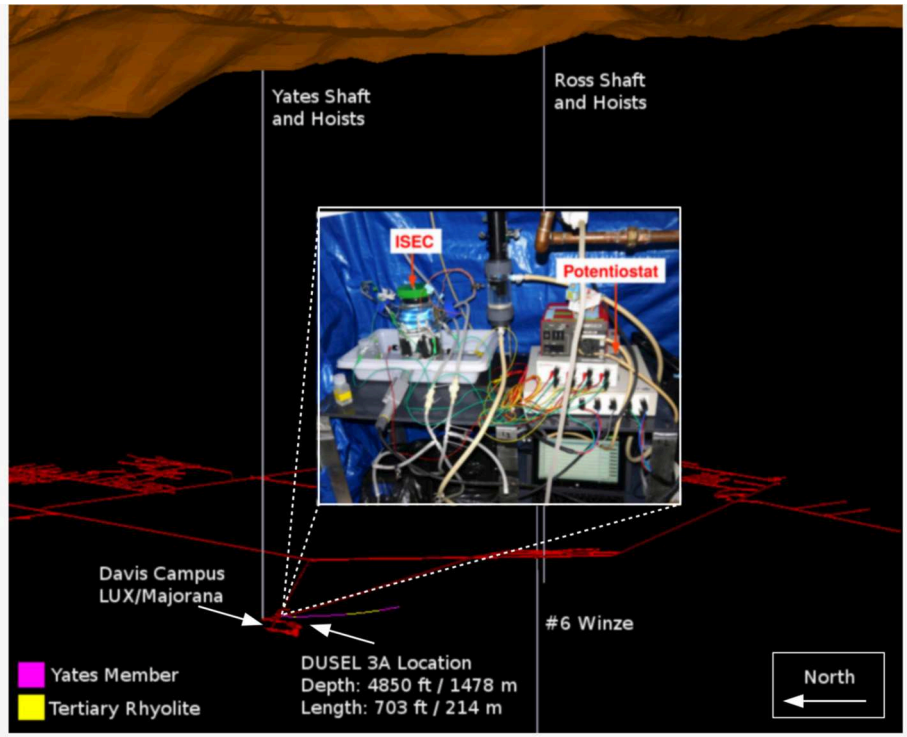

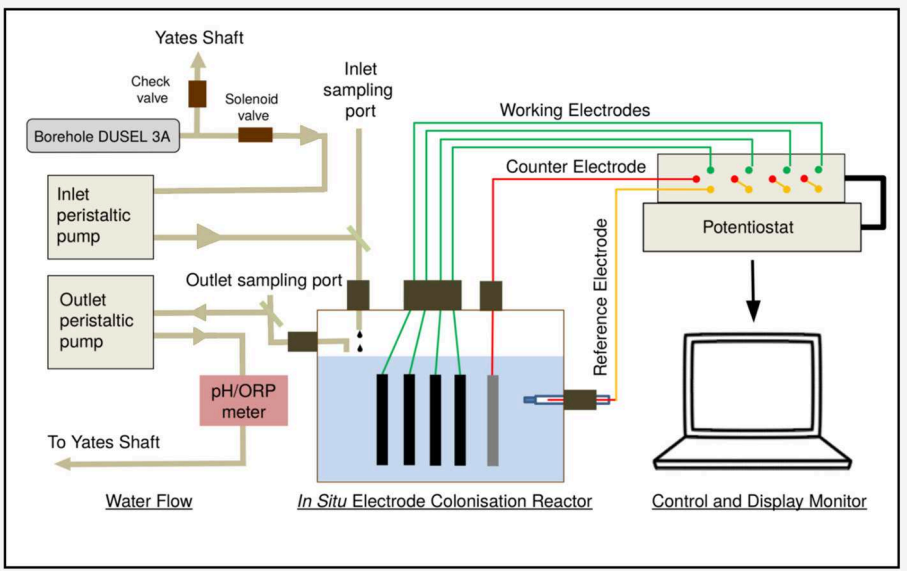

FIGURE 1 | (Top) A 3-dimensional layout of Sanford Underground Research Facility (image to scale). DUSEL 3A, located at 4,850 ft level close to Davis Campus cutting the iron-rich Precambrian Yates member, was selected as the site for *in situ* electrochemical colonization (ISEC) reactor deployment. An image of the ISEC reactor after deployment (Dec 2014) is shown in the inset. **(Bottom)** Schematic diagram of ISEC reactor. The four carbon cloth working electrodes were poised at −0.19, +0.01, +0.26, and +0.53 V vs. SHE, respectively, using a 4-channel potentiostat acting as electron donors and acceptors in a single reactor. DUSEL 3A fluid was fed directly into the reactor and the effluent was pumped out to Yates shaft.

(0.5 g), vitamins, and trace minerals (Kieft et al., 1999). Media was maintained at pH ∼ 7.5 using phosphate buffer (10 mM). Enrichment of microbes capable of using electrode as electron donor was performed by augmenting SURF base media with sodium bicarbonate (10 mM), poising electrodes at −0.19 and +0.01 V vs. SHE, and continuous purging of a gas mix (CO_2: air v:v 20:80) in the electrochemical cell. To enrich for microbes capable of using the electrode as the terminal electron acceptor, media was augmented with sodium acetate (5 mM), electrodes were poised at +0.26 and +0.53 V vs. SHE, and continuous

N_2 gas purging was used to maintain anoxic conditions. These secondary electrochemical enrichments were performed in batch mode (media changed every 7–10 days) for 2 months.

Active Microbial Community Analysis

The active microbial community was analyzed by extracting 16S ribosomal RNA (rRNA) transcripts from: (1) dehumidifier fluid (as a potential contaminant) (2 L), (2) DUSEL 3A fluid (2 L), (3) electrode-attached biofilms in ISEC (3 × 4 cm), (4) electrode-attached biofilms of the laboratory electrochemical enrichments (1 × 0.5 cm), and (5) Control. The DUSEL 3A and dehumidifier fluid were filtered through 0.22 μm sterivex filters (Millipore, USA) to collect microbiological samples. All microbiological samples were immediately placed on dry ice for transportation to the University of Southern California and kept in a −80°C freezer in the laboratory until extraction. Total RNA was extracted from the filters and electrode-attached biofilms (ISEC and secondary laboratory electrochemical enrichments) via physical (freeze, thaw, vortex), chemical (sodium dodecyl sulfate and EDTA), and biological (lysozyme) disruption of the cell wall prior to phenol-chloroform extraction as described previously (Reese et al., 2018). A control that included only reagents and no sample material was extracted alongside the samples to confirm lack of contamination. Any residual DNA was digested using TURBO DNA-free TM Kit (ThermoFisher Scientific, USA) and verified to be free of DNA by running a PCR of the RNA extraction. The samples were sent to Molecular Research DNA (Shallowater, TX, USA) for reverse transcription, library preparation, and high throughput sequencing. At the facility, sequencing library preparation included reverse transcribing to cDNA the hypervariable region V4 of the bacterial 16S rRNA transcript using 806R (Caporaso et al., 2011). Specifically, cDNA sequencing steps included purification and generation of blunt end cDNA followed by ligation to sequencing adapters, amplification using 515F and 806R priming set (Caporaso et al., 2011), denaturation, and sequencing. A total of 250 ng of double strand cDNA from each sample was used to prepare the libraries. All amplicons from different samples were pooled (10 pM each) and purified using Agencourt Ampure beads (Agencourt Bioscience Corporation, MA, USA). Deep sequencing was performed on Roche 454 FLX titanium platform using recommended reagents.

The sequences were processed using mothur (v 1.36.1) pipeline (Schloss et al., 2009). The barcodes and the primers were removed from each sequence, followed by trimming to remove any ambiguous base calls, average quality scores <20, and homopolymer runs more than 8 bp. A total of 422,490 high-quality unique sequences remained and the resulting average sequence length was 260 bp for all samples. The trimmed sequences were aligned with the SILVA-based reference alignment (Pruesse et al., 2007) using the Needleman-Wunsch pairwise alignment method (Needleman and Wunsch, 1970). Chimeras were removed using UCHIME (Edgar et al., 2011), and a distance matrix was created. The sequences were clustered to identify unique operational taxonomical units (OTUs) at the 97% level, followed by creating a shared OTU file amongst various samples, and the taxonomy was assigned using mothur formatted Ribosomal Database Project (RDP) training set version 16. The resultant microbiome was processed using "Phyloseq," "Microbiome," and "Vegan" package available in R (version 3.5.2). The dataset (OTU shared file, taxonomy file, and the metadata file) were introduced as a phyloseq objects in R. The microbiome data was pre-processed by removing contaminant OTUs from the extraction reagent. OTUs not represented in the DUSEL 3A (source fluid) were also removed from the dataset to account for any contamination from initial dehumidifier backflow. The resulting filtered microbiome data (including absolute abundance data from DUSEL 3A, ISEC, and Laboratory enrichments) was used to calculate the diversity indices, MDS plots, and statistics including Adonis and betadisper. The absolute abundance microbiome data of m phylotype/OTUs and n samples [$C = (c_{ij}) \in \mathbb{N}^{m \times n}$, where c_{ij} are the number of reads for a phylotype/OTU (i) in the sample (j)] was transformed into the relative abundances by total sum scaling ($k_{ij} = \frac{c_{ij}}{\sum_{i=1}^{m} c_{ij}}$). Next, to study the variation of relative abundance of a phylotype/OTU across sample the dataset was normalized to the maximum $f_{ij} = \frac{k_{ij}}{J_i}$ *where* $J_i = maximum\{k_{ij}\}$. The raw sequencing data have been uploaded to National Center for Biotechnology Information (NCBI) Sequence Read Archive (SRA) database (accession number: SRR8537881-SRR8537882) under BioProject PRJNA262938. Custom scripts used for analysis the sff files via MOTHUR and further sequence processing via R can be found at https://github.com/yaminijangir/SURF_scripts.

Isolation and Electrochemical Measurements of Pure Isolates

Electrode-attached biomass from each of WE1 and WE4 was streaked on R2A agar plates (Reasoner and Geldreich, 1985) and incubated at 30°C to obtain single colonies. Morphologically distinct colonies were re-streaked on fresh R2A agar plates, resulting in multiple isolates. For taxonomic classification, isolates were grown to late exponential phase in liquid R2A at 30°C and DNA extraction performed using the UltraClean® Microbial DNA Isolation kit (Mo Bio Laboratories, Carlsbad, CA, USA). The bacterial 16S rRNA gene was PCR-amplified from the extracted DNA using primers 8F and 1492R (Integrated DNA Technologies, USA). The purified PCR product (PureLink PCR Purification Kit, Life Technologies, CA, USA) was sent for sanger sequencing to Genewiz (South Plainfield, NJ, USA) from the 1492R primer. The 600 bp length sequences of the isolated strains have been deposited to NCBI SRA (accession numbers: MK483257, MK483258). The chronoamperometry (i.e., current vs. time at a fixed potential) measurement of each isolate was performed in a standard three-electrode glass electrochemical cell (50 mL volume) in triplicates.

Comamonas sp. (designated strain WE1-1D1) was grown aerobically to stationary phase from frozen stocks (−80°C in 20% glycerol) in R2A media and the culture was used to inoculate 750 mL of SURF base medium at 1% (v:v). After reaching the mid-exponential phase, the culture was pelleted by centrifugation at 5,369 × g for 10 min, washed three times and re-suspended in 15 mL fresh SURF base medium without sodium bicarbonate, yeast extract, and trace minerals.

Five milliliters of this suspension was introduced into three separate electrochemical cells, already containing 50 mL SURF base medium (excluding sodium bicarbonate, yeast extract, and trace minerals), after the abiotic current was stabilized to a steady baseline. The electrochemical cell was continuously purged with 100% purified compressed air, and chronoamperometry was performed with the working electrode poised at −0.012 V vs. SHE. After cyclic voltammetry was completed at a scan rate of 1 mV/s, chronoamperometric measurement was resumed at −0.012 V vs. SHE, and ∼10.7 mM potassium cyanide was added after ∼1.75 h. Cell densities were determined by plate counts.

Bacillus sp. (designated strain WE4-1A1-BC) was grown aerobically to stationary phase from frozen stocks (−80°C in 20% glycerol) in R2A media and the culture was used to inoculate 500 mL of SURF base medium at 1% (v:v). After reaching mid-exponential phase, the culture was pelleted by centrifugation at 7,000 × g for 10 min, washed two times and resuspended in 10 mL fresh SURF base medium without sodium acetate. A total of 5 mL of the suspension was introduced into the electrochemical cell, containing 50 mL SURF base medium augmented with sodium acetate (5 mM), after the abiotic current was stabilized to a steady baseline. The electrochemical cell was continuously purged with N_2 to maintain anaerobic conditions, and chronoamperometry was performed with the working electrode poised at +0.53 V vs. SHE. Cell densities were determined by plate counts. The reproducibility of the experiment was tested in triplicates.

Microscopy

For scanning electron microscopy (SEM), electrode samples were fixed overnight in 2.5% glutaraldehyde. Samples were then subjected to an ethanol dehydration series (25, 50, 75, 90, and 100% v/v ethanol for 15 min each treatment) and critical point drying (Autosamdri 815 critical point drier, Tousimis Inc., Rockville, MD, USA). The samples were then mounted on aluminum stubs, coated with gold (Sputter coater 108, Cressington Scientific), and imaged at 5 keV using a JEOL JSM 7001F low vacuum field emission SEM.

RESULTS AND DISCUSSION

In situ Current Response and Active Microbial Community Composition

Large negative currents were detected on both WE1 and WE2, −276.68 ± 43.80 μA and −168.76 ± 26.82 μA, respectively, consistent with the expected cathode oxidation conditions. While significantly smaller in magnitude, negative currents were also detected on WE3 and WE4 at higher (nominally anodic) potentials (**Table 2**). It is important to note that the currents observed in the ISEC reactor are a combination of both biotic and abiotic redox reactions occurring on electrode surfaces. Dissolved oxygen of the SURF 3A liquid varied decreased from 3.79 mg/L to zero during the course of ISEC deployment causing oxygen leakage into the reactor and associated abiotic oxygen reduction currents. In May 2015 (during decommissioning of the ISEC reactor), ORP values of DUSEL 3A fluid and the effluent of the ISEC reactor were −50 mV (**Table 1**) and 200 mV (**Table 2**), respectively; confirming oxygen leakage inside the ISEC reactor. The dissolved organic carbon measured at SURF 3A hole during installation of ISEC was 239.04 ± 1.96 μM.

TABLE 2 | Mean current (last 40 days) observed at various redox potentials in the *in situ* electrochemical colonization (ISEC) reactor and aqueous water chemistry of ISEC reactor effluent.

Applied voltage	Average current (μA) ± standard deviation
−0.19 V vs. SHE	−276.68 ± 43.80
+0.01 V vs. SHE	−168.76 ± 26.82
+0.26 V vs. SHE	−0.15 ± 0.09
+0.53 V vs. SHE	−1.47 ± 0.11
ISEC reactor effluent aqueous chemistry	
pH	7.5
Temperature (°C)	19
Conductance (μS/cm)	11000
ORP (mV)	+200

Nucleic-acid analysis has proven to be effective for characterizing the phylogenetic, taxonomic, and functional structure of microbial assemblages. Since extracted DNA may originate from extracellular DNA pools, dead, and/or dormant cells, sequenced 16S rRNA genes represent the total microbial community rather than its active fraction. On the other hand, ribosomal RNA transcripts describe the active portion of the microbial community (Jansson et al., 2012) and hence, an RNA-based molecular approach was chosen for this study. Herein we present the taxonomic assignments in terms of relative percent of classified sequences with respect to the total number of sequences.

The *in situ* microbial community analyses determined by pyrosequencing the 16S rRNA transcripts, revealed that bacteria dominated DUSEL 3A fluid (99.65%). The bacterial sequences most closely matched the phyla *Proteobacteria* (83.23%), *Bacteroidetes* (10.14%), *Firmicutes* (0.50%), *Chloroflexi* (0.13%), *Planctomycetes* (0.003%). Some sequences (5.82%) did not match to any phyla and have been labeled as unclassified. Within *Proteobacteria*, the majority of sequences were identified as *Gammaproteobacteria* (26.03%), followed by unclassified *Proteobacteria* class (24.45%), *Deltaproteobacteria* (17.78%), *Alphaproteobacteria* (10.30%), and *Betaproteobacteria* (4.66%) (**Figure 2**). The archaeal community in DUSEL 3A fluid was dominated by sequences related to *Crenarchaeota* (0.19%), *Euryarchaeota* (0.13%), and *Thaumarchaeota* (0.03%). In a DNA-based study, Osburn et al. (2014) also observed a predominance of Bacteria over Archaea in the *in situ* fluid at the 4,850-ft level of SURF. They further observed a higher abundance of *Firmicutes*, which we attribute to the DNA- vs. RNA-based microbial community analysis because this phylum has been shown to experience dormancy through sporulation. Additionally, this difference can also arise from the *Firmicutes* exhibiting large 16S rRNA gene copy number (Větrovsk and Baldrian, 2013).

Importantly, the active microbial community structure revealed some shifts between the DUSEL 3A *in situ* fluid

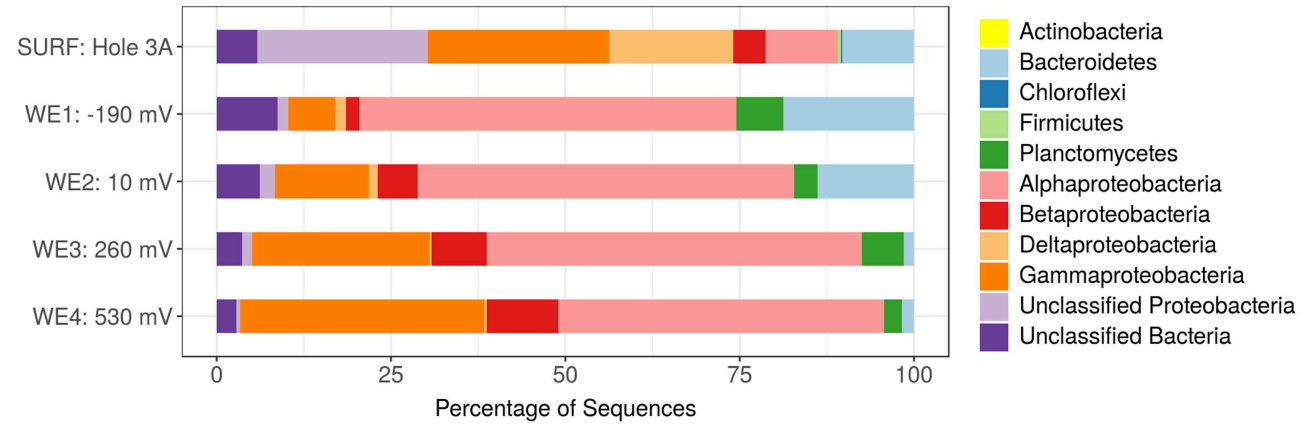

FIGURE 2 | Phylum classification of the active *in situ* bacterial community of DUSEL 3A fluid (labeled SURF: Hole 3A) and the four separate working electrodes in the *in situ* electrochemical colonization (ISEC) reactor (labeled WE1-WE4). The unclassified (e.g., putatively novel microbiota) were relatively more abundant at the reducing potential (−0.19 V vs. SHE) where bacteria use the electrode as the electron donor.

and the electrode-attached biofilms of the ISEC reactor. The majority of sequences obtained from electrode-attached biomass of ISEC working electrodes were most closely related to the *Proteobacteria*, specifically the *Alphaproteobacteria* (46.75–54.03%), *Gammaproteobacteria* (6.68–35.96%), *Betaproteobacteria* (1.98–10.24%), unclassified (0.57–2.17%), and *Deltaproteobacteria* (0.29–1.54%). The increased relative abundance of sequences identified as *Gammaproteobacteria* and *Betaproteobacteria* was observed with increasing electrode potential. The overall relative abundance of sequences related to *Planctomycetes* phylum substantially increased from the DUSEL 3A fluid (0.003%) to ISEC working electrodes (3–6%). On the other hand, the relative abundance of sequences identified as *Chloroflexi* and *Firmicutes* phyla decreased from 0.13 and 0.49% to 0.001 and 0.002%, respectively. The relative abundance of sequences related to *Bacteroidetes* from the electrode-attached biofilm (across different working electrodes) of the ISEC reactor ranged from 1.45 to 18.76% and unclassified OTUs at the phyla level ranged from 2.83 to 8.72%. The ISEC reactor captured the majority of the bacterial community, but some members, including *Methanobacteria*, unclassified *Clostridia*, *Methylophilaceae*, and *Moraxellaceae*, were not represented. These populations were originally present in low abundances (<0.13%) in DUSEL 3A fluid. Suspected oxygen leakage into the ISEC reactor potentially hindered the survival of obligate anaerobes belonging to the class *Methanobacteria* and *Clostridia* (Dworkin and Falkow, 2006). Many OTUs which were unclassified (at the phylum level) along with *Bacteroidetes* and *Alphaproteobacteria* favored the lower potential electrodes; this observation highlights the potential for largely uncharacterized microbial lineages to perform extracellular electron uptake in subsurface environments. Within the sequences classified as Archaea, the phylum *Thaumarchaeota* (ammonia-oxidizing *Candidatus Nitrosoarchaeum*) was identified on all ISEC working electrodes. However, *Crenarchaeota* sequences (0.002%) were only present at an electrode potential of −0.19 V. It is important to note the universal primers (515F and 806R) employed in this study may underestimate the diversity of archaea present in the environment and primers specific for archaeal domain should be employed (Bahram et al., 2019).

Based on the 16S rRNA sequencing data, the bacterial communities of the electrode attached biofilms demonstrated potential-dependent distribution patterns (**Figure 3**). Below we discuss these patterns in light of previously reported physiotypes. However, we stress that the presence of specific lineages on electrodes is not in itself evidence of EET, since poised electrodes may support microbial consortia capable of diverse metabolisms, including syntrophy, heterotrophy or fermentation, depending on the microenvironment formed at the electrodes. This makes isolation and electrochemical characterization fundamental to confirming and investigating EET processes from the electrode-attached biofilm community.

At a potential of −0.19 V (WE1), chosen to mimic sulfur oxidation, the electrode was dominated by sequences closely related to the families *Bdellovibrionaceae, Chitinophagaceae, Flavobacteraceae, Legionellaceae, Patulibacteraceae, Psuedomonadaceae, Saprospiraceae, Solimonas, Sphingomonadaceae, Xanthomonadaceae,* and unclassified *Desulfuromonadales* (**Figure 3A**). Consistent with this, members of *Flavobacterium* (within the *Flavobacteraceae* family) have been shown to attach to and metabolize sulfur minerals, and this has been postulated to create micro-oxic environments for sulfur oxidizers (Wright et al., 2013). Some *Flavobacteria* genera have also co-existed with mat-forming neutrophilic iron oxidizers (Fleming et al., 2014), and some Mn-oxidizing strains belonging to *Flavobacterium* have been isolated from caves of upper Tennessee river basin (Carmichael et al., 2013). A *Pseudomonas/Pseudoalteromonas*-like *Gammaproteobacteria* was previously shown to putatively catalyze iron(II) oxidation under micro-aerobic conditions, isolated from volcanic seamount (Sudek et al., 2009), which may contribute to the formation of iron mats in

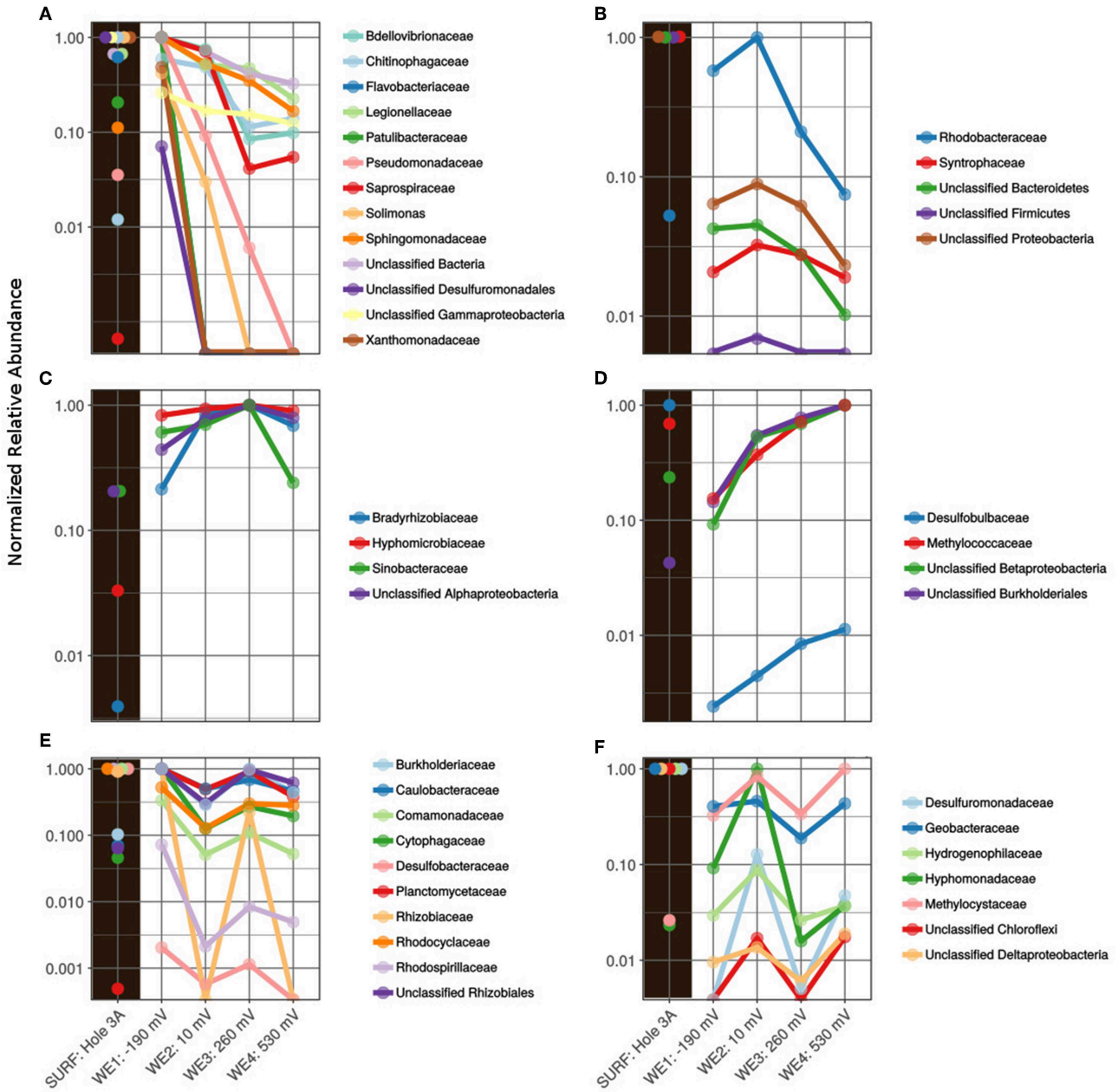

FIGURE 3 | Active family-level normalized relative abundance of bacterial community present in the *in situ* electrochemical colonization (ISEC) reactor sorted by poised electrodes: **(A)** maximum at WE1: −0.19 V vs. SHE, **(B)** maximum at WE2: +0.01 V vs. SHE, **(C)** maximum at WE3: + 0.26 V vs. SHE, **(D)** maximum at WE4: +0.53 V vs. SHE, **(E)** maximum at WE1 and WE3, and **(F)** maximum at WE2 and WE4, with reference to the inoculum-fluid of SURF DUSEL 3A (labeled as SURF: Hole 3A).

the deep marine subsurface. Other lineages captured at this potential included *Patulibacteraceae, Saprospiraceae, Chitinophagaceae, Sphingomonadaceae,* and *Solimonas,* each putatively containing aerobic respiratory metabolism among their members (Saddler and Bradbury, 2005; Takahashi et al., 2006; Glaeser and Kämpfer, 2014; Kim et al., 2014; McIlroy and Nielsen, 2014; Rosenberg, 2014). The potential +0.01 V vs. SHE (WE2), chosen to mimic iron oxidation, favored the colonization of members from bacterial families *Rhodobacteraceae*, *Syntrophaceae*, and many OTUs were identified as unclassified at the phyla level (**Figure 3B**). The *Rhodobacteraceae* family has been widely studied to understand banded iron formation in early Earth (Kappler et al., 2005; Hegler et al., 2008). The abundance of many unclassified from the *Desulfuromonadales*, *Gammaproteobacteria*, *Bacteroidetes*, *Firmicutes*, and *Proteobacteria* at the lower electrode potentials highlights the importance of alternate sources of reducing power available in the subsurface. The families *Bradyrhizobiaceae* and

Hyphomicrobiaceae, were predominantly abundant on WE3 poised at +0.26 V vs. SHE (**Figure 3C**). Sequences related to mesophilic sulfate-reducing *Desulfobulbaceae* (Kuever, 2014) and type 1 methanotrophic *Methylococcaceae* (Bowman, 2014) were relatively dominant on WE4 poised at +0.53 V vs. SHE, which was chosen to mimic manganese reduction (**Figure 3D**).

Some microbes adapt to broad ranges of environments ("habitat generalists") as their key survival strategy, while others specialize in certain niches ("habitat specialists") (Tienderen and Van, 1991). In this study, we observed that some bacterial populations colonized working electrodes specific to a particular habitat—low and high electrode potential (**Figures 3E,F**, respectively). Among these, members of the bacterial families *Comamonadaceae*, *Rhodocyclaceae*, *Burkholderiaceae*, *Caulobacteraceae, Hyphomonadaceae, Hydrogenophilaceae*, *Desulfobacteraceae*, *Desulfuromonadaceae*, *Geobacteraceae*, have been shown to interact with minerals (Lovley, 1991). *Rhodoferax ferrireducens* sp. Strain T118^T, a member of the *Comamonadaceae* family, can support growth by oxidizing acetate with iron(III) reduction (Finneran et al., 2003). Also, novel strains from the *Delftia* genus (*Comamonadaceae*) and *Azonexus* (*Rhodocyclaceae*) were demonstrated to donate electrons to poised electrodes (+0.522 V vs. SHE) in anaerobic conditions (Jangir et al., 2016). A member of the *Burkholderiaceae* family, metallophilic gram-negative *Cupriavidus metallidurans,* has demonstrated to actively biomineralized particulate Au (Reith et al., 2009). *Desulfuromonadaceae* family contains members are capable of sulfur and Fe(III) reduction (Greene, 2014), and more recently *Desulfuromonas soudanensis* WTL was isolated using electrochemical enrichments from anoxic deep subsurface brine (Badalamenti et al., 2016) with 38 multiheme cytochromes. In this study, the relative predominance of *Desulfuromonadaceae* at lower and higher potentials indicates their ability to survive/grow in niches (**Figure 3F**). Finally, *Geobacteraceae*, consisting of the widely studied genus *Geobacter*, has been documented to putatively reduce insoluble Fe(III) and Mn(IV) (Röling, 2014) and mimicked on electrodes for anode reduction (Bond and Lovley, 2003). This group has also been shown to uptake electron from graphite electrodes coupled with anaerobic respiration (Gregory et al., 2004).

To summarize, the ISEC reactor captured a wide range of metabolically active bacteria, including (but not exclusively) well-studied groups, such as *Geobacteraceae,* shown to be capable of microbe-mineral interactions in earlier studies.

Current Production and Microbial Community Composition in Laboratory Electrochemical Enrichment

After 5 months of *in situ* colonization at SURF, sections of biomass-containing electrodes from ISEC reactor were transferred to laboratory electrochemical reactors. Within 8 days, currents developed on both cathodic (−0.19 and +0.01 V vs. SHE) and anodic potentials (+0.26 and +0.53 V vs. SHE), which will be henceforth named as cathodic current (transfer of electrons from electrode to microbe) and anodic current (transfer of electrons from microbe to electrode). Since the WE3 (+0.26 V vs. SHE) was lost due to an electrical short between the counter and the working electrode on the 42nd day of laboratory incubation, further analysis was performed only on WE1, WE2, and WE4 of the laboratory electrochemical enrichments. The average currents (for the last media change) corresponding to WE1 and WE4 were −43.46 ± 7.76 μA, −0.83 ± 0.06 μA, and 582.56 ± 63.14 μA, respectively (**Figure 4**). Separate incubation with sterile media under identical operating conditions (abiotic control) resulted in an average current of −24.976 ± 0.74 μA at WE1, −1.705 ± 0.128 μA at WE2, and 0.925 ± 0.23 μA at WE4. The observed cathodic or anodic currents from laboratory electrochemical enrichments at WE1 and WE4 were very large compared to the sterile controls demonstrating electron uptake and donation to poised electrodes via enriched microbes. However, the sterile (control) cathodic current at WE2 was higher than laboratory enrichments indicating that at this potential it is difficult to interpret the difference between the abiotic oxygen reduction with microbially mediated oxygen reduction at the electrode. Hence, cyclic voltammetry (CV) was performed to diagnose the reaction with a scan rate of at 10 mV/s on the biofilms of colonized electrodes of WE1, WE2, and WE4 and compared to the abiotic control (**Figure 4**). CV of electrode-attached biofilm at WE1 and WE2 revealed presence of reversible diffusion controlled peaks indicating presence of redox active mediators shown to enhance EET (Marsili et al., 2008; Von Canstein et al., 2008). CV of electrode-attached biofilm at WE4 revealed the classic sigmoidal shape (Torres et al., 2008) previously observed for pure EET-capable strains under turnover conditions, suggesting enrichment for biofilm containing electrode-bound, non-diffusing, redox enzymes capable of coupling oxidation of the electron donor (in this case acetate) to reduction of the electrode. Interestingly, the formal potential (as defined in Richter et al., 2009) of this biofilm as +0.2 V vs. SHE lies between the formal potential of *G. sulfurreducens* WT as −0.15 V vs. SHE (Richter et al., 2009) and the peak potential of outer-membrane cytochromes of *S. oneidensis* MR-1 as +0.21 V vs. SHE (Xu et al., 2016). The overall increase in the potentiostatic current, the difference in the biotic cyclic voltammogram (compared to abiotic control) and cell biomass on the electrodes observed through SEM image (**Figure 5**), point to the electrochemical enrichment of bacterial communities capable of electron transfer to/from the electrode.

The active bacterial community analysis of the laboratory electrochemical enrichments indicates growth of multiple unclassified bacterial phyla on reducing (cathodic) potentials, similar to the ISEC reactor (**Figure 6**). The dominance of *Desulfuromonadaceae* and *Geobacteraceae* observed at the most oxidizing (anodic) potential of +0.53 V vs. SHE (mimicking manganese reduction) (**Figure 6**) explains the high anodic current and the classic catalytic sigmoidal CV signature (Torres et al., 2008). Members of these families are capable of anaerobic respiration utilizing a variety of compounds as electron acceptors, including sulfur, Mn(IV), Fe(III), and poised electrodes (Lovley, 2006). Interestingly, *Comamonadaceae* and *Rhodocyclaceae* were present in all the poised electrodes suggesting an ability to transfer electrons to/from the poised electrodes. Many diverse bacterial families were enriched at the lower/reducing potentials −0.19 and +0.01 V vs. SHE mimicking sulfur and iron

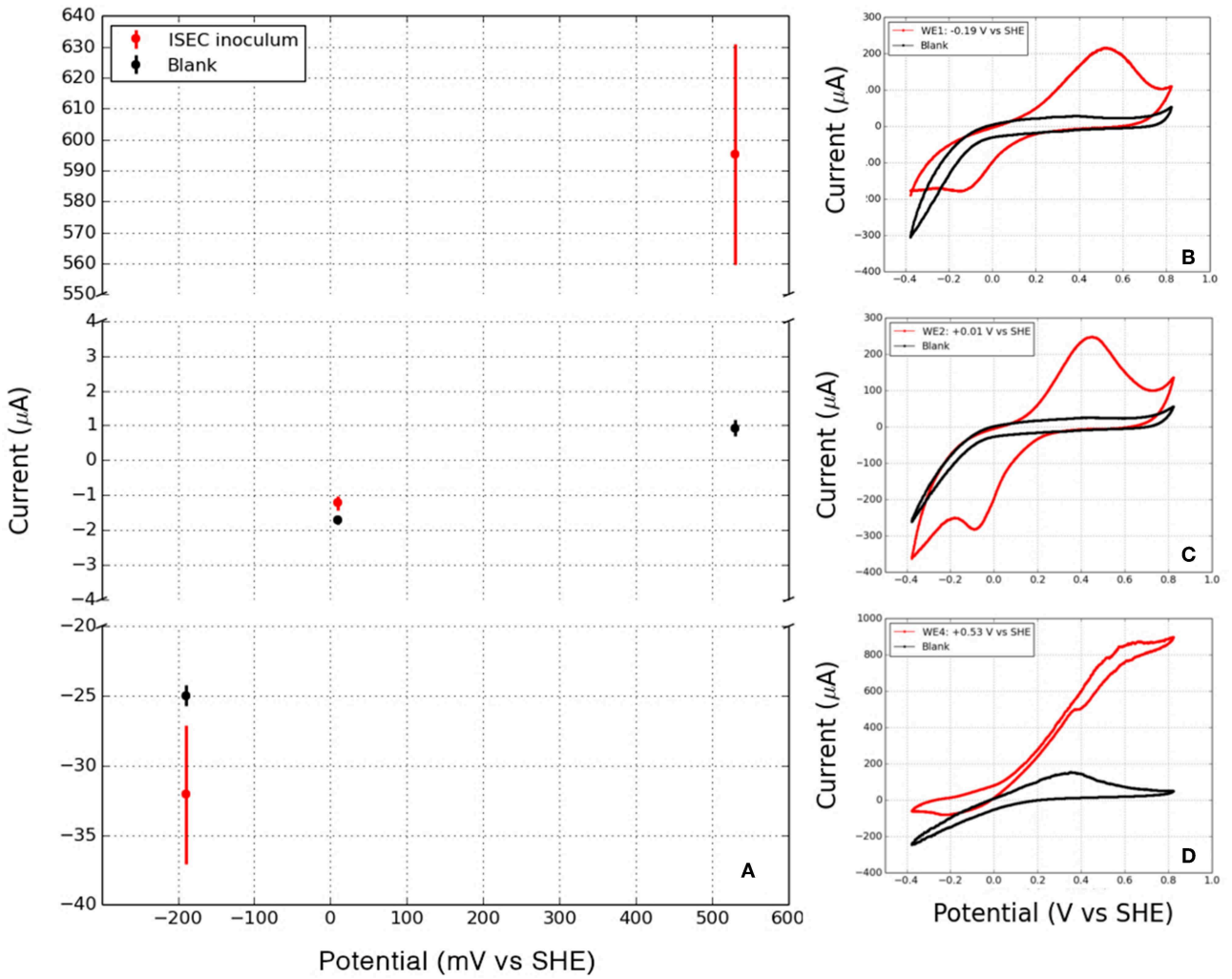

FIGURE 4 | (A) Mean cathodic and anodic currents observed in laboratory enrichments at WE1 (−0.19 V vs. SHE), WE2 (+0.01 V vs. SHE) and WE4 (+0.53 V vs. SHE). Cyclic voltammetry of the working electrodes (including attached biofilms) and the corresponding abiotic controls (blank) at various potentials: **(B)** WE1: −0.19 V vs. SHE, **(C)** WE2: +0.010 V vs. SHE, and **(D)** WE4: +0.53 V vs. SHE, points to redox activity mediated by the *in situ* microorganisms.

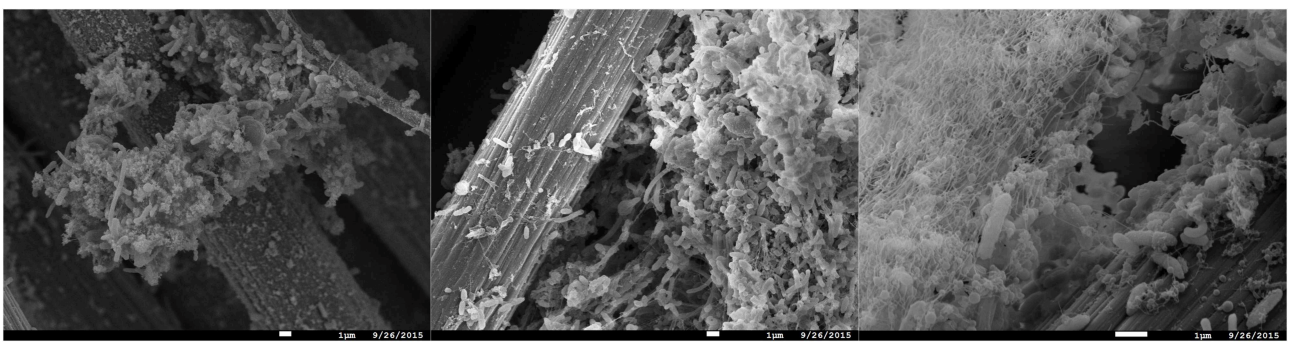

FIGURE 5 | Scanning electron micrograph of the enrichment electrode-associated biomass at WE1 at −0.19 V vs. SHE **(left)**, WE2 at +0.01 V vs. SHE **(center)**, and WE4 at 0.53 V vs. SHE **(right)** (scale = 1 μm).

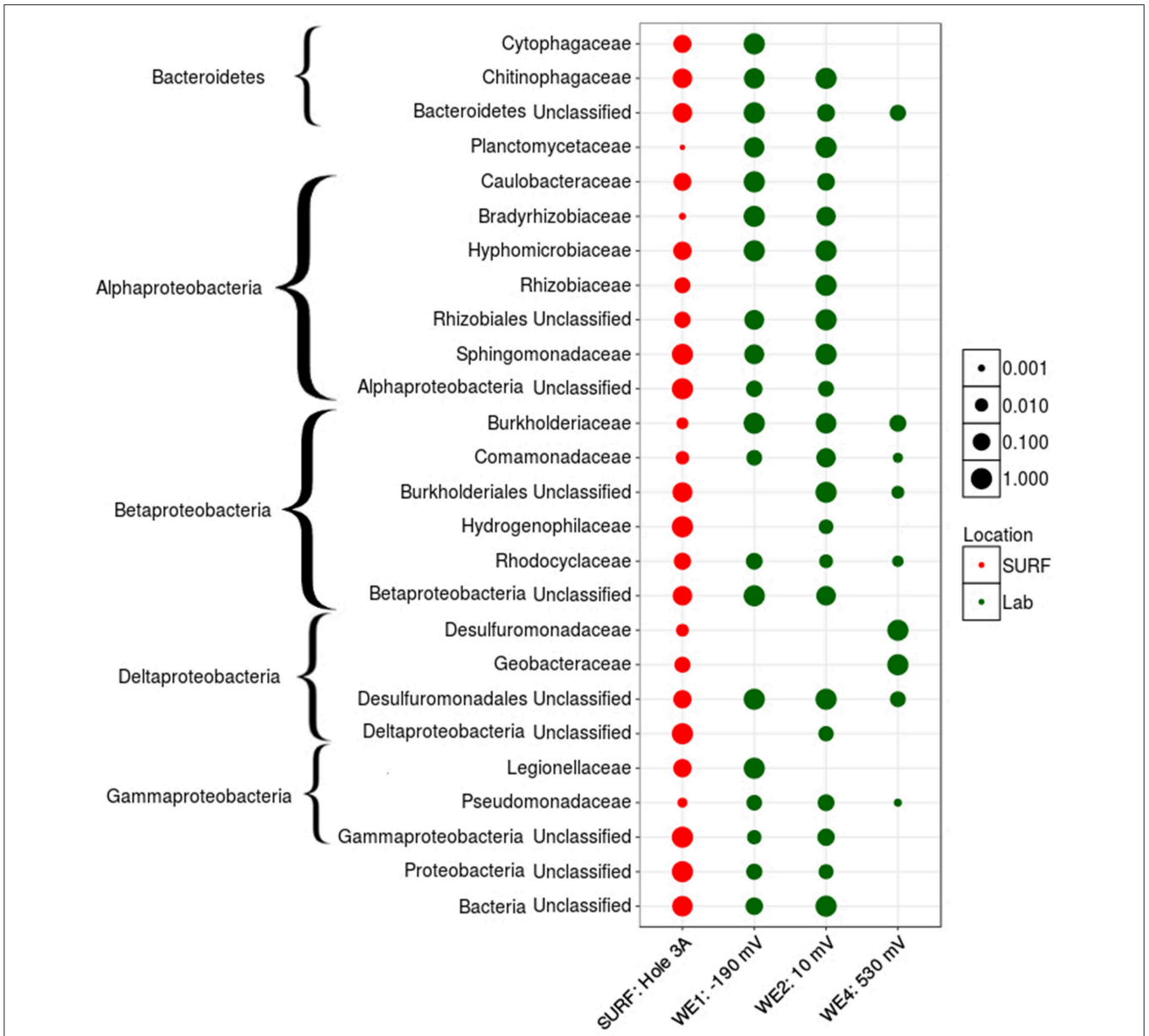

FIGURE 6 | Active family-level normalized relative abundance of bacterial community present in laboratory electrochemical enrichment. The size of the symbol represents the normalized relative abundance of that group across various habitat types (depicted by different colors).

oxidation) including the *Plactomycetaceae, Caulobacteraceae, Bradyrhizobiaceae, Hyphomicrobiaceae, Sphingomonadaceae,* and *Hydrogenophilaceae.* The higher diversity of subsurface organisms at lower potential electrodes, including those that could not be unclassified at the phyla level, stress the need for further experiments to investigate extracellular electron uptake pathways.

Microbial Community Structure Diversity Measurements

The observed richness (number of OTUs) decreased from the source with various electrochemical enrichments (**Figure 7**). Nevertheless, ISEC was able to capture at least 50% of the observed OTUs at DUSEL 3A. Based on Shannon's diversity index, there was only weak statistical evidence (Welch Two Sample *T*-test) of similarities in microbial community structures between DUSEL 3A and ISEC ($t = 3.2394$, $p = 0.04235$) or between DUSEL 3A and laboratory enrichment ($t = 3.2527$, $p = 0.07365$). It is interesting to note that the bacterial community attached to electrode poised at +0.01 V vs. SHE (mimicking iron oxidation) has consistent higher Shannon diversity index than the communities on differently poised electrodes. OTU evenness remains constant from DUSEL 3A to ISEC and laboratory enrichment (except for the laboratory electrode poised at +0.53 V vs. SHE). The consistent lower alpha diversity of biofilm enriched

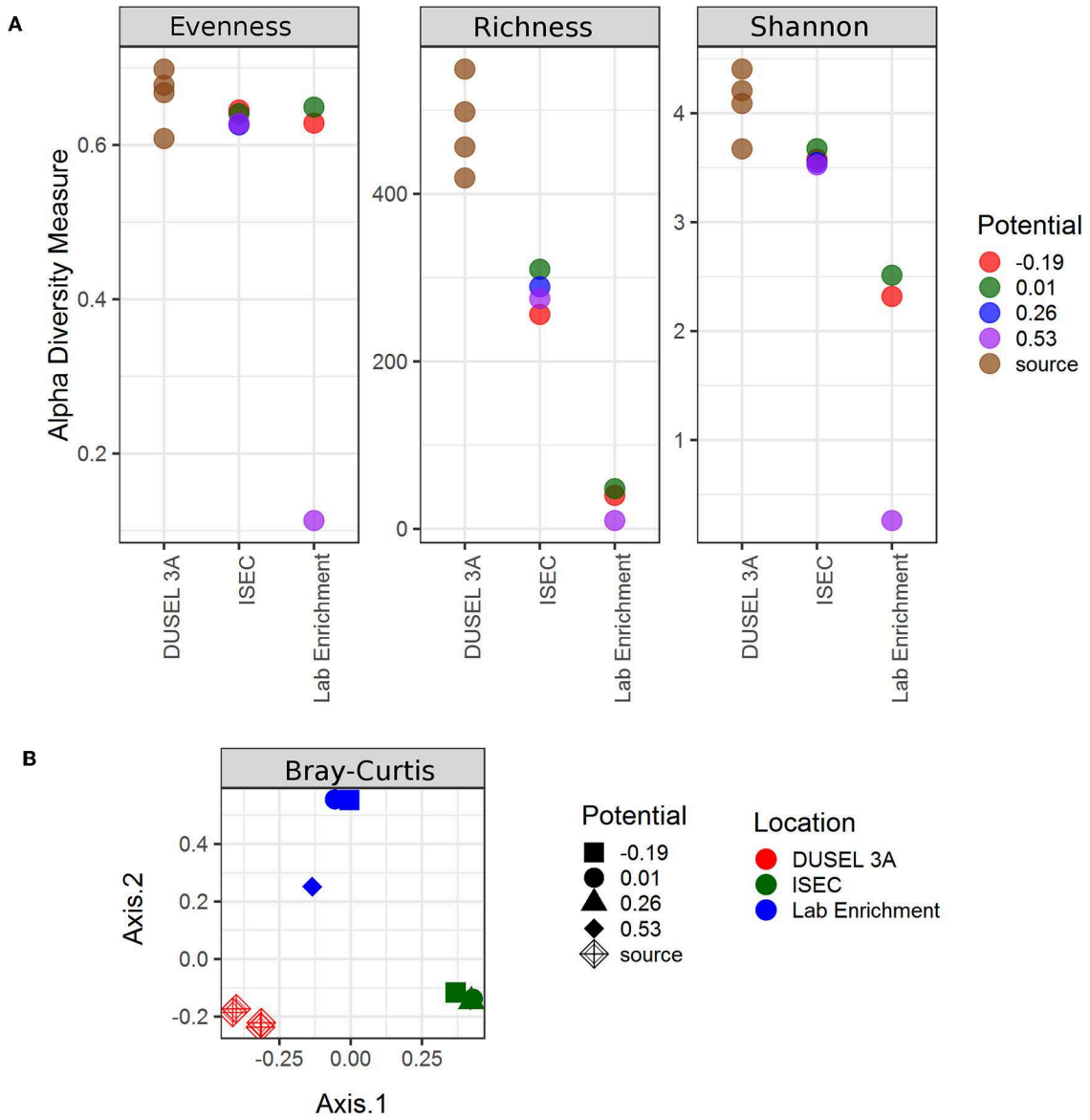

FIGURE 7 | Alpha and beta diversity indices evaluated for the samples. Both the indices point to variation in the microbial community structure from ISEC to lab electrochemical enrichment. **(A)** Estimates of evenness, richness, and Shannon diversity index of the microbial community as a function of location. **(B)** Multidimensional scaling plot evaluated using Bray–Curtis method to the clustering of the microbial community based on location.

on the electrode poised at +0.53 V vs. SHE (laboratory) is likely due to the fact that acetate was the only energy source provided. Multidimensional scaling (via PCoA analysis), evaluated using various methods, points to clustering based on enrichment (**Figure 7**). Further Adonis tests performed on Bray-Curtis points to variation with each enrichment step [$R^2 = 0.54918$, $\Pr(>F) = 0.001$].

Isolation and Electrochemical Characterization of Isolated Strains

Bacterial strains were isolated as pure cultures originating from the biomass associated with WE1 (0.19 V vs. SHE) and WE4 (+0.53 V vs. SHE). Phylogenetic analyses of the 16S rRNA gene sequences demonstrated that these strains belonged to the genera *Bacillus, Anaerospora, Cupriavidus, Azonexus, and Comamonas*. While *Bacillus, Anaerospora, Cupriavidus*, and *Azonexus* were isolated from WE4 (+0.53 V vs. SHE), two strains of *Comamonas* were isolated from both WE1 (−0.19 V vs. SHE) and WE4 (+0.53 V vs. SHE). *Bacillus*, *Anaerospora,* and *Comamonas* were isolated on heterotrophic media R2A. Whereas, *Cupriavidus* and *Azonexus* were enriched as iron-reducers on Fe(III)-NTA and poorly crystalline iron oxide, respectively (Lovley, 1991). Further electrochemical studies were performed on isolated *Comamonas* sp. (strain WE1-1D1) from WE1 (−0.19 V vs. SHE) and *Bacillus* sp. (strain WE4-1A1-BC) from WE4 (+0.53 V vs. SHE).

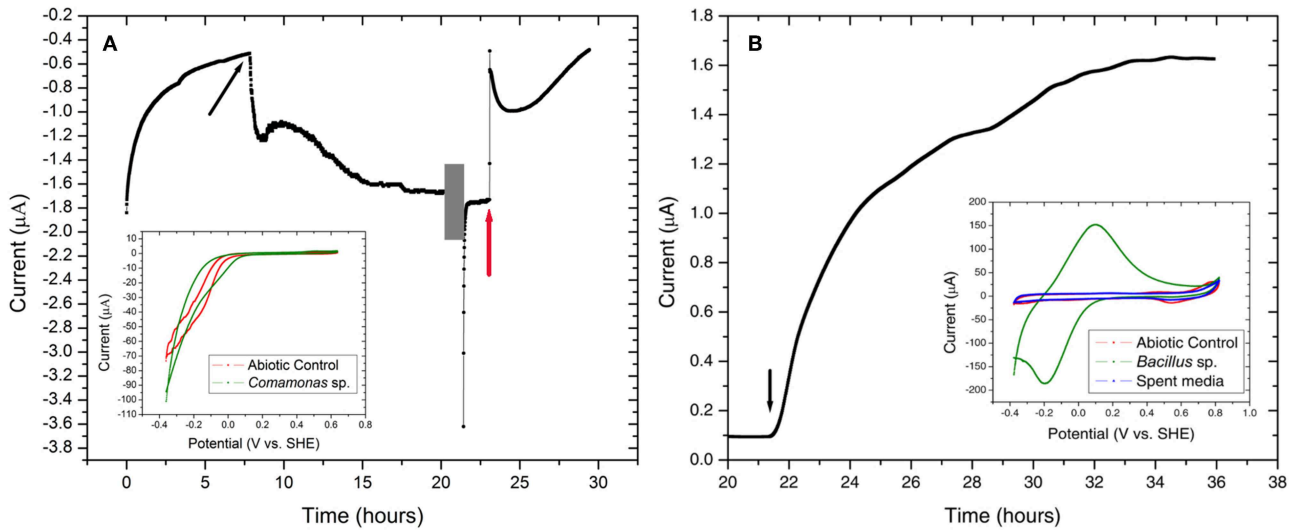

FIGURE 8 | Chronoamperometry of the isolated strains **(A)** *Comamonas* sp. (strain WE1-1D1) and **(B)** *Bacillus* sp. (strain WE4-1A1-BC) grown at −0.012 V vs. SHE and +0.53 V vs. SHE, respectively. **(A)** An increase in cathodic current was observed with the addition of *Comamonas* sp. (strain WE1-1D1) (black arrow) to the electrochemical cell. At 20 h (gray box), CV (inset) was performed on the electrode-attached biofilm and potassium cyanide was injected at 23 h (red arrow). **(B)** *Bacillus* sp. (strain WE4-1A1-BC) was enriched on working electrode poised at +0.53 V vs. SHE with acetate as the electron donor and carbon source. Black arrow indicates the time point when the bioreactor was inoculated with the cells. Cyclic voltammogram of the abiotic control, electrode-attached biofilm and the spent media is shown in the inset.

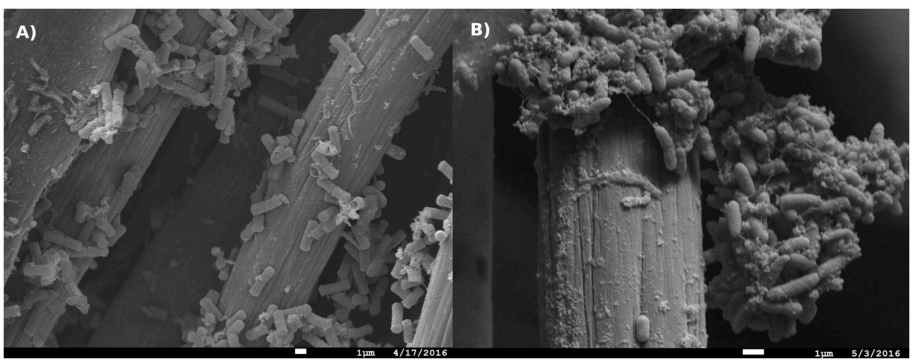

FIGURE 9 | Scanning electron micrograph of **(A)** *Bacillus* sp. (strain WE4-1A1-BC) and **(B)** *Comamonas* sp. (strain WE1-1D1) biomass associated with the working electrodes (Scale = 1 μm).

Both gram-negative *Comamonas* and gram-positive *Bacillus* have previously been reported in microbial fuel cell communities. While the genus *Comamonas* has been previously enriched on both cathodic and anodic communities of microbial fuel cells (Xing et al., 2010; Ishii et al., 2012; Sun et al., 2012), the genus *Bacillus* has only been reported from anodic communities (Nimje et al., 2009; Ismail and Jaeel, 2013; Tang et al., 2014). Some species of these genera are capable of interacting with minerals. The *Comamonas* sp. strain IST-3 oxidizes Fe(II) for energy gain (Blöthe and Roden, 2009) and *Bacillus* can reduce Fe(III) but without conserving energy through this interaction (de Castro and Ehrlich, 1970).

Comamonas sp. (designated strain WE1-1D1) was studied in a half-cell reactor for electron uptake at working potential of −0.012 V vs. SHE. The media was constantly purged with 100% purified compressed air to supply oxygen as the electron acceptor. Upon inoculation of *Comamonas* sp. (designated strain WE1-1D1) to the reactors, the cathodic current (electron uptake from electrodes) increased from −0.51 to −1.67 μA (**Figure 8**), the planktonic cell density increased from $7 \pm 1 \times 10^8$ to $2 \pm 1 \times 10^9$ CFU/mL and SEM images confirmed cellular attachment with the formation of a monolayer biofilm on the WE (**Figure 9**). To further validate electron uptake by the strain, potassium cyanide (an electron transport chain inhibitor) was added resulting in the collapse of the cathodic current (**Figure 8**). Cyclic voltammetry shows a catalytic wave (reflecting cathode oxidation) with an onset potential of 50–100 mV (**Figure 8**). Taken together, the rise in the planktonic cell

density, increase in the cathodic current, and presence of cells on the WE (**Figure 9**), point to electron uptake from the poised electrode by *Comamonas* sp. (strain WE1-1D1). Previously, electrochemical studies performed on the mineral oxidizing bacteria show a diversity of EET mechanisms (Summers et al., 2013; Bose et al., 2014; Deutzmann et al., 2015; Ishii et al., 2015; Rowe et al., 2015). Further characterization of the isolate is essential in understanding its potential for EET and pinpoint the mechanisms.

Bacillus sp. (strain WE4-1A1-BC) was studied in a half-cell reactor with working electrode poised at +0.53 V vs. SHE. Upon inoculation of *Bacillus* sp. (strain WE4-1A1-BC) to the electrochemical reactors, the anodic current rose from 0.1 to 1.6 μA (**Figure 8**) and SEM images confirmed cellular attachment with the formation of a monolayer biofilm (**Figure 9**). The total planktonic cell density decreased from $2 \pm 1 \times 10^8$ to $4 \pm 1 \times 10^6$ CFU/mL indicating possible cell lysis as free planktonic cells. Cyclic voltammetry shows a reversible peak centered at 0 V vs. SHE in the biofilm-associated working electrode. To study whether this peak arose from any soluble redox mediators released by the organism, cyclic voltammetry was performed on the spent media (planktonic cells were spun down 15× at 7,000 × g). Cyclic voltammogram of the spent media also lacked the reversible peak indicating that redox components bound to the gram-positive bacteria (**Figure 8**) were responsible for EET. Furthermore, HPLC measurements, as described previously (Bretschger et al., 2010), confirmed a decrease in acetate concentration by 0.8 mM (12%) in 13 h. Based on these measurements, the coulombic efficiency was calculated as 1.81% using the ratio of the total coulombs produced during the experiment to the theoretical amount of coulombs assuming oxidation of acetate to CO_2. In comparison, coulombic efficiency of a well-known electrode reducer *S. oneidensis* MR-1 for electricity generation from lactate (to acetate) is ∼20% (Watson and Logan, 2010). Taken collectively, the overall increase in anodic current, reduction in acetate concentration, the shift in biotic cyclic voltammogram relative to abiotic CV, and presence of cells on the WEs (**Figure 9**), suggest that *Bacillus* sp. (strain WE4-1A1-BC) is capable of electron transfer to the poised electrode. Additional genetic and physical studies are required to investigate the precise EET mechanism from this strain.

CONCLUSIONS

Our results highlight the potential for poised electrodes to serve as *in situ* observatories to capture for further downstream studies electrochemically active microbes in the deep terrestrial subsurface. The *in situ* electrodes deployed at the SURF captured many families represented in the borehole fluid, while also showing potential-dependent clear shifts in the relative abundance of specific lineages. Although the ISEC reactor electrodes were poised to mimic sulfur oxidation, iron oxidation and manganese reduction, the microbial community structure pointed to sequences matching families capable of diverse metabolisms, likely reflecting interactions within and across the microbial communities colonizing separate electrochemical niches in the single cultivation vessel. Since downstream laboratory incubations were performed in separate electrochemical cells with different environmental conditions, the microbial structure of the anode-attached biofilms differed significantly from the cathode-attached biofilm. Using this workflow we were able to separately enrich and ultimately isolate cathode-oxidizing and anode-reducing microbes originating from the same environment. Further genetic and physical studies are needed to elucidate the mechanisms responsible for EET in the isolated strains.

DATA AVAILABILITY STATEMENT

The datasets generated for this study can be found in the NCBI Accession numbers: SRR8537881, SRR8537882, MK483257, and MK483258.

AUTHOR CONTRIBUTIONS

ME-N, JA, and YJ: conception or design of the work. YJ, BR, GW, and CA: field work. YJ, AK, NB, and LZ: data collection. YJ and ME-N: data analysis and interpretation. YJ and ME-N: drafting the article. ME-N, JA, and BR: critical revision of the article.

FUNDING

This work was supported by the NASA Astrobiology Institute (Life Underground project) under cooperative agreement NNA13AA92A. AK and NB were supported by the National Science Foundation DIMENSIONS grant DEB-1542527 for electrochemical characterization of the isolated strains.

ACKNOWLEDGMENTS

We acknowledge the science and support staff at SURF, including Jaret Heise, Tom F. Regan, Kathy Hart, and Oren T. Loken, for mine access, reactor deployment, and facilitating sample collection. We are also grateful to Oxana Gorbantenko and Forrest Cain, of Black Hills State University, for monitoring the ISEC reactor during the extended deployment. In addition, we acknowledge Duane Moser, Ken Nealson, Magdalena Osburn, Douglas LaRowe, Shuai Xu, Pratixaben Savalia, Lina Bird, and Annette Rowe for providing their valuable input. Scanning Electron Microscopy was performed at the University of Southern California's Core Center of Excellence in Nanoscale Imaging. This manuscript has been released as a pre-print at bioRxiv (Jangir et al., 2019).

REFERENCES

Bach, W., and Edwards, K. J. (2003). Iron and sulfide oxidation within basalt ocean crust: implications for chemolithoautotrophic microbial biomass production. *Geochim. Cosmochim. Acta* 67, 3871–3887. doi: 10.1016/S0016-7037(03)00304-1

Badalamenti, J. P., Summers, Z. M., Chan, C. H., Gralnick, J. A., and Bond, D. R. (2016). Isolation and genomic characterization of 'Desulfuromonas soudanensis WTL', a metal- and electrode-respiring bacterium from anoxic deep subsurface brine. *Front. Microbiol.* 7:913. doi: 10.3389/fmicb.2016.00913

Bahram, M., Anslan, S., Hildebrand, F., Bork, P., and Tedersoo, L. (2019). Newly designed 16S rRNA metabarcoding primers amplify diverse and novel archaeal taxa from the environment. *Environ. Microbiol. Rep.* 11, 487–494. doi: 10.1111/1758-2229.12684

Beese-Vasbender, P. F., Nayak, S., Erbe, A., Stratmann, M., and Mayrhofer, K. J. J. (2015). Electrochemical characterization of direct electron uptake in electrical microbially influenced corrosion of iron by the lithoautotrophic SRB Desulfopila corrodens strain IS4. *Electrochim. Acta* 167, 321–329. doi: 10.1016/j.electacta.2015.03.184

Blöthe, M., and Roden, E. E. (2009). Microbial iron redox cycling in a circumneutral-pH groundwater seep. *Appl. Environ. Microbiol.* 75, 468–473. doi: 10.1128/AEM.01817-08

Bond, D. R. (2010). "Electrodes as electron acceptors, and the bacteria who love them," in *Geomicrobiology: Molecular and Environmental Perspective*, eds L. Barton, M. Mandl, and A. Loy (Dordrecht: Springer), 385–399. doi: 10.1007/978-90-481-9204-5_18

Bond, D. R., Holmes, D. E., Tender, L. M., and Lovley, D. R. (2002). Electrode-reducing microorganisms that harvest energy from marine sediments. *Science* 295, 483–485. doi: 10.1126/science.1066771

Bond, D. R., and Lovley, D. R. (2003). Electricity production by geobacter sulfurreducens attached to electrodes electricity production by *Geobacter sulfurreducens* attached to electrodes. *Appl. Environ. Microbiol.* 69, 1548–1555. doi: 10.1128/AEM.69.3.1548-1555.2003

Bose, A., Gardel, E. J., Vidoudez, C., Parra, E. A., and Girguis, P. R. (2014). Electron uptake by iron-oxidizing phototrophic bacteria. *Nat. Commun.* 5:3391. doi: 10.1038/ncomms4391

Bowman, J. P. (2014). "The family Methylococcaceae," in *The Prokaryotes*, eds E. Rosenberg, E. F. DeLong, S. Lory, E. Stackebrandt, and F. Thompson (Berlin; Heidelberg: Springer), 411–440. doi: 10.1007/978-3-642-38922-1_237

Bretschger, O., Cheung, A. C. M., Mansfeld, F., and Nealson, K. H. (2010). Comparative microbial fuel cell evaluations of *Shewanella* spp. *Electroanalysis* 22, 883–894. doi: 10.1002/elan.200800016

Caddey, S. W., Bachman, R. L., Campbell, T. J., Reid, R. R., and Otto, R. P. (1991). *The Homestake Gold Mine, an Early Proterozoic Iron-Formation-Hosted Gold Deposit*. Lawrence County, SD: Bulletin. Available online at: https://pubs.er.usgs.gov/publication/b1857J (accessed April 19, 2018).

Caporaso, J. G., Lauber, C. L., Walters, W. A., Berg-Lyons, D., Lozupone, C. A., Turnbaugh, P. J., et al. (2011). Global patterns of 16S rRNA diversity at a depth of millions of sequences per sample. *Proc. Natl. Acad. Sci. U.S.A.* 108 (Suppl. 1), 4516–4522. doi: 10.1073/pnas.1000080107

Carmichael, M. J., Carmichael, S. K., Santelli, C. M., Strom, A., and Auer, S. L. B. (2013). Mn(II)-oxidizing bacteria are abundant and environmentally relevant members of ferromanganese deposits in caves of the upper tennessee river basin. *Geomicrobiol. J.* 30, 779–800. doi: 10.1080/01490451.2013.769651

Carmona-Martínez, A. A., Harnisch, F., Kuhlicke, U., Neu, T. R., and Schröder, U. (2013). Electron transfer and biofilm formation of *Shewanella putrefaciens* as function of anode potential. *Bioelectrochemistry* 93, 23–29. doi: 10.1016/j.bioelechem.2012.05.002

de Castro, A. F., and Ehrlich, H. L. (1970). Reduction of iron oxide minerals by a marine Bacillus. *Antonie Van Leeuwenhoek* 36, 317–327. doi: 10.1007/BF02069033

Deutzmann, J. S., Sahin, M., and Spormann, A. M. (2015). Extracellular enzymes facilitate electron uptake in biocorrosion and bioelectrosynthesis. *MBio* 6, e00496–e00415. doi: 10.1128/mBio.00496-15

Dworkin, M., and Falkow, S. (2006). *The Prokaryotes: A Handbook on the Biology of Bacteria*. New York, NY: Springer. doi: 10.1007/0-387-30743-5

Edgar, R. C., Haas, B. J., Clemente, J. C., Quince, C., and Knight, R. (2011). UCHIME improves sensitivity and speed of chimera detection. *Bioinformatics* 27, 2194–2200. doi: 10.1093/bioinformatics/btr381

Edwards, K. J., Bach, W., and McCollom, T. M. (2005). Geomicrobiology in oceanography: microbe-mineral interactions at and below the seafloor. *Trends Microbiol.* 13, 449–456. doi: 10.1016/j.tim.2005.07.005

Fedorovich, V., Knighton, M. C., Pagaling, E., Ward, F. B., Free, A., and Goryanin, I. (2009). Novel electrochemically active bacterium phylogenetically related to *Arcobacter butzleri*, isolated from a microbial fuel cell. *Appl. Environ. Microbiol.* 75, 7326–7334. doi: 10.1128/AEM.01345-09

Finneran, K. T., Johnsen, C. V., and Lovley, D. R. (2003). *Rhodoferax ferrireducens* sp. nov., a psychrotolerant, facultatively anaerobic bacterium that oxidizes acetate with the reduction of Fe(III). *Int. J. Syst. Evol. Microbiol.* 53, 669–673. doi: 10.1099/ijs.0.02298-0

Fleming, E. J., Cetinić, I., Chan, C. S., Whitney King, D., and Emerson, D. (2014). Ecological succession among iron-oxidizing bacteria. *ISME J.* 8, 804–815. doi: 10.1038/ismej.2013.197

Fredrickson, J. K., and Zachara, J. M. (2008). Electron transfer at the microbe-mineral interface: a grand challenge in biogeochemistry. *Geobiology* 6, 245–253. doi: 10.1111/j.1472-4669.2008.00146.x

Glaeser S. P., and Kämpfer P. (2014). "The family Sphingomonadaceae," in *The Prokaryotes*, eds E. Rosenberg, E. F. DeLong, S. Lory, E. Stackebrandt, and F. Thompson (Berlin; Heidelberg: Springer).

Gorby, Y. A., Yanina, S., McLean, J. S., Rosso, K. M., Moyles, D., Dohnalkova, A., et al. (2006). Electrically conductive bacterial nanowires produced by *Shewanella oneidensis* strain MR-1 and other microorganisms. *Proc. Natl. Acad. Sci. U.S.A.* 103, 11358–11363. doi: 10.1073/pnas.0604517103

Greene, A. C. (2014). "The family Desulfuromonadaceae," in *The Prokaryotes*, eds E. Rosenberg, E. F. DeLong, S. Lory, E. Stackebrandt, and F. Thompson (Berlin; Heidelberg: Springer).

Gregory, K. B., Bond, D. R., and Lovley, D. R. (2004). Graphite electrodes as electron donors for anaerobic respiration. *Environ. Microbiol.* 6, 596–604. doi: 10.1111/j.1462-2920.2004.00593.x

Hart, K., Trancynger, T. C., Roggenthen, W., and Heise, J. (2014). "Topographic, geologic, and density distribution modeling in support of physics experiments at the Sanford Underground Research Facility (SURF)," in *Proceedings of the South Dakota Academy of Science*, *Vol. 93*, 33–41.

Hartshorne, R. S., Reardon, C. L., Ross, D., Nuester, J., Clarke, T. A., Gates, A. J., et al. (2009). Extracellular electron transfer via microbial nanowires. *Proc. Natl. Acad. Sci.* 106, 3968–3973. doi: 10.1073/pnas.0900086106

Hegler, F., Posth, N. R., Jiang, J., and Kappler, A. (2008). Physiology of phototrophic iron(II)-oxidizing bacteria: implications for modern and ancient environments. *FEMS Microbiol. Ecol.* 66, 250–260. doi: 10.1111/j.1574-6941.2008.00592.x

Heise, J. (2015). The Sanford underground research facility at homestake. *J. Phys. Conf. Ser.* 606:012015. doi: 10.1088/1742-6596/606/1/012015

Hirose, A., Kasai, T., Aoki, M., Umemura, T., Watanabe, K., and Kouzuma, A. (2018). Electrochemically active bacteria sense electrode potentials for regulating catabolic pathways. *Nat. Commun.* 9:1083. doi: 10.1038/s41467-018-03416-4

Holmes, D. E., Bond, D. R., O'Neil, R. A., Reimers, C. E., Tender, L. R., and Lovley, D. R. (2004). Microbial communities associated with electrodes harvesting electricity from a variety of aquatic sediments. *Microb. Ecol.* 48, 178–190. doi: 10.1007/s00248-003-0004-4

Ishii, S., Logan, B. E., and Sekiguchi, Y. (2012). Enhanced electrode-reducing rate during the enrichment process in an air-cathode microbial fuel cell. *Appl. Microbiol. Biotechnol.* 94, 1087–1094. doi: 10.1007/s00253-011-3844-8

Ishii, T., Kawaichi, S., Nakagawa, H., Hashimoto, K., and Nakamura, R. (2015). From chemolithoautotrophs to electrolithoautotrophs: CO_2 fixation by Fe(II)-oxidizing bacteria coupled with direct uptake of electrons from solid electron sources. *Front. Microbiol.* 6:994. doi: 10.3389/fmicb.2015.00994

Ismail, Z. Z., and Jaeel, A. J. (2013). Sustainable power generation in continuous flow microbial fuel cell treating actual wastewater: influence of biocatalyst type on electricity production. *ScientificWorldJournal* 2013:713515. doi: 10.1155/2013/713515

Jangir, Y., French, S., Momper, L. M., Moser, D. P., Amend, J. P., and El-Naggar, M. Y. (2016). Isolation and characterization of electrochemically

active subsurface *Delftia* and *Azonexus* species. *Front. Microbiol.* 7:756. doi: 10.3389/fmicb.2016.00756

Jangir, Y., Karbelkar, A. A., Beedle, N. M., Zinke, L. A., Wanger, G., Anderson, C. M., et al. (2019). *In situ* electrochemical studies of the terrestrial deep subsurface biosphere at the sanford underground research facility, South Dakota, USA. *bioRxiv [Preprint]*. doi: 10.1101/555474

Jansson, J. K., Neufeld, J. D., Moran, M. A., and Gilbert, J. A. (2012). Omics for understanding microbial functional dynamics. *Environ. Microbiol.* 14, 1–3. doi: 10.1111/j.1462-2920.2011.02518.x

Kappler, A., Pasquero, C., Konhauser, K. O., and Newman, D. K. (2005). Deposition of banded iron formations by anoxygenic phototrophic Fe(II)-oxidizing bacteria. *Geology* 33:865. doi: 10.1130/G21658.1

Kawaichi, S., Yamada, T., Umezawa, A., McGlynn, S. E., Suzuki, T., Dohmae, N., et al. (2018). Anodic and cathodic extracellular electron transfer by the filamentous bacterium *Ardenticatena maritima* 110S. *Front. Microbiol.* 9:68. doi: 10.3389/fmicb.2018.00068

Kieft, T. L., Fredrickson, J. K., Onstott, T. C., Gorby, Y. A., Kostandarithes, H. M., Bailey, T. J., et al. (1999). Dissimilatory reduction of Fe(III) and other electron acceptors by a Thermus isolate. *Appl. Environ. Microbiol.* 65, 1214–21.

Kim, B. H., Park, H. S., Kim, H. J., Kim, G. T., Chang, I. S., Lee, J., et al. (2004). Enrichment of microbial community generating electricity using a fuel-cell-type electrochemical cell. *Appl. Microbiol. Biotechnol.* 63, 672–681. doi: 10.1007/s00253-003-1412-6

Kim, S.-J., Moon, J.-Y., Weon, H.-Y., Ahn, J.-H., Chen, W.-M., and Kwon, S.-W. (2014). *Solimonas terrae* sp. nov., isolated from soil. *Int. J. Syst. Evol. Microbiol.* 64, 1218–1222. doi: 10.1099/ijs.0.055574-0

Kracke, F., Vassilev, I., and Krömer, J. O. (2015). Microbial electron transport and energy conservation - The foundation for optimizing bioelectrochemical systems. *Front. Microbiol.* 6:575. doi: 10.3389/fmicb.2015.00575

Kuever, J. (2014). "The family Desulfobulbaceae," in *The Prokaryotes* (Berlin; Heidelberg: Springer), 75–86. doi: 10.1007/978-3-642-39044-9_267

Lesko, K. T. (2015). The Sanford underground research facility at homestake (SURF). *Phys. Proc.* 61, 542–551. doi: 10.1016/j.phpro.2014.12.001

Lovley, D. R. (1991). Dissimilatory Fe(III) and Mn(IV) reduction. *Microbiol. Rev.* 55, 259−287. doi: 10.1016/S0065-2911(04)49005-5

Lovley, D. R. (2006). Bug juice: harvesting electricity with microorganisms. *Nat. Rev. Microbiol.* 4, 497–508. doi: 10.1038/nrmicro1442

Lovley, D. R., and Phillips, E. J. P. (1988). Novel mode of microbial energy metabolism: organic carbon oxidation coupled to dissimilatory reduction of iron or manganese. *Appl. Environ. Microbiol.* 54, 1472–1480.

Marsili, E., Baron, D. B., Shikhare, I. D., Coursolle, D., Gralnick, J. A., and Bond, D. R. (2008). *Shewanella* secretes flavins that mediate extracellular electron transfer. *Proc. Natl. Acad. Sci. U.S.A.* 105, 3968–3973. doi: 10.1073/pnas.0710525105

McIlroy S. J., and Nielsen P. H. (2014). "The family Saprospiraceae," in *The Prokaryotes*, eds E. Rosenberg, E. F. DeLong, S. Lory, E. Stackebrandt, and F. Thompson (Berlin; Heidelberg: Springer).

Meyer, J. L., Jaekel, U., Tully, B. J., Glazer, B. T., Wheat, C. G., Lin, H. T., et al. (2016). A distinct and active bacterial community in cold oxygenated fluids circulating beneath the western flank of the Mid-Atlantic ridge. *Sci. Rep.* 6, 1–14. doi: 10.1038/srep22541

Murdoch, L. C., Germanovich, L. N., Wang, H., Onstott, T. C., Elsworth, D., Stetler, L., et al. (2012). Hydrogeology of the vicinity of Homestake mine, South Dakota, USA. *Hydrogeol. J.* 20, 27–43. doi: 10.1007/s10040-011-0773-7

Myers, C. R., and Myers, J. M. (1992). Localization of cytochromes to the outer membrane of anaerobically grown *Shewanella putrefaciens* MR-1. *J. Bacteriol.* 174, 3429–3438. doi: 10.1128/jb.174.11.3429-3438.1992

Myers, C. R., and Nealson, K. H. (1988). Bacterial manganese reduction and growth with manganese oxide as the sole electron acceptor. *Science* 240, 1319–1321. doi: 10.1126/science.240.4857.1319

Nealson, K. H., Belz, A., and McKee, B. (2002). Breathing metals as a way of life: geobiology in action. *Antonie van Leeuwenhoek.* 81, 215–222. doi: 10.1023/A:1020518818647

Needleman, S. B., and Wunsch, C. D. (1970). A general method applicable to the search for similarities in the amino acid sequence of two proteins. *J. Mol. Biol.* 48, 443–453. doi: 10.1016/0022-2836(70)90057-4

Nevin, K. P., Hensley, S. A., Franks, A. E., Summers, Z. M., Ou, J., Woodard, T. L., et al. (2011). Electrosynthesis of organic compounds from carbon dioxide is catalyzed by a diversity of acetogenic microorganisms. *Appl. Environ. Microbiol.* 77, 2882–2886. doi: 10.1128/AEM.02642-10

Nimje, V. R., Chen, C.-Y., Chen, C.-C., Jean, J.-S., Reddy, A. S., Fan, C.-W., et al. (2009). Stable and high energy generation by a strain of *Bacillus subtilis* in a microbial fuel cell. *J. Power Sources* 190, 258–263. doi: 10.1016/j.jpowsour.2009.01.019

Orcutt, B. N., Sylvan, J. B., Knab, N. J., and Edwards, K. J. (2011). Microbial ecology of the dark ocean above, at, and below the seafloor. *Microbiol. Mol. Biol. Rev.* 75, 361–422. doi: 10.1128/MMBR.00039-10

Osburn, M. R., LaRowe, D. E., Momper, L. M., and Amend, J. P. (2014). Chemolithotrophy in the continental deep subsurface: Sanford Underground Research Facility (SURF), USA. *Front. Microbiol.* 5:610. doi: 10.3389/fmicb.2014.00610

Pruesse, E., Quast, C., Knittel, K., Fuchs, B. M., Ludwig, W., Peplies, J., et al. (2007). SILVA: a comprehensive online resource for quality checked and aligned ribosomal RNA sequence data compatible with ARB. *Nucleic Acids Res.* 35, 7188–7196. doi: 10.1093/nar/gkm864

Rabaey, K., and Verstraete, W. (2005). Microbial fuel cells: novel biotechnology for energy generation. *Trends Biotechnol.* 23, 291–298. doi: 10.1016/j.tibtech.2005.04.008

Reasoner, D. J., and Geldreich, E. E. (1985). A new medium for the enumeration and subculture of bacteria from potable water. *Appl. Environ. Microbiol.* 49, 1–7.

Reese, B. K., Zinke, L. A., Sobol, M. S., LaRowe, D. E., Orcutt, B. N., Zhang, X., et al. (2018). Nitrogen cycling of active bacteria within oligotrophic sediment of the Mid-Atlantic Ridge Flank. *Geomicrobiol. J.* 35, 468–483. doi: 10.1080/01490451.2017.1392649

Reguera, G., McCarthy, K. D., Mehta, T., Nicoll, J. S., Tuominen, M. T., and Lovley, D. R. (2005). Extracellular electron transfer via microbial nanowires. *Nature* 435, 1098–1101. doi: 10.1038/nature03661

Reimers, C. E., Girguis, P., Stecher, H. A., Tender, L. M., Ryckelynck, N., and Whaling, P. (2006). Microbial fuel cell energy from an ocean cold seep. *Geobiology* 4, 123–136. doi: 10.1111/j.1472-4669.2006.00071.x

Reith, F., Etschmann, B., Grosse, C., Moors, H., Benotmane, M. A., Monsieurs, P., et al. (2009). Mechanisms of gold biomineralization in the bacterium *Cupriavidus metallidurans*. *Proc. Natl. Acad. Sci. U.S.A.* 106, 17757–17762. doi: 10.1073/pnas.0904583106

Richter, H., Nevin, K. P., Jia, H., Lowy, D. A., Lovley, D. R., and Tender, L. M. (2009). Cyclic voltammetry of biofilms of wild type and mutant Geobacter sulfurreducens on fuel cell anodes indicates possible roles of OmcB, OmcZ, type IV pili, and protons in extracellular electron transfer. *Energy Environ. Sci.* 2:506. doi: 10.1039/b816647a

Röling W. F. M. (2014). "The family Geobacteraceae," in *The Prokaryotes*, eds E. Rosenberg, E. F. DeLong, S. Lory, E. Stackebrandt, and F. Thompson (Berlin; Heidelberg: Springer).

Rosenberg, E. (2014). "The family Chitinophagaceae," in *The Prokaryotes*, eds E. Rosenberg, E. F. DeLong, S. Lory, E. Stackebrandt, and F. Thompson (Berlin; Heidelberg: Springer).

Ross, D. E., Flynn, J. M., Baron, D. B., Gralnick, J. A., and Bond, D. R. (2011). Towards electrosynthesis in *Shewanella*: energetics of reversing the Mtr pathway for reductive metabolism. *PLoS ONE* 6:e16649. doi: 10.1371/journal.pone.0016649

Rowe, A. R., Chellamuthu, P., Lam, B., Okamoto, A., and Nealson, K. H. (2015). Marine sediments microbes capable of electrode oxidation as a surrogate for lithotrophic insoluble substrate metabolism. *Front. Microbiol.* 6:784. doi: 10.3389/fmicb.2014.00784

Rowe, A. R., Rajeev, P., Jain, A., Pirbadian, S., Okamotao, A., Gralnick, J. A., et al. (2017a). Tracking electron uptake from a cathode into *Shewanella* cells: implications for generating maintenance energy from solid substrates. *bioRxiv [Preprint]*. doi: 10.1128/mBio.02203-17

Rowe, A. R., Yoshimura, M., LaRowe, D. E., Bird, L. J., Amend, J. P., Hashimoto, K., et al. (2017b). *In situ* electrochemical enrichment and isolation of a magnetite-reducing bacterium from a high pH serpentinizing spring. *Environ. Microbiol.* 19, 2272–2285. doi: 10.1111/1462-2920.13723

Saddler G. S., and Bradbury J. F. (2005). "Xanthomonadales ord. nov.," in *Bergey's Manual® of Systematic Bacteriology*, eds D. J. Brenner, N. R. Krieg, J. T. Staley, and G. M. Garrity (Boston, MA: Springer).

Schloss, P. D., Westcott, S. L., Ryabin, T., Hall, J. R., Hartmann, M., Hollister, E. B., et al. (2009). Introducing mothur: open-source, platform-independent, community-supported software for describing and comparing microbial communities. *Appl. Environ. Microbiol.* 75, 7537–7541. doi: 10.1128/AEM.01541-09

Shi, L., Dong, H., Reguera, G., Beyenal, H., Lu, A., Liu, J., et al. (2016). Extracellular electron transfer mechanisms between microorganisms and minerals. *Nat. Rev. Microbiol.* 14, 651–662. doi: 10.1038/nrmicro.2016.93

Southam, G. (2012). Minerals as substrates for life: the prokaryotic view. *Elements* 8, 101–106. doi: 10.2113/gselements.8.2.101

Sudek, L. A., Templeton, A. S., Tebo, B. M., and Staudigel, H. (2009). Microbial ecology of Fe (hydr)oxide mats and basaltic rock from Vailulu'u Seamount, American Samoa. *Geomicrobiol. J.* 26, 581–596. doi: 10.1080/01490450903263400

Summers, Z. M., Gralnick, J. A., and Bond, D. R. (2013). Cultivation of an obligate Fe(II)-oxidizing lithoautotrophic bacterium using electrodes. *MBio* 4:e00420-12. doi: 10.1128/mBio.00420-12

Sun, Y., Wei, J., Liang, P., and Huang, X. (2012). Microbial community analysis in biocathode microbial fuel cells packed with different materials. *AMB Express* 2:21. doi: 10.1186/2191-0855-2-21

Takahashi, Y., Matsumoto, A., Morisaki, K., and Omura, S. (2006). *Patulibacter minatonensis* gen. nov., sp. nov., a novel actinobacterium isolated using an agar medium supplemented with superoxide dismutase, and proposal of Patulibacteraceae fam. nov. *Int. J. Syst. Evol. Microbiol.* 56, 401–406. doi: 10.1099/ijs.0.63796-0

Tang, J., Yang, G., Wen, J., Yu, Z., Zhou, S., and Liu, Z. (2014). *Bacillus thermophilum* sp. nov., isolated from a microbial fuel cell. *Arch. Microbiol.* 196, 629–634. doi: 10.1007/s00203-014-1001-3

Tender, L. M., Reimers, C. E., Stecher, H. A., Holmes, D. E., Bond, D. R., Lowy, D. A., et al. (2002). Harnessing microbially generated power on the seafloor. *Nat. Biotechnol.* 20, 821–825. doi: 10.1038/nbt716

Tienderen, P. H., Van (1991). Evolution of generalists and specialist in spatially heterogeneous environments. *Evolution* 45:1317. doi: 10.2307/2409882

Torres, C. I., Marcus, A. K., Parameswaran, P., and Rittmann, B. E. (2008). Kinetic experiments for evaluating the nernst–monod model for anode-respiring bacteria (ARB) in a biofilm anode. *Environ. Sci. Technol.* 42, 6593–6597. doi: 10.1021/es800970w

Větrovsk,ý, T., and Baldrian, P. (2013). The variability of the 16S rRNA gene in bacterial genomes and its consequences for bacterial community analyses. *PLoS ONE* 8:e57923. doi: 10.1371/journal.pone.0057923

Von Canstein, H., Ogawa, J., Shimizu, S., and Lloyd, J. R. (2008). Secretion of flavins by *Shewanella* species and their role in extracellular electron transfer. *Appl. Environ. Microbiol.* 74, 615–623. doi: 10.1128/AEM.01387-07

Watson, V. J., and Logan, B. E. (2010). Power production in MFCs inoculated with *Shewanella oneidensis* MR-1 or mixed cultures. *Biotechnol. Bioeng.* 105, 489–498. doi: 10.1002/bit.22556

White, G. F., Shi, Z., Shi, L., Wang, Z., Dohnalkova, A. C., Marshall, M. J., et al. (2013). Rapid electron exchange between surface-exposed bacterial cytochromes and Fe(III) minerals. *Proc. Natl. Acad. Sci. U.S.A.* 110, 6346–6351. doi: 10.1073/pnas.1220074110

White, H. K., Reimers, C. E., Cordes, E. E., Dilly, G. F., and Girguis, P. R. (2009). Quantitative population dynamics of microbial communities in plankton-fed microbial fuel cells. *ISME J.* 3, 635–646. doi: 10.1038/ismej.2009.12

Wright, K. E., Williamson, C., Grasby, S. E., Spear, J. R., and Templeton, A. S. (2013). Metagenomic evidence for sulfur lithotrophy by Epsilonproteobacteria as the major energy source for primary productivity in a sub-aerial arctic glacial deposit, Borup Fiord Pass. *Front. Microbiol.* 4:63. doi: 10.3389/fmicb.2013.00063

Wrighton, K. C., Agbo, P., Warnecke, F., Weber, K. A., Brodie, E. L., DeSantis, T. Z., et al. (2008). A novel ecological role of the Firmicutes identified in thermophilic microbial fuel cells. *ISME J.* 2, 1146–1156. doi: 10.1038/ismej.2008.48

Xing, D., Cheng, S., Logan, B. E., and Regan, J. M. (2010). Isolation of the exoelectrogenic denitrifying bacterium *Comamonas denitrificans* based on dilution to extinction. *Appl. Microbiol. Biotechnol.* 85, 1575–1587. doi: 10.1007/s00253-009-2240-0

Xing, D., Zuo, Y., Cheng, S., Regan, J. M., and Logan, B. E. (2008). Electricity generation by *Rhodopseudomonas palustris* DX-1. *Environ. Sci. Technol.* 42, 4146–4151. doi: 10.1021/es800312v

Xu, S., Jangir, Y., and El-Naggar, M. Y. (2016). Disentangling the roles of free and cytochrome-bound fl avins in extracellular electron transport from *Shewanella oneidensis* MR-1. *Electrochim. Acta* 198, 49–55. doi: 10.1016/j.electacta.2016.03.074

Conflict of Interest: The authors declare that the research was conducted in the absence of any commercial or financial relationships that could be construed as a potential conflict of interest.

frontiers in Energy Research

ORIGINAL RESEARCH
published: 01 November 2019
doi: 10.3389/fenrg.2019.00119

Long Term Feasibility Study of In-field Floating Microbial Fuel Cells for Monitoring Anoxic Wastewater and Energy Harvesting

Pierangela Cristiani[1]*, *Iwona Gajda*[2], *John Greenman*[2], *Francesca Pizza*[3], *Paolo Bonelli*[4] and *Ioannis Ieropoulos*[2]

[1] Ricerca sul Sistema Energetico - RSE S.p.A., Milan, Italy, [2] Bristol Robotics Laboratory, Bristol BioEnergy Centre, University West England, Bristol, United Kingdom, [3] MilanoDepur SpA, WWTP of Milano-Nosedo, Milan, Italy, [4] CISE2007, Milan, Italy

In the present work different prototypes of floating MFCs have been tested in anoxic water environments of wastewater plants in Italy, over a period of 3 years. Several configurations of horizontal (flat) and vertical (tubular) MFCs were assembled, using low-cost and light-weight materials, such as plastic lunch boxes, polystyrene or wood to keep the systems afloat, and ceramics for the MFCs. Untreated carbon cloth or veil was used for both anode and cathode electrodes. Felt (flat MFCs) or clay (tubular MFCs) was used as the cation-exchange separator. Single flat MFCs generated power up to 12 mW/m^2 while a 32 cylindrical MFC stack generated up to 18 mW/m^2. The testing lasted for more than 2 years and there was no inoculation other than exposing the MFCs to the denitrification environment. The cathodes of the flat MFCs were spontaneously colonized by algae and plants, and this did not affect the stability of the systems. Natural light increased the power output of the flat MFCs which were smaller than 50 × 50 cm. Diurnal oscillation of temperature and periodic water flow did not significantly affect the performance of the MFCs. The largest flat MFC produced the highest absolute power, although in a disrupted way. A new, simple low-energy remote monitoring system, based on LoRa technology was used for data transmission over distances of >500 m. This is a piece of hardware that could potentially be suitable for remote monitoring as part of a network, as it can be directly powered by the deployed MFCs.

Keywords: floating microbial fuel cells, wastewaters monitoring, low-energy remote data transmission, in-field MFC tests, anossic wastewater, long term field operation

OPEN ACCESS

Edited by:
Eileen Hao Yu,
Newcastle University, United Kingdom

Reviewed by:
Nan Li,
Tianjin University, China
Fang Zhang,
Tsinghua University, China

***Correspondence:**
Pierangela Cristiani
pierangela.cristiani@rse-web.it

Specialty section:
This article was submitted to Bioenergy and Biofuels, a section of the journal Frontiers in Energy Research

Received: *15 March 2019*
Accepted: *11 October 2019*
Published: *01 November 2019*

Citation:
Cristiani P, Gajda I, Greenman J, Pizza F, Bonelli P and Ieropoulos I (2019) Long Term Feasibility Study of In-field Floating Microbial Fuel Cells for Monitoring Anoxic Wastewater and Energy Harvesting. Front. Energy Res. 7:119. doi: 10.3389/fenrg.2019.00119

HIGHLIGHTS

- Prototypes of floating MFCs producing power for energy harvesting in anoxic wastewater.
- 0.4–3 mW (0.2–0.6 V) was generated by the MFCs connected to a DC/DC converter.
- More than 2 years continuous operation of tubular MFCs set in floaters.
- Large flat MFCs more productive than a set of smaller flat MFC of equivalent electrodes surface.
- Light cycle strongly influences the productivity of small flat MFCs.
- Floating MFCs as energy-autonomous sensors of biodegradation for remote monitoring systems.

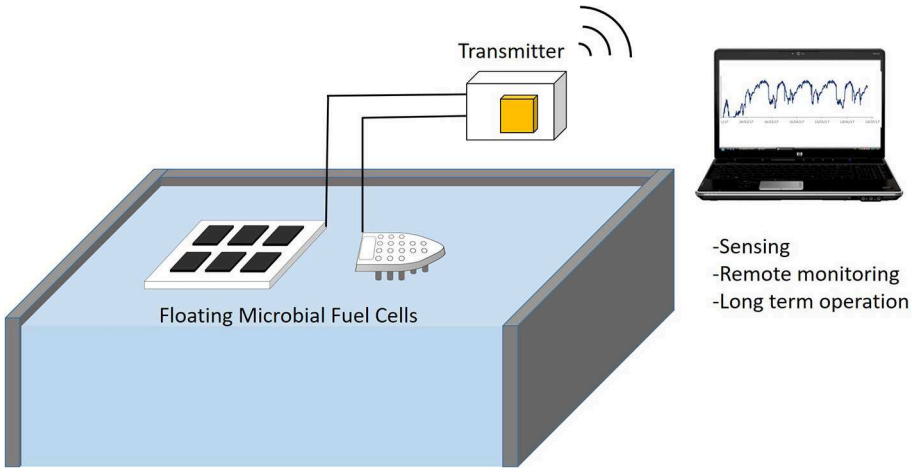

GRAPHICAL ABSTRACT |

INTRODUCTION

The biotechnological purification of wastewater is based on complex and strictly interconnected physico-chemical and biological processes. The efficiency of the process is achieved only through careful and correct control of crucial parameters, such as nutrient content, organic loading and aerobic/anaerobic conditions. Therefore, regular measurement of physicochemical parameters such as temperature, water flow, dissolved oxygen, organic load is regularly carried out in wastewater treatment plants (WWTPs). The concentration of biodegradable organic matter is the most important parameter of the process, which would require closer monitoring. The frequency of analysis is governed by the instability of the system operation, which is normally more pronounced in smaller treatment plants where the demand for a greater number of controls is often challenged by the availability of resources (human and technical ones). On-line monitoring devices are often used in modern WWTPs, depending on their dimensions, practice and available resources (Bourgeois et al., 2001), whereas the strict control of the water treatment in emerging economies is often unsustainable, if at all supported. Nevertheless, sensing is becoming increasingly important as a function performed to protect and preserve natural ecosystems, whether in developed or emerging economies.

There are currently numerous sensing technologies that are being used for monitoring different environmental parameters, many of which can operate for prolonged periods. The cost however, could be disproportionately high for those WWTPs also requiring strict maintenance regimes, high energy and plenty of consumables. In this context, Microbial Fuel Cells (MFCs) are a promising technology with the dual purpose of harvesting energy and sensing aquatic environments, especially but not exclusively wastewater. Several sediment MFCs have been previously investigated (Reimers et al., 2001) and an MFC-powered rowing float (called Row-bot) has also been recently reported for wastewater environments (Philamore et al., 2015), which is based on the EcoBot principle of operation (Ieropoulos and Melhuish, 2005; Ieropoulos et al., 2010). Several other laboratory experiments confirmed the possibility of using MFCs as sensors for biodegradation in the water (Kim et al., 2003; Tront et al., 2008). The challenge, however, remains as one of scale up for self-powering MFC sensors for water quality and establishing real environmental (even remote) monitoring networks, where electricity may not be available. More recently floating systems (Martinucci et al., 2015; Schievano et al., 2017) have also been proposed, with promising results. The low concentration of biodegradable organic matter (10's of mgL^{-1} COD) dissolved in the water of the anoxic tank strongly limits the power production of this kind of MFC (Martinucci et al., 2015). The scaling up of such simple systems, based on microbial catalysis at anode and cathode, would be needed in order to be performing well-enough for the desired objectives (power and sensing), optimizing the cell geometry and connecting in series parallel several MFC units (Ieropoulos et al., 2008).

In the present study, the performance of floating MFCs suitably designed for anaerobic water environments was tested both for energy harvesting and sensing purposes, in long-term experiments (more than 3 years) in denitrification tanks of WWTPs, as part of a longer term study (Martinucci et al., 2015). A particular focus was the selection of low cost and readily available materials, parts, electronic components and open-source software, for the purpose of wastewater monitoring and for a possible development of monitoring networks, acknowledging the sense of emerging "citizen science" of the industrialized world (Wildschut, 2017). Different designs and geometries of flat and tubular cells were investigated, with electrodes assembled in horizontal and vertical configurations, using plastic lunch boxes or polystyrene to keep the system afloat in contact with the anoxic wastewater. The MFC configuration

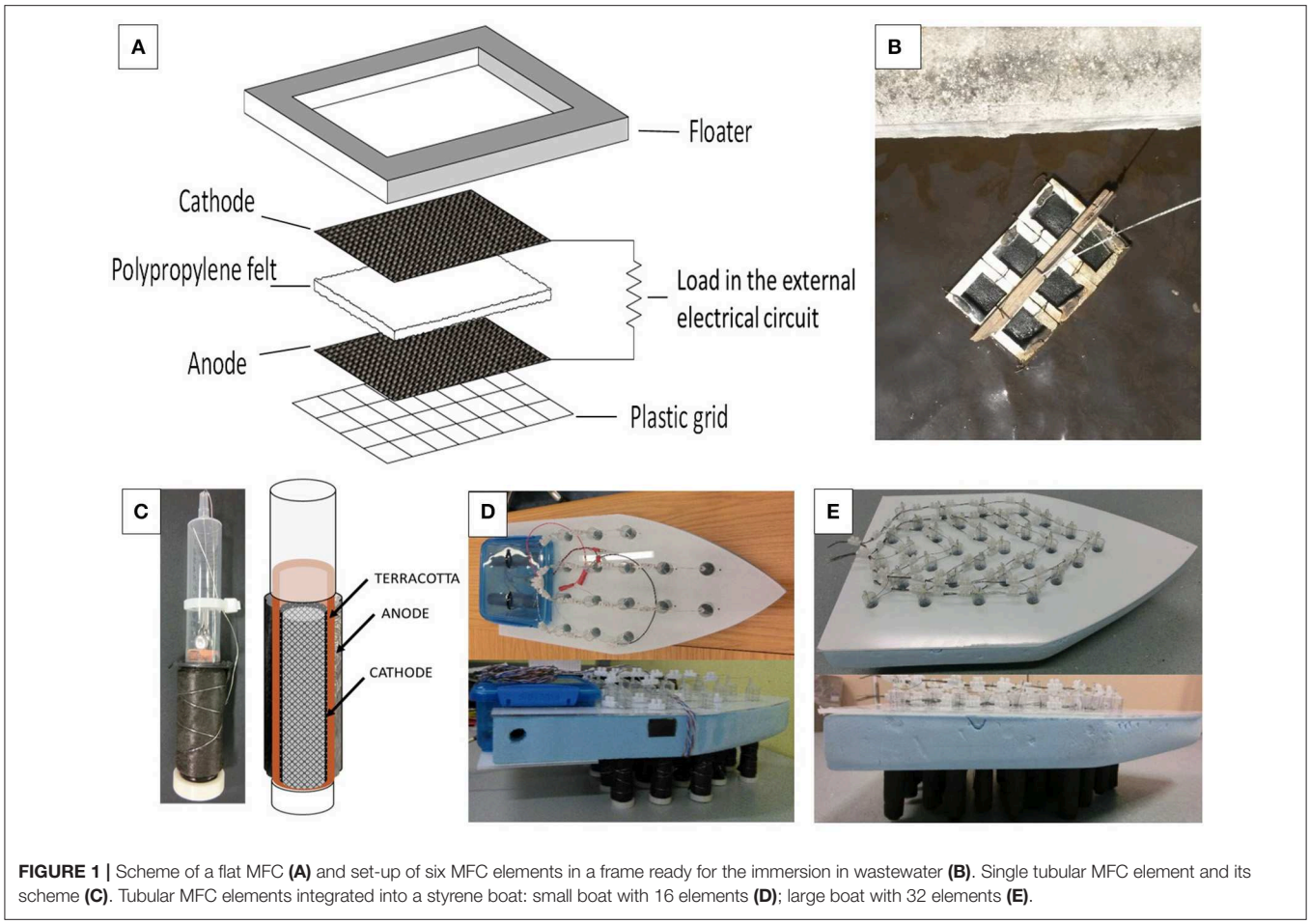

FIGURE 1 | Scheme of a flat MFC **(A)** and set-up of six MFC elements in a frame ready for the immersion in wastewater **(B)**. Single tubular MFC element and its scheme **(C)**. Tubular MFC elements integrated into a styrene boat: small boat with 16 elements **(D)**; large boat with 32 elements **(E)**.

was based on carbon electrodes avoiding any chemical catalysts or pretreatment, and a simple inert separator (polypropylene or ceramic) between anode and cathode (**Figure 1**). Experiments were carried out in two Italian WWTP, at the Milano-Nosedo WWTP (2014–2018) and subsequently at the Carimate WWTP (2017–2019). Milano-Nosedo is the largest WWTP serving a population of 1.25 million in the city of Milan, whereas Carimate is one order of magnitude smaller, but with similar aerobic and anoxic treatment processes. Previous work performed with the same flat MFC configuration at the same Milano-Nosedo WWTP demonstrated the possibility to produce energy from such MFC configurations (Martinucci et al., 2015) and higher power densities were achieved reducing the electrode area from 0.125 m^2 (40 × 30 cm) to 0.03 m^2 (20 × 15 cm). The present study was conducted with the aim of *in situ* assessing such MFC systems in producing power and sensing, whilst exposed to the elements (diurnal cycle, weather conditions) and water parameters (temperature, flow, organic content, etc.). A new generation of low-energy remote data logging system (LoRa) was also developed and integrated into the electronic circuitry, to utilize the generated power from MFCs and transmit signals over long distances; the near-term vision is that such systems become an integral part of a full MFC sensing package for remote area access and telemetry.

MATERIALS AND METHODS

Experiments

Several flat MFCs units of different dimensions were operated in a denitrification anoxic pool at the Milano-Nosedo WWTP during a trial period of more than 3 years (2014–2017). Some flat MFCs units were operated as individual units and the output was monitored through a resistance of 100 Ω while other units, usually the better performing, were occasionally disconnected from the resistance and connected in parallel with other units, to harvest the generated energy (data not shown). A schematic representation alongside photos to illustrate the system are shown in **Figures 1A,B**. Another long term testing of six flat MFCs with small electrodes and anodes short-circuited all together was operated in the anoxic basin of a different WWTP located at Carimate (Milan, Italy) since June 2017, for about 1 year. The generated electricity from these MFCs was also monitored through a connected 100 Ω electrical resistance.

Several tubular MFCs inserted in a polystyrene frame shaped like a boat were also tested close to the flat ones in the same denitrification anoxic pool at Milano-Nosedo WTTP (**Figures 1C–E**). The tubular ceramic MFC units shown in the picture and diagram of **Figure 1C** were connected in two different floating stacks, one with 16 MFC units (Small

TABLE 1 | Characteristics of the MFCs types.

Type, materials	Electrodes geometry	Name	Number
Flat, carbon cloth electrodes and PPE felt (1 cm)	50 × 50 cm	Flat-large	1
Flat, carbon cloth electrodes, PPE felt (1 cm)	18 × 18 cm	Flat-medium	4
Flat, carbon cloth electrodes, PPE felt (1 cm)	10 × 13 cm	Flat-small	6
Flat, carbon cloth electrodes, PPE felt (1 cm) anode shorted all together	10 × 13 cm	Flat-small	6
Tubular, terracotta (thickness = 0.2 cm L = 7 cm, d = 1.5 cm), filled with activated carbon (cathode); anode in carbon fiber outside	Anode: 280 cm^2 Cathode: 20 cm^2	Small boat	16
Tubular, terracotta (thickness = 0.2 cm L = 7 cm, d = 1.5 cm), filled with activated carbon (cathode); anode in carbon fiber outside	Anode of 280 cm^2 Cathode of 20 cm^2	Big boat	32

boat, **Figure 1D**) and the other with 32 MFC units (Big boat, **Figure 1E**). All the MFCs units of each boat were electrically connected in parallel using stainless steel wire and terminal blocks and an external resistance of 100 Ω was connected between them. The small boat (16 tubular MFCs) was introduced into the Milano-Nosedo WTTP since 2014, close to the flat MFCs of various geometries and was removed in 2018, after more than 3 years of continuous operation. The big boat (32 tubular MFCs) started to operate at the beginning of March in 2016 and was removed with all the other MFCs in 2018. The different geometries of flat MFCs were operated in the same period.

The trends of power generated in long time experiments by the different flat and tubular MFCs, summarized in **Table 1**, are discussed in this work. The flat MFC geometries tested at Milano-Nosedo WWTP are named: Flat-large (one, with 50 × 50 cm electrodes), Flat-medium (four, with 18 × 18 cm electrodes) and Flat-small (six, with 10 × 13 cm electrodes). Six more Flat-small MFCs with anodes electrically connected together were the ones tested at the Carimate WWTP.

A detailed description of the Milano-Nosedo WWTP, one of the largest plants in Europe, for 1,250,000 Population equivalent (PE) and water parameters, has been reported previously (Martinucci et al., 2015). In brief, the anoxic water is characterized by an incoming BOD_5 of around 170 mgL^{-1} reduced through biodegradation for 99% (<5 mgL^{-1} outlet); an incoming COD of about 300 ± 100 mgL^{-1} and COD <15 mgL^{-1} in the outlet. The residual COD concentration in the anoxic tank is around 20 mgL^{-1} measured on a filtrated (0.45 μ) sample, excluding the activated sludge.

The Carimate WWTP is a smaller waterworks facility and serves about 70,221 inhabitants in an area close to Milan, producing about 5,000,000 m^3/y of wastewater. Part of the treatment is for industrial wastewater, which is about 1,000,000 m^3/y and which corresponds to 4,000–5,000 more population equivalent, (as BOD_5). The dissolved COD in the anoxic wastewater of this plant is a little higher than in the Milano-Nosedo plant, usually ranging between 10 and 80 mgL^{-1}.

Flat MFCs Fabrication

Schematic diagrams for the flat MFC are presented in **Figure 1A**. The two electrodes of each MFC had the same area and were placed parallel to each other at a distance of 1 cm, separated by a polypropylene (PPE) felt. The cathode and anode were both made of carbon cloth, which was free of any chemical catalyst (cod. SCCT-8, SAATI, Legnano, Italy). An electrical resistance of 100 Ω was connected in the external circuit of each MFC, between anode(s) and cathode.

Tubular Ceramic MFCs Building

Tubular MFCs were assembled using terracotta cylinders (L = 7 cm, d = 1.5 cm, thickness 0.2 cm) that were sealed at one end with a plastic stopper. The anodes were made from carbon fiber veil (280 cm^2 per MFC) that was folded, wrapped around the cylinder and secured with stainless steel wire (**Figure 1C**). The cathodes made of activated carbon as previously described (Gajda et al., 2015) were inserted into the cylinders and connected with stainless steel crocodile clips to the wire. A 10 mL plastic syringe was attached to the top of the ceramic cylinder in order to fit the MFCs into the floating "boat"-like polystyrene material. In this way, the activated carbon is exposed to air through the open top connected to the syringe in the floating part of the boat.

Data Acquisition and Transmission

For each tested flat MFC, the voltage V through the R (100 Ω) resistance was recorded every 10 min, using a multichannel data logger made with Arduino hardware and open-source software, as described in Supporting Information (**Figure S1**). The generated power P (V × I), where I is the current flowing through the external resistance R, was calculated using Ohm's low (V = I × R). The data acquired were then transmitted using a LoRa low energy transmission system described in **Figures S1, S2**, which was set up and tested for data transmission over distances of >500 m.

RESULTS AND DISCUSSION

Both the flat MFCs and the tubular MFCs types were immersed in the denitrification tank without prior inoculation. The electrode facing the anoxic water quickly developed a biofilm fueled by the residual organics dissolved into the water in contact with the electrode. In the case of the flat MFCs whose electrodes were separated though a porous PPE felt, without any electrolytic membrane, biofilm grew also on the cathode sustaining the catalysis of the cathodic reaction (biocathode). Previous works on laboratory-based systems reported that the air-breathing biocathode of single chamber and membraneless MFCs using the

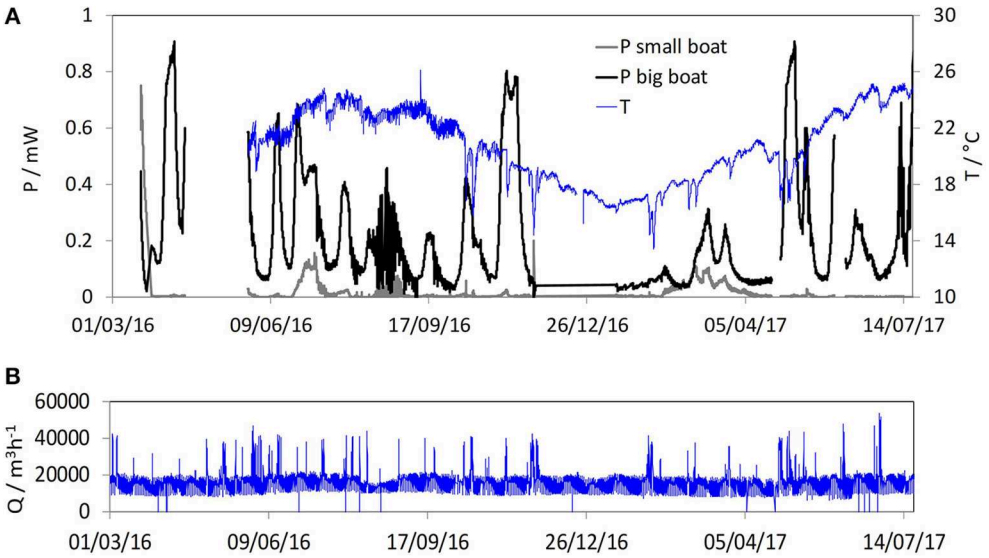

FIGURE 2 | Power trends of the Small boat and Large boat MFCs during more than 1 year (April 2016–July 2017) in an anoxic tank (Milano-Nosedo WWTP) **(A)**; trends of temperature and wastewater flow incoming in the plant is also reported **(B)**.

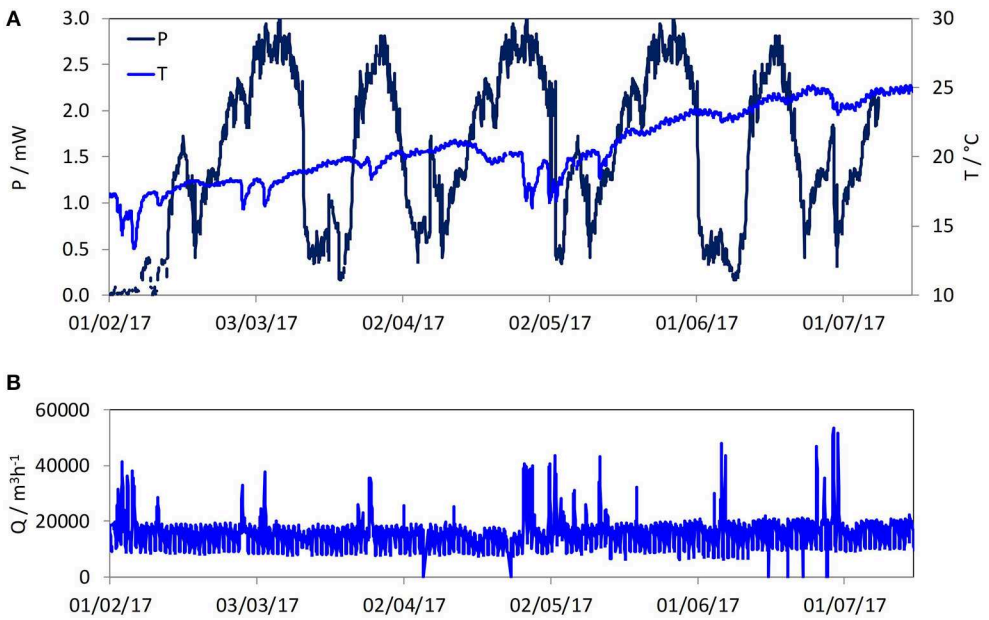

FIGURE 3 | Power trend of the Flat-large MFC (50 × 50 cm) operated from January to July 2017 (Milano-Nosedo WWTP) **(A)**; trends of temperature and incoming wastewater flow in the plant **(B)**.

same anoxic wastewater from the Milano-Nosedo plant quickly become anaerobic developing a biofilm rich of bacteria of the sulfur and nitrogen cycles (Guerrini et al., 2014; Rago et al., 2017). The same microorganisms differently enrich the anode and the cathode, but alone or in synergy with other microorganisms, such as Spirochetes and photosynthetic anaerobic bacteria are able to sustain a good cathodic catalytic activity using atmospheric oxygen just as the end-terminal electron acceptor (Cristiani et al., 2013). This mechanism allows the flat floating MFCs to perform in the anoxic tank. The development of the biofilm at the cathode was inhibited in the case of tubular ceramic MFCs, as the ceramic porosity does not allow the passage of bacteria (Rago et al., 2018), but also due to the fact that the internal cavities of the ceramic cylinders were not directly exposed to the anoxic water. The cathodic operation, in this case, was facilitated by the activated carbon, whose cathodic catalytic properties, which are higher

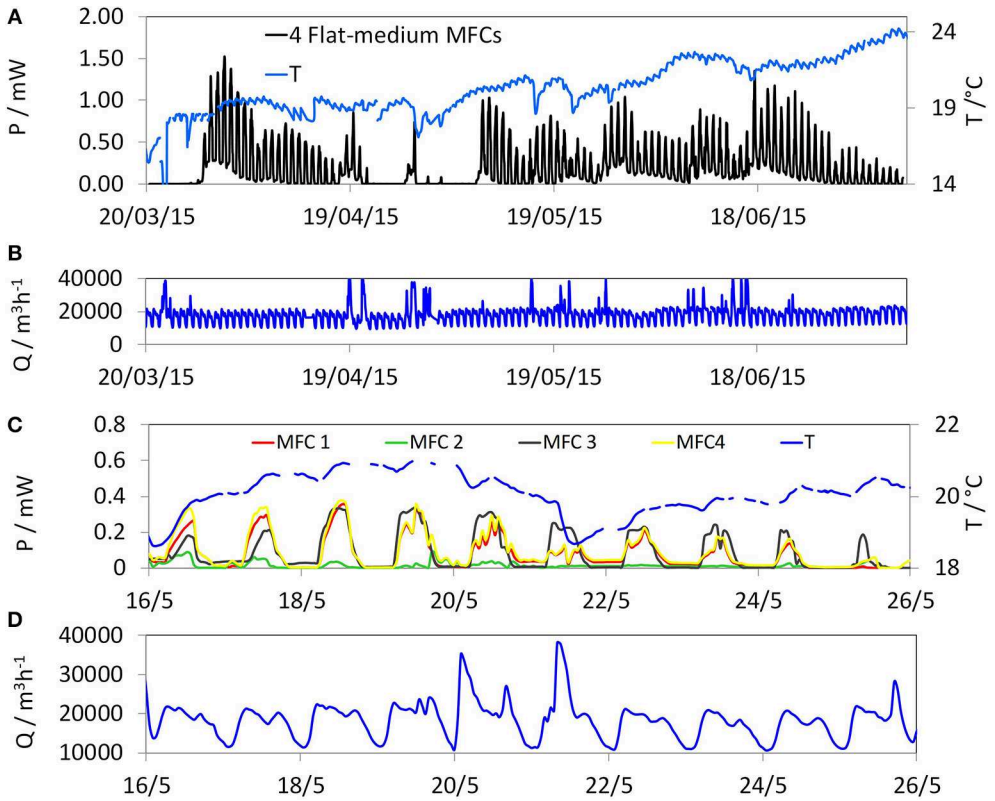

FIGURE 4 | Power trends of the Flat-medium MFCs (18 × 18 cm) operated from April to July 2017 (Milano-Nosedo WWTP) **(A)**; trends of temperature and wastewater flow incoming in the plant **(B)**; zoomed view of the power trends at daily scale **(C)**; zoomed view of temperature and wastewater flow at daily scale **(D)**.

than the plain carbon cloth, have been well-documented (Dong et al., 2012; Wei et al., 2012; Gajda et al., 2014; Santoro et al., 2017).

MFC Power Performance

The power output from the flat and tubular MFC systems (boats) floating in anoxic wastewater, over a long period of time, is shown in **Figures 2**–**7**. The lack of data in **Figure 2** (May 2016) is due to technical issues with the data acquisition system and is not an indication of the MFCs ceasing to work. The data shown represent significant parts of the whole 3-year operational period. After approximately 2 weeks from the initial immersion, all the MFCs reached a maximum voltage, varying between 0.2 and 0.5 V depending on the type. In the case of the small boat, a peak voltage of 0.7 V (about 2 mW of power) was produced within the first month of operation (**Figure S1**). Output levels suddenly dropped, before stabilizing, possibly due to humidity, which would have caused short-circuiting and the uptake of atmospheric oxygen. The small boat had been generating power in the range of 0.04–0.31 mW, showing power density up to 9.6 mW/m^2 especially during the first period of the operation, although not continuously. Performance, however, dropped continuously in the second year, when the Big boat was put side by side (**Figure 2**), which outperformed the smaller boat. The big boat MFCs swiftly reached a power output of 1.15 mW in November 2015 and reached about 0.9 mW (**Figure 2**), corresponding to a power density of 14 mW/m^2 and continued to generate power with a similar trend during the whole experimental period. The better performance of the big boat, compared to the smaller one, is not simply due to the higher number of MFCs connected in series/parallel (32 instead of 16) alone, but also due to the fact that the MFCs in the small boat had probably undergone cathode clogging due to moisture penetration and sludge accumulation resulting from water splashes, as it was operating for a longer period of time. Hence, the decrease in the oxygen supply to the cathode had probably caused a decrease of MFC performance.

The flat MFCs required slightly longer periods to start power generation, but all reached a peak in <1 month from the immersion. The Flat-large MFC produced higher absolute power, with peaks of 3 mW (**Figure 3**) corresponding to a density of 12 mW/m^2, which were more evident over weekly rather than daily periods. Nevertheless, a minimum of ∼0.4 mW was consistently generated. Oscillation trends were already shown in previous experiments (Martinucci et al., 2015), and it was particularly highlighted in smaller flat MFCs (**Figures 4**–**7**).

Figure 4 shows the trend of power produced by four identical flat-medium MFCs during about 4 months of continuous operation. The maximum peak power (1.5 mW) was almost half compared to Flat-large MFC with a similar power density (12 mWm^2), since the total electrode area (1,296 cm^2) was approximately half. On average, the performance was generally

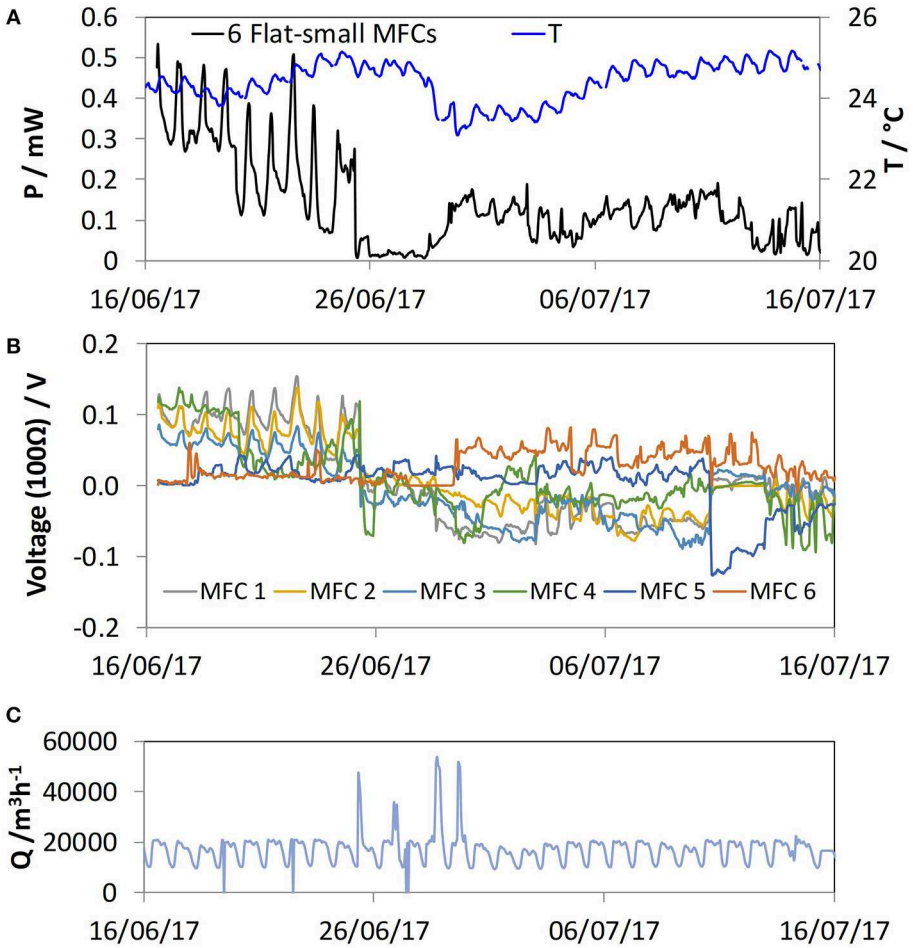

FIGURE 5 | Total power **(A)** and individual voltage trends **(B)** produced by six Flat-small MFCs (10 × 13 cm) during 1 month operation (June–July 2017) at Milano-Nosedo WWTP. Wastewater temperature **(A)** and flow **(C)**.

inferior. The inferior performance, more marked in the case of the Flat-small MFCs, can be attributed to high variability of the power produced by the single MFCs (**Figure S2**). Indeed, the performance between the four MFCs was inconsistent with some producing less power than others, in this way negatively affecting the power density. The power trend produced from six of this MFC type is shown in **Figure 5**. The power produced peaked at 0.5 mW, corresponding to a power density of 6.4 mWm^2, which was inferior to the larger ones.

Figure 6 shows three (out of six) of the better performing Flat-small MFCs, which produced 13.6, 9.4, and 4.6 mWm^2, respectively. These results point to a severe concern regarding the achievement of a stable power from the smaller MFCs for energy harvesting. In fact, the problem of spatial distribution and stability affected these flat MFC more than the others, especially in cases of storms and pronounced changes in water flow. The increased rate between perimeter and area characterizing the electrodes of the smallest flat MFCs resulted in the anaerobic conditions becoming rate-limiting for the anode, which operated next to the water surface. Consequently, the possibility of polarity reversal of the cells has to be taken into account for these MFCs, causing the decay of produced power. A phenomenon such as this is reported in **Figure 6**, documented in the power trends of the six Flat small MFCs operating in the Summer of 2017.

MFC Output vs. Temperature and Water Flow

The generated power by the tubular MFCs on the boat and the relationship with temperature and water flow (Q) measured at the plant inlet during the same period of time is reported in **Figure 2**. The variation of power appears to be affected by the large variation of flow rate that was consistent with the adverse weather events (mainly rainfall and storms) which diluted the incoming wastewater whilst increasing the flow causing temporary decreases. No direct correlation of power with the water temperature is noticeable, neither for the diurnal cycle nor for the whole experimental period. Nevertheless, the MFC performance decreased to very low levels during wintertime, when the environment temperature generally dropped below 15°C impacting the temperature of the first layer of water. This result is consistent with mesophilic bacterial metabolism, which has an optimum between 20 and 35°C, in the context

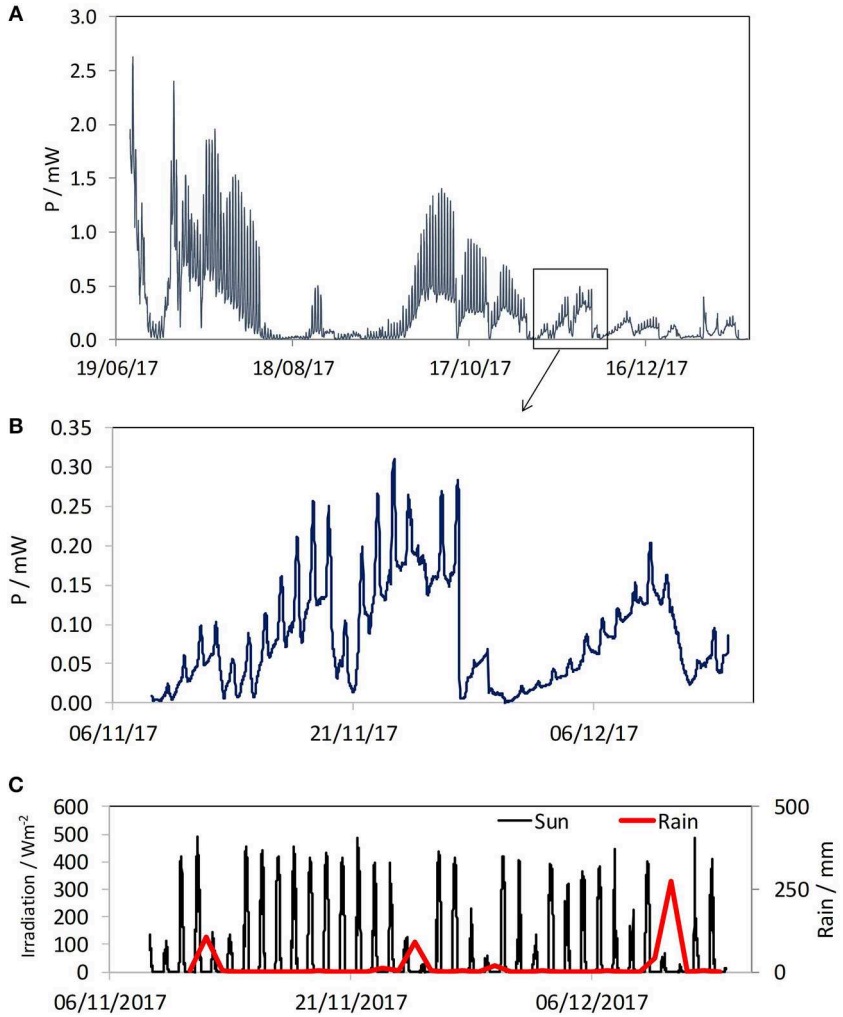

FIGURE 6 | Power trend of six Flat-small MFCs (10 × 13 cm) with shortened anodes (Carimate WWTP) **(A)**. A detail of power trend between November and December 2017 **(B)**; with meteorological measurements: sun irradiation and rain **(C)**.

of the Arrhenius law of temperature. The daily oscillation of power from both Small and Big boats were negligible, like in the case of the flat MFC with much larger cathodes (**Figure 3**). In fact, cylindrical cathodes of the boats were not exposed to light since they are positioned inside the terracotta cylinder and immersed in water. The observed increases in power can be consequently, correlated with the diurnal cycle and also with the concentration of organic substance through the anodes. Also, the power oscillations of Flat-large MFC are only marginally dependent on the temperature and water flow as for MFC boats (**Figure 3**). In fact, the decay in performance was mainly coinciding with periods of intense rain and other events that significantly diluted the dissolved organic substance, changing the organic load in the stream.

The daily power oscillations of Flat-medium MFCs are evidenced in **Figure 4**, which is also highlighted in the zoomed graph of the power trends of the single MFCs during 10 days of June 2015. This graph shows for all the four MFCs a daily variation of power much more pronounced than the weekly or multi-day variation, which results synchronized with the sun hours and the variation of flow rate rather with the temperature variation. The same oscillating behavior was noticed for Flat-small MFCs (**Figures 5–7**). Daily power trends of Flat-small MFCs (three of six) and of both boats during a single day are shown in **Figure 6** with Temperature, Q and COD concentration of the wastewater sampled at the plant inlet (20–21 June 2017). The graphs show that the MFC performance improves concurrently with daytime, the increase of the COD dissolved and the increase in water flow. A noticeable power peak for the Flat-small MFCs is, in fact, in advance of hours with respect to the water temperature variation.

It could be inferred that the cathode electrode was limiting in the case of small size MFCs, not able to sustain the anodic oxidation, especially when anodes are exposed to very low substrate levels (10–20 mg/L COD). The presence of microalgae could favor the local increase in the concentration of oxygen

on the cathode resulting in higher power output (Gajda et al., 2015) when exposed to light, and higher power over the long term. Also, a contribution of photosynthetic microorganisms in producing the power could be responsible for MFCs performing well-during the hours of solar radiation. Several microorganisms as well as cyanobacteria could be involved, as reported in the literature (Rosenbaum et al., 2010; Huarachi-Olivera et al., 2018). For instance, purple non-sulfur bacteria were frequently detected in biocathodes of single chamber microbial fuel cells (Cristiani et al., 2013) during previous tests performed at laboratory level using the same wastewater from the nitrification tank of the Milano-Nosedo WWTP (Cristiani et al., 2013; Rago et al., 2017). This aspect deserves further investigation in any future analyses.

It may be finally noted that the black color of the material used for the cathode electrode could increase the temperature oscillation in it, affecting the intensity of the MFC response due to sun exposure. Nevertheless, a test performed with a thermoresistance (PT 100) placed on the electrode surface of a flat MFC exposed to the sun demonstrated that the temperature variation during insulation did not vary more than 2–3°C with respect to the temperature of the water bulk, thereby excluding the immediate effect of temperature.

MFC Output vs. Environmental Factors

Figure 6 shows the trend of the six floating cells immersed in the anoxic basin of the Carimate WWTP, with electrodes measuring 10 × 13 cm and anodes short-circuited. In this way, the different output of the single cell is due to the cathode performance and not to the (common) anode. The figure show daily oscillating power trends as already registered for the smallest flat MFCs operated at the Milano Nosedo WWTP. Therefore, the power limit, in this case as in the case of the other small flat MFCs, is underlined with the underperforming cathodes. The graph shows a strong daily variability, especially during the first months. At the end of November, the cathodes were variously covered by a layer of mud that strongly limited the exchange with the oxygen of the air as well as impeding, to some extent, the arrival of light on the cell. In that period, the power, and also the daily variation, were much more contained, although a direct relationship of power production with sun irradiation and meteorological events was still maintained. The presence of photosynthetic anaerobic bacteria producing hydrogen in such conditions could play a relevant role, enhancing the cathodic reaction in synergy with the rich anaerobic pool (Cristiani et al., 2013; Rago et al., 2015). This phenomenon deserves further investigation to be confirmed. **Figure 6** shows also a zoom of the voltage trend of the six flat cells immersed in the anoxic tank of the Carimate WWTP with the solar irradiation measured with a commercial solarimeter (Futura electronics, code 8220-DVM1307). Rain precipitation, expressed as mm of water, is also reported in the graph. The rain causes the dilution of the wastewater, and consequently a reduction of the organic content. This phenomenon can be easily correlated with the power drop.

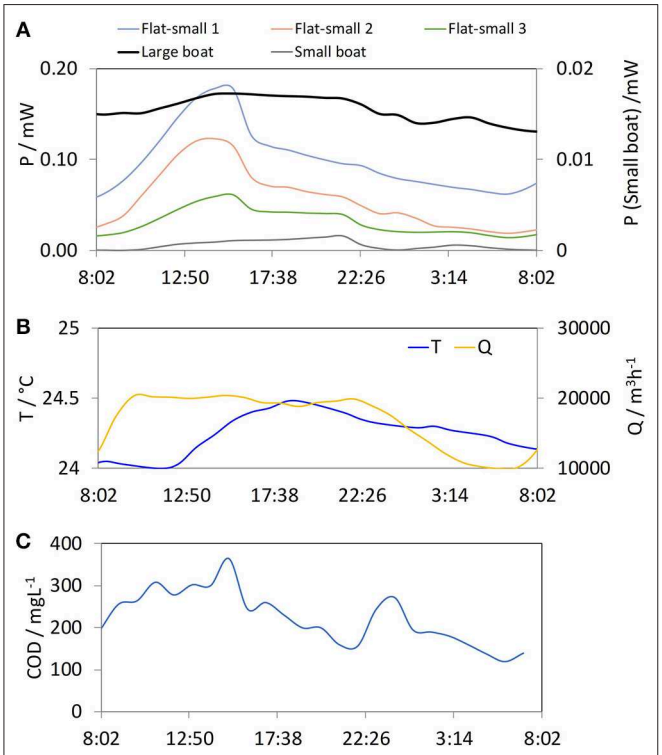

FIGURE 7 | One day (20–21 June 2017) power trends of three Flat-small MFCs and the two boats **(A)**. Temperature, flow **(B)**, and COD **(C)** concentration in the wastewater sampled at the inlet of the Milano-Nosedo WWTP is also reported.

MFC Output vs. COD Concentration

The trend of COD concentration measured by colorimetric method (Hatch Lange kits and instrumentation) every hour at the inlet of the (Milano–Nosedo) WWTP during 1 day (20–21 June 2017) with power trends of the Flat-small MFCs and of both the boat MFCs immersed in the same anoxic tank is reported in the **Figure 7**. The graph shows a significant difference in the trend of the different MFC types.

The correlation between the increase in the signal and the period of light is evident for the Flat-small MFCs, even if, in this period, it is not the sole phenomenon that determines the intensity of the power.

The COD fluctuation in the denitrification tank also affected the MFC power production of each type and size. The larger boat output could be better correlated to the COD level than the others exposed to the light and also the small boat, as it was not performing well-during that period. The dynamic behavior of nutrient concentration could then be monitored via an on-line signal, and the treatment could be more efficiently controlled, and therefore cost-effective in the long term (Tanwar et al., 2008).

Energy Harvesting and Data Transmission

The simple low-energy remote system (LoRa) that was set for the MFC data transmission is described in Supplementary Information (**Figures S3, S4**). It was successfully tested over a distance of 500 m, between the transmitter and the receiver installed at the WTTPs. This system requires a minimum tension of 3.3 V and 0.3 mA (about 1 mW) to operate in sleeping mode

and consumes about 130 mA (during the data transmission, that lasts only about 70 μs).

Based on the results achieved, it could be concluded that a single Flat-large MFC which produced continuously an average between 0.4 and 3 mW (0.2–0.6 V) connected to a DC/DC converter in a harvesting circuit, like those described in previous works (Schievano et al., 2017), is able to supply enough power for the transmitter. For a two time a day message, the additional power of 858 mW for 140 μs is needed, which is, in terms of energy (0.12 mWs), negligible if compared to the sleeping mode consume.

In the case of Big boat, the minimum requested power of 0.4 mW is not produced in continuous mode. Therefore, the number of MFCs for the future construction of the boat should be increased.

In both cases, due to the variability of the produced power in time, the connection of two or more MFC systems should be recommended to reliably power the LoRa transmitter.

Post-operation Observation of Flat MFCs

Image of immersed flat and cylindrical reactors in MFC boats during operation are reported in **Figures S5, S6**. Post-operation observations of flat MFCs are reported in **Figure S7**.

The flat MFCs were quickly covered by photosynthetic organisms (**Figure S7**). As time progressed, spontaneous vegetation of grass, herbs and shrubs grew on the cathode of these MFCs (top surface, exposed to air), somewhat demonstrating a wetland phenomenon, whose root system gently covered the electrode without damaging it, allowing the oxygen to reach cathode and preventing its permeation through (**Figure S7**). This phenomenon probably allowed Flat-large MFC to outperform other set-ups in long time. For the tubular configuration in the boats, there was no vegetation growth on the cathodes. Differently, activate sludge can excessively accumulate on the cathodes, inhibiting the power production. The tubular cathodes, i.e., internal cathodes, suffered for sludge incoming which obstructed aeration, especially the ones in the small boat as they operated for a longer period time (since 2014). This last phenomenon, in particular, resulted critical and has to be prevented for using the small size of both kinds of MFC.

CONCLUSIONS

Both the tested floating MFCs types (flat and tubular) were demonstrated to be able to provide electric power for years, although with oscillations, despite the low concentration of organic matter in the wastewater of the denitrification tanks. They clearly demonstrated the viability of the MFC system as an energy harvester in a real environment.

The dissolved COD in the wastewater as well as the meteorological conditions (sun irradiation and rainfall), mainly caused the oscillation in MFC's output. The daily temperature and water flow variations had a negligible effect.

Floating MFCs reached a power peak in about 2 weeks from the installation and do not need maintenance during the whole experimental period. Photosynthetic species (bacteria, microalgae, and plants) growing on the floating MFCs have a positive effect, both as visual impact and in avoiding mud encrustation on the cathodes. These aspects allowed a long-time operation of the MFCs. On the contrary, sludge accumulation on the cathodes of both tubular and flat MFCs resulted in a much-reduced output and most critically required prevention in future designs of MFC's as sensors and energy harvesters. A new, simple low-energy remote transmission system (LORA) successfully tested, shows great promise for a cost-effective way of data transmission that could be implemented in monitoring and controlling water quality based on floating MFCs.

A single unit of Flat-large MFCs and boats can guarantee energy enough for daily remote transmission of signals from the tested system, although not continuously.

The simplicity in setting up such a monitoring system lends itself well-toward the development of citizen science and for remote environmental control.

DATA AVAILABILITY STATEMENT

All datasets generated for this study are included in the article/**Supplementary Material**.

AUTHOR CONTRIBUTIONS

PC: experiment design, analyses of data, writing parts, and revising the manuscript. IG: MFC prototypes building, data acquisition and elaboration, writing part of the article, and final approval of the version to be submitted. II: design of the test, interpretation of data, revising of the manuscript, and final approval of the version to be submitted. FP: supervision of the experiment in plant, revising the manuscript, and final approval of the version to be submitted. JG: contribution on biological aspects revising of the manuscript, and final approval of the version to be submitted. PB: set-up of data acquisition and transmission device, writing a part of the manuscript, and final approval of the version to be submitted.

FUNDING

This work has been financed by the Research Fund for the Italian Electrical System in compliance with the Decree of Minister of Economic Development April 16, 2018. The work done for the boat MFC made in the Bristol BioEnergy Centre, has been funded by the Bill & Melinda Gates Foundation (Grant No. OPP1094890) and the EPSRC, UK (Grant No. EP/L002132/1).

SUPPLEMENTARY MATERIAL

The Supplementary Material for this article can be found online at: https://www.frontiersin.org/articles/10.3389/fenrg.2019.00119/full#supplementary-material

REFERENCES

Bourgeois, W., Burgess, J.E., and Stuetz, R. M. (2001). On-line monitoring of wastewater quality: a review. *J. Chem. Technol. Biotechnol.* 76, 337–348. doi: 10.1002/jctb.393

Cristiani, P., Franzetti, A., Gandolfi, I., Guerrini, E., and Bestetti, G.. (2013). Bacterial DGGE fingerprints of biofilms on electrodes of membraneless microbial fuel cells. *Int. Biodeterior. Biodegradation* 84, 211–219. doi: 10.1016/j.ibiod.2012.05.040

Dong, H., Yu, H., and Wang, X. (2012). Catalysis kinetics and porous analysis of rolling activated carbon-PTFE air-cathode in microbial fuel cells. *Env. Sci. Technol.* 46, 13009–13015. doi: 10.1021/es303619a

Gajda, I., Greenman, J., Melhuish, C., and Ieropoulos, I. (2015). Simultaneous electricity generation and microbially-assisted electrosynthesis in ceramic MFCs. *Bioelectrochemistry* 104, 58–64. doi: 10.1016/j.bioelechem.2015.03.001

Gajda, I., Greenman, J., Melhuish, C., Santoro, C., Li, B., Cristiani, P., et al. (2014). Water formation at the cathode and sodium recovery using microbial fuel cells (MFCs). *Sustain. Energy Technol. Assessments* 7, 187–194. doi: 10.1016/j.seta.2014.05.001

Guerrini, E., Grattieri, M., Trasatti, S., Bestetti, M., and Cristiani, P. (2014). Performance explorations of single chamber microbial fuel cells by using various microelectrodes applied to biocathodes. *Int. J. Hydrogen Energy* 39, 21837–21846. doi: 10.1016/j.ijhydene.2014.06.132

Huarachi-Olivera, R., Dueñas-Gonza, A., Yapo-Pari, U., Vega, P., Romero-Ugarte, M., Tapia, J., et al. (2018). Bioelectrogenesis with microbial fuel cells (MFCs) using the microalga *Chlorella vulgaris* and bacterial communities. *Electron. J. Biotechnol.* 31, 34–43. doi: 10.1016/j.ejbt.2017.10.013

Ieropoulos, I., Greenman, J., and Melhuish, C. (2008). Microbial fuel cells based on carbon veil electrodes: stack configuration and scalability. *Int. J. Energy Res.* 32, 1228–1240. doi: 10.1002/er.1419

Ieropoulos, I., Greenman, J., Melhuish, C., and Horsfield, I. (2010). "EcoBot-III-A robot with guts," in *Proceedings of the Alife XII Conference* (Odense), 733–740.

Ieropoulos, I., and Melhuish, C. (2005). EcoBot-II: an artificial agent with a natural metabolism. *J. Adv. Robot. Syst.* 2, 295–300. doi: 10.5772/5777

Kim, B. H., Chang, I. S., Gil, G. C., Park, H. S., and Kim, H. J. (2003). Novel BOD (biological oxygen demand) sensor using mediator-less microbial fuel cell. *Biotechnol. Lett.* 25, 541–545.

Martinucci, E., Pizza, F., Perrino, D., Colombo, A., Trasatti, S. P. M., Barnabei, L., et al. (2015). Energy balance and microbial fuel cells experimentation at wastewater treatment plant Milano-Nosedo. *Int. J. Hydrogen Energy* 40, 14683–14689. doi: 10.1016/j.ijhydene.2015.08.100

Philamore, H., Rossiter, J., Stinchcombe, A., and Ieropoulos, I. (2015). "Row-bot: an energetically autonomous artificial water boatman," in *2015 IEEE/RSJ International Conference on Intelligent Robots and Systems (IROS)* (IEEE), 3888–3893.

Rago, L., Cristiani, P., Villa, F., Zecchin, S., Colombo, A., Cavalca, L., et al. (2017). Influences of dissolved oxygen concentration on biocathodic microbial communities in microbial fuel cells. *Bioelectrochemistry* 116, 39–51. doi: 10.1016/j.bioelechem.2017.04.001

Rago, L., Ruiz, Y., Baeza, J. A., Guisasola, A., and Cortés, P. (2015). Microbial community analysis in a long-term membrane-less microbial electrolysis cell with hydrogen and methane production. *Bioelectrochemistry* 106, 359–368. doi: 10.1016/j.bioelechem.2015.06.003

Rago, L., Zecchin, S., Marzorati, S., Goglio, A., Cavalca, L., Cristiani, P., et al. (2018). A study of microbial communities on terracotta separator and on biocathode of air breathing microbial fuel cells. *Bioelectrochemistry* 120, 18–26. doi: 10.1016/j.bioelechem.2017.11.005

Reimers, C. E., Tender, L. M., Fertig, S., and Wang, W. (2001). Harvesting energy from the marine sediment–water interface. *Env. Sci. Technol.* 35, 192–195. doi: 10.1021/es001223s

Rosenbaum, M., He, Z., and Angenent, L.T. (2010). Light energy to bioelectricity: photosynthetic microbial fuel cells. *Curr. Opin. Biotechnol.* 21, 259–264. doi: 10.1016/j.copbio.2010.03.010

Santoro, C., Arbizzani, C., Erable, B., and Ieropoulos, I. (2017). Microbial fuel cells: from fundamentals to applications. A review. *J. Power Sources* 356, 225–244. doi: 10.1016/j.jpowsour.2017.03.109

Schievano, A., Colombo, A., Grattieri, M., Trasatti, S. P., Liberale, A., Tremolada, P., et al. (2017). Floating microbial fuel cells as energy harvesters for signal transmission from natural water bodies. *J. Power Sour.* 340, 80–88. doi: 10.1016/j.jpowsour.2016.11.037

Tanwar, P., Nandy, T., Ukey, P., and Manekar, P. (2008). Correlating on-line monitoring parameters, pH, DO and ORP with nutrient removal in an intermittent cyclic process bioreactor system. *Bioresour. Technol.* 99, 7630–7635. doi: 10.1016/j.biortech.2008.02.004

Tront, J. M., Fortner, J. D., Plötze, M., Hughes, J. B., and Puzrin, A. M. (2008). Microbial fuel cell biosensor for in situ assessment of microbial activity. *Biosens. Bioelectron.* 24, 586–590. doi: 10.1016/j.bios.2008.06.006

Wei, B., Tokash, J. C., Chen, G., Hickner, M. A., and Logan, B. E. (2012). Development and evaluation of carbon and binder loading in low-cost activated carbon cathodes for air-cathode microbial fuel cells. *RSC Adv.* 2, 12751–12758. doi: 10.1039/C2RA21572A

Wildschut, D. (2017). The need for citizen science in the transition to a sustainable peer-to-peer-society. *Futures* 91, 46–52. doi: 10.1016/j.futures.2016.11.010

Conflict of Interest: PC was employed by company Ricerca sul Sistema Energetico – RSE SpA. FP was employed by company MilanoDepur SpA.

The remaining authors declare that the research was conducted in the absence of any commercial or financial relationships that could be construed as a potential conflict of interest.

frontiers in Energy Research

ORIGINAL RESEARCH
published: 05 December 2019
doi: 10.3389/fenrg.2019.00135

Comparative Performance of Microbial Desalination Cells Using Air Diffusion and Liquid Cathode Reactions: Study of the Salt Removal and Desalination Efficiency

Marina Ramírez-Moreno[1], Pau Rodenas[1], Martí Aliaguilla[2], Pau Bosch-Jimenez[2], Eduard Borràs[2], Patricia Zamora[3], Víctor Monsalvo[3], Frank Rogalla[3], Juan M. Ortiz[1]* and Abraham Esteve-Núñez[1,4]*

[1] IMDEA Water Institute, Parque Científico Tecnológico de la Universidad de Alcalá, Alcalá de Henares, Spain, [2] LEITAT Technological Center, Barcelona, Spain, [3] FCC Aqualia S.A., Madrid, Spain, [4] Department of Analytical Chemistry, Physical Chemistry and Chemical Engineering Department, Universidad de Alcalá, Alcalá de Henares, Spain

OPEN ACCESS

Edited by:
Uwe Schröder,
Technische Universitat Braunschweig, Germany

Reviewed by:
Carlo Santoro,
University of the West of England, United Kingdom
Mohanakrishna Gunda,
Qatar University, Qatar

***Correspondence:**
Patricia Zamora
patricia.zamora@fcc.es
Juan M. Ortiz
juanma.ortiz@imdea.org

Specialty section:
This article was submitted to Bioenergy and Biofuels, a section of the journal Frontiers in Energy Research

Received: 25 July 2019
Accepted: 11 November 2019
Published: 05 December 2019

Citation:
Ramírez-Moreno M, Rodenas P, Aliaguilla M, Bosch-Jimenez P, Borràs E, Zamora P, Monsalvo V, Rogalla F, Ortiz JM and Esteve-Núñez A (2019) Comparative Performance of Microbial Desalination Cells Using Air Diffusion and Liquid Cathode Reactions: Study of the Salt Removal and Desalination Efficiency. Front. Energy Res. 7:135. doi: 10.3389/fenrg.2019.00135

Microbial Desalination Cell (MDC) represents an innovative technology which accomplishes simultaneous desalination and wastewater treatment without external energy input. MDC technology could be employed to provide freshwater with low-energy input, for example, in remote areas where organic wastes (i.e., urban or industrial) are available. In addition, MDC technology has been proposed as pre-treatment in conventional reverse osmosis plants, with the aim of saving energy and avoiding greenhouse gases related to conventional desalination processes. The use of oxygen reduction (i.e. $O_2 + 2H_2O + 4e^- \rightarrow 4\ OH^-$, $E^{0'} = 0.815$ V, pH = 7) was usually implemented as cathodic reaction in most of the MDCs reported in literature, whereas other strategies based on liquid catholytes have been also proposed, for example, ferro-ferricyanide redox couple (i.e. $Fe(CN)_6^{3-} + 1e^- \rightarrow Fe(CN)_6^{4-}$, $E^0 = 0.37$ V). As the MDC designs in the literature and operation modes (i.e., batch, continuous, semi-continuous, etc.) are quite different, the available MDC studies are not directly comparable. For this reason, the main objective of this work was to have a proper comparison of two similar MDCs operating with two different catholyte strategies, and compare performance and desalination efficiencies. In this sense, this study compares the desalination performance of two laboratory-scale MDCs located in two different locations for brackish water and sea water using two different strategies. The first strategy consisted of an air cathode for efficient oxygen reduction, while the second strategy was based on a liquid catholyte with Fe^{3+}/Fe^{2+} solution (i.e., ferro-ferricyanide complex). Both strategies achieved desalination efficiency above 90% for brackish water. Nominal desalination rates (NDR) were in the range of 0.17–0.14 $L{\cdot}m^{-2}{\cdot}h^{-1}$ for brackish and seawater with air diffusion cathode MDC, respectively, and 1.5–0.7 $L{\cdot}m^{-2}{\cdot}h^{-1}$ when using ferro-ferricyanide redox MDC. Organic matter present in wastewater was effectively removed at 0.9 and 1.1 kg $COD{\cdot}m^{-3}{\cdot}day^{-1}$ using the air diffusion cathode MDC for brackish and

sea water, respectively, and 7.1 and 19.7 kg COD·m^{-3}·day^{-1} with a ferro-ferricyanide redox MDC. Both approaches used a laboratory MDC prototype without any energy supply (excluding pumping energy). Pros and cons of both strategies are discussed for subsequent upscaling of MDC technology.

Keywords: microbial desalination cell, wastewater treatment, air cathode, sea water, brackish water

INTRODUCTION

More than 700 million people worldwide do not have access to enough clean water and the number is expected to rise up to 1.8 billion people in the next decade (Talbot, 2015). The water sources in regions like the Mediterranean coast, Mexican Gulf or California coast start to be depleted by an increasing demand of drinking water, agriculture, or industry use, while the Middle East region, one of the most water-scarce regions of the world, copes with similar water scarcity problems (Water Scarcity, 2019). Consequently, current desalination technologies have a huge impact on society due to the increasing demand of water worldwide (Badiuzzaman et al., 2017; Chowdhury et al., 2018). However, the high energy cost continues to be a major concern, with energy consumption accounting for 75% of the desalination operating costs when excluding capital costs, or 40% including capital costs (Elmekawy et al., 2014). This energy cost for desalination is about 10 times higher than for conventional water sources, leading to high water prices.

In this context, the most extended desalination technology is reverse osmosis (RO) with an associated energy consumption of 3.5 kWh·m^{-3} (50% recovery) (MacHarg et al., 2008). Temperature-driven technologies such as multi stage flash (MSF) and multi effect distillation (MED) consume even larger amounts of energy (5.5–40 kWh·m^{-3}), thus limiting their use only in countries with low fuel cost (Sharon and Reddy, 2015). Electrodialysis (ED) desalination is mainly suitable for brackish water applications since energy costs depends on the salinity of the water source (Ortiz et al., 2005). Other emerging membrane technologies like forward osmosis (FO), membrane distillation (MD), and capacitive deionization (CDI) have been shown to be only suitable for specific treatment applications (Yuan et al., 2012; Shaffer et al., 2014; Wang and Chung, 2015).

Microbial Desalination Cell (MDC) is a novel technology able to produce sustainable drinking water by using the energy provided from the metabolism of electroactive bacteria when organic matter is degraded, allowing simultaneous desalination of water, treatment of waste water and production of electricity. MDC consists of an electrochemical device with three compartments (Cao et al., 2009). The anodic compartment comprises an electrode covered by a biofilm that oxidizes the organic matter contained in the wastewater, transferring electrons from the substrate (i.e., organic matter) to the electrode. Then, the electrons use an external circuit to reach the cathodic compartment, where the reduction reaction takes place. The electric potential forces the migration of ions. Therefore, desalination takes place when positive ions move through the cation exchange membrane (CEM) from the saline compartment to the cathode and negative ions move through the anion exchange membrane (AEM) from saline to the anodic compartment.

The first concept of MDC was proposed by Cao et al. in a cell of 9 cm^2 (cross section) with a saline volume chamber of 11 mL, achieving 90% of salt removal batchwise, at initial salt concentrations ranging from 5 to 35 NaCl g·L^{-1} (Cao et al., 2009). Different MDC configurations have been reported in the literature, including cubic and tubular reactors (Mehanna et al., 2010; Jacobson et al., 2011a,b; Ping and He, 2013), stacked cells (Chen et al., 2011; Kim and Logan, 2011), using batch recirculation (Chen et al., 2012; Qu et al., 2012), biocathodes (Wen et al., 2012), increasing water production by applying external voltage (Ge et al., 2014), or integrating innovative membranes (forward osmosis) (Zhang and He, 2012; Yuan et al., 2015), ion exchange resins in the compartments (Zhang et al., 2012), or microfiltration processes (Zuo et al., 2017, 2018). Up to date, the biggest MDC ever built (100 L) was reported to achieve partial desalination of sea water with a nominal desalination rate of 0.077 L·m^{-2}·h^{-1} (Zhang and He, 2015).

Cathode reaction is considered one of the main bottlenecks in microbial electrochemical technologies (METs) (Freguia et al., 2008). Most of the MDC studies have been carried out by implementing oxygen reduction in the cathodic compartment by taking advantage of the gained experience in the field of microbial electrochemical systems using oxygen as electron acceptor (i.e. $O_2 + 2H_2O + 4e^- \rightarrow 4\ OH^-$, $E^{0'} = 0.815$ V, pH = 7). Current challenges are to develop air-cathodes with high oxygen reduction reaction (ORR) performance, long term stability and low cost (Freguia et al., 2007; Lu and Li, 2012). Zhao et al. studied three main factors that affect air cathodes performance: the solution pH, the catholyte concentration and the catalyst load (Zhao et al., 2006). Precious metals (Pt, Pd, Au, or Ag) are used as catalysts in electrochemical devices to reduce oxygen in different pH conditions (Ge et al., 2015). Liu et al. showed operative oxygen reduction potential on MFCs between 0.17 to 0.26 V using MnOx as alternative catalyst instead of precious metals (i.e., Pt, Pd) (Zhao et al., 2006; Liu et al., 2010). Also other metal oxides or metal-organic catalysts from the transition metal group (FeOOH, CoOOH, MnOx, WO_3, Co-PPY) have been developed to reduce the capital costs (Bashyam and Zelenay, 2006; Lu and Li, 2012; Wang et al., 2015; Zhang et al., 2016). Among these transition metals, nickel has been shown good performance when surface properties are modified to facilitate ORR (Vij et al., 2017). Additionally, iron is also another promising transition metal for ORR on microbial electrochemical devices (Lefèvre et al., 2009). For example, Harnish et al. demonstrated the versatility of iron-phthalocyanine as catalyst for oxygen reduction on MFCs at

TABLE 1 | Main features for MDC experimental setups.

Location	LEITAT Lab	IMDEA Water Lab
Cross section (cm^2)	100	100
Dimensions active area (cm)	10 × 10	10 × 10
Number of unit cells	1	1
ANODE		
Electric collector	Stainless steel	Isostatic graphite plate (Grade 2114-45)
Electrode	SGL Unidirectional Carbon Fiber Felt	RVG 2000 MERSEN Carbon Felt
Electrode thickness (mm)	5.0	4.6
Compartment thickness (mm)	8.7	9
CATHODE		
Electric collector	Stainless steel 316 frame + carbon fibers mesh	Isostatic graphite plate (Grade 2114-45)
Electrode	Carbon nanofibers doped with iron nanoparticles	RVG 2000 MERSEN Carbon Felt
Electrode thickness (mm)	0.6	4.6
Compartment thickness (mm)	8.7	9
SALINE COMPARTMENT		
Compartment thickness (mm)	8.7	9
ION EXCHANGE MEMBRANES		
Anionic membrane	Neosepta AMX	
Electric resistance ($\Omega \cdot cm^2$)*	2.4	
Permselectivity (%) **	>93	
Thickness (μm)*	0.14	
Cationic membrane	Neosepta CMX	
Electric resistance ($\Omega \cdot cm^2$)*	3.0	
Permselectivity (%)**	>90	
Thickness (μm)*	0.17	
OPERATIONAL CONDITIONS		
Operation mode	Batch (3 streams)	Batch (3 streams)
Flow rate ($mL \cdot min^{-1}$)	95	95
Temperature (°C)	25–30°C	25–30°C
External load (Ω)	2.5	2.5
STREAMS		
Anolyte	FWM + 2.5 g/L Sodium Acetate	FWM + 1.65 $g \cdot L^{-1}$ Sodium Acetate
Catholyte	0.1 M PBS	0.06 M $K_3Fe(CN)_6$
Saline stream	NaCl	NaCl
TANKS		
Anolyte Volume (mL)	2,500	2,000
Catholyte Volume (mL)	2,500	2,000
Saline Volume (mL)	500	370
Rate V_{an}:V_{saline}:$V_{catholyte}$	5:1:5	5:1:5
START-UP OPERATION		
Initial inoculum	Electroactive biofilm from an operating MFC	Pure culture *Geobacter sulfurreducens*
Period (hours)	158	140

**Equilibrated with 0.5N-NaCl solution, at 25°C (data provided by the manufacturer).*
***Measured at the laboratory. Membrane equilibrated with 0.1 M NaCl and 0.5 M NaCl solutions.*

neutral pH (Harnisch et al., 2009). Activated carbons, carbon fibers, carbon black and graphene are also use on ORR due to their tuneable surface properties and high surface (Yuan et al., 2016). More recently, air diffusion cathodes using nanofibers doped with transition metal (Bosch-Jimenez et al., 2017) has been proposed for microbial fuel cells.

Despite the extensive use of oxygen as electron acceptor in METs, the proof of concept of MDC was developed using a ferricyanide catholyte (i.e. $Fe(CN)_6^{3-} + 1e^- \rightarrow Fe(CN)_6^{4-}$, $E^0 = 0.36$ V) (Cao et al., 2009). Salt removal up to 94%, and energy production of 2 $W \cdot m^{-2}$ were achieved, thus increasing significantly the performance of the system compared to that when using ORR as cathodic reaction. Nevertheless, due to high cost of reagents, the use of ferro-ferricyanide catholyte (or other redox mediators/compounds) would be only feasible from a technical point of view in MDCs if: (i) the redox mediator is low cost or (ii) an easy and cheap strategy is developed for regeneration of catholyte solution once depleted.

This work presents the results obtained in parallel in two laboratories (LEITAT and IMDEA Water) for the development of MDC technology for low-energy drinking water production. Similar MDC configurations and experimental methodology have been implemented in both locations in order to compare two different approaches:

a) MDC operating using oxygen reduction as cathodic reaction.
b) MDC operating using the ferro-ferricyanide redox couple as cathodic reaction.

For the first approach, an air diffusion cathode made of carbon nanofibers and iron nanoparticle as catalyst (produced by electrospinning and pyrolysis) was developed as suitable low-cost electrode for environmental applications (i.e., no use of Pt as catalyst).

In the second approach, a ferro-ferricyanide redox catholyte was studied as an alternative to oxygen reduction, in order to enhance the available potential in the MDC and allow for an improved performance.

Finally, salt removal (SR), nominal desalination rate (NDR), current efficiency, specific energy production (SEP), COD removal rate (COD_{rate}), coulombic efficiency (CE), total circulated charge (Q), and water transport are discussed to compare the pros and cons of the aforementioned MDC approaches.

MATERIALS AND METHODS

Microbial Desalination Cell Set Up

Table 1 shows the main features for both MDCs used in this study. The laboratory MDCs consisted of a three-compartment compact stack design with neoprene gaskets for a hermetical seal (see **Figure 1**). Graphite felt RVG2000 (MERSEN) and UDCF (SGL) were used as anode electrodes, and isostatic graphite (Grade 2114-45, MERSEN) and stainless steel AISI 316 as anode electric collectors. In the first approach, a novel air diffusion cathode using carbon nanofibers with iron nanoparticles as catalyst was implemented (see section Start-up protocol), and metal frame -stainless steel frame with UDCFs mesh (SGL) as electric collector—was used in the cathodic compartment. For the second approach (i.e., ferro-ferricyanide redox MDC), the materials were the same of the anode compartment. Finally, two

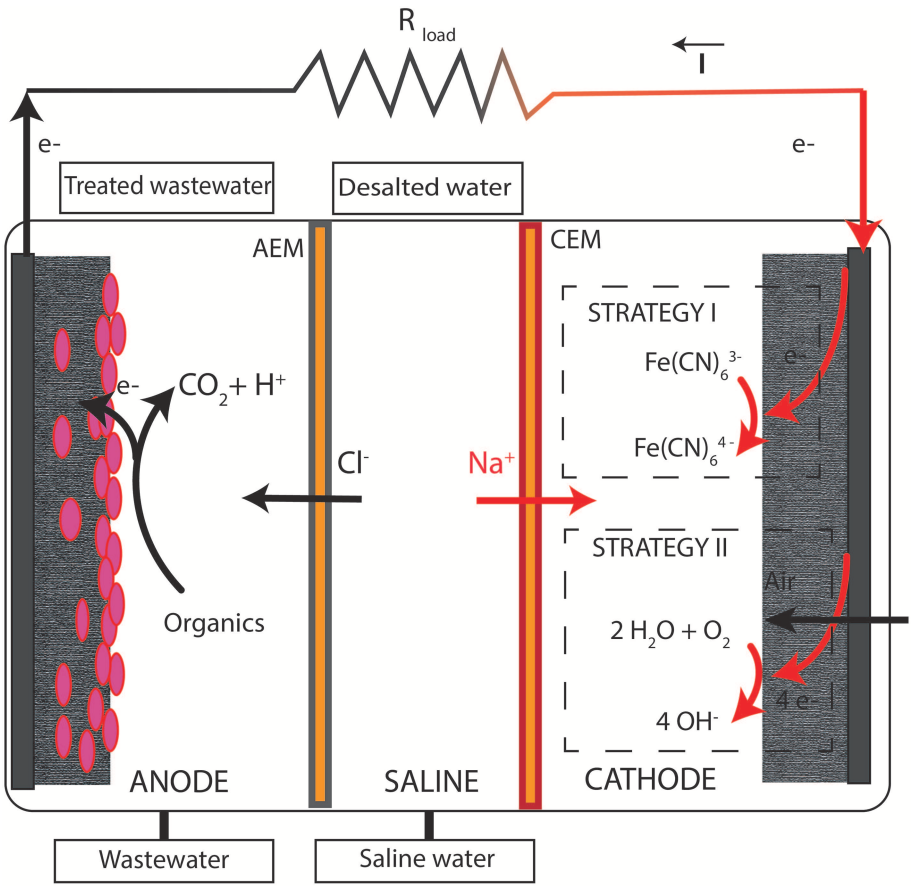

FIGURE 1 | Diagram of an MDC unit. AEM, anion exchange membrane; CEM, cation exchange membrane.

stainless steel end plates were used to close the cell on both ends with a Torque of 10 and 6 N·m for the liquid and air cathode MDCs, respectively.

Figure 2 depicts the diagram of the MDC experimental setup at IMDEA Water and LEITAT facilities (see pictures in **Supplementary Figure 1**). In both cases, the systems were operated in batch mode with recirculation at flow rate of 75 $mL{\cdot}min^{-1}$ (for all streams), and in a temperature-controlled room at 30°C.

The anolyte solution used at LEITAT consisted of a solution containing 0.45 $g{\cdot}L^{-1}$ NaCl, 0.165 $g{\cdot}L^{-1}$ $MgCl_2{\cdot}6H_2O$, 0.0136 $g{\cdot}L^{-1}$ $CaCl_2$, 0.0153 $g{\cdot}L^{-1}$ Mg_2SO_4, 8.4 $g{\cdot}L^{-1}$ $NaHCO_3$, 0.128 $g{\cdot}L^{-1}$ KH_2PO_4, 0.925 $mL{\cdot}L^{-1}$ of NH_4Cl 1 M solution, 1 $mL{\cdot}L^{-1}$ of trace element solution and 0.5 $mL{\cdot}L^{-1}$ of Wolfe's vitamins solution, and 20 mM sodium acetate as organic substrate. The catholyte solution consisted of 100 mM Phosphate Buffered Solution (PBS). Saline media was prepared by dissolving 5 $g{\cdot}L^{-1}$ NaCl for brackish water solution and 35 $g{\cdot}L^{-1}$ NaCl for seawater solution.

Similarly, the anolyte solution used at IMDEA Water consisted of fresh water media (FWM) containing 0.1 $g{\cdot}L^{-1}$, KCl, 2.5 $g{\cdot}L^{-1}$ $NaHCO_3$, 0.6 $g{\cdot}L^{-1}$ KH_2PO_4, 0.5 $g{\cdot}L^{-1}$ NH_4Cl, 10 $mL{\cdot}L^{-1}$ of trace element solution and 1 $mL{\cdot}L^{-1}$ of Wolfe's vitamins solution and 20 mM sodium acetate as organic substrate. The catholyte solution consisted of a $K_3Fe(CN)_6$ 100 mM solution. Saline media was prepared by dissolving 5 $g{\cdot}L^{-1}$ NaCl for brackish water solution and 35 $g{\cdot}L^{-1}$ NaCl for seawater solution.

Air Diffusion Cathode

Air cathode was composed of three parts as depicted in **Figure 3**: (i) an external membrane (high density polyethylene fibers textile), impermeable to water and permeable to oxygen; (ii) a conductive material, in this case carbon nanofibers with iron nanoparticles to allow ORR; and (iii) an internal semipermeable membrane (treated high density polyethylene fibers textile) to allow proton exchange.

Start-Up Protocol

A previously reported start-up procedure was followed for both MDCs under study (Borjas et al., 2017). The anolyte, saline, and catholyte streams were firstly sterilized and recirculated through the lab-MDCs. Then, 200 mL of inoculum containing electrogenic bacteria was introduced in the anodic chamber of the MDCs by recirculation with a peristaltic pump.

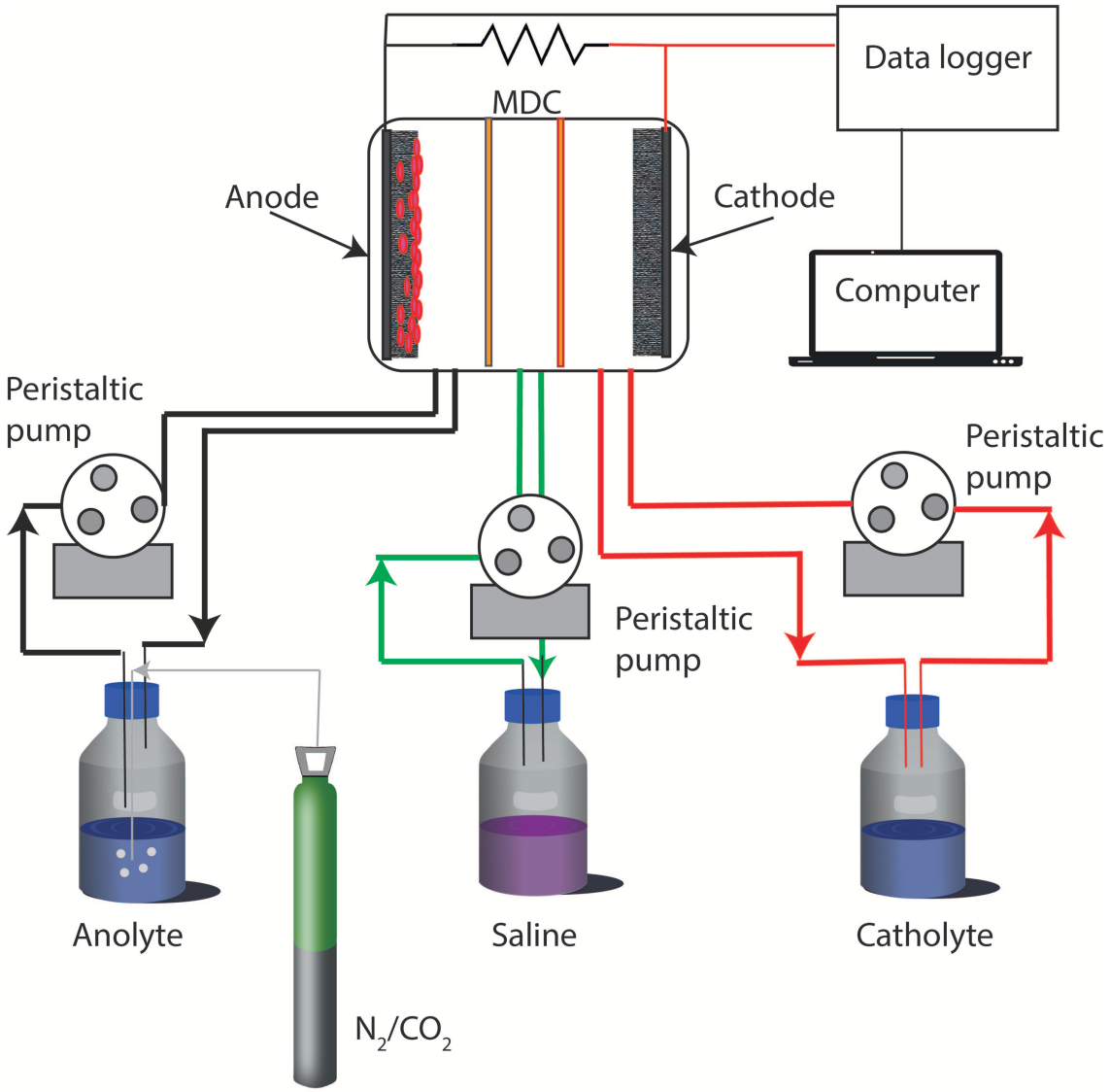

FIGURE 2 | Microbial Desalination Cells set-up.

For the air cathode MDC approach, as initial inoculum for start-up, an anodic-electroactive mixed culture from a long term (>3 years) operating Microbial Fuel Cell (MFC) was employed. Initial microbial population content, characterized by MiSeq Illumina platform, accounted for a mixture of Bacteroidetes (6.7%), Fermicutes (3.1%), Proteobacteria (65.9%), Spirochaetes (4.8%), Thermotogae (2.8%), and Verrucomicrobia (9.0%). A selective pressure through a redox potential gradient was applied to the anode in order to promote the growth and attachment of electroactive bacteria onto the electrode. Anode was properly inoculated when current density achieved values higher than 0.15 $mA{\cdot}cm^{-2}$. After that, it was transferred to the MDC.

In the case of the ferro-ferricyanide redox MDC, a pure culture of *Geobacter sulfurreducens* (strain DL1) was used as inoculum. Exponential-phase culture ($OD_{600nm} = 0.4$) was used for the inoculation into the anode compartment in the start-up protocol.

After inoculation of the anodes, the peristaltic pump was switched off overnight, allowing the microorganism to start growing on the anode surface (i.e., graphite felt). After incubation, the pumps were switched on to recirculate the anolyte, catholyte, and saline solutions through the system.

Once the bioanode was considered stable (i.e., no significant variation of electric current), the first desalination cycle was performed with newly-prepared solutions to ensure reproducibility among subsequent desalination cycles. The desalination cycles were finished when the conductivity of the saline tank was below of 1 $mS{\cdot}cm^{-1}$, as this threshold could be

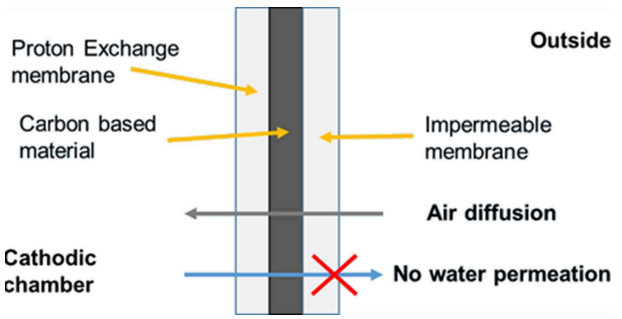

FIGURE 3 | Air cathode configuration.

considered as optimum value for water quality (Council Directive 75/440/EEC, 1975).

Calculations

The following equations were used to determine the main parameters of the MDCs performance. Current density, j ($mA{\cdot}cm^{-2}$), was calculated by:

$$j = \frac{I}{A_m} \tag{1}$$

where I is the electric current (mA) and A_m is the effective electrode surface area (cm^2).

Salt removal, SR (%), refers to the percentage of NaCl removed during every desalination cycle, and it can be expressed by:

$$SR = \frac{c_s^i - c_s^f}{c_s^i} \tag{2}$$

where c_s^i *and* c_s^f represent the initial and final molar concentrations of salt in the saline tank (mol m^{-3}), respectively.

Nominal Desalination rate, NDR ($L{\cdot}m^{-2}{\cdot}h^{-1}$), refers to the normalized amount of fresh water per square meter of membrane during every desalination cycle, and it can be expressed by:

$$NDR = \frac{Q_t}{A_m \cdot t_d} \tag{3}$$

where, t_d is the desalination time (h) (i.e., conductivity of saline tank below of 1 $mS{\cdot}cm^{-1}$), and Q_t is the volume of desalinated water (L).

Specific energy production, SEP ($kWh{\cdot}m^{-3}$), defines the energy produced by the MDC per cubic meter of fresh water, and it can be expressed by:

$$SEP = \frac{1}{Q_t}\int E_{cell} I\,(t)\,dt \tag{4}$$

where E_{cell} is the electric potential provided by the MDC device (V).

Current efficiency, η_c (%), defines the percentage of the total charge associated to the salt removed from the saline compartment to the amount of electric charge transferred across the membranes (ECT, $C{\cdot}m^{-3}$) over a complete process of desalination. η_c and ECT were calculated using Equations 5 and 6, respectively.

$$\eta_c = \frac{\upsilon\, z\, F\,(c_s^i - c_s^f)}{ECT} \tag{5}$$

$$ECT = \frac{1}{Q_t}\int I\,(t)\,dt \tag{6}$$

where, $\boldsymbol{\nu}$ and z represent the stoichiometric coefficient and the valence of the salt ions, respectively, and F is the Faraday constant (96,485 $C{\cdot}mol^{-1}$).

Coulombic efficiency, η_{Cb}, is defined as the ratio of total electric charge transferred to the anode from the consumed organic substrate and it can be expressed by:

$$\eta_{Cb} = \frac{M\int I\,(t)\,dt}{F \cdot b \cdot Q_{An} \cdot \triangle COD} \tag{7}$$

where M is the molecular weight of oxygen (32 $g{\cdot}mol^{-1}$), b is the number of electrons exchanged per mole of oxygen (b = 4), Q_{An} is the volume of the anolyte tank (L), and ΔCOD is the change in chemical oxygen demand (COD) for the experiment ($mg\ O_2{\cdot}L^{-1}$).

COD removal rate, COD_{rate} ($kg{\cdot}m^{-3}{\cdot}day^{-1}$), was calculated using the next expression:

$$COD_{rate} = \frac{\triangle COD}{V_A t_d} \tag{8}$$

where V_A is the volume of liquid in the anode compartment (m^3).

The total circulated charge, Q (Coulomb), was calculated according to Equation 9:

$$Q = \int I\,(t)\,dt \times t_d \tag{9}$$

RESULTS AND DISCUSSION

Both MDC strategies (i.e., ORR as cathodic reaction, ferro-ferricyanide redox system as cathodic reaction) were compared using laboratory-scale MDCs with 100 cm^2 of cross section (or geometric electrode surface). Experimental results are showed in **Figure 4**. Experiments were carried out at two different initial saline concentrations: brackish water range (NaCl 7.5–10 $g{\cdot}L^{-1}$) with an initial electric conductivity of 13.9 and 17.5 $mS{\cdot}cm^{-1}$ for ferro-ferricyanide redox and air cathode approach, respectively, and seawater range (NaCl 35 $g{\cdot}L^{-1}$), with an initial electric conductivity of 51.5 and 53.3 $mS{\cdot}cm^{-1}$ for ferro-ferricyanide redox and air cathode approach. Nominal desalination rate, salt removal, current efficiency and COD removal rate were compared between both strategies to compare the feasibility of MDC technology, understand its limitations, describe its advantages and disadvantages and elucidate which strategy is more convenient for scaling up of the technology in real environments.

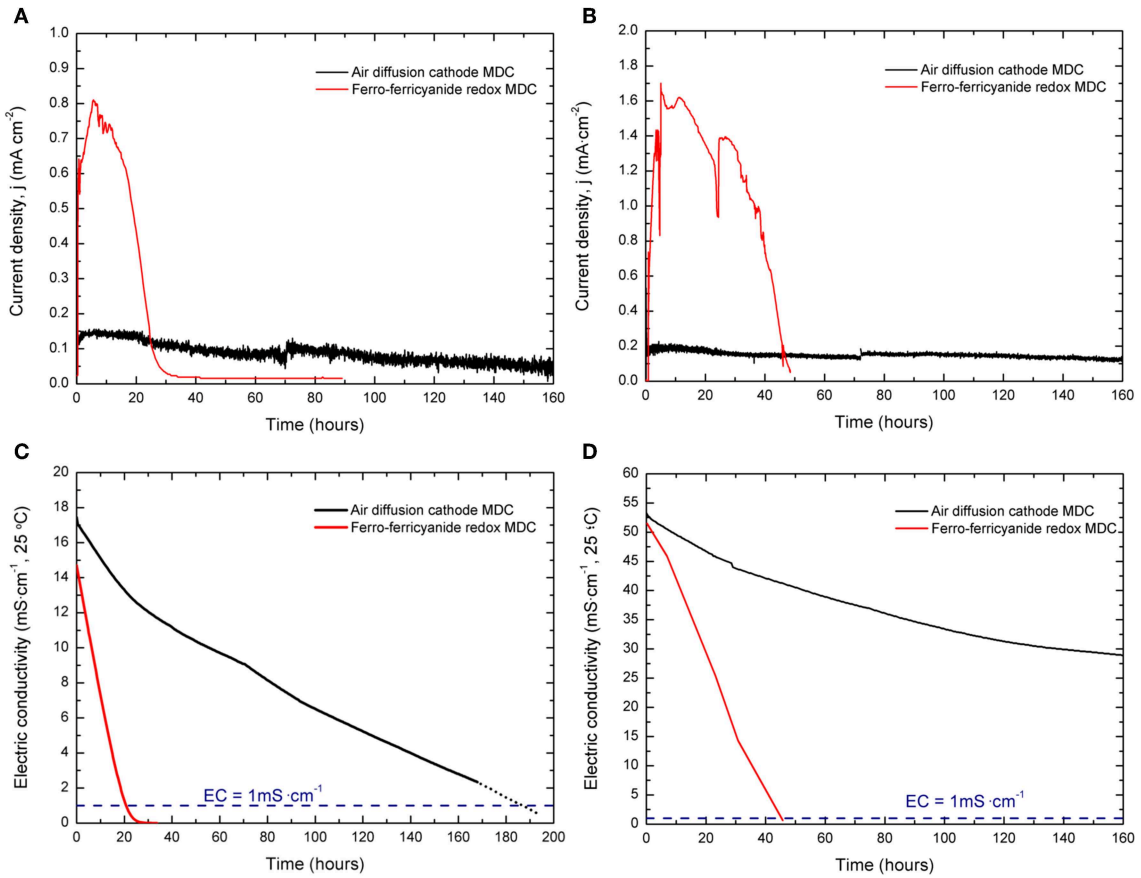

FIGURE 4 | Experimental results for air diffusion cathode MDC (black) and ferro-ferricyanide redox MDC (red). **(A,B)** Current density vs. time for brackish and sea water desalination. **(C,D)** Conductivity vs. time for brackish and sea water desalination. Horizontal line shows the threshold for conductivity 1 mS·cm^{-1}. The dotted line for the air diffusion cathode MDC results from an interpolation of the electric conductivity below 1 mS·cm^{-1} for comparative purposes.

Brackish Water Desalination

Figure 4A shows the electric current for brackish water desalination experiments using the aforementioned strategies. Maximum current densities for air diffusion and ferro-ferricyanide cathode were 0.14 and 0.81 mA·cm^{-2}, respectively. As both devices used the same external load (2.5 Ω) and analogous anodes and configurations, the higher electric current obtained when using the ferro-ferricyanide redox MDC may be directly related to the cathode reaction, which provide higher available potential to drive the desalination process.

In general, it could be stated that from the thermodynamic point of view, the available potential in the MDC to perform the desalination process is higher when oxygen reduction is used in the cathode [$E^{0'}_{MDC} = E^{0'}_{cathode}$-$E^{0'}_{anode} = 0.81$ V—(−0.3 V) = 1.11 V]. However, oxygen reduction reaction provides less potential than expected in the range of current densities (i.e., 0.2–1.5 mA cm^{-2}) used for desalination in MDC systems, and it is mainly related to slow kinetics associated to this reaction at pH = 7 (or neutral), that is common in microbial electrochemical systems. On the other hand, regardless the lower thermodynamic potential when ferri-ferrocyanide reduction is used in the cathode compartment [$E^{0'}_{MDC} = 0.36$—(−0.3 V) = 0.66 V], fast kinetic provides more available potential when implemented in MDC systems. Thus, the lower potential available is the reason behind the poor desalination performance when oxygen reduction is used as cathodic reaction.

Figure 4C shows the electric conductivity for brackish water desalination using the aforementioned strategies. As the electric current is also directly related to migration of ion species, the desalination time (i.e., time required to achieve the threshold conductivity of 1 mS·cm^{-1}) for the ferro-ferricyanide redox MDC is lower compared to the air cathode MDC.

As shown in **Figure 4C**, the current density in ferro-ferricyanide redox cathode experiment decreased from 0.81 mA·cm^{-2} in 16 h to 0.08·mA cm^{-2}. This decrease is attributable to the drop in conductivity of the salinity compartment from 14 to 0.56 mS·cm^{-1}. In the case of the air cathode experiment, the current density dropped from 0.14 to 0.08 mA·cm^{-2} in 160 h, decreasing the conductivity in the saline compartment from 16 to 2.4 mS·cm^{-1}.The decrease of current density in both MDC cases could be linked to the increase of the internal resistance of the MDC, as electric conductivity decreases during

TABLE 2 | Initial and final salinity, salt removal, desalination time, current efficiency, nominal desalination rate, COD removal rate, anode coulombic efficiency, specific energy production, total circulated charge and volume variation for air diffusion cathode and ferro-ferricyanide redox MDC experiments for brackish water desalination.

	Air-diffusion cathode MDC	Ferro-ferricyanide redox MDC
Initial salinity ($g \cdot L^{-1}$)	10.7	7.3
Final salinity ($g \cdot L^{-1}$)	0.5	0.5
Salt removal (%)	93.6	93.3
Desalination time (h)	205	23
NDR ($L \cdot m^{-2} \cdot h^{-1}$)*	0.17**	1.5
Current efficiency (%)	162	81.1
COD removal rate (kg $COD \cdot m^{-3} \cdot day^{-1}$)***	0.94	7.14
Coulombic efficiency (%)	6.5	91.0
Specific energy production ($kWh \cdot m^{-3}$)	0.017	0.7
Total circulated charge (Q)	5086	5165
Volume variation (%)	−36.0	−8.1

*Calculated considering the final volume of saline tank.
**Extrapolated from experimental results.
***Considering the volume of anolyte compartment.

TABLE 3 | Initial and final salinity, salt removal, desalination time, current efficiency, nominal desalination rate, COD removal rate, anode coulombic efficiency, specific energy production, total circulated charge and volume variation for air diffusion cathode and ferro-ferricyanide redox MDC experiments for sea water desalination.

	Air-diffusion cathode MDC**	Ferro-ferricyanide redox MDC
Initial salinity ($g \cdot L^{-1}$)	33.5	35.0
Final salinity ($g \cdot L^{-1}$)	17.4	0.5
Salt removal (%)	48.2	98.6
Desalination time (h)	–	43
NDR ($L \cdot m^{-2} \cdot h^{-1}$)*	0.14	0.7
Current efficiency (%)	145	108
COD removal rate (kg $COD \cdot m^{-3} \cdot day^{-1}$)	1.07	19.7
Coulombic efficiency (%)	10.3	61.0
Specific Energy Production ($kWh \cdot m^{-3}$)	0.055	5.4
Total circulated charge (Q)	8,994	19,354
Volume variation (%)	−2	−19

*Calculated considering the final volume of saline tank.
**Calculated for partial desalination.

the experiments. These observations are in accordance with previous MDC behavior operating in batch mode (Borjas et al., 2017).

It is worthwhile to mention that the air diffusion cathode developed in this study (Fe-doped C-NF) displayed higher current densities compared with analogous studies in the literature (in the range of 0.084 $mA \cdot cm^{-2}$, using Pt coated air diffusion cathode when desalinating 10 $g \cdot L^{-1}$ brackish water) (Jafary et al., 2018). **Table 2** shows the main experimental performance parameters for brackish water desalination using both cathodic reactions

For both desalination cycles the salt removal exceeded 90%, indicating proper performance of both MDCs as desalination devices. Regarding nominal desalination rate (NDR), the ferro-ferricyanide redox MDC was able to produce almost six times higher amount of desalinated water (1.54 $L \cdot m^2 \cdot h^{-1}$) compared to that of the air diffusion cathode MDC (0.17 $L \cdot m^2 \cdot h^{-1}$). Current efficiencies were 162% and 81.1% for air diffusion cathode and ferro-ferricyanide redox MDC, respectively. As current efficiency determines the rate of current that is used for ion migration, values above 100% means that an additional transport phenomena occurred during the experiment, i.e., diffusion from saline to adjacent compartments.

From the point of view of waste water treatment, COD removal rates for both air diffusion cathode and ferro-ferricyanide redox MDCs were 0.94 and 7.14 kg $COD \cdot m^{-3} \cdot day^{-1}$. This parameter is related to the current density and desalination performance, as consumption of COD provides the electric current to drive the desalination process. The coulombic efficiency decayed at longer desalination times (t_d), as it is the case of the air diffusion cathode MDC experiment. This fact may be due to a competition between electrogenic and anaerobic microorganism since the latter do not contribute to electric current generation.

Specific energy production (SEP) was 0.02 and 0.8 $kWh \cdot m^{-3}$ for air diffusion cathode and ferro-ferricyanide redox MDC, respectively. This fact indicates that in both cases it is possible to generate a significant amount of electric energy simultaneously with desalinated water production and waste water treatment, as reported in the literature (Sophia et al., 2016; Sevda and Abu-Reesh, 2018).

Finally, the water transport was measured by determining the change in the final volume of the saline tank. Water transport across membranes was remarkable for air diffusion cathode MDC experiment, accounting for 36% decrease (v/v). In the case of the ferro-ferricyanide redox MDC, the volume decrease remained below 10% (v/v). Water transport may be attributable to osmosis and/or electrosomosis phenomena (i.e., water transport due to electric charge). As the desalination conditions were similar for both cases (i.e., electric charge to perform desalination, see **Table 2**), the water transport could be attributed to osmosis. In this sense, for a similar water flux due to osmosis, a higher desalination time allows for a higher osmosis water transport, as indicated in **Table 2** for the air diffusion cathode experiment.

Seawater Desalination

Figure 4B shows the electric current for sea water desalination experiments. In this case, air diffusion cathode MDC and ferro-ferricyanide redox MDC experiments achieved maximum current densities of 0.20 and 1.70 $mA \cdot cm^{-2}$, respectively. Similarly to the previously discussed results, the current density for ferro-ferricyanide redox MDC decreased from 1.7 to 0.1 $mA \cdot cm^{-2}$ in 48 h due to the drop in the conductivity of the salinity compartment (from 50 to 0.6 $mS \cdot cm^{-1}$) as depicted in **Figure 4B**. For the air cathode MDC experiment, the current

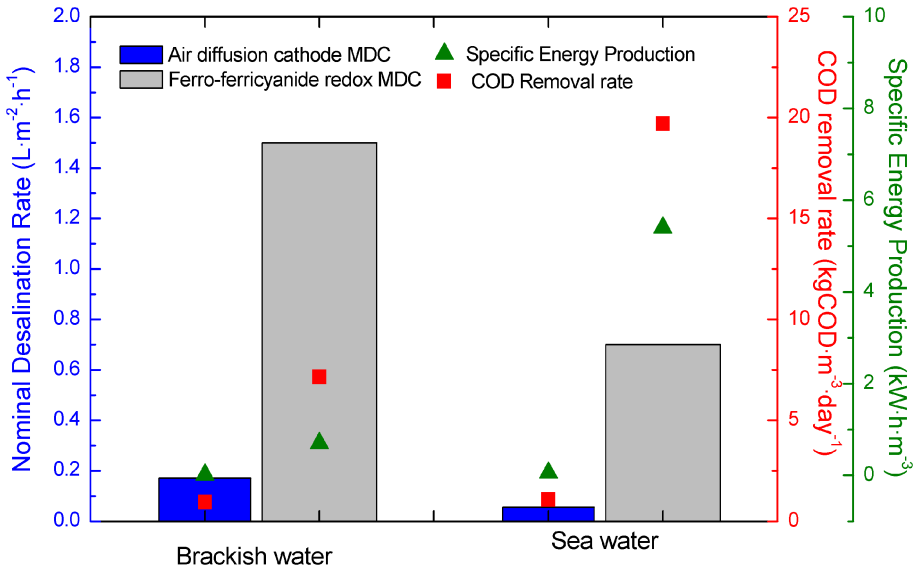

FIGURE 5 | Nominal desalination rate (NDR) (bar plot), COD removal rate (black line), and specific energy production (SEP) (green line) for both MDC strategies.

density dropped from 0.2 to 0.12 mA·cm^{-2} in 160 h, while decreasing the salinity from 51 to 28 mS·cm^{-1}.

Figure 4D shows the electric conductivity for sea water desalination. In this case, the air diffusion cathode MDC was not able to accomplish complete desalination (i.e., electric conductivity below threshold value of 1 mS·cm^{-1}). **Table 3** shows the main experimental performance parameters for the sea water desalination experiment.

It is important to note that for the air diffusion cathode MDC, the salt removal was around 20%, indicating that only partial desalination was achieved. The partial desalination has been also reported in the literature with similar MDC configuration using oxygen reduction as cathode reaction (decrease of 58 to 22 mS·cm^{-1}, salt removal 50%) (Zhang and He, 2015; Moruno et al., 2018). This effect could be attributed to the low available potential to drive the migration of the ions. When the electric conductivity increased in the anodic/cathode chamber due to the migration of the ions from the saline compartment during the desalination cycle, back-diffusion transport of salt started to be significant, and eventually this ionic transport was equal to the ionic transport due to migration. This resulted in a zero net balance of salinity in the saline compartment (Ping et al., 2016). This effect could be observed in **Figure 4D** from the asymptotic trend of the electric conductivity for the air diffusion cathode MDC (28 mS·cm^{-1}). In the case of ferro-ferricyanide redox MDC, complete desalination was achieved, being the desalination time 43 h (t_d).

NDR values were 0.14 L·m^{-2}·h^{-1} for partial desalination (air diffusion cathode MDC), and 0.7 L·m^{-2}·h^{-1} for the ferro-ferricyanide redox MDC. This latter value is slightly higher compared to analogs MDC systems operating with ferro-ferricyanide catholyte (Cao et al., 2009; Luo et al., 2012; Kalleary et al., 2014; Chen et al., 2015) likely due to recirculation, thickness of the saline compartment and low external load value. Current efficiencies were above 100%, indicating higher ion migration which could be attributed to the electric current achieved. Thus, diffusion from saline compartment to adjacent compartments was more significant for sea water desalination compared to brackish water desalination (see **Tables 2**, **3**). Regarding volume variation, it could be attributed to osmotic processes due to the longer duration in the air cathode MDC configuration as well as different initial conductivity in catholyte solutions in both configurations.

Figure 5 summarizes the main experimental results for both MDC strategies for brackish and sea water desalination. As stated, NDR was higher for brackish and sea water when the ferro-ferricyanide redox MDC was used, and only complete desalination could be achieved using air diffusion cathode MDC for brackish water desalination (i.e., partial desalination for sea water). From the point of view of COD removal rate, desalination of sea water increased the waste water capacity of the MDC, and this effect was related to the increase in the generation of electric current. Similarly, specific energy production (SEP) was higher for seawater desalination compared to brackish water's.

From the point of view of real application, brackish water desalination can be accomplished by both strategies. As oxygen is a simple and available reagent, air diffusion cathode MDC is more suitable for brackish water desalination, but water production (i.e., NDR) should be maximized by complete optimization of the system. In the case of sea water desalination, only ferro-ferricyanide redox MDC could achieve complete desalination, so air diffusion MDC strategy could be adopted as a suitable approach for pre-desalination step applications (for example, coupled to a RO conventional plant Elmekawy et al., 2014. Obviously, even if ferro-ferricyanide redox catholyte allows the increase of the desalination efficiency, waste water treatment, fresh water, and energy production in the MDC device, it should

be regenerated when depleted due to the high costs of reagents, as previously discussed in the literature Cao et al., 2009. For this reason, low-cost and effective strategies for regeneration of the redox mediator catholyte need to be explored in next studies, for instance, using renewable energy (i.e., photovoltaic, wind energy) or other microbial electrochemical processes (i.e., biocathodes).

Finally, the experimental results of this study have been obtained in two different laboratories, with systematic experimental approach and in close collaboration. The consistent and reproducible experimental results shall help the further development of MDC technology and to speed up their scaling-up for operation in real environments.

CONCLUSIONS

Microbial Desalination Cell constitutes an innovative technology where microbial fuel cells and electrodialysis merge in the same device for obtaining fresh water with no energy-associated costs, while treating wastewater and producing energy. One of the main limitations for MDC technology is the low available potential for desalination when oxygen reduction is used as cathodic reaction, as partial desalination is obtained when sea water is used as feed stream. The ferro-ferricyanide redox MDC strategy has been proposed in the literature in order to enhance the performance of MDC technology and provide total desalination of sea water. Two analogous MDC experimental setups with different cathode strategy (air diffusion and ferro-ferricyanide redox) allow to compare the desalination performance of both systems, and to understand the main limitations for the technology development. Air cathode approach may be suitable for brackish water desalination, even though nominal desalination rates are near one order of magnitude lower than those obtained using a ferro-ferricyanide redox mediator. Seawater desalination could be better addressed by a ferro-ferricyanide redox MDC; however, catholyte regeneration routes should be explored to reduce costs and allow for low-cost and efficient desalination. A compromise between MDC performance and costs should be made for further upscaling and application in real environments. Finally, the proposed methodology could be an interesting approach for inter laboratory collaboration for further MDC studies.

DATA AVAILABILITY STATEMENT

The datasets generated for this study are available on request to the corresponding author.

AUTHOR CONTRIBUTIONS

MR-M performed the experiments related to ferro/ferricyanide catholyte. PR helped in the experimental stage, collected and organized all the experimental data, and wrote the manuscript. MA and PB-J performed the manufacturing process and experiments related to air diffusion cathode. EB also participated in the air-cathode design and supervised the experimental work. PZ coordinated and supervised the inter-laboratory experimental work and corrected the manuscript. VM and FR supervised the experimental work. JO and AE-N designed experiments related to ferro/ferricyanide catholyte and critically reviewed the manuscript. All authors participated in manuscript writing.

FUNDING

Project MIDES – H2020 has received funding from the European Union's Horizon 2020 research and innovation programme under grant agreement No. 685793. MR-M acknowledges the financial support of Consejería de Educación e Investigación de la Comunidad de Madrid and Fondo Social Europeo (Ref: PEJD-2018-PRE/AMB-8721). JO acknowledges the financial support of Agencia Estatal de Investigación (AEI) and Fondo Europeo de Desarrollo Regional (FEDER) (Proyecto BioDES, CTM2015-74695-JIN).

SUPPLEMENTARY MATERIAL

The Supplementary Material for this article can be found online at: https://www.frontiersin.org/articles/10.3389/fenrg.2019.00135/full#supplementary-material

REFERENCES

Badiuzzaman, P., McLaughlin, E., and McCauley, D. (2017). Substituting freshwater: can ocean desalination and water recycling capacities substitute for groundwater depletion in California? *J. Environ. Manage.* 203, 123–135. doi: 10.1016/j.jenvman.2017.06.051

Bashyam, R., and Zelenay, P. (2006). A class of non-precious metal composite catalysts for fuel cells. *Nature* 443, 63–66. doi: 10.1038/nature05118

Borjas, Z., Esteve-Núñez, A., and Ortiz, J. M. (2017). Strategies for merging microbial fuel cell technologies in water desalination processes: start-up protocol and desalination efficiency assessment. *J. Power Sources* 356, 519–528. doi: 10.1016/j.jpowsour.2017.02.052

Bosch-Jimenez, P., Martinez-Crespiera, S., Amantia, D., Della Pirriera, M., Forns, I., Shechter, R., et al. (2017). Non-precious metal doped carbon nanofiber air-cathode for Microbial Fuel Cells application: oxygen reduction reaction characterization and long-term validation. *Electrochim. Acta* 228, 380–388. doi: 10.1016/j.electacta.2016.12.175

Cao, X., Huang, X., Liang, P., Xiao, K., Zhou, Y., Zhang, X., et al. (2009). A new method for water desalination using microbial desalination cells. *Environ. Sci. Technol.* 43, 7148–7152. doi: 10.1021/es901950j

Chen, S., Luo, H., Hou, Y., Liu, G., Zhang, R., and Qin, B. (2015). Comparison of the removal of monovalent and divalent cations in the microbial desalination cell. *Front. Environ. Sci. Eng.* 9, 317–323. doi: 10.1007/s11783-013-0596-y

Chen, X., Liang, P., Wei, Z., Zhang, X., and Huang, X. (2012). Sustainable water desalination and electricity generation in a separator coupled stacked microbial desalination cell with buffer free electrolyte circulation. *Bioresour. Technol.* 119, 88–93. doi: 10.1016/j.biortech.2012.05.135

Chen, X., Xia, X., Liang, P., Cao, X., Sun, H., and Huang, X. (2011). Stacked microbial desalination cells to enhance water desalination efficiency. *Environ. Sci. Technol.* 45, 2465–2470. doi: 10.1021/es103406m

Chowdhury, A. H., Scanlon, B. R., Reedy, R. C., and Young, S. (2018). Fingerprinting groundwater salinity sources in the Gulf Coast Aquifer System, USA. *Hydrogeol. J.* 26, 197–213. doi: 10.1007/s10040-017-1619-8

Council Directive 75/440/EEC (1975). Council Directive 75/440/EEC of 16 June 1975 concerning the quality required of surface water intended for the abstraction of drinking water in the Member States.

Elmekawy, A., Hegab, H. M., and Pant, D. (2014). The near-future integration of microbial desalination cells with reverse osmosis technology. *Energy Environ. Sci.* 7, 3921–3933. doi: 10.1039/C4EE02208D

Freguia, S., Rabaey, K., Yuan, Z., and Keller, J. (2007). Non-catalyzed cathodic oxygen reduction at graphite granules in microbial fuel cells. *Electrochim. Acta* 53, 598–603. doi: 10.1016/j.electacta.2007.07.037

Freguia, S., Rabaey, K., Yuan, Z., and Keller, J. (2008). Sequential anode–cathode configuration improves cathodic oxygen reduction and effluent quality of microbial fuel cells. *Water Res.* 42, 1387–1396. doi: 10.1016/j.watres.2007.10.007

Ge, X., Sumboja, A., Wuu, D., An, T., Li, B., Goh, F. W. T., et al. (2015). Oxygen reduction in alkaline media: from mechanisms to recent advances of catalysts. *ACS Catal.* 5, 4643–4667. doi: 10.1021/acscatal.5b00524

Ge, Z., Dosoretz, C. G., and He, Z. (2014). Effects of number of cell pairs on the performance of microbial desalination cells. *Desalination* 341, 101–106. doi: 10.1016/j.desal.2014.02.029

Harnisch, F., Wirth, S., and Schröder, U. (2009). Effects of substrate and metabolite crossover on the cathodic oxygen reduction reaction in microbial fuel cells: platinum vs. iron(II) phthalocyanine based electrodes. *Electrochem. Commun.* 11, 2253–2256. doi: 10.1016/j.elecom.2009.10.002

Jacobson, K. S., Drew, D. M., and He, Z. (2011a). Efficient salt removal in a continuously operated upflow microbial desalination cell with an air cathode. *Bioresour. Technol.* 102, 376–380. doi: 10.1016/j.biortech.2010.06.030

Jacobson, K. S., Drew, D. M., and He, Z. (2011b). Use of a liter-scale microbial desalination cell as a platform to study bioelectrochemical desalination with salt solution or artificial seawater. *Environ. Sci. Technol* 45, 4652–4657. doi: 10.1021/es200127p

Jafary, T., Daud, W. R. W., Aljlil, S. A., Ismail, A. F., Al-Mamun, A., Baawain, M. S., et al. (2018). Simultaneous organics, sulphate and salt removal in a microbial desalination cell with an insight into microbial communities. *Desalination* 445, 204–212. doi: 10.1016/j.desal.2018.08.010

Kalleary, S., Mohammed Abbas, F., Ganesan, A., Meenatchisundaram, S., Srinivasan, B., Packirisamy, A. S. B., et al. (2014). Biodegradation and bioelectricity generation by Microbial Desalination Cell. *Int. Biodeterior. Biodegrad.* 92, 20–25. doi: 10.1016/j.ibiod.2014.04.002

Kim, Y., and Logan, B. E. (2011). Series assembly of microbial desalination cells containing stacked electrodialysis cells for partial or complete seawater desalination. *Environ. Sci. Technol.* 45, 5840–5845. doi: 10.1021/es200584q

Lefèvre, M., Proietti, E., Jaouen, F., and Dodelet, J.-P. (2009). Iron-based catalysts with improved oxygen reduction activity in polymer electrolyte fuel cells. *Science* 324, 71–74. doi: 10.1126/science.1170051

Liu, X.-W., Sun, X.-F., Huang, Y.-X., Sheng, G.-P., Zhou, K., Zeng, R. J., et al. (2010). Nano-structured manganese oxide as a cathodic catalyst for enhanced oxygen reduction in a microbial fuel cell fed with a synthetic wastewater. *Water Res.* 44, 5298–5305. doi: 10.1016/j.watres.2010.06.065

Lu, M., and Li, S. F. Y. (2012). Cathode reactions and applications in microbial fuel cells: a review. *Crit. Rev. Environ. Sci. Technol.* 42, 2504–2525. doi: 10.1080/10643389.2011.592744

Luo, H., Xu, P., and Ren, Z. (2012). Long-term performance and characterization of microbial desalination cells in treating domestic wastewater. *Bioresour. Technol.* 120, 187–193. doi: 10.1016/j.biortech.2012.06.054

MacHarg, J. P., Seacord, T. F., and Sessions, B. (2008). ADC baseline tests reveal trends in membrane performance. *Desalin. Water Reuse* 18, 1–9. Available online at: http://citeseerx.ist.psu.edu/viewdoc/download?doi=10.1.1.608.2998&rep=rep1&type=pdf

Mehanna, M., Saito, T., Yan, J., Hickner, M., Cao, X., Huang, X., et al. (2010). Using microbial desalination cells to reduce water salinity prior to reverse osmosis. *Energy Environ. Sci.* 3, 1114–1120. doi: 10.1039/c002307h

Moruno, F. L., Rubio, J. E., Santoro, C., Atanassov, P., Cerrato, J. M., and Arges, C. G. (2018). Investigation of patterned and non-patterned poly(2,6-dimethyl 1,4-phenylene) oxide based anion exchange membranes for enhanced desalination and power generation in a microbial desalination cell. *Solid State Ionics* 314, 141–148. doi: 10.1016/j.ssi.2017.11.004

Ortiz, J. M., Sotoca, J. A., Expósito, E., Gallud, F., García-García, V., Montiel, V., et al. (2005). Brackish water desalination by electrodialysis: batch recirculation operation modeling. *J. Memb. Sci.* 252, 65–75. doi: 10.1016/j.memsci.2004.11.021

Ping, Q., and He, Z. (2013). Improving the flexibility of microbial desalination cells through spatially decoupling anode and cathode. *Bioresour. Technol.* 144, 304–310. doi: 10.1016/j.biortech.2013.06.117

Ping, Q., Porat, O., Dosoretz, C. G., and He, Z. (2016). Bioelectricity inhibits back diffusion from the anolyte into the desalinated stream in microbial desalination cells. *Water Res.* 88, 266–273. doi: 10.1016/j.watres.2015.10.018

Qu, Y., Feng, Y., Wang, X., Liu, J., Lv, J., He, W., et al. (2012). Simultaneous water desalination and electricity generation in a microbial desalination cell with electrolyte recirculation for pH control. *Bioresour. Technol.* 106, 89–94. doi: 10.1016/j.biortech.2011.11.045

Sevda, S., and Abu-Reesh, I. M. (2018). Improved salt removal and power generation in a cascade of two hydraulically connected up-flow microbial desalination cells. *J. Environ. Sci. Heal. Part A* 53, 326–337. doi: 10.1080/10934529.2017.1400805

Shaffer, D. L., Werber, J. R., Jaramillo, H., Lin, S., and Elimelech, M. (2014). Forward osmosis: where are we now?. *Desalination* 356, 271–284. doi: 10.1016/j.desal.2014.10.031

Sharon, H., and Reddy, K. S. (2015). A review of solar energy driven desalination technologies. *Renew. Sustain. Energy Rev.* 41, 1080–1118. doi: 10.1016/j.rser.2014.09.002

Sophia, A. C., Bhalambaal, V. M., Lima, E. C., and Thirunavoukkarasu, M. (2016). Microbial desalination cell technology: contribution to sustainable waste water treatment process, current status and future applications. *J. Environ. Chem. Eng.* 4, 3468–3478. doi: 10.1016/j.jece.2016.07.024

Talbot, D. (2015). *The World's Largest and Cheapest Reverse-Osmosis Desalination Plant is up and Running in Israel*. MIT Technology Review.

Vij, V., Sultan, S., Harzandi, A. M., Meena, A., Tiwari, J. N., Lee, W.-G., et al. (2017). Nickel-based electrocatalysts for energy-related applications: oxygen reduction, oxygen evolution, and hydrogen evolution reactions. *ACS Catal.* 7, 7196–7225. doi: 10.1021/acscatal.7b01800

Wang, P., and Chung, T.-S. (2015). Recent advances in membrane distillation processes: membrane development, configuration design and application exploring. *J. Memb. Sci.* 474, 39–56. doi: 10.1016/j.memsci.2014.09.016

Wang, Q., Huang, L., Yu, H., Quan, X., Li, Y., Fan, G., et al. (2015). Assessment of five different cathode materials for Co(II) reduction with simultaneous hydrogen evolution in microbial electrolysis cells. *Int. J. Hydrogen Energy* 40, 184–196. doi: 10.1016/j.ijhydene.2014.11.014

Water Scarcity (2019). *UN Water*. Available online at: http://www.unwater.org/water-facts/scarcity/ (accessed April 1, 2019).

Wen, Q., Zhang, H., Chen, Z., Li, Y., Nan, J., and Feng, Y. (2012). Using bacterial catalyst in the cathode of microbial desalination cell to improve wastewater treatment and desalination. *Bioresour. Technol.* 125, 108–113. doi: 10.1016/j.biortech.2012.08.140

Yuan, H., Abu-Reesh, I. M., and He, Z. (2015). Enhancing desalination and wastewater treatment by coupling microbial desalination cells with forward osmosis. *Chem. Eng. J.* 270, 437–443. doi: 10.1016/j.cej.2015.02.059

Yuan, H., Hou, Y., Abu-Reesh, I. M., Chen, J., and He, Z. (2016). Oxygen reduction reaction catalysts used in microbial fuel cells for energy-efficient wastewater treatment: a review. *Mater. Horizons* 3, 382–401. doi: 10.1039/C6MH00093B

Yuan, L., Yang, X., Liang, P., Wang, L., Huang, Z.-H., Wei, J., et al. (2012). Capacitive deionization coupled with microbial fuel cells to desalinate low-concentration salt water. *Bioresour. Technol.* 110, 735–738. doi: 10.1016/j.biortech.2012.01.137

Zhang, B., and He, Z. (2012). Integrated salinity reduction and water recovery in an osmotic microbial desalination cell. *RSC Adv.* 2:3265. doi: 10.1039/c2ra20193c

Zhang, B., Zheng, X., Voznyy, O., Comin, R., Bajdich, M., García-Melchor, M., et al. (2016). Homogeneously dispersed multimetal oxygen-evolving catalysts. *Science* 352, 333–337. doi: 10.1126/science.aaf1525

Zhang, F., Chen, M., Zhang, Y., and Zeng, R. J. (2012). Microbial desalination cells with ion exchange resin packed to enhance desalination at low salt concentration. *J. Memb. Sci.* 417–418, 28–33. doi: 10.1016/j.memsci.2012.06.009

Zhang, F., and He, Z. (2015). Scaling up microbial desalination cell system with a post-aerobic process for simultaneous wastewater treatment and seawater desalination. *Desalination* 360, 28–34. doi: 10.1016/j.desal.2015.01.009

Zhao, F., Harnisch, F., Schröder, U., Scholz, F., Bogdanoff, P., and Herrmann, I. (2006). Challenges and constraints of using oxygen cathodes in microbial fuel cells. *Environ. Sci. Technol.* 40, 5193–5199. doi: 10.1021/es060332p

Zuo, K., Chang, J., Liu, F., Zhang, X., Liang, P., and Huang, X. (2017). Enhanced organics removal and partial desalination of high strength industrial wastewater with a multi-stage microbial desalination cell. *Desalination* 423, 104–110. doi: 10.1016/j.desal.2017.09.018

Zuo, K., Chen, M., Liu, F., Xiao, K., Zuo, J., Cao, X., et al. (2018). Coupling microfiltration membrane with biocathode microbial desalination cell enhances advanced purification and long-term stability for treatment of domestic wastewater. *J. Memb. Sci.* 547, 34–42. doi: 10.1016/j.memsci.2017.10.034

Conflict of Interest: The authors declare that the research was conducted in the absence of any commercial or financial relationships that could be construed as a potential conflict of interest.

frontiers in Energy Research

ORIGINAL RESEARCH
published: 25 February 2020
doi: 10.3389/fenrg.2020.00020

Membrane Selection for Electrochemical Treatment of Septage

*Guruprasad V. Talekar and Srikanth Mutnuri**

Applied Environmental Biotechnology Laboratory, Department of Biological Sciences, Birla Institute of Technology and Science, Sancoale, India

The development of economically feasible and efficient decentralized onsite treatment of septic tank water or blackwater is the need of the hour. In recent years, Electrochemical oxidation (EO) has been proven to be an efficient alternative treatment technology for use in small-scale, onsite wastewater treatment operations. Recently, the electrochemical treatment of wastewater in membrane divided cells has been reported to be of superior efficiency with regards to chemical oxygen demand (COD) removal while producing fewer disinfection by-products. In this study, a reduction of all the major wastewater defining parameter in both the anode and cathode chambers of an Anionic exchange membrane divided electrochemical reactor (AEM-ECR) and a Cationic exchange membrane divided electrochemical reactor (CEM-ECR) were obtained after the electrolysis of real septage and septage that had passed a vertical flow constructed wetland (VFCW), respectively. The results of these batch electrolysis experiments in AEM-ECR and CEM-ECR using septage as feed concluded that among the two studied membranes, AEM usage in ECR is optimal. The reduction in COD, Total Organic Carbon (TOC), and Total ortho-phosphate (TP) after electrolysis in AEM based ECR was found to be double that achieved in CEM-ECR. The charge supplied and power required were 7794 ± 10 coulombs L^{-1} and 48 ± 6.7 Wh L^{-1}. Further, the results of the batch electrolysis experiments in AEM-ECR with VFCW treated septage as feed concluded that the optimum feed to the AEM-ECR is VFCW treated septage since the charge and power requirement for treatment of VFCW treated septage is 42.5 and 35% lower, respectively, to that required for septage for similar percentage reductions in COD, TOC, and TP. The charge supplied and power required was 4482 ± 846 coulombs L^{-1} and 31 ± 1.6 Wh L^{-1}. Finally, the continuous flow experiments AC_{AEM} and CA_{AEM} concluded that, regarding the double-chambered membrane ECR, a feed flow mode from anode to cathode results in maximum reduction in COD, TOC, TP, and coliforms in a double-chambered membraned ECR. The power required for treatment was 21.2 Kwh/m^3.

Keywords: electrooxidation, electro disinfection, membrane divided cells, anion exchange membrane, cation exchange membrane

OPEN ACCESS

Edited by:
Subba Rao Chaganti, University of Michigan, United States

Reviewed by:
Makarand M. Ghangrekar, Indian Institute of Technology Kharagpur, India
Qaisar Mahmood, COMSATS University, Islamabad Campus, Pakistan

****Correspondence:***
Srikanth Mutnuri
srikanth@goa.bits-pilani.ac.in

Specialty section:
This article was submitted to Bioenergy and Biofuels, a section of the journal Frontiers in Energy Research

Received: *19 September 2019*
Accepted: *04 February 2020*
Published: *25 February 2020*

Citation:
Talekar GV and Mutnuri S (2020) Membrane Selection for Electrochemical Treatment of Septage. Front. Energy Res. 8:20. doi: 10.3389/fenrg.2020.00020

INTRODUCTION

The development of economically feasible and efficient decentralized onsite treatment of septic tank water or blackwater is the need of the hour for many upper and lower middle-income countries due to a lack of centralized treatment infrastructure. In India, according to the Central Pollution control board (CPCB), existing centralized treatment facilities can treat only 38% (22963 MLD) of the total generated sewage (61754 MLD). About 62% of the generated sewage (38791 MLD) is discharged untreated, directly into nearby water bodies causing immense degradation of the ecosystem and environmental health. Globally, as reported by UNESCO in 2017, over 80% of all wastewater is discharged without treatment.

More than 70 different onsite systems exist which have been practiced over the century (Science and Ho, 2016). Media filters (Intermittent sand filters and Rotating sand filters), Lagoons (Facultative, aerated, aerobic, and anaerobic lagoons), Sequential batch reactors and constructed wetlands are some examples. However, none of them have been specifically used for blackwater treatment (Massoud et al., 2009). Simultaneously, electrochemical technologies have also been investigated as effluent treatment processes (Chen, 2004). Electrochemical treatment has shown to lower the Biochemical oxygen demand (BOD), chemical oxygen demand (COD), and nitrogen concentration (Huang et al., 2016), and has been extensively described for industrial and domestic wastewater treatment by processes like electrocoagulation, electrooxidation, electrodisinfection, electroflotation, and electrosorption (Tennakoon et al., 1996; Grimm et al., 1998; Vlyssides and Israilides, 1998; Feng et al., 2003; Tartakovsky et al., 2011; Kim et al., 2013; Samir and Abbas, 2013; Hong et al., 2014).

In recent years, Electrochemical oxidation (EO), has proven to be an efficient alternative treatment technology for use in small-scale onsite wastewater treatment operations. EO of wastewater can be carried out in single cells, membrane separated cells or porous disc separated cells. Membrane separated cells or divided cells consist of a membrane between the anode and cathode chamber. The membrane is either an Anion Exchange membrane (AEM) or a Cation Exchange membrane (CEM), depending on the type of nutrients to be recovered from the wastewater. Membrane separated cells are preferred over single cells when nutrient recovery from the waste streams is the additional objective apart from treating the wastewater in terms of COD, BOD, and Ammonium (NH_4^+). The CEM divided cell electrolytic reactors have been reported to separate and concentrate NH_4^+ from synthetic wastewater (Gildemyn et al., 2015; Ren et al., 2017), urine (Luther et al., 2015), and anaerobic digestate (Desloover et al., 2015). The AEM divided cell reactors have been reported for phosphate (PO_4^{3-}) recovery (Zhang et al., 2013; Chen et al., 2017; Ledezma et al., 2017; Ren et al., 2017). NH_4^+ and PO_4^{3-} recoveries up to 90% have been demonstrated. Further, the use of AEM and CEM divided cells to treat latrine wastewater and recovery of NH_4^+ and PO_4^{3-} has been reported very recently (Yang et al., 2019). The study also reports that 39% less chlorate (ClO_3^-) and 92% less chlorinated organic by-products are produced in a membrane divided cell than in a membrane-free reactor. In another study by Drennan et.al., higher COD removal during greywater treatment with less energy demand was reported in a membrane divided cell compared to the undivided cell. The study also reported no formation of perchlorate but removal of Halo acetic acids(HAAs) and Trihalomethanes(THAs) on the cathode side (Drennan et al., 2019). Hence the membrane divided cell provides a promising sustainable electrochemical process when optimized, for onsite treatment of wastewater. Resource recovery is among the primary objectives in many studies reported on membrane divided cells. This, however, requires a recovery solution in one of the chambers during recirculation. The use of such a recovery solution will increase the operational costs of the process. Avoiding the use of a recovery solution by passing the feed from one chamber of the electrochemical cell to another, could prove to be advantageous if wastewater treatment is the sole purpose of the process. Our previous research demonstrated the use of a CEM divided cell for electrochemical treatment and disinfection of constructed wetland treated septage without the use of any recovery solution (Talekar et al., 2018). The COD, Total Kjeldahl Nitrogen (TKN), Total Ammoniacal Nitrogen (TAN), Total orthophosphates (TP) removal percentages were 75 ± 3, 30 ± 4, 20 ± 4, and 14 ± 3%, respectively. The $\log_{10}$ reduction of coliform was 5 ± 1.2. The power requirement was 16 ± 3 KWh/m^3 for septage disinfection.

The aim of this study is to further investigate and optimize the aforementioned electrochemical process. We evaluated the performance efficiency of the AEM divided cell in comparison to the CEM divided cell, to select an optimal membrane. The performance efficiency of the AEM divided cell with two types of feed (septage and septage partially treated by a Vertical flow constructed wetland) were studied to optimize the electrolysis process to achieve a maximum reduction of COD, TOC, TN, TAN, coliform and the chlorine production at the anode. This was in contrast to our previous study where the electrolysis process in the CEM divided cell was optimized for a maximum coliform removal.

MATERIALS AND METHODS

Laboratory Scale Double Chambered Membraned Electrochemical Reactor

The Electrochemical reactor (ECR) was a plate and frame type as described earlier (Rabaey et al., 2005; Talekar et al., 2018). It had two chambers, an anode, and a cathode chamber, separated by an ion-exchange membrane (**Figure 1**). Two types of ion-exchange membranes were used, a CEM during the first set of experiments and an AEM in the second set of experiments. Both the CEM (CMI-7000) and the AEM (AMI-7001) were procured from Membrane International Inc. NJ, USA. The volumes of the anode and cathode chambers were 128 ml ($8 \times 8 \times 2$ cm^3) each, while the active volume of both the chambers was 96 ml ($8 \times 6 \times 2$ cm^3). An IrOx Mixed Metal Oxide (MMO) mesh (Magneto, The Netherlands) (8×8 cm^2) was used as the Anode and a stainless-steel mesh (SS 304, 600 Micron, 8×8 cm^2) was used as the cathode. A DC power supply unit (GW-Instek, SPS 606) was

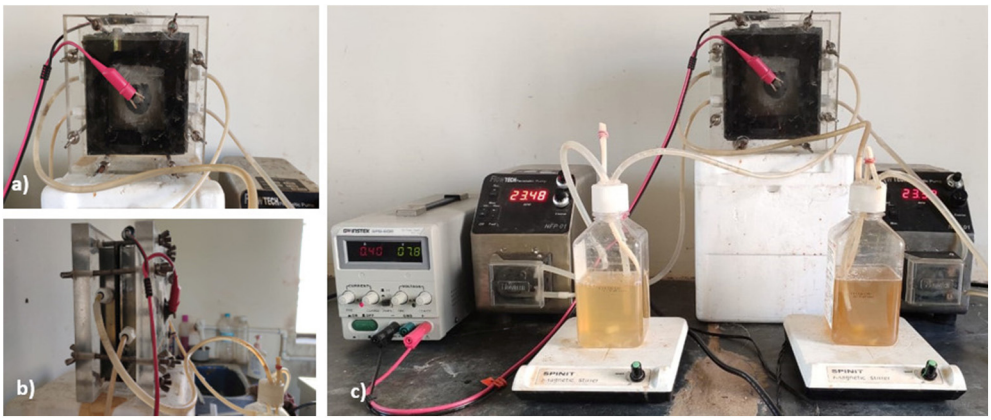

FIGURE 1 | (a) Front view of the double chamber electrochemical cell assembly. **(b)** Side view of the assembly showing anodic chamber with inlet at the bottom and cathodic chamber with outlet at the top. **(c)** Complete experimental setup for batch electrolysis experiments.

used. The feed was fed and/or recirculated into the reactor using peristaltic pumps (NFP-01, Flowtech, India) with variable flow rates ranging from 0.6 to 100 ml/min. This ECR configuration was employed for all the lab-scale experiments conducted during this study.

Influent and Effluent Wastewater Parameter Analysis

In all the experiments conducted, the septage used was obtained from the septic tank (6 m^3). The wetland passed water was obtained from a reservoir that collects the effluent of the second stage VFCW, which is a component of a community-scale integrated treatment system described earlier (Talekar et al., 2018). The influent and effluent samples generated during the lab-scale experiments were analyzed for COD, Total Nitrogen (TN), TAN, TP, TOC, Total Carbon (TC), Inorganic Carbon (IC), chloride, total chlorine, and Coliform Forming Unit (CFU). The concentration of COD, TP, TAN, and chloride were measured by the closed reflux—colorimetric method, the vanado—molybdophosphoric acid colorimetric method, the titrimetric method, and Mohr's titration, respectively. The TN, TOC, TC, and IC were obtained using a TOC analyzer with a detection limit of 4 μg/L (TOC-L PC controlled model, Shimadzu). The total chlorine was measured by using a commercially available chlorine test kit (Merck, Germany) based on the DPD photometric method. The CFU was obtained by the spread plate method using MacConkey Agar.

The precipitate from the surface of the MMO anode and the stainless-steel cathode in the EC collected after batch electrolysis was analyzed by Scanning electron microscopy (SEM). The SEM images and elemental analysis were done by a field emission gun scanning microscope (Quanta FEG-250) coupled with energy dispersive spectroscopy (EDAX, Ametek 174422 Smart Insight) operated at 10 kV.

Electrolysis Experiments

All the experiments conducted during the study, using the above described ECR are described in **Table 1**. Batch electrolysis experiments, using real septage/blackwater as the feed, were conducted employing the CEM divided ECR (CEM-ECR) and AEM divided ECR (AEM-ECR). The analysis of the results from these experiments dictated the choice of the membrane employed in further experiments. Subsequently, batch electrolysis experiments were conducted using the VFCW treated septage as feed in the divided ECR with the selected membrane (AEM_W). The results of this experiment dictated the choice of feed to the ECR and the necessity of pre-treatment of the septage before electrochemical treatment. Following the choice of the membrane in the ECR and the type of feed to the ECR, continuous flow electrolysis experiments were conducted. Two continuous feed flow electrolysis experiments were conducted: (i) Anode to cathode flow via. reservoir (AEM_W-AC), and (ii) Cathode to Anode flow via. reservoir (AEM_W-CA).

During the batch experiments, 500 ml of feed was circulated through each chamber simultaneously via a reservoir of 1 L capacity, as shown in the schematic diagram (**Figure 2**). The recirculation rate was 20 ml/min. The content in the reservoirs was mixed using a magnetic stirrer to avoid the settling of solids. Once the flow reached a steady state, the voltage supply was

TABLE 1 | List of electrolysis experiments conducted in the divided ECR.

Experiment number	Acronym	Membrane and feed used	Flow pattern
1	Batch-AEM_S	AEM and Septage	Septage recirculated through anode and cathode chamber separately
2	Batch-CEM_S	CEM and Septage	
3	Batch-AEM_W		
4	Continuous-AEM_W-AC	AEM and VFCW treated septage	Feed passes through anode chamber and then through cathode chamber
5	Continuous-AEM_W-CA		Feed passes through cathode chamber and then through anode chamber

switched on to start electrolysis. The DC supply was operated in constant current mode with the current set to 0.8 A. The electrolysis was carried out for 120 min and sampling was carried out from both the reservoirs every 30 min. The samples were analyzed for the above-mentioned wastewater parameters. The power and charge requirements per liter of feed for a desired level of treatment were calculated. All batch experiments were conducted in triplicates.

During the continuous experiments the feed was passed through the reactor in two directions in two separate electrolysis experiments: (i) Anode to cathode passage where the feed was first passed through the anode chamber then through cathode via. the reservoir (**Figure 3**). (ii) Cathode to Anode passage where the feed was first passed through the cathode chamber then through the anode chamber via. the reservoir (**Figure S1**). The contents of all the reservoirs were mixed using a magnetic stirrer. In both the experiments, the flow was allowed to reach a steady-state after which the voltage supply was switched on and a constant current was maintained. The feed was set at a rate of 4 ml/min. After 100 min, three replicates of the effluent samples were collected

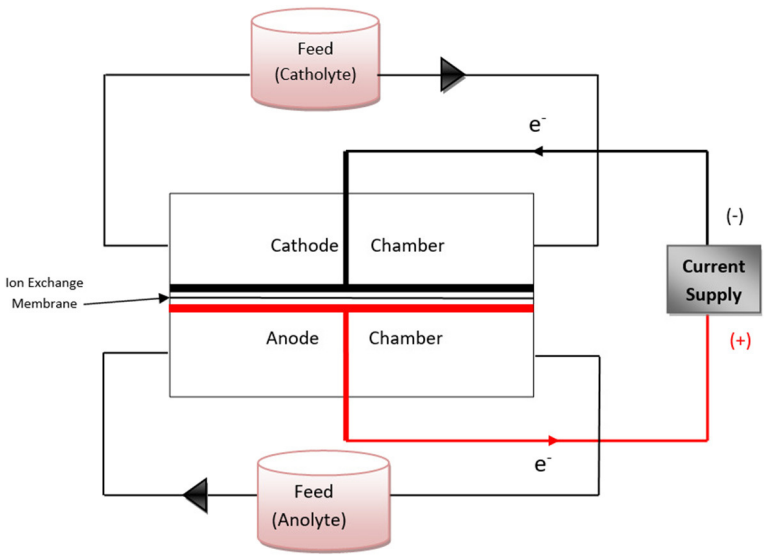

FIGURE 2 | Schematic diagram showing the flow pattern of the feed through the electrochemical reactor in batch electrolysis experiments.

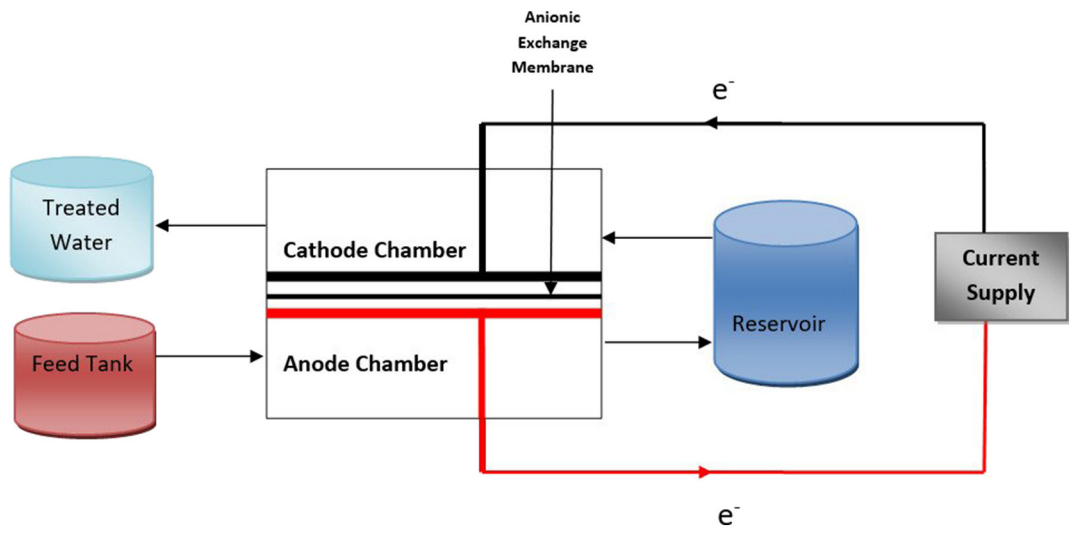

FIGURE 3 | Schematic diagram showing the flow pattern of the feed (VFCW passed septage) through the electrochemical reactor in continuous-AEM$_W$-AC electrolysis experiment.

and analyzed for the above-mentioned wastewater parameters. The voltage reading was noted down at regular intervals.

RESULTS

Batch Electrolysis With Septage as Feed in AEM Divided ECR and CEM Divided ECR

During the electrolysis of septage in the AEM-ECR, it was observed that a higher reduction in various selected wastewater parameters occurred in the cathode chamber compared to that in the anode chamber. The percentage reduction in COD, TOC, TP, TN, and TAN in the cathode chamber were 84.3 ± 3.8, 79 ± 1.6, 92.7 ± 0.7, 41.3 ± 21.4, and 38.73 ± 15.62, respectively. While in the anode chamber the percentage reduction in COD, TOC, TP, TN, and TAN were 20 ± 1.1, 8.2 ± 1.2, −22 ± 4.2, 17.7 ± 5, and −0.73 ± 0.71, respectively. The $\log_{10}$ reduction of the coliform count per mL in the anode and cathode chambers, after 30 min of electrolysis were 2 and 1.14 ± 0.25. This increased to 2.69 after 60 min of electrolysis in both chambers. However, the color of the septage after treatment did not change after the electrolysis in the cathode recirculation.

During the septage electrolysis experiments in a CEM-ECR, the percentage reduction in COD, TOC, TP, TN, and TAN in the anode chamber were 53.21 ± 0.01, 40.06 ± 1.1, 35.6 ± 4.2, 97.2 ± 1.2, and 52.8 ± 12.7, respectively. While in the cathode chamber, the percentage reduction in COD, TOC, TP, TN, and TAN were 28.9 ± 12.8, 13.6 ± 2, 72.32 ± 3.8, −29.5 ± 36.2, and −48.7 ± 7.5, respectively. The $\log_{10}$ reduction of the coliform count per mL in the anode and cathode chambers after 30 min of electrolysis were 3.2 ± 1.2 and 3.5 ± 0.5. The Log_{10} reduction after 90 min in both the chambers was 5.3 ± 1.3.

Batch Electrolysis With VFCW Treated Septage as Feed in AEM Based ECR

Similar to the results obtained with the electrolysis of septage in the AEM-ECR, the reduction of selected wastewater parameters during the cathode chamber recirculation was higher than during the anode chamber recirculation, as is evident from **Figures 8**, **9**. The percentage reduction in COD, TOC, TP, TN, and TAN in the cathode chamber was 75.8 ± 8.6, 82.2 ± 3.7, 90.9 ± 0.64, 13.5 ± 4.2, and 9.9 ± 7, respectively. In the anode chamber the percentage reduction in COD, TOC, TP, TN, and TAN was 28.12 ± 1.5, 6.6 ± 3.3, 19.15± 3.5, −16.54 ± 5.3, and 10.67 ± 3.2, respectively. A 4 $\log_{10}$ reduction in CFU was obtained after 30 and 60 min of electrolysis in the anode and cathode chamber recirculation, respectively.

Continuous VFCW Treated Septage Treatment by Electrolysis in AEM Based ECR

Continuous feed experiments were conducted in two modes as mentioned above in the AEM based ECR:

(i) Anode to cathode flow mode (AC_{AEM})
(ii) Cathode to anode flow mode (CA_{AEM})

Based on the results of the batch experiments AEM_W, the charge required to treat a defined amount of VFCW treated septage was determined. This, in turn, determined the flow rate to the ECR and the hydraulic retention time (HRT) in the ECR of the feed, for a fixed current. In the continuous feed experiments (both AC_{AEM} and CA_{AEM}), the flowrate maintained was 5 mL/min with HRT = 22 min in each chamber and current fixed at 0.4 A (Current density = 62.5 A/m^2). The overall percentage reduction in COD, TOC, TP, TN, TAN, TC, and TIC achieved in AC_{AEM} was 74 ± 0.9, −1.2 ± 1.4, 54 ± 0.28, 34.7 ± 3.5, 17 ± 1.7, 48.3 ± 0.14, and 82.5 ± 2.5, respectively. In the CA_{AEM}, the percentage reduction in COD, TOC, TP, TN, TAN, TC, and TIC were 80.8 ± 15.4, −4.38 ± 8.07, 33.4 ± 1.7, 9.5 ± 2.11, −5 ± 5.7, 46.7 ± 2.02, and 83.2 ± 2.2, respectively. The $\log_{10}$ reduction in CFU obtained after AC_{AEM} and CA_{AEM} was 3.5 ± 0.6 and 2.4, respectively.

DISCUSSIONS

The results of the batch electrolysis experiments using septage as feed in the AEM-ECR (experiment 1) are represented in **Figures 5**, **6**. The reduction of COD and TOC occurred in both the anodic and cathodic chamber recirculation. In the cathodic recirculation, the COD and TOC reduction was 64.3 and 71% higher than the reduction achieved in the anodic recirculation. The reduction in the anodic chamber recirculation could have been partially due to direct oxidation of the organics on the surface of the electrode and majorly due to indirect oxidation in the bulk anolyte by the reactive chlorine species generated from inherent chloride (50–185 mg/L) present in the wastewater (Martínez-Huitle and Ferro, 2006; Fajardo et al., 2017). In the cathode chamber, the COD and TOC reduction could be majorly due to movement of the negatively charged smaller sized organics, the phospho-sugars like GDP-D- Glucose, CDP-D-Glucose, etc. and the short-chain fatty acids (Høverstad et al., 2018) to the anode chamber. The removal was due to the coagulation of organic matter at higher pH and subsequent sedimentation.

The TP reduction in the anode chamber (**Figure 6**) was primarily due to the precipitation of the phosphates as calcium phosphates and magnesium phosphates in the vicinity of the anode electrode on the membrane surface and also in the bulk (anolyte). The elemental analysis of the anodic precipitate by EDAX showed that oxygen (47.5 wt.%), calcium (27.5 wt.%), phosphorus (14.2 wt.%), and magnesium (9.9 wt.%) were the predominant elements precipitated. The atomic O/Ca and Ca/P ratio was 1.72 and 1.93, respectively. The SEM images of the precipitate showed sharp needlelike structures among button headlike structures (formed by several layers of stacked circular structures). The needle-shaped structures were calcium phosphates similar to the structures reported by Drevet et. al. (Drevet and Benhayoune, 2012). The button headlike structures were similar to the calcium oxide nanoparticles encountered by Balaganesh et al. (2018). From the elemental analysis (EDAX) results (**Figure S2**) and SEM images (**Figure 4**), it was inferred that the precipitates were primarily constituted of calcium oxides and calcium phosphates. Magnesium oxides and magnesium

phosphates were also present in the precipitate in low amounts as inferred from the EDAX results.

The TP removal in the cathode chamber (**Figure 7**) was due to the transfer of phosphate ions from the cathode to the anode chamber across the AEM.

The reduction in TN was observed in both the anodic and cathodic chamber recirculations. Similar to the COD and TOC, the removal percentage was higher in the cathodic chamber than in the anodic chamber. The removal of TN in the anode chamber was due to indirect oxidation of nitrogenous organic matter (Urea) (Hanson et al., 2016) to ammonia and its further oxidation to nitrogen, nitrates, nitrous oxides under acidic pH conditions by OH radicals and by hypochlorous acid (Kim et al., 2005). In the cathode chamber, the TN decrease was due to the movement of nitrates and nitrites from the cathode chamber to the anode chamber across AEM and also due to ammonia volatilization.

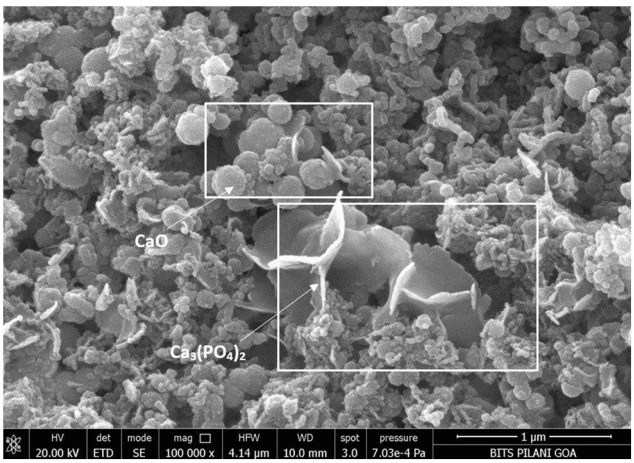

FIGURE 4 | SEM images of anodic precipitate at 100,000× magnification showing circular button head like structures of calcium oxide and needle shaped calcium phosphates.

The TAN removal in the anode chamber was primarily due to the partial decomposition of ammonia to nitrogen by OH radicals (Kim et al., 2005) and indirect oxidation in the anolyte by chlorine species generated from chloride and less likely by the direct oxidation of ammonium on the surface of the Ti/IrO_2 and Ti/RuO_2 anodes (Li and Liu, 2009) under acidic anolyte conditions. In the cathode chamber, the TAN decreased due to the volatilization of ammonium ions as ammonia from a highly basic catholyte (11 ± 0.1). **Figure 7**, summarizes all the major reactions occurring in the anode and the cathode chambers, leading to pollutant removal.

The coliform disinfection in the anode chamber was due to the combined effect of acidic pH (2 ± 0.14)(Pearson et al., 1987; Wahyuni, 2015) and active chlorine species (Kraft, 2008; Cho et al., 2014), while in the cathode chamber, it was solely due to the high pH (11 ± 0.1) (Pearson et al., 1987). The charge supplied and power required to achieve the mentioned reduction was 7794 ± 10 coulombs L^{-1} and 48 ± 6.7 Wh L^{-1}. The total chlorine concentration in the treated septage in the anode recirculation and the power required per gram of chlorine production was 3.65 mg L^{-1} and 13 Kwh gm^{-1} chlorine.

In the case of septage electrolysis in the CEM-ECR (experiment 2), as expected and shown in our previous research (Talekar et al., 2018), a significant reduction in most of the parameters occurred in the anode chamber compared to the cathode chamber. The mechanisms involved in the reduction of various parameters in anode and cathode chambers in a CEM-ECR are described in detail in our previous research (Talekar et al., 2018). The charge and power required was 8,640 coulombs L^{-1} and 42.12 ± 4 Wh L^{-1}. The total chlorine concentration in the treated septage in the anode recirculation and the power required per gram of chlorine production was 1.975 mg L^{-1} and 21 Kwh gm^{-1} chlorine.

On comparing the results obtained from experiments 1 and 2, as represented in **Figures 5**, **6**, it can be seen that the COD, TOC, and TP reduction was highest in the cathode chamber recirculation in the AEM-ECR. The highest removal of TN

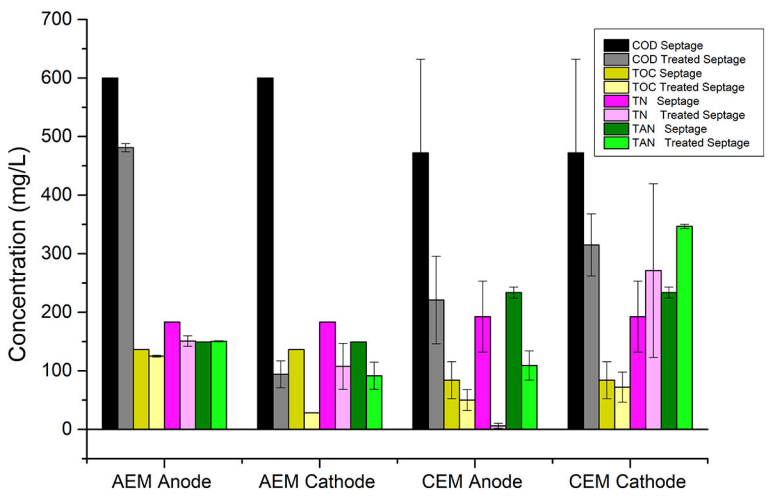

FIGURE 5 | Variation in wastewater parameters of septage/blackwater after 90 min of electrolysis in anode and cathode chamber recirculation in ECR with AEM and ECR with CEM.

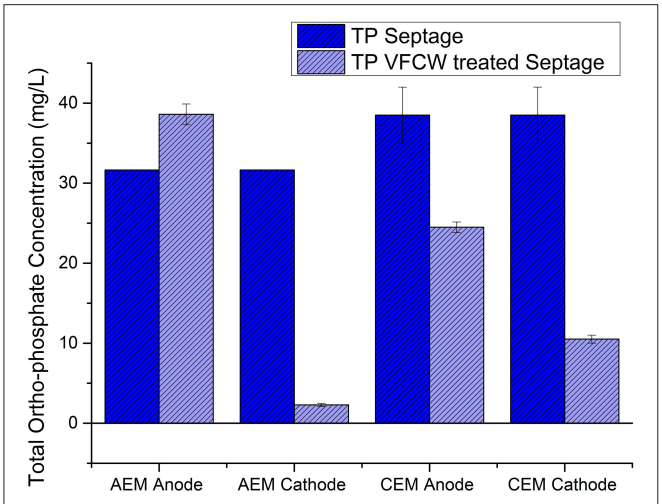

FIGURE 6 | Variation in ortho-phosphate concentration of septage/blackwater after 90 min of electrolysis in anode and cathode chamber recirculation in ECR with AEM and ECR with CEM.

and TAN was seen in the anode chamber recirculation in the CEM-ECR. The TN removal in the anode chamber in the CEM-ECR was double the reduction achieved in the cathode chamber of the AEM-ECR. The TAN removal in the anode chamber of CEM-ECR was 14% higher than that achieved in the cathode chamber of AEM-ECR. With respect to coliform removal, complete removal was achieved after 60 min in both the anode and cathode recirculations in the AEM-ECR, while it took 90 min in both the anode and cathode recirculations in the CEM-ECR.

The charge requirement in the case of AEM-ECR electrolysis was 10% lower than that required in CEM-ECR electrolysis. However, the power consumption of the AEM-ECR was 8% more than the requirement of the CEM-ECR. Even though the CEM-ECR seems to be promising in terms of power consumption, the AEM-ECR outweighs the CEM -ECR in terms of COD, TOC, TP reduction, and chlorine production. Chlorine, contributing to the oxidation of organics and coliform removal, production in the anode chamber of the AEM-ECR was around 82% higher. Hence it was concluded that the optimized membrane between

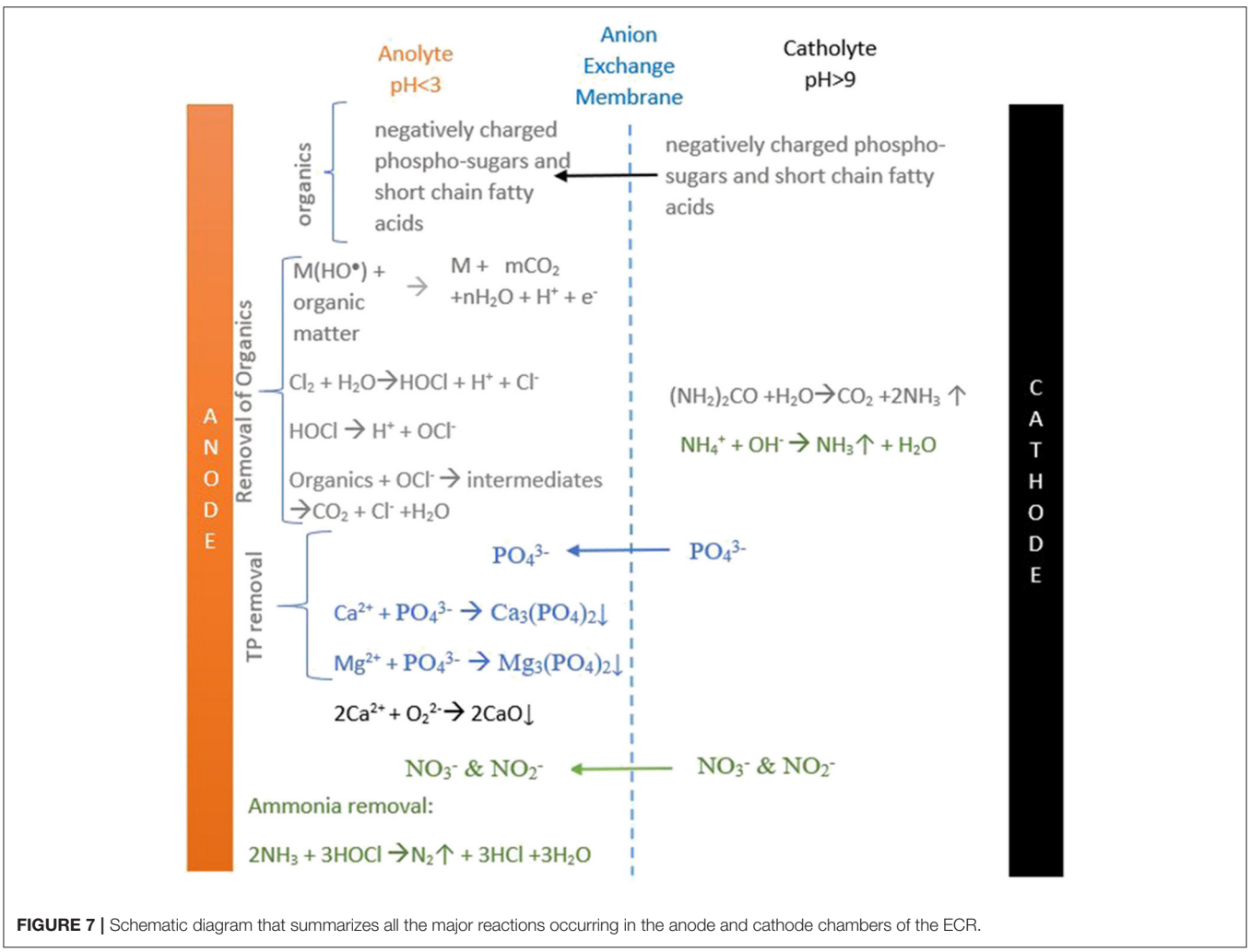

FIGURE 7 | Schematic diagram that summarizes all the major reactions occurring in the anode and cathode chambers of the ECR.

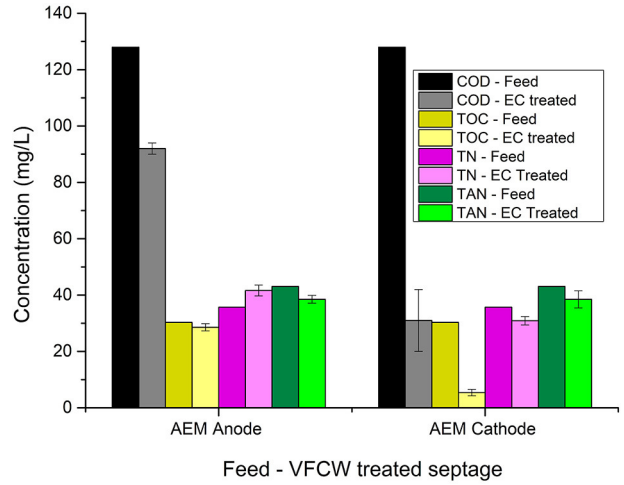

FIGURE 8 | Variation in wastewater parameters of VFCW treated septage after 90 min of electrolysis in anode and cathode chamber recirculation in ECR with AEM.

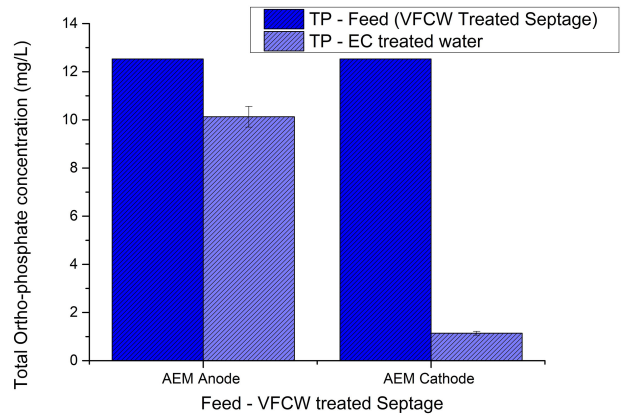

FIGURE 9 | Variation in ortho-phosphate concentration of VFCW treated septage after 90 min of electrolysis in anode and cathode chamber recirculation in ECR with AEM.

anode and cathode chamber was the AEM. Therefore, further experiments were conducted with the AEM-ECR.

The electrolysis experiment (experiment 3) following the membrane selection, was carried out with the AEM-ECR using VFCW treated septage as the feed. The results showed that the COD, TOC, TP, and TN reduction were 48, 75.6, 71.75, and 13.5% higher, respectively, in the cathode chamber to that achieved in the anode chamber. TAN removal was similar in both the chambers. Mechanisms of removal of considered parameters in anode and cathode chambers have been discussed above. The charge supplied and power required to achieve the mentioned reduction was 4482 ± 846 coulombs L^{-1} and 31 ± 1.6 Wh L^{-1}. The average total chlorine concentration in the treated septage in anode recirculation and the average power required per gram of chlorine production was 3.125 mg L^{-1} and 9.9 Kwh gm^{-1} chlorine.

On comparing the results of experiments 1 and 3 (**Table 2**), it was seen that the percentage removal of COD, TOC, TP from septage and VFCW treated septage in the cathodic chamber recirculation after electrolysis was almost the same, except in the case of TN and TAN. The removal percentage of TN and TAN was higher in the case of septage as feed. This may mislead one to conclude that septage could be the optimum feed to the process. However, the charge and power requirements for achieving the mentioned reduction were significantly lower for electrolysis of the VFCW treated septage than for that of septage. The charge and power requirements for VFCW treated septage were 42.5 and 35% lower, respectively to those for septage. This was for the obvious reason that the VFCW treated septage had lower organic loads. Power requirements per gram of chlorine production from the VFCW treated water was 38.1% lower than the requirements for electrolysis of septage. Hence from this result analysis, it was concluded that a pre-treatment of the septage by a VFCW before the electrolysis was advantageous in terms of lowering power requirements. Therefore, VFCW treated septage was considered the preferred feed to the AEM-ECR.

Hence, at the end of the batch experiments, it was concluded that the ECR performance was optimal with the AEM as the membrane between the anode and cathode chambers and VFCW treated septage as feed. Therefore, the following continuous experiments were conducted in the AEM-ECR with VFCW treated septage.

In the AC_{AEM} experiment, during electrolysis (**Table 3**), as the feed passed the anode chamber, the COD reduced by 80%. Further, as the anode passed feed passed through the cathode chamber, the COD increased by around 42%. The unusual increase in [COD] observed after the cathode passage could be due to the detection of the small chain peptides in the cathode effluent sample by the dichromate method of COD estimation. These small chain peptides could be formed by the denaturation of macromolecular proteins at a higher pH (Min et al., 2018). However, the overall reduction was 74 ± 0.9%. In the case of TOC, after the anodic passage, the TOC increased very slightly (by 2 mg/l) and then further decreased as the anode passed feed flowed through the cathode (**Table 3**). The decrease in the TOC in the cathode chamber was partially due to coagulation at higher pH and subsequent sedimentation and predominantly due to the chemical conversion of organic carbon species to inorganic carbon species as evident from **Table 3**. Overall there was no removal in the TOC.

A TP reduction, in this flow mode, was seen after the cathodic passage of the feed due to a transfer of the phosphate ions to the anode chamber forming white-colored precipitates of calcium (oxides and phosphates) and magnesium (oxides and phosphates) as discussed previously. The un-combined phosphate ions were added to the pre-existing phosphates in the anolyte and hence there was an increase in $[PO_4^{3-}]$ in the anolyte.

The TN initially increased by 19% after anode passage and then decreased as the anode passed feed passed through the cathode chamber. The increase in TN was possibly due to the addition of nitrites and nitrates from the catholyte to the anolyte

TABLE 2 | Variation of wastewater parameters of the feed in the cathode chamber recirculation of AEM-ECR, feed being septage, and VFCW septage.

Parameters	Septage			VFCW treated Septage		
	Influent $n = 3$	Effluent $n = 3$	Percentage removal	Influent $n = 3$	Effluent $n = 3$	Percentage removal
COD (mg/L)	600 ± 24	94 ± 23	84.3 ± 3.8	136 ± 8	31 ± 11	75.8 ± 8.6
TOC (mg/L)	136.2 ± 1.29	28.28	79.2 ± 1.6	30.32 ± 0.64	5.4 ± 1.12	82.2 ± 3.7
TP (mg/L)	31.65 ± 0.32	2.3 ± 0.2	92.7 ± 0.7	12.53 ± 0.07	1.14 ± 0.08	90.9 ± 0.64
TN (mg/L)	183.3 ± 2.16	107.6 ± 39.3	41.3 ± 21.4	35.72 ± 0.17	30.895 ± 1.5	13.5 ± 4.2
TAN (mg/L)	149.3	91.46 ± 23.3	38.73 ± 15.62	43.1	38.85 ± 3.05	9.9 ± 7
pH	7.25	11.49 ± 0.085	NA	6.1	11.01 ± 0.1	NA
Charge requirement		7794 ± 10 coulombs L^{-1}			4482 ± 846 coulombs L^{-1}	
Power requirement		48 ± 6.7 Wh L^{-1}			31 ± 1.6 Wh L^{-1}	

NA, not applicable.

TABLE 3 | Variation in selected wastewater parameters as the feed flows through the chambers of the ECR in experiments AC_{AEM} and CA_{AEM}.

Parameters	Anode to cathode flow mode (AC_{AEM})				Cathode to anode flow mode (CA_{AEM})			
	Influent	Post-anode passage	Reservoir	Effluent (Post-cathode)	Influent	Post-cathode passage	Reservoir	Effluent (Post-anode)
pH	7.34 ± 0.04	2.27 ± 0.04	2.3 ± 0.02	9 ± 0.1	7.19 ± 0.01	10.64 ± 0.15	9.82 ± 0.25	2.69 ± 0.19
COD (mg/L)	104	20 ± 2	19 ± 1	27 ± 1	104	26 ± 10	29 ± 11	20 ± 16
TOC (mg/L)	17.48 ± 1.25	22.85 ± 0.015	23.57 ± 0.27	17.69 ± 1.02	17.34	9.7 ± 0.1	10.8 ± 1.2	18.1 ± 1.4
Ortho-phosphate (mg/L)	7.8 ± 0.4	9.3 ± 0.7	8.81 ± 0.69	3.6 ± 0.4	7.4	2.5 ± 0.2	2.5 ± 0.05	4.5 ± 0.13
TN (mg/L)	53.53 ± 0.29	63.84 ± 3	60.07 ± 3.5	35 ± 2.05	54.4	39.22 ± 1.62	41 ± 2.3	49.2 ± 1.15
TAN (mg/L)	40 ± 1	45 ± 0.6	40 ± 0.6	33.15 ± 0.15	37.3	43.1 ± 2.8	36.6 ± 1.6	39.15 ± 2.15
TC (Total Carbon) (mg/L)	43 ± 0.7	29 ± 0.05	24.7 ± 0.7	22.2 ± 0.3	41.57	23.86 ± 0.26	29.88 ± 1.75	22.16 ± 0.84
TIC (Total Inorganic Carbon) (mg/L)	25.52 ± 0.52	5.7 ± 0.07	1.05 ± 0.35	4.47 ± 0.7	24.24	14.17 ± 0.2	19 ± 0.5	4.08 ± 0.55
Log_{10}(CFU/ml)	5.02 ± 0.11	nd	nd	nd	3.95	1.8	2.6	1.5

nd, not detected.

via the AEM. The decreased TN in the cathode chamber was possibly due to the decomposition of organic nitrogen (Urea) in basic catholyte conditions (pH $\leq$ 9) (Zhigang et al., 2008), volatilization of ammonia and movement of nitrites and nitrates to the anode chamber. The TAN remained almost constant as the feed flowed through the anode chamber and reached the reservoir. It decreased, however, as the feed from the reservoir passed through the cathode. The decrease, as mentioned earlier, was due to the volatilization of ammonia at high pH (pH>9) (Desloover et al., 2012). The TC of the feed exhibited a decreasing trend throughout as the feed flowed through the anode and then through the cathode via the reservoir.

In the CA_{AEM} experiment, the COD of the feed decreased after cathodic passage and showed a further reduction after anodic passage, as shown in **Table 3**. The TOC variation trend was opposite to that seen in the AC_{AEM}. The TOC after cathodic passage decreased, then increased as the cathode passed feed in the reservoir flowed through the anode chamber. Overall there was no TOC removal. The TP concentration decreased as the feed passed the cathode chamber and increased as the cathode effluent passes through the anode chamber. The decrease observed in the cathode effluent was due to the transfer of PO_4^{3-} ions from the catholyte to the anolyte. These transferred phosphates further precipitated in the anode chamber as discussed before. The TP concentration of the final effluent in comparison to the cathode passed feed was higher due to the accumulation of uncombined PO_4^{3-} ions added from the catholyte to the anolyte across the membrane. The TN decreased after cathodic passage and then increased as the cathode passed feed flowed through the anode chamber, a trend opposite to that seen in AC_{AEM}. The ammoniacal nitrogen increased as the feed passed the cathode chamber, and remained the same as the cathode passed feed flowed through anode chamber. The increase in the cathode chamber was due to the high pH of the catholyte at which nitrogen exists predominantly as ammonium. The TC concentration was shown to decrease after both cathode and subsequent anode passage. The value of various parameters at every sampling point during the flow of the feed through the

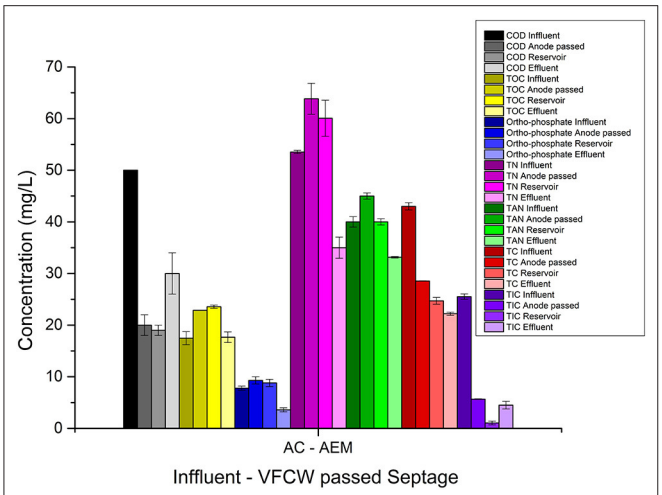

FIGURE 10 | Graphical representation of variation in wastewater parameters as the feed flows through the anode chamber and then through the cathode chamber via reservoir during electrolysis in AEM based ECR.

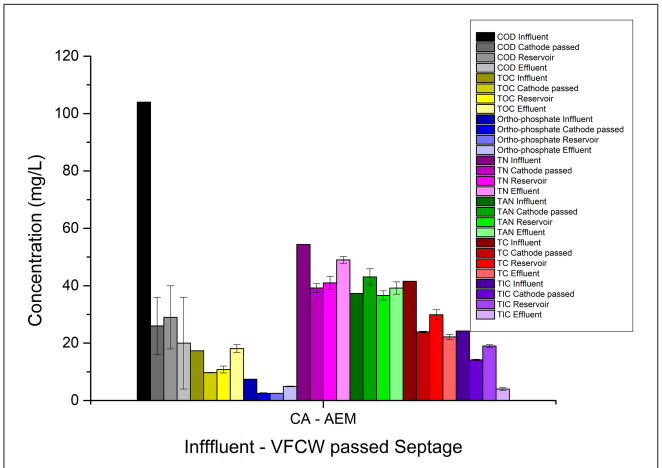

FIGURE 11 | Graphical representation of variation in wastewater parameters as the feed flows through the cathode chamber and then through the anode chamber via reservoir during electrolysis in AEM based ECR.

ECR in AC_{AEM} flow mode and CA_{AEM} flow mode is shown in **Figures 10**, **11**.

It was seen that the percentage reduction in TP, TN, TAN, TC, and TIC in AC_{AEM} was higher than in the case of CA_{AEM} (**Table 4**). The TOC reduction in both the flow modes was negligible or equal to zero and COD removal in AC_{AEM} is almost similar to the reduction reached in CA_{AEM}. The [COD], $[PO_4^{3-}]$, and [TN] removal achieved in AC_{AEM} and CA_{AEM} was 128.33, 7, 38.83, and 140, 4.83, 8.66 g/m^2 day, respectively. The power consumption in the AC_{AEM} and CA_{AEM} flow modes was calculated to be 21.2 and 21.46 Kwh/m^3, respectively. The effluent pH of the AC_{AEM} was in the permissible range for environmental discharge, while the effluent pH of CA_{AEM} was more acidic. Hence among both the flow modes tested, AC_{AEM} can be chosen

TABLE 4 | Percentage reduction in wastewater parameters achieved in Batch-AEM_W, AC_{AEM}, and CA_{AEM} experiments.

Parameters	Batch-AEM_W cathode recirculation	AC_{AEM}	CA_{AEM}
COD	75.8 ± 8.6	74 ± 0.1	80.8 ± 15.4
TOC	82.2 ± 3.7	−1.27 ± 1.38	−4.4 ± 8
Ortho-phosphate	90.9 ± 0.64	54 ± 2.8	33.5 ± 1.7
TN	13.5 ± 4.2	34.8 ± 3.5	9.5 ± 2.1
TAN	9.9 ± 7	17.1 ± 1.7	−5 ± 5.75
TC (Total Carbon)	62.3 ± 3.7	48.3 ± 0.14	46.7 ± 2.02
TIC (Total Inorganic Carbon) (mg/L)	54.5 ± 3.5	82.53 ± 1.7	83.2 ± 2.25

as the optimum mode of flow of feed through the ECR in consideration of the higher reduction in $[PO_4^{3-}]$, [TN] and similar [COD] removal. Furthermore, the energy consumption in the AC_{AEM} was lower than the consumption in the AC_{CEM} (28 Kwh/ m^3) as shown in our previous study (Talekar et al., 2018). The effluent quality meets the Indian CPCB standards mentioned for release in inland surface water.

In the future, septage treatment in the modified ECR configuration consisting of both the AEM and CEM will be studied to recover NH_4^+ and PO_4^{3-} simultaneously and its scaleup feasibility.

CONCLUSION

In the present study, an attempt was made to optimize the type of the ion exchange membrane and the type of feed used in the double-chambered electrochemical reactor. The results of the batch electrolysis experiments in AEM-ECR and CEM-ECR using septage as feed lead to the conclusion that among the two studied membranes, the AEM was optimal. The reduction in COD, TOC, and TP after electrolysis in the AEM-ECR was double the reduction achieved in the CEM-ECR. The charge supplied and power required were 7794 ± 10 coulombs L^{-1} and 48 ± 6.7 Wh L^{-1}.

Further, the batch electrolysis experiments in AEM-ECR using VFCW treated septage as feed concluded that the optimum feed to the ECR with AEM was VFCW treated septage. The charge and power requirement for treating wetland (VFCW) treated septage was 42.5 and 35% lower, respectively, than that required for septage. The charge supplied and power required was 4482 ± 846 coulombs L^{-1} and 31 ± 1.6 Wh L^{-1}.

Finally, the continuous flow experiments, AC_{AEM} and CA_{AEM} lead to the conclusion that an anode to cathode flow mode was the optimal mode of flow of feed. The power required for treatment was 21.2 Kwh/m^3. The developed process showed promise in small scale on-site electrochemical treatment of wastewater. The treated water could be used for agricultural purposes. However, the work demands further long-term lab-scale studies and pilot studies to determine the durability of the AEM membrane which will dictate the scale-up feasibility of the

process developed. Further, studies about the disinfection by-products (DBP's like HAAs, THM's, perchlorates) released after electrolysis is required for promoting commercialization of the system in the future.

DATA AVAILABILITY STATEMENT

The raw data supporting the conclusions of this article will be made available by the authors, without undue reservation, to any qualified researcher on request.

AUTHOR CONTRIBUTIONS

GT completed all the lab-scale experiments, analysis, and manuscript writing. SM contributed to the design of the experiments and supported us with his expertise throughout the study. Both the authors read and approved the final manuscript.

FUNDING

This work was financed from the funds provided by DBT-BIRAC and Bill & Melinda Gates Foundation issued for the Reinvent the Toilet Challenge initiative.

SUPPLEMENTARY MATERIAL

The Supplementary Material for this article can be found online at: https://www.frontiersin.org/articles/10.3389/fenrg.2020.00020/full#supplementary-material

REFERENCES

Balaganesh, A. S., Sengodan, R., Ranjithkumar, R., and Chandarshekar, B. (2018). Synthesis and characterization of porous calcium oxide nanoparticles (CaO NPS). *Int. J. Innov. Technol. Explor Eng.* 8, 312–314.

Chen, G. (2004). Electrochemical technologies in wastewater treatment. *Sep. Purif. Technol.* 38, 11–41. doi: 10.1016/j.seppur.2003.10.006

Chen, X., Gao, Y., Hou, D., Ma, H., Lu, L., Sun, D., et al. (2017). The microbial electrochemical current accelerates urea hydrolysis for recovery of nutrients from source-separated urine. *Environ. Sci. Technol. Lett.* 4, 305–310. doi: 10.1021/acs.estlett.7b00168

Cho, K., Qu, Y., Kwon, D., Zhang, H., Cid, C. A., Aryanfar, A., et al. (2014). Effects of anodic potential and chloride ion on overall reactivity in electrochemical reactors designed for solar-powered wastewater treatment. *Environ. Sci. Technol.* 48, 2377–2384. doi: 10.1021/es404137u

Desloover, J., Abate Woldeyohannis, A., Verstraete, W., Boon, N., and Rabaey, K. (2012). Electrochemical resource recovery from digestate to prevent ammonia toxicity during anaerobic digestion. *Environ. Sci. Technol.* 46, 12209–12216. doi: 10.1021/es3028154

Desloover, J., Vrieze, J., De, V.ijver, M., Van De, Mortelmans, J., and Rozendal, R. (2015). Electrochemical nutrient recovery enables ammonia toxicity control and biogas desulfurization in anaerobic digestion. *Environ. Sci. Technol.* 49, 948–955. doi: 10.1021/es504811a

Drennan, D. M., Koshy, R. E., Gent, D. B., and Schaefer, C. E. (2019). Electrochemical treatment for greywater reuse: effects of cell configuration on COD reduction and disinfection byproduct formation and removal. *Water Sci. Technol. Water Supply* 19, 891–898. doi: 10.2166/ws.2018.138

Drevet, R., and Benhayoune, H. (2012). "Electrochemical deposition of calcium phosphate coatings on a prosthetic titanium alloy substrate," in *Calcium Phosphate: Structure, Synthesis, Properties, and Applications*, ed. R. B. Heimann (New York, NY: Nova Science Publishers), 231–252.

Fajardo, A. S., Seca, H. F., Martins, R. C., Corceiro, V. N., Freitas, I. F., Quinta-ferreira, M. E., et al. (2017). Electrochemical oxidation of phenolic wastewaters using a batch-stirred reactor with NaCl electrolyte and Ti/RuO 2 anodes. *J. Electroanal. Chem.* 785, 180–189. doi: 10.1016/j.jelechem.2016.12.033

Feng, C., Sugiura, N., Shimada, S., and Maekawa, T. (2003). Development of a high performance electrochemical wastewater treatment system. *J. Hazard. Mater.* 103, 65–78. doi: 10.1016/S0304-3894(03)00222-X

Gildemyn, S., Luther, A. K., Andersen, S. J., Desloover, J., and Rabaey, K. (2015). Electrochemically and bioelectrochemically induced ammonium recovery. *J. Vis. Exp.* 2015, 1–12. doi: 10.3791/52405

Grimm, J., Bessarabov, D., and Sanderson, R. (1998). Review of electro-assisted methods for water purification. *Desalination* 115, 285–294. doi: 10.1016/S0011-9164(98)00047-2

Hanson, A. M., Lee, G. F., Hanson, A. M., and Lee, G. F. (2016). Forms of organic nitrogen in domestic wastewater. *J. Water Pollut. Control Fed.* 43, 2271–2279. Available online at: http://www.jstor.org/stable/25037233

Hong, K. H., Kim, W. Y., Son, D. J., Yun, C. Y., Chang, D., Bae, H. S., et al. (2014). Characteristics of organics and nutrients removal in municipal wastewater treatment by electrolysis using copper electronic conductor. *Int. J. Electrochem. Sci.* 9, 3979–3989.

Høverstad, T., Fausa, O., Bjørneklett, A., Bøhmer, T., and Bjrneklett, T. H. F. A. (2018). Short-chain fatty acids in the normal human feces short-chain fatty acids in the normal human feces. *Scand. J. Gastroenterol.* 19:5521. doi: 10.1080/00365521.1984.12005738

Huang, X., Qu, Y., Cid, C. A., Finke, C., Hoffmann, M. R., Lim, K., et al. (2016). Electrochemical disinfection of toilet wastewater using wastewater electrolysis cell. *Water Res.* 92, 164–172. doi: 10.1016/j.watres.2016.01.040

Kim, D. G., Kim, W. Y., Yun, C. Y., Son, D. J., Chang, D., Bae, H. S., et al. (2013). Agro-industrial wastewater treatment by electrolysis technology. *Int. J. Electrochem. Sci.* 8, 9835–9850.

Kim, K. W., Kim, Y. J., Kim, I. T., Park, G. I., and Lee, E. H. (2005). The electrolytic decomposition mechanism of ammonia to nitrogen at an IrO2 anode. *Electrochim. Acta* 50, 4356–4364. doi: 10.1016/j.electacta.2005.01.046

Kraft, A. (2008). Electrochemical water disinfection: a short review. *Platin. Met. Rev.* 52, 177–185. doi: 10.1595/147106708X329273

Ledezma, P., Jermakka, J., Keller, J., and Freguia, S. (2017). Recovering nitrogen as a solid without chemical dosing: bio-electroconcentration for recovery of nutrients from urine. *Environ. Sci. Technol. Lett.* 4, 119–124. doi: 10.1021/acs.estlett.7b00024

Li, L., and Liu, Y. (2009). Ammonia removal in electrochemical oxidation: mechanism and pseudo-kinetics. *J. Hazard. Mater.* 161, 1010–1016. doi: 10.1016/j.jhazmat.2008.04.047

Luther, A. K., Desloover, J., Fennell, D. E., and Rabaey, K. (2015). Electrochemically driven extraction and recovery of ammonia from human urine. *Water Res.* 87, 367–377. doi: 10.1016/j.watres.2015.09.041

Martínez-Huitle, C. A., and Ferro, S. (2006). Electrochemical oxidation of organic pollutants for the wastewater treatment: direct and indirect processes. *Chem. Soc. Rev.* 35, 1324–1340. doi: 10.1039/B517632H

Massoud, M. A., Tarhini, A., and Nasr, J. A. (2009). Decentralized approaches to wastewater treatment and management: applicability in developing countries. *J. Environ. Manage.* 90, 652–659. doi: 10.1016/j.jenvman.2008.07.001

Min, C., Won, S., Cho, K., and Ho, M. R. (2018). Degradation of organic compounds in wastewater matrix by electrochemically generated reactive chlorine species : kinetics and selectivity. *Catalysis Today* 313, 189–195. doi: 10.1016/j.cattod.2017.10.027

Pearson, H. W., Mara, D. D., Mills, S. W., and Smallman, D. J. (1987). Physico-chemical parameters influencing faecal bacterial survival in waste stabilization ponds. *Water Sci. Technol.* 19, 145–152. doi: 10.2166/wst.1987.0139

Rabaey, K., Lissens, G., and Verstraete, W. (2005). "Microbial fuel cells: performances and perspectives," in *Biofuels for Fuel Cells: Renewable Energy*

From Biomass Fermentation. 377–399. Available online at: http://hdl.handle.net/1854/LU-328755 (accessed August 03, 2018).

Ren, S., Li, M., Sun, J., Bian, Y., Zuo, K., and Zhang, X. (2017). Short communication: a novel electrochemical reactor for nitrogen and phosphorus recovery from domestic wastewater. *Front. Environ. Sci. Eng.* 11:17. doi: 10.1007/s11783-017-0983-x

Samir, A., and Abbas, S. A. (2013). Combination of electrocoagulation and electro-oxidation processes of textile wastewaters treatment. *Civil Environ. Res.* 3, 61–74.

Science, W., and Ho, G. (2016). Technology for sustainability: the role of onsite, small and community scale technology. *Water Sci. Technol.* 51, 15–20. doi: 10.2166/wst.2005.0346

Talekar, G. V., Sharma, P., Yadav, A., and Clauwaert, P. (2018). Sanitation of blackwater via sequential wetland and electrochemical treatment. *NPJ Clean Water* 1, 1–9. doi: 10.1038/s41545-018-0014-x

Tartakovsky, B., Mehta, P., Bourque, J. S., and Guiot, S. R. (2011). Electrolysis-enhanced anaerobic digestion of wastewater. *Bioresour. Technol.* 102, 5685–5691. doi: 10.1016/j.biortech.2011.02.097

Tennakoon, C. L. K., Bhardwaj, R. C., and Bockris, J. O. (1996). Electrochemical treatment of human wastes in a packed bed reactor. *J. Appl. Electrochem.* 26, 18–29. doi: 10.1007/BF00248184

Vlyssides, A. G., and Israilides, C. J. (1998). Electrochemical oxidation of a textile dye and finishing wastewater using a Pt/Ti electrode. *J. Environ. Sci. Heal. A* 33, 847–862. doi: 10.1080/10934529809376765

Wahyuni, E. A. (2015). The influence of pH characteristics on the occurance of coliform bacteria in Madura Strait. *Proc. Environ. Sci.* 23, 130–135. doi: 10.1016/j.proenv.2015.01.020

Yang, Y., Lin, L., Tse, L. K., Dong, H., Yu, S., and Hoffmann, M. R. (2019). Membrane-separated electrochemical latrine wastewater treatment. *Environ. Sci.* 5, 51–59. doi: 10.1039/c8ew00698a

Zhang, Y., Desmidt, E., Van Looveren, A., Pinoy, L., Meesschaert, B., and Van Der Bruggen, B. (2013). Phosphate separation and recovery from wastewater by novel electrodialysis. *Environ. Sci. Technol.* 47, 5888–5895. doi: 10.1021/es4004476

Zhigang, L. I. U., Qingliang, Z., Kun, W., Duujong, L. E. E., Wei, Q. I. U., and Jianfang, W. (2008). Urea hydrolysis and recovery of nitrogen and phosphorous as MAP from stale human urine. 20, 1018–1024. doi: 10.1016/S1001-0742(08)62202-0

Conflict of Interest: The authors declare that the research was conducted in the absence of any commercial or financial relationships that could be construed as a potential conflict of interest.

Advantages of publishing in Frontiers

OPEN ACCESS
Articles are free to read for greatest visibility and readership

FAST PUBLICATION
Around 90 days from submission to decision

HIGH QUALITY PEER-REVIEW
Rigorous, collaborative, and constructive peer-review

TRANSPARENT PEER-REVIEW
Editors and reviewers acknowledged by name on published articles

Frontiers
Avenue du Tribunal-Fédéral 34
1005 Lausanne | Switzerland

Visit us: www.frontiersin.org
Contact us: info@frontiersin.org | +41 21 510 17 00

REPRODUCIBILITY OF RESEARCH
Support open data and methods to enhance research reproducibility

DIGITAL PUBLISHING
Articles designed for optimal readership across devices

FOLLOW US
@frontiersin

IMPACT METRICS
Advanced article metrics track visibility across digital media

EXTENSIVE PROMOTION
Marketing and promotion of impactful research

LOOP RESEARCH NETWORK
Our network increases your article's readership